



EMIL WOLF
EDITOR

PROGRESS IN OPTICS

VOLUME 55

CONTRIBUTORS

M. Bellini, J. Evers, G. Gbur, C.H. Keitel, M. Kiffner,
G. Li, M. Macovei, M. Premaratne,
T.D. Visser, A. Zavatta

PROGRESS IN OPTICS

VOLUME 55

EDITORIAL ADVISORY BOARD

G.S. Agarwal	<i>Stillwater, USA</i>
T. Asakura	<i>Sapporo, Japan</i>
M.V. Berry	<i>Bristol, England</i>
C. Brosseau	<i>Brest, France</i>
A.T. Friberg	<i>Stockholm, Sweden</i>
F. Gori	<i>Rome, Italy</i>
D.F.V. James	<i>Toronto, Canada</i>
P. Knight	<i>London, England</i>
G. Leuchs	<i>Erlangen, Germany</i>
P. Milonni	<i>Los Alamos, NM, USA</i>
J.B. Pendry	<i>London, England</i>
J. Peřina	<i>Olomouc, Czech Republic</i>
J. Pu	<i>Quanzhou, PR China</i>
W. Schleich	<i>Ulm, Germany</i>

PROGRESS IN OPTICS

VOLUME 55

EDITED BY

E. Wolf

University of Rochester, N.Y., U.S.A.

Contributors

M. Bellini, J. Evers, G. Gbur, C.H. Keitel, M. Kiffner,
G. Li, M. Macovei, M. Premaratne,
T.D. Visser, A. Zavatta



Amsterdam • Boston • Heidelberg • London • New York • Oxford • Paris
San Diego • San Francisco • Singapore • Sydney • Tokyo

Elsevier
Radarweg 29, PO Box 211, 1000 AE Amsterdam, The Netherlands
Linacre House, Jordan Hill, Oxford OX2 8DP, UK
360 Park Avenue South, New York, NY 10010-1710

First edition 2010

Copyright © 2010, Elsevier B.V. All rights reserved.

No part of this publication may be reproduced, stored in a retrieval system or transmitted in any form or by any means electronic, mechanical, photocopying, recording or otherwise without the prior written permission of the publisher.

Permissions may be sought directly from Elseviers Science & Technology Rights Department in Oxford, UK: phone (+44) (0) 1865 843830; fax (+44) (0) 1865 853333; email: permissions@elsevier.com. Alternatively you can submit your request online by visiting the Elsevier web site at <http://elsevier.com/locate/permissions>, and selecting *Obtaining permission to use Elsevier material*.

Notice

No responsibility is assumed by the publisher for any injury and/or damage to persons or property as a matter of products liability, negligence or otherwise, or from any use or operation of any methods, products, instructions or ideas contained in the material herein. Because of rapid advances in the medical sciences, in particular, independent verification of diagnoses and drug dosages should be made.

Library of Congress Cataloging-in-Publication Data

A catalog record for this book is available from the Library of Congress

British Library Cataloguing in Publication Data

A catalogue record for this book is available from the British Library

ISBN: 978-0-444-53705-8

ISSN: 0079-6638

For information on all Elsevier publications
visit our web site at elsevierdirect.com

Printed and bounded in Great Britain
10 11 12 13 10 9 8 7 6 5 4 3 2 1

Working together to grow
libraries in developing countries

www.elsevier.com | www.bookaid.org | www.sabre.org

ELSEVIER BOOK AID International Sabre Foundation

CONTENTS

<i>Preface</i>	ix
1. Optical Pulse Propagation in Biological Media: Theory and Numerical Methods	
Malin Premaratne	1
1. Introduction	1
2. Light Scattering	4
2.1. Classification of Scattering	5
2.2. Quantitative Modeling	6
3. Photon Transport Equation	8
3.1. Radiance	8
3.2. Radiance Transport Equation	10
3.3. Scattering Phase Function	11
4. Numerical Methods	18
4.1. Two-Flux and Multi-Flux Methods	21
4.2. Spectral Methods	24
4.3. Finite Volume Method	26
4.4. Method of Lines	29
4.5. Method of Characteristics	30
4.6. Time Shift and Superposition Method	32
5. Concluding Remarks	33
References	34
2. Manipulating Light States by Single-Photon Addition and Subtraction	
Marco Bellini and Alessandro Zavatta	41
1. Introduction	42
2. Single-Photon Operators for Manipulating Quantum Information	43
2.1. Continuous-Variable Quantum State Engineering	43
2.2. Unified Treatment of Experimental Single-Photon Addition and Subtraction Implementations	44
3. Single-Photon Addition	48
3.1. Single-Photon-Added Coherent States	49
3.2. Single-Photon-Added Thermal States	53
3.3. Tests of Nonclassicality	56

4.	Single-Photon Subtraction	61
4.1.	Photon Subtraction from Arbitrary Light States	61
4.2.	De-Gaussification of Squeezed States and Generation of Schrödinger's Kittens	64
4.3.	Increasing Entanglement and Nonlocality by Single-Photon Subtraction	69
5.	Sequences and Superpositions of Single-Photon Operators	72
5.1.	Sequences of Creation and Annihilation Operators	72
5.2.	Superpositions of Quantum Operators	73
6.	Conclusions	76
7.	Acknowledgments	77
A.	Quantum Tomography	77
	References	79
3.	Vacuum-Induced Processes in Multilevel Atoms	85
	M. Kiffner, M. Macovei, J. Evers, and C. H. Keitel	
1.	Introduction	86
2.	Mathematical Model	87
2.1.	Description of the System	88
2.2.	General Reservoir Theory	92
2.3.	Derivation of the Master Equation	94
2.4.	Master Equation for Radiatively Coupled Multilevel Systems	105
3.	Single-Particle Processes	111
3.1.	Single-Particle Spontaneous Decay	112
3.2.	Spontaneous Decay-Induced Coherences	127
4.	Collective Processes	150
4.1.	Pair of Dipole–Dipole Interacting Two-Level Atoms	151
4.2.	Experimental Verification of the Dipole–Dipole Interaction	155
4.3.	Dipole–Dipole Interaction beyond the Two-Level Approximation	160
4.4.	Impact of the Dipole–Dipole Interaction	175
4.5.	Multi-Particle Quantum Dynamics	177
	Acknowledgments	183
	References	184
4.	Adaptive Lens	199
	Guoqiang Li	
1.	Introduction	200
2.	Adaptive Liquid Crystal Lens	203
2.1.	Liquid Crystal Cell	203
2.2.	Liquid Crystal Lens	207
2.3.	Refractive Liquid Crystal Lens Using Discrete Electrodes	208
2.4.	Diffractive Liquid Crystal Lens Using Discrete Electrodes	211
2.5.	Liquid Crystal Lens Based on Hole-Patterned Electrode	242
2.6.	Liquid Crystal Lens Formed by a Glass/Polymer Lens/Shell and Flat LC Layer(s)	249
2.7.	Modal Liquid Crystal Lens Based on Resistive Electrode	252
2.8.	Lens Using Polymer/Liquid Crystal Composites	254
2.9.	Microlens with Hybrid Alignment	256
2.10.	Polarization-Independent LC Lens	258

3. Adaptive Liquid Lens	258
3.1. Liquid Lenses Based on Fluid-Membrane Interaction	259
3.2. Liquid Lenses Based on Electrowetting Effect	264
3.3. Liquid Microlenses Based on Dielectrophoretic Effect	268
3.4. Liquid Microlenses Based on Hydrogel and Thermal Effect	273
4. Examples of Applications of the Adaptive Lenses	274
4.1. Correction of Presbyopia	274
4.2. Zoom Lens, Optical Tweezer, and Biomedical Imaging	276
4.3. Aberration Correction	277
5. Conclusion	278
Acknowledgments	278
References	278
 5. The Structure of Partially Coherent Fields	 285
G. Gbur and T.D. Visser	
1. Preface	285
2. The Space-Frequency Representation	287
3. Partially Coherent Fields in Young's Experiment	291
4. The Evolution of Partially Coherent Beams	296
5. Focusing of Partially Coherent Wave Fields	302
6. Scattering of Partially Coherent Wave Fields by Random and Deterministic Media	308
7. Phase Singularities of Coherence Functions	314
8. The Coherent Mode Representation	320
9. Numerical Simulation of Partially Coherent Fields	324
10. Direct Applications of Coherence Theory	326
References	329
 <i>Author Index of Volume 55</i>	 343
<i>Subject Index of Volume 55</i>	359
<i>Contents of Previous Volumes</i>	367
<i>Cumulative Index – Volumes 1–55</i>	381

This page intentionally left blank

PREFACE

This volume presents five chapters, which deal with recent theoretical and experimental developments in modern optics.

The first chapter by Malin Premaratne discusses research on optical pulse propagation in biological materials. Specifically, it presents a review of recent advances in modeling of short optical pulses interacting with biological media at sufficiently low-power levels, which do not induce physical or chemical changes in the material.

The second chapter by Marco Bellini and Alessandro Zavatta presents a review of recent experimental developments regarding manipulation of optical fields by controlled addition and subtraction of single photons. The accurate engineering of the quantum state of light made possible by such operations has been used for generating novel, rather exotic nonclassical states and for testing fundamental laws of quantum physics. Applications of these techniques in the field of quantum information processing are likely to enhance the performances of existing protocols and lead to entirely new ones.

The third chapter by M. Kiffner, M. Macovei, J. Evers, and C. H. Keitel reviews researches on vacuum-induced processes in multilevel atoms. Based on the master equation, the underlying physical mechanisms are elucidated, both for single particles and also for collective atomic systems. Particular emphasis is placed on modifying or controlling the impact of vacuum-induced processes on the overall system dynamics, for example, by means of coherent laser fields. Numerous applications are discussed.

The fourth chapter by Guoqiang Li reviews recent advances that have been made in the field of adaptive lenses, varifocal lenses (Alvarez-Lohmann lenses), utilizing lateral shift between two conjugate components of cubic surfaces. It discusses the progress made in production of single-element adaptive lenses, including liquid crystal lenses. Refractive and diffractive lenses based on discrete electrodes, hole-patterned electrodes, modal control electrode, hybrid liquid-crystal alignment, polymer/LC materials are also described. Liquid lenses based on mechanical pressure, electrowetting effect, dielectric effect, and thermal effects are also discussed.

The concluding chapter by G. Gbur and T. Visser gives an overview of recent developments and applications, both theoretical and experimental, of light of different coherence properties. It includes accounts of researches on focusing and scattering of beams of any state of coherence, and it also discusses phase singularities of coherence functions and some applications.

Emil Wolf

Department of Physics and Astronomy
and The Institute of Optics,
University of Rochester,
Rochester, New York 14627, USA

October 2010

CHAPTER 1

Optical Pulse Propagation in Biological Media: Theory and Numerical Methods

Malin Premaratne

*Advanced Computing and Simulation Laboratory (AxL),
Department of Electrical and Computer Systems Engineering,
Monash University, Clayton, Victoria, Australia
E-mail address: malin@eng.monash.edu.au.*

Contents		
1.	Introduction	1
2.	Light Scattering	4
2.1.	Classification of Scattering	5
2.2.	Quantitative Modeling	6
3.	Photon Transport Equation	8
3.1.	Radiance	8
3.2.	Radiance Transport Equation	10
3.3.	Scattering Phase Function	11
4.	Numerical Methods	18
4.1.	Two-Flux and Multi-Flux Methods	21
4.2.	Spectral Methods	24
4.3.	Finite Volume Method	26
4.4.	Method of Lines	29
4.5.	Method of Characteristics	30
4.6.	Time Shift and Superposition Method	32
5.	Concluding Remarks	33
	References	34

1. INTRODUCTION

Science fiction captures the imagination of human mind and inspires us to make the dreams of today a reality tomorrow. Different versions



FIGURE 1 Usage of Starfleet Tricorder in Star-Trek series © Paramount Pictures and CBS Studios.

of the “Tricorder” device used in Star-Trek science fiction series can noninvasively scan any physical, chemical, or biological entity and cure ailments by hovering over their bodies (Figure 1). Recent advances in ultrasound and electromagnetics (including optics) could make “Tricorder” a reality. Increasingly, novel innovative ways of using light for clinical applications are developed by researchers all around the world (Wilson, Tuchin, & Taney, 2005). For example, optical probes capable of carrying out tissue diagnosis offer significant advantages over standard biopsy and cytology techniques, in terms of both patient care and medical costs (Mourant et al., 1998). These probes have the capability to detect cancerous tissues because the interaction of light with tissue is strongly influenced by the composition and the cellular structure of tissue, which is obviously different for cancerous and healthy tissues (Wilson et al., 2005). Similarly, photodynamic therapy is increasingly used as a replacement or alternative way of treating cancerous cells with minimal side effects (Gobin et al., 2007; Prasad, 2003). Photodynamic therapy is the use of drugs (photosensitizers) that are activated by visible or near infrared light to produce specific biological effects in cells or tissues that can be exploited to achieve a particular clinical endpoint (Wilson et al., 2005). Recently, nanoshells have also been used as the activating medium (Gobin et al., 2007). When photosensitive dyes are used, cancerous cells are killed by injecting them in the vicinity of the cancerous cells and then transferring them to a toxic state using laser light (Niemz, 2004). In case of nanoshells, the heat generated by the nanoshells irradiated with resonant laser light causes the destruction of cancerous cells (Gobin et al., 2007). Laser-induced interstitial thermotherapy (LITT) is another technique used for tumor treatment, which makes use of the possibility of localized tissue coagulation (Niemz, 2004).

LITT was recently introduced to treat tumors in retina, brain, prostate, liver, and uterus (Niemz, 2004). Lasers are also being used for diagnostic and therapeutic purposes in ophthalmology, where the conventional incoherent light sources fail. For example, retinal glaucoma and retinal detachment can be accurately assessed and diagnosed by using confocal laser microscopy (Niemz, 2004).

All these developments relies on having a detailed understanding of light propagation through tissue. Such understanding can only be gained by creating sufficiently accurate models that can capture the essence of light interaction with biological media. Experiments are a vital part of this model-making process where they provide a solid basis and sound understanding necessary to conceptualize the fundamental ideas/axioms central to a model. Good models enable one to make predictions beyond their initial experimental base and discover novel phenomena. For engineers, these models eventually provide a way to optimize and fine tune techniques/devices that would have not been possible in other means. For example, heat is generated due to the interaction with light and tissue. The resulting local tissue temperature is of prime importance in laser surgery and depends, in turn, on the spatial distribution of the incident radiation. A detailed modeling is required to determine the duration of the laser light exposure of tissue for a successful surgical outcome. Errors cannot be tolerated in such clinical settings where the outcome might decide the fate of a patient undergoing laser surgery! Moreover, the development of diagnostic techniques such as optical coherence tomography, confocal microscopy, light scattering spectroscopy, and optical reflectance microscopy requires a fundamental understanding of how light scatters from normal and pathological structures within tissue (Wilson et al., 2005). In addition to these, lasers are used in ophthalmology, gynecology, urology, and many other fields (Huang et al., 1991; Niemz, 2004; Webb, 1996). Therefore, it is important to understand the effects of various optical parameters (i.e., model parameters) and their effect on the incident and scattered light to interpret these measurements appropriately (Mourant et al., 1998).

Increasingly, it has become clear that much can be learned about biological media by using temporal optical interactions. Most importantly, different cross-talk problems (i.e., interfering signals) arising in the steady-state optical interactions with biological media can be mitigated using properly executed temporal probing techniques (Tuchin, 2007; Welch & van Gemert, 1995). For example, short light pulses can be used to enhance image resolution in optical tomography techniques as cleverly exploited in the time-resolved spectroscopy area (Arridge, 1999). Another area of importance is optical coherence tomography (OCT), which uses low-coherence interferometry to produce a two-dimensional

image of optical scattering from internal tissue microstructures in a way that is analogous to ultrasonic pulse-echo imaging (Huang et al., 1991). Both low-coherence light and ultrashort laser pulses can be used to map internal structures of biological systems. An optical signal that is transmitted through or reflected from a biological tissue will contain time-of-flight information, which in turn yields spatial information about tissue microstructure (Huang et al., 1991).

Given the many facets of recent advances in biology and optics, and the pace and overdrive of the innovation, it is a formidable or even an impossible task to map the current state of these technologies in a single snapshot. Many articles have comprehensively covered the trends and techniques in **static** optical fields interacting with biological media (Peraiah, 2002; Pomeraning, 2005; Welch & van Gemert, 1995). Therefore, our primary aim is to cover the **transient** characteristics of optical fields propagating through biological media at sufficiently low power levels, which do not induce physical or chemical changes in the material. We specifically look at short, low-intensity pulses interacting with biological media and discard any light-induced permanent changes (e.g., tissue damage and ablation) or secondary emission processes (e.g., fluorescence and phosphorescence). This review is organized as follows: In the Section 2, we review the basic features of light scattering from biological media. We point out some specific features and provide pointers to literature for specific details. In Section 3, we look at the quantitative aspects of light propagation through tissue by discussing the general structure of the transient photon transport equation and related quantities. One major component of the photon transport equations is the scattering phase function, which takes care of the details of specific features of the scattering objects. We provide a catalog of many known phase functions and highlight their features, so reader can make an informed decision when selecting a phase function for analysis of biological media. We specifically point out the fact that further research needs to be done in coming up with better phase functions for biological media. Section 4 shows various ways of solving the transient photon transport equation and highlights the strengths and weakness of each method briefly. Most importantly, it is expected that this section provides enough pointers to literature where the reader can learn analogous variants of the methods covered in this section. Thereafter, we conclude this review in Section 5.

2. LIGHT SCATTERING

Scattering of light is a fundamental property of any heterogenous optical medium. Any medium other than a vacuum is heterogenous in some sense

and hence scatter light (Bohren & Huffman, 1983). Light gets redirected or scattered when it encounters an electromagnetically active obstacle or inhomogeneity. Such redirection of energy can be used to learn about the scattering objects and thus enable one to do measurements and characterization of objects remotely/noninvasively. However, to gain a deeper understanding about how this can be achieved, it is vital to build an intuitive understanding of light interaction with material. Among the plethora of interactive mechanisms initiated due to such interactions, light scattering dominates. Having said that, it is important to understand that scattering does not always take place when photons interact with material (Born & Wolf, 1999). In certain instances, photons could get absorbed by the media and the energy in the photon may get dissipated as heat. In other instances, the absorbed light may get re-emitted after a time delay with a less energetic photon (Barron, 2004). This process is known as fluorescence. However, in certain fluorescence materials, multiple photons get absorbed and high-energetic photons get emitted. If the fluorescence takes places slowly for longer hours, the associated process is known as phosphorescence (Hercules, 1966).

If a photon gets absorbed by a certain media, then the energy of the absorbed photon must correspond to the energy required to make a discrete transition from a lower-energy level to higher-energy level in a material. In contrast, scattering of photons from a material could take place regardless of the structure of allowable energy transitions in the material. If the incident photon interacts with a characteristic energy level, there is a very good probability for the generation of photons with different energies compared with the incident photon energy. Interestingly, if the incident photon energy is close to an allowed energy transition in the scattering material and interacts with one of these characteristic energy levels, significant enhancement in the scattering strength can be observed. This type of enhanced scattering, usually called “resonance scattering,” has characteristics significantly different to “normal scattering” (Kokhanovsky, 2001).

2.1. Classification of Scattering

If the scattered photon energy is exactly equal to the incident photon energy, then the scattering event is termed “elastic.” Example of elastic scattering include Mie scattering and Rayleigh scattering observed in scattering from objects such as large dielectric objects (size is measured relative to wavelength of the incident radiation) and biological cells (Bohren & Huffman, 1983). Because biological media are made of many dissimilar constituents, their optical scattering properties including scattering strength provide a natural basis for their classification (Tuchin, 1997).

Strongly scattering (opaque) media examples include skin, brain tissue, vascular walls, blood, and sclera where multiple scattering dominates and

Weakly scattering (transparent) media examples include the cornea and lens in the anterior eye chamber where low-order, independent scattering events dominate.

However, it is to be noted that most of the biological media are anisotropic (i.e., have different properties in different directions), and hence it is important to account for scattering anisotropy especially in small-volume scattering studies. This has been somewhat successfully achieved by introducing scattering phase functions that describe the probability of scattering in a particular direction relative to incident radiation. Most widely used phase functions include Henyey–Greenstein phase function (Henyey & Greenstein, 1941), Gegenbauer kernel phase function (Yaroslavsky, Yaroslavsky, Goldbach, & Schwarzmaier, 1997), and Mie phase function (van de Hulst, 1981). In conjunction with these different variants of phase functions, empirical figure-of-merit (FoM) parameters known as similarity-rules have been widely used in tissue-optics community to concisely capture diffusive and anisotropic features in a cohesive platform (van de Hulst & Graaff, 1996). However, apart from their intuitive appeal, such classifications do not provide adequate quantitative assistance for analysis. Even though not that widely investigated yet, two other complexities of prime importance are the influence of medium on the coherence of light interacting with the medium and its state of polarization (Nieto-Vesperinas, 2006; Wolf, 2007).

2.2. Quantitative Modeling

A detailed quantitative understanding of how light propagates in tissue requires the incorporation of key relevant parameters needed for describing an optical signal in a medium, namely, wavelength, absorption, diffusion, anisotropy of scattering, coherence, and polarization. Such an understanding is paramount for the interpretation of diagnostic measurements to render meaningful results and for the development of therapeutic techniques. However, a simple relationship among the above fundamental parameters cannot be made because of the intricate dependency of the biological and optical properties of the biological medium on the local light intensity. For example, diagnostic methods that use fluorescence require a thorough understanding of targeted molecular energy absorption and emission rates at both exciting and emission wavelengths (Welch & van Gemert, 1995).

In addition, living biological media constantly change their properties due to intrinsic biochemical processes and external stimulations (Alberts

et al., 1998; Saterbak, McIntire, & San, 2007). This time-dependency further complicates the mathematical description and subsequent numerical solution. In principle, Maxwell's equations can be integrated to calculate the optical response of a biological medium excited by an external/internal optical source. However, this can only be accomplished by having a detailed knowledge of tissue dielectric properties that is hard to acquire or even represent in current computing platforms (Barnes & Greenebaum, 2007; Foster & Schwan, 1989). Lack of this detailed knowledge of dielectric properties of tissue forces us to seek approximate methods that nonetheless provide sufficient information to describe almost all experimental results. One such method is photon transport theory that exploits the wide knowledge and experience of radiation transport in stellar atmosphere and propagation of neutrons in a nuclear reactors (Chandrasekhar, 1960; Pomraning, 2005; Rybicki & Lightman, 2004). Photon transport theory essentially ignores the wave features of propagating electromagnetic fields such as diffraction and interference but complies with other essential principles such as conservation of energy and momentum (Pomraning, 2005). Photon transport theory is based on the conservation of energy along an infinitesimal line segment in the scattering media and hence it could accurately predict light intensity distributions within biological media (Premaratne, Premaratne, & Lowery, 2005). However, as many authors have reported, it fails to account for observed coherent back-scattering peaks from dense scattering media including tissues (Yoo, Liu, & Alfano, 1990). Moreover, there is much controversy about how inhomogeneous media (i.e., those with varying refractive index, varying scattering parameters, and varying absorption properties) are to be handled in the photon transport framework (Bal, 2006; Premaratne et al., 2005). Without dwelling on this debate on the intricacies and on the precise format of photon transport equation, we can study different analytical and numerical strategies applicable under general conditions. Any variants from the standard techniques can be handled very easily because only trivial changes need to be made to underlying algorithms/concepts.

Even though monochromatic, steady-state photon transport in biological media found some applications in optical tomography and sensing areas, higher sensitivities or resolutions can be achieved by resorting to temporal and/or frequency domain methods (Leitgeb, Hitzenberger, & Fercher, 2003; Pal, Basu, Mitra, & Vo-Dinh, 2006; Yun, Tearney, de Boer, Iftimia, & Bouma, 2003). Especially, temporal waveforms (e.g., pulses) can be used to selectively excite certain types of molecules and to reduce the overall cross-talk due to different inhomogeneous features contributing significant amount of scattered light to the boundary where a detector is placed. When operated in steady state, there is no simple way to distinguish between these separate contributions from the main signal and cross-talk because such phenomena inevitably introduce measurement

errors or measurement ambiguities. In contrast to this, if sufficiently small (both in energy and duration) optical pulses are used for probing the medium, it is possible to differentiate between different or spatially-dispersed scattering centers at the boundary/detector due to differences in the propagation delay.

In frequency domain methods, modulated sinusoidal signals are detected using their amplitude and phase information (Yun et al., 2003). Unlike steady-state methods, where only intensity, which is related to amplitude, is detected, the additional information carried by the relative phase shift of the detected signal provides better separation between the contributions from the scattering and absorption properties of the medium.

In contrast to this, short pulses and pulse-trains can be used to probe scattering media (Pal et al., 2006). In these techniques, it is possible to change pulse shape, pulse width, and pulse energy and to monitor the resulting variations in the signal passing through the probed media. Changes in the signal parameters and the reception delay can then be directly mapped to different features of the medium, providing a detailed map of the medium properties. What is interesting is that such pulses, when combined to make a pulse train, can provide more information because it enables one to introduce additional dimensions to this measuring problem by varying spacing between pulses and their peak-intensity or relative-energy.

3. PHOTON TRANSPORT EQUATION

According to our present understanding, electromagnetic fields are made of photons with properties precisely described by the laws of quantum field theory (Greiner & Reinhardt, 2002; Peskin & Schroeder, 1995). One consequence of this wave-particle duality is that electromagnetic fields, in certain cases, can be described using Maxwell's equations and, in other cases, using particle features including energy $h\nu$ contained in each photon, where h is the Planck's constant and ν is the frequency of the light in vacuum (Baierlein, 2001). Therefore, for monochromatic light, it is easy to relate the number of photons contained in an electromagnetic field to its associated photon number. However, this becomes almost impossible for optical fields that have broad spectral features or deviate from ideal monochromatic conditions.

3.1. Radiance

When studying light propagation in biological media, photons are not counted directly to measure the energy transported by them, but analogous variables are used. The variable used in radiometry for this purpose is called "radiance," which measures the power transmitted per unit solid

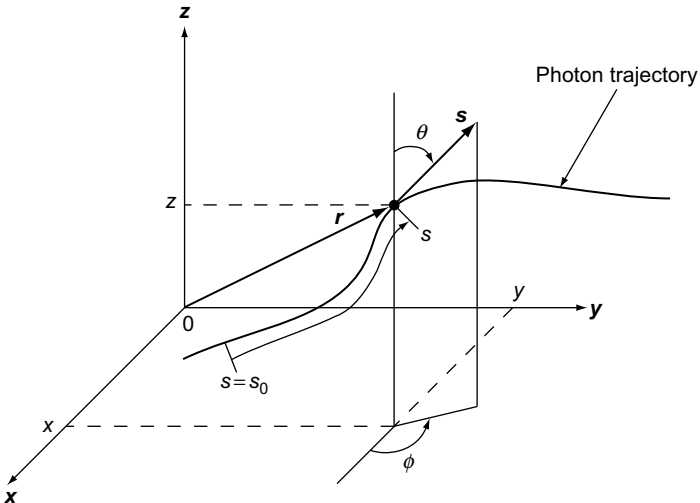


FIGURE 2 Coordinate system adopted for describing the photon transport equation. The distance along the photon trajectory, s , is measured relative to an arbitrary fixed point along the trajectory. Here, θ is called the polar (or zenith) angle and ϕ , is called the azimuthal angle.

angle in a certain ray (direction) per unit projected area perpendicular to the ray (Nicodemus, 1963). One advantage of this definition is that the “radiance” measure provides an intuitive feel because it is synonymous with the words “brightness” and “luminance.”¹

We used the coordinate system shown in Figure 2 to describe the evolution equation for radiance. Owing to the definition adopted for radiance I , we need to have two vector quantities and a scalar to define it at a point; these quantities are position vector r , unit vector along the propagation direction s and time t (see Figure 3). The radiance vector $I(t, r, s)$ has SI units of $\text{W} \cdot \text{m}^{-2} \cdot \text{sr}^{-1}$. Radiance characterizes the total amount of radiation present, at all frequencies. However, in some instances, it is important to distinguish each frequency in the spectrum separately. This is achieved by introducing a quantity called “spectral radiance,” which uses frequency variable v as a separate labeling parameter. The spectral radiance $I(t, r, s, v) \equiv I_v(t, r, s)$ has SI unit of $\text{W} \cdot \text{m}^{-2} \cdot \text{sr}^{-1} \cdot \text{Hz}^{-1}$. It is well known that intensity of a point source decreases as inverse square of the distance from the source in vacuum. Interestingly, due to its definition per solid angle, radiance is invariant everywhere surrounding a source point. More generally, using geometric optics arguments, it possible to

¹This statement is only approximately true because the sensitivity of the human eye to light is characterized by the luminous efficiency function. The integral of the spectral radiance over the visible spectrum weighted by the luminous efficiency is called the luminance.

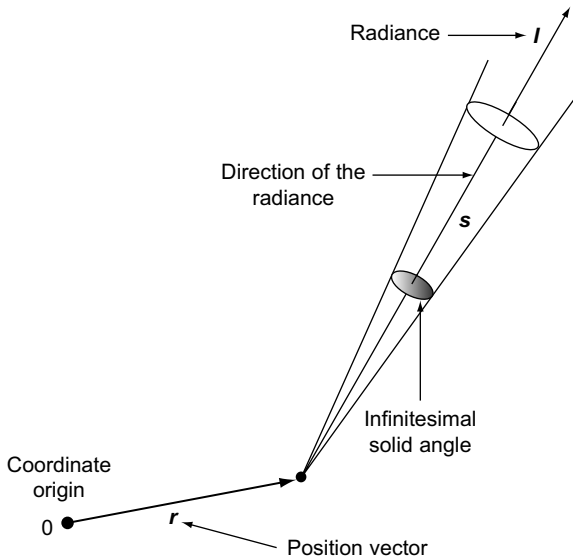


FIGURE 3 Radiance, I , at position \mathbf{r} , along with the unit vector \mathbf{s} at a given time t measures the power transmitted per unit solid angle per unit projected area perpendicular to the ray as shown here.

show that the quantity $I(t, \mathbf{r}, \mathbf{s})/n^2(\mathbf{r}, v)$ is invariant along a ray path in a lossless, homogeneous, and isotropic medium with refractive index, $n(\mathbf{r}, v)$ (Born & Wolf, 1999).

3.2. Radiance Transport Equation

Radiance variation along a ray path in a biological medium is given by the photon transport equation (PTE). The PTE expresses the energy balance in a unit solid angle of $d\Omega$ about the ray direction \mathbf{s} (see Figure 3) within a frequency interval dv about v (Premaratne et al., 2005). Using the coordinate system described in Figure 2, it can be written as

$$\frac{1}{v_g(v)} \frac{\partial I_v(t, \mathbf{r}, \mathbf{s})}{\partial t} + \mathbf{s} \cdot \nabla_{\mathbf{r}} I_v(t, \mathbf{r}, \mathbf{s}) = -\sigma_a(t, \mathbf{r}) I_v(t, \mathbf{r}, \mathbf{s}_i) - \sigma_s(t, \mathbf{r}) I_v(t, \mathbf{r}, \mathbf{s}_i) + \sigma_s(t, \mathbf{r}) \int_{4\pi} I_v(t, \mathbf{r}, \mathbf{s}_i) \Phi_v(\mathbf{s}_i \rightarrow \mathbf{s}, t, \mathbf{r}) d\Omega_{\mathbf{s}_i} + F_v(t, \mathbf{r}, \mathbf{s}), \quad (3.1a)$$

$$+ \sigma_s(t, \mathbf{r}) \int_{4\pi} I_v(t, \mathbf{r}, \mathbf{s}_i) \Phi_v(\mathbf{s}_i \rightarrow \mathbf{s}, t, \mathbf{r}) d\Omega_{\mathbf{s}_i} + F_v(t, \mathbf{r}, \mathbf{s}), \quad (3.1b)$$

where $v_g(v)$ is the group velocity of light in the scattering medium at frequency v , $\sigma_s(t, \mathbf{r})$ is the scattering coefficient of the medium, $\sigma_a(t, \mathbf{r})$ is the attenuation coefficient of the medium, and $F_v(t, \mathbf{r}, s)$ is the intrinsic power source density in the medium. In most cases, because no internal sources in the medium are present, power source density can be safely neglected in calculations. It is to be noted that in Equation (3.1), we have allowed both scattering and attenuation coefficients to vary with both spatial variable \mathbf{r} and time variable t for a given frequency (or wavelength). However, the group velocity in the medium is assumed to be constant. This is because if the refractive index (and hence the group velocity) is allowed to vary within the scattering volume, the streaming part of Equation (3.1a) requires additional terms as described by Premaratne et al. (2005). In conventional derivation of the radiative transport equation, the divergence of rays are ignored (i.e., $\nabla_{\mathbf{r}} \cdot \mathbf{s} \equiv 0$). However, if the refractive index varies across the scattering medium, light rays do not travel in straight lines but instead follow curved paths. In such situations, it is possible to show that ray divergence has a nonzero value and thus corrections need to be made to account for it as shown by Premaratne et al. (2005) so that the transport equation assumes the following form:

$$\begin{aligned} \frac{n_v(\mathbf{r})}{c} \frac{\partial}{\partial t} I_v(t, \mathbf{r}, s) + \left(\frac{1}{R_1(s)} + \frac{1}{R_2(s)} \right) I_v(t, \mathbf{r}, s) + n_v^2(\mathbf{r}) \frac{\partial^2}{\partial s^2} \frac{I_v(t, \mathbf{r}, s)}{n_v^2(\mathbf{r})} \\ = -\sigma_a(t, \mathbf{r}) I_v(t, \mathbf{r}, s_i) - \sigma_s(t, \mathbf{r}) I_v(t, \mathbf{r}, s_i) \\ + \sigma_s(t, \mathbf{r}) \int_{4\pi} I_v(t, \mathbf{r}, s_i) \Phi_v(s_i \rightarrow s, t, \mathbf{r}) d\Omega_{s_i} + F_v(t, \mathbf{r}, s), \end{aligned} \quad (3.2)$$

where $n_v(\mathbf{r})$ is the spatially varying refractive index of the medium, c is the speed of light in vacuum, s is the arc length along a light ray path of interest, and $R_1(s)$ and $R_2(s)$ are the principal radii of curvatures of the geometric wavefront (Premaratne et al., 2005).

3.3. Scattering Phase Function

In Equation (3.1b), the function $\Phi_v(s_i, s)$ describes the probability of the photon with frequency v scattering from incident direction s_i to direction s after interacting with a scattering center (see Figure 4). This function is widely known as the scattering phase function of the medium. The scattering phase function provides a mechanism for quantifying elastic optical scattering in a medium and relates energy losses and energy increments to comply with constraints imposed by Maxwell's equations. However, it is important to note that this definition of scattering function ignores the

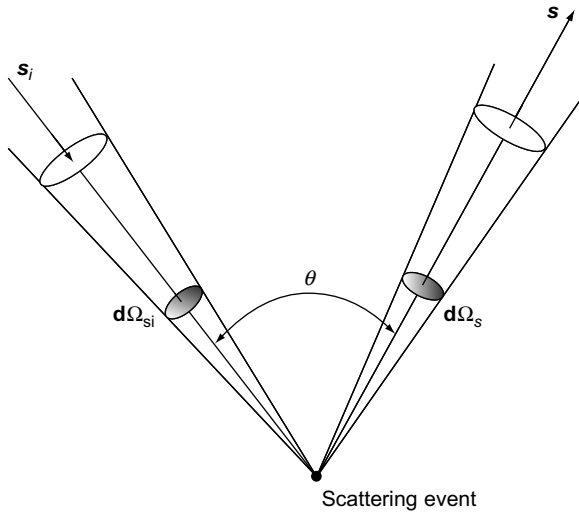


FIGURE 4 Scattering of light incident on a scattering-center from direction s_i within the solid-angle $d\Omega_{si}$ to solid-angle $d\Omega_s$ in the direction s . The angle between vectors s_i and s is given by θ .

changes in the polarization or frequency due to scattering. Thus, our analysis is limited to elastic scattering events and needs to be modified if above effects need to be taken into account. Most importantly, such a change from elastic to inelastic domain includes a complete reformulation of the photon transport equation as shown in Liou (1975); Mishchenko, Travis, & Lacis (2006) Mishchenko, Travis, and Lacis (2006), and Liou (1975). In such a framework, the scattering phase function needs to be replaced by a matrix (called the scattering phase matrix), which describes both self- and cross-scattering probabilities of energies.

Given that the scattering phase function is also a probability density function, we could arrive at the following normalization conditions. Consider light incident on a scattering center from direction s_i scattering into a cone with solid-angle $d\Omega_s$ in the direction of s as shown in Figure 4. Because we do not consider scattering center to absorb the incoming photons, the scattered photon detection probability should be equal to 1 when summed for all such directions surrounding the scattering center: i.e.,

$$\int_{4\pi} \Phi_v(s_i \rightarrow s, t, r) d\Omega_s = 1, \quad \forall s_i, t, r. \quad (3.3)$$

Owing to this normalization condition, scattering phase function has units of sr^{-1} . If one wishes to make the scattering phase function dimensionless,

the above normalization condition needs to be replaced by the following:

$$\int_{4\pi} \Phi_v(\mathbf{s}_i \rightarrow \mathbf{s}, t, \mathbf{r}) d\Omega_s = 4\pi, \quad \forall \mathbf{s}_i, t, \mathbf{r}. \quad (3.4)$$

In general, scattering phase function does not obey the reciprocity conditions for the scattering directions (i.e., $\Phi_v(\mathbf{s}_i \rightarrow \mathbf{s}, t, \mathbf{r}) \neq (\Phi_v(-\mathbf{s} \rightarrow -\mathbf{s}_i, t, \mathbf{r}), \forall \mathbf{s}_i, \mathbf{s}, t, \mathbf{r})$). However, many phase functions used in modeling biological media are axisymmetric for the incident ray direction

$$\Phi_v(\mathbf{s}_i \rightarrow \mathbf{s}, t, \mathbf{r}) \equiv \Phi_v(\mathbf{s}_i \cdot \mathbf{s}, t, \mathbf{r}), \quad \forall \mathbf{s}_i, \mathbf{s}, t, \mathbf{r} \quad (3.5)$$

and hence reciprocity conditions are satisfied. These axisymmetric scattering phase functions can be elegantly written using geometrical arguments. The angle θ between the unit vectors \mathbf{s}_i and \mathbf{s} is given by (see Figure 4)

$$\cos(\theta) = \mathbf{s}_i \cdot \mathbf{s}. \quad (3.6)$$

The scattering event is termed forward scattering if $\cos(\theta)$ term assumes a positive value. A scattering event where $\cos(\theta)$ term is negative is referred to as backward scattering event. It is instructive to look at several possible phase functions to see how the above concepts are applied in practice. However, most of the phase functions we discuss below are just convenient models and have no physical basis. We also provide references to more accurate computations of scattering properties from Maxwell's equations such as Mie phase functions for spherical particles. However, even exact results derived from these approaches have limited use because most scattering particles found in practice do not have perfect spherical shapes or ideal, lossless dielectric characteristics. Strictly speaking, it is not possible to ignore absorption and just consider pure refractive properties due to causality driven Kramers–Kronig relationships (Waters, Mobley, & Miller, 2005). However, it is also not possible to simply include loss/gain in such analysis due to the existence of many outstanding issues. Therefore, further studies that preserve causality (or that take into account causality) must be carried out in this area (refer to (Mishchenko, 2008) for a detailed discussion of this topic).

3.3.1. Rayleigh Phase Function

If the incident light wavelength is far from a resonant frequency of a scatterer, its light scattering characteristics closely resemble that of an induced dipole oscillator. It is possible to show that isotropic scatterers react to

unpolarized light in a manner resembling the following phase function, which is known as Rayleigh phase function, $\Phi_R(\cos(\theta))$:

$$\Phi_R(\cos(\theta)) = \frac{3}{16\pi} (1 + \cos^2(\theta)). \quad (3.7)$$

This scattering relationship is true for Rayleigh regime where size parameter $a = 2\pi r/\lambda$ is significantly less than 1 for the spherical scatterer radius r and incident light wavelength λ . Even though this phase function matches reasonably well with Mie scattering results for small particles, further improvements can be made by extending the functional format to have a power series representation of $\cos(\theta)$ to fourth or fifth order. A study by Sharma, Roy, and Somerford (1998) found that such an extension sometimes give physically unrealistic/impossible results (e.g., negative values for the phase function) for certain scattering angles or fails to reproduce multiple minima. Detailed empirical analytical expressions for Mie phase function covering above scenarios can be found in the study by Caldas and Semiao (2001).

3.3.2. Liu Phase Function

A two-parameter phase function, $\Phi_L(\cos(\theta), \varepsilon, n_p)$, was proposed by Liu (1994) to provide a better match with Mie scattering results.

$$\Phi_L(\cos(\theta), \varepsilon, m) = \frac{\varepsilon(2m+1)(1+\varepsilon\cos(\theta))^{2m}}{2\pi((1+\varepsilon)^{2m+1} - (1-\varepsilon)^{2m+1})}, \quad (3.8)$$

where ε is the characteristic factor and m is the anisotropy index. The anisotropy index, m , which can only assume positive integer values to ensure that the phase function remains positive in the permissible region. Scattering anisotropy of the Liu phase function increases with increasing values of m . Positive characteristic factors lead to strong forward scattering whereas negative characteristic factors lead to strong backscattering. The Liu phase function loses its dependency on the scattering angle θ if the characteristic factor is identically equal to zero, i.e., if the medium is isotropic.

The Liu phase function is very suitable for studying biological tissue because it can represent strong, near-forward scattering features accurately.² It can be said that Liu designed a phase function that is constrained to reproduce the forward scattering correctly. Numerical comparisons of this phase function with the Henyey–Greenstein (HG) phase function

² $\Phi_L(\cos(\theta), \varepsilon, m)$ is very accurate for scattering events with average $\cos(\theta)$ in the range $0.8 \leq \langle \cos(\theta) \rangle \leq 1.0$.

(see Section 3.3.3) shows that the former constitutes substantial improvement over the latter in the near-forward direction. Closer examination shows that the accuracy of the Liu phase function is restricted to $0.8 < g < 1.0$, which is the typical range for the asymmetry parameter of biomedical tissues.

A special case of the Liu phase function results if $\varepsilon = 1$. The resulting phase function, $\Phi_B(\cos(\theta), m)$, is called the binomial phase function (Sharma et al., 1998) defined by

$$\Phi_B(\cos(\theta), m) = \frac{1}{4\pi} \frac{(2m+1)}{2^{2m}} (1 + \cos(\theta))^{2m}, \quad (3.9)$$

where m is a positive integer.

Another variant is the delta-Eddington phase function $\Phi_{DE}(\cos(\theta), g, \alpha)$, which allows the reduction of the transport equation to the diffusion equation

$$\Phi_{DE}(\cos(\theta), g, \alpha) = \frac{1}{4\pi} [2\alpha\delta(1 - \cos(\theta)) + (1 - \alpha)(1 + 3g\cos(\theta))], \quad (3.10)$$

where $\delta(\cdot)$ is the delta function (Kanwal, 2004), f is a weighting factor in the range 0 to 1, which determines the amount of light in forward peak, and g is an asymmetry factor, very similar to an analogous variable in the Henyey–Greenstein phase function in Equation 3.11. When the parameter $\alpha = 0$, the Liu phase function reduces to Eddington phase function, which was widely used in early stage works in the radiative transfer research.

3.3.3. Henyey–Greenstein Phase Function

The Henyey–Greenstein (HG) phase function was introduced to describe scattering of radiation in galaxies (Henyey & Greenstein, 1941). This function was used in bio-optics area first by Pedersen, McCormick, & Reynolds (1976) to calculate the oxygen saturation levels in blood using light scattering data. It is a single-parameter, scattering phase function with many convenient analytical numerical/computational properties. The HG phase function can reasonably well describe the strongly forward scattering particles with dimensions much larger than the wavelength of the scattered light. The HG phase function can be written using the cosine of the scattering angle, $\mu \equiv \cos(\theta)$ as (see Figure 4)

$$\Phi_{HG}(\cos(\theta), g) = \frac{1}{4\pi} \frac{1 - g^2}{(1 + g^2 - 2g\cos(\theta))^{3/2}}, \quad (3.11)$$

where g is called the asymmetry parameter. It can be calculated by taking the mean value of the HG phase function with respect to all feasible scattering solid angles around a scattering point (i.e., by integrating over 4π steradian) as given below

$$g \equiv 2\pi \int_{-1}^{+1} \mu \Phi_{\text{HG}}(\mu, g) d\mu. \quad (3.12)$$

The HG phase function obeys the normalization condition given in Equation 3.3 for all the permissible values of the asymmetric parameter g because

$$2\pi \int_{-1}^{+1} \Phi_{\text{HG}}(\mu, g) d\mu = 1. \quad (3.13)$$

However, it is very clear from literature that the popularity of the HG phase function in radiative transfer theory is mainly due to its remarkably simple expansion in terms of the associated Legendre polynomial of order n , $P_n^1(\cos(\theta))$,

$$\Phi_{\text{HG}}(\cos(\theta), g) = \frac{1}{4\pi} \sum_{n=0}^{\infty} (2n + 1) g^n P_n^1(\cos(\theta)) \quad (3.14)$$

useful for many algorithms such as discrete ordinate method. This phase function has the ability to represent either the experimentally observed pronounced forward scattering peak or the backward scattering peak by using an appropriately chosen asymmetry parameter value. However, these pronounced forward and backward peaks are not isolated events but occur simultaneously. Because the HG phase function with a single parameter could not, in principle, account for these two distinct scattering events at once, a modified three-parameter HG-type phase function, which is a linear combination of two HG functions was introduced by Irvin (1965). The three-parameter scattering phase function of Irvin, $\Phi_I(\cos(\theta), g_1, g_2, \alpha)$, has the following form

$$\Phi_I(\cos(\theta), g_1, g_2, \alpha) = \alpha \Phi_{\text{HG}}(\cos(\theta), g_1) + (1 - \alpha) \Phi_{\text{HG}}(\cos(\theta), g_2), \quad (3.15)$$

where α is a real number between 0 and 1, and $0 \leq g_1 \leq 1$ and $-1 \leq g_2 \leq 0$ are analogous parameters to g in the HG phase function. These parameters can be determined by using well-known regression methods (Kattawar, 1975). A special case of the above three parameter $\Phi_I(\cos(\theta), g_1, g_2, \alpha)$ can

be found by assigning $g_1 = 0$. This leads to a two-parameter HG-type phase function with isotropically scattering part. This phase function is called modified Henyey–Greenstein phase function, $\Phi_{\text{MHG}}(\cos(\theta), g, \alpha)$ in literature (Jacques, Alter, & Prahl, 1987) and given by

$$\Phi_{\text{MHG}}(\cos(\theta), g, \alpha) = \frac{\alpha}{4\pi} + (1 - \alpha)\Phi_{\text{HG}}(\cos(\theta), g). \quad (3.16)$$

Experimental evidence shows that modified HG phase function can accurately represent single-particle scattering in human dermis (Jacques et al., 1987) and human aorta (Yoon, 1988) very well. The Henyey–Greenstein phase function reduces to isotropic scattering phase function, Φ_{Iso} , when $|g| \rightarrow 0$.

$$\Phi_{\text{Iso}} = \frac{1}{4\pi}. \quad (3.17)$$

However, as explained in the Section 3.3.1, when $|g| \rightarrow 0$, the scattering phase function should converge to Rayleigh scattering phase function. Noting this, Cornette and Shanks (1992) introduced the following hybrid phase function, $\Phi_{\text{CS}}(\cos(\theta))$, which is a product of the Rayleigh phase function and the HG phase function:

$$\Phi_{\text{CS}}(\cos(\theta), g) = \frac{24\pi}{2 + g^2}\Phi_{\text{R}}(\cos(\theta))\Phi_{\text{HG}}(\cos(\theta), g). \quad (3.18)$$

A generalization, $\Phi_{\text{D}}(\cos(\theta), \alpha, g)$, of this Cornette and Shanks phase function was given by Draine (2003)

$$\Phi_{\text{D}}(\cos(\theta), \alpha, g) = \frac{1 + \alpha \cos^2(\theta)}{1 + \alpha(1 + 2g^2)/3}\Phi_{\text{HG}}(\cos(\theta), g). \quad (3.19)$$

This phase function reduces to $\Phi_{\text{R}}(\cos(\theta))$ when $g = 0$ and $\alpha = 1$, and to $\Phi_{\text{CS}}(\cos(\theta), g)$ when $\alpha = 1$. Even with these enhancements, all these phase functions have many deficiencies in representing realistic light scattering features in practically important scenarios (see, e.g., (Draine, 2003; Yaroslavsky et al., 1997)).

3.3.4. Reynolds–McCormick Phase Function

This phase function is also known as the Gegenbauer kernel phase function because of its equivalent series representation using Gegenbauer orthogonal polynomials (Reynolds & McCormick, 1980). This phase function was proposed by Reynolds and McCormick after observing significant discrepancy between electromagnetic scattering theory results and

those obtained from radiative transfer framework using the HG phase function. Reynolds–McCormick (RM) phase function generalizes the HG-type phase function to multiple dimensions. The RM phase function $\Phi_{\text{RM}}(\cos(\theta), g, \alpha)$ has two parameters, $\alpha > -1/2$ and g (which is similar to the asymmetry parameter in the HG function with $|g| \leq 1$)

$$\Phi_{\text{RM}}(\cos(\theta), g, \alpha) = \frac{\alpha g}{\pi \left((1+g)^{2\alpha} - (1-g)^{2\alpha} \right)} \frac{(1-g^2)^{2\alpha}}{(1+g^2 - 2g \cos(\theta))^{-(\alpha+1)}}. \quad (3.20)$$

It is easy to verify that this phase function reduces to the well-known HG phase function for $\alpha = 1/2$. Similarly, as for the HG phase function (see Equation 3.14), there is an analogous orthogonal expansion for Equation 3.20 (Reynolds & McCormick, 1980)

$$\Phi_{\text{GK}}(\cos(\theta), g, \alpha) = \frac{2\alpha g (1-g^2)^{2\alpha-1}}{\pi \left((1+g)^{2\alpha} - (1-g)^{2\alpha} \right)} \sum_0^{\infty} \left(1 + \frac{n}{\alpha} \right) g^n G_n^{\alpha}(\cos(\theta)), \quad (3.21)$$

where $G_n^{\alpha}(\cos(\theta))$ is the Gegenbauer polynomials of order n . Detailed studies have shown that the RM phase function can reasonably well represent single scattering properties of human blood cells (Flock, Wilson, & Patterson, 1987; Hammer, Schweitzer, Michel, Thamm, & Kolb, 1998). However, as for the HG phase function, the Gegenbauer kernel phase function (i.e., the RM phase function) was widely applied because of the simplicity it brought to scattering calculations due to the attractive properties of the orthogonal polynomial expansion in Equation 3.21 (Yaroslavsky et al., 1997).

4. NUMERICAL METHODS

Even though the photon transport equation (PTE) looks very simple, solving it numerically is difficult because its actual functional form can vary depending on the medium properties and boundary conditions. For example, the steady-state PTE is of Fredholm type whereas the transient PTE is of Volterra type in its integral formulation (Wu & Wu, 2000a). Moreover, if there is intrinsic coupling between time, space, and frequency variables through material parameters, and hence the related coefficients (e.g., scattering and absorption) vary rapidly between relatively large magnitudes, most of the existing numerical schemes/libraries cannot be readily used for numerical solution. In particular, in mixed regimes where diffusion and ballistic-transport dominates at different spatial locations, conventional solvers and preconditioning methods become ineffective due to extremely poor convergence rates (Wu & Wu, 2000a).

Broadly, numerical solutions strategies for **transient** photon transport equation can be classified into three major groups:

Stochastic/probabilistic methods: In these schemes, radiance is described using a collection of localized energy packets (not necessarily a single photon but a collection of photons) into point-like particles that move independently of one another, even if the radiance itself is spread continuously over space. These packets gain or lose energy as they travel through the medium and get absorbed under certain conditions. Therefore, these descriptions treat photons like energy packets in totally different form to actual photons because photons do not spread out as they propagate or lose energy continuously in linear absorbing media. In these methods, photon energy packet trajectory is shaped probabilistically by the material properties and boundary conditions as described by the photon transport equation. Examples include standard (conventional) Monte Carlo method (Guo, Kumar, & San, 2000; Sawetprawichkul, Hsu, Mitra, & Sakami, 2000) and reverse Monte Carlo Method (Lu & Hsu, 2005).

Deterministic methods: In these schemes, well-known analytical methods or partial differential equation solution methods are applied to solve the photon transport equation. Sometimes, the photon transport equation is discretized without changing its functional form. However, different variants of the original equation, in principle equivalent to the original formulation but numerically tractable because they possess many favorable stability features, are frequently used. Especially noteworthy alternative formulations include approximations such as the diffusion approximation, which is valid only if a large number of scattering events take place within the medium. Examples include discrete ordinates method (Boulanger & Charette, 2005; Sakami, Mitra, & Hsu, 2000; Sakami et al., 2002), integral formulation (Tan & Hsu, 2001; Wu & Wu, 2000b), modified method of characteristics (Katika & Pilon, 2006), discrete transfer method (Rath, Mishra, Mahanta, Saha, & Mitra, 2003), Galerkin method (Okutucu & Yener, 2006; Okutucu, Yener, & Busnaina, 2007), Laguerre Runge–Kutta–Fehlberg method (Handapangoda, Premaratne, Yeo, & Friend, 2008), radiation element method (Guo & Kumar, 2001), spherical harmonics (Klose & Larsen, 2006; Kumar & Mitra, 1999), and finite volume method (Mishra, Chugh, Kumar, & Mitra, 2006).

Hybrid methods: In these methods, both analytical and stochastic/probabilistic methods are interchangeably used to solve the transient photon transport equation. Examples include transport-diffusion method (Densmore, Urbatsch, Evans, & Buksas, 2007), accelerated Monte Carlo method (Kong, Ambrose, & Spanier, 2008),

condensed-history method (Bhan & Spanier, 2007), and symbolic Monte Carlo method (Clouet & Samba, 2003).

Note that we do not explicitly take into account the polarization aspects of light in our description. However, in principle, such generalization is possible by introducing Stokes parameters, which leads to four coupled photon transport equations instead of the one in Equation 3.1. Such generalization clutters the basic approach with intricate details peculiar to different solution methods and makes the subsequent presentation and analysis overly complex. However, this is warranted if it adds a great deal to the present understanding and improves the accuracy and validity of the method. On the contrary, (Svaasand & Gomer, 1990) presented evidence that in a tissue-like medium, incident light rapidly becomes unpolarized as it propagates through the scattering medium and hence accounting for polarization in such analysis is unnecessary.

The solution of photon transport equation under steady-state conditions (using both stochastic and deterministic methods) has been the subject of several books and monographs (Chandrasekhar, 1960; Mishchenko et al., 2006; Pomraning, 2005; Sobolev & Gaposchkin, 1963). Therefore, we mainly focus on the novel methods applicable to the solution of transient photon transport equation in this review. Our selection and presentation of methods are not chronological and purely focus on the distinct ideas that may seed future developments in this area.

It is important to understand that the solution of photon transport equation is generally considered difficult compared with many other equations found in theoretical physics because it is an integro-differential equation with six independent variables: three spatial coordinates, two angular variables for propagation direction, and time (i.e., x , y , z , θ , ϕ , and t). Figure 2 shows these variables relative to the photon trajectory. It is interesting to note that most of the known methods of solution of the photon transport equation use a hybrid coordinate system where position of a photon is described using the Cartesian coordinates, but the direction of propagation is given using spherical coordinates (a moving coordinate system in this case). It is possible to establish one-to-one relation between these coordinates using projections as can be clearly seen in Figure 5. Boundary conditions play a crucial role in the solution process because they are incomplete at each boundary (i.e., there is partial information at each boundary) and can vary with time or move spatially with time. In almost all the methods used for solving the photon transport equation, some form of discrete mesh is formed in the six-dimensional space and quantities of interest such as radiance are tracked/traced discretely along the lattice points of the discrete mesh. The accuracy of the solution is ensured by either implicitly or explicitly making these discrete

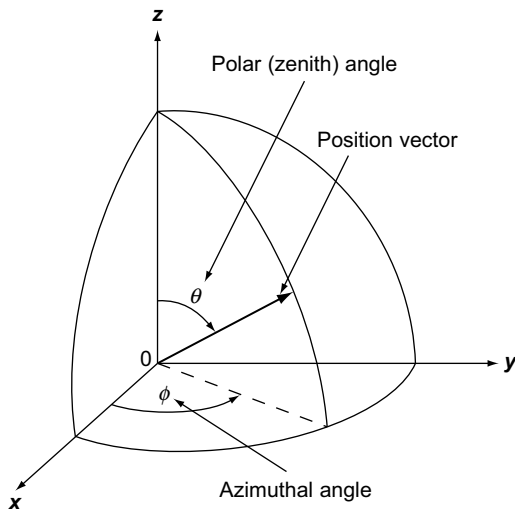


FIGURE 5 A spherical coordinate system with azimuthal and polar (zenith) angles combined with a Cartesian coordinates system.

solutions comply with the photon transport equation. In some instances, such compliance is guaranteed at each point of the discrete mesh whereas in other instances, convergence is achieved iteratively. However, recently, several schemes that do not require regular, prespecified grid for solving transient photon transport equation have appeared (Sadat, 2006; Tan, Liu, & Li, 2006).

4.1. Two-Flux and Multi-Flux Methods

One of the most simple ways of solving the photon transport equation is to use forward and backward scattering fluxes at a point that represent the integrals of radiance over the two hemispheres symmetrically in those directions as shown in Figure 6. Therefore, this method is known as the two-flux method (Schuster, 1905; Thomas & Stammes, 1999). Owing to this averaging (i.e., integration), it is implicitly assumed that radiances are constant over the respective hemispheres. One of the main advantages of this strategy is that isotropic scattering properties are inherently built into this approximation and thus no further simplification is needed. As we will see later in this review, this two-flux formulation is a rather crude approximation to finite volume method for solving photon transport equation. However, if low accuracy of the final result is acceptable, the two-flux method provides an excellent approximation to photon transport equation. If the anisotropy of the scattering medium cannot be

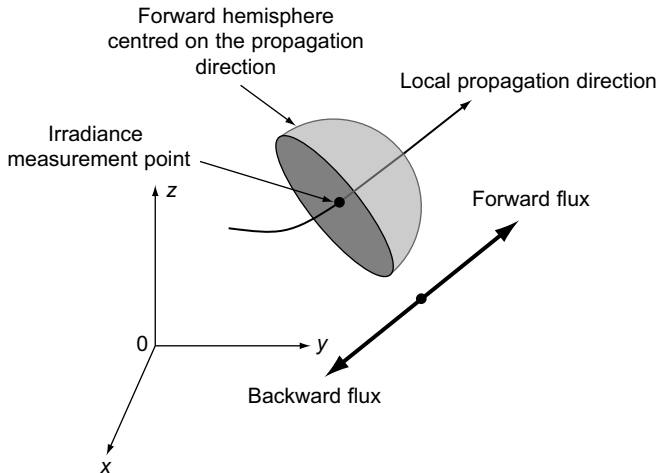


FIGURE 6 Forward hemispherical flux calculation for mapping radiance to irradiance. Mirror image of the hemisphere is used for calculating the backward hemispherical flux.

neglected, the quality of this approximation deteriorates and thus modifications need to be introduced. For example, Churchill and coworkers (Chin & Churchill, 1965; Chu & Churchill, 1960) extended the two-flux model to strongly anisotropic media subject to collimated illumination. In addition to the usual forward and backward components, they also introduced four other components directed sideways. No definitive guidelines exist for the placement of these components, and thus, problem-specific strategies need to be adopted in practice, especially for multidimensional problems (Daniel, Laurendeau, & Incropera, 1979; Sasse, Konigsdorff, & Frank, 1995).

In the two-flux method, light propagation is essentially considered in one dimension. Therefore, it is better to recast the previous three-dimensional radiance transport equation in one dimension as

$$\frac{1}{v_g(v)} \frac{\partial}{\partial t} I_v(t, z, \mu) + \frac{\partial}{\partial z} I_v(t, z, \mu) = -\sigma_a(t, z) I_v(t, z, \mu) - \sigma_s(t, z) I_v(t, z, \mu) \\ + \sigma_s(t, z) \int_{-1}^{+1} I_v(t, z, \mu_i) \Phi_v(\mu_i \rightarrow \mu, t, z) d\mu_i + F_v(t, z, \mu), \quad (4.1)$$

where z is the one-dimensional spatial coordinate, $\mu = \cos(\theta)$, where θ is the zenith angle of the coordinate system as shown in Figure 2, $v_g(v)$ is the group velocity of light in the scattering medium at frequency v , $\sigma_s(t, z)$ is

the scattering coefficient of the medium, $\sigma_a(t, z)$ is the attenuation coefficient of the medium, and $F_v(t, z, \mu)$ is the intrinsic power source density in the medium. The phase function Φ_v is assumed to be normalized to unity as for the three-dimensional case.

In the two-flux method, the scattered intensity is considered to be constant over the forward- and the backward-facing hemispheres and assumes the following form (Mitra & Kumar, 1999)

$$I_v(t, z, \mu) = \begin{cases} I_{v+}(t, z) & \mu \geq 0 \\ I_{v-}(t, z) & \mu < 0 \end{cases} \quad (4.2)$$

and thus effectively removes the dependency of radiance $I_v(t, z, \mu)$ on μ . This decomposition can also be seen as an averaging operation on each hemisphere with respect to μ . Substituting Equation (4.2) into Equation (4.1) and integrating with respect to μ in its positive and negative ranges, we get

$$\begin{aligned} \frac{1}{v_g(v)} \frac{\partial}{\partial t} I_{v+}(t, z) + \frac{\partial}{\partial z} I_{v+}(t, z) &= -\sigma_a(t, z) I_{v+}(t, z) - \sigma_s(t, z) I_{v+}(t, z) \\ &+ \sigma_s(t, z) B(I_{v+}(t, z) - I_{v-}(t, z)) + \int_0^1 F_v(t, z, \mu) d\mu, \end{aligned} \quad (4.3)$$

$$\begin{aligned} \frac{1}{v_g(v)} \frac{\partial}{\partial t} I_{v-}(t, z) + \frac{\partial}{\partial z} I_{v-}(t, z) &= -\sigma_a(t, z) I_{v-}(t, z) - \sigma_s(t, z) I_{v-}(t, z) \\ &+ \sigma_s(t, z) B(I_{v-}(t, z) - I_{v+}(t, z)) \int_{-1}^0 F_v(t, z, \mu) d\mu, \end{aligned} \quad (4.4)$$

where the parameter B is known as the back-scatter fraction defined by

$$B = \int_0^1 \int_{-1}^0 I_v(t, z, \mu_i) \Phi_v(\mu_i \rightarrow \mu, t, z) d\mu_i d\mu. \quad (4.5)$$

These hyperbolic equations can be integrated using well-known finite difference schemes (Mitra & Kumar, 1999). Multiflux methods have a similar format but involve additional coupled equations to relate the different flux components to each other.

4.2. Spectral Methods

Spectral methods approximate the radiance using a linear combination of continuous functions with superior convergence properties. Spectral methods have been widely used recently to seek solutions of transient photon transport equation because such expansions enable one to preserve certain critical features of the solutions. For example, in the Laguerre–Runge–Kutta–Fehlberg (LRKF) method reported in Handapangoda et al. (2008), radiance is expanded in Laguerre functions to preserve causality properties during the time-marching stages. In general, spectral methods reduce the integro-differential equation of photon transfer to a set of coupled differential equations. Most of the base function families used in spectral methods are orthogonal and hence the resulting coupled differential equations can be derived easily. Orthogonality property also reduces the coupling complexity of resulting equations, making them very suitable for numerical work. Thereafter, standard yet powerful numerical techniques used for solving coupled differential equations are employed to tackle them under various boundary and initial conditions.

Kim and coworkers (Kim & Ishimaru, 1999; Kim & Moscoso, 2002) expanded the radiance in a Fourier series of the periodic azimuthal angle with the resulting Fourier coefficients expressed using Chebyshev polynomials (Kim & Moscoso, 2002):

$$I_{vn}(t, z, \mu) \cong \sum_{k=0}^N a_k(\mu, t) T_k(z), \quad (4.6)$$

where $I_{vn}(t, z, \mu)$ is the nth Fourier coefficient of the radiance and $T_k(z)$ are the orthogonal Chebyshev polynomials (Canuto, Hussaini, Quarteroni, & Zang, 1988). Such an expansion is favored for studying light propagation in biological tissue because it enables one to successfully tackle the anisotropic scattering by focussing attention on the corresponding integral terms of the photon transport equation. Moreover, it provides the added flexibility to handle complex boundary conditions with ease. In this method, the Chebyshev polynomials are only used to approximate the spatial component of the radiance and hence lead to a system of integral equations for the angularly dependent Chebyshev modes. The resulting linear system of equations has a bordered, blockbanded sparsity structure that can be efficiently solved using a deflated block elimination method (Chan & Resasco, 1986). Thereafter, time-marching is done using the well-known Crank–Nicholson method (Kim & Ishimaru, 1999; Kim & Moscoso, 2002).

In the study by Handapangoda et al. (2008), time dependency of the radiance was expanded using Laguerre functions:

$$I_v(t, z, \mu) \cong \sum_{k=0}^N B_k(z, \mu) L_k(t), \quad (4.7)$$

where $L_k(t)$ are the orthogonal Laguerre polynomials (Abramowitz & Stegun, 1965). The discrete ordinates method was used to discretize the resulting equations for azimuthal and zenith angles. This transformation reduces the original integro-differential equation to a single-variable ordinary differential equation, which can then be solved using the fourth-order Runge–Kutta–Fehlberg method (Handapangoda et al., 2008). Since the time dependence is expanded using a Laguerre basis, all the sampling points in the time domain are obtained in a single execution, as opposed to time-marching techniques used in existing solution methods. Owing to Laguerre polynomials forming a very efficient orthogonal basis in real space, any arbitrary incident pulse can be approximated using a relatively small number of Laguerre polynomials. The causality of the system is implicitly imposed by the causal Laguerre polynomials because such expansions are a linear superposition of causal Laguerre polynomials. The use of the very robust and efficient Runge–Kutta–Fehlberg integration method in the spatial domain makes this technique eminently suitable for inhomogeneous scattering media with complex boundary conditions (Handapangoda & Premaratne, 2009).

The previous two methods expanded the radiance $I_v(t, z, \mu)$ using z or t variables. In addition, the radiance parametrically depends on $\mu \equiv \cos(\theta)$, which is a function of θ , the zenith angle of the coordinate system (see Figure 2). Therefore, it is interesting to look at how such a decomposition can be made to improve the computation aspects of radiance, $I_v(t, z, \mu)$. In literature, such expansions are known as P_N methods (Bayazitoglu & Higenyi, 1979) or the method of spherical harmonics (Kourganoff, 1963). Even though strictly not belonging to the conventional spectral methods, P_N methods bear a close resemblance to them. The general P_N method models the radiance by expanding it as a series of Legendre polynomials in μ

$$I_v(t, z, \mu) \cong \sum_{m=0}^N I_{vm}(t, z) p_m(\mu), \quad (4.8)$$

which is then substituted into the photon transport equation. The photon transport equation is subsequently multiplied by a Legendre polynomial P_m of order m (less than or equal to N) and integrated with respect to μ

(Mitra & Kumar, 1999). Use of the orthogonality property of the Legendre polynomials results in a differential equation for each expansion coefficient $I_{vm}(t, z)$ of Equation (4.8). These equations are relatively simple and well-behaved, so it is fairly easy to solve them using standard numerical techniques. One of the main deficiencies of this method is that low-order approximations such as P_1 approximation is usually only accurate in media with near-isotropic properties. The accuracy can be increased by taking higher-order approximations, but the resulting improvements are very marginal and, in most instances, are masked by the added mathematical complexity of the resulting equations. Empirical numerical evidence suggests that even-order P_N approximations are less accurate than their nearest lower odd-order approximates. Therefore, even-order P_N approximations such as P_2 are never used in practice. In the study by Mitra, Lai, and Kumar (1997), a P_1 approximation was used to model transient radiative transfer in a rectangular enclosure. Mitra and Kumar (1997) carried out a comparison of the P_N against two-flux and discrete ordinate methods. Photon transport equation under radiative transfer was investigated by Wu and Ou (2002) under a hybrid P_1 and P_3 formulation. A modified differential equation in one dimension was used for carrying out the analysis for collimated irradiation.

4.3. Finite Volume Method

Discrete ordinate method can be identified as the most widely used method of solving the photon transport equation. The derivation of the photon transport equation matches the photon energy entering an infinitesimal volume from a given direction to that leaving, thus providing local and overall energy conservation. However, numerical solution of the photon transport equation is obtained by approximating the scattering integrals by algebraic equations that use constraints such as symmetry or equivalence of first few moments (i.e., moment matching) to derive the ordinates and weights of the approximate sum. Even though this rigor is somewhat relaxed for solid-angle discretization of an infinitesimal volume element where weighting factors are ignored. The accuracy of treating anisotropic scattering is related to the number of points used in the solid-angle discretization procedure. Owing to all these numerical approximations, discrete ordinate method suffers from many drawbacks such as false scattering, ray-effects, and nonconservation of photon energy (Kourganoff, 1963; Welch & van Gemert, 1995). The last is the most troublesome because it violates one of the fundamental laws of physics/nature.

A way to overcome the violation of energy conservation during numerical calculation is to adopt a finite volume method for the photon transport equation. Finite volume methods are designed to enforce several

conservation laws related to mass, momentum, energy, or charge. In finite volume methods, the computation domain is first divided into sufficiently small volume elements and appropriate conservation laws are applied to each such element. Owing to the fact that fluxes leaving one volume element become the incoming source for the adjacent elements, such judicious application of a conservation laws leads to a system of coupled equations, that can be solved using an appropriate method. Briggs and coworkers (Briggs, Miller, & Lewis, 1975) pioneered the application of finite volume method to photon transport equation.³ Thereafter, Raithby and Chui (Chui & Raithby, 1993; Raithby & Chui, 1990) and Chai and coworkers (Chai, Lee, & Patankar, 1994; Chai, Parthasarathy, Lee, & Patankar, 1995) introduced different variants of the implementation applicable to the PTE-type equations. In the study by (Chai et al., 1994), the radiance along a given direction is assumed to be uniform over the boundary of the volume element of concern, whereas the study by Raithby and Chui (1990) breaks the volume element boundary into two sections and assigns uniform radiance values for each of these sections.

The first step in implementing finite volume method is to re-write the photon transport equation along a certain direction as shown by Chai et al. (2004). Suppose the unit vector in the direction of interest is given by s_l and the path length is given by l , then, we could replace the scalar product $s_l \cdot \nabla_r I_v(t, \mathbf{r}, s_l)$ in Equation (3.1) by the partial derivative with respect to l to get

$$\frac{1}{v_g(v)} \frac{\partial}{\partial t} I_v(t, \mathbf{r}, s_l) + \frac{\partial}{\partial l} I_v(t, \mathbf{r}, s_l) = f_v(t, \mathbf{r}, I_v(t, \mathbf{r}, s_l), \sigma_a(t, \mathbf{r}), \sigma_s(t, \mathbf{r})), \quad (4.9)$$

where $f_v(t, \mathbf{r}, I_v(t, \mathbf{r}, s_l), \sigma_a(t, \mathbf{r}), \sigma_s(t, \mathbf{r}))$ is a function of attenuation, scattering, and source terms as described in Equation (3.1). The finite volume approach is carried out by taking the volume integration of the differential equation over a domain V and solid-angle $d\Omega_s$

$$\frac{1}{v_g(v)} \int \int_V \frac{\partial}{\partial t} I_v dV d\Omega_s + \int \int_V \frac{\partial}{\partial l} I_v dV d\Omega_s = \int \int_V f_v dV d\Omega_s. \quad (4.10)$$

All the terms except the second term (i.e., the integral with directional derivative) in the above equation can be handled easily using conventional quadrature methods. In the finite volume method, the directional derivative is very accurately integrated using the following procedure.

For the general irregular regions handled by the finite volume method, we consider the general domain depicted in Figure 7. The quadrilateral

³However, their application was in the field of neutron transport.

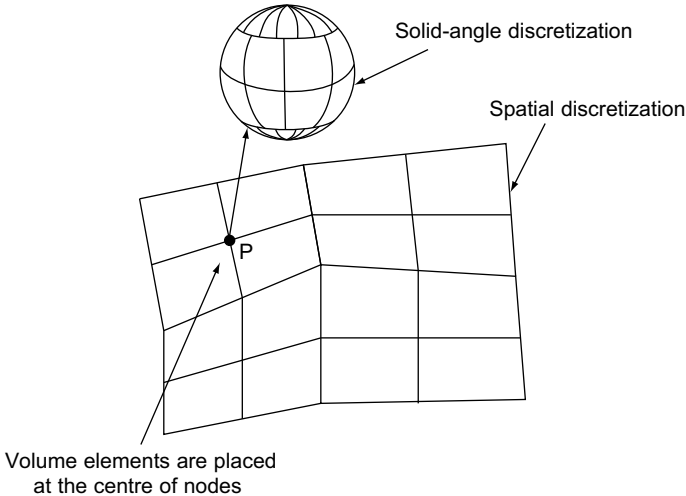


FIGURE 7 Discrete grid used in finite volume method.

volumes depicted in Figure 7 follow the convention used by Chai and coworkers (Chai et al., 1995), where nodes are placed at the center of each volume element. Both spatial and solid angles are discretized using appropriate fineness and format to enable the application of numerical quadrature schemes. One of the simplest schemes for discretizing the 4π solid angle associated with a point is to use the nonoverlapping areas on the surface of a unit sphere defined by lines of longitude and latitude (Modest, 2003). For each volume element such as the one surrounding point P in Figure 7, Equation (4.10) is integrated over the volume element and over each of the solid-angle elements, Ω_i , following (Modest, 2003)

$$\int \int \int_{\Omega_i} \frac{\partial}{\partial l} I_v dV d\Omega_s = \int \int \int_{\Omega_i} \mathbf{s}_l \cdot \nabla I_v dV d\Omega_s = \int \int \int_{\Omega_i} \nabla \cdot (\mathbf{s}_l I_v) dV d\Omega_s, \quad (4.11)$$

where we used the fact that directional coordinates are independent of spatial coordinates and hence the relation $\nabla \mathbf{s} = 0$ holds. We now apply the Gauss theorem⁴ to get

$$\int \int \int_{\Omega_i} \frac{\partial}{\partial l} I_v dV d\Omega_s = \int \int \int_{\Omega_i} I_v \mathbf{s}_l \cdot \mathbf{n} d\Gamma d\Omega_s, \quad (4.12)$$

⁴This is a special case of Stokes' theorem. If ω is an $(n - 1)$ -form with compact support on manifold M and ∂M denotes its boundary with its induced orientation, then $\int_M d\omega = \int_{\partial M} \omega$, where d is the exterior derivative.

where Γ is the surface of the volume element and n is the outward surface normal as indicated in Figure 7. The fundamental difference among the different algorithms used in finite volume method relies on the approach taken to discretize this integral. In the simplest implementations, the radiance is assumed to be constant across each element of the elementary volume as well as over the solid-angle Ω_i (Chai et al., 1994; Modest, 2003). However, for example, the study by Raithby and Chui (1990) breaks the volume element boundary into two sections and assigns uniform radiance values for each of these sections. This approach used two different spatial discretization schemes called step and CLAM to solve photon transport equation in one-dimensional and three-dimensional geometries. For identical grids, the CLAM scheme captures the penetration depths of light more accurately than the step scheme. Finite volume method was extended to unstructured meshes in the study by Murthy and Mathur (1998), but great care needs to be taken to reduce false scattering, which depends on the spatial discretization scheme used (Chai et al., 2004). Different time-marching strategies can be adopted to enhance the performance of the algorithm (Chai et al., 2004). If the time discretization is ignored in these calculations, one may even be tempted to use a sure and well-established technique such as the method of lines discussed below.

4.4. Method of Lines

Method of lines (MOL) solution of the photon transport equation is an explicit/implicit solution method, which enables one to utilize higher-order spatial and angular discretization methods. It requires no additional effort in formulation and readily allows one to use state-of-the-art ordinary differential equation solution method for temporal integration (Ayrancı & Selcuk, 2004; Cayan & Selcuk, 2007; Demirkaya, Arinc, Selcuk, & Ayrancı, 2005). The basic idea of the MOL is to replace the spatial/angular derivatives in the photon transport equation with algebraic approximations but to retain the temporal evolution term (see Equation (3.1)). Thereafter, the photon transport equation becomes a system of coupled first-order ordinary differential equations in the temporal variable (Ayrancı & Selcuk, 2004). The solution techniques for first-order coupled system of ordinary differential equations are well-matured and widely available (Press, Teukolsky, Vetterling, & Flannery, 2007). Therefore, one could solve the resulting set of equations efficiently with very high accuracy. This step takes away the burden of time discretization and provides a way to set the time steps in such a way as to maintain the accuracy and stability of the evolving solution. Thus, one of the salient features of MOL approach is the ability to use higher-order, implicit, and hence stable numerical algorithms for time integration (Press et al., 2007).

4.5. Method of Characteristics

When dealing with propagation of energy through space or material media, one can find curves that are called “characteristic curves” on which the underlying partial differential equation (or the propagation equation) reduces to an ordinary differential equation. Once the parametric equation of these curves are found by taking the “time” as a parameter, it is possible to replace the partial differential equation by ordinary differentials with respect to the parameter describing the characteristic curves. In general, it is possible to show that the method of characteristics (or direct marching method) is valid for any hyperbolic differential equation including the time-dependent photon transport equation. There is a physically appealing intuitive way to understand the meaning of these characteristic curves. It is possible to construct the Poynting vector of the propagating wave and to show that its direction matches with the tangent to a characteristic curve at that point. Hence, characteristic curves represent the photon paths or trajectories through the scattering media. Therefore, wave propagation through the scattering media can be traced using the Lagrangian formulation, where the wave propagation is calculated by tracing the photon transport along the characteristic curve starting from an initial position. Similar to the method of lines, once the equivalent ordinary differential equation is found along the characteristic curves, well-established, widely available solvers can be used for solution (Press et al., 2007). Even though this procedure seems straightforward, it may introduce some problems in practice because when adaptive solution routines are used, time increments along different characteristic curves may be different. So the time discretization/gridding on different characteristic curves may need to be different. In nonuniform, inhomogeneous media, the characteristic curves may coalesce or spread apart due to nonuniform velocities resulting in a highly distorted grid (Hoffman, 1998).

To understand how we can reduce the partial differential equation to an ordinary differential equation on a characteristics line, consider the scenario shown in Figure 8. We assume that the propagation velocity of a photon on the characteristics at any general point is given by $v_g(v)$, where parameter v denotes the optical frequency of the photon being tracked. Assume the velocity vector has the direction given by azimuthal angle ϕ and polar angle θ in the (x, y, z) rectangular coordinate systems given there. Then, the propagation velocity of the photon can be projected onto x -, y -, and z -axes as follows:

$$\frac{dx}{dt} = v_g(v) \sin(\theta) \cos(\phi) \quad (4.13a)$$

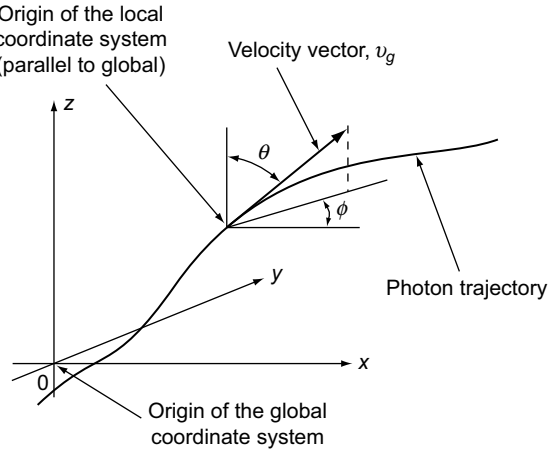


FIGURE 8 Coordinates and notation used in describing the method of characteristics.

$$\frac{dy}{dt} = v_g(v) \sin(\theta) \sin(\phi) \quad (4.13b)$$

$$\frac{dz}{dt} = v_g(v) \cos(\theta). \quad (4.13c)$$

Suppose the unit tangent vector on the characteristic at this point is given by s_c . Then, we could write the total derivative of the radiance, $I_v(t, r, s_c)$ along the direction s_c as

$$\frac{DI_v}{Dt} \equiv \frac{\partial I_v}{\partial t} + \frac{dx}{dt} \frac{\partial I_v}{\partial x} + \frac{dy}{dt} \frac{\partial I_v}{\partial y} + \frac{dz}{dt} \frac{\partial I_v}{\partial z}. \quad (4.14)$$

If $\{i, j, k\}$ are the unit vectors in the direction of (x, y, z) axes, then we could write the velocity of the particle using (4.13) as

$$\frac{dx}{dt} i + \frac{dy}{dt} j + \frac{dz}{dt} k = v_g(v) s_c \quad (4.15)$$

because the tangent vector of the characteristic curve can be written as $s_c \equiv \sin(\theta) \cos(\phi) i + \sin(\theta) \sin(\phi) j + \cos(\theta) k$. Therefore, we could write the total derivative (4.14) as

$$\frac{DI_v}{Dt} = \frac{\partial I_v}{\partial t} + v_g(v) s_c \cdot \nabla I_v, \quad (4.16)$$

which matches with the left-hand side of the equation (4.9) giving the following equality:

$$\frac{1}{v_g(v)} \frac{D}{Dt} I_v(t, \mathbf{r}, \mathbf{s}_c) = f_v(t, \mathbf{r}, I_v(t, \mathbf{r}, \mathbf{s}_c), \sigma_a(t, \mathbf{r}), \sigma_s(t, \mathbf{r})). \quad (4.17)$$

This formulation transforms the partial differential equation of propagation into a total differential equation. This form of formulation was used by Rukolaine, Vasilyev, Yuferev, and Galyukov (2002) to solve photon transport equation in axisymmetric domains (e.g., cylindrical media) with diffuse and specularly reflecting boundaries. However, owing to the significant dependence of this formulation on symmetry properties of the medium, it cannot be adopted for general media. Moreover, this method cannot simulate transient phenomena. A variant of this method called the “modified method of characteristic” was proposed by Katika and Pilon (2006). Unlike the conventional method where photons only travel in the forward direction (i.e., along the propagation direction), the photons were allowed to propagate in the backward direction along a characteristic. Moreover, prespecified space and time sampling points along the characteristics were used for carrying out numerical integration. Therefore, the generated solutions were sampled at the same times along each characteristic and thus naturally overcame the problems related to grid deformation mentioned previously.

4.6. Time Shift and Superposition Method

If the scattering medium is linear and does not enclose any energy sources, then the behavior of such a medium can be described using a conventional linear time invariant transfer function. The time shift and superposition method proposed by Liu and Hsu (2008) for solving the photon transport equation takes advantage of this property in a clever way. It uses the response of the medium to a short square pulse and then repeatedly uses time shift and superposition to construct the response of an arbitrary pulse incident on the medium. It is very clear that this approach provides a very significant computational saving for solving the photon transport equation.

Suppose $f_1(t, \mathbf{r}, s)$ is the resultant waveform (i.e., the response) after photons pass through a source-free, linear scattering medium subjected to a square pulse input radiance $I_{in}(t) = H(t) - H(t - T)$, where T is the time width (i.e., the duration) of the square pulse and $H(t)$ is the Heaviside step function. If the medium properties are time-invariant (i.e., medium parameters do not depend on time), then the medium properties remain the same regardless of the time at which the input pulse first interacts

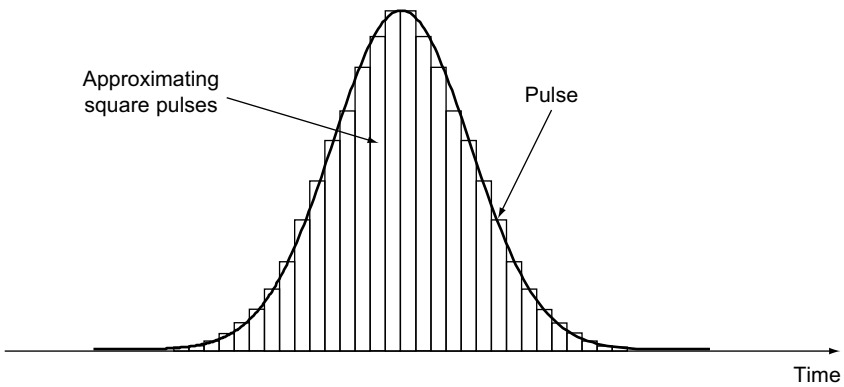


FIGURE 9 Approximating an arbitrary pulse using time shift and superposition of square pulses.

with the medium. Therefore, it is easy to see that $f_1(t - t_0, \mathbf{r}, \mathbf{s})$ is the response of the medium to the input pulse shifted (i.e., delayed) t_0 seconds; $I_{in}(t - t_0) = H(t - t_0) - H(t - t_0 - T)$. If the width of the square pulse is sufficiently small, then it is possible to approximate any arbitrary pulse shape closely as shown in Figure 9. The height of the square pulse is modulated by using different multiplication factors, but width is kept constant. For example, if the input pulse shape is given by $g(t)$, then it can be written approximately using this scheme as

$$g(t) \approx \sum_i g(t_i) [H(t - t_i) - H(t - t_i - T)], \quad (4.18)$$

where index i spans through the subdivisions as shown in Figure 9. Therefore, the resulting output pulse shape, $f(t)$ can be written as

$$f(t) \approx \sum_i g(t_i) f_1(t - t_i, \mathbf{r}, \mathbf{s}). \quad (4.19)$$

A detailed analysis to show the validity of this method compared with standard discrete ordinate method and discrete finite element methods was reported by Liu and Hsu (2008). Discrete finite element method to calculate the response $f_1(t, \mathbf{r}, \mathbf{s})$ to square inputs was also used.

5. CONCLUDING REMARKS

Photon transport in biological tissue is an emerging area that needs to be made rigorous. Recently, time-varying fields and time-varying biological

media have attracted much attention due to the many potential applications in diagnostic sensing and therapy areas. Photon transport analysis borrows different theoretical tools from classical and quantum optics, but no unified theory exists yet which is capable of cohesively representing all relevant fundamental concepts and observed effects. For example, the photon transport equation cannot be exactly matched with Maxwell's equations when diffractive phenomena dominate. Moreover, neither photon statistical aspects nor stimulated/spontaneous emission concepts can be described using the photon transport equation without making major approximations or adjustments. The need for such a fundamental understanding arises from the applications that require a precise control of light interaction with tissue in the presence of foreign substances. One example would be where photo-active substances are injected into biological tissue and light is used to initiate and steer reactions in photo-dynamic therapy area for treating cancerous cells. Another example is the routine use of noninvasive laser surgery for treating vision impairments. Specifically for the ophthalmological treatment, a detailed understanding of the light interaction with biological substances and their reaction to local light intensity is paramount for successful application of the technique. Existing methods are not adequate for providing a high accuracy and predictability normally required in clinical settings. Therefore, further work must be done to improve the existing numerical techniques and to make the theoretical descriptions much more accurate and computationally efficient.

REFERENCES

- Abramowitz, M., & Stegun, I. A. (1965). Orthogonal polynomials. In *Handbook of mathematical functions with formulas, graphs and mathematical tables* (pp. 773–784). Dover, New York, USA.
- Alberts, B., Bray, D., Johnson, A., Lewis, J., Raff, M., Roberts, K., et al. (1998). *Essential cell biology: An introduction to the molecular biology of the cell*. Garland Publishing Inc., New York, USA.
- Arridge, S. R. (1999). Optical tomography in medical imaging. *Inverse Problems*, 15, R41–R93.
- Ayrancı, I., & Selcuk, N. (2004). Mol solution of dom for transient radiative transfer in 3-d scattering media. *Journal of Quantitative Spectroscopy & Radiative Transfer*, 84, 409–422.
- Baierlein, R. (2001). *Newton to Einstein: The trail of light: An excursion to the wave-particle duality and the special theory of relativity*. Cambridge University Press, Cambridge, UK.
- Bal, G. (2006). Radiative transfer equations with varying refractive index: A mathematical perspective. *Journal of the Optical Society of America*, 23, 1639–1644.
- Barnes, F. S., & Greenebaum, B. (Eds.). (2007). *Bioengineering and biophysical aspects of electromagnetic fields*. CRC Press, Florida, USA.
- Barron, L. (2004). *Molecular light scattering and optical activity* (2nd ed.). Cambridge University Press, Cambridge, UK.
- Bayazitoglu, Y., & Higenyi, J. (1979). The higher order differential equations of radiative transfer: p_3 approximation. *AIAA J.*, 17, 424–431.

- Bhan, K., & Spanier, J. (2007). Condensed history monte carlo methods for photon transport problems. *Journal of Computational Physics*, 225, 1673–1694.
- Bohren, C. F., & Huffman, D. R. (1983). *Absorption and scattering of light by small particles*. Wiley Interscience, New York, USA.
- Born, M., & Wolf, E. (1999). *Principles of optics: Electromagnetic theory of propagation, interference and diffraction of light* (7th ed.). Cambridge University Press, Cambridge, UK.
- Boulanger, J., & Charette, A. (2005). Numerical developments for short-pulsed near infrared laser spectroscopy: I. direct treatment. *Journal of Quantitative Spectroscopy & Radiative Transfer*, 91, 189–209.
- Briggs, L. L., Miller, J. W. F., & Lewis, E. E. (1975). Ray-effect mitigation in discrete ordinate-like angular finite element approximations in neutron transport. *Nuclear Science and Engineering*, 57, 205–217.
- Caldas, M., & Semiao, V. (2001). Radiative properties of small particles: Extension of the pennendorf model. *Journal of Optical Society of America A*, 18, 831–838.
- Canuto, C., Hussaini, M. Y., Quarteroni, A., & Zang, T. A. (1988). *Spectral methods in fluid dynamics*. Springer-Verlag, New York, USA.
- Cayan, F. N., & Selcuk, N. (2007). The method of lines solution of discrete ordinates method for non-grey media. *Journal of Quantitative Spectroscopy & Radiative Transfer*, 104, 228–237.
- Chai, J. C., Hsu, P. F., & Lam, Y. C. (2004). Three-dimensional transient radiative transfer modeling using the finite-volume method. *Journal of Quantitative Spectroscopy & Radiative Transfer*, 86, 299–313.
- Chai, J. C., Lee, H. S., & Patankar, S. V. (1994). Finite volume method for radiation heat transfer. *Journal of Thermophysics and Heat Transfer*, 8, 419–425.
- Chai, J. C., Parthasarathy, G., Lee, H. S., & Patankar, S. V. (1995). Finite volume method radiative heat transfer procedure for irregular geometries. *Journal of Thermophysics and Heat Transfer*, 9, 410–415.
- Chan, T. F., & Resasco, D. C. (1986). Generalized deflated block-elimination. *SIAM Journal on Numerical Analysis*, 23, 913–924.
- Chandrasekhar, S. (1960). *Radiative transfer*. Dover Publications Inc., New York, USA.
- Chin, J. H., & Churchill, S. W. (1965). Anisotropic, multiply scattered radiation from an arbitrary, cylindrical source in an infinite slab. *ASME Journal of Heat Transfer*, 87, 167–172.
- Chu, C. M., & Churchill, S. W. (1960). Numerical solution of problems in multiple scattering of electromagnetic radiation. *Journal of Physical Chemistry*, 59, 855–863.
- Chui, E. H., & Raithby, G. D. (1993). Computation of radiant heat transfer on a nonorthogonal mesh using the finite volume method. *Numerical Heat Transfer Part B: Fundamentals*, 23, 269–288.
- Clouet, J. F., & Samba, G. (2003). A hybrid symbolic monte-carlo method for radiative transfer equations. *Journal of Computational Physics*, 188, 139–156.
- Cornette, W. M., & Shanks, J. G. (1992). Physically reasonable analytic expression for the single-scattering phase function. *Applied Optics*, 31, 3152–3160.
- Daniel, K. J., Laurendeau, N. M., & Incropera, F. P. (1979). Prediction of radiation absorption and scattering in turbid water bodies. *ASME Journal of Heat Transfer*, 101, 63–67.
- Demirkaya, G., Arinc, F., Selc-uk, N., & Ayrancı, I. (2005). Comparison between performances of monte carlo method and method of lines solution of discrete ordinates method. *Journal of Quantitative Spectroscopy & Radiative Transfer*, 93, 115–124.
- Densmore, J. D., Urbatsch, T. J., Evans, T. M., & Buksas, M. W. (2007). A hybrid transport-diffusion method for monte carlo radiative-transfer simulations. *Journal of Computational Physics*, 222, 485–503.
- Draine, B. T. (2003). Scattering by interstellar dust grains. i. optical and ultraviolet. *The Astrophysical Journal*, 598, 1017–1025.

- Flock, S. T., Wilson, B. C., & Patterson, M. S. (1987). Total attenuation coefficient and scattering phase function of tissues and photon materials at 633nm. *Medical Physics*, 14, 826–834.
- Foster, K. R., & Schwan, H. P. (1989). Dielectric properties of tissues and biological materials: A critical review. *Critical Reviews in Biomedical Engineering*, 17, 25–104.
- Gobin, A. M., Lee, M. H., Halas, N. J., James, W. D., Drezek, R. A., & West, J. L. (2007). Near-infrared resonant nanoshells for combined optical imaging and photothermal cancer therapy. *Nano Letters*, 7, 1929–1934.
- Greiner, W., & Reinhardt, J. (2002). *Quantum electrodynamics*. Springer, New York, USA.
- Guo, Z., & Kumar, S. (2001). Radiation element method for transient hyperbolic radiative transfer in plane-parallel inhomogeneous media. *Numerical Heat Transfer, Part B Fundamentals*, 39, 371–387.
- Guo, Z., Kumar, S., & San, K.-C. (2000). Multidimensional monte carlo simulation of short-pulse transport in scattering media. *Journal of Thermophysics and Heat Transfer*, 14, 504–511.
- Hammer, M., Schweitzer, D., Michel, B., Thamm, E., & Kolb, A. (1998). Single scattering by red blood cells. *Applied Optics*, 37, 7410–7418.
- Handapangoda, C. C., & Premaratne, M. (2009). Implicitly causality enforced solution of multidimensional transient photon transport equation. *Optics Express*, 17, 23423–23442.
- Handapangoda, C. C., Premaratne, M., Yeo, L., & Friend, J. (2008). Laguerre runge–kutta–fehlberg method for simulating laser pulse propagation in biological tissue. *IEEE Journal of Selected Topics in Quantum Electronics*, 14, 105–112.
- Henyey, L. G., & Greenstein, J. L. (1941). Diffuse radiation in the galaxy. *Astrophysical Journal*, 93, 70–83.
- Hercules, D. M. (Eds.). (1966). *Fluorescence and phosphorescence analysis: Principles and applications*. Interscience Publishers, New York, USA.
- Hoffman, J. D. (1998). *Numerical methods for engineers and scientists*. McGraw Hill, New York, USA.
- Huang, D., Swanson, E. A., Lin, C. P., Schuman, J. S., Stinson, W. G., Chang, W., et al. (1991). Optical coherence tomography. *Science*, 254, 1178–1181.
- Irvin, W. M. (1965). Multiple scattering by large particles. *Astrophysical Journal*, 142, 1563–1575.
- Jacques, S. L., Alter, C. A., & Prahl, S. A. (1987). Angular dependence of hene laser light scattering by human dermis. *Lasers Life Science*, 1, 309–333.
- Kanwal, R. P. (2004). *Generalized functions: Theory and applications*. Birkhauser, Boston, USA.
- Katika, K. M., & Pilon, L. (2006). Modified method of characteristics in transient radiation transfer. *Journal of Quantitative Spectroscopy & Radiative Transfer*, 98, 220–237.
- Kattawar, G. W. (1975). A three-parameter analytic phase function for multiple scattering calculations. *Journal of Quantitative Spectroscopy & Radiative Transfer*, 15, 839–849.
- Kim, A. D., & Ishimaru, A. (1999). Chebyshev spectral method for radiative transfer equations applied to electromagnetic wave propagation and scattering in a discrete random medium. *Journal of Computational Physics*, 152, 264–280.
- Kim, A. D., & Moscoso, M. (2002). Chebyshev spectral methods for radiative transfer. *SIAM Journal on Scientific Computing*, 23, 2075–2095.
- Klose, A. D., & Larsen, E. W. (2006). Light transport in biological tissue based on the simplified spherical harmonics equations. *Journal of Computational Physics*, 220, 441–470.
- Kokhanovsky, A. A. (2001). *Optics of light scattering media, problems and solutions* (2nd ed.). Springer PRAXIS, Chichester, UK.
- Kong, R., Ambrose, M., & Spanier, J. (2008). Efficient, automated monte carlo methods for radiation transport. *Journal of Computational Physics*, 227, 9463–9476.
- Kourganoff, V. (1963). *Basic methods in transfer problems*. Dover Publications, New York, USA.
- Kumar, S., & Mitra, K. (1999). Microscale aspects of thermal radiation transport and laser applications. *Advanced Heat Transfer*, 33, 187–294.

- Leitgeb, R., Hitzenberger, C. K., & Fercher, A. F. (2003). Performance of fourier domain vs. time domain optical coherence tomography. *Optics Express*, 11, 889–894.
- Liou, K.-N. (1975). Theory of the scattering-phase-matrix determination for ice crystals. *Journal of Optical Society of America A*, 65, 159–162.
- Liu, P. (1994). A new phase function approximating to mie scattering for radiative transprot equations. *Physics in Medicine and Biology*, 39, 1025–1036.
- Liu, L. H., & Hsu, P. F. (2008). Time shift and superposition method for solving transient radiative transfer equation. *Journal of Quantitative Spectroscopy & Radiative Transfer*, 109, 1297–1308.
- Lu, X., & Hsu, P.-F. (2005). Reverse monte carlo simulations of light pulse propagation in nonhomogeneous media. *Journal of Quantitative Spectroscopy & Radiative Transfer*, 93, 349–367.
- Mishchenko, M. I. (2008). Broadband electromagnetic scattering by particles. *Journal of Optical Society of America A*, 25, 2893–2895.
- Mishchenko, M. I., Travis, L. D., & Lacis, A. A. (2006). *Multiple scattering of light by particles: Radiative transfer and coherent backscattering*. Cambridge University Press, Cambridge, UK.
- Mishra, S. C., Chugh, P., Kumar, P., & Mitra, K. (2006). Development and comparison of the dtm, the dom and the fvm formulations for the short-pulse laser transport through a participating medium. *International Journal of Heat and Mass Transfer*, 49, 1820–1832.
- Mitra, K., & Kumar, S. (1999). Development and comparison of models for light-pulse transport through scattering absorbing media. *Applied Optics*, 38, 188–196.
- Mitra, K., Lai, M. S., & Kumar, S. (1997). Transient radiation transport in participating media within a rectangular enclosure. *AIAA Journal of Thermophysics and Heat Transfer*, 11, 409–414.
- Modest, M. F. (2003). *Radiative heat transfer* (2nd ed.). Academic Press, San Diego, USA.
- Mourant, J. R., Freyer, J. P., Hieltscher, A. H., Eick, A. A., Shen, D., & Johnson, T. M. (1998). Mechanisms of light scattering from biological cells relevant to noninvasive optical-tissue diagnostics. *Applied Optics*, 37, 3586–3593.
- Murthy, J. Y., & Mathur, S. R. (1998). Finite volume method for radiative heat transfer using unstructured meshes 1998. *Journal of Thermophysics and Heat Transfer*, 12, 313–321.
- Nicodemus, F. E. (1963). Radiance. *American Journal of Physics*, 31, 368–377.
- Niemz, M. H. (2004). *Laser-Tissue interactions: Fundamentals and applications* (3rd ed.). Springer, New York, USA.
- Nieto-Vesperinas, M. (2006). *Scattering and diffraction in physical optics* (2nd ed.). Wold Scientific, Singapore.
- Okutucu, T., & Yener, Y. (2006). Radiative transfer in participating media with collimated short-pulse gaussian irradiation. *Journal of Physics D: Applied Physics*, 39, 1976–1983.
- Okutucu, T., Yener, Y., & Busnaina, A. A. (2007). Transient radiative transfer in participating media with pulse-laser irradiationan approximate galerkin solution. *Journal of Quantitative Spectroscopy & Radiative Transfer*, 103, 118–130.
- Pal, G., Basu, S., Mitra, K., & Vo-Dinh, T. (2006). Time-resolved optical tomography using short-pulse laser for tumor detection. *Applied Optics*, 45, 6270–6282.
- Pedersen, G. D., McCormick, N. J., & Reynolds, L. O. (1976). Transport calculations for light scattering in blood. *Biophysical Journal*, 16, 199–207.
- Peraiah, A. (2002). *An introduction to radiative transfer: Methods and applications in astrophysics*. Cambridge University Press, Cambridge, UK.
- Peskin, M. E., & Schroeder, D. V. (1995). *An introduction to quantum field theory (frontiers in physics)*. Westview Press, Boulder, USA.
- Pomraning, G. C. (2005). *The Equations of radiation hydrodynamics*. Dover Publications Inc., New York, USA.

- Prasad, P. N. (2003). *Introduction to biophotonics*. John Wiley and Sons, New York, USA.
- Premaratne, M., Premaratne, E., & Lowery, A. (2005). The photon transport equation for turbid biological media with spatially varying isotropic refractive index. *Optics Express*, 13(2), 389–399.
- Press, W. H., Teukolsky, S. A., Vetterling, W. T., & Flannery, B. P. (2007). *Numerical recipes the art of scientific computing* (3rd ed.). Cambridge University Press, Cambridge, UK.
- Raithby, G. D., & Chui, E. H. (1990). A finite-volume method for predicting a radiant heat transfer enclosures with participating media. *ASME Journal of Heat Transfer*, 112, 415–423.
- Rath, P., Mishra, S. C., Mahanta, P., Saha, U. K., & Mitra, K. (2003). Discrete transfer method applied to transient radiative transfer problems in participating medium. *Numerical Heat Transfer, Part A: Applications*, 44, 183–197.
- Reynolds, L. O., & McCormick, N. J. (1980). Approximate two-parameter phase function for light scattering. *Journal of Optical Society of America A*, 70, 1206–1212.
- Rukolaine, S. A., Vasilyev, M. G., Yuferev, V. S., & Galyukov, A. O. (2002). Numerical solution of axisymmetric radiative heat transfer problems in arbitrary domains using the characteristic method. *Journal of Quantitative Spectroscopy & Radiative Transfer*, 73, 205–217.
- Rybicki, G. B., & Lightman, A. P. (2004). *Radiative processes in astrophysics*. Wiley–VCH, Berlin, Germany.
- Sadat, H. (2006). On the use of a meshless method for solving radiative transfer with discrete ordinates formulations. *Journal of Quantitative Spectroscopy & Radiative Transfer*, 101, 263–268.
- Sakami, M., Mitra, K., & Hsu, P.-F. (2000). Transient radiative transfer in anisotropically scattering media using monotonicity-preserving schemes. *Proceedings of the ASME*, 366, 135–143.
- Sakami, S., Mitra, K., & Hsu, P.-F. (2002). Analysis of light transport through two-dimensional scattering and absorbing media. *Journal of Quantitative Spectroscopy & Radiative Transfer*, 73, 169–179.
- Sasse, C., Konigsdorff, R., & Frank, S. (1995). Evaluation of an improved hybrid six-flux/zone model for radiative transfer in rectangular enclosures. *International Journal of Heat and Mass Transfer*, 38, 3423–3431.
- Saterbak, A., McIntire, L. V., & San, K.-Y. (2007). *Bioengineering fundamentals*. Pearson Prentice Hall, New Jersey, USA.
- Sawetprawichkul, A., Hsu, P.-F., Mitra, K., & Sakami, M. (2000). A monte carlo study of transient radiative transfer within the one-dimensional multi-layered slab. *Proceedings of the ASME*, 366, 145–153.
- Schuster, A. (1905). Radiation through a foggy atmosphere. *Astrophysical Journal*, 21, 1–22.
- Sharma, S. K., Roy, A. K., & Somerford, D. J. (1998). New approximate phase functions for scattering of unpolarized light by dielectric particles. *Journal of Quantitative Spectroscopy & Radiative Transfer*, 60, 1001–1010.
- Sobolev, V. V., & Gaposchkin, S. I. (1963). *A treatise on radiative transfer*. Van Nostrand, New York, USA.
- Svaasand, L. O., & Gomer, C. J. (1990). Chapter optics in tissue. In G. J. Müller & D. H. Sliney (Eds.), *Dosimetry of laser radiation in medicine and biology* (vol. IS-5, pp. 114–132). Bellingham: SPIE Optical Engineering.
- Tan, J. Y., Liu, L. H., & Li, B. X. (2006). Least-squares collocation meshless approach for transient radiative transfer. *Journal of Thermophysics and Heat Transfer*, 20, 912–918.
- Tan, Z.-M., & Hsu, P.-F. (2001). An integral formulation of transient radiative transfer. *ASME Journal of Heat Transfer*, 123, 466–475.
- Thomas, G. E., & Stammes, K. (1999). *Radiative transfer in the atmosphere and ocean*. Cambridge University Press, Cambridge, UK.

- Tuchin, V. (2007). *Tissue optics: Light scattering methods and instruments for medical diagnosis* (2nd ed.). SPIE Publications.
- Tuchin, V. V. (1997). Light scattering study of tissues. *Physics—Uspekhi*, 40(5), 495–515.
- van de Hulst, H. C. (1981). *Light scattering by small particles*. New York: Dover.
- van de Hulst, H. C., & Graaff, R. (1996). Aspects of similarity in tissue optics with strong forward scattering. *Physics in Medicine and Biology*, 41, 2519–2531.
- Waters, K. R., Mobley, J., & Miller, J. G. (2005). Causality-imposed (kramers-kronig) relationships between attenuation and dispersion. *IEEE Transactions on Ultrasonics, Ferroelectrics, and Frequency Control*, 52, 822–833.
- Webb, R. H. (1996). Confocal optical microscopy. *Reports on Progress in Physics*, 59, 427–471.
- Welch, A. J., & van Gemert, M. J. C. (Eds.). (1995). *Optical-response of laser-irradiated tissue (lasers, photonics, and electro-optics)*. Springer, New York, USA.
- Wilson, C. B., Tuchin, V. V., & Tanev, S. (2005). *Advances in biophotonics*. IOS Press, Amsterdam, Netherlands.
- Wolf, E. (2007). *Introduction to the theory of coherence and polarization of light*. Cambridge University Press, Cambridge, UK.
- Wu, C. Y., & Ou, N. R. (2002). Differential approximation for transient radiative transfer through a participating medium exposed to collimated irradiation. *Journal of Quantitative Spectroscopy & Radiative Transfer*, 73, 111–120.
- Wu, C.-Y., & Wu, S.-H. (2000a). Integral equation formulation for transient radiative transfer in an anisotropically scattering medium. *International Journal of Heat and Mass Transfer*, 43, 2009–2020.
- Wu, S.-H., & Wu, C.-Y. (2000b). Integral equation solution for transient radiative transfer in nonhomogeneous anisotropically scattering media. *ASME Journal of Heat Transfer*, 122, 818–822.
- Yaroslavsky, A. N., Yaroslavsky, I. V., Goldbach, T., & Schwarzmaier, H.-J. (1997). Different phase-function approximations to determine optical properties of blood: A comparison. *Proceedings of SPIE*, 2982, 324–330.
- Yoo, K. M., Liu, F., & Alfano, R. R. (1990). Biological materials probed by the temporal and angular profiles of the backscattered ultrafast laser pulses. *Journal of Optical Society of America B*, 7, 1685–1693.
- Yoon, G. (1988). *Absorption and scattering of laser light in biological media—mathematical modeling and methods for determining optical properties*. PhD thesis, University of Texas at Austin.
- Yun, S. H., Tearney, B. J., de Boer, J. F., Iftimia, N., & Bouma, B. E. (2003). High-speed optical frequency-domain imaging. *Optics Express*, 11, 2953–2963.

This page intentionally left blank

CHAPTER 2

Manipulating Light States by Single-Photon Addition and Subtraction

Marco Bellini^{a,b} and Alessandro Zavatta^{a,b}

^{a,b}*Istituto Nazionale di Ottica (INO - CNR), Florence, Italy*

^{a,b}*LENS and Department of Physics, University of Firenze,
Florence, Italy*

Contents		
1.	Introduction	42
2.	Single-Photon Operators for Manipulating Quantum Information	43
2.1.	Continuous-Variable Quantum State Engineering	43
2.2.	Unified Treatment of Experimental Single-Photon Addition and Subtraction Implementations	44
3.	Single-Photon Addition	48
3.1.	Single-Photon-Added Coherent States	49
3.2.	Single-Photon-Added Thermal States	53
3.3.	Tests of Nonclassicality	56
4.	Single-Photon Subtraction	61
4.1.	Photon Subtraction from Arbitrary Light States	61
4.2.	De-Gaussification of Squeezed States and Generation of Schrödinger's Kittens	64
4.3.	Increasing Entanglement and Nonlocality by Single-Photon Subtraction	69
5.	Sequences and Superpositions of Single-Photon Operators	72
5.1.	Sequences of Creation and Annihilation Operators	72
5.2.	Superpositions of Quantum Operators	73

6. Conclusions	76
7. Acknowledgments	77
A. Quantum Tomography	77
References	79

1. INTRODUCTION

The annihilation operator \hat{a} and its creation counterpart \hat{a}^\dagger operate on a state with a precisely defined number of excitation quanta (a so-called Fock or number state $|n\rangle$) by decreasing or increasing this number by exactly one unit, according to

$$\hat{a}|n\rangle = \sqrt{n}|n-1\rangle \quad (1.1)$$

$$\hat{a}^\dagger|n\rangle = \sqrt{n+1}|n+1\rangle. \quad (1.2)$$

Differently from the conventional deterministic addition and subtraction of objects from an ensemble, the creation and annihilation operators work in a probabilistic way, i.e., the probability of success is proportional to the number of particles originally present in the state because of the \sqrt{n} and $\sqrt{n+1}$ terms in Equations (1.1) and (1.2). Accordingly, for a general state being in a given superposition or mixture of Fock states, the application of the \hat{a} and \hat{a}^\dagger operators not only shifts the excitation number distribution by one unit toward lower or higher values, but also deeply reshapes it by increasing the weight of terms containing a higher number of excitation quanta.

Even if creating and annihilating quanta with the \hat{a}^\dagger and \hat{a} operators is, thus, quite different from a classical deterministic addition or removal of a single object from an ensemble, the application of \hat{a}^\dagger and \hat{a} is nevertheless often referred to as single-photon “addition” and “subtraction” in the case of light fields. Here we will keep using this notation while pointing out that it may be somewhat misleading if interpreted in strictly classical terms (further discussions on the interpretation of the general process of photon addition and subtraction, especially in the context of photodetection, can be found in, e.g., Mollow, 1968; Moya-Cessa, Chavez-Cerda, & Vogel, 1999; Srinivas & Davies, 1981). As a simple example, the fact that \hat{a} operates differently from a classical picture of particle subtraction is evident from the observation that, by definition, coherent states do not change under such an operation.

Although the effect of photon addition and subtraction on light states has been discussed for a long time (Agarwal & Tara, 1991, 1992), neither operation was experimentally demonstrated till recently. In 2004, Wenger, Tualle-Brouri, & Grangier (2004) were able to subtract a single photon from a traveling field using a beam-splitter and a photodetector. In the same year, a single-photon addition scheme was demonstrated by Zavatta,

Viciani, & Bellini (2004a). Since then, these basic quantum operations have been applied to several classical and nonclassical light states, and very recently, the possibility to combine them in sequences (Parigi, Zavatta, Kim, & Bellini, 2007) and coherent superpositions (Zavatta, Parigi, Kim, Jeong, & Bellini, 2009) has been demonstrated.

2. SINGLE-PHOTON OPERATORS FOR MANIPULATING QUANTUM INFORMATION

2.1. Continuous-Variable Quantum State Engineering

Quantum information protocols like quantum teleportation, quantum cloning, and quantum cryptography, mainly devised for spin-1/2 systems (especially polarization-entangled photons) can be efficiently realized also in the continuous-variable (CV) regime. Here, the quadratures $\hat{x} = (\hat{a} + \hat{a}^\dagger)/2$ and $\hat{y} = i(\hat{a}^\dagger - \hat{a})/2$, describing the single-mode light field, assume a range of continuous values and can be used to encode the quantum information. In this regime, particular attention has been devoted to the so-called Gaussian states, which are those with a Gaussian Wigner function and include squeezed, coherent, and thermal states (Braunstein & van Loock, 2005). However, non-Gaussian states and operations are now increasingly viewed as fundamental ingredients for continuous-variable quantum technologies. Eisert, Scheel, and Plenio (2002), Fiurášek (2002) and Giedke and Cirac (2002) demonstrated that Gaussian states and Gaussian operations (linear optical elements and squeezers) are not a sufficient resource to perform important communication tasks like entanglement distillation. However, recent results have shown that this is possible by using non-Gaussian states (Dong et al., 2008; Hage et al., 2008) or non-Gaussian operations (Takahashi et al., 2008). Furthermore, Cerf, Krüger, Navez, Werner, and Wolf (2005) showed that the cloning of coherent states achieved by a non-Gaussian bimodal state is optimal. The growing interest in applications of non-Gaussian states is also demonstrated by the growing need of defining a measure for the non-Gaussian character of a quantum state (Genoni, Paris, & Banaszek, 2007).

The basic quantum processes of photon addition and subtraction are formidable tools for generating non-Gaussian and highly nonclassical states. Besides their implications for advanced quantum information protocols and emerging quantum technologies (e.g., Adesso, Dell'Anno, Siena, Illuminati, & Souza, 2009), they have recently shown their huge potential for completely engineering quantum light states and testing the foundations of quantum physics.

The use of photon subtraction was first proposed by Opatrný, Kurizki, and Welsch (2000) as a conditional measurement to increase the degree of entanglement of a two-mode state and its effectiveness in CV teleportation. Here, photon subtraction selects a subensemble of more entangled

states from a two-mode squeezed (or Einstein–Podolsky–Rosen, EPR) state generated by a parametric amplifier, thus leading to an improvement of the fidelity in CV teleportation (Cochrane, Ralph, & Milburn, 2002; Olivares, Paris, & Bonifacio, 2003). The annihilation of a single photon from a quantum state does not produce nonclassicality by itself but is, however, able to convert Gaussian states into non-Gaussian ones (Kim, Park, Knight, & Jeong, 2005; Wenger et al., 2004). Recently, the use of single-photon annihilation as a tool to produce non-Gaussian CV light states has been proposed and demonstrated (Ourjoumtsev, Tualle-Brouri, Laurat, & Grangier, 2006; Parigi et al. 2007; Wenger et al. 2004). However, in order to turn any classical state into a nonclassical and non-Gaussian state, one just needs to excite it by a single quantum with a photon-addition operation (Agarwal & Tara, 1991; Zavatta, Parigi, & Bellini, 2007; Zavatta et al. 2004a, 2005). Dakna, Clausen, Knöll, and Welsch (1999) proved that any single-mode quantum state can be generated starting from the vacuum state with alternate application of the displacement and the creation operator. More recently, Fiurášek, García-Patrón, and Cerf (2005) showed that a similar degree of control on state generation can be achieved by means of squeezing and photon subtraction.

The realization of the Schrödinger cat-like states, together with the complete quantum state engineering by conditional measurement on a beam splitter were proposed by Dakna, Anhut, Opatrný, Knöll, and Welsch (1997) and Dakna, Knöll, and Welsch (1998). Based on these seminal ideas, the realization of nonclassical superpositions of coherent states has been achieved in several experimental configurations (Neergaard-Nielsen, Nielsen, Hettich, Molmer, & Polzik, 2006; Ourjoumtsev, Dantan, Tualle-Brouri, & Grangier, 2007; Ourjoumtsev, Ferreyrol, Tualle-Brouri, & Grangier, 2009; Ourjoumtsev et al. 2006; Wakui, Takahashi, Furusawa, & Sasaki, 2007) and new proposals for generating arbitrary state superpositions have recently appeared (Marek, Jeong, & Kim, 2008; Takeoka & Sasaki, 2007).

Even more recently, the combination of the elementary operations of photon addition and subtraction has been also proposed as a tool to implement several useful quantum operations on light states, including Kerr nonlinearities and noiseless linear amplification (Fiurášek, 2009; Marek & Filip, 2010). A few exciting experiments along these new lines have just started to appear (Usuga et al., 2010; Zavatta, Fiurášek, & Bellini, 2010).

2.2. Unified Treatment of Experimental Single-Photon Addition and Subtraction Implementations

Although different proposals have been put forward for the experimental implementation of single-photon addition and subtraction operations (Dakna et al., 1998; Kim, 2008), so far, only two approaches have

demonstrated their feasibility in experiments and have been extensively used to manipulate the light states. Both schemes involve a probabilistic realization of the quantum operations, conditioned on the detection of a single photon in an ancillary mode. These conditional schemes have already proved successful for the generation of single-photon Fock states (Lvovsky et al., 2001; Zavatta, Viciani, & Bellini, 2004b) and constitute the main idea behind the proposal of measurement-induced nonlinearities in linear-optics quantum computation (Knill, Laflamme, & Milburn, 2001).

The main devices for the implementation of the creation and annihilation operators are the parametric down-converter and the beam-splitter, schematically shown in Figure 1. Although apparently quite different, they share a very similar quantum description, and the explanation of their inner working will follow strictly parallel routes.

A parametric down-conversion (PDC) crystal produces pairs of daughter photons from a single pump one. Because the energy and momentum conservation laws have to be obeyed in the process, the spatiotemporal characteristics of the emitted photons are highly quantum correlated. The detection of one photon of the pair in a particular mode then precisely localizes the twin photon in space and time if the pump characteristics are well known.

Given the interaction Hamiltonian

$$\hat{H}_{\text{PDC}} = -i\hbar g(\hat{a}\hat{b} - \hat{a}^\dagger\hat{b}^\dagger), \quad (2.1)$$

where \hat{a} and \hat{b} represent the annihilation operators of modes a and b , respectively, and g accounts for the $\chi^{(2)}$ nonlinearity of the crystal and the amplitude of the pump field (assumed undepleted), the corresponding

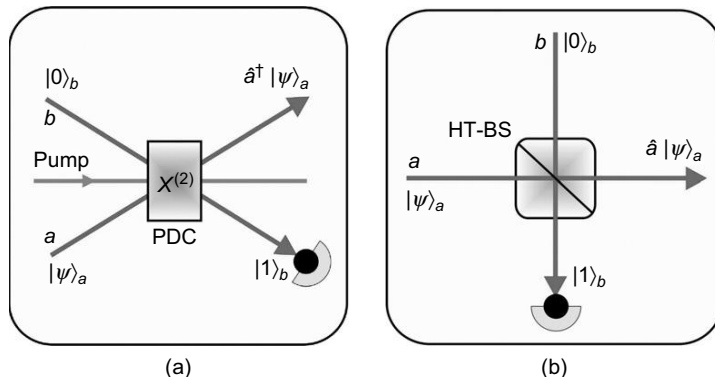


FIGURE 1 Scheme of the experimental devices for the implementation of the creation and annihilation operators. (a) PDC: parametric down-conversion. (b) HT-BS: high-transmission beam-splitter.

two-mode squeezing or parametric down-conversion operator is

$$\hat{S} = e^{-\lambda(\hat{a}\hat{b} - \hat{a}^\dagger\hat{b}^\dagger)} \quad (2.2)$$

with $\lambda = gt$. If the coupling is not too strong ($\lambda \ll 1$) and one of the input modes is initially empty (i.e., the input b mode is in the vacuum state $|0\rangle_b$), the first-order perturbation theory predicts that the output state has the form:

$$|\psi_{\text{out}}\rangle \approx \left[1 - \lambda(\hat{a}\hat{b} - \hat{a}^\dagger\hat{b}^\dagger) \right] |\psi\rangle_a |0\rangle_b \approx |\psi\rangle_a |0\rangle_b + \lambda\hat{a}^\dagger|\psi\rangle_a |1\rangle_b, \quad (2.3)$$

where a pure state $|\psi\rangle_a$ has been assumed for simplicity at the input mode a of the parametric crystal. Although most of the times no down-conversion occurs and the input state is unchanged, the rare occurrence of a single photon in the output mode b (also defined the *idler* or *trigger* mode in the following) leaves the output mode a (defined as the *signal* mode in the following) in a single-photon-excited version of the input state. Thus, one has conditionally implemented the action of the creation operator \hat{a}^\dagger onto the initial state $|\psi\rangle_a$.

For a generic signal input, the output state of the parametric amplifier can be written as

$$\hat{\rho}_{\text{out}} = \sum_m P_m |\psi_{\text{out}_m}\rangle \langle \psi_{\text{out}_m}|, \quad (2.4)$$

where the input mixed state is $\hat{\rho} = \sum_m P_m |\psi_m\rangle \langle \psi_m|$ and P_m is the probability for the state $|\psi_m\rangle$. If we condition the preparation of the signal state to single-photon detection on the idler channel, we obtain the desired photon-added state

$$\hat{\rho}_a^{(add)} = \text{Tr}_b(\hat{\rho}_{\text{out}} |1\rangle_b \langle 1|) = |g|^2 \hat{a}^\dagger \hat{\rho} \hat{a}. \quad (2.5)$$

A similar description can be used for the effect of a beam-splitter (BS) on two input states, one of which is the vacuum. The expression for the beam-splitter operator

$$\hat{B} = e^{-\theta(\hat{a}^\dagger\hat{b} - \hat{a}\hat{b}^\dagger)} \quad (2.6)$$

where $R = \sin^2(\theta)$ is the intensity reflectivity, looks very similar to Equation (2.2) and, indeed, when the reflectivity is low enough ($\theta \ll 1$), the

detection of a single photon in its output mode b projects the other output mode a in a photon-subtracted version of the initial state:

$$|\psi_{\text{out}}\rangle \approx \left[1 - \theta(\hat{a}^\dagger \hat{b} - \hat{a}\hat{b}^\dagger) \right] |\psi\rangle_a |0\rangle_b \approx |\psi\rangle_a |0\rangle_b + \theta \hat{a} |\psi\rangle_a |1\rangle_b \quad (2.7)$$

and thus implements the action of the annihilation operator \hat{a} onto the input state in mode a .

In the more general case of mixed input states and realistic single-photon detectors, the discussions above may be taken to the next level. By indicating the input state in mode a by its density matrix operator $\hat{\rho}_a$, and describing the on-off photodetection process (i.e., the action of a real avalanche-type detector, which is able to discern there being photons but is not able to discriminate how many) in output mode b with the operator $\hat{M}_b = \mathbf{1} - |0\rangle_b \langle 0|$, then the output state in mode a is given by:

$$\hat{\rho}_a^{(\text{out})} = \mathcal{N} \text{Tr}_b (\hat{M}_b \hat{U} \hat{\rho}_a |0\rangle_b \langle 0| \hat{U}^\dagger) \quad (2.8)$$

where the operator \hat{U} stands for the PDC or BS operators introduced above according to the process we are considering (see Figure 2 for a general scheme of this conditional photon addition/subtraction implementation).

An analytic expression for the output states can be obtained by a Taylor expansion (Kim, 2008) of \hat{U} in Equation (2.8) under the condition that both the beam-splitter reflectivity and the crystal parametric gain are very low ($\lambda, \theta \ll 1$). In these conditions, the density matrices for the output states,

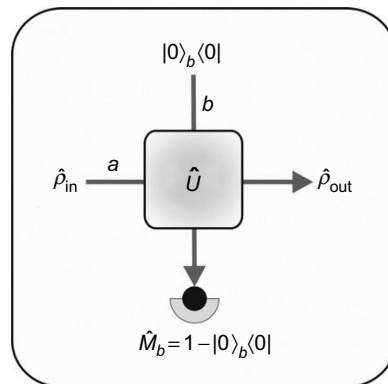


FIGURE 2 General scheme for the implementation of conditional photon addition/subtraction.

truncated to $O(\lambda^5)$ and $O(\theta^5)$ are

$$\hat{\rho}_a^{(\text{add})} = \mathcal{N} \left(\left(\lambda^2 + \frac{\lambda^4}{3} \right) \hat{a}^\dagger \hat{\rho}_a \hat{a} - \frac{\lambda^4}{2} \left(\hat{a}^\dagger \hat{\rho}_a \hat{a} \hat{a} \hat{a}^\dagger + \hat{a} \hat{a}^\dagger \hat{a}^\dagger \hat{\rho}_a \hat{a} - \hat{a}^\dagger \hat{a}^\dagger \hat{\rho}_a \hat{a} \hat{a} \right) \right) \quad (2.9)$$

$$\hat{\rho}_a^{(\text{sub})} = \mathcal{N} \left(\left(\frac{\theta^2}{4} - \frac{\theta^4}{48} \right) \hat{a} \hat{\rho}_a \hat{a}^\dagger - \frac{\theta^4}{32} \left(\hat{a} \hat{\rho}_a \hat{a}^\dagger \hat{a}^\dagger \hat{a} + \hat{a}^\dagger \hat{a} \hat{a} \hat{\rho}_a \hat{a}^\dagger - \hat{a} \hat{a} \hat{\rho}_a \hat{a}^\dagger \hat{a}^\dagger \right) \right) \quad (2.10)$$

for the addition and subtraction cases, respectively. When the probability of there being a large number of photons is negligible, only the first term dominates in Equations (2.9) and (2.10), showing that these experimental approaches are indeed good implementations of the action of single-photon creation and annihilation operators \hat{a}^\dagger and \hat{a} on arbitrary light states. This is normally the case in all the experiments reported later; however, when dealing with large numbers of photons, one has to take care because the other terms in the expansion start to acquire weight and the experimental states may digress from the desired ones (a more complete description of the process, without these assumptions, can be found in Dodonov & Mizrahi (2009) and Hayrynen, Oksanen, & Tulkki (2009)).

3. SINGLE-PHOTON ADDITION

The operation of adding a single quantum of excitation to an arbitrary light field automatically converts it into a nonclassical state. The simple removal of the vacuum contribution in the photon number probability distribution is enough to generate nonclassicality, as demonstrated by Lee (1995). Of course, the effect is stronger for states that have a significant vacuum component to start from, whereas it may be almost unnoticeable for states with larger intensities. Therefore, single-photon addition is a very attractive tool for generating quantum states with different degrees of nonclassicality and explore the boundary between classical and quantum behavior (Zavatta et al., 2004a, 2005). It may also be used to put to a stringent test different experimental criteria to measure the nonclassical character of a state (Zavatta et al., 2007).

It is very interesting to note that the addition of a single photon to a field by means of the creation operator \hat{a}^\dagger can be seen as the fundamental event of stimulated emission. Going back to Equation (2.3), in the case of vacuum injection, one is dealing with plain spontaneous emission of photons into unoccupied modes, and the probability of this process to happen is proportional to $|\lambda|^2$. However, it is easy to see that, given a pure seed field $|\psi\rangle$, the probability of success of the addition event is $|\lambda|^2(1 + \bar{n})$, where

$\bar{n} = \langle \psi | \hat{a}^\dagger \hat{a} | \psi \rangle$ is the average number of photons in the input state (this can be straightforwardly shown to hold also for a generic input mixed state). As Einstein predicted, the probability of stimulated emission of photons into a well-defined mode scales as the number of photons already there. Therefore, by following the evolution of the photon-added output state while the input field intensity increases starting from vacuum, one can directly witness the gradual transition from the spontaneous to the stimulated regimes of light emission.

Quite interestingly, this effect can also be used to obtain an absolute experimental calibration of the intensity of the seed fields injected in the PDC signal mode by measuring the rate of counts in the idler channel and comparing it with the unseeded case. As shown earlier, the ratio of such rates equals $(1 + \bar{n})$, due to the enhancement of emission probability characteristic of stimulated emission in bosonic fields, and the mean number of photons in the input field can thus be easily measured. The same scheme was originally proposed by Klyshko (1977) as a metrological tool for absolute radiance measurements (Kitaeva, Penin, Fadeev, & Yanait, 1979; Migdall, 1999).

3.1. Single-Photon-Added Coherent States

A coherent state $|\alpha\rangle$, the eigenstate of the photon annihilation operator $\hat{a}|\alpha\rangle = \alpha|\alpha\rangle$ by definition (Glauber, 1963), is the closest analog to a classical light field and exhibits a Poisson photon number distribution with an average photon number of $|\alpha|^2$ and a width of $|\alpha|$. Coherent states possess well-defined amplitude and phase, whose uncertainties are the minimum permitted by the Heisenberg uncertainty principle. On the contrary, a Fock state, the eigenstate of the photon number operator $\hat{a}^\dagger \hat{a}|n\rangle = n|n\rangle$, is obtained by repeated application of the creation operator \hat{a}^\dagger onto the vacuum state $|0\rangle$, contains a perfectly defined number of quanta of field excitation, and is strictly quantum-mechanical, with no classical analog. Moreover, being the intensity of a Fock state defined without uncertainty, its phase is completely undefined.

In 1991, Agarwal and Tara (1991) introduced a new class of states, defined by the repeated (m times) application of the photon creation operator \hat{a}^\dagger to the coherent state,

$$|\alpha, m\rangle \propto \hat{a}^{\dagger m} |\alpha\rangle. \quad (3.1)$$

Such photon-added coherent states essentially represent the result of successive elementary one-photon excitations of a classical coherent field and occupy an intermediate position between the Fock and the coherent states, reducing to the two limit cases for $\alpha \rightarrow 0$ or $m \rightarrow 0$, respectively. When

just a single quantum of field excitation is added to a coherent field, the single-photon-added coherent state (SPACS) reads as follows:

$$|\alpha, 1\rangle = \frac{\hat{a}^\dagger |\alpha\rangle}{\sqrt{1 + |\alpha|^2}}. \quad (3.2)$$

SPACSSs can be expanded in terms of Fock states as

$$|\alpha, 1\rangle = \frac{e^{-\frac{|\alpha|^2}{2}}}{\sqrt{1 + |\alpha|^2}} \sum_{n=0}^{\infty} \frac{\alpha^n}{\sqrt{n!}} \sqrt{n+1} |n+1\rangle \quad (3.3)$$

where the lack of the vacuum term contribution is evident. Accordingly, the density matrix elements for the SPACSSs are

$$\rho_{ij} = \langle i | \hat{\rho} | j \rangle = \frac{ij}{\sqrt{i!j!}} \frac{e^{-\frac{|\alpha|^2}{2}}}{1 + |\alpha|^2} \alpha^{(i-1)} \alpha^{*(j-1)} \quad (3.4)$$

and the effect of single-photon excitation can be readily observed in the plots of Figure 4(a) where the absolute value of the theoretical matrix elements are reported for the single-photon Fock state and for a SPACS derived from a coherent state with $\alpha \approx 1$.

Unlike the operation of photon annihilation, the single-photon excitation of a coherent state changes it into something quite different, especially for low values of α , where the absence of the vacuum term has a stronger impact. In the extreme case of an initial vacuum state $|0\rangle$, the addition of one photon, indeed, transforms it into the very nonclassical single-photon Fock state $|1\rangle$, which exhibits negative values of the Wigner function around the origin. On the opposite extreme, it is quite intuitive that the addition of a single photon to an intense coherent field should not change much its classical wave-like character. So, by simply varying the amplitude α of the initial coherent state, the character of the final state can be continuously tuned between completely quantum and almost completely classical. This allows one to closely follow the evolution of the generated state from a particle-like one, characterized by a circularly symmetric and negative-valued single-photon Wigner function, through an intermediate region characterized by the gradual appearance of a phase, toward the wave-like classical coherent state (see Zavatta et al., 2004a,b).

The Wigner function for a single-photon-added coherent state of arbitrary amplitude α can be expressed as follows:

$$W(z) = \frac{-2(1 - |2z - \alpha|^2)}{\pi(1 + |\alpha|^2)} e^{-2|z - \alpha|^2} \quad (3.5)$$

(where $z = x + iy$) and can clearly become negative, a proof of its nonclassical character, whenever the condition

$$|2z - \alpha|^2 < 1 \quad (3.6)$$

is satisfied. In addition to the negativity of the Wigner function, SPACSS also exhibit a definite squeezing in their field quadratures that can be readily observed. Given a generic field quadrature $\hat{x}_\theta = \frac{1}{2}(\hat{a}e^{-i\theta} + \hat{a}^\dagger e^{i\theta})$, its fluctuations amount to

$$[\Delta x_\theta]_\alpha^2 = \langle x_\theta^2 \rangle_\alpha - \langle x_\theta \rangle_\alpha^2 = \frac{1}{4} + \frac{1 - |\alpha|^2 \cos(2\theta)}{2(1 + |\alpha|^2)^2}. \quad (3.7)$$

Clearly, the quadrature obtained by choosing $\theta = 0$ exhibits reduced fluctuations with respect to the coherent state for $|\alpha| > 1$, and is thus squeezed. It is interesting to note that, differently from Fock and Gaussian squeezed states, SPACSS combine both the key features normally associated to quantum states: the negativity of the Wigner function and the reduced fluctuations along one quadrature.

The experimental apparatus used to generate and analyze the SPACS is schematically drawn in Figure 3. A mode-locked Ti:sapphire laser, emitting 1.5-ps long pulses at 786 nm and at a repetition rate of 82 MHz is used as the primary source. The laser pulses are frequency doubled to 393 nm in a LBO crystal (Ramazza, Ducci, Zavatta, Bellini, & Arecchi, 2002). The UV beam then serves as a pump for a 3-mm thick, type-I BBO crystal which generates spontaneous parametric down-conversion (SPDC) at the same wavelength of the laser source. The crystal is slightly tilted from the collinear configuration in order to obtain an exit cone beam with an angle of $\sim 3^\circ$ from which symmetric signal and idler modes are roughly selected by means of irises.

In order to remotely select a pure state on the signal channel, idler photons undergo narrow spatial and frequency filtering before detection; indeed the remotely prepared signal state will only approach a pure state if the filter transmission function is much narrower than the momentum and spectral widths of the pump beam generating the SPDC pair (Aichele, Lvovsky, & Schiller, 2002; Bellini, Marin, Viciani, Zavatta, & Arecchi, 2003; Ou, 1997; Viciani, Zavatta, & Bellini, 2004). The idler beam is, thus, passed through a pair of etalon interference filters, which perform a narrow spectral selection and is then coupled into a single-spatial-mode fiber before impinging onto an on-off photodetector.

The weak coherent state α is obtained by controlled attenuation (VF in the figure) of a small portion of the laser emission, which is fed into the signal mode of the parametric crystal and is then directed to a 50/50

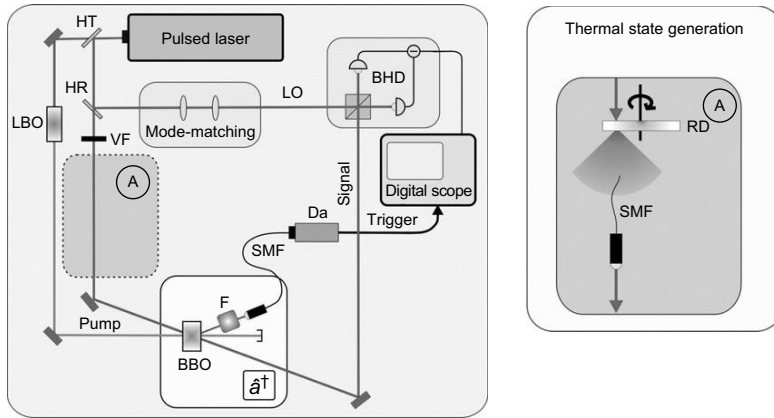


FIGURE 3 Experimental apparatus for conditional single-photon addition: HT (HR): high-transmission (high-reflection) beam-splitter; LBO: lithium triborate crystal; VF: variable attenuation filter; BBO-I: type-I β -barium borate down-converter crystal; BHD: balanced homodyne detector; F: spectral filter; Da: single-photon counting module; LO: local oscillator; SMF: single-mode fiber (spatial filter). Inset (A) shows the configuration for thermal state generation, which is included in the setup as described in Section 3.2. RD: rotating ground glass disk.

beam-splitter. Here it is overlapped with a second (intense) coherent state (again obtained from a portion of the original laser pulses), which is spatially mode-matched to the conditionally prepared SPACS by the insertion of appropriate lens combinations along its path and serves as the local oscillator (LO) for homodyne measurements (Reynaud, Heidmann, Giacobino, & Fabre, 1992). Measurements are performed at different values of the coherent seed amplitude $|\alpha|$; as seen earlier, a calibration of such an amplitude is simply obtained from a measurement of the increase in the idler count rate as described in Section 3.

In Figure 4, a sequence of reconstructed density matrices (b) and Wigner functions (c) (see Appendix 7, pattern function method) for SPACSSs is shown for two values of the seed coherent field amplitude $|\alpha|$. The first one (top of columns b and c), obtained with a blocked input, corresponds to the single-photon Fock state obtained by conditional preparation from the two-photon wavefunction of SPDC (Lvovsky et al., 2001; Zavatta et al., 2004b) and clearly exhibits classically impossible negative values around the center of the circularly symmetric (due to the undefined value of the phase) distribution. When the coherent seed is switched on, the Wigner function loses its circular symmetry while moving away from the origin because of the appearance of a defined phase, but it still exhibits a clear nonclassical nature as indicated by its partial negativity. For increasing seed amplitudes, the negativity gradually gets

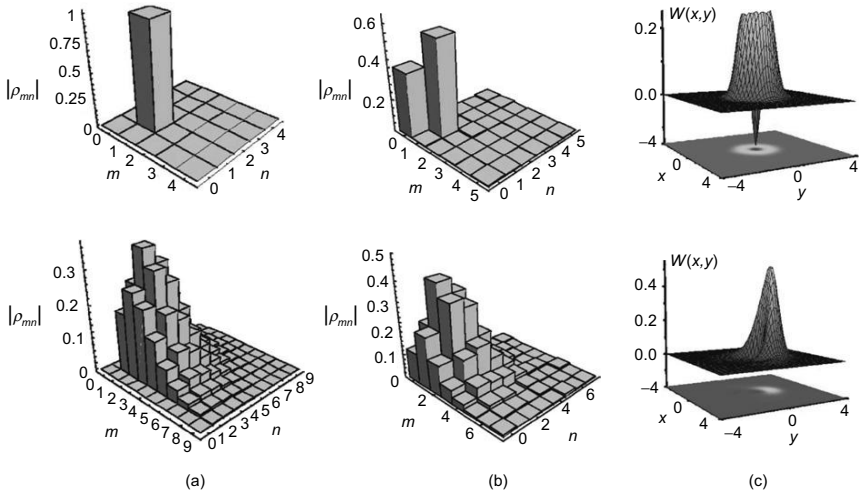


FIGURE 4 Column (a) Theoretical density matrices of SPACSSs for $|\alpha| = 0$, i.e., single-photon Fock state, and $|\alpha| = 1$ (bottom). Column (b) Experimental density matrices of SPACSSs as reconstructed from the experimental data with corresponding Wigner functions (column c) for $|\alpha| = 0$ and $|\alpha| = 0.95$.

less evident making it more and more similar to the Gaussian typical of a classical coherent field (Zavatta et al., 2004a).

When comparing the reconstructed Wigner functions and density matrix elements with the theoretical ones for the corresponding quantum states, one has to take into account the limited efficiency, which does not allow one to generate and analyze pure states but involves here some mixing with the vacuum. The limited efficiency enters both in the preparation of the quantum state (dark counts and the nonideal conditioning in the idler channel do not allow one to generate a pure state in the signal channel) and in the homodyne detection process (limited efficiency of the photodiodes and imperfect mode-matching of the signal field to the LO). The Wigner function and density matrix elements of SPACSSs in the presence of limited efficiency (i.e., vacuum contamination) have been reported by Zavatta et al. (2004b): it can be easily seen that the nonunit detection efficiency reduces the nonclassical character of experimentally observed SPACSSs and, especially for higher values of the seed amplitude $|\alpha|$, may completely mask it in the presence of reconstruction noise.

3.2. Single-Photon-Added Thermal States

Coherent states are still at the border between the quantum and classical behavior of light, so it is interesting to extend the earlier procedures for

producing nonclassical states by photon addition to real classical ones. The generation and the analysis of single-photon-added thermal states (SPATSS), i.e., completely classical states excited by a single photon, was first introduced and studied by Agarwal and Tara (1992). The peculiar nonclassical behavior of SPATSS has recently triggered an interesting debate (Diósi, 2000; Vogel, 2000) and has been described in several theoretical articles (Agarwal & Tara, 1992; Diósi, 2000; Jones, Haight, & Lee, 1997; Kim et al., 2005; Lee, 1995); their experimental generation has also been proposed with more complex schemes (Dakna et al., 1998; Jones et al., 1997; Kim et al., 2005).

When the input $\hat{\rho}$ of Equation (2.5) is a thermal state with mean photon number \bar{n} , one obtains that the single-photon-added thermal state is described by the following density operator expressed in the Fock base:

$$\hat{\rho}^{(\text{add})} = \frac{1}{\bar{n}(\bar{n} + 1)} \sum_{n=0}^{\infty} \left(\frac{\bar{n}}{1 + \bar{n}} \right)^n n|n\rangle\langle n|. \quad (3.8)$$

Again, the lack of the vacuum term and the rescaling of higher excited terms are evident in this expression. The P phase-space representation can be easily calculated and is given by Agarwal and Tara (1992)

$$P(z) = \frac{1}{\pi \bar{n}^3} \left[(1 + \bar{n})|z|^2 - \bar{n} \right] e^{-|z|^2/\bar{n}}, \quad (3.9)$$

while the corresponding Wigner function reads as

$$W(z) = \frac{2}{\pi} \frac{|2z|^2(1 + \bar{n}) - (1 + 2\bar{n})}{(1 + 2\bar{n})^3} e^{-2|z|^2/(1+2\bar{n})}. \quad (3.10)$$

Quite interestingly, SPATSS have a well-behaved P -function, which is always negative around $z = 0$; this feature is also present in the Wigner function and assures their nonclassicality. However, both $P(0)$ and $W(0)$ tend to zero in the limit of $\bar{n} \rightarrow \infty$.

The experimental setup used to produce SPATSS is very similar to the one described in Section 3.1. In order to avoid the technical problems connected to the handling of a true high-temperature thermal source, a pseudo-thermal one, obtained by inserting a rotating ground glass disk (RD) in a portion of the laser beam (see inset of Figure 3), was used. The scattered light forms a random spatial distribution of speckles whose average size is larger than the core diameter of a single-mode fiber used to collect it. When the ground glass disk rotates, light exits the fiber in a clean collimated spatial mode with random amplitude and phase fluctuations yielding the photon distribution typical of a thermal source (Arecchi,

1965). Indeed, if the rate of addition events is smaller than the inverse coherence time of the state (mainly dictated by the rotation speed of the disk), then photon addition is performed on a sequence of completely uncorrelated (both in amplitude and phase) coherent states, i.e., a thermal state by definition (Parigi, Zavatta, & Bellini, 2009).

Because the involved light states do not exhibit any phase dependence, homodyne data acquisition is performed without actively scanning the phase of the local oscillator. A maximum likelihood estimation (see Appendix 7) procedure is then used to reconstruct the diagonal density matrix elements of the states. The results are shown in Figure 5, together with the corresponding reconstructed Wigner functions for a given injected thermal state (Zavatta et al., 2005). One expects the measured negativity of the Wigner function at the origin to rapidly get smaller as the mean photon number of the input thermal state is increased. With the level of efficiency and reconstruction accuracy reported in Zavatta et al. (2005), one may expect to experimentally detect Wigner function negativity above the reconstruction noise, and thus prove the state non-classicality, up to about $\bar{n} \approx 1.5$ (also see Figure 6(a)). However, it should be noted that, even for a single-photon Fock state, the Wigner function loses its negativity for efficiencies lower than 50%, so that surpassing

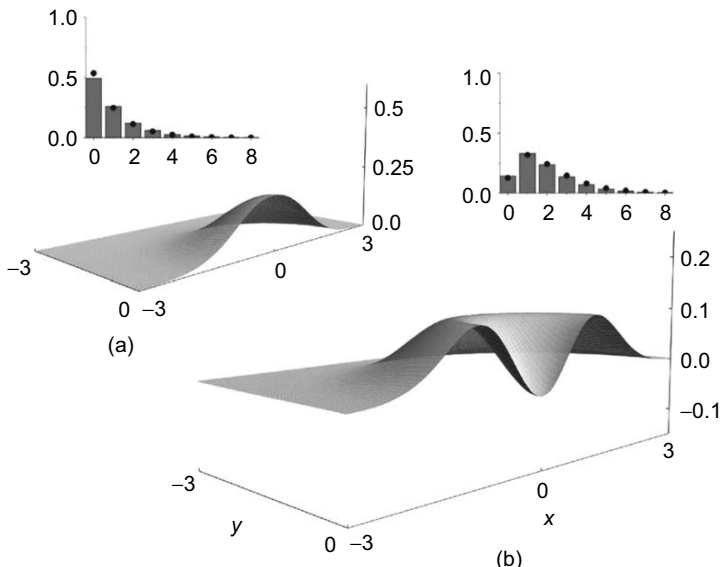


FIGURE 5 Experimentally reconstructed diagonal density matrix elements and Wigner functions for thermal states (a) and SPATSSs (b) with $\bar{n} = 1.15$. Filled circles indicate the density matrix elements calculated for thermal states and SPATSSs with the expected efficiencies.

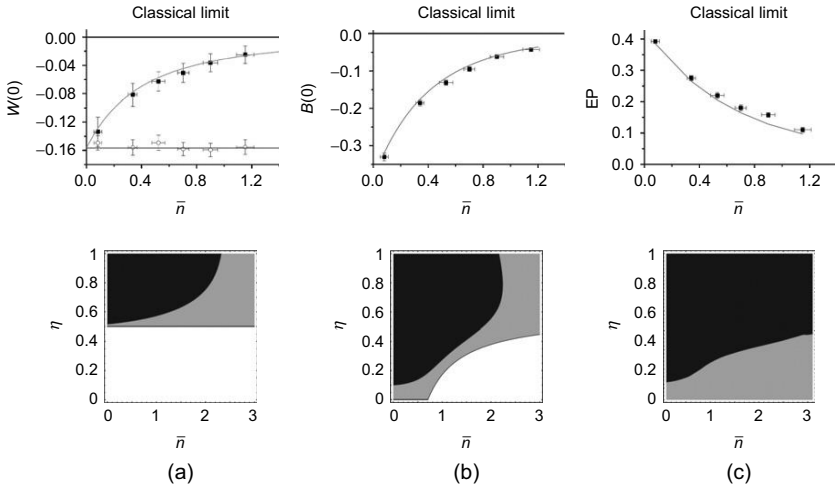


FIGURE 6 (a) Experimental values for the minimum of the Wigner function $W(0)$ as a function of \bar{n} for SPATSs (solid squares) and for single-photon Fock states (empty circles). (b) Experimental data (squares) and calculated values (solid curve) of $B(0)$ (see text): negative values indicate nonclassicality of the state. (c) The same as above for the entanglement potential (EP) of the SPATSs; here nonclassicality is demonstrated by EP values greater than zero. Contour plots in the lower panels show the calculated regions of nonclassical behavior of SPATSs as a function of \bar{n} and η according to the different criteria. White areas indicate classical behavior; grey areas indicate where a potentially nonclassical character is not measurable because of the experimental reconstruction noise (estimated as the average error on the experimentally reconstructed parameters); black areas indicate regions where the nonclassical character is measurable given the current statistical uncertainties.

this experimental threshold is an essential requisite in order to use this nonclassicality criterion.

3.3. Tests of Nonclassicality

The definition and the measurement of the nonclassicality of a quantum light state is an important and widely discussed topic in the quantum information community; nonclassical light is the starting point for generating even more nonclassical states (Jeong, Lund, & Ralph, 2005; Lund, Jeong, Ralph, & Kim, 2004) or producing the entanglement that is essential to implement quantum information protocols with continuous variables (Braunstein & van Loock, 2005; Kim, Son, Bužek, & Knight, 2002).

A variety of nonclassical states has recently been characterized by means of the negativeness of their Wigner function (Lvovsky et al., 2001;

Zavatta et al., 2004a,b, 2005), but this is just a sufficient and not necessary condition for nonclassicality; for instance, squeezed states are nonclassical, but they possess a positive Wigner function (Lvovsky & Shapiro, 2002). Therefore, it is still an open question which is the universal way to experimentally characterize the nonclassicality of a quantum state.

In general, a quantum state is said to be nonclassical when it cannot be written as a mixture of coherent states. A general mixed quantum state $\hat{\rho}$ can be characterized by the Glauber–Sudarshan P -function (Glauber, 1963; Sudarshan, 1963)

$$\hat{\rho} = \int d^2\alpha P(\alpha)|\alpha\rangle\langle\alpha|. \quad (3.11)$$

Formally, the resulting expressions for expectation values of normally ordered operator functions are equivalent to classical statistical mean values, where the P -function plays the role of a probability density. However, in general, the Glauber–Sudarshan P -function is not constrained to exhibit all the properties of a classical probability density, and whenever it cannot be interpreted as such, that is, whenever it becomes negative or highly singular, then the state is defined as nonclassical (Mandel, 1986; Titulaer & Glauber, 1965). For instance, the P -function of a single-photon Fock state is

$$P(\alpha) = \left(1 + \frac{\partial}{\partial\alpha} \frac{\partial}{\partial\alpha^*}\right) \delta(\alpha), \quad (3.12)$$

a highly singular distribution, which clearly cannot be interpreted as a classical probability. Most of the nonclassical states generated so far in a laboratory have highly singular P -functions, whose reconstruction is, therefore, experimentally impossible.

Other criteria for experimentally evaluating the nonclassical character of a state have thus been developed. As shown earlier, photon-added coherent and thermal states have the interesting property of presenting a controllable degree of nonclassicality and can thus be used as an ideal test-bed for such different criteria. In particular, although the Wigner function negativeness for SPATSS in Section 3.2 has already clearly shown the nonclassicality of these states for all the investigated values of \bar{n} , it is interesting to directly compare this criterion to other indicators of the nonclassical character of the measured states.

Vogel (2000) has recently proposed a nonclassicality test based on the characteristic function (the Fourier transform) of the quadrature distributions. At the first-order, the criterion defines a phase-independent state as nonclassical if the characteristic function of the state is greater than the

characteristic function of the vacuum for some values. In other words, the evidence of structures narrower than those associated to vacuum in the quadrature distribution is a sufficient condition to define a nonclassical state (Lvovsky & Shapiro, 2002). However, it has been shown that nonclassical states exist (as pointed out by Diósi (2000) for a vacuum-lacking thermal state, which is very similar to SPATSs) that fail to fulfil such inequality; when this happens, the first-order Richter–Vogel (RV) criterion has to be extended to higher orders (Richter & Vogel, 2002). However, as higher orders are investigated, the increasing sensitivity to experimental and statistical noise may soon become unmanageable. Applying this criterion to the experimental SPATSs data, Zavatta et al. (2007) found that the nonclassical, first-order RV criterion is only satisfied for very low values of \bar{n} , whereas it is necessary to extend the criterion to the second order to just barely show nonclassicality for $\bar{n} = 0.53$. At higher values of \bar{n} , no sign of nonclassical behavior is experimentally evident with this approach, although the Wigner function of the corresponding states still clearly exhibits a measurable negativity (see Figure 6(a)). Depending on the particular state under examination, also the reverse situation may happen. Lvovsky and Shapiro (2002) proved that mixtures of vacuum and single-photon Fock states can be nonclassical according to the RV criterion, while failing to show any negativity in their Wigner function.

The tomographic reconstruction used for determining the negativity of the Wigner function, can also be exploited to test alternative criteria: for example, by reconstructing the photon-number distribution $\rho_n = \langle n | \hat{\rho}_{\text{meas}} | n \rangle$, and then looking for strong modulations in neighboring photon probabilities by the following relationship (D'Ariano, Sacchi, & Kumar, 1999; Klyshko, 1996)

$$B(n) \equiv (n+2)\rho_n\rho_{n+2} - (n+1)\rho_{n+1}^2 < 0, \quad (3.13)$$

which is known to hold for nonclassical states. In the ideal situation of unit efficiency, SPATSs should always give $B(0) < 0$ because of the absence of the vacuum term ρ_0 , in agreement with Lee (1995). The experimental results obtained for $B(0)$ by using the reconstructed density matrices are presented in Figure 6(a,b) together with those calculated for the state with the measured experimental efficiency. This efficiency level should in principle allow one to find negative values of $B(0)$ even for large values of \bar{n} ; however, if one takes reconstruction errors as a result of statistical noise into account, the maximum \bar{n} for which the corresponding SPATS can be safely declared nonclassical is of the order of 2. It should be noted that, differently from the Wigner function approach, here nonclassicality can be proved even for experimental efficiencies much lower than 50%, as far as the mean photon number of the thermal state is not too high (see Figure 6(b)).

Finally, it is particularly interesting to measure the entanglement potential (EP) of SPATSs as recently proposed by Asboth, Calsamiglia, and Ritsch (2005). This measurement is based on the fact that, when a nonclassical state is mixed with vacuum on a 50/50 beam splitter, some amount of entanglement (depending on the nonclassicality of the input state) appears between the BS outputs. No entanglement can be produced by a classical initial state (see also Springer, Lee, Bellini, & Kim, 2009). For a given single-mode density operator $\hat{\rho}$, one calculates the entanglement of the bipartite state at the BS outputs $\hat{\rho}' = \hat{B}(\hat{\rho}|0\rangle\langle 0|)\hat{B}^\dagger$ by means of the logarithmic negativity $E_N(\hat{\rho}')$, based on the Peres separability criterion and defined by Vidal & Werner (2002), where \hat{B} is the 50/50 BS transformation of Equation (2.6) with $\theta = \pi/4$. The computed entanglement potentials for the reconstructed SPATS density matrices are shown in Figure 6(c) together with those expected at the experimentally evaluated efficiency. The EP is definitely greater than zero (by more than 13σ) for all the detected states, thus confirming that they are indeed nonclassical, in agreement with the findings obtained by the measurement of $B(0)$ and $W(0)$. As a comparison, the EP would be equal to unity for a pure single-photon Fock state, while it would reduce to 0.43 for a single-photon state mixed with vacuum $\hat{\rho} = (1-\eta)|0\rangle\langle 0| + \eta|1\rangle\langle 1|$ with the experimental efficiency $\eta=0.62$.

A comparison of the effectiveness of the three tomographic approaches to test nonclassicality is presented in the lower panel of Figure 6, in which the calculated indicators, $W(0)$, $B(0)$, and EP, from the model state are shown as a function of \bar{n} and η . It is evident that the Wigner function negativity only works for sufficiently high efficiencies, while both $B(0)$ and EP are able to detect nonclassical behavior even for $\eta < 50\%$. In particular, the entanglement potential is clearly seen as the most powerful criterion, at least for these particular states, that allows for an experimental proof of nonclassicality for all combinations of \bar{n} and η , as long as reconstruction errors can be neglected.

As seen earlier in Equation (3.9), the P -function of SPATSs is well-behaved but violates the properties of a classical probability density (Agarwal & Tara, 1992), giving rise to the question whether its experimental determination could be possible (Richter, 2001). In the zero-temperature limit, the SPATS includes the special case of the one-photon Fock state with the highly singular P -function given in Equation (3.12). In this sense, the SPATS represents a single photon whose P -function is regularized by a controlled thermal background.

The P characteristic function $\Phi(k, \theta)$ can be easily obtained (Vogel & Welsch, 2006) from the characteristic function of the observable quadrature $\hat{x}(\theta)$. As discussed earlier, the latter can be retrieved as the Fourier transform of the measured quadrature distributions (see (Lvovsky & Shapiro, 2002)). For many states, the P characteristic function can directly

display nonclassicality by violating the condition $|\Phi(k, \theta)| \leq 1$ (cf. Richter & Vogel, 2002; Vogel, 2000). However, even when this condition is fulfilled, $\Phi(k, \theta)$ may still be integrable and then the P -function can be obtained as a simple inverse Fourier transform to directly verify nonclassicality. SPATSSs belong to this category: for sufficiently high \bar{n} , most criteria for nonclassicality fail (Zavatta et al., 2007), but it is still possible to retrieve a well-behaved negative P -function.

Kiesel, Vogel, Parigi, Zavatta, and Bellini (2008) performed the first reconstruction of a nonclassical P -function (see Figure 7) from its characteristic function, directly retrieved from experimental quadrature data of SPATSSs. Because the measured states are independent of the phase, the reconstructed P -function is phase-independent as well. It is clearly seen that the P -function attains negative values, so that it fails to have the properties of a classical probability density. This is the first direct proof of nonclassicality based on its original definition (Mandel, 1986; Titulaer & Glauber, 1965).

It is important to note that the reconstruction of the P -function is also possible for large thermal photon number \bar{n} . On the contrary, all the other criteria for nonclassicality described earlier start to fail for increasing values of \bar{n} . To show the power of the reconstruction of the P -function under such conditions, its use at the limits was demonstrated for a SPATS with $\bar{n} = 3.71$ additionally contaminated with a 19% admixture of the corresponding thermal background. One still obtains a P -function being negative within one standard deviation (see Figure 7(b)), whereas other nonclassical signatures do not survive for this state.

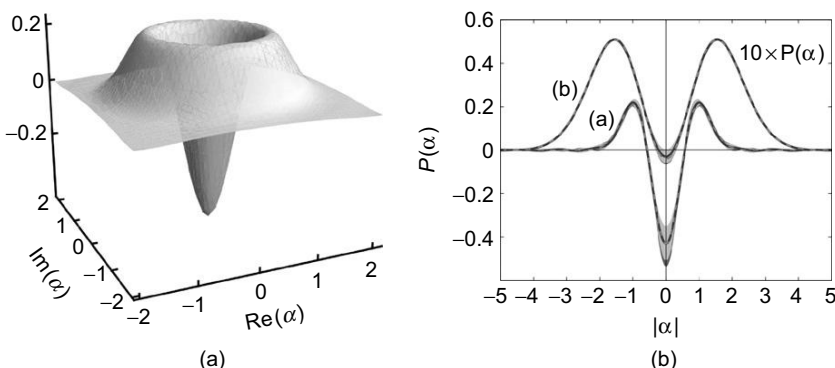


FIGURE 7 Experimentally reconstructed P -function of a SPATS. Also shown are two sections for (a) $\bar{n} = 1.11$ and (b) $\bar{n} = 3.71$, compared with the corresponding theoretical fits (dashed curves). The standard deviations (bright-shaded areas) and the systematic errors (dark-shaded areas) are also given.

The P -function has other interesting properties: for example, in the case of imperfect detection ($\eta < 1$), the measured homodyne quadrature distributions are convoluted with Gaussian noise, whose variance increases with decreasing η (Vogel & Grabow, 1993). In the Wigner function, this increasing noise smoothes out its structures and destroys negativities. On the contrary, for the P -function, experimental inefficiencies only lead to a rescaling of the quadrature variable (e.g., Semenov, Vasylyev, & Lev, 2006), and the P -function obtained by perfect detection is related to $P_\eta(\alpha)$, obtained with the quantum efficiency η , via

$$P(\alpha) = \eta P_\eta(\sqrt{\eta}\alpha). \quad (3.14)$$

Singularities in the P -function are, thus, often preserved in case of experimental losses, making it impossible to reconstruct it from experimental data. However, the negativities of $P(\alpha)$ are, in principle, preserved even for a small efficiency, whereas for other phase-space distributions, such as the Wigner function, they are quickly lost.

4. SINGLE-PHOTON SUBTRACTION

4.1. Photon Subtraction from Arbitrary Light States

The general scheme for conditional single-photon subtraction by using a low-reflectivity beam-splitter has been recently applied in a systematic way by Zavatta, Parigi, Kim, & Bellini (2008) to a set of paradigmatic states of light. It has been shown that single-photon subtraction has rather peculiar effects on the mean number of photons, strictly depending on the statistics of the initial state. In particular, it has been verified that the final photon-subtracted state contains a larger, smaller, or equal mean number of photons according to whether the initial state has a super-, sub-, or Poissonian distribution.

As already shown in the context of photodetection theory (Mizrahi & Dodonov, 2002; Srinivas & Davies, 1981; Ueda, Imoto, & Ogawa, 1990), one finds that the average number of photons in the photon-subtracted state, \bar{n}_{sub} , is related to the initial one, \bar{n} , as $\bar{n}_{\text{sub}} = \bar{n} - 1 + F$, where F is the Fano factor of the initial state, simply given by the ratio between the photon number variance and the mean, which is greater, equal to, or less than unity for super-Poissonian, Poissonian, or sub-Poissonian initial states, respectively. For a Fock state, the most sub-Poissonian state available ($F = 0$), the number of photons in the field is precisely known and the subtraction of a single photon works in an intuitive way, decreasing such a number by exactly one unit. In the case of a thermal state, a super-Poissonian one with $F = \bar{n} + 1$, the mean photon number doubles to $2\bar{n}$ after

photon subtraction, a very counter-intuitive result if one just thinks of it in classical deterministic terms. This, however, is not an entirely quantum effect, because similar results may also be obtained by means of classical statistics when starting from appropriate photon/particle number probability distributions (Kim, 2008). Finally, as the coherent state is a Poissonian one ($F = 1$), its mean photon number does not change after subtracting a photon by means of the \hat{a} operator. Note that this happens also for phase-diffused coherent states, whose density matrix is diagonal, but still Poissonian weighted, in the Fock basis. However, in the case of a pure coherent state, being an eigenstate of \hat{a} implies that not only its mean photon number and photon probability distribution, but also the whole state (represented by its density matrix or Wigner function) is left completely untouched by its application (Glauber, 1963).

The experimental setup used to perform photon subtraction is similar to the one described earlier for the case of photon addition (see Figure 1). Coherent states are simply obtained by splitting off (by means of a high-reflectivity beam splitter, HR) a small portion of the main laser output and properly attenuating it by means of neutral density filters (VF); on the other hand, thermal states are produced by inserting a rotating ground glass disk (RD) in the coherent laser beam. Subtraction of a single photon from a Fock state is performed by means of a double-conditioning scheme. In the first stage, a single-photon Fock state is conditionally prepared based on the spontaneous parametric down-conversion in the nonlinear crystal. In the second stage, a conditional photon subtraction is performed with the beam-splitter setup. When both trigger detectors fire, a single photon is subtracted from a single-photon Fock state.

It is interesting to note that all these measurements are based on simple variations upon a basic scheme (see Figure 8). A module for single-photon creation (implemented by conditional parametric down-conversion and denoted by \hat{a}^\dagger) is placed between two modules for single-photon annihilation (implemented by means of low-reflectivity beam splitters and denoted by \hat{a}). In this case, one can use the triggers from one or both subtraction modules for single- or double-photon subtraction from a state. However, the subtraction of a single photon from the Fock state is conditioned upon a double-click from the second or third modules, when seeding is blocked and only the vacuum field is fed as the input.

The reconstructed density matrix elements and the corresponding Wigner functions for a thermal state with $\bar{n}_{\text{th}} = 0.36 \pm 0.05$ and for its photon-subtracted version are reported in Figure 9(a) and 9(b). A reshaping and broadening of the photon number distribution is evident and the final reconstructed mean photon number $\bar{n}_{\text{th,sub}} = 0.69 \pm 0.07$ is in agreement with the expected $\bar{n}_{\text{th,sub}} = 2\bar{n}_{\text{th}}$ within the experimental errors. A flattening of the Wigner function is also visible in Figure 9(b), and the

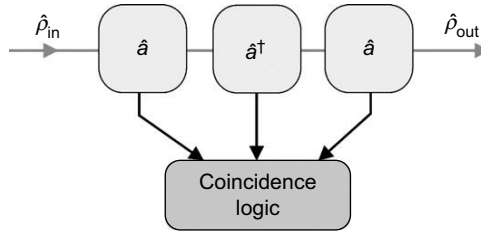


FIGURE 8 Schematic representation of the modular scheme for implementing various combinations of conditional single-photon operations. The \hat{a} blocks are two subtraction modules based on low-reflectivity beam-splitters, while the \hat{a}^\dagger block is an addition module based on conditional stimulated down-conversion. Depending on the combination of clicks in the coincidence logic, either single operations or simple sequences can be applied to arbitrary input states.

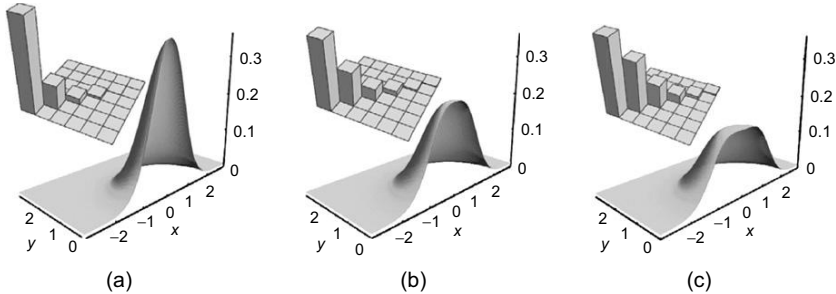


FIGURE 9 Reconstructed density matrix elements and Wigner functions for: (a) a thermal state with $\bar{n} = 0.36$. (b) The same state after a single-photon subtraction. (c) The state resulting from a sequence of two single-photon subtractions. The de-Gaussification of the state is evident.

departure from a Gaussian state can be estimated by calculating the kurtosis of the measured quadrature distributions.

A sequence of two single-photon subtractions (double-clicks from the first and third modules in Figure 8) is also performed in this case and the results are quite intriguing (see Figure 9(c)): the photon number distribution gets even broader and the final reconstructed mean photon number becomes $\bar{n}_{\text{th,sub,sub}} = 1.03 \pm 0.05$, as expected by the theoretical value $\bar{n}_{\text{th,sub,sub}} = 3\bar{n}_{\text{th}}$: subtracting more and more photons from a thermal state results in larger and larger mean photon numbers. This apparently contradictory behavior can be explained by the fact that this is not the simple deterministic extraction of particles from an initial state. Instead, one is dealing with a probabilistic annihilation of photons, whose probability

is proportional to the number of photons in the initial field. Thus, a subensemble of states with higher photon number is selected by means of photon subtraction.

On the contrary, the result of photon subtraction from a Fock state is far from surprising: in this case, it is intuitively clear that sending a one-photon state through a beam splitter yields the vacuum in one arm if a click is registered in the other. A single-photon Fock state with a negative Wigner function is thus Gaussified by converting it into a pure vacuum state (with a positive Gaussian Wigner function) by a single-photon subtraction. The fact that a single-photon split between two paths can only be detected in one of them is indeed a rather standard way to characterize single-photon sources in anticoincidence experiments. Such a direct and complete tomographic characterization of this phenomenon had, nonetheless, never been performed before Zavatta et al. (2008).

Finally, photon subtraction from a coherent state was performed. A comparison of the reconstructed density matrices for the initial and final states confirmed that the operation of single-photon subtraction has no measurable effect on the incoming field, within the experimental errors. With a fidelity of $F = 0.98$ between the initial coherent state and the photon-subtracted one, the experiment by Zavatta et al. (2008) is, thus, the first direct experimental proof of the fact that coherent states are eigenstates of the \hat{a} operator (Glauber, 1963).

4.2. De-Gaussification of Squeezed States and Generation of Schrödinger's Kittens

Photon subtraction is an efficient de-Gaussification tool when acting on certain kinds of states. The use of single-photon annihilation for producing non-Gaussian and nonclassical CV light states has been demonstrated in several recent experiments (Ourjoumtsev et al., 2006; Parigi et al., 2007; Wenger et al., 2004).

In its first experimental realization by Wenger et al. (2004), short pulses of squeezed light were de-Gaussified in an attempt to produce approximate linear superpositions of coherent states, or Schrödinger's cats. The experimental scheme is schematically shown in Figure 10 and is based on a cavity-dumped Ti:sapphire laser-emitting femtosecond pulses of moderate energy (about 40 nJ) at a repetition rate < 1 MHz. These pulses are frequency doubled in a single pass through a thin crystal of potassium niobate (KNbO_3), cut and temperature tuned for noncritical type-I phase matching. The second harmonic power is large enough to obtain a significant single-pass parametric gain in a similar KNbO_3 crystal used in a type-I spatially degenerate configuration. Differently from the above examples,

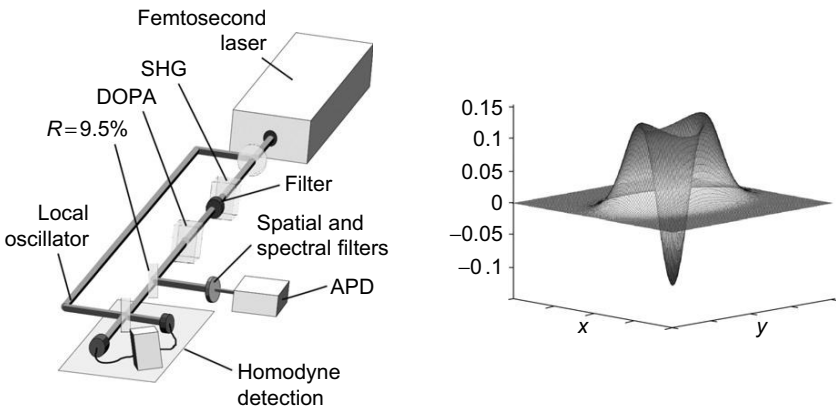


FIGURE 10 Scheme of the experimental apparatus to produce photon-subtracted squeezed vacuum states (Ourjoumtsev et al., 2006). Also shown is the reconstructed Wigner function of the states, clearly showing negative regions and closely resembling that of a low-amplitude Schrödinger's cat.

where the down-converted photons appeared in different directions corresponding to the idler and signal modes, here the down-converted photons share the same spatial mode, collinear with the pump.

Thanks to the relatively high-gain, higher-order terms (beyond pair production) have explicitly to be included in the description of the emitted light states and play an essential role in the understanding of the phase dependence of the data. An unconditional homodyne analysis of the emitted state proved its squeezed character, with the variance of the squeezed quadrature distribution 1.75 dB below the shot noise level. Although nonclassical, at this stage, the emitted state was still Gaussian.

A good physical insight of the process can be gained by considering the simple case of an expansion of the emitted squeezed vacuum up to $n = 4$ in the Fock basis. The squeezed vacuum state can then be written as

$$|\psi_s\rangle = \alpha|0\rangle + \beta|2\rangle + \gamma|4\rangle \quad (4.1)$$

with $\alpha = 0.96$, $\beta = 0.27$, and $\gamma = 0.10$ for the degree of squeezing reached in the experiment.

The squeezed vacuum state was then subjected to conditional single-photon subtraction by means of a low-reflectivity beam-splitter and an avalanche on-off photodiode (APD). Denoting the reflectivity and transmittance of the beam splitter, as r and t , respectively, the two-mode

entangled squeezed state emerging at its two outputs can be written as

$$\begin{aligned} |\psi_{s,\text{out}}\rangle &= \left(\alpha|0\rangle_a + t^2\beta|2\rangle_a + t^4\gamma|4\rangle_a \right) |0\rangle_b \\ &+ \left(\sqrt{2}rt\beta|1\rangle_a + 2rt^3\gamma|3\rangle_a \right) |1\rangle_b + O(2) \end{aligned} \quad (4.2)$$

and the term $O(2)$ denotes Fock state terms higher than 1 on the reflected beam, which can be neglected in this simplified calculation, given the assumption $r \ll 1$. Triggering the time-domain homodyne detector only on APD photon-counting events in mode b reduces the transmitted state in mode a to

$$|\psi_{s,\text{sub}}\rangle \propto \beta|1\rangle_a + \sqrt{2}\gamma t^2|3\rangle_a \quad (4.3)$$

a nonclassical coherent superposition of odd Fock states.

As in other similar experiments, and because of the very broad spectral and angular bandwidth of the parametric crystal, the filtering system placed in the reflected BS channel has to be adjusted very carefully to ensure that the photons detected by the APD are optimally matched to the mode defined by the homodyne detection.

The first version of the experiment was able to demonstrate a clear de-Gaussification of the Wigner function of the photon-subtracted squeezed vacuum, but the experimental inefficiencies were too high to allow for the observation of a negative Wigner function. This was achieved in a successive experiment (Ourjoumtsev et al., 2006) where, with a similar but improved setup, small Wigner negativities were observed even without recurring to corrections for the finite-detection efficiency (see Figure 10).

After the first pulsed scheme, generation of photon-subtracted squeezed vacuum was achieved also in a continuous wave (cw) regime by Neergaard-Nielsen et al. (2006) and Wakui et al. (2007). Such schemes were able to produce narrow-band states by making use of optical parametric oscillators (OPOs) for the generation of the initial squeezed field. With frequency-tunable bandwidths around 10 MHz, these sources are compatible with atomic memories and may become part of future quantum information networks.

Although the general scheme of the cw experiments is similar to the pulsed case, important differences arise in the mode selection of the investigated states. In an OPO, the nonlinear optical medium is placed inside an optical resonator, thus providing light generated within well-defined frequency and spatial modes. However, the OPO cavity has to be locked on resonance with the laser frequency to make sure that the degenerate down-conversion mode is efficiently generated. Differently from other cw

experiments, squeezing has to be observed across the entire theoretical bandwidth of the OPO and not just within a narrow frequency band. This is necessary because photon subtraction (by the usual combination of a low-reflectivity beam-splitter and an on-off photodiode) takes place in a well-defined temporal mode, and the final photon-subtracted squeezed state then has to be analyzed in that particular mode with a conditional time-domain homodyne-detection scheme.

Besides the degenerate squeezed mode, the OPO generates thousands of (nondegenerate) modes that are also phase-matched and resonant with the cavity. Photons in these modes produce unwanted counts in the photon-subtraction subtraction channel, and therefore have to be filtered out. To this purpose, light reflected by the beam-splitter is filtered with three consecutive cavities and a spectral filter, which block all the OPO output modes except for the degenerate-squeezed squeezed mode, on its way to the APD (see Figure 11). Because the local oscillator (derived from the laser output) is a continuous wave field, which does not define a precise temporal mode for homodyne detection, an optimized mode function has to be used to integrate the acquired continuous homodyne data and turn them into discrete field quadrature measurements.

In the first works on photon-subtracted squeezed states, potassium niobate (KNbO_3) crystals were used as nonlinear optical media for the pulsed optical parametric amplifier (OPA) (Ourjoumtsev et al., 2006), and for the

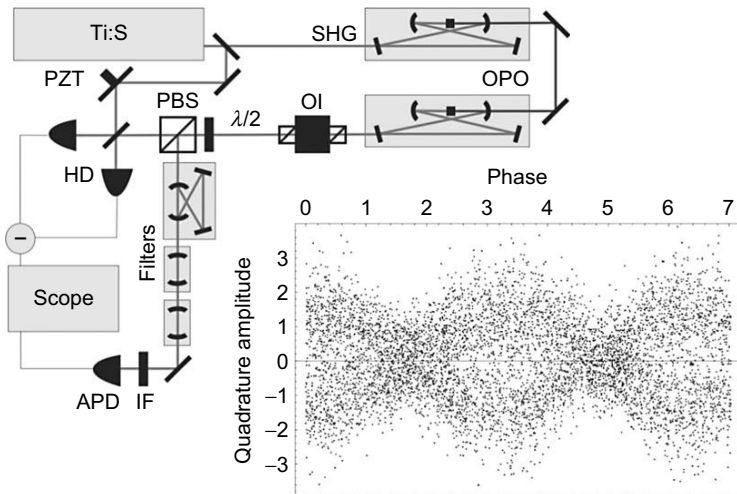


FIGURE 11 Experimental setup and raw quadrature data obtained as a function of the phase of the local oscillator of the photon-subtracted squeezed vacuum state obtained by Neergaard-Nielsen et al. (2006).

cw optical parametric oscillator (OPO) (Neergaard-Nielsen et al., 2006). In the case of experiments with KNbO₃, however, a big source of loss, referred to as (pump) blue light-induced infrared absorption (BLIIRA), is present. This loss weakens the entanglement between the two modes into which the squeezed vacuum is split, and yields uncorrelated trigger photons. To avoid these problems, the latest experiments with cw OPO were performed by Wakui et al. (2007) by making use of periodically poled KTiOPO₄ (PPKTP), which had not shown any BLIIRA effect in cw squeezing experiments. A value of -0.083 at the origin of the Wigner function of the photon-subtracted squeezed vacuum state was obtained in this case, which is the largest ever observed without any correction for experimental imperfections.

The lack of the vacuum term in the expression for the state expansion in Fock terms is already a clear indication of the nonclassicality of the state, but the main interest in photon-subtracted squeezed vacuum states is in the fact that they closely resemble linear superpositions of low-amplitude coherent states, or Schrödinger's kittens. A coherent state $|\alpha\rangle$ is considered to be at the boundary of the classical and nonclassical worlds and its superpositions are accepted to show the quantum nature of the Schrödinger's cat paradox. Producing such superposition state in a traveling field has always been difficult because of the unavailability of the extremely high nonlinearity required. Given the Fock state expansion of a coherent state

$$|\alpha\rangle = e^{-|\alpha|^2/2} \sum_{n=0}^{\infty} \frac{\alpha^n}{\sqrt{n!}} |n\rangle \quad (4.4)$$

a so-called odd Schrödinger's cat has the form

$$|\alpha\rangle + |-\alpha\rangle \propto \sum_{n=0}^{\infty} \frac{\alpha^{2n+1}}{\sqrt{(2n+1)!}} |2n+1\rangle \quad (4.5)$$

and it is easy to observe that it has nonzero probabilities only for odd numbers of photons. By restricting to just the first two terms, this closely resembles the approximate expression of a photon-subtracted squeezed vacuum state given in Equation (4.3). The raw quadrature data presented in the inset of Figure 11 for a varying value of the local oscillator phase clearly illustrate this behavior by showing a superposition of two wave-like oscillations with opposite phases. The reconstructed density matrix elements and Wigner function for the Schrödinger's kitten obtained by Neergaard-Nielsen et al. (2006) is also shown in Figure 12. Although the fidelity of the photon-subtracted squeezed state to a kitten state can be increased by properly choosing the amount of squeezing for low coherent

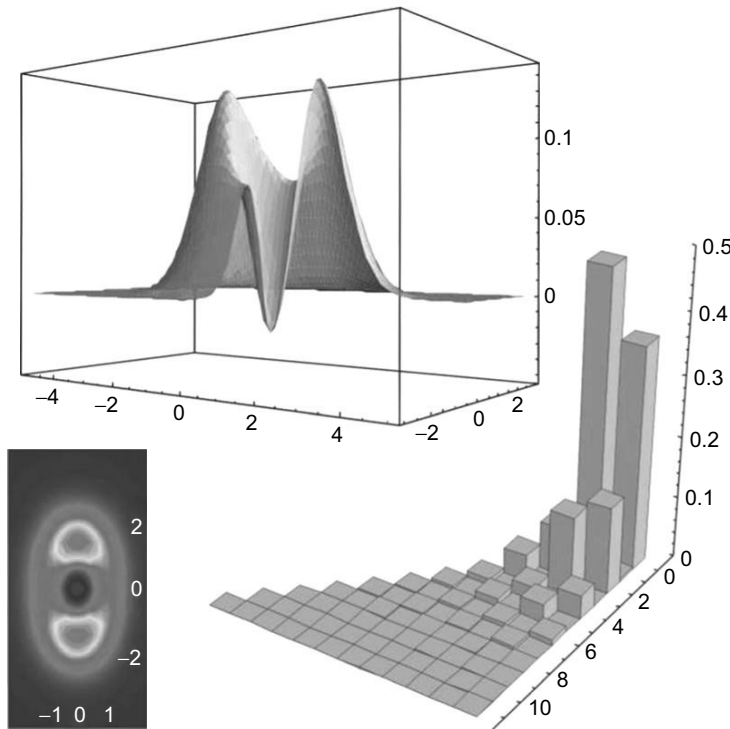


FIGURE 12 Experimentally reconstructed Wigner function and density matrix elements for the Schrödinger's kitten produced in the cw setup of Neergaard-Nielsen et al. (2006).

state amplitudes, it quickly starts to drop for bigger cats. Recent schemes of time-separated two-photon subtraction from a squeezed vacuum state have demonstrated progress in this direction by producing the largest amplitude coherent state superpositions with a negative Wigner function (Takahashi et al., 2008).

However, several schemes have also been devised to breed small-amplitude Schrödinger's kittens to larger cats, which may become useful for future quantum information protocols (e.g., Jeong, Kim, Ralph, & Ham, 2004; Lund et al., 2004).

4.3. Increasing Entanglement and Nonlocality by Single-Photon Subtraction

Entanglement plays a crucial role in quantum-information processing. In the case of CV systems, optical parametric amplification allows one to produce quadrature-entangled beams, but the entanglement is often

insufficient for efficiently performing given tasks, or may quickly degrade due to losses. Entanglement distillation constitutes the basis of quantum repeaters, which are thus essential for long-distance quantum communications. As mentioned earlier, Gaussian entanglement distillation requires non-Gaussian operations. Among several proposals, one of the simplest is the conditional subtraction of photons from Gaussian-entangled beams (Cochrane et al., 2002; Kitagawa, Takeoka, Sasaki, & Chefles, 2006; Opatrný et al., 2000; Yang & Li, 2009).

In order to provide realistic experimental schemes for demonstrating CV nonlocality, Nha and Carmichael (2004) and García-Patrón et al. (2004) suggested to apply the CHSH version of Bells inequality to a two-mode squeezed state, conditional on subtraction of a photon from each mode of the state. They suggested to extract the dichotomic observables needed for the nonlocality test from homodyne measurements, which has high-detection efficiency compared with photon counters and allows one, in principle, to avoid a detection loophole. They found that the CHSH Bell's inequality can be violated even when the squeezing parameter is as small as 0.48, as long as the reflectivity of the beam splitter is low enough. They also found that the scheme is quite insensitive to the detection efficiency of the on/off detector. As in most of these schemes, losing a photon in the heralding channel is not a big problem because, if a photon is not detected, no measurement will be performed anyway.

Finally, an entangled two-mode squeezed state of the form

$$|\psi\rangle = \sqrt{1 - |\lambda|^2} \sum_{n=0}^{\infty} \lambda^n |n\rangle |n\rangle \quad (4.6)$$

has been proposed as a resource for CV quantum teleportation. The prospects for realizing such teleportation are limited by the available squeezing of the entangled two-mode state and perfect teleportation can only be achieved with an infinitely squeezed vacuum, which is not experimentally available. In the first demonstration of continuous-variable teleportation by Furusawa et al. (1998), the low degree of squeezing resulted in a low entanglement and, finally, in a low fidelity of the teleported state. In order to improve the fidelity of quantum teleportation, Opatrný et al. (2000) suggested to perform a conditional photon subtraction in each mode of the two-mode squeezed state. In the case of coincident detection of a single photon in both the fields reflected by the subtraction beam-splitters, they showed that the degree of entanglement between the transmitted modes could be increased, as well as the fidelity of the teleported state. Later, Olivares et al. (2003) considered (the so-called inconclusive) photon subtraction using realistic on-off photodetectors

and showed that an improvement of quantum teleportation can still be achieved, depending on the various parameters involved.

Despite the many theoretical studies on increasing nonlocality and teleportation fidelity, so far, no experiment has succeeded in subtracting photons from each mode of the field. This is mainly because the probability of subtracting a photon from one mode is already very low, so that coincidence subtraction of two photons is technically extremely demanding. However, a less demanding scheme has been recently devised in which only one photon subtraction is involved to increase entanglement. Ourjoumtsev et al. (2007) subtracted only one photon from their two-mode squeezed state but, by erasing the information on the path information of the subtracted photon, they were nevertheless able to increase the degree of entanglement. An optical parametric amplifier was used to produce Gaussian quadrature-entangled light pulses, and small fractions of these beams were picked off and interfered with a well-defined phase on a 50/50 beam splitter (see Figure 13). By detecting photons in only one of the BS outputs, a single delocalized photon is subtracted from the two-mode state. Operating with single photon counts rather than with coincidences, this protocol allows for much higher generation rates and produces states more robust to experimental imperfections. Besides, it is more efficient at moderate OPA gain: for example, in the zero-gain limit, the detection of a photon transforms a state with almost no entanglement into a maximally entangled $1/\sqrt{2}(|1\rangle|0\rangle - |0\rangle|1\rangle)$ e-bit state. In order to quantify the

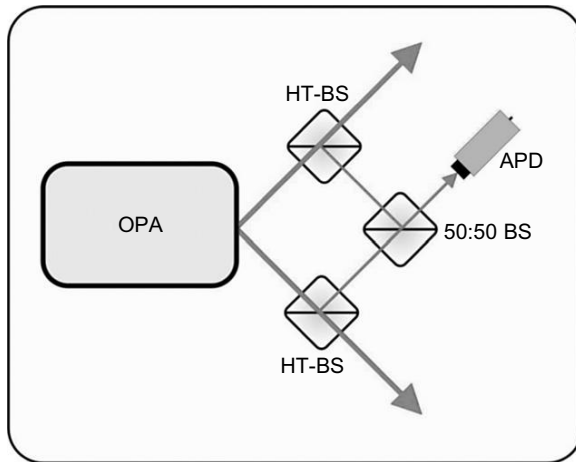


FIGURE 13 Simplified scheme of the experimental entanglement increase setup by means of photon subtraction as realized by Ourjoumtsev et al. (2007).

variation of the entanglement between the two modes before and after photon subtraction, the signal and idler beams were analyzed by two phase-correlated, time-resolved homodyne detectors sampling each individual pulse by measuring quadrature values in phase with two local oscillator fields. The reconstruction of the two-mode Wigner function allowed one to calculate the density matrix of the states and quantify their entanglement by means of the negativity $\mathcal{N} = \frac{\|\rho^{T_1}\|_1 - 1}{2}$, where T_1 is the partial transposition operation (Vidal & Werner, 2002). Based on the fact that the partial transpose of a two-mode system has to be positive definite for a separable state, the appearance of negative eigenvalues is a sufficient condition for entanglement. The monotone character of the negativity can be used for quantifying entanglement and was thus adopted here as a measure of its increase by photon subtraction.

5. SEQUENCES AND SUPERPOSITIONS OF SINGLE-PHOTON OPERATORS

5.1. Sequences of Creation and Annihilation Operators

After the successful application of isolated single-photon operations onto different light states, Parigi et al. (2007) have recently extended the experimental range of state-manipulation techniques by applying the two basic operations of photon addition and subtraction in alternated sequences ($\hat{a}\hat{a}^\dagger$ or $\hat{a}^\dagger\hat{a}$). As already described above, and as shown in Figure 8, a clever combination of three basic modules has been used, each one conditionally implementing the action of a specific quantum operator on the input light state. Then, by choosing the right combination of clicks coming from the module detectors, one can select the desired quantum operation, or any sequence of them. A single click simply conditions the generation of a photon-added or photon-subtracted thermal state, while a double click can either produce a first-subtracted-then-added thermal state or vice versa, depending on the order of clicks.

The upper panel of Figure 14 shows the experimental quadrature distributions for the states obtained from an initial thermal distribution, together with those calculated while keeping all experimental inefficiencies into account (Parigi et al., 2007). The corresponding photon number probability distributions are plotted in the central panel of Figure 14 as theoretically calculated and as reconstructed from the experimental data by means of an iterative maximum likelihood algorithm (see Appendix 7), correcting for the finite-detection efficiency. The experimentally reconstructed density matrix elements for the states have then been used to obtain their corresponding Wigner functions (lower panel of Figure 14).

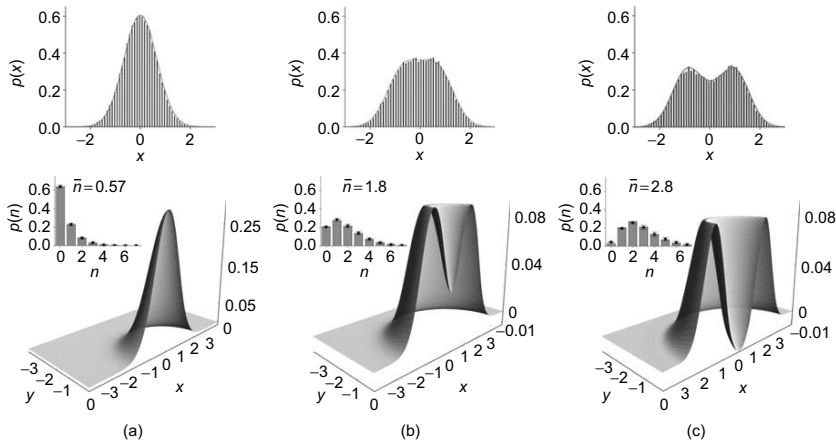


FIGURE 14 Quadrature distributions (top); reconstructed photon number distributions (center) and Wigner functions (bottom) for: (a) Initial thermal state. (b) State resulting from the subtraction-after-addition sequence. (c) From the addition-after-subtraction sequence.

The two final states resulting from the application of the $\hat{a}\hat{a}^\dagger$ and $\hat{a}^\dagger\hat{a}$ sequences are completely different from each other and from the original thermal one. This provides the first direct experimental verification of the noncommutativity of the quantum bosonic creation and annihilation operators, and gives a visually convincing demonstration that a simple view of classical particle addition and subtraction is incorrect in this case.

For both operator sequences, the Wigner function of the output states exhibits a clear central dip, which is absent in the case of the thermal field; such a dip reaches negative values (which survive even without correcting for detection losses) for the subtract-then-add sequence, while it stays well in the positive region for the add-then-subtract sequence. In this case, the Wigner function positivity is theoretically expected and is not due to experimental imperfections. As for squeezed states, the resulting state can be shown to be nonclassical (with a negative P -function) although possessing a positive Wigner function.

5.2. Superpositions of Quantum Operators

The possibility of superposing different arbitrary operators \hat{A} and \hat{B} to form the general operator superposition (or cat operation) $\alpha\hat{A} + \beta\hat{B}$, where α and β are complex amplitudes, is an important corner stone for the complete engineering of light states. Because the superposition principle relies on the indistinguishability among different alternatives, the experimental

implementation of quantum operators heralded by a single-photon detection offers a very convenient way to achieve this goal. If the herald field modes of different operators are properly mixed by means of a beam splitter, the information about the origin of a click in the herald photodetector is erased, and a coherent superposition of the different operators can be conditionally implemented.

Similar schemes have been recently proposed and experimentally implemented for increasing the entanglement of bipartite Gaussian quantum states by inconclusive photon subtraction (Olivares et al., 2003; Ourjoumtsev et al., 2007, 2009) toward the implementation of a quantum repeater for long-haul quantum communication (Kimble, 2008) in ionic systems (Yuan et al., 2008), and for the remote delocalization of a single photon over distinct temporal modes (Zavatta, D'Angelo, Parigi, & Bellini, 2006).

As recently proposed by Kim, Jeong, Zavatta, Parigi, and Bellini (2008), this scheme for operator superposition is also crucial for the proof of the bosonic commutation relation

$$[\hat{a}, \hat{a}^\dagger] = \hat{a}\hat{a}^\dagger - \hat{a}^\dagger\hat{a} = \mathbf{1}, \quad (5.1)$$

which is at the heart of many important consequences of quantum mechanics. The experiments by Parigi et al. (2007) described above were only able to demonstrate noncommutativity of \hat{a} and \hat{a}^\dagger , but they were not able to completely verify their commutation relation. In order to achieve the superposition of Equation (5.1), the single-photon addition and subtraction operations as described in the experimental scheme discussed in Section 5.1 had to be combined as shown in Figure 15. The implementation of the desired superposition of operator sequences is determined by the coincidence (C) between a click from the on-off photodetector heralding photon addition (Da) and one from a second photodetector (Ds), placed after a -3-db fibre coupler (FC, corresponding to the action of a 50/50 BS) combining the herald signals from the two subtraction modules. By a click from detector Ds, one knows that a single photon has been subtracted, but cannot identify if it was before or after the photon addition. In these conditions, a coincidence event heralds the application of the general cat operation $\hat{a}\hat{a}^\dagger - e^{i\phi}\hat{a}^\dagger\hat{a}$ with an adjustable phase ϕ , to any input light field. By varying the phase ϕ , any arbitrary-balanced superposition of the two operator sequences can be obtained. In particular, by setting $\phi = 0$ or $\phi = \pi$, one can directly realize the commutator or the anticommutator of the creation and annihilation operators, respectively.

Figure 16(a) shows a sequence of histograms of raw homodyne data acquired while scanning the phase of the superposition. The remote

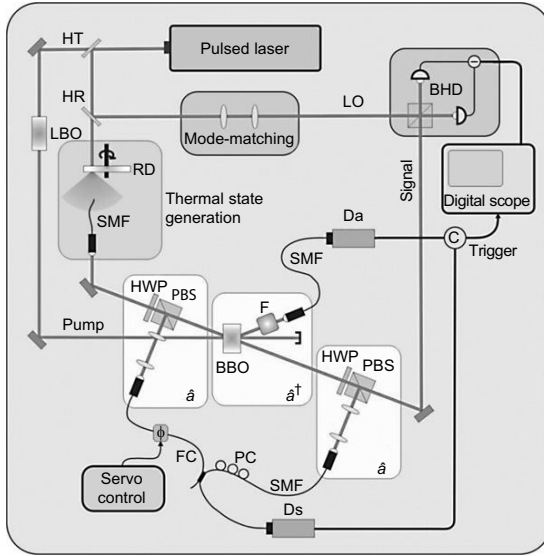


FIGURE 15 Experimental scheme for producing superpositions of alternated single-photon addition/subtraction sequences. A given operator superposition is heralded by the coincidence (C) between clicks from the Da and Ds on-off photodetectors.

manipulation of the state by the implementation of different superpositions of creation and annihilation sequences is clearly observed.

The Wigner functions of the original thermal state and those resulting from the experimental realization of the commutator and anticommutator between \hat{a} (obtained by setting $\phi = 0$) and \hat{a}^\dagger (obtained by setting $\phi = \pi$) are presented in Figure 17. Note that the phase change would not have resulted in such different output states if the operations had just been statistical mixtures. The fidelity $F = |\text{Tr} \sqrt{\sqrt{\hat{\rho}_{\text{in}}} \hat{\rho}_{\text{out}} \sqrt{\hat{\rho}_{\text{in}}}}|^2$ between the original thermal state and the final one (represented by their reconstructed density operators $\hat{\rho}_{\text{in}}$ and $\hat{\rho}_{\text{out}}$, respectively) is about $F = 0.992$ for the commutator case ($\phi = 0$). However, this only demonstrates that the implemented operator superposition is essentially equivalent to the identity operator up to a multiplicative constant (K) because of the normalization of quantum states. The exact value of the constant K strongly affects the state resulting from the anticommutator setup, and it can thus be readily retrieved from the experimental data. Figure 16(b) reports the measured homodyne quadrature distribution for the same initial thermal state after the application of the anticommutator operator (i.e., $\phi = \pi$). Also reported are the theoretical distributions calculated for the same experimental

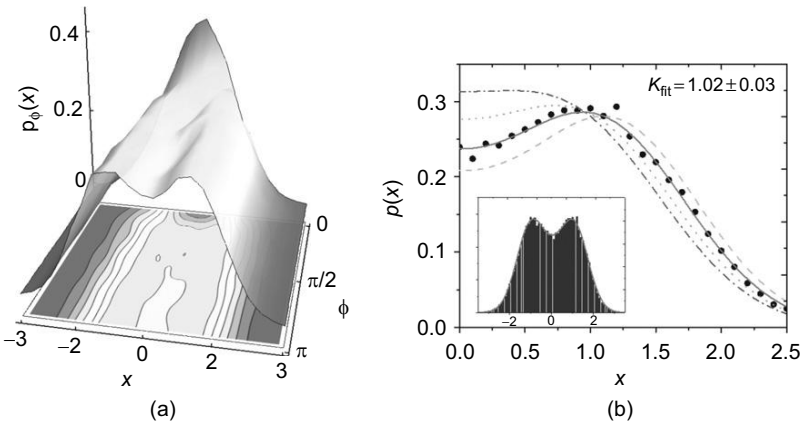


FIGURE 16 (a) Sequence of raw homodyne data histograms for the final state as a function of the normalized quadrature x and of the superposition phase ϕ . (b) Histogram of raw quadrature data (solid dots) for the anticommutator setup at $\phi = \pi$. Also shown are theoretical curves calculated for the experimental parameters and different values of the commutator ($K = 0$: dashed; $K = 2$: dotted; $K = 3$: dash-dotted). The solid curve is the result of the best fit to the experimental data.

parameters but with a few different values of the constant K . A best fit of the experimental homodyne data gives $K = 1.02(3)$, thus quantitatively demonstrating the bosonic commutation relation (Zavatta et al., 2009).

6. CONCLUSIONS

The fundamental quantum operations of single-photon addition and subtraction are promising tools for completely engineering quantum light states and testing the principles of quantum physics. The additional capability of combining such basic operations in sequences and arbitrary superpositions has further extended the range of possible light state manipulations. As an example, the scheme for producing general operator superpositions can be straightforwardly extended to the superposition of \hat{a} and \hat{a}^\dagger (thus implementing “position” and “momentum” operators in the phase space) by letting the creation and annihilation herald photons interfere at a beam splitter. These approaches can even be generalized to realize various superpositions of higher-order operators in terms of \hat{a} and \hat{a}^\dagger . Because any quantum state can be written as $\sum_n C_n \hat{a}^{\dagger n} |0\rangle$, where C_n are complex amplitudes, arbitrary states can, in principle, be generated by applying the appropriate superposition of photon creation operators.

The recent experimental demonstrations reported in this review have opened new exciting perspectives in the accurate generation and manipulation of photonic states and will certainly provide an important basis toward the application of quantum physics to future technologies.

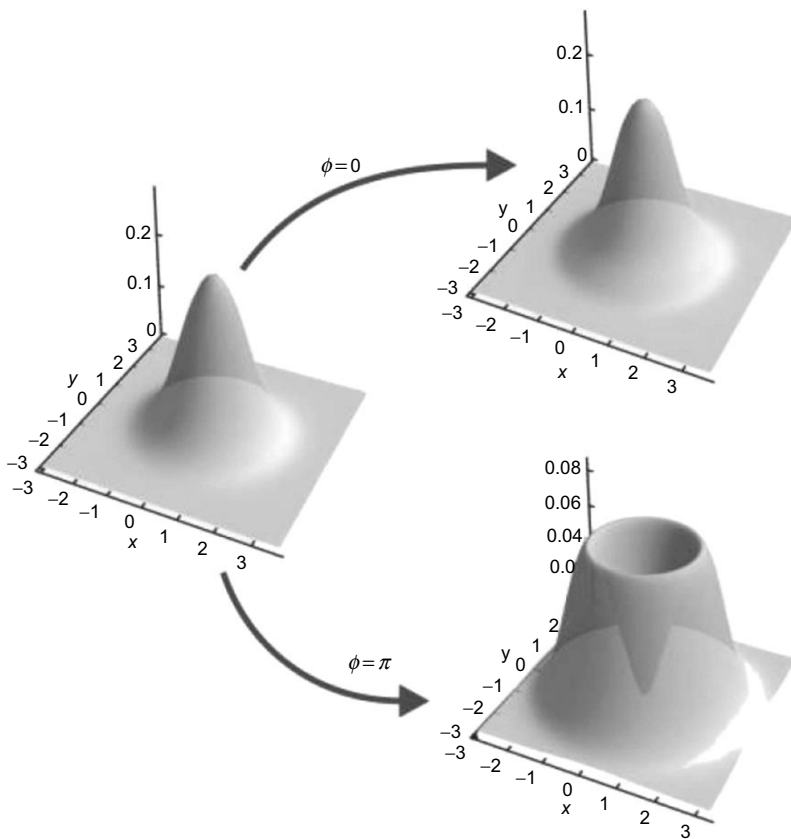


FIGURE 17 Experimentally reconstructed Wigner functions of the original thermal state and of those resulting from the application of the commutator and anticommutator superpositions.

7. ACKNOWLEDGMENTS

The authors gratefully acknowledge the support of Ente Cassa di Risparmio di Firenze and Regione Toscana under project CTOTUS.

A. QUANTUM TOMOGRAPHY

Balanced homodyne detection allows the measurement of the electric field quadratures $\hat{x}_\theta = \hat{x} \cos \theta + \hat{y} \sin \theta$ of a signal mode as a function of the phase θ relative to an intense, coherent, local oscillator field LO. The two orthogonal field quadratures \hat{x} and \hat{y} are defined as $\hat{x} = \frac{1}{2}(\hat{a} + \hat{a}^\dagger)$ and $\hat{y} = \frac{i}{2}(\hat{a}^\dagger - \hat{a})$, with $[\hat{x}, \hat{y}] = i/2$. By performing a series of homodyne

measurements on equally prepared states it is possible to obtain the probability distributions $p(x, \theta)$ of the quadrature operator $\hat{x}_\theta = \frac{1}{2}(\hat{a}e^{-i\theta} + \hat{a}^\dagger e^{i\theta})$ that are simply seen to correspond to the marginals of the Wigner quasi-probability distribution $W(x, y)$ (Vogel & Risken, 1989):

$$p(x, \theta) = \int_{-\infty}^{+\infty} W(x \cos \theta - y \sin \theta, x \sin \theta + y \cos \theta) dy. \quad (7.1)$$

Given a sufficient number of quadrature distributions at different values of the phase $\theta \in [0, \pi]$, one is able to reconstruct the quantum state of the field under study (Leonhardt, 1997). The elements of the density matrix $\hat{\rho}$ of the state in the number-state representation can be obtained by averaging the so-called “pattern functions” $f_{nm}(x, \theta)$ over the outcomes of the quadrature operator and over the phase θ as

$$\langle n | \hat{\rho} | m \rangle = \frac{1}{\pi} \int_0^{\pi} d\theta \int_{-\infty}^{+\infty} dx p(x, \theta) f_{nm}(x, \theta), \quad (7.2)$$

where the pattern functions can be implemented for unit quantum efficiency with stable numerical algorithms (D'Ariano, 1997; Leonhardt, 1997). The Wigner function can then be obtained by means of the following transformation:

$$W(x, y) = \sum_{n, m}^M \rho_{n, m} W_{n, m}(x, y) \quad (7.3)$$

where $W_{n, m}(x, y)$ is the Wigner function of the operator $|n\rangle\langle m|$. Note that, using this procedure, the Wigner function of the state is reconstructed from a truncated density matrix of dimension $M \times M$. This implies a finite resolution in the reconstructed function which, however, can be adapted to the particular physical situation of interest in order to avoid loss of information on the state.

An alternative reconstruction procedure involves the maximum likelihood estimation introduced by Banaszek, D'Ariano, Paris, and Sacchi (1999), which gives the density matrix that most likely represents the measured homodyne data. First, one builds the likelihood function contracted for a density matrix truncated to M diagonal elements (with the constraints of Hermiticity, positivity, and normalization), then the function is maximized by an iterative procedure (Hradil, Mogilevtsev, & Rehacek, 2006; Lvovsky, 2004), and the errors on the reconstructed density matrix

elements are evaluated using the Fisher information (Hradil et al., 2006; Rehacek, Mogilevtsev, & Hradil, 2008).

All the homodyne measurements described in this review are characterized by the fact that they necessarily have to work in the time domain and analyze well-defined temporal modes, heralded by clicks in some on-off photodetector. Several experimental setups are now performing such tasks with good efficiency (see Lvovsky & Raymer, 2009), and a few of them have pushed the frequency of operation to the full repetition rate of common mode-locked lasers (Huisman et al., 2009; Okubo, Hirano, Zhang, & Hirano, 2008; Zavatta, Bellini, Ramazza, Marin, & Arecchi, 2002).

REFERENCES

- Adesso, G., Dell'Anno, F., Siena, S. D., Illuminati, F., & Souza, L. A. M. (2009). Optimal estimation of losses at the ultimate quantum limit with non-gaussian states. *Physical Review A*, 79, 040305.
- Agarwal, G. S., & Tara, K. (1991). Nonclassical properties of states generated by the excitations on a coherent state. *Physical Review A*, 43, 492.
- Agarwal, G. S., & Tara, K. (1992). Nonclassical character of states exhibiting no squeezing or sub-poissonian statistics. *Physical Review A*, 46, 485.
- Aichele, T., Lvovsky, A. I., & Schiller, S. (2002). Optical mode characterization of single photons prepared by means of conditional measurements on a biphoton state. *European Physical Journal D*, 18, 237.
- Arecchi, F. T. (1965). Measurement of the statistical distribution of gaussian and laser sources. *Physical Review Letters*, 15, 912.
- Asboth, J. K., Calsamiglia, J., & Ritsch, H. (2005). Computable measure of nonclassicality for light. *Physical Review Letters*, 94, 173602.
- Banaszek, K., D'Ariano, G. M., Paris, M. G. A., & Sacchi, M. F. (1999). Maximum-likelihood estimation of the density matrix. *Physical Review A*, 61, 010304.
- Bellini, M., Marin, F., Viciani, S., Zavatta, A., & Arecchi, F. T. (2003). Nonlocal pulse shaping with entangled photon pairs. *Physical Review Letters*, 90, 043602.
- Braunstein, S. L., & van Loock, P. (2005). Quantum information with continuous variables. *Reviews of Modern Physics*, 77, 513.
- Cerf, N. J., Krüger, O., Navez, P., Werner, R. F., & Wolf, M. M. (2005). Non-gaussian cloning of quantum coherent states is optimal. *Physical Review Letters*, 95, 070501.
- Cochrane, P. T., Ralph, T. C., & Milburn, G. J. (2002). Teleportation improvement by conditional measurements on the two-mode squeezed vacuum. *Physical Review A*, 65, 062306.
- Dakna, M., Anhut, T., Opatrný, T., Knöll, L., & Welsch, D.-G. (1997). Generating schrödinger-cat-like states by means of conditional measurements on a beam splitter. *Physical Review A*, 55, 3184.
- Dakna, M., Clausen, J., Knöll, L., & Welsch, D.-G. (1999). Generation of arbitrary quantum states of traveling fields. *Physical Review A*, 59, 1658.
- Dakna, M., Knöll, L., & Welsch, D.-G. 1998. Quantum state engineering using conditional measurement on a beam splitter. *European Physical Journal D*, 3, 295.
- D'Ariano, G. M. (1997). Measuring quantum states. In T. Hakioğlu & A. S. Shumovsky (Eds.), *Quantum optics and spectroscopy of solids* (pp. 175–202). Kluwer Academic Publishers, Amsterdam

- D'Ariano, G. M., Sacchi, M. F., & Kumar, P. (1999). Tomographic measurements of nonclassical radiation states. *Physical Review A*, 59, 826.
- Diósi, L. (2000). Comment on nonclassical states: An observable criterion. *Physical Review Letters*, 85, 2841.
- Dodonov, A. V., & Mizrahi, S. S. (2009). Smooth quantum-classical transition in photon subtraction and addition processes. *Physical Review A*, 79, 023821.
- Dong, R., Lassen, M., Heersink, J., Marquardt, C., Filip, R., Leuchs, G., et al. (2008). Experimental entanglement distillation of mesoscopic quantum states. *Nature Physics*, 4, 919–923.
- Eisert, J., Scheel, S., & Plenio, M. B. (2002). Distilling gaussian states with gaussian operations is impossible. *Physical Review Letters*, 89, 137903.
- Fiurášek, J. (2002). Gaussian transformations and distillation of entangled gaussian states. *Physical Review Letters*, 89, 137904.
- Fiurášek, J., García-Patrón, R., & Cerf, N. J. (2005). Conditional generation of arbitrary single-mode quantum states of light by repeated photon subtractions. *Physical Review A*, 72, 033822.
- Fiurášek, J. (2009). Engineering quantum operations on traveling light beams by multiple photon addition and subtraction. *Physical Review A*, 80, 053822.
- Furusawa, A., Sørensen, J. L., Braunstein, S. L., Fuchs, C. A., Kimble, H. J., & Polzik, E. S. (1998). Unconditional quantum teleportation. *Science*, 282, 706–709.
- García-Patrón, R., Fiurášek, J., Cerf, N. J., Wenger, J., Tualle-Brouri, R., & Grangier, P. (2004). Proposal for a loophole-free bell test using homodyne detection. *Physical Review Letters*, 93, 130409.
- Genoni, M. G., Paris, M. G. A., & Banaszek, K. (2007). Measure of the non-gaussian character of a quantum state. *Physical Review A*, 76, 042327.
- Giedke, G., & Cirac, I. J. (2002). Characterization of gaussian operations and distillation of gaussian states. *Physical Review A*, 66, 032316.
- Glauber, R. J. (1963). Coherent and incoherent states of the radiation field. *Physical Review*, 131, 2766.
- Hage, B., Samblowski, A., DiGuglielmo, J., Franzen, A., Fiurášek, J., & Schnabel, R. (2008). Preparation of distilled and purified continuous-variable entangled states. *Nature Physics*, 4, 915–918.
- Hayrynen, T., Oksanen, J., & Tulkki, J. (2009). Exact theory for photon subtraction for fields from quantum to classical limit. *EPL (Europhysics Letters)*, 87(4), 44002–44006.
- Hradil, Z., Mogilevtsev, D., & Rehacek, J. (2006). Biased tomography schemes: An objective approach. *Physical Review Letters*, 96, 230401.
- Huisman, S. R., Jain, N., Babichev, S. A., Vewinger, F., Zhang, A. N., Youn, S. H., et al. (2009). Instant single-photon fock state tomography. *Optics Letters*, 34, 2739–2741.
- Jeong, H., Kim, M. S., Ralph, T. C., & Ham, B. S. (2004). Generation of macroscopic superposition states with small nonlinearity. *Physical Review A*, 70, 061801.
- Jeong, H., Lund, A. P., & Ralph, T. C. (2005). Production of superpositions of coherent states in traveling optical fields with inefficient photon detection. *Physical Review A*, 72, 013801.
- Jones, G. N., Haight, J., & Lee, C. T. (1997). Nonclassical effects in the photon-added thermal state. *Quantum and Semiclassical Optics: Journal of the European Optical Society Part B*, 9, 411.
- Kiesel, T., Vogel, W., Parigi, V., Zavatta, A., & Bellini, M. (2008). Experimental determination of a nonclassical Glauber-Sudarshan P function. *Physical Review A*, 78, 021804.
- Kim, M. (2008). Recent developments in photon-level operations on travelling light fields. *Journal of Physics B*, 41, 133001.
- Kim, M. S., Jeong, H., Zavatta, A., Parigi, V., & Bellini, M. (2008). Scheme for proving the bosonic commutation relation using single-photon interference. *Physical Review Letters*, 101, 260401.

- Kim, M. S., Park, E., Knight, P. L., & Jeong, H. (2005). Nonclassicality of a photon-subtracted gaussian field. *Physical Review A*, 71, 043805.
- Kim, M. S., Son, W., Bužek, V., & Knight, P. L. (2002). Entanglement by a beam splitter: Nonclassicality as a prerequisite for entanglement. *Physical Review A*, 65, 032323.
- Kimble, H. J. (2008). The quantum internet. *Nature*, 453, 1023–1030.
- Kitaeva, G. K., Penin, A. N., Fadeev, V. V., & Yanait, Y. A. (1979). Measurement of brightness of light fluxes using vacuum fluctuations as a reference. *Soviet Physics Doklady*, 24, 564.
- Kitagawa, A., Takeoka, M., Sasaki, M., & Chefles, A. (2006). Entanglement evaluation of non-gaussian states generated by photon subtraction from squeezed states. *Physical Review A*, 73, 042310.
- Klyshko, D. N. (1977). Utilization of vacuum fluctuations as an optical brightness standard. *Soviet Journal of Quantum Electronics*, 7, 591.
- Klyshko, D. N. (1996). Observable signs of nonclassical light. *Physics Letters A*, 231, 7.
- Knill, E., Laflamme, R., & Milburn, G. J. (2001). A scheme for efficient quantum computation with linear optics. *Nature*, 409, 46–52.
- Lee, C. T. (1995). Theorem on nonclassical states. *Physical Review A*, 52, 3374.
- Leonhardt, U. (1997). *Measuring the quantum state of light*. Cambridge, MA: Cambridge University Press.
- Lund, A. P., Jeong, H., Ralph, T. C., & Kim, M. S. (2004). Conditional production of superpositions of coherent states with inefficient photon detection. *Physical Review A*, 70, 020101(R).
- Lvovsky, A. I. (2004). Iterative maximum-likelihood reconstruction in quantum homodyne tomography. *Journal of Optics B, Quantum and Semiclassical Optics*, 6, S556.
- Lvovsky, A. I., Hansen, H., Aichele, T., Benson, O., Mlynek, J., & Schiller, S. (2001). Quantum state reconstruction of the single-photon fock state. *Physical Review Letters*, 87, 050402.
- Lvovsky, A. I., & Raymer, M. G. (2009). Continuous-variable optical quantum-state tomography. *Reviews of Modern Physics*, 81, 299.
- Lvovsky, A. I., & Shapiro, J. H. (2002). Nonclassical character of statistical mixtures of the single-photon and vacuum optical states. *Physical Review A*, 65, 033830.
- Mandel, L. (1986). Non-classical states of the electromagnetic field. *Physica Scripta*, T12, 34.
- Marek, P., & Filip, R. (2010). Coherent-state phase concentration by quantum probabilistic amplification. *Physical Review A*, 81, 022302.
- Marek, P., Jeong, H., & Kim, M. S. (2008). Generating “squeezed” superpositions of coherent states using photon addition and subtraction. *Physical Review A*, 78, 063811.
- Midgall, A. (1999). Correlated-photon metrology without absolute standards. *Physics Today*, 52, 41.
- Mizrahi, S. S., & Dodonov, V. V. (2002). Creating quanta with an annihilation operator. *Journal of Physics A: Mathematical and General*, 35(41), 8847–8857.
- Mollow, B. R. (1968). Quantum theory of field attenuation. *Physical Review*, 168, 1896–1919.
- Moya-Cessa, H., Chavez-Cerda, S., & Vogel, W. (1999). Adding and subtracting energy quanta of the harmonic oscillator. *Journal of Modern Optics*, 46, 1641–1656.
- Neergaard-Nielsen, J. S., Nielsen, B. M., Hettich, C., Molmer, K., & Polzik, E. S. (2006). Generation of a superposition of odd photon number states for quantum information networks. *Physical Review Letters*, 97, 083604.
- Nha, H., & Carmichael, H. J. (2004). Proposed test of quantum nonlocality for continuous variables. *Physical Review Letters*, 93, 020401.
- Okubo, R., Hirano, M., Zhang, Y., & Hirano, T. (2008). Pulse-resolved measurement of quadrature phase amplitudes of squeezed pulse trains at a repetition rate of 76 mhz. *Optics Letters*, 33, 1458–1460.

- Olivares, S., Paris, M. G. A., & Bonifacio, R. (2003). Teleportation improvement by inconclusive photon subtraction. *Physical Review A*, 67, 032314.
- Opáčný, T., Kurizki, G., & Welsch, D.-G. (2000). Improvement on teleportation of continuous variables by photon subtraction via conditional measurement. *Physical Review A*, 61, 032302.
- Ou, Z. Y. (1997). Parametric down-conversion with coherent pulse pumping and quantum interference between independent fields. *Quantum and Semiclassical Optics: Journal of the European Optical Society Part B*, 9, 599.
- Ourjoumtsev, A., Dantan, A., Tualle-Brouri, R., & Grangier, P. (2007). Increasing entanglement between gaussian states by coherent photon subtraction. *Physical Review Letters*, 98, 030502.
- Ourjoumtsev, A., Ferreyrol, F., Tualle-Brouri, R., & Grangier, P. (2009). Preparation of non-local superpositions of quasi-classical light states. *Nature Physics*, 5, 189–192.
- Ourjoumtsev, A., Tualle-Brouri, R., Laurat, J., & Grangier, P. (2006). Generating optical schrodinger kittens for quantum information processing. *Science*, 312, 83.
- Parigi, V., Zavatta, A., & Bellini, M. (2009). Implementation of single-photon creation and annihilation operators: Experimental issues in their application to thermal states of light. *Journal of Physics B: Atomic, Molecular and Optical Physics*, 42, 114005.
- Parigi, V., Zavatta, A., Kim, M. S., & Bellini, M. (2007). Probing quantum commutation rules by addition and subtraction of single photons to/from a light field. *Science*, 317, 1890.
- Ramazza, P. L., Ducci, S., Zavatta, A., Bellini, M., & Arecchi, F. T. (2002). Second-harmonic generation from a picosecond tisla laser in lbo: Conversion efficiency and spatial properties. *Applied Physics B Lasers and Optics*, 75, 53.
- Rehacek, J., Mogilevtsev, D., & Hradil, Z. (2008). Tomography for quantum diagnostics. *New Journal of Physics*, 10, 043022.
- Reynaud, S., Heidmann, A., Giacobino, E., & Fabre, C. (1992). Quanutm fluctuations in optical systems. In E. Wolf, (Ed.), *Progress in optics*. (Vol. 30, p. 1). Amsterdam: Elsevier.
- Richter, T. (2001). A new view on the Perina-Mišta form of the Glauber-Sudershan P function. *Journal of Modern Optics*, 48, 1881.
- Richter, T., & Vogel, W. (2002). Nonclassicality of quantum states: A hierarchy of observable conditions. *Physical Review Letters*, 89, 283601.
- Semenov, A. A., Vasylyev, D. Y., & Lev, B. I. (2006). Nonclassicality of noisy quantum states. *Journal of Optics B, Quantum and Semiclassical Optics*, 39, 905.
- Springer, S. C., Lee, J., Bellini, M., & Kim, M. S. (2009). Conditions for factorizable output from a beam splitter. *Physical Review A*, 79, 062303.
- Srinivas, M. D., & Davies, E. B. (1981). Photon counting probabilities in quantum optics. *Optica Acta: International Journal of Optics*, 28(7), 981–996.
- Sudarshan, E. C. G. (1963). Equivalence of semiclassical and quantum mechanical descriptions of statistical light beams. *Physical Review Letters*, 10, 277.
- Takahashi, H., Wakui, K., Suzuki, S., Takeoka, M., Hayasaka, K., Furusawa, A., et al. (2008). Generation of large-amplitude coherent-state superposition via ancilla-assisted photon subtraction. *Physical Review Letters*, 101, 233605.
- Takeoka, M., & Sasaki, M. (2007). Conditional generation of an arbitrary superposition of coherent states. *Physical Review A*, 75, 064302.
- Titulaer, U. M., & Glauber, R. J. (1965). Correlation functions for coherent fields. *Physical Review*, 140, B676.
- Ueda, M., Imoto, N., & Ogawa, T. (1990). Quantum theory for continuous photodetection processes. *Physical Review A*, 41, 3891–3904.
- Usuga, M. A., Mueller, C. R., Wittmann, C., Marek, P., Filip, R., Marquardt, C., et al. (2010). Noise-powered probabilistic concentration of phase information. *Nature Physics*, 6, 767–771.

- Viciani, S., Zavatta, A., & Bellini, M. (2004). Nonlocal modulations on the temporal and spectral profiles of an entangled photon pair. *Physical Review A*, *69*, 053801.
- Vidal, G., & Werner, R. F. (2002). Computable measure of entanglement. *Physical Review A*, *65*, 032314.
- Vogel, W. (2000). Nonclassical states: An observable criterion. *Physical Review Letters*, *84*, 1849.
- Vogel, K., & Risken, H. (1989). Determination of quasiprobability distributions in terms of probability distributions for the rotated quadrature phase. *Physical Review A*, *40*, R2847.
- Vogel, W., & Grabow, J. (1993). Statistics of difference events in homodyne detection. *Physical Review A*, *47*, 4227.
- Vogel, W., & Welsch, D.-G. (2006). *Quantum optics*. Weinheim: Wiley-VCH.
- Wakui, K., Takahashi, H., Furusawa, A., & Sasaki, M. (2007). Photon subtracted squeezed states generated with periodically poled ktpo4. *Optics Express*, *15*, 3568.
- Wenger, J., Tualle-Brouri, R., & Grangier, P. (2004). Non-gaussian statistics from individual pulses of squeezed light. *Physical Review Letters*, *92*, 153601.
- Yang, Y., & Li, F.-L. (2009). Entanglement properties of non-gaussian resources generated via photon subtraction and addition and continuous-variable quantum-teleportation improvement. *Physical Review A*, *80*, 022315.
- Yuan, Z.-S., Chen, Y.-A., Zhao, B., Chen, S., Schmiedmayer, J., & Pan, J.-W. (2008). Experimental demonstration of a BDCZ quantum repeater node. *Nature*, *454*, 1098–1101.
- Zavatta, A., Bellini, M., Ramazza, P. L., Marin, F., & Arecchi, F. T. (2002). Time-domain analysis of quantum states of light: Noise characterization and homodyne tomography. *Journal of the Optical Society of America B*, *19*, 1189.
- Zavatta, A., D'Angelo, M., Parigi, V., & Bellini, M. (2006). Remote preparation of arbitrary time-encoded single-photon ebits. *Physical Review Letters*, *96*, 020502.
- Zavatta, A., Fiurášek, J., & Bellini, M. (2010). A high-fidelity noiseless amplifier for quantum light states. quant-ph/1004.3399v1 and Nature Photonics, to appear.
- Zavatta, A., Parigi, V., & Bellini, M. (2007). Experimental nonclassicality of single-photon-added thermal light states. *Physical Review A*, *75*, 052106.
- Zavatta, A., Parigi, V., Kim, M. S., & Bellini, M. (2008). Subtracting photons from arbitrary light fields: Experimental test of coherent state invariance by single-photon annihilation. *New Journal of Physics*, *10*, 123006.
- Zavatta, A., Parigi, V., Kim, M. S., Jeong, H., & Bellini, M. (2009). Experimental demonstration of the bosonic commutation relation via superpositions of quantum operations on thermal light fields. *Physical Review Letters*, *103*, 140406.
- Zavatta, A., Viciani, S., & Bellini, M. (2004a). Quantum-to-classical transition with single-photon-added coherent states of light. *Science*, *306*, 660.
- Zavatta, A., Viciani, S., & Bellini, M. (2004b). Tomographic reconstruction of the single-photon fock state by high-frequency homodyne detection. *Physical Review A*, *70*, 053821.
- Zavatta, A., Viciani, S., & Bellini, M. (2005). Single-photon excitation of a coherent state: Catching the elementary step of stimulated light emission. *Physical Review A*, *72*, 023820.

This page intentionally left blank

CHAPTER 3

Vacuum-Induced Processes in Multilevel Atoms

**M. Kiffner^{*,a}, M. Macovei, J. Evers^b, and
C. H. Keitel**

Max Planck Institute for Nuclear Physics, Heidelberg, Germany

**Present address: Technische Universität München, Physik*

Department I / T34, James Franck Strasse, Garching, Germany

E-mail address: ^amartin.kiffner@ph.tum.de,

^bjoerg.evers@mpi-hd.mpg.de

Contents		
1.	Introduction	86
2.	Mathematical Model	87
2.1.	Description of the System	88
2.2.	General Reservoir Theory	92
2.3.	Derivation of the Master Equation	94
2.4.	Master Equation for Radiatively Coupled Multilevel Systems	105
3.	Single-Particle Processes	111
3.1.	Single-Particle Spontaneous Decay	112
3.2.	Spontaneous Decay-Induced Coherences	127
4.	Collective Processes	150
4.1.	Pair of Dipole–Dipole Interacting Two-Level Atoms	151
4.2.	Experimental Verification of the Dipole–Dipole Interaction	155
4.3.	Dipole–Dipole Interaction beyond the Two-Level Approximation	160
4.4.	Impact of the Dipole–Dipole Interaction	175
4.5.	Multi-Particle Quantum Dynamics	177
	Acknowledgments	183
	References	184

1. INTRODUCTION

Atoms commonly do not act as isolated objects, but rather are open quantum systems, as they interact with the environment. Typically, this environment is formed by the electromagnetic vacuum field. The interaction of atoms with the environment modifies the atomic dynamics, with spontaneous emission as the most obvious example. Spontaneous emission is generally recognized as incoherent process, which leads to decoherence and, therefore, forms a major limitation for many schemes of current theoretical and experimental interest. But vacuum-induced processes can also generate coherent time evolution. In view of spontaneous emission, this appears surprising. However, the starting point for the description of decoherence is a Hamiltonian governing the combined dynamics of atoms and environment that describes a completely unitary time evolution. From this point of view, it is natural that vacuum-induced processes can be coherent, even though they often indeed induce nonunitary time evolutions. Such vacuum-induced unitary dynamics can be observed most readily if multilevel atoms are considered. For example, spontaneous emission can lead to the formation of atomic coherences, albeit subject to stringent conditions on the level scheme. These coherences can be interpreted as arising from vacuum-induced transitions between different atomic states. The situation becomes even more interesting if different atoms can exchange energy via the vacuum. Such dipole–dipole interactions induce both coherent and incoherent atomic dynamics, leading to significant deviations from the single-atom properties. Finally, a complex interplay of vacuum-induced interatomic and intraatomic dynamics may arise if several multilevel atoms are considered. These vacuum-induced processes form the basis for a large number of applications, for which the vacuum-induced dynamics can be favorable, perturbing, or even both. For example, while spontaneous emission induces detrimental decoherence, it at the same time is often facilitated for the detection of the quantum state of the system. Most applications can be improved, if the vacuum-induced processes can be modified or even controlled. Thus, a profound understanding of vacuum-induced processes is desirable.

Motivated by this, in this review, we discuss vacuum-induced processes in multilevel atoms. It is based on a rather general master equation describing the interaction of multilevel atoms with the vacuum, which we introduce and discuss in Section 2. The following Section 3 focusses on coherent and incoherent vacuum-induced processes in single atoms. Key topics are the modification of spontaneous emission, spontaneously generated coherences, and engineering of vacuum-induced coherences. The following Section 4 is devoted to collective vacuum-induced processes, with the emphasis on a pair of dipole–dipole interacting multilevel atoms.

In the final part, related many-particle phenomena are discussed. Our aim is to provide a deep understanding of vacuum-induced processes by illuminating different aspects of the atom-vacuum interaction in a unified way. The different physical mechanisms are traced back to the founding master equation and interpreted in terms of the same underlying conditions and principles.

2. MATHEMATICAL MODEL

The various systems that are in the focus of Sections 3 and 4 of this review deal with single atoms and ensembles of atoms that interact with the quantized electromagnetic radiation field. The aim of this section is to provide a general model that allows to describe most of the effects and physical processes in these systems. We thus consider an ensemble of M identical multilevel atoms with a complex internal level structure that interact with the radiation field. This general model allows to describe the single-atom systems that are discussed in Section 3, as well as collective effects that are in the focus of Section 4. Although we will frequently refer to the emitters as atoms, they could be molecules or, in principle, any other quantum system that exhibits discrete energy levels. It is assumed that the internal level structure of each emitter is comprised of two near-degenerate multiplets with an arbitrary number of states, and we explicitly allow the states within each multiplet to be nondegenerate. An example for multiplets in realistic systems is given by angular momentum eigenstates of atoms, where the level splitting within each manifold can be identified with the Zeeman splitting of the magnetic sublevels. A detailed description of the system we are considering is provided in Section 2.1, where we also set up its Hamiltonian.

We describe the quantum dynamics of the system in the master equation approach (Agarwal, 1974; Breuer & Petruccione, 2006; Ficek & Swain, 2005; Lehmberg, 1970a,b) that provides an effective theory for the time evolution of the atomic degrees of freedom. It is important to stress that the atomic subsystem alone constitutes an open quantum system (Breuer & Petruccione, 2006) since it is coupled to a second system represented by the infinite number of field modes. Formally, the quantum state of the atomic degrees of freedom is obtained if a partial trace over the field modes is taken in the density operator of the composite system, and the time evolution of this reduced density operator is governed by the master equation. In contrast to closed quantum systems, this time evolution will not, in general, follow a unitary dynamics due to the coupling between the atoms and the radiation field. An outstanding strength of the master equation approach is that the infinite number of modes of the radiation field can be often regarded as a reservoir, which changes

only slightly due to the presence of the atoms. It is then justified to introduce a number of approximations that simplify the equation of motion for the atomic system considerably. Since the master equation only allows to determine the quantum state of the atomic subsystem, the quantum state of the radiation field is inaccessible. Fortunately, physical observables, which involve correlation functions of the electromagnetic field can be expressed in terms of correlation functions of atomic operators. Since these correlation functions can be evaluated in turn via the master equation and the quantum regression theorem (Breuer & Petruccione, 2006; Carmichael, 1993; Lax, 1963), it is generally not required to determine the quantum state of the radiation field. This fact contributes considerably to the power and applicability of the master equation approach.

The master equation technique is a standard tool for the description of atom-field interactions and has been applied to various systems. While the master equation for a single two-level atom is a standard component of most textbooks on quantum optics, the master equation for the quite general multiatom, multilevel system described in Section 2.1 is not part of the standard literature yet. We thus provide a detailed and instructive derivation of its explicit form in Sections 2.2 and 2.3. Starting from Zwanzig's exact master equation for the reduced density operator of the atoms, we recall the major steps that lead to the general master equation in Born approximation in Section 2.2. We then discuss all approximations and their scope of validity that lead to the master equation in its final form that is presented in Section 2.4. We emphasize that this last Section 2.4 is independent of Sections 2.2 and 2.3, and thus the two latter sections can be left out. Due to the generality of the master equation introduced in Section 2.4, it does not only constitute the basis for the discussion of the systems in Sections 3 and 4 but may also serve as a starting point for future studies of dipole-dipole interacting multilevel systems.

2.1. Description of the System

We consider a collection of M identical atoms that are located at different positions $\mathbf{r}_\mu (\mu \in \{1, \dots, M\})$ in space. An example for a geometrical setup of four atoms is shown in Figure 1(a). Each atom is modeled by a finite number of L atomic states, and the k -th state of atom μ is labeled by $|k_\mu\rangle$ ($k \in \{1, \dots, L\}$). Since we consider a collection of identical atoms, we assume that the states $|k_\mu\rangle$ and $|k_\nu\rangle$ for $\mu \neq \nu$ represent the same physical state within each atom. The subscript μ indicates that $|k_\mu\rangle$ belongs to the state space of atom μ , and the energy of state $|k_\mu\rangle$ is denoted by E_k .

We assign to each dipole transition of the atomic level scheme a number i and a transition frequency ω_i . This assignment can be chosen at will, but must be kept fixed throughout the derivation. The total number of

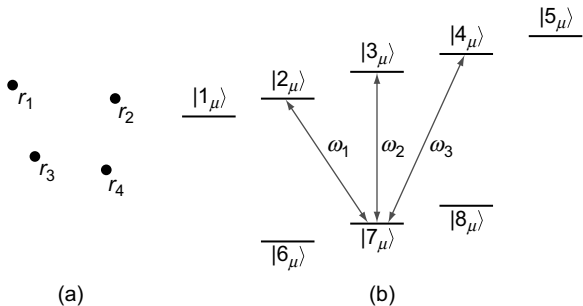


FIGURE 1 (a) Geometrical setup of $M = 4$ atoms. We neglect the center of mass motion of the atoms and assume their positions to be fixed. (b) Level scheme with $L = 8$ states. The ground- and excited-state multiplets consist of three and five states, respectively. In order to keep the drawing concise, only those dipole transitions that involve the ground state $|7_\mu\rangle$ are indicated by arrows, and the transition frequencies are labeled by ω_i . Note that the splitting of the excited- and ground-state multiplets is not to scale. In particular, all frequency differences ($\omega_i - \omega_j$) are assumed to be much smaller than the frequencies ω_i themselves.

dipole transitions is denoted by D . To the i -th dipole transition of atom μ corresponds a pair of raising and lowering operators that are labeled by $S_{i+}^{(\mu)}$ and $S_{i-}^{(\mu)}$, respectively. These transition operators are defined as

$$S_{i+}^{(\mu)} = |l_\mu\rangle\langle k_\mu| \quad \text{and} \quad S_{i-}^{(\mu)} = |k_\mu\rangle\langle l_\mu|, \quad (2.1)$$

where $|k_\mu\rangle$ is the ground state, and $|l_\mu\rangle$ is the excited state of the i -th dipole transition. For example, in Figure 1(b), the raising operator on the first transition is given by $S_{1+}^{(\mu)} = |2_\mu\rangle\langle 7_\mu|$.

Although the number of the relevant atomic states L is arbitrary, we assume that the atomic levels can be divided into a group of ground states and a group of excited states. In particular, we suppose that the ground- and excited-state multiplets are near-degenerate and that transitions among states of the same multiplet are not dipole-allowed. This means that the frequency splitting between any two states that belong to the same multiplet is much smaller than all dipole-allowed transition frequencies ω_i . It follows that all possible differences $(\omega_i - \omega_j)$ are much smaller than the mean transition frequency ω_0 ,

$$(\omega_i - \omega_j) \ll \omega_0, \quad \text{where} \quad \omega_0 = \frac{1}{D} \sum_{i=1}^D \omega_i \quad \text{and} \quad i, j \in \{1, \dots, D\}. \quad (2.2)$$

An example for an atomic level scheme with $L = 8$ states is shown in Figure 1(b). Here the ground- and excited-state multiplets consist of three

and five states, respectively. In general, the dynamics of the system may involve several near-degenerate multiplets of the internal level scheme, and the extension of our scheme to this situation is outlined in Section 2.4.

After the introduction of these definitions, we can establish the Hamiltonian of the complete system, which is comprised of three parts,

$$H = H_A + H_F + V. \quad (2.3)$$

Although H_A and H_F describe the free time evolution of the atoms and the radiation field, respectively, the interaction Hamiltonian V accounts for the coupling between these two subsystems. The first term in Equation (2.3) is given by

$$H_A = \sum_{\mu=1}^M \sum_{k=1}^L E_k A_{kk}^{(\mu)}, \quad (2.4)$$

where $A_{kk}^{(\mu)} = |k_\mu\rangle\langle k_\mu|$, and the Hamiltonian of the radiation field is

$$H_F = \sum_{ks} \hbar \omega_k a_{ks}^\dagger a_{ks}. \quad (2.5)$$

In the latter equation, $a_{ks}(a_{ks}^\dagger)$ are the annihilation (creation) operators that correspond to a field mode with wave vector k , unit polarization vector ϵ_{ks} ($s \in \{1, 2\}$), and frequency ω_k . In electric-dipole approximation, the interaction between the atoms and the radiation field is described by (Cohen-Tannoudji, Dupont-Roc, and Grynberg (1997); Cohen-Tannoudji, Dupont-Roc, and Grynberg, 1998)

$$V = - \sum_{\mu=1}^M \hat{\mathbf{d}}^{(\mu)} \cdot \hat{\mathbf{E}}(\mathbf{r}_\mu), \quad (2.6)$$

where $\hat{\mathbf{d}}^{(\mu)}$ is the electric-dipole moment operator of atom μ ,

$$\hat{\mathbf{d}}^{(\mu)} = \sum_{i=1}^D [d_i S_{i+}^{(\mu)} + \text{H.c.}] . \quad (2.7)$$

The complex vector d_i denotes the dipole moment of the i -th dipole transition, and the electric field operator $\hat{\mathbf{E}}$ is defined as

$$\hat{\mathbf{E}}(\mathbf{r}) = i\hbar \sum_{ks} u_{ks}(\mathbf{r}) a_{ks} + \text{H.c..} \quad (2.8)$$

In this equation, the mode function $u_{ks}(\mathbf{r})$ reads

$$u_{ks}(\mathbf{r}) = \frac{1}{\hbar} \sqrt{\frac{\hbar\omega_k}{2\varepsilon_0 v}} \epsilon_{ks} e^{ik \cdot \mathbf{r}}, \quad (2.9)$$

where v is the quantization volume, and ϵ_{ks} is the unit polarization vector that corresponds to the wave vector k ($s \in \{1, 2\}$).

The Hamiltonian V in Equation (2.6) describes the interaction of the atoms with the radiation field in electric-dipole coupling. The validity of this model rests on the assumption that the spatial variation of the electromagnetic field can be neglected on the length scale of the atom. In addition, the interaction of the atom with high-frequency field modes that lead to relativistic effects are not correctly described by V (Cohen-Tannoudji et al., 1997). For these two reasons, we introduce a cutoff in the summation on the wave vectors k in the electric field operator in Equation (2.6) and consider only wave vectors that obey $|k| \leq k_C$, where the cutoff wave number k_C is taken to be of the order of $1/a_0$ and a_0 is the Bohr radius. With this choice, only photons with wavelengths larger than typical atomic dimensions contribute to V . Since a wave number of $1/a_0$ corresponds to an energy of $m_e c^2 \alpha$, where $\alpha = 1/137$ is the fine structure constant and m_e the electron mass, our choice of the cutoff wave number excludes “relativistic modes” with an energy larger than $m_e c^2$. On the other hand, all relevant transition frequencies ω_i of the atomic system are typically much smaller than the cutoff frequency $\omega_C = ck_C$. It follows that our model describes quasi-resonant absorption and emission processes correctly, but virtual emissions and reabsorptions of high-frequency photons are not taken into account. We will discuss the implications of the frequency cutoff on the validity of the effects described by our model in detail in Section 2.3.

The interaction Hamiltonian V is the dipolar term of the multipolar Hamiltonian that is obtained from the Hamiltonian in minimal coupling via the Power–Zienau–Woolley transformation (Cohen-Tannoudji et al., 1997; Davidovich, 1975; Power & Zienau, 1959; Woolley, 1971). For completeness, we note that we omitted in Equation (2.3) the self-energy term

$$H_{\text{self}} = \frac{1}{\varepsilon_0} \sum_{\mu=1}^M \int d^3 r \mathbf{P}_{\perp}^{(\mu)}(\mathbf{r}) \cdot \mathbf{P}_{\perp}^{(\mu)}(\mathbf{r}) + \frac{1}{\varepsilon_0} \sum_{\substack{\mu, \nu=1 \\ \mu \neq \nu}}^M \int d^3 r \mathbf{P}^{(\mu)}(\mathbf{r}) \cdot \mathbf{P}^{(\nu)}(\mathbf{r}), \quad (2.10)$$

where $\mathbf{P}^{(\mu)}$ is the polarization density of atom μ , and $\mathbf{P}_{\perp}^{(\mu)}$ is its transverse component. The first term is a sum over single-atom self-energies that contribute to the Lamb shift of the individual atoms. As we will discuss in

Section 2.3, our model established in this section is not suited for a correct description of the Lamb shift, and thus, we disregard this term. In the second term of Equation (2.10), only products $\mathbf{P}^{(\mu)}(\mathbf{r}) \cdot \mathbf{P}^{(\nu)}(\mathbf{r})$ with $\mu \neq \nu$ contribute. Since the polarization $\mathbf{P}^{(\mu)}(\mathbf{r})$ is strictly zero outside of atom μ , and since we assume that the atomic separation is always larger than the extend of the atomic clouds, each of these products are identically equal to zero (see, e.g., complement AIV and CIV in the study by Cohen-Tannoudji et al. (1997)). It is thus justified that we did not include H_{self} in the system Hamiltonian H in Equation (2.3).

2.2. General Reservoir Theory

The Hamiltonian in Equation (2.3) determines the quantum dynamics of the system described in Section 2.1 via Schrödinger's equation. In the interaction picture with respect to the Hamiltonian $H_A + H_F$ describing the free time evolution of the atoms and the radiation field, the density operator $\tilde{\varrho}$ of the system obeys

$$\partial_t \tilde{\varrho}(t) = -\frac{i}{\hbar} [V(t), \tilde{\varrho}(t)] = -\frac{i}{\hbar} \mathcal{L}(t) \tilde{\varrho}(t). \quad (2.11)$$

Here $V(t)$ is the interaction Hamiltonian in the interaction picture with respect to $H_A + H_F$,

$$V(t) = U^\dagger(t) V U(t), \quad \text{where} \quad U(t) = \exp[-i(H_A + H_F)t/\hbar], \quad (2.12)$$

and the second equality in Equation (2.11) defines the Liouville superoperator $\mathcal{L}(t)$ of the system. Since the radiation field is characterized by infinitely many degrees of freedom, a direct integration of Equation (2.11) for the complete system is intractable. Fortunately, in most situations, it is sufficient to know the reduced density operator $\tilde{\varrho}_A = \text{Tr}_F[\tilde{\varrho}]$ of the atomic subsystem, where the trace runs over the degrees of freedom of the radiation field. By means of projection operator techniques, Equation (2.11) can be transferred into an exact equation of motion for the reduced density operator $\tilde{\varrho}_A$ of the atoms (Agarwal, 1974; Breuer & Petruccione, 2006; Mandel & Wolf, 1995; Zwanzig, 1961),

$$\begin{aligned} i\hbar \partial_t \mathcal{P} \tilde{\varrho}(t) &= \mathcal{P} \mathcal{L}(t) \mathcal{P} \tilde{\varrho} + \mathcal{P} \mathcal{L}(t) \mathcal{Q} \\ &\left[\mathcal{U}(t, 0) \mathcal{Q} \tilde{\varrho}(0) - \frac{i}{\hbar} \int_0^t d\tau \mathcal{U}(t, \tau) \mathcal{Q} \mathcal{L}(\tau) \mathcal{P} \tilde{\varrho}(\tau) \right]. \end{aligned} \quad (2.13)$$

Here the time-independent projection operator \mathcal{P} is defined as

$$\mathcal{P} \tilde{\varrho}(t) = \varrho_F(0) \otimes \text{Tr}_F[\tilde{\varrho}(t)] = \varrho_F(0) \otimes \tilde{\varrho}_A(t), \quad (2.14)$$

and $\varrho_F(0) = \text{Tr}_A[\tilde{\varrho}(0)]$ denotes the reduced density operator of the radiation field at $t = 0$. The projection operator \mathcal{P} satisfies $\mathcal{P}^2 = \mathcal{P}$, and $\mathcal{P}\tilde{\varrho}$ is essentially given by the reduced density operator $\tilde{\varrho}_A$ of the atoms that we are interested in. $\mathcal{Q} = \mathbb{1} - \mathcal{P}$ is the complementary projection operator to \mathcal{P} , and

$$\mathcal{U}(t, \tau) = \mathcal{T} \exp \left[-\frac{i}{\hbar} \int_{\tau}^t \mathcal{Q}\mathcal{L}(t') dt' \right] \quad (2.15)$$

is the time evolution operator. In this equation, \mathcal{T} denotes the time-ordering operator that arranges the operators such that the time arguments increase from right to left. Equation (2.13) is known as the Nakajima–Zwanzig equation and is an effective equation of motion for the atomic degrees of freedom under the influence of the coupling to the radiation field. The atomic subsystem is an example for an open quantum system since it is coupled to a second quantum system, which is usually referred to as the environment. In our case, this environment is represented by the infinitely many modes of the electromagnetic radiation field. The interaction between the open system and the environment creates correlations between the two subsystems such that it is impossible, in general, to represent the time evolution of $\mathcal{P}\tilde{\varrho}$ by a unitary dynamics.

In order to simplify the exact master Equation (2.13), we make the following two assumptions:

1. The expectation value of the interaction Hamiltonian V with respect to $\varrho_F(0)$ vanishes, $\text{Tr}_F[\varrho_F(0)V(t)] = 0$.
2. The total density operator factorizes into a product state at the initial time $t = 0$, $\tilde{\varrho}(0) = \varrho_F(0) \otimes \tilde{\varrho}_A(0)$.

The first condition implies $\mathcal{P}\mathcal{L}(t)\mathcal{P} = 0$, and thus, the first term in Equation (2.13) vanishes. Since the application of the projection operator \mathcal{Q} to the product state $\varrho_F(0) \otimes \tilde{\varrho}_A(0)$ yields zero, i.e., $\mathcal{Q}\tilde{\varrho}(0) = 0$, assumption (2) eliminates the second term in Equation (2.13), which then reduces to

$$\partial_t \mathcal{P}\tilde{\varrho}(t) = -\frac{1}{\hbar^2} \int_0^t d\tau \mathcal{P}\mathcal{L}(t)\mathcal{Q}\mathcal{U}(t, \tau)\mathcal{Q}\mathcal{L}(\tau)\mathcal{P}\tilde{\varrho}(\tau). \quad (2.16)$$

It should be noted that Equation (2.16) is still an exact equation for $\mathcal{P}\tilde{\varrho}$ that holds if conditions (1) and (2) are satisfied.

We now introduce the first approximation, which is known as the Born approximation. The right-hand side of Equation (2.16) is at least of second order in the interaction Hamiltonian V . Higher orders arise since the

time evolution operator \mathcal{U} also contains \mathcal{L} . If the coupling between the atoms and the radiation field is sufficiently weak, it is justified to restrict the analysis to the leading order in V . This amounts to approximate the time evolution operator in Equation (2.15) by the identity superoperator, $U(t, \tau) \approx \mathbb{1}$. The Born approximation means that an emitted photon does not react back on the atom. In this weak coupling limit, we obtain the following master equation for the reduced density operator of the atoms $\tilde{\rho}_A$ in the interaction picture,

$$\partial_t \tilde{\rho}_A(t) = \frac{1}{\hbar^2} \int_0^t d\tau \text{Tr}_F \left\{ [V(t - \tau) \rho_F \otimes \tilde{\rho}_A(t - \tau), V(t)] + \text{H.c.} \right\}, \quad (2.17)$$

where the short-hand notation $\rho_F(0) = \rho_F$ has been introduced and we changed the integration variable from τ to $t - \tau$.

Apart from the two assumptions (1) and (2) and the Born approximation, the master equation in Equation (2.17) has been derived under quite general conditions and thus applies to various other systems. But since Equation (2.17) is an integrodifferential equation, it is still very difficult to solve in practice. In Section 2.3, we describe in detail the various approximations and their scope of validity that allow to transfer Equation (2.17) into a much simpler form that is well suited for practical purposes.

2.3. Derivation of the Master Equation

We now derive from Equation (2.17) the explicit form of the master equation for the system described in Section 2.1. In order to evaluate the right-hand side of Equation (2.17), we transform the interaction Hamiltonian V in Equation (2.6) into the interaction picture with respect to $H_A + H_F$, where H_A and H_F are defined in Equations (2.4) and (2.5), respectively,

$$V(t) = - \sum_{\mu=1}^M \sum_{i=1}^D \left[S_{i+}^{(\mu)} e^{i\omega_i t} \mathbf{d}_i \cdot \hat{\mathbf{E}}(\mathbf{r}_\mu, t) + S_{i-}^{(\mu)} e^{-i\omega_i t} \mathbf{d}_i^* \cdot \hat{\mathbf{E}}(\mathbf{r}_\mu, t) \right], \quad (2.18)$$

and $\hat{\mathbf{E}}(\mathbf{r}_\mu, t) = \exp[iH_F t/\hbar] \hat{\mathbf{E}}(\mathbf{r}_\mu) \exp[-iH_F t/\hbar]$. After some rearrangement, the master Equation (2.17) can be written as

$$\begin{aligned} \partial_t \tilde{\rho}_A(t) = & \sum_{\mu, \nu=1}^M \sum_{i,j=1}^D \left\{ \left[S_{j-}^{(\nu)} A_{ij}^{\mu\nu}(t), S_{i+}^{(\mu)} \right] e^{i(\omega_i - \omega_j)t} + \left[S_{j+}^{(\nu)} B_{ij}^{\mu\nu}(t), S_{i-}^{(\mu)} \right] e^{-i(\omega_i - \omega_j)t} \right. \\ & \left. + \left[S_{j+}^{(\nu)} C_{ij}^{\mu\nu}(t), S_{i+}^{(\mu)} \right] e^{i(\omega_i + \omega_j)t} + \left[S_{j-}^{(\nu)} D_{ij}^{\mu\nu}(t), S_{i-}^{(\mu)} \right] e^{-i(\omega_i + \omega_j)t} + \text{H.c.} \right\}, \end{aligned} \quad (2.19)$$

where the operators $A_{ij}^{\mu\nu}$, $B_{ij}^{\mu\nu}$, $C_{ij}^{\mu\nu}$, and $D_{ij}^{\mu\nu}$ are defined as

$$A_{ij}^{\mu\nu}(t) = \int_0^t d\tau \left[\mathbf{d}_i^T G^{\mu\nu}(t, \tau) \mathbf{d}_j^* \right] e^{i\omega_j \tau} \tilde{\varrho}_A(t - \tau), \quad (2.20a)$$

$$B_{ij}^{\mu\nu}(t) = \int_0^t d\tau \left[(\mathbf{d}_i^*)^T G^{\mu\nu}(t, \tau) \mathbf{d}_j \right] e^{-i\omega_j \tau} \tilde{\varrho}_A(t - \tau), \quad (2.20b)$$

$$C_{ij}^{\mu\nu}(t) = \int_0^t d\tau \left[\mathbf{d}_i^T G^{\mu\nu}(t, \tau) \mathbf{d}_j \right] e^{-i\omega_j \tau} \tilde{\varrho}_A(t - \tau), \quad (2.20c)$$

$$D_{ij}^{\mu\nu}(t) = \int_0^t d\tau \left[(\mathbf{d}_i^*)^T G^{\mu\nu}(t, \tau) \mathbf{d}_j^* \right] e^{i\omega_j \tau} \tilde{\varrho}_A(t - \tau), \quad (2.20d)$$

and \mathbf{d}^T denotes the transposed of \mathbf{d} . These operators are comprised of integrals over the past of the atomic density operator $\tilde{\varrho}_A$, an exponential term that oscillates at atomic frequencies $\pm\omega_j$ and the tensor of the electromagnetic field $G^{\mu\nu}$. The Cartesian components of this tensor are defined as ($p, q \in \{1, 2, 3\}$)

$$G_{pq}^{\mu\nu}(t, \tau) = \frac{1}{\hbar^2} \text{Tr}_F \left\{ \left[\mathbf{e}_p \cdot \hat{\mathbf{E}}(\mathbf{r}_\mu, t) \right] \left[\mathbf{e}_q \cdot \hat{\mathbf{E}}(\mathbf{r}_\nu, t - \tau) \right] \varrho_F \right\}, \quad (2.21)$$

where \mathbf{e}_p are Cartesian unit vectors. In general, this tensor depends on time t and the integration variable τ . Here we consider the special case of stationary reservoirs, i.e., the state $\varrho_F(0)$ of the radiation field is stationary with respect to the free time evolution of the reservoir governed by H_F ,

$$[H_F, \varrho_F(0)] = 0. \quad (2.22)$$

With this assumption, the operators $\exp[\pm iH_F t/\hbar]$ commute with $\varrho_F(0)$. In combination with the invariance of the trace under cyclic permutations of the arguments, Equation (2.22) leads to homogeneous correlation functions in time that are independent of t ,

$$G_{pq}^{\mu\nu}(\tau) = \frac{1}{\hbar^2} \text{Tr}_F \left\{ \left[\mathbf{e}_p \cdot \hat{\mathbf{E}}(\mathbf{r}_\mu, \tau) \right] \left[\mathbf{e}_q \cdot \hat{\mathbf{E}}(\mathbf{r}_\nu, 0) \right] \varrho_F \right\}. \quad (2.23)$$

Stationary reservoirs are particularly relevant, since physical reservoirs like thermal fields (including the vacuum) are of this type. On the other

hand, the most prominent example for a nonstationary reservoir that leads to t -dependent correlation functions is represented by a squeezed vacuum or squeezed thermal field. Master equations for atoms in squeezed reservoirs can be found in the studies carried out by Breuer and Petruccione (2006), Enaki and Macovei (2000), Ficek and Tanaś (2002), Gardiner (1986), Gardiner and Collet (1985), and Scully and Zubairy (1997) and will not be investigated further in this review. With the definition of the electric field operator in Equation (2.8), the explicit form of the tensor components in Equation (2.23) is given by

$$G_{pq}^{\mu\nu}(\tau) = - \sum_{\substack{ks \\ k's'}} \left\{ [e_p \cdot u_{ks}(r_\mu)] [e_q \cdot u_{k's'}(r_\nu)] \text{Tr}_F[a_{ks}a_{k's'}^\dagger \varrho_F] e^{i\omega_k \tau} \right. \quad (2.24)$$

$$- [e_p \cdot u_{ks}(r_\mu)] [e_q \cdot u_{k's'}^*(r_\nu)] \text{Tr}_F[a_{ks}a_{k's'}^\dagger \varrho_F] e^{-i\omega_k \tau}$$

$$- [e_p \cdot u_{ks}^*(r_\mu)] [e_l \cdot u_{k's'}(r_\nu)] \text{Tr}_F[a_{ks}^\dagger a_{k's'} \varrho_F] e^{i\omega_k \tau}$$

$$\left. + [e_p \cdot u_{ks}^*(r_\mu)] [e_q \cdot u_{k's'}^*(r_\nu)] \text{Tr}_F[a_{ks}^\dagger a_{k's'}^\dagger \varrho_F] e^{-i\omega_k \tau} \right\}.$$

The evaluation of this expression involves the mean values $\text{Tr}_F[\dots \varrho_F]$ with respect to the initial state of the radiation field.

In many physical situations, the integrals in Equation (2.20) can be simplified considerably. The reduced density operator $\tilde{\varrho}_A$ in the interaction picture evolves typically on a timescale that is determined by the lifetimes $T_A = 1/\gamma$ of the atomic levels. On the contrary, the τ dependence of the correlation functions $G_{pq}^{\mu\nu}(\tau)$ in Equation (2.23) is independent of the atomic system and solely defined by the properties of the reservoir. Here we assume that the correlation functions in Equation (2.23) are approximately zero if τ is much larger than a typical correlation time τ_c . If the correlation time τ_c is much smaller than the atomic lifetimes, i.e., $\tau_c \ll T_A$, the atomic variables evolve on a much slower timescale than the correlation functions. It is then justified to introduce two approximations in Equation (2.20). First, we can assume that the interaction with the radiation field does not change the atomic state $\tilde{\varrho}_A(t)$ appreciably during the correlation time τ_c . Therefore, we can replace $\tilde{\varrho}_A(t - \tau)$ by $\tilde{\varrho}_A(t)$ in Equation (2.20). In addition, it is justified to extend the upper bound in the integration over τ in Equation (2.20) to infinity. These two approximations are known as the Markov approximation (Agarwal, 1974; Breuer & Petruccione, 2006; Cohen-Tannoudji et al., 1998; Mandel & Wolf, 1995) and allow to cast Equation (2.20) into the following form,

$$A_{ij}^{\mu\nu}(t) = \tilde{\varrho}_A(t) \mathcal{A}_{ij}^{\mu\nu}, \quad B_{ij}^{\mu\nu}(t) = \tilde{\varrho}_A(t) \mathcal{B}_{ij}^{\mu\nu}, \quad (2.25a)$$

$$C_{ij}^{\mu\nu}(t) = \tilde{\varrho}_A(t) \mathcal{C}_{ij}^{\mu\nu}, \quad D_{ij}^{\mu\nu}(t) = \tilde{\varrho}_A(t) \mathcal{D}_{ij}^{\mu\nu}, \quad (2.25b)$$

where the complex-valued coefficients $\mathcal{A}_{ij}^{\mu\nu}$, $\mathcal{B}_{ij}^{\mu\nu}$, $\mathcal{C}_{ij}^{\mu\nu}$, and $\mathcal{D}_{ij}^{\mu\nu}$ are given by

$$\mathcal{A}_{ij}^{\mu\nu} = \int_0^\infty d\tau \left[\mathbf{d}_i^T G^{\mu\nu}(\tau) \mathbf{d}_j^* \right] e^{i\omega_j \tau}, \quad \mathcal{B}_{ij}^{\mu\nu} = \int_0^\infty d\tau \left[(\mathbf{d}_i^*)^T G^{\mu\nu}(\tau) \mathbf{d}_j \right] e^{-i\omega_j \tau}, \quad (2.26a)$$

$$\mathcal{C}_{ij}^{\mu\nu} = \int_0^\infty d\tau \left[\mathbf{d}_i^T G^{\mu\nu}(\tau) \mathbf{d}_j \right] e^{-i\omega_j \tau}, \quad \mathcal{D}_{ij}^{\mu\nu} = \int_0^\infty d\tau \left[(\mathbf{d}_i^*)^T G^{\mu\nu}(\tau) \mathbf{d}_j^* \right] e^{i\omega_j \tau}. \quad (2.26b)$$

The Markov approximation is usually very well justified in quantum optical systems. In particular, it is possible to calculate the correlation functions in Equation (2.23) for some initial states of the radiation field directly, e.g., for a thermal field at temperature T (Breuer & Petruccione, 2006; Cohen-Tannoudji et al., 1997, 1998; Trippenbach, Gao, Cooper, & Burnett, 1992a). This analysis shows that the typical correlation time of the functions $G^{\mu\nu}$ corresponding to a single point in space ($\mu = \nu$) is even shorter than the period $2\pi/\omega_0$ of the relevant dipole transitions. Since typical lifetimes of excited states in the optical regime are of the order of $10^{-6} - 10^{-9}$ s and transition frequencies are of the order of 10^{15} s⁻¹, the condition $\tau_c \ll T_A$ is very well satisfied. Similarly, one can show that the correlation functions that refer to two different points in space ($G^{\mu\nu}$ with $\mu \neq \nu$) decay sufficiently fast provided that $R_{\mu\nu}/c \ll T_A$, i.e., the passage time of photons between pairs of atoms must be small as compared with the typical timescale of the atomic evolution. For microscopic ensembles of atoms, this condition is also easily met.

There are several important points that are associated with the Markov approximation that we would like to mention. First of all, decaying correlation functions that are equal to zero for $\tau \gg \tau_c$ can only be realized for a continuum of frequencies in the reservoir (Breuer & Petruccione, 2006). Therefore, the summation over k vectors in Equation (2.24) has to be replaced by an integration. At the heart of the Markov approximation is the assumption that $\hat{\rho}_A(t)$ does not change on a timescale defined by the correlation time τ_c . The master equation in Markov approximation thus describes the time evolution of the reduced atomic density operator on a coarse-grained time axis (Cohen-Tannoudji et al., 1998) that does only resolve temporal events on a timescale $\Delta t \gg \tau_c$. This instance has two important consequences. First, retardation effects that occur due to the finite passage time of photons between the atoms are not correctly described. These effects have been studied for a pair of two-level atoms by Milonni and Knight (1974, 1975), where it has been shown that retardation effects are important for times $t \approx R_{\mu\nu}/c$ and atomic separations larger

than half of the transition wavelength. Extensions to smaller distances have been discussed by Dung and Ujihara (1999). On the other hand, retardation effects average out for $t \gg R_{\mu\nu}/c$ and can thus be disregarded in the long-time limit. Second, in order to be consistent with the fact that events on a timescale defined by the correlation time of the reservoir functions are not resolved, all terms in the master equation that cause a time evolution on this timescale have to be eliminated. Formally, this can be achieved if the master equation is averaged over a time interval Δt with $\tau_c \ll \Delta t \ll T_A$. This averaging procedure is usually referred to as rotating-wave approximation (RWA) and eliminates all terms proportional to $S_{i+}^{(\mu)} S_{j+}^{(\nu)}$ and $S_{i-}^{(\mu)} S_{j-}^{(\nu)}$ that oscillate at a frequency $\pm(\omega_i + \omega_j)$. On the contrary, the terms proportional to $S_{i+}^{(\mu)} S_{j-}^{(\nu)}$ and $S_{i-}^{(\mu)} S_{j+}^{(\nu)}$ oscillate at a frequency $\pm(\omega_i - \omega_j)$. We assume that the differences $(\omega_i - \omega_j)$ between the resonance frequencies are much smaller than the frequencies ω_i themselves, and in particular that $|\omega_i - \omega_j| \Delta t \ll 1$ such that these terms are not affected by the temporal averaging. After the transformation of Equation (2.19) into the Schrödinger picture and the RWA, we thus obtain

$$\begin{aligned} \partial_t \varrho_A(t) = & -\frac{i}{\hbar} [H_A, \varrho_A(t)] \\ & + \sum_{\mu, \nu=1}^M \sum_{i, j=1}^D \left\{ \mathcal{A}_{ij}^{\mu\nu} \left[S_{j-}^{(\nu)} \varrho_A(t), S_{i+}^{(\mu)} \right] + \mathcal{B}_{ij}^{\mu\nu} \left[S_{j+}^{(\nu)} \varrho_A(t), S_{i-}^{(\mu)} \right] + \text{H.c.} \right\}. \end{aligned} \quad (2.27)$$

We emphasize that the RWA performed in Equation (2.19) is not equivalent to a RWA on the level of the interaction Hamiltonian V (Agarwal, 1974). In particular, we would miss important terms that contribute to the energy shifts of collective states in multiatom systems if we had performed the RWA already in Equation (2.6). Moreover, it has been shown (Breuer & Petruccione, 2006; Davies, 1974; Dümcke & Spohn, 1979) that the master equation in Born–Markov approximation without performing the RWA may not give rise to a completely positive density operator. Since this is an unphysical result, the Markov approximation enforces the RWA in the weak coupling limit.

In contrast to Equation (2.19), Equation (2.27) is an ordinary differential equation for the reduced density operator of the atoms ϱ_A . The influence of the reservoir is accounted for by the complex-valued parameters $\mathcal{A}_{ij}^{\mu\nu}$ and $\mathcal{B}_{ij}^{\mu\nu}$. Since these coefficients are time independent, the master Equation (2.27) describes a quantum Markov process (Breuer & Petruccione, 2006). According to Equation (2.26a), the coefficients that appear in the master equation in Born–Markov approximation always have the structure of a tensor coupling, no matter what the initial state of the radiation field is. The choice of a specific reservoir determines the electromagnetic field

tensor in Equation (2.24), and once this tensor is known, the parameters $\mathcal{A}_{ij}^{\mu\nu}$ and $\mathcal{B}_{ij}^{\mu\nu}$ can be evaluated via Equation (2.26a).

In order to give an example for the parameters $\mathcal{A}_{ij}^{\mu\nu}$ and $\mathcal{B}_{ij}^{\mu\nu}$ and the further evaluation of Equation (2.27), we assume that the radiation field is initially in the vacuum state, i.e., $\varrho_F(0) = |0\rangle\langle 0|$. With this choice, the various field correlation functions that enter Equation (2.24) are given by

$$\begin{aligned}\text{Tr}_F[a_{ks}a_{k's'}^\dagger \varrho_F] &= \text{Tr}_F[a_{ks}^\dagger a_{k's'}^\dagger \varrho_F] = \text{Tr}_F[a_{ks}^\dagger a_{k's'} \varrho_F] = 0, \\ \text{Tr}_F[a_{ks}a_{k's'}^\dagger \varrho_F] &= \delta_{kk'}\delta_{ss'}.\end{aligned}\quad (2.28)$$

Note that the initial state $\varrho_F(0) = |0\rangle\langle 0|$ fulfills the two assumptions in Section 2.2 that allowed to establish the master Equation (2.17) in Born approximation. We continue with the evaluation of the parameters $\mathcal{A}_{ij}^{\mu\nu}$ and $\mathcal{B}_{ij}^{\mu\nu}$ in Equation (2.26a). First, we replace the summation over the discrete wave vectors k in Equation (2.24) by an integral over the continuum modes,

$$\sum_{ks} \rightarrow \frac{v}{(2\pi c)^3} \int_0^{\omega_C} d\omega_k \omega_k^2 \int d\Omega_k \sum_s. \quad (2.29)$$

Here we expressed the integral over the three-dimensional k -space in terms of spherical coordinates and changed the integration over k into an integral over frequencies $\omega_k = ck$. Note that the integration over ω_k extends from 0 to ω_C , where ω_C is the cutoff frequency that has been introduced in Section 2.1. Next, we use the relation $\int_0^\infty e^{ix\tau} d\tau = \pi\delta(x) + i\mathcal{P}_c 1/x$ (here \mathcal{P}_c denotes the Cauchy principal part) and evaluate the integrals over τ in Equation (2.26a). This yields

$$\mathcal{A}_{ij}^{\mu\nu} = \left(\Gamma_{ij}^{\mu\nu} + iM_{ij}^{\mu\nu} \right) \quad \text{and} \quad \mathcal{B}_{ij}^{\mu\nu} = -i \left(P_{ij}^{\mu\nu} \right)^*, \quad (2.30)$$

where

$$\Gamma_{ij}^{\mu\nu} = \frac{\pi}{2\varepsilon_0 \hbar (2\pi c)^3} \int_0^{\omega_C} d\omega_k \omega_k^3 \left[\mathbf{d}_i^T F(\omega_k/c, \mathbf{R}_{\mu\nu}) \mathbf{d}_j^* \right] \delta(\omega_k - \omega_0), \quad (2.31)$$

$$P_{ij}^{\mu\nu} = \frac{1}{2\varepsilon_0 \hbar (2\pi c)^3} \mathcal{P}_c \int_0^{\omega_C} d\omega_k \omega_k^3 \left[\mathbf{d}_i^T F(\omega_k/c, \mathbf{R}_{\mu\nu}) \mathbf{d}_j^* \right] \frac{1}{\omega_0 + \omega_k}, \quad (2.32)$$

$$M_{ij}^{\mu\nu} = \frac{1}{2\varepsilon_0 \hbar (2\pi c)^3} \mathcal{P}_c \int_0^{\omega_C} d\omega_k \omega_k^3 \left[\mathbf{d}_i^T F(\omega_k/c, \mathbf{R}_{\mu\nu}) \mathbf{d}_j^* \right] \frac{1}{\omega_0 - \omega_k}. \quad (2.33)$$

In this equation, the vector $\mathbf{R}_{\mu\nu} = \mathbf{r}_\mu - \mathbf{r}_\nu$ denotes the relative coordinates of atom μ with respect to atom ν . Note that the integrals in Equations (2.32) and (2.33) would be divergent if we had not introduced the cutoff frequency ω_C . In these definitions, we approximated the frequencies ω_i and ω_j by the mean frequency $\omega_0 = (1/D) \sum_{i=1}^D \omega_i$. This is justified since we assumed that the differences $(\omega_i - \omega_j)$ are much smaller than the mean transition frequency ω_0 . The Cartesian components of the tensor F in Equations (2.31)–(2.33) are given by (Craig & Thirunamachandran, 1984; Friedberg, Hartmann, & Manassah, 1973; McLone & Power, 1965) ($p, q \in \{1, 2, 3\}$)

$$\begin{aligned} F_{pq}(k, \mathbf{R}) &= \int d\Omega_k \sum_s e^{ik \cdot \mathbf{R}} [\epsilon_{ks}]_p [\epsilon_{ks}^*]_q \\ &= 4\pi \left\{ \delta_{pq} \left[\left(\frac{1}{\zeta} - \frac{1}{\zeta^3} \right) \sin \zeta + \frac{1}{\zeta^2} \cos \zeta \right] \right. \\ &\quad \left. - \frac{[\mathbf{R}]_p [\mathbf{R}]_q}{R^2} \left[\left(\frac{1}{\zeta} - \frac{3}{\zeta^3} \right) \sin \zeta + \frac{3}{\zeta^2} \cos \zeta \right] \right\}, \end{aligned} \quad (2.34)$$

where $\zeta = kR$. Since the range of integration extends over the complete solid angle, the tensor in Equation (2.34) depends only on the absolute value of k . In addition, the components of this tensor are real, and the parameters in Equations (2.31)–(2.33) obey the following symmetry relations,

$$\Gamma_{ij}^{\mu\nu} = (\Gamma_{ji}^{\nu\mu})^*, \quad P_{ij}^{\mu\nu} = (P_{ji}^{\nu\mu})^*, \quad M_{ij}^{\mu\nu} = (M_{ji}^{\nu\mu})^*. \quad (2.35)$$

These relations together with Equation (2.30) allow us to cast the master Equation (2.19) into the following form,

$$\begin{aligned} \partial_t \varrho_A(t) &= -\frac{i}{\hbar} [H_A, \varrho_A(t)] + i \sum_{\mu, \nu=1}^M \sum_{i=1}^D \sum_{j=1}^D \Omega_{ij}^{\mu\nu} \left[S_{i+}^{(\mu)} S_{j-}^{(\nu)}, \varrho_A(t) \right] \\ &\quad - \sum_{\mu, \nu=1}^M \sum_{i=1}^D \sum_{j=1}^D \Gamma_{ij}^{\mu\nu} \left(S_{i+}^{(\mu)} S_{j-}^{(\nu)} \varrho_A(t) + \varrho_A(t) S_{i+}^{(\mu)} S_{j-}^{(\nu)} - 2S_{j-}^{(\nu)} \varrho_A(t) S_{i+}^{(\mu)} \right) \\ &\quad - i \sum_{\mu=1}^M \sum_{i=1}^D \sum_{j=1}^D \left\{ M_{ij}^{\mu\mu} \left[S_{i+}^{(\mu)} S_{j-}^{(\mu)}, \varrho_A(t) \right] - (P_{ij}^{\mu\mu})^* \left[S_{i-}^{(\mu)} S_{j+}^{(\mu)}, \varrho_A(t) \right] \right\}. \end{aligned} \quad (2.36)$$

We first concentrate on the two terms in the last line of Equation (2.36), which depend on $M_{ij}^{\mu\mu} = M_{ij}$ and $P_{ij}^{\mu\mu} = P_{ij}$. Note that we omitted the

index μ since the parameters in Equations (2.32) and (2.33) depend only on the indices i and j if $\mu = \nu$. In order to give an interpretation for the parameters M_{ij} and P_{ij} for $i = j$, let $S_{i+}^{(\mu)} = |k_\mu\rangle\langle l_\mu|$ be the transition operator from state $|l_\mu\rangle$ of atom μ to state $|k_\mu\rangle$ of the same atom. Since $S_{i+}^{(\mu)}S_{i-}^{(\mu)} = |k_\mu\rangle\langle k_\mu| = A_{kk}^{(\mu)}$ and $S_{i-}^{(\mu)}S_{i+}^{(\mu)} = A_{ll}^{(\mu)}$, the parameters M_{ii} and P_{ii} represent a frequency shift of the atomic levels, which is related to the Lamb shift.

However, we emphasize that the correct values for the Lamb shift of the atomic levels cannot be obtained within the framework of the present theory. A rigorous treatment of this effect requires a fully relativistic theory and renormalization procedures. In addition, it is well known that the Lamb shift can only be evaluated correctly if all atomic states, including the continuum, are included. Here we assume that the correct values for the atomic level shifts have been incorporated into the energies of the atomic states.

We proceed with a short discussion of the parameters M_{ij} and P_{ij} for $i \neq j$. In this case, the terms proportional to M_{ij} and P_{ij} represent a coherent coupling between two atomic levels of the same atom. The influence of these terms on the system dynamics is rather small and has been investigated by Akram, Ficek, and Swain (2000), Cardimona and Stroud (1983), and Ficek and Swain (2005). In particular, the terms M_{ij} and P_{ij} do not contribute at all unless two conditions are simultaneously fulfilled. First, the dipole moments \mathbf{d}_i and \mathbf{d}_j must be nonorthogonal since $M_{ij}, P_{ij} \sim \mathbf{d}_i \cdot \mathbf{d}_j^*$. Second, at least one of the operators $S_{i+}^{(\mu)}S_{j-}^{(\mu)}$ or $S_{i-}^{(\mu)}S_{j+}^{(\mu)}$ must be different from zero (for $i \neq j$). These two conditions can be met simultaneously in artificial atoms, but not in transitions between two atomic angular momentum multiplets. We thus omit these terms in the following.

In conclusion, we can remove all terms in the last line of Equation (2.36) if the Lamb shifts are incorporated into the energies of the atomic levels.

The parameters $\Omega_{ij}^{\mu\nu}$ with $\mu \neq \nu$ occur in the second term of the first line in Equation (2.36) and are defined as $\Omega_{ij}^{\mu\nu} = P_{ij}^{\mu\nu} - M_{ij}^{\mu\nu}$. It follows from Equations (2.32) and (2.33) that they can be written as

$$\Omega_{ij}^{\mu\nu} = \frac{1}{\varepsilon_0 \hbar (2\pi c)^3} \mathcal{P}_c \int_0^{\omega_C} d\omega_k \left[\mathbf{d}_i^T F(\omega_k/c, \mathbf{R}_{\mu\nu}) \mathbf{d}_j^* \right] \frac{\omega_k^4}{\omega_k^2 - \omega_0^2}. \quad (2.37)$$

In order to evaluate the integral, we replace the sharp frequency cut-off at ω_C by a smooth step function and extend the upper integration limit to infinity, i.e., we exchange $\int_0^{\omega_C} d\omega_k$ by $\int_0^\infty d\omega_k \omega_C^2 / (\omega_k^2 + \omega_C^2)$. The smooth step function $\omega_C^2 / (\omega_k^2 + \omega_C^2)$ is approximately equal to unity for

$\omega_k \ll \omega_C$ and approximately zero for $\omega_k \gg \omega_C$. Note that this choice of the regularization function is not unique, and other forms have been used in the literature (Craig & Thirunamachandran, 1984). If the sin and cos functions appearing in the definition of the tensor F are decomposed in exponential functions, it is straightforward to evaluate the principal value integrals in Equation (2.37) with the method of Residues,

$$\Omega_{ij}^{\mu\nu} = \frac{k_0^3}{4\pi\epsilon_0\hbar} \left\{ \mathbf{d}_i \cdot \mathbf{d}_j^* \left[\left(\frac{1}{\eta} - \frac{1}{\eta^3} \right) \cos \eta - \frac{1}{\eta^2} \sin \eta + \mathcal{C}_1(\eta, \kappa) \right] \right. \quad (2.38)$$

$$\left. - \frac{[\mathbf{d}_i \cdot \mathbf{R}_{\mu\nu}] [\mathbf{d}_j^* \cdot \mathbf{R}_{\mu\nu}]}{R_{\mu\nu}^2} \left[\left(\frac{1}{\eta} - \frac{3}{\eta^3} \right) \cos \eta - \frac{3}{\eta^2} \sin \eta + \mathcal{C}_2(\eta, \kappa) \right] \right\}.$$

In this equation, the functions \mathcal{C}_1 and \mathcal{C}_2 depend on the frequency cutoff via the parameter $\kappa = R_{\mu\nu}k_C$ and are given by ($\eta = k_0R_{\mu\nu}$)

$$\mathcal{C}_1(\eta, \kappa) = \frac{1}{\kappa^2 + \eta^2} \left[e^{-\kappa} (1 + \kappa + \kappa^2) \frac{\kappa^2}{\eta^3} + (1 - \eta^2) \frac{\cos \eta}{\eta} + \sin \eta \right], \quad (2.39a)$$

$$\mathcal{C}_2(\eta, \kappa) = \frac{1}{\kappa^2 + \eta^2} \left[e^{-\kappa} (3 + 3\kappa + \kappa^2) \frac{\kappa^2}{\eta^3} + (3 - \eta^2) \frac{\cos \eta}{\eta} + 3 \sin \eta \right]. \quad (2.39b)$$

The functions \mathcal{C}_1 and \mathcal{C}_2 vanish as κ approaches infinity, i.e., $\lim_{\kappa \rightarrow \infty} \mathcal{C}_1(\eta, \kappa) = \lim_{\kappa \rightarrow \infty} \mathcal{C}_2(\eta, \kappa) = 0$. For a finite value of κ , the contribution of \mathcal{C}_1 and \mathcal{C}_2 to $\Omega_{ij}^{\mu\nu}$ is negligible provided that $1/\kappa^2 \ll 1$ and $\exp(-\kappa)\kappa^2 \ll 1$. This is clearly the case if $\kappa = R_{\mu\nu}k_C$ is sufficiently larger than unity. It follows that \mathcal{C}_1 and \mathcal{C}_2 can be neglected if the atomic separation is larger than the inverse cutoff wave number, $R_{\mu\nu} \gg k_C^{-1}$. Since we set $k_C^{-1} = a_0/(2\pi)$, where a_0 is the Bohr radius, this means that the latter inequality holds provided that the atomic clouds are well separated, which is one of the underlying assumptions of our model established in Section 2.1. We will thus neglect the contribution of \mathcal{C}_1 and \mathcal{C}_2 to Equation (2.38) from now on.

The discussion below Equation (2.39) shows that the expression for $\Omega_{ij}^{\mu\nu}$ is to a good approximation independent of the frequency cutoff as long as the inequality $R_{\mu\nu} \gg k_C^{-1}$ holds. Corrections due to the frequency cutoff become important if the atomic separation is of the order of the wavelength that is associated with the cutoff wave number, i.e., if $R \approx \lambda_C = 2\pi/k_C$. Physically, the frequency cutoff corresponds to a spatial

average over a region with linear dimension of the order of k_C^{-1} (Cohen-Tannoudji et al., 1997). Therefore, the frequency cutoff effectively results in a finite size of the emitters. As long as the atomic separation is much larger than this size k_C^{-1} due to the averaging in position space, the atoms appear as point-like emitters. On the other hand, it is expected that the frequency cutoff becomes important as soon as the distance between the emitters is of the order of their size. This explains why the functions \mathcal{C}_1 and \mathcal{C}_2 in $\Omega_{ij}^{\mu\nu}$ are important for $R_{\mu\nu} \leq \lambda_C = 2\pi/k_C$ but can be neglected if $R_{\mu\nu} \gg \lambda_C$. Note that this result is independent of our particular choice of the cutoff parameter k_C . We can thus conjecture that for a given distance $R_{\mu\nu}$, the parameters $\Omega_{ij}^{\mu\nu}$ will be independent of the cutoff wave number provided that we choose the cutoff to be larger than $2\pi/R_{\mu\nu}$. It follows that field modes with wave number $k \geq 2\pi/R_{\mu\nu}$ have a negligible contribution to the parameters $\Omega_{ij}^{\mu\nu}$. We are now able to identify the field modes that contribute the most to the coherent dipole–dipole interaction in Equation (2.38). Since the density of modes increases quadratically with frequency, field modes with larger frequencies contribute more than those with smaller frequencies. It follows that the dominant contribution to $\Omega_{ij}^{\mu\nu}$ stems from modes for which the wave number k is on the order of the inverse distance between the atoms. We thus conclude that the nonrelativistic model established in Section 2.1 allows to determine the dipole–dipole interaction accurately if the electronic clouds of the emitters do not overlap. Formally, the contribution of high-frequency modes to $\Omega_{ij}^{\mu\nu}$ is eliminated by the phase factor $\exp(ik \cdot R_{\mu\nu})$. Note that the integrals $P_{ij}^{\mu\mu}$ and $M_{ij}^{\mu\mu}$ in Equation (2.36) that contribute to the Lamb shift of the individual atomic levels refer to a single atom and thus miss this phase factor. A correct description of these terms thus requires a relativistic description of the atom-field interactions.

The dipole–dipole interaction between pairs of atoms is distinguished from the ordinary Lamb shift of single quantum systems by another fact. While a correct model for the Lamb shift requires that all bound and continuum states have to be considered, we show that in second order in the interaction Hamiltonian V , there are no corrections to the parameters $\Gamma_{ij}^{\mu\nu}$ and $\Omega_{ij}^{\mu\nu}$ due to the presence of additional (continuum) states. To this end, we calculate the coupling parameters $\Omega_{ij}^{\mu\nu}$ and $\Gamma_{ij}^{\mu\nu}$ in second-order perturbation theory and consider two dipole transitions i and j in different atoms. Transition i in atom μ couples the ground and excited states $|g_\mu\rangle$ and $|e_\mu\rangle$, respectively. Similarly, the transition j in atom ν is characterized by the states $|g_\nu\rangle$ and $|e_\nu\rangle$. We consider the transition amplitude from the initial state $|\psi_{\text{init}}\rangle = |e_\mu, g_\nu, 0_F\rangle$ to the final state $|\psi_{\text{fin}}\rangle = |g_\mu, e_\nu, 0_F\rangle$, where $|0_F\rangle$ is the vacuum state of the radiation field. This corresponds to a process where the excitation of atom μ is transferred to atom ν via the radiation

field. According to second-order perturbation theory (Cohen-Tannoudji et al., 1998), the transition amplitude for this process is

$$\mathcal{A}_{\text{init} \rightarrow \text{fin}} = TA \frac{\sin [(E_{\text{fin}} - E_{\text{init}})T/(2\hbar)]}{(E_{\text{fin}} - E_{\text{init}})T/(2\hbar)}, \quad (2.40)$$

where T is the interaction time, E_{init} and E_{fin} are the energies of the initial and final states, respectively, and

$$A = -\frac{i}{\hbar} \lim_{\eta \rightarrow 0^+} \sum_{ks} \left\{ \frac{\langle g_\mu, e_\nu, 0_F | V | g_\mu, g_\nu, \{k, s\} \rangle \langle g_\mu, g_\nu, \{k, s\} | V | e_\mu, g_\nu, 0_F \rangle}{\hbar(\omega_0 - c|k|) + i\eta} \right. \\ \left. - \frac{\langle g_\mu, e_\nu, 0_F | V | e_\mu, e_\nu, \{k, s\} \rangle \langle e_\mu, e_\nu, \{k, s\} | V | e_\mu, g_\nu, 0_F \rangle}{\hbar(\omega_0 + c|k|) + i\eta} \right\}. \quad (2.41)$$

If we replace the sum over the wave vectors of the radiation field by an integral according to Equation (2.29) and with the identity $\lim_{\eta \rightarrow 0^+} 1/(x + i\eta) = \mathcal{P}1/x - i\pi\delta(x)$, we obtain

$$A = -\left(\Gamma_{\mu\nu}^{ij} + i\Omega_{\mu\nu}^{ij} \right)^*. \quad (2.42)$$

The important point that should be noticed is that there are only two types of intermediate states that can contribute to Equation (2.41). The first type corresponds to both atoms in the ground state and one photon $\{k, s\}$ with wave vector k and polarization s , $|g_\mu, g_\nu, \{k, s\}\rangle$. The second type consists of both atoms in the excited state and one photon, $|e_\mu, e_\nu, \{k, s\}\rangle$. Even in a model with infinitely many states, in second order in V there are no other intermediate states that can mediate a transition from $|e_\mu, g_\nu\rangle$ to $|g_\mu, e_\nu\rangle$. This result substantiates that the dipole-dipole interaction can be calculated correctly in the context of the model described in Section 2.1.

A diagrammatic representation of the two terms in Equation (2.41) that correspond to the two types of intermediate states is given in Figure 2. The first term corresponds to the process in subfigure (a), where atom μ emits a photon first, and both atoms are in the ground state in the intermediate step. This photon is subsequently reabsorbed by atom ν . The second term corresponds to the process in subfigure (b), where atom ν emits a photon by a transition from the ground state to its excited state, and both atoms are in the excited state in the intermediate step. The reabsorption of the photon is accompanied by a transition from the excited state to the ground state of atom μ . Note that the overall process from the initial to the final state is resonant, but the exchanged photons in general

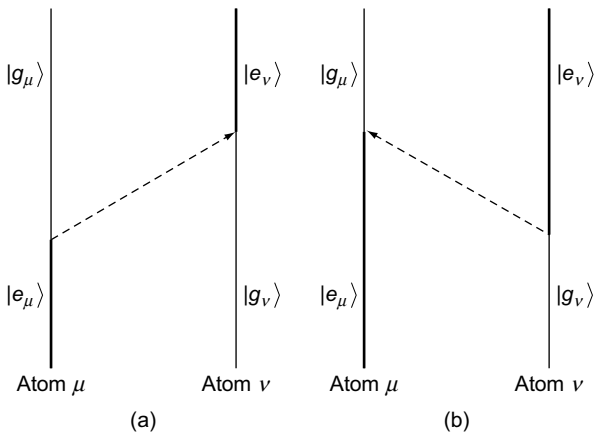


FIGURE 2 Diagrammatic representation of the processes that contribute to the transition amplitude in Equation (2.41). (a) The intermediate state $|g_\mu, g_v, \{k, s\}\rangle$ is reached by the emission of a photon from atom μ . In the final step, the photon is reabsorbed by the excitation of atom ν . (b) This shows the time-reversed process, where atom ν emits a photon by a transition from the ground state to its excited state. The subsequent transition from the intermediate state $|e_\mu, e_v, \{k, s\}\rangle$ to the final state $|\psi_{\text{fin}}\rangle$ corresponds to the reabsorption of the photon by the de-excitation of atom μ .

do not match the frequency of the atomic transition. Therefore, the photons that mediate the dipole–dipole interaction are called virtual, since they cannot be observed. Finally, we mention that the dipole–dipole interaction in electric-dipole coupling appears as a purely retarded exchange interaction. The reason is that the operator \hat{E} that appears in the interaction Hamiltonian in Equation (2.6) actually represents the transverse dielectric displacement, which coincides with the total electric field outside the system of charges (Cohen-Tannoudji et al., 1997).

2.4. Master Equation for Radiatively Coupled Multilevel Systems

Here we present the final result for the master equation that determines the density operator ϱ_A of M identical multilevel atoms that are coupled via the vacuum,

$$\partial_t \varrho_A(t) = -\frac{i}{\hbar} [H_A, \varrho_A(t)] + \mathcal{L}_\gamma \varrho_A(t) + \mathcal{L}_{\text{col}} \varrho_A(t). \quad (2.43)$$

In this equation, the Hamiltonian H_A describes the free evolution of the atoms and is defined in Equation (2.4) of Section 2.1. The second term

in Equation (2.43) describes the spontaneous emission of the individual atoms,

$$\mathcal{L}_\gamma \varrho_A(t) = - \sum_{\mu=1}^M \sum_{i,j=1}^D \gamma_{ij} \left(S_{i+}^{(\mu)} S_{j-}^{(\mu)} \varrho_A(t) + \varrho_A(t) S_{i+}^{(\mu)} S_{j-}^{(\mu)} - 2 S_{j-}^{(\mu)} \varrho_A(t) S_{i+}^{(\mu)} \right). \quad (2.44)$$

Note that the second summation in Equation (2.44) is a double sum over the D dipole transitions in each atom. The parameters γ_{ij} are given by (Agarwal, 1974; Cardimona, Raymer, & Stroud, 1982; Fleischhauer, Keitel, Narducci, Scully, Zhu, & Zubairy, 1992; Imamoğlu, 1989)

$$\gamma_{ij} = \Gamma_{ij}^{\mu\mu} = \sqrt{\gamma_i \gamma_j} \frac{\mathbf{d}_i \cdot \mathbf{d}_j^*}{|\mathbf{d}_i| |\mathbf{d}_j|}, \quad (2.45)$$

and

$$\gamma_i = \frac{\omega_0^3 |\mathbf{d}_i|^2}{6\pi \epsilon_0 \hbar c^3}. \quad (2.46)$$

For $i = j$, $\gamma_{ii} = \gamma_i$ is the half-decay rate of the i -th atomic dipole transition, and the parameters γ_{ij} for $i \neq j$ describe the cross-damping between a pair of transitions i and j of the same atom. According to Equation (2.45), the cross decay rates γ_{ij} depend on the mutual orientation of the associated dipole moments \mathbf{d}_i and \mathbf{d}_j . These parameters describe the decay-induced coherence between atomic dipole transitions and will be discussed in detail in Section 3.2. In particular, we show that these spontaneously created coherences give rise to quantum interference effects. Note that the cross decay rates γ_{ij} contribute to the master equation provided that the dipole moments \mathbf{d}_i and \mathbf{d}_j are nonorthogonal. Due to the term $S_{j-}^{(\mu)} \varrho_A(t) S_{i+}^{(\mu)}$ in the first line of Equation (2.50), it is not required that one of the operators $S_{i+}^{(\mu)} S_{j-}^{(\mu)}$ or $S_{i-}^{(\mu)} S_{j+}^{(\mu)}$ is different from zero at the same time. This is in contrast to the parameters M_{ij} and P_{ij} ($i \neq j$) which were discussed below Equation (2.36) in Section 2.3.

The last term in Equation (2.43) describes the coupling between different atoms that arises due to the interaction with the radiation field and consists of two terms,

$$\mathcal{L}_{\text{col}} \varrho_A(t) = -\frac{i}{\hbar} [H_\Omega, \varrho_A(t)] + \mathcal{L}_\Gamma \varrho_A(t). \quad (2.47)$$

The first term gives rise to a coherent time evolution that is governed by the Hamiltonian

$$H_\Omega = -\hbar \sum_{\substack{\mu, \nu=1 \\ \mu \neq \nu}}^M \sum_{i,j=1}^D \Omega_{ij}^{\mu\nu} S_{i+}^{(\mu)} S_{j-}^{(\nu)}. \quad (2.48)$$

The parameters

$$\begin{aligned} \Omega_{ij}^{\mu\nu} = & \frac{3}{2} \frac{\sqrt{\gamma_i \gamma_j}}{|\mathbf{d}_i| |\mathbf{d}_j|} \left\{ \mathbf{d}_i \cdot \mathbf{d}_j^* \left[\left(\frac{1}{\eta} - \frac{1}{\eta^3} \right) \cos \eta - \frac{1}{\eta^2} \sin \eta \right] \right. \\ & \left. - \frac{[\mathbf{d}_i \cdot \mathbf{R}] [\mathbf{d}_j^* \cdot \mathbf{R}]}{R^2} \left[\left(\frac{1}{\eta} - \frac{3}{\eta^3} \right) \cos \eta - \frac{3}{\eta^2} \sin \eta \right] \right\} \end{aligned} \quad (2.49)$$

with $\eta = k_0 R_{\mu\nu}$ describe the *coherent* coupling between two dipole transitions of different atoms. This is a remarkable result since this coherent interaction arises solely from the vacuum-mediated coupling between different atoms.

The second term in Equation (2.47) accounts for the modification of spontaneous emission of one atom due to the presence of the other atoms,

$$\mathcal{L}_\Gamma \varrho_A(t) = - \sum_{\substack{\mu, \nu=1 \\ \mu \neq \nu}}^M \sum_{i,j=1}^D \Gamma_{ij}^{\mu\nu} \left(S_{i+}^{(\mu)} S_{j-}^{(\nu)} \varrho_A(t) + \varrho_A(t) S_{i+}^{(\mu)} S_{j-}^{(\nu)} - 2 S_{j-}^{(\nu)} \varrho_A(t) S_{i+}^{(\mu)} \right), \quad (2.50)$$

where the parameters

$$\begin{aligned} \Gamma_{ij}^{\mu\nu} = & \frac{3}{2} \frac{\sqrt{\gamma_i \gamma_j}}{|\mathbf{d}_i| |\mathbf{d}_j|} \left\{ \mathbf{d}_i \cdot \mathbf{d}_j^* \left[\left(\frac{1}{\eta} - \frac{1}{\eta^3} \right) \sin \eta + \frac{1}{\eta^2} \cos \eta \right] \right. \\ & \left. - \frac{[\mathbf{d}_i \cdot \mathbf{R}] [\mathbf{d}_j^* \cdot \mathbf{R}]}{R^2} \left[\left(\frac{1}{\eta} - \frac{3}{\eta^3} \right) \sin \eta + \frac{3}{\eta^2} \cos \eta \right] \right\} \end{aligned} \quad (2.51)$$

can be interpreted as collective decay rates and $\eta = k_0 R_{\mu\nu}$.

Note that terms with $\mu = \nu$ are excluded in the summation over the atomic indices μ and ν in Equations (2.48) and (2.50). This reflects the fact that the contribution $\mathcal{L}_{\text{col}} \varrho_A(t)$ in Equation (2.47) describes the coupling between pairs of atoms. For a single atom, this term does not contribute to the master equation. The coupling parameters $\Omega_{ij}^{\mu\nu}$ and $\Gamma_{ij}^{\mu\nu}$ have the

structure of a tensorial coupling between two dipoles d_i and d_j that belong to different atoms and can be written as

$$\Omega_{ij}^{\mu\nu} = \frac{1}{\hbar} \left[d_i^T \overset{\leftrightarrow}{\chi}_{\text{re}}(\mathbf{R}_{\mu\nu}) d_j^* \right], \quad (2.52)$$

$$\Gamma_{ij}^{\mu\nu} = \frac{1}{\hbar} \left[d_i^T \overset{\leftrightarrow}{\chi}_{\text{im}}(\mathbf{R}_{\mu\nu}) d_j^* \right]. \quad (2.53)$$

Here $\overset{\leftrightarrow}{\chi}_{\text{re}}$ and $\overset{\leftrightarrow}{\chi}_{\text{im}}$ denote the real and imaginary part of the tensor $\overset{\leftrightarrow}{\chi}$, respectively, and the Cartesian components $p, q \in \{1, 2, 3\}$ of this tensor are

$$\overset{\leftrightarrow}{\chi}_{pq}(\mathbf{R}) = \frac{k_0^3}{4\pi\varepsilon_0} \left[\delta_{pq} \left(\frac{1}{\eta} + \frac{i}{\eta^2} - \frac{1}{\eta^3} \right) - \frac{[\mathbf{R}]_p [\mathbf{R}]_q}{R^2} \left(\frac{1}{\eta} + \frac{3i}{\eta^2} - \frac{3}{\eta^3} \right) \right] e^{i\eta}, \quad (2.54)$$

where $\eta = k_0 R$. The parameters $\Omega_{ij}^{\mu\nu}$ and $\Gamma_{ij}^{\mu\nu}$ obey an important symmetry property, which allows us to reduce the number of independent parameters in the master Equation (2.43). According to their definitions in Equations (2.51) and (2.49), $\Gamma_{ij}^{\mu\nu}$ and $\Omega_{ij}^{\mu\nu}$ depend on the atomic indices μ, ν via the atomic separation vector $\mathbf{R}_{\mu\nu} = \mathbf{r}_\mu - \mathbf{r}_\nu$. Since the tensor $\overset{\leftrightarrow}{\chi}(\mathbf{R})$ in Equation (2.54) does not depend on the sign of the vector \mathbf{R} ,

$$\overset{\leftrightarrow}{\chi}(-\mathbf{R}) = \overset{\leftrightarrow}{\chi}(\mathbf{R}), \quad \text{we have} \quad \Gamma_{ij}^{\mu\nu} = \Gamma_{ij}^{\nu\mu} \quad \text{and} \quad \Omega_{ij}^{\mu\nu} = \Omega_{ij}^{\nu\mu}. \quad (2.55)$$

Together with Equation (2.35), we can establish the following relations,

$$\begin{aligned} \Gamma_{ij}^{\mu\nu} &= \Gamma_{ij}^{\nu\mu} = (\Gamma_{ji}^{\mu\nu})^* = (\Gamma_{ji}^{\nu\mu})^*, \\ \Omega_{ij}^{\mu\nu} &= \Omega_{ij}^{\nu\mu} = (\Omega_{ji}^{\mu\nu})^* = (\Omega_{ji}^{\nu\mu})^*. \end{aligned} \quad (2.56)$$

In particular, this shows that the parameters $\Gamma_{ii}^{\mu\nu}$ and $\Omega_{ii}^{\mu\nu}$ are real.

So far, we only considered the interaction of M atoms via the vacuum field. In the presence of external laser fields, an additional term $-i/\hbar [H_L(t), \varrho_A(t)]$ has to be added to the right-hand side of Equation (2.43),

$$\partial_t \varrho_A(t) = -\frac{i}{\hbar} [H_A, \varrho_A(t)] - \frac{i}{\hbar} [H_L(t), \varrho_A(t)] + \mathcal{L}_\gamma \varrho_A(t) + \mathcal{L}_{\text{col}} \varrho_A(t). \quad (2.57)$$

Here the time-dependent Hamiltonian $H_L(t)$ describes the interaction between the atoms and the laser fields. In the following, we assume that the Rabi frequencies and detunings that are associated with the laser fields

are much smaller than the mean transition frequency ω_0 . In this case, it is justified to assume that the other terms in Equation (2.43), which arise due to the atom–vacuum coupling, are not affected by the presence of the laser fields (Cohen-Tannoudji et al., 1998).

The master equation in Equation (2.43) can be applied to a broad range of systems. In this last paragraph, we outline the scope of its validity and recall the approximations that we used in the derivation process.

The starting point of our derivation is the master equation in Born approximation, see Section 2.2. This approximation implies that only processes up to second order in the interaction between the atoms and the radiation field are taken into account. This approximation eventually breaks down for very small atomic separations (Craig & Thirunamachandran, 1984). Atom-field interactions that are of higher order than the second-order processes considered here then lead to the well-known van der Waals shift of the ground and excited states. However, it is difficult to specify the range of validity of the Born approximation since it depends on the atomic species as well as on the physical observable one is interested in. A figure of merit is the van der Waals radius of the considered atomic species, which is typically on the order of a few nanometers for alkali atoms. If the atomic separation is smaller than or on the order of the van der Waals radius, corrections to the second-order dipole–dipole interaction are expected.

We describe the interaction between atoms and the radiation field within the framework of a nonrelativistic model and the electric-dipole approximation. In order to account for the limitations of our model, we introduced a cutoff in all summations over wave vectors of the radiation field, and this cutoff has been chosen to be on the order of the inverse Bohr radius. It is well known that the Lamb shift of individual atomic levels cannot be correctly described in such an approach. On the contrary, we have shown that our model yields a valid description of the dipole–dipole interaction provided that the atomic clouds of the individual atoms do not overlap. Furthermore, we point out that an equivalent master equation is obtained if the interaction between the atoms and the radiation field is described in minimal coupling rather than in electric-dipole coupling (Agarwal, 1974; Brooke, Marzlin, Cresser, & Sanders, 2008; Craig & Thirunamachandran, 1984).

The key approximation in the derivation of the master equation in Section 2.3 is the Markov approximation that relies on the existence of two very different timescales: The typical correlation time of the reservoir correlation functions is supposed to be much smaller than the lifetime of the atomic levels. This approximation is usually very well justified in quantum optical systems, in particular if realistic reservoir states like a thermal field are considered. The Markov approximation implies that the time evolution of the density operator ϱ_A is described on a coarse-grained

time axis where processes of the order of the reservoir correlation times are not resolved. It thus requires that the rotating-wave approximation (RWA) is assumed, which amounts to average the master equation over a timescale that is long as compared with the reservoir correlation functions, but much smaller than the lifetimes of the atomic levels.

In the description of our model in Section 2.1, we claimed that the master Equation (2.43) can be easily generalized to systems where the internal level structure consists of more than two near-degenerate multiplets. This is indeed possible if the difference between the mean transition frequencies of the various multiplet transitions are much larger than the inverse lifetimes of the atomic states. In this case, all terms that introduce a coupling between transitions belonging to different multiplet pairs are eliminated by the RWA. It follows that each excited- and ground-state multiplet can be treated independently, and the contributions from all pairs of multiplets can be added to obtain the total master equation.

A key assumption of our model is that the atoms are identical. In realistic systems, however, one may frequently encounter a situation where the atoms are nonidentical, e.g., due to an inhomogeneous magnetic field. In general, the mean transition frequency in Equation (2.2) will then vary from atom to atom and should be labeled by $\omega_0^{(\mu)}$, where μ runs over the number of atoms. A careful analysis of the derivation in Section 2.3 reveals that the generalization of Equation (2.43) to the case of nonidentical atoms is straightforward, provided that the variation of the mean transition frequencies $\omega_0^{(\mu)}$ is small as compared with the mean value $\tilde{\omega}_0$ of all frequencies $\omega_0^{(\mu)}$. In this case, Equation (2.43) remains valid provided that the following replacements everywhere in Equation (2.47) that defines $\mathcal{L}_{\text{colQA}}(t)$ are being carried out:

$$\omega_0^{(\mu)} \sim \tilde{\omega}_0 = \frac{1}{M} \sum_{\mu=1}^M \omega_0^{(\mu)}, \quad d_i \sim d_i^{(\mu)}, \quad \text{and} \quad d_j \sim d_j^{(\nu)}. \quad (2.58)$$

Finally, we address the center-of-mass motion of the atoms that has been omitted so far. In single-atom systems, the influence of spontaneous emission on the center-of-mass motion has been studied extensively in the context of laser cooling and trapping (Chu & Wieman, 1989). The dipole–dipole interaction in multi-atom systems has an additional impact on the center-of-mass motion since it gives rise to a potential between pairs of atoms. A semi-classical description of the center-of-mass motion in the presence of the dipole–dipole interaction can be achieved by phase space methods (Ellinger, Cooper, & Zoller, 1994) or by the introduction of classical trajectories. In the latter case, the master Equation (2.43) remains a valid description for the internal degrees of freedom of the atoms if the Doppler shifts associated with the movement of the atoms are sufficiently

small (Trippenbach et al., 1992a) and if the separation vectors $R_{\mu\nu}$ are replaced by the time-dependent trajectories $R_{\mu\nu}(t)$. This approach has been frequently used to describe laser cooling mechanisms in the presence of the dipole–dipole interaction (Goldstein, Pax, & Meystre, 1996; Smith & Burnett, 1991, 1992a,b; Smith, Burnett, & Cooper, 1992). A quantized treatment of the center-of-mass motion that includes the dipole–dipole interaction is presented by Guo (1994) and Guo and Cooper (1995).

3. SINGLE-PARTICLE PROCESSES

This section focuses on vacuum-induced processes in single multilevel atoms. The simplest example is spontaneous emission (SE), the ubiquitous incoherent relaxation between the different atomic states by emission of photons. The realization that spontaneous emission is not an immutable property of the atom itself (Kleppner, 1981; Purcell, 1946) has led to a great variety of attempts to modify it, as discussed in Section 3.1. SE amounts to the emission of a real photon, and the origin of this process is virtual photon exchange with the vacuum, which can be visualized as the emission of a virtual photon together with the transition of the atom to a different atomic state, followed by a reabsorption of the virtual photon on the same transition (Agarwal, 1974). A different vacuum-induced process is the emission of a virtual photon on one atomic transition followed by a reabsorption on a different transition in the same atom. This gives rise to spontaneously generated coherences (SGC) and is often accompanied by interference effects in spontaneous emission (Ficek & Swain, 2005). These additional coherences and interferences lead to many fascinating features summarized in Section 3.2. It should be noted, however, that many of the schemes analyzed theoretically cannot straightforwardly be realized in atomic systems due to stringent conditions on the level scheme for spontaneously generated coherences to occur. Nevertheless, these works are of significance, mainly for three reasons. First, there are realistic atomic level schemes that exhibit spontaneously generated coherences, as reviewed in Section 3.2. Second, these schemes can be realized in other quantum systems, such as quantum dots, as discussed in Section 3.2.4. Finally, it is possible to induce or engineer spontaneously generated coherences in atomic systems, as summarized in Section 3.3.

Regarding the theoretical description, in the case of a single atom, the master Equation (2.43) simplifies considerably, since the contributions $\mathcal{L}_{\text{col}}\rho_A(t)$ describing interactions between different particles vanish. To reduce the notation, in this section, the superscript (μ) denoting the atom number is dropped, and we replace the atomic operators $S_{i\pm}$ by operators $S_{ij} = |i\rangle\langle j|$ directly indicating the involved states $i, j \in \{1, \dots, L\}$. In the simplest case of a single two-level system, the excited and ground

states will be denoted $|e\rangle$ and $|g\rangle$, respectively, and we further introduce the inversion operator $S_z = (S_{ee} - S_{gg})/2$ for later use.

3.1. Single-Particle Spontaneous Decay

The basis of this section is the well-known fact that excited atomic states in general are not stable, but rather spontaneously decay to states of lower energy under emission of photons. Typically, decays to different ground states are possible, and each transition is assigned a decay rate γ_i related to the Einstein A coefficient describing the probability of the decay through this channel. For example, apart from possible modifications at very short timescales, in free space, a single-excited two-level atom decays according to an exponential law (Agarwal, 1974; Breuer & Petruccione, 2006; Cohen-Tannoudji et al., 1998; Weisskopf & Wigner, 1930),

$$\langle S_z(t) \rangle = (\langle S_z(0) \rangle + 1/2)e^{-\gamma t} - 1/2, \quad (3.1)$$

where $\langle S_z(0) \rangle$ is the inversion at $t = 0$. Spontaneous emission is one of the most frequently occurring physical processes and as such its control is of vital importance also for almost every stimulated operation. Furthermore, many applications are limited by incoherent processes such as spontaneous emission. Well-known examples are noise in quantum measurements or amplifiers, as exemplified by the fluctuation-dissipation theorem, or decoherence in quantum information science. This raises the fundamental problem of controlling spontaneous emission. It can be concluded from the derivation of the master equation in Section 2 that the reason for the occurrence of spontaneous emission is the interaction of the atom with the surrounding electromagnetic vacuum field by means of emission and absorption of virtual photons, i.e., vacuum fluctuations stimulate the atom to emit spontaneously a real photon. Therefore, it is not surprising that the decay rate can be written as (Agarwal, 1974; Scully & Zubairy, 1997; Weisskopf & Wigner, 1930),

$$\gamma_i = 2\pi |g(\omega_i)|^2 \mathcal{D}(\omega_i), \quad (3.2)$$

where $\mathcal{D}(\omega_i)$ is the vacuum mode density at the corresponding transitions frequency ω_i , and $g(\omega_i)$ is a coefficient describing the atom-field coupling strength. As mentioned above, a central theme of this section is the question whether spontaneous emission and its consequences can be modified or even controlled to one's advantage. Equation (3.2) suggests a natural separation into different approaches. First, in Section 3.1.1, we briefly discuss schemes that make use of a modification of the surrounding vacuum, i.e., $\mathcal{D}(\omega_i)$. We then proceed to review *dynamical* approaches based on the influence of the atomic properties and the atom-field coupling g on SE in Section 3.1.2.

3.1.1. Modification of the Vacuum Mode Density

A modification of the vacuum mode density suitable for significant change in the spontaneous emission is possible, for instance, in optical cavities or photonic band gap materials. In both cases, boundary conditions imposed by the environment modify the structure of the vacuum, thereby allowing for the control of the spontaneous decay. Enhancement of the mode density allows to increase spontaneous emission and to imprint a different directional pattern on the emitted light. For example, enhancing emission in one spatial direction allows to direct spontaneously emitted photons toward a detector (Berman, 1984; Knight, 1981). Similarly, a reduction of the mode density suppresses spontaneous emission into a particular direction. Note, however, that a suppression of the total decay rate in general requires the reduction of the mode density in three spatial dimensions, which is technically challenging.

The possibility to enhance the spontaneous emission rate in a single-mode cavity was recognized for radio frequencies already by Purcell (1946). Experimental observation of the Purcell effect was reported, e.g., by Goy, Raimond, Gross, and Haroche (1983). Kleppner (1981) discovered that the radiation rate can be suppressed by means of a cavity, if the mode density is low at the atomic transition frequency. The inhibition of spontaneous decay was first reported in Rydberg atoms (Hulet, Hilfer, & Kleppner, 1985) and between cyclotron states in a Penning trap (Gabrielse & Dehmelt, 1985). For optical transitions, complete suppression is challenging because very high fundamental frequencies of the resonator are required (Heinzen, Childs, Thomas, & Feld, 1987; Jhe et al., 1987; Kreuter et al., 2004; Martini, Innocenti, Jacobovitz, & Mataloni, 1987).

A simple example is the case in which the atomic transition frequency is below the fundamental mode frequency of the surrounding cavity. These results can be understood by analyzing a two-level atom coupled to a low-quality optical resonator. For a low-quality cavity, the cavity damping rate κ is much larger than the atom-cavity coupling strength g . This allows to eliminate the cavity degrees of freedom, and the master equation describing this system becomes (Garraway & Knight, 1996)

$$\frac{d}{dt}\rho = i\delta_{eg}[S_z, \rho] - \Gamma\{[S_{eg}, S_{ge}\rho] + [\rho S_{eg}, S_{ge}]\}. \quad (3.3)$$

Here, $\Gamma = g^2\kappa/(\kappa^2 + \Delta^2)$ is the spontaneous decay rate, and $\delta_{eg} = g^2\Delta/(\kappa^2 + \Delta^2)$ describes the Lamb shift. $\Delta = \omega_c - \omega_{eg}$ is the detuning of the cavity carrier frequency ω_c from the atomic transition frequency ω_{eg} . The solution to Equation (3.3) is of similar form as Equation (3.1). In particular, for a resonant cavity $\Delta = 0$, the Lamb shift $\delta_{eg} = 0$ and the decay rate is $\Gamma = g^2/\kappa$. Cavity-induced enhancement occurs if g^2/κ is larger than

the free space decay rate. As the cavity is detuned, Γ decreases, which is Kleppner's result for a single-mode cavity.

Analogous modification of spontaneous emission has also been observed for atoms placed in front of a mirror (Eschner, Raab, Schmidt-Kaler, & Blatt, 2001; Morawitz, 1969). This effect can be enhanced with the help of left-handed materials (Kästel & Fleischhauer, 2005; Li, Evers, & Keitel, 2009a; Xu, Yang, Lin, & Zhu, 2009; Yannopapas, Paspalakis, & Vitanov, 2009).

As was mentioned above, another method to influence the spontaneous emission decay via modifying the surrounding vacuum modes consists in placing the emitter into a photonic band gap material (Angelakis, Knight, & Paspalakis, 2004; Bykov, 1972; John, 1987; John & Quang, 1994; Lodahl et al., 2004; Petrov, Bogomolov, Kalosha, & Gaponenko, 1998; Schriemer, van Driel, Koenderink, & Vos, 2001; Yablonovitch, 1987; Zhu, Li, Yang, & Li, 2003; Zhu, Yang, Chen, Zheng, & Zubairy, 2000). This leads to many remarkable effects, such as the appearance of photon-atom bound states (Bay, Lambropoulos, & Mølmer, 1997; John & Quang, 1994; Kofman, Kurizki, & Sherman, 1994), transient lasing without inversion (Angelakis, Paspalakis, & Knight, 2001), coexistence of accelerated and decelerated spontaneous emission processes (Megens, Wijnhoven, Lagendijk, & Vos, 1999; Petrov et al.; Yang, Fleischhauer, & Zhu, 2003; Zhu et al., 2003), the possibility to control light with light (Florescu & John, 2004), possible modification of the Planck blackbody radiation in microstructured metals (Cornelius & Dowling, 1999; Fleming, Lin, El-Kady, Biswas, & Ho, 2002), and enhancement of interference effects (Li et al., 2009a; Quang, Woldeyohannes, John, & Agarwal, 1997; Zhu, Chen, & Huang, 1997). Photonic crystals have been reviewed recently by Angelakis et al. (2004), Benisty and Weisbuch (2006), and Joannopoulos, Johnson, Winn, and Meade (2008).

The photonic crystal case differs from all other systems studied in this review in that the Markov approximation no longer applies, and the master Equation (2.43) is not suitable to describe the dynamics. Therefore, in the following, we review the main steps to calculate the quantum dynamics of an excited two-level atom embedded in a photonic band gap medium. The Hamiltonian of the system in the interaction picture takes the form (Angelakis et al., 2004; Bykov, 1972; John, 1987; John & Quang, 1994; Yablonovitch, 1987)

$$H_i = i \sum_k g_k (a_k^\dagger S_{ge} e^{i\Delta_k t} - S_{eg} a_k e^{-i\Delta_k t}). \quad (3.4)$$

Here a_k and a_k^\dagger are the radiation field annihilation and creation operators, and $\Delta_k = \omega_k - \omega_{eg}$ is the atom-field detuning. The atomic field coupling constant $g_k = (\omega_{eg} d_{eg}/\hbar) \sqrt{\hbar/(2\epsilon_0 \omega_k v)} (\vec{e}_\lambda \cdot \vec{u}_d)$, and d_{eg} and \vec{u}_d are

the magnitude and unit direction vector of the atomic dipole moment, respectively. v is the quantization volume, \vec{e}_λ are the two transverse polarization unit vectors, and ϵ_0 is the vacuum permittivity. If initially the atom is in the excited state $|e\rangle$ and the field is in the vacuum state $|\{0\}\rangle$, then the state vector of the system can be written as

$$|\Psi(t)\rangle = c_e(t)|e, \{0\}\rangle + \sum_k c_{gk}(t)|g, \{1_k\}\rangle. \quad (3.5)$$

The state $|g, \{1_k\}\rangle$ describes the atom in its ground state $|g\rangle$ and a single photon in mode k . The time-dependent Schrödinger equation leads to

$$\frac{d}{dt}c_e(t) = - \sum_k g_k c_{gk}(t) e^{-i\Delta_k t}, \quad (3.6a)$$

$$\frac{d}{dt}c_{gk}(t) = g_k c_e(t) e^{i\Delta_k t}, \quad (3.6b)$$

which combines to

$$\frac{d}{dt}c_e(t) = - \sum_k g_k^2 \int_0^t dt' c_e(t') e^{-i\Delta_k(t-t')}. \quad (3.7)$$

Performing the Laplace transform $\tilde{c}_e(s) = \int_0^\infty dt e^{-st} c_e(t)$, rewriting the mode sum over transverse plane waves into a continuous integral, and integrating over the angular degrees of freedom gives

$$\tilde{c}_e(s) = \left[s + \frac{\omega_{eg}^2 d_{eg}^2}{6\pi^2 \epsilon_0 \hbar} \int_0^\Lambda \frac{k^2 dk}{\omega_k(s + i\Delta_k)} \right]^{-1}, \quad (3.8)$$

and Λ is a cutoff frequency for the wave number. In structureless reservoirs with broadband mode densities, such as in plain vacuum, one can use Markov and Wigner–Weisskopf approximations, i.e.,

$$\lim_{s \rightarrow 0^+} \frac{1}{s + i\Delta_k} = -iP \frac{1}{\Delta_k} + \pi \delta(\Delta_k). \quad (3.9)$$

Substituting Equation (3.9) in Equation (3.8) yields $\tilde{c}_e(s) = [s + i\delta_{eg} + \gamma/2]^{-1}$, with δ_{eg} the Lamb shift and γ the spontaneous emission rates, respectively (John & Quang, 1994). Upon Laplace back transformation, we recover the result of purely exponential decay of Section 2. In contrast, in structured reservoirs such as in a photonic band gap material, in which the mode density changes considerably in the vicinity of the atomic transition

frequency, these approximations no longer apply. Instead, the dispersion relation near the band edge ω_c of a three-dimensional periodic dielectric can be approximated by (John & Wang, 1990)

$$\omega_k = \omega_c + A(k - k_0)^2, \quad (3.10)$$

where $A \approx \omega_c/k_0^2$ and $k \approx k_0 \equiv \pi/L$ with L the lattice constant. Using Equation (3.10), we evaluate Equation (3.8) as

$$\tilde{c}_e(s) = \frac{(s - i\delta)^{1/2}}{s(s - i\delta)^{1/2} - (i\beta)^{3/2}}. \quad (3.11)$$

Here $\beta^{3/2} = \omega_{eg}^{7/2} d_{eg}^2 / (6\pi\epsilon_0\hbar c^3)$ and $\delta = \omega_{eg} - \omega_c$. Finally, the inverse Laplace transform of Equation (3.11) yields (John & Quang, 1994)

$$\begin{aligned} c_e(t) = & 2b_1 x_1 e^{(\beta x_1^2 + i\delta)t} + b_2 (x_2 + y_2) e^{(\beta x_2^2 + i\delta)t} \\ & - \sum_{j=1}^3 b_j y_j \left[1 - \Phi\left(\sqrt{\beta x_j^2 t}\right) \right] e^{(\beta x_j^2 + i\delta)t}, \end{aligned} \quad (3.12)$$

where

$$x_1 = (A_+ + A_-) e^{i\pi/4}, \quad (3.13a)$$

$$x_2 = (A_+ e^{-i\pi/6} - A_- e^{i\pi/6}) e^{-i\pi/4}, \quad (3.13b)$$

$$x_3 = (A_+ e^{i\pi/6} - A_- e^{-i\pi/6}) e^{3i\pi/4}, \quad (3.13c)$$

$$A_{\pm} = \left[\frac{1}{2} \pm \frac{1}{2} \sqrt{1 + \frac{4}{27} \frac{\delta^3}{\beta^3}} \right]^{1/3}, \quad (3.13d)$$

$$b_j = \frac{x_j}{(x_j - x_i)(x_j - x_k)} \quad (i \neq k \neq j \in \{1, 2, 3\}), \quad (3.13e)$$

$$y_j = \sqrt{x_j^2} \quad (j \in \{1, 2, 3\}), \quad (3.13f)$$

and $\Phi(x)$ is the error function. The decaying atom is dressed by its own radiation field, leading to the first two terms in Equation (3.12), which correspond to the shifted dressed states. The first dressed state is a photon-atom bound state located inside the band gap region, which does not decay spontaneously, since any light emitted is reflected back onto the atom due to the lack of a mode for light propagation. It is interesting to note that this term already occurs if the atomic transition frequency is close to the band edge, but outside the gap. The second dressed state is

located outside the band gap and thus leads to decay. In total, the excited-state population exhibits oscillatory decay, with fractional steady-state population in the upper state due to the photon-atom bound state (John, 1987; John & Quang, 1994). The atomic level splitting, oscillatory behavior, and fractional steady-state atomic population in the excited state are all direct consequences of strong interaction between the atom and its own localized radiation when the atomic resonant frequency lies near the edge of a perfect photonic band gap and thus strongly dependent on the detuning of the resonant atomic frequency ω_{eg} from the band-edge frequency ω_c .

Enhancement or quenching of spontaneous emission has also been reported in various other systems. For instance, an experimental and theoretical study of the fluorescence rate of a single molecule as a function of its distance to a laser-irradiated gold nanoparticle was presented by Anger, Bharadwaj, and Novotny (2006). By varying the distance between molecule and nanoparticle, a continuous transition from fluorescence enhancement to fluorescence quenching could be demonstrated experimentally.

3.1.2. Dynamic Control of Spontaneous Decay

We now turn to methods to control spontaneous emission that are not based on a modification of the vacuum mode density. Different levels of control have to be distinguished. For example, spontaneous emission can be quenched at a particular emission frequency, while the total spontaneous emission rate integrated over all frequencies remains unaltered. These approaches can be summarized as a modification of the spontaneous emission spectrum. A more challenging task is to suppress the total integrated spontaneous emission rate. One approach to control the spontaneous emission is to effectively modify the coupling between the quantum system and the vacuum, which typically is achieved by applying external fields. Therefore, we denote the methods presented in this section as dynamical control.

3.1.2.1. Quantum Zeno and Anti-Zeno Effect A well-known example is the quantum Zeno effect, in which frequent measurements performed on a quantum system modify the temporal dynamics of the quantum system. For a recent review on this subject, see the study by Facchi and Pascazio (2001). This idea in principle can be applied to spontaneous decay of an unstable quantum system. The key mechanism is that a measurement collapses the wave function, and if these collapses occur on timescales small as compared with the free system evolution, then the evolution effectively freezes (Misra & Sudarshan, 1977). For this, however, the measurements have to be faster than the natural coherence time of the system, which in free space is so small that this condition usually cannot

be met. Also, the effect of frequent measurements crucially depends on the measurement rate and the spectrum of the vacuum reservoir. More recent work (Facchi & Pascazio, 2001; Kofman & Kurizki, 2000; Schulman, 1997) suggests that the repeated measurements can also lead to the so-called quantum anti-Zeno effect, i.e., a measurement induced acceleration of decay.

In the following section, we examine an alternative method to control the spontaneous emission that is similar in spirit to the Zeno approach, but does not require frequent measurements (Agarwal, Scully, & Walther, 2001b). Instead, the spontaneous decay is manipulated dynamically by applying 2π pulses between the decaying upper level and another atomic state. This constitutes a unitary evolution and does not lead to wave function collapse. Therefore, it differs from the Zeno effect.

We consider a two-level particle that decays from the upper level $|a\rangle$ to a lower level $|b\rangle$ with the decay rate γ (see Figure 3). The Hamiltonian in the interaction picture can be written as follows:

$$H_i = \hbar \sum_k [g_k a_k^\dagger S_{ba} e^{i\Delta_k t} + g_k^* a_k S_{ab} e^{-i\Delta_k t}], \quad (3.14)$$

where a_k^\dagger and a_k are the creation and annihilation operators for the k -th mode in the vacuum with frequency ω_k and $\Delta_k = \omega_k - \omega_{ab}$ ($\hbar\omega_{ab}$ is the energy difference between the two levels). g_k is the atom-field coupling constant. The usual spontaneous emission decay process can be efficiently modified by applying a series of 2π pulses with period τ to couple the upper level and another level $|c\rangle$ (see Figure 3). The evolution matrix U describing a single pulse can be written as

$$\begin{aligned} U_{2\pi} &= \exp\left[-\frac{i\Omega t_d}{2}(|a\rangle\langle c| + |c\rangle\langle a|)\right] \\ &= \cos\left(\frac{\Omega t_d}{2}\right)(|a\rangle\langle a| + |c\rangle\langle c|) - i \sin\left(\frac{\Omega t_d}{2}\right)(|a\rangle\langle c| + |c\rangle\langle a|). \end{aligned} \quad (3.15)$$

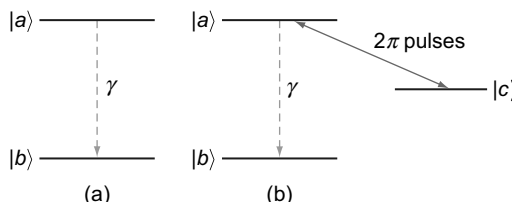


FIGURE 3 (a) Energy levels of a spontaneously decaying two-state atom. (b) Dynamic control of spontaneous emission on the transition $|a\rangle \rightarrow |b\rangle$ by application of a series of 2π pulses on the $|a\rangle \leftrightarrow |c\rangle$ transition.

Here Ω and t_d are the Rabi frequency and duration of the pulse, respectively, which are adjusted such that $\Omega t_d = 2\pi$. If the duration of each pulse is sufficiently short compared with the period τ , then $U_{2\pi} \approx -(|a\rangle\langle a| + |c\rangle\langle c|)$, and each pulse effectively changes the coherence between the upper level $|a\rangle$ and the lower level $|b\rangle$ by a phase π . The total time evolution matrix after $2N$ pulses can be written as

$$\begin{aligned} U^{(w)}(t_{2N}, t_0) &= U_{2\pi} U(t_{2N}, t_{2N-1}) U_{2\pi} U(t_{2N-1}, t_{2N-2}) \\ &\quad \cdots U_{2\pi} U(t_2, t_1) U_{2\pi} U(t_1, t_0), \end{aligned} \quad (3.16)$$

with $t_{2N} - t_{2N-1} = \cdots = t_2 - t_1 = t_1 - t_0 = \tau$, and the time-evolution matrix for the atomic decay during the time $t_k - t_{k-1} = \tau$ is

$$U(t_k, t_{k-1}) = \exp \left[-\frac{i}{\hbar} \int_{t_{k-1}}^{t_k} dt' H_i(t') \right]. \quad (3.17)$$

Without the series of 2π pulses, one has the usual decay process as a reference, and the total evolution matrix U can be represented as

$$U^{(0)}(t_{2N}, t_0) = U(t_{2N}, t_{2N-1}) U(t_{2N-1}, t_{2N-2}) \cdots U(t_2, t_1) U(t_1, t_0). \quad (3.18)$$

The time evolution of the population in the lower level $|b\rangle$ for the atom initially in the upper level can be determined from

$$P_b^{(i)}(t) = \sum_k |\langle b, 1_k | U^{(i)}(t, 0) | a, 0 \rangle|^2, \quad (3.19)$$

where $i \in \{w, 0\}$, depending on whether the pulses are applied or not. The population dynamics can be obtained by inserting Equation (3.16) and Equation (3.18) in Equation (3.19). As an example, in what follows, we show the time-evolution operator after two pulses (from t_0 to t_2) to the first order in the coupling constant:

$$\begin{aligned} U^{(w)}(t_2, t_1) &= 1 - \frac{i}{\hbar} \int_{t_0}^{t_1} dt' H_i(t') + \frac{i}{\hbar} \int_{t_1}^{t_2} dt' H_i(t') \\ &= 1 - i \left[- \sum_k g_k a_k^\dagger S_{ba} e^{i\Delta_k t_0} \left(1 - e^{i\Delta_k \tau} \right)^2 / (i\Delta_k) + \text{H.c.} \right] \\ &= 1 - \left[\sum_k g_k a_k^\dagger S_{ba} e^{i\Delta_k t_0} \left(1 - e^{2i\Delta_k \tau} \right) (i \tan \Delta_k \tau / 2) / \Delta_k - \text{H.c.} \right]. \end{aligned} \quad (3.20)$$

We now compare the time-evolution matrix for the interrupted damping (3.20) to the uninterrupted decay:

$$\begin{aligned} U^{(0)}(t_2, t_1) &= 1 - \frac{i}{\hbar} \int_{t_0}^{t_1} dt' H_i(t') - \frac{i}{\hbar} \int_{t_1}^{t_2} dt' H_i(t') \\ &= 1 - \left[\sum_k g_k a_k^\dagger S_{ba} e^{i\Delta_k t_0} (e^{2i\Delta_k \tau} - 1) / \Delta_k - \text{H.c.} \right]. \end{aligned} \quad (3.21)$$

Comparing Equations (3.20) and (3.21), the only difference between the two expressions is the additional factor $i \tan(\Delta_k \tau/2)$. It arises due to the change of coherence between the upper and lower levels by the 2π pulses. We can now split the total time $t = t_{2N}$ into N equal intervals. Then, the time-evolution operators $U^{(0)}(t_{2N}, 0)$ and $U^{(w)}(t_{2N}, 0)$ for the two cases can be obtained from Equations (3.16), (3.18), (3.20), and (3.21) by retaining only the terms linear in g_k . Finally, the population in the lower level can be represented as (Agarwal et al., 2001b)

$$\begin{aligned} P_b^{(0)}(t_{2N}) &= \sum_k \left| (g_k/\Delta_k) (e^{2i\Delta_k \tau} - 1) \sum_{j=1}^N e^{2i\Delta_k(j-1)\tau} \right|^2 \\ &= \int d\omega_k |g(\omega_k)|^2 D(\omega_k) \frac{\sin^2(\Delta_k t/2)}{(\Delta_k/2)^2}, \end{aligned} \quad (3.22)$$

and

$$\begin{aligned} P_b^{(w)}(t_{2N}) &= \sum_k \left| (g_k/\Delta_k) (1 - e^{2i\Delta_k \tau}) (i \tan \Delta_k \tau/2) \sum_{j=1}^N e^{2i\Delta_k(j-1)\tau} \right|^2 \\ &= \int d\omega_k |g(\omega_k)|^2 D(\omega_k) (\tan \Delta_k \tau/2)^2 \left(\frac{\sin^2(\Delta_k t/2)}{(\Delta_k/2)^2} \right). \end{aligned} \quad (3.23)$$

We replaced the summation over k by an integration over ω_k , with $D(\omega_k)$ the density of states and $t = 2N\tau$. Again, the only difference between the two cases is the presence of a single term $\tan^2(\Delta_k \tau/2)$. Provided that the pulse interval τ and the detuning Δ_k are chosen such that $\Delta_k \tau \ll 1$, the application of the sequence of 2π pulses on the auxiliary transition leads to the suppression of the spontaneous decay. The suppression can be interpreted as arising from a destructive interference of transition amplitudes induced by the pulses. This destructive interference is due to a phase change of the state $|a\rangle$ by π due to the application of the 2π pulse.

The requirement for application of measurements or pulses with high repetition rate can be alleviated if the upper state consists of a manifold of two or more decaying substates. Interference between different decay channels out of this manifold leads to a sequence of quiescent and burst phases in which the spontaneous decay of the manifold is much slower or much faster than the corresponding decay of a single state. Based on this observation, Frishman and Shapiro (2001) developed a method to suppress the spontaneous decay of the manifold via infrequent interruptions, which essentially keeps the system in a quiescent phase. Then, the timescale for the interruptions is determined by the decay rate, which is much longer than usual Zeno times. For example, the spontaneous emission of a visible photon out of an ensemble of excited electronic states of an atom or a molecule can be completely suppressed by the application of suitable microwave pulses with a separation of a few nanoseconds.

It has also been pointed out that counter-rotating terms, i.e., those additionally included if the rotating-wave-approximation is not applied, can significantly modify the short-time evolution. In particular, then the Zeno time is much larger, which is of relevance for attempts to experimentally verify the Zeno effect (Zheng, Zhu, & Zubairy, 2008).

3.1.2.2. Multiphoton Pathway Interference A different approach to the modification of the spontaneous emission rate relies on multiphoton pathway interference (Akram, Evers, & Keitel, 2005; Berman, 2004; Evers & Keitel, 2002, 2004a,b; Feranchuk, Komarov, and Ulyanenkov, 2002; Kofman, 2004). The basic idea is to induce different multiphoton transitions as the interfering pathways. Such interference among different multiphoton channels between bound states also occurs in other level schemes (Abi-Salloum, Davis, Lehman, Elliott, & Narducci, 2007) and has been observed experimentally (Chen, Yin, & Elliott, 1990), even up to interference between four-wave and six-wave channels (Zhang, Khadka, Anderson, & Xiao, 2009). Similar effects have also been observed, e.g., in field ionization (Schumacher, Weihe, Muller, & Bucksbaum, 1994). More applications and further references can be found in the studies by Král, Thanopoulos, and Shapiro (2007), Protopapas and Knight (1995), Zhang et al. In these examples, the interfering fields are coherent driving fields. In contrast, in the following, we will analyze interference among multiphoton pathways, which include a spontaneously emitted photon. In particular, we discuss the general idea for the example of a dipole-forbidden transition.

We consider a two-level atom with a dipole-forbidden transition between upper state $|e\rangle$ and lower state $|g\rangle$, driven by a coherent field with frequency much lower than the atomic transition frequency (Akram et al., 2005). Then, the decay of the excited state in leading order is mediated by three processes. First, the atom can decay via two-photon spontaneous

emission (note that here for simplicity we neglect processes beyond the dipole approximation such as electric quadrupole transitions). Second, the atom can absorb or emit a low-frequency field (LFF) photon together with the emission of a single photon into the vacuum, which we denote as induced emission. To illustrate the basic principle, we assume that the driving field is sufficiently strong such that the induced decay channels dominate over the two-photon spontaneous decay. The system can then be described in an interaction picture by the interaction Hamiltonian V and the wave function $|\Psi(t)\rangle$ given as (Cardimona, Kovanis, & Sharma, 1993; Evers & Keitel, 2004b),

$$V = \hbar \sum_k \left(\alpha_1 b e^{-i\omega t} + \alpha_2 b^\dagger e^{i\omega t} \right) a_k S_{eg} e^{i(\omega_{eg} - \omega_k)t} + \text{H.c.}, \quad (3.24)$$

$$|\Psi(t)\rangle = \sum_n E_n(t) |e, n, 0\rangle + \sum_n \sum_k G_n^k(t) a_k^\dagger |g, n, 0\rangle. \quad (3.25)$$

Here, a_k [a_k^\dagger] is a vacuum photon annihilation [creation] operator, and b [b^\dagger] are the corresponding photon operators of the driving field. $|i, n, 0\rangle$ denotes the atom in state $|i\rangle$, the n photon state of the driving field, and no photons in the vacuum. $E_n(t)$ is the amplitude for the atom in the excited state with n photons in the LFF mode, but no photons in the vacuum. $G_n^k(t)$ corresponds to the atom in the ground state with one spontaneous photon in the vacuum. Eliminating the vacuum using a Wigner–Weisskopf-like calculation as in Section 2, the equation for each upper-state amplitude E_n can be written as (Akram et al., 2005)

$$\frac{d}{dt} E_n(t) = -\beta_0 E_n(t) - \beta_1 e^{2i\omega t} E_{n-2}(t) - \beta_2 e^{-2i\omega t} E_{n+2}(t), \quad (3.26)$$

where $\beta_0, \beta_1, \beta_2$ are combinations of the coupling constants α_i ($i \in \{1, 2\}$), which depend on the specific atomic system being considered. β_0 corresponds to a LFF-induced two-photon decay. This exponential decay, however, is modified by the presence of the contributions proportional to β_1, β_2 , if the frequency ω is smaller than the (natural and induced) decay width. Otherwise, the terms with β_1, β_2 average out due to the fast oscillation of the exponential functions. This can be interpreted as interference between the induced decay pathways from the excited to the ground state. This interference takes place, if the pathways cannot be identified by the frequency of the involved photons, i.e., if ω is smaller than the transition width. Note, however, that the two-photon spontaneous decay channel does not interfere with the induced pathways, as it can be distinguished via the frequency of the spontaneous photons. Thus, this system allows for a control of induced emission via multiphoton pathway interference,

whereas the (naturally slow) two-photon spontaneous emission is essentially unaltered.

An example for the time evolution of the total population $\Pi(t)$ in the atomic upper state $|e\rangle$ versus time is shown in Figure 4(a). The driving field is chosen as a coherent state. It can be seen that depending on the phase of the coherent state, the induced decay can be either enhanced or reduced as compared with the case without pathway interference ($\beta_1 = \beta_2 = 0$) or to the case of unknown driving field phase. These results may be interpreted as constructive or destructive interference of the induced decay pathways, controlled by the coherent phase of the LFF. From Equation (3.26), one can see that states with a relative phase $\pm 2\phi$ are coupled, such that results with $\phi = n\pi$ ($n \in \{0, 1, \dots\}$) coincide. The maximum destructive interference is obtained for $\phi = \pi/2$ or $2\phi = \pi$, which corresponds to a relative minus sign between the coupled amplitudes, inducing cancellation. In Figure 4(b), the dependence of the system evolution on the LFF frequency is plotted. As expected from the interpretation based on pathway interference, the population trapping vanishes with increasing ω .

The advantage of using a dipole forbidden transition is that since the one-photon decay is forbidden, all relevant natural and induced transitions are of the same (second) multiphoton order. Therefore, the induced multiphoton processes can dominate the system dynamics even if the driving LFF intensity is moderate. The modification of spontaneous decay on a dipole-allowed transition is more challenging. It requires that the one-photon spontaneous decay channel interferes with three-photon transitions induced by the driving LFF (Berman, 2004; Evers & Keitel,

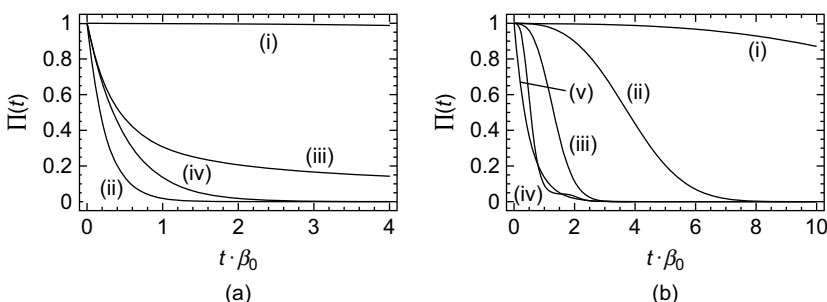


FIGURE 4 (a) Total upper-state population decay with respect to time for LFF frequency $\omega = 0.01 \beta_0$. (i) $\beta_1 = \beta_2 = 0.5 \beta_0$, coherent state phase $\phi = \pi/2$, (ii) $\beta_1 = \beta_2 = 0.5 \beta_0, \phi = 0$ or π , (iii) $\beta_1 = \beta_2 = 0.5 \beta_0$, average over all possible values of ϕ , and (iv) reference curve for the case $\beta_1 = \beta_2 = 0$ (no interference) and arbitrary ϕ . (b) Total upper-state population decay with respect to time for $\beta_1 = \beta_2 = 0.5 \beta_0$, $\phi = \pi/2$, and different ω : (i) $\omega = 0.01 \beta_0$, (ii) $\omega = 0.1 \beta_0$, (iii) $\omega = 0.5 \beta_0$, (iv) $\omega = 2 \beta_0$, and (v) reference curve for the case $\beta_1 = \beta_2 = 0$ without interference effects. Reproduced from Akram et al. (2005). Copyright (2005) by Institute of Physics Publishing.

2002; Evers & Keitel, 2004a; Evers & Keitel, 2004b; Kofman, 2004). The suppression of the induced three-photon processes has to be compensated by a rather intense LFF inducing the multiphoton transitions, which may lead to complications such as ionization. The Hamiltonian for the dipole-allowed case is a straightforward extension to the two-photon Hamiltonian in Equation (3.24) (Evers & Keitel, 2002, 2004b).

3.1.2.3. Dressed-State Level Crossing Finally, we turn to a scheme in which a strong coherent field substantially modifies the spontaneous decay of an atom due to level crossing. The atom is assumed to have three states $|1\rangle$, $|2\rangle$, and $|3\rangle$ with energies in ascending order, and the coherent field is applied between the two upper states (see Figure 5). If the applied field is sufficiently strong, one of the dressed states $|\tilde{2}\rangle$ and $|\tilde{3}\rangle$ is ac-Stark shifted below the bare ground state $|1\rangle$ (Kocharovskaya, Mandel, & Scully, 1995; Kocharovskaya, Radeonychev, Mandel, & Scully, 1999). This can lead to an anomalous atomic response yielding maximal coherence, vanishing absorption, and large index of refraction (Kocharovskaya et al., 1995, 1999; Löfller, Nikonov, Kocharovskaya, & Scully, 1997). Also, the structure of the spontaneous emission channels is modified due to the level crossing. If the Stark-shifted state $|\tilde{2}\rangle$ is shifted below the bare ground state $|1\rangle$, the previously stable ground state $|1\rangle$ becomes unstable and can decay spontaneously to $|\tilde{2}\rangle$. To show this, we assume $\omega_{32} \gg \Omega \gg \omega_{21}$, and write the master equation describing the processes indicated in Figure 5 as (Kocharovskaya et al., 1999)

$$\begin{aligned} \dot{\rho} + i\Omega[S_z, \rho] = & -\frac{\gamma_3}{4}\{[S_{\tilde{3}\tilde{2}}, S_{\tilde{2}\tilde{3}}\rho] + [S_{\tilde{2}\tilde{3}}, S_{\tilde{3}\tilde{2}}\rho] + [S_z, S_z\rho]\} \\ & -\frac{\tilde{\gamma}_2}{2}\{[S_{1\tilde{2}}, S_{\tilde{2}1}\rho] + [S_{\tilde{3}1}, S_{1\tilde{3}}\rho]\} + \text{H.c..} \end{aligned} \quad (3.27)$$

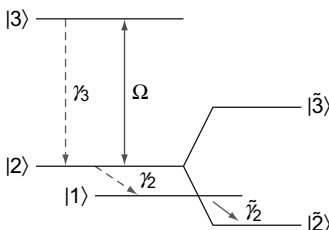


FIGURE 5 Energy levels of a strongly driven three-level particle. Here, Ω is the Rabi frequency corresponding to the $|3\rangle \leftrightarrow |2\rangle$ atomic transition while γ_3 and γ_2 are the spontaneous emission decays of the upper state $|3\rangle$ and $|2\rangle$, respectively. $|\tilde{3}\rangle$ and $|\tilde{2}\rangle$ indicate the dressed states. $\tilde{\gamma}_2$ is the spontaneous decay on $|1\rangle \rightarrow |\tilde{2}\rangle$ transition when $\Omega \gg \omega_{21}$.

Here, $S_z = S_{\tilde{3}\tilde{3}} - S_{\tilde{2}\tilde{2}}$ and $\tilde{\gamma}_2 = 4\Omega^3 d_{21}^2 / (3\hbar c^3)$. Equation (3.27) leads to the equations of motion for the dressed-state populations

$$\begin{aligned}\frac{d}{dt}\langle S_{\tilde{3}\tilde{3}} \rangle &= -(\gamma_3/2 + \tilde{\gamma}_2)\langle S_{\tilde{3}\tilde{3}} \rangle + \gamma_3\langle S_{\tilde{2}\tilde{2}} \rangle/2, \\ \frac{d}{dt}\langle S_{11} \rangle &= -\tilde{\gamma}_2(\langle S_{11} \rangle - \langle S_{\tilde{3}\tilde{3}} \rangle), \\ \langle S_{\tilde{2}\tilde{2}} \rangle &= 1 - (\langle S_{\tilde{3}\tilde{3}} \rangle + \langle S_{11} \rangle).\end{aligned}\quad (3.28)$$

In steady state, one obtains $\langle S_{\tilde{3}\tilde{3}} \rangle = (\gamma_3/2)/(\tilde{\gamma}_2 + 3\gamma_3/2)$, $\langle S_{11} \rangle = \langle S_{\tilde{3}\tilde{3}} \rangle$, and $\langle S_{\tilde{2}\tilde{2}} \rangle = 1 - 2\langle S_{\tilde{3}\tilde{3}} \rangle$. Thus, if $\tilde{\gamma}_2 \gg \gamma_3$, all atoms are trapped in sublevel $|\tilde{2}\rangle$, even though $|\tilde{2}\rangle$ consists of a superposition of the two excited states $|2\rangle$ and $|3\rangle$. A complete population of $|\tilde{2}\rangle$, however, requires a relatively large dipole moment and mode density at the low-frequency $|2\rangle \leftrightarrow |1\rangle$ transition. Further analysis shows that trapping of atoms in one of the two dressed states also modifies both the resonance fluorescence and the probe field absorption spectra in a substantially different way than in the case of strongly driven two-level system (Kocharovskaya et al., 1995).

3.1.3. Spectral Control of Spontaneous Emission

Compared with a suppression of the total spontaneous emission rate of a given system, a modification of the emission spectrum is often more straightforward. Considerable interest has been devoted to the generation of narrow lines in the resonance fluorescence spectrum, which typically can be associated to the occurrence of long-lived, metastable states. This can, for example, be achieved by coupling the decaying state to a metastable state (Garraway, Kim, & Knight, 1995; Hegerfeldt & Plenio, 1995; Manka, Doss, Narducci, Ru, & Oppo, 1991; Narducci, Scully, Oppo, Ru, & Tredicce, 1990), by spontaneous emission interference as discussed in Section 3.2 (Cardimona et al., 1982; Ficek & Swain, 2004; Zhou & Swain, 1996) or by surrounding the atom in modified reservoirs (Carmichael, Lane, & Walls, 1987; Keitel, Knight, Narducci, & Scully, 1995). Similarly, individual spectral regions can also be strongly suppressed (Scully & Zhu, 1998; Zhu & Scully, 1996). Ultrasharp lines in the absorption or emission spectra of a two-level atom were shown to occur (Freedhoff & Quang, 1994) in the resonance fluorescence of a V-type three-level atom excited by a single-mode laser field when the dipole moments are nearly parallel (Zhou & Swain, 1996) and in the resonance spectrum of a three-level setup with dark state suppression (Evers et al., 2002). The emission spectrum can also be controlled using the phase of applied laser fields (Evers, 2005; Martinez, Herczfeld, Samuels, Narducci, & Keitel, 1997; Paspalakis & Knight, 1998). Narrow spectral lines can also appear due to spontaneous emission

interference between two dipole transitions in a single atom (Kiffner, Evers, & Keitel, 2006a). Analogous spectral control can also be achieved in interacting ensembles of atoms (Agarwal, Brown, Narducci, & Vetrí, 1977; Macovei, Evers, & Keitel, 2003; Macovei & Keitel, 2003).

In the following section, we outline one mechanism for the line width reduction of radiatively broadened spectral lines in the traditional setting of resonance fluorescence (Keitel, Narducci, & Scully, 1995). We consider a three-level system in the V -configuration with upper states $|1\rangle$ and $|2\rangle$ and lower state $|3\rangle$. The two driving fields on the $|3\rangle \leftrightarrow |1\rangle$ and $|3\rangle \leftrightarrow |2\rangle$ transitions have coupling constants Ω_1 and Ω_2 , respectively, and the spontaneous emission rates on these transitions are γ_1 and γ_2 . The resonance fluorescence spectrum emitted on the transition $|3\rangle \leftrightarrow |1\rangle$ is given by the real part of the half-sided Fourier transform of the atomic dipole correlation function (Cohen-Tannoudji, 1977)

$$S(\omega) \propto \text{Re} \lim_{t \rightarrow \infty} \int_0^t d\tau e^{i(\omega_{13}-\omega)\tau} \langle S_{13}(t+\tau)S_{31}(t) \rangle. \quad (3.29)$$

As we are interested in the resonant strong-field limit $\Omega \equiv \sqrt{\Omega_1^2 + \Omega_2^2} \gg \gamma_i$ ($i \in \{1, 2\}$), we transfer to the dressed-state picture given by (Keitel et al., 1995; Macovei et al., 2003)

$$|3\rangle = \frac{1}{\sqrt{2}}\{|\Psi_1\rangle + |\Psi_2\rangle\}, \quad (3.30a)$$

$$|2\rangle = \frac{\Omega_1}{\Omega}|\Psi_3\rangle + \frac{\Omega_2}{\sqrt{2}\Omega}|\Psi_2\rangle - \frac{\Omega_2}{\sqrt{2}\Omega}|\Psi_1\rangle, \quad (3.30b)$$

$$|1\rangle = -\frac{\Omega_2}{\Omega}|\Psi_3\rangle + \frac{\Omega_1}{\sqrt{2}\Omega}|\Psi_2\rangle - \frac{\Omega_1}{\sqrt{2}\Omega}|\Psi_1\rangle. \quad (3.30c)$$

The operators $R_{\alpha\beta} = |\Psi_\alpha\rangle\langle\Psi_\beta|$ describe dressed-state transition operators for $\alpha \neq \beta$ and dressed-state populations if $\alpha = \beta$ ($\alpha, \beta \in \{1, 2, 3\}$). Introducing Equation (3.30) in Equation (3.29) and performing the secular approximation, one arrives at

$$\begin{aligned} S(\omega) = \frac{1}{2} \text{Re} \lim_{t \rightarrow \infty} \int_0^t d\tau e^{i(\omega_{13}-\omega)\tau} & \left\{ \frac{\Omega_2^2}{\Omega^2} (\langle R_{31}(\tau)R_{13} \rangle_s + \langle R_{32}(\tau)R_{23} \rangle_s) \right. \\ & \left. + \frac{\Omega_1^2}{2\Omega^2} (\langle R_{21}(\tau)R_{12} \rangle_s + \langle R_z(\tau)R_z \rangle_s + \langle R_{12}(\tau)R_{21} \rangle_s) \right\}. \end{aligned} \quad (3.31)$$

In general, the resonance fluorescence spectrum consists of many spectral lines. However, the first two lines depend on the dressed-state population ($\langle R_{33} \rangle$) that is unpopulated in our case, i.e., $\langle R_{33} \rangle_s = 0$. Therefore, the spectrum reduces to

$$S(\omega) = \frac{\Omega_1^2}{4\Omega^2} \left\{ \frac{1}{2} \frac{6\Gamma}{36\Gamma^2 + (\Delta + 2\Omega)^2} + \frac{4\Gamma_2}{16\Gamma^2 + \Delta^2} + \frac{1}{2} \frac{6\Gamma}{36\Gamma^2 + (\Delta - 2\Omega)^2} \right\}. \quad (3.32)$$

Here $\Delta = \omega_{13} - \omega$ and $\Gamma = (\gamma_1\Omega_1^2 + \gamma_2\Omega_2^2)/(4\Omega^2)$. Without additional field Ω_2 , we find that $\Gamma = \gamma_1/4$. But if $\Omega_1 \ll \Omega_2$ and $\gamma_2 < \gamma_1$, $\Gamma \approx \gamma_2/4$, and one finds spectral narrowing on the $|1\rangle \rightarrow |3\rangle$ bare-state transition. This approach can be implemented, for example, by choosing one optical transition and one transition with higher- or lower-transition frequency ω . Since the spontaneous decay rate scales with ω^3 , the condition $\gamma_2 < \gamma_1$ can be achieved. It can be seen from Equation (3.32) that together with the line width the line intensities are also reduced. One way to overcome this has been suggested by Keitel (1999) using a four-level setup including incoherent pumping. An alternative approach is to use collective interaction among many three-level particles (Macovei, Evers, & Keitel, 2004).

3.2. Spontaneous Decay-Induced Coherences

Throughout the derivation of the general master equation for radiatively coupled atoms in Section 2, we encountered terms that can be interpreted as decay-induced coherences between atomic dipole transitions. Even though effects of this type were noted already in the early days of quantum mechanics (Landau, 1927), it was later work (Agarwal, 1974; Cardimona et al., 1982; Faist, Capasso, Sirtori, West, & Pfeiffer, 1997; Fleischhauer, Keitel, Narducci, Scully, Zhu, & Zubairy, 1992; Gong, Paspalakis, & Knight, 1998; Imamoğlu, 1989; Javanainen, 1992; Paspalakis & Knight, 1998; Schmidt, Campman, Gossard, & Imamoğlu, 1997; Zhou & Swain, 1996; Zhu, Chan, & Lee, 1995; Zhu & Scully, 1996) that sparked widespread interest in these coherences. Many applications have been proposed (Ficek & Swain, 2005), including population trapping (Agarwal, 1974; Gong et al., Lee, Polynkin, Scully, & Zhu, 1997), modification of the resonance fluorescence (Cardimona et al., 1982; Keitel, 1999; Zhou & Swain, 1996; Zhu et al., 1995) and probe absorption (Zhou & Swain, 1997), lasing without inversion (Fleischhauer, Keitel, Narducci, Scully, Zhu, & Zubairy, 1992), phase control (Evers, 2005; Paspalakis & Knight, 1998),

dark-state suppression (Evers et al., 2002), spontaneous emission in band gap structures (Zhu et al., 1997), group velocity control (Bortman-Arbiv, Wilson-Gordon, & Friedmann, 2001), optical bistability (Joshi, Yang, & Xiao, 2003; Liu, Gong, Fan, & Xu, 2004), squeezing (Gao, Li, & Zhu, 2002; Gonzalo, Antón, Carreño, & Calderón, 2005), enhancing of Kerr nonlinearity (Niu & Gong, 2006), entanglement evolution (Derkacz & Jakóbczyk, 2006), and quantum interference enforced by time-energy complementarity (Kiffner, Evers, & Keitel, 2006b).

From Equation (2.45), it can be seen that the corresponding coupling constant γ_{ij} for coherences arising due to the interaction of transitions i and j vanish if the two transition dipole moments are orthogonal. At the same time, transferring the master equation into a suitable interaction picture reveals that these coupling terms typically average out in an approximation similar to the rotating-wave approximation if the two transition frequencies ω_i and ω_j are large compared with the respective atomic widths γ_i and γ_j . This poses stringent conditions on the atomic level structure for these coherences to become of relevance, and it should be noted that for many level schemes discussed in the literature, these conditions are not met by any known atomic species. Particularly, the well-known Λ - and V -type three-level schemes with near-degenerate nonorthogonal transition dipole moments frequently discussed in theoretical works cannot be found in real atomic systems. Nevertheless, decay-induced coherences are of relevance mainly for three reasons. First, nonatomic systems and, in particular, artificial quantum systems can be found where the mentioned conditions can be fulfilled also for three-level setups. Second, schemes have been devised, which either simulate few-level setups with decay-induced coherences or allow to induce similar coherences. Third, there are different realistic level schemes in which decay-induced coherences crucially determine the system dynamics. All three approaches will be discussed in more detail throughout this section.

3.2.1. Basic Analysis, Three-Level Systems

We begin by explaining the relevant basic features of decay-induced coherences, which motivate the great interest they receive. Despite the fact that the real atomic V -type systems do not exhibit decay-induced coherences, we follow the original discussion in the literature and begin by analyzing a V -type system with near-degenerate nonorthogonal transition dipole moments. This discussion provides the basis to understand the more advanced schemes considered in the following sections.

The system consists of two upper levels $|1\rangle$ and $|2\rangle$ spontaneously decaying to a common ground state $|3\rangle$, see Figure 6(a). The transition between the two upper states is dipole-forbidden. The system master

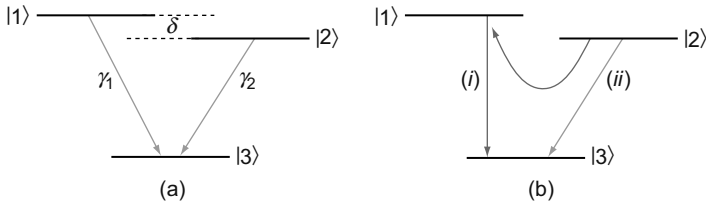


FIGURE 6 Atomic three-level system in V -configuration exhibiting spontaneous emission interference. (a) Relevant level scheme. (b) Schematic depiction of the cross-coupling processes.

equation follows from Equation (2.43) as (Agarwal, 1974; Ficek & Swain, 2005)

$$\begin{aligned} \frac{\partial \rho}{\partial t} = & -i[\omega_{13}S_{11} + \omega_{23}S_{22}, \rho] \\ & -\frac{\gamma_1}{2}([S_{13}, S_{31}\rho] + [\rho S_{13}, S_{31}]) - \frac{\gamma_2}{2}([S_{23}, S_{32}\rho] + [\rho S_{23}, S_{32}]) \\ & -\frac{\gamma_{12}}{2}([S_{13}, S_{32}\rho] + [\rho S_{23}, S_{31}]) - \frac{\gamma_{12}}{2}([S_{23}, S_{31}\rho] + [\rho S_{13}, S_{32}]). \end{aligned} \quad (3.33)$$

Here, $S_{\alpha\beta} = |\alpha\rangle\langle\beta|$ describes the atomic lowering or raising operators when $\alpha \neq \beta$ and populations if $\alpha = \beta$ ($\{\alpha, \beta \in 1, 2, 3\}$). The terms proportional to γ_α describe the independent spontaneous emission on the two transitions, whereas the terms with γ_{12} are the vacuum-induced cross terms. For simplicity, we consider the case of degenerate transition frequencies and equal spontaneous emission rates, $\gamma = \gamma_1 = \gamma_2$. Further, we denote the cosine of the angle between the two transition dipole moments as p , $0 \leq p \leq 1$, such that the cross-coupling rate in Equation (3.33) becomes $\gamma_{12} = p\gamma$.

The equations of motion for the upper-states population $\mathcal{P}(t) = \langle S_{11} \rangle + \langle S_{22} \rangle$ and the coherences $\mathcal{C}(t) = \langle S_{12} \rangle + \langle S_{21} \rangle$ are

$$\frac{d}{dt}\mathcal{P}(t) = -\gamma\mathcal{P}(t) - p\gamma\mathcal{C}(t), \quad (3.34a)$$

$$\frac{d}{dt}\mathcal{C}(t) = -\gamma\mathcal{C}(t) - p\gamma\mathcal{P}(t), \quad (3.34b)$$

and can be solved to give

$$\mathcal{P}(t) = \frac{1}{2}[\mathcal{P}(0) + \mathcal{C}(0)]e^{-\gamma(1+p)t} + \frac{1}{2}[\mathcal{P}(0) - \mathcal{C}(0)]e^{-\gamma(1-p)t}, \quad (3.35)$$

with $\mathcal{P}(0)$ and $\mathcal{C}(0)$ being the initial conditions. If $p = 0$, one finds a true exponential decay of the total upper-state population. But if $p \neq 0$, the decay is modified. In particular, for $p = 1$, the initial population fraction $(\mathcal{P}(0) - \mathcal{C}(0))/2$ is trapped completely, while the part corresponding to $(\mathcal{P}(0) + \mathcal{C}(0))/2$ does decay. To interpret this situation, we apply a basis transformation to the symmetric and antisymmetric combination of the two upper states (Agarwal, 1974; Ficek & Swain, 2005),

$$|S\rangle = \frac{1}{\sqrt{2}} (|1\rangle + |2\rangle), \quad |A\rangle = \frac{1}{\sqrt{2}} (|1\rangle - |2\rangle), \quad (3.36)$$

and note that $(\mathcal{P}(0) + \mathcal{C}(0))/2$ [$(\mathcal{P}(0) - \mathcal{C}(0))/2$] is the initial population in $|S\rangle$ [$|A\rangle$]. The master Equation (3.33), then reads (Ficek & Swain, 2005)

$$\begin{aligned} \frac{\partial \rho}{\partial t} = & -\frac{\gamma}{2} (1+p) (|S\rangle \langle S| \rho + \rho |S\rangle \langle S| - 2|3\rangle \langle S| \rho |S\rangle \langle 3|) \\ & -\frac{\gamma}{2} (1-p) (|A\rangle \langle A| \rho + \rho |A\rangle \langle A| - 2|3\rangle \langle A| \rho |A\rangle \langle 3|). \end{aligned} \quad (3.37)$$

It can easily be seen that the symmetric state $|S\rangle$ decays with the modified decay rate $(1+p)\gamma$, whereas the asymmetric state $|A\rangle$ decays with the rate $(1-p)\gamma$. Thus, for parallel dipole moments ($p = 1$), the decay of the asymmetric state is completely suppressed, as was already apparent in Equation (3.35). The symmetric state, on the other hand, decays with twice the natural decay rate γ . Some examples for the time evolution are given in Figure 7.

The complete trapping for all times, however, is very fragile. Both if the dipole moments are not entirely parallel ($p \neq 1$), or if the two upper states are not completely degenerate ($\omega_{13} \neq \omega_{23}$), in the long-time limit only the ground state $|3\rangle$ is populated. The reason is that for $p \neq 1$, both symmetric and antisymmetric states have a nonvanishing decay rate. If the states are not degenerate, then the symmetric and the antisymmetric states are coupled, such that the antisymmetric state is depleted via the coupling to the symmetric state, even though it does not decay spontaneously to the ground state by itself. Nevertheless, in both cases, a considerable slowing down of the decay from the antisymmetric state as compared with the natural decay rates is possible if the perturbation from the ideal conditions is moderate.

An interpretation of this population trapping can be given in terms of quantum coherence and interference. The idea is that a photon emitted by one of the transitions can be reabsorbed by the other transition, if the above conditions for the cancellation of spontaneous emission are met. This process is shown in Figure 6(b) where the two interfering decay paths (i) and (ii) are indicated. Obviously, it is only possible if both the dipole

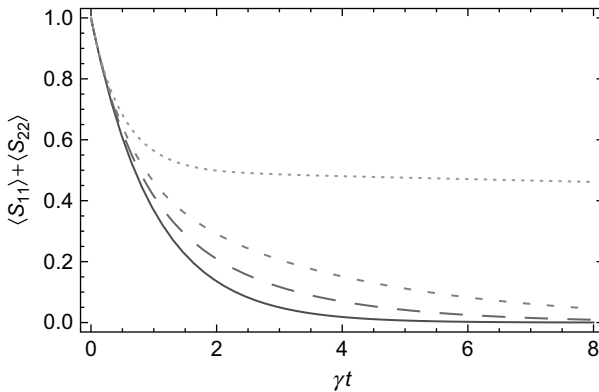


FIGURE 7 Upper-states population $\langle S_{11}(t) \rangle + \langle S_{22}(t) \rangle$ as function of γt . Here $\langle S_{11}(0) \rangle + \langle S_{22}(0) \rangle = 1$ and $\langle S_{21}(0) \rangle = \langle S_{12}(0) \rangle = 0$. The different curves show the cases $p = 0$ (solid line), $p = 0.5$ (dashed), $p = 0.7$ (short-dashed) and $p = 0.99$ (dotted), respectively.

moments and the transition frequencies of the two transitions match. This vacuum-mediated coupling gives rise to a so-called spontaneously generated coherence between the two upper states (Agarwal, 1974). The extra coherence then prohibits the spontaneous emission to the ground states, just as in the case of coherent population trapping in a corresponding three-level system in Λ -configuration (Scully & Zubairy, 1997).

In a sense, this vacuum-mediated coupling can be interpreted as a generalized complex Lamb shift (Cohen-Tannoudji et al., 1998). The difference is that the Lamb shift arises from a process in which a photon is emitted on an atomic transition, and then reabsorbed on the same transition, whereas here the photon is absorbed on a different transition. This interpretation as a generalized Lamb shift can also be applied to the case of dipole–dipole interacting samples of atoms (Dicke, 1954). There, the dipole–dipole interaction arises from a process in which a photon is emitted by one atom, and then reabsorbed in a different atom. Thus, the dipole–dipole coupling requires similar conditions to be fulfilled as spontaneous emission interference, but applied to transitions in different atoms. These vacuum-induced interparticle-couplings will be reviewed in Section 4.

3.2.2. The $J = 1/2 - J = 1/2$ Scheme

In this section, we demonstrate that realistic level schemes do exist in which spontaneously generated coherences can be observed. It is easy to see that the conditions for SGC are satisfied in a four-level system in $J = 1/2 \leftrightarrow J = 1/2$ configuration as shown in Figure 8(a), by the two

π -transitions preserving the magnetic quantum number m_j . This level structure can be found, e.g., in mercury ions and was studied related to the resonance fluorescence spectrum (Kiffner et al. 2006a; Polder & Schuurmans, 1976; Tan, Xia, & Li, 2009), squeezing (Jakob & Bergou, 1999; Lützenhaus, Cirac, & Zoller, 1998), time-energy complementarity (Kiffner et al. 2006b), spontaneously generated coherences in experimentally realizable level schemes (Kiffner et al., 2006a), and photon-photon correlations (Das & Agarwal, 2008). Light scattering from trapped mercury ions has already been studied experimentally (Eichmann et al., 1993; Itano et al., 1998). But in the $J = 1/2 \leftrightarrow J = 1/2$ system, the two π transitions do not share common states, and thus it is not clear if an atom can absorb photons on the one transition after having emitted on the other transition. On the other hand, one finds that in the equations of motion, there are indeed terms which resemble typical SGC contributions. Thus, the question arises whether SGC and vacuum-induced interferences take place in this realistic system (Kiffner et al., 2006a,b).

This question can be addressed by assuming that the two π -transitions are driven by a single laser field and by calculating the fluorescence intensity and the fluorescence spectrum emitted on these transitions. Both can be calculated in terms of the steady-state two-time correlation function

$$\left\langle [\vec{e}_z \cdot \hat{E}^{(-)}(\vec{r}, t + \tau)] [\vec{e}_z \cdot \hat{E}^{(+)}(\vec{r}, t)] \right\rangle_{t \rightarrow \infty},$$

where $\hat{E}^{(\pm)}$ are the positive and negative frequency part of the quantized electromagnetic field, \vec{r} is the detector position, and \vec{e}_z is the unit polarization vector. The fluorescence intensity follows with $\tau = 0$, and it is found that it is not affected by SGC or interference because the terms in the equations of motion turn out to be proportional to $\langle |1\rangle \langle 3| |4\rangle \langle 2| \rangle_{t \rightarrow \infty}$, which is zero because of the orthogonality of the ground states. Thus, the more general level scheme suppresses the SGC contributions in the equations of motion as suspected above.

But, in contrast, surprisingly the fluorescence spectrum does show signatures of interference, as can be seen from Figure 8(b). A closer analysis reveals that for the spectrum, the two operators $|1\rangle \langle 3|$ and $|4\rangle \langle 2|$ have to be evaluated at different times, $\tau \neq 0$. Then, they are no longer orthogonal and the SGC contributions can contribute. Thus, it can be concluded that the presented system indeed is a realistic setup to verify the as yet unobserved presence of SGC in atomic systems (Kiffner et al., 2006b).

But perhaps even more interesting is the interpretation of the results reveals that they arise from complementarity of energy and time (Kiffner et al., 2006a). If the observer decides to measure the total intensity, then the detector does not detect the energies of the different photons. Since

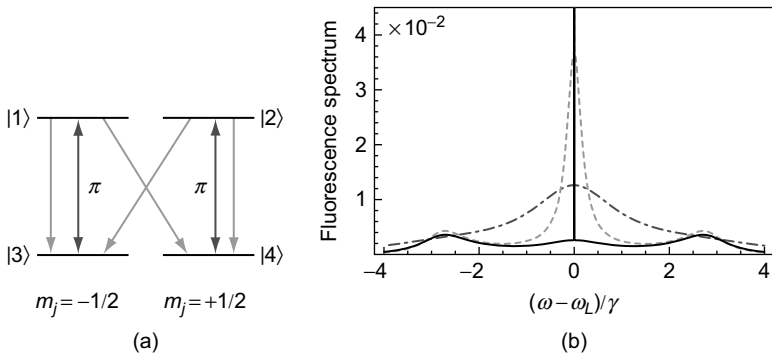


FIGURE 8 (a) Four-level atom in $J = 1/2 \leftrightarrow J = 1/2$ configuration as found, e.g., in mercury ions. Single arrows denote spontaneous emission channels, and double arrows indicate coherent driving with frequency ω_L on the so-called π transitions. (b) Resonance fluorescence spectrum emitted from the π transitions. The solid line shows the complete fluorescence spectrum for perfect detector resolution. The dashed line is the spectrum with interference terms artificially omitted. The vertical line at $\omega = \omega_L$ denotes the elastic Rayleigh peak that is present both with and without interference terms. If observed with a finite-frequency resolution of order of the natural decay rate γ , the spectra with and without interference terms are virtually identical (dash-dotted line). Reproduced from Kiffner et al. (2006b). Copyright (2006) by the American Physical Society.

there is no spectral information, complementarity does not impose any restrictions on the time resolution of such a measurement, and hence it is in principle possible to detect the photons in a time-resolved way. Thus, the experimental conditions allow, at least in principle, to determine the atomic ground state immediately after the detection of a π -photon. This implies that the π -photons cannot interfere, since one could decide on which of the two π -transitions the photon was emitted and hence reveal the quantum path taken by the system.

This completely changes if the spectrum of resonance fluorescence is measured. Here, the observer decides to measure the photon energies precisely. Since time and energy are complementary observables, no information on the time sequence of the emission can be obtained simultaneously, and the photon emission times are indeterminate. In contrast to the measurement of the total intensity, it is now impossible to decide on which transition the π -photon has been emitted, such that different indistinguishable pathways are possible. Therefore, the SGC can contribute and interference occurs. A similar argument explains why interference was observed in a recent attosecond time-energy double-slit experiment (Lindner et al., 2005), where the spectral resolution of the detector makes the “time slits” indistinguishable.

A quantitative analysis is possible in terms of the time-energy uncertainty relation, supported by a calculation for spectral measurements with variable frequency resolution. Also, a dressed-state analysis allows to clearly identify the interfering pathways, further supporting the above interpretation (Kiffner et al., 2006a,b). Interestingly, the spontaneously generated coherences summarized here can interplay with the related vacuum-mediated couplings between different atoms (Schmid & Evers, 2009).

3.2.3. The N-Type Scheme

Quantum coherence between the different atomic states and the related quantum interference between different transition pathways are key ingredients to a multitude of quantum optical effects (Ficek & Swain, 2005). A primary example is electromagnetically induced transparency (EIT) (Fleischhauer, Imamoğlu, & Marangos, 2005; Harris, 1997). EIT occurs, for example, in a three-level atomic system with two ground and one excited state, and with both transitions from the ground to the excited state driven by coherent laser fields. If the two-photon Raman detuning of the two fields is zero, the atom evolves into a superposition of the ground states only, which is known as a dark state. Further excitation to the excited state is suppressed due to destructive interference. Thus, if one of the applied fields is seen as probe field, then the application of the second control laser field renders the medium transparent—hence the name EIT. A related effect is the so-called electromagnetically induced absorption (EIA), in which the absorption of a probe laser field is substantially enhanced due to additional control laser fields. In the study by Akulshin, Barreiro, and Lezama (1998), EIA was experimentally observed in the absorption on the D_2 line of rubidium vapor under excitation of two copropagating optical waves with variable frequency offset. The control field was tuned to the center of the absorption line, while the frequency of the weak probe field was scanned around the control field frequency. Narrow spectral structures occurred at the zero-frequency offset. Based on the experimental results, it was concluded that EIA occurs in a degenerate two-level system if the following conditions are satisfied (Lezama, Barreiro, & Akulshin, 1999): (i) the ground level must be degenerate in order to allow the long-lived Zeeman coherence; (ii) the total angular momentum of the excited level F_e must be larger than the total momentum of the ground level F_g , and (iii) the transition $F_g \rightarrow F_e$ should be a closed transition. It was argued that EIA can be explained in terms of a spontaneous transfer of coherence from the excited to the ground states, a mechanism directly connected to the SGC discussed in this section (Failache, Valente, Ban, Lorent, & Lezama, 2003; Spani Molella, Rinkleff, & Danzmann, 2005; Taichenachev,

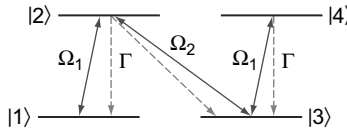


FIGURE 9 Atomic four-level system in N -configuration exhibiting spontaneous emission interference. Here Ω_1 and Ω_2 are the corresponding Rabi frequencies, while Γ is the spontaneous emission decay rate of the upper states.

Tumaikin, & Yudin, 1999a). It should be noted, however, that EIA was also observed in systems violating the above conditions (Kim, Moon, Kim, & Kim, 2003). This type of EIA cannot be explained by transfer of coherence, but by multiphoton atom-probe field interactions (Chou & Evers, 2010).

In the following section, we describe a theoretical model that reproduces EIA for a certain class of level schemes, which was introduced by Taichenachev, Tumaikin, and Yudin (1999b). This model relies crucially on the spontaneous transfer of coherence, a phenomenon closely related to vacuum-induced coherences. It considers a four-state atom in N -configuration, see Figure 9. The states $|1\rangle$ and $|3\rangle$ are nondecaying ground states with zero energy, while the excited states $|2\rangle$ and $|4\rangle$ have energy $\hbar\omega_0$ and decay spontaneously with decay rate Γ . The transition $|1\rangle \leftrightarrow |4\rangle$ is forbidden by selection rules. The transition dipole moments are such that a single control field with frequency ω_1 drives the two transitions $|1\rangle \rightarrow |2\rangle$ and $|3\rangle \rightarrow |4\rangle$ simultaneously with Rabi frequency Ω_1 . The weak field at frequency ω_2 probes the transition $|3\rangle \rightarrow |2\rangle$ with Rabi frequency Ω_2 (see Figure 9). In an interaction picture, assuming rotating-wave and dipole approximations, the free Hamiltonian H_0 and the interaction Hamiltonian H_i can be written as

$$H_0 = \hbar\Delta_1|1\rangle\langle 1| + \hbar\Delta_2|3\rangle\langle 3| + \hbar(\Delta_2 - \Delta_1)|4\rangle\langle 4|, \quad (3.38a)$$

$$H_i = \hbar\Omega_1\hat{Q}_1 + \hbar\Omega_2\hat{Q}_2 + H.c., \quad (3.38b)$$

where $\Delta_q = \omega_q - \omega_0$ are the detunings ($q \in \{1, 2\}$). The operators \hat{Q}_q are given by

$$\hat{Q}_1 = \alpha|2\rangle\langle 1| + |4\rangle\langle 3|, \quad \hat{Q}_2 = \beta|2\rangle\langle 3|, \quad \alpha^2 + \beta^2 = 1, \quad (3.39)$$

where the real numbers α and β govern the relative transition amplitudes. Assuming a closed atomic system, the master equation was given in the

study by Taichenachev et al. (1999b) as

$$\frac{d}{dt}\rho = -\frac{i}{\hbar}[H_0 + H_i, \rho] - \frac{1}{2}\Gamma\{P_e, \rho\}_+ + \Gamma \sum_{q=1,2} \hat{Q}_q^\dagger \rho \hat{Q}_q, \quad (3.40)$$

where $P_e = |2\rangle\langle 2| + |4\rangle\langle 4|$ is the projector onto the excited levels. This master equation can be rewritten in the notation of Equation (2.44) as

$$\frac{d}{dt}\rho = -\frac{i}{\hbar}[H_0 + H_i, \rho] - \sum_{i,j=1}^3 \gamma_{ij} (S_{i+}S_{j-}\rho + \rho S_{i+}S_{j-} - 2S_{j-}\rho S_{i+}), \quad (3.41)$$

if the atomic raising operators are defined as $S_{1+} = S_{21}$, $S_{2+} = S_{23}$, and $S_{3+} = S_{43}$, and the nonvanishing decay coefficients as $\gamma_{11} = |\alpha|^2\Gamma$, $\gamma_{22} = |\beta|^2\Gamma$, $\gamma_{33} = \Gamma$, $\gamma_{13} = \alpha\Gamma$, and $\gamma_{31} = \gamma_{13}^*$. The second term on the right-hand side of Equation (3.40) having the structure of an anticommutator contributes to the radiative damping of the excited-state populations and coherences. The last term contains the transfer of populations and low-frequency coherences from the excited level to the ground state, which can be written in this form since $S_{1+}S_{3-} = 0$ such that parts of the cross-terms in Equation (3.41) vanish.

The probe field absorption is determined by the steady-state probe transition coherence $\langle S_{32} \rangle$, which follows from Equation (3.40) as

$$\langle S_{32} \rangle = \frac{i\Omega_1(\langle S_{42} \rangle - \alpha\langle S_{31} \rangle) + i\beta\Omega_2(\langle S_{22} \rangle - \langle S_{33} \rangle)}{\Gamma/2 - i\Delta_2}. \quad (3.42)$$

The terms proportional to Ω_1 in Equation (3.42) describe modifications to the probe field absorption due to light-induced low-frequency coherences and spontaneous transfer of coherences. To understand the role of these contributions, we introduce a prefactor p characterizing the magnitude of the transfer by replacing $\gamma_{31} \rightarrow p\gamma_{31}$. For $p = 0$, no spontaneous coherence transfer takes place, while $p = 1$ corresponds to Equation (3.40). We analyze the probe absorption spectrum in linear order of the probe field Rabi frequency Ω_2 , the low-saturation regime $\Omega_1 < \Gamma$, and focus on the resonant case $\Delta_1 = \Delta_2 = 0$. Then (Taichenachev et al., 1999b),

$$\langle S_{32}^{(1)} \rangle = i\frac{\beta\Omega_2}{\Gamma/2} \left[\langle S_{33}^{(0)} \rangle + f(p) \right], \quad (3.43)$$

where the first term proportional to the zeroth-order population $\langle S_{33}^{(0)} \rangle$ describes the usual linear absorption in the absence of the control field,

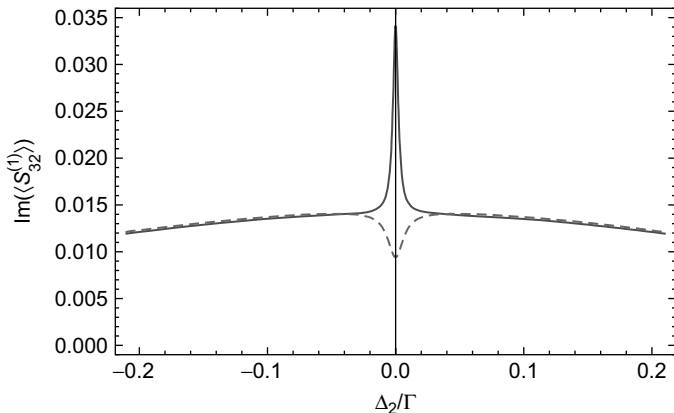


FIGURE 10 Imaginary part of $\langle S_{32}^{(1)} \rangle$ as function of Δ_2/Γ . Here $\Omega_1 = 0.05\Gamma$, $\Omega_2 = 0.01\Gamma$, $\Delta_1 = 0$, and $\alpha = \beta = 1/\sqrt{2}$. The solid curve is for $p = 1$, whereas the dashed line stands for $p = 0$.

and $f(p)$ describes the modification due to the control field Ω_1 and the coherence transfer (the expression for $\langle S_{32}^{(1)} \rangle$ at arbitrary detunings is given by Taichenachev et al. (1999b)). In the absence of coherence transfer, one finds $f(p=0) = -|\alpha|^2/(1+|\alpha|^2) \langle S_{33}^{(0)} \rangle$, which is negative and thus indicates electromagnetically induced transparency, i.e., a suppression of the usual absorption. In contrast, with coherence transfer, $f(p=1) = \alpha/(1-|\alpha|^2) \langle S_{33}^{(0)} \rangle$, which is positive and thus indicates an enhancement of absorption, i.e., electromagnetically induced absorption. An example for the corresponding probe field spectra is shown in Figure 10. It can thus be concluded that the spontaneous transfer of coherence is the origin of EIA in this system.

3.2.4. Experimental Evidence

In the introduction of this section, we discussed the stringent conditions on the atomic structure that need to be fulfilled in order for spontaneous coherences to occur. Thus, it is not surprising that the first experimental demonstration by Xia et al. (1996) did not make use of atoms, but rather involved sodium dimers. These dimers can be described by a five-level scheme with one ground state $|3\rangle$, two intermediate states $|1\rangle$, $|2\rangle$, and two upper states $|e_1\rangle$, $|e_2\rangle$ as shown in Figure 11. The system is excited from the ground state to the excited states via a two-photon process and then spontaneously decays via either of the intermediate states to the ground state. The crucial feature of this scheme is that the two transition dipole

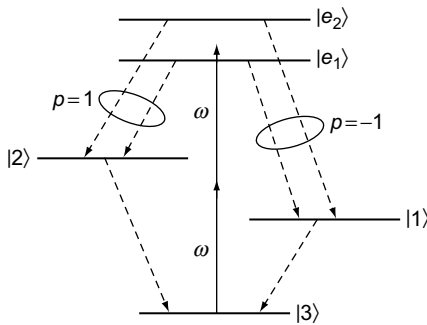


FIGURE 11 The relevant level scheme of sodium dimers used in the experiment by Xia, Ye, and Zhu (1996). The ground state $|3\rangle$ is excited via a two-photon process to the two excited states $|e_1\rangle, |e_2\rangle$. These decay to the ground state either via intermediate state $|1\rangle$ or $|2\rangle$. The transition dipole moments from the excited states to $|1\rangle$ are parallel ($p = 1$), whereas the dipole moments to $|2\rangle$ are antiparallel ($p = -1$). The exciting field frequency is ω .

moments from the excited states to the first intermediate state $|1\rangle$ are parallel ($p = 1$), while the corresponding dipole moments to the second intermediate state are antiparallel ($p = -1$). Thus, two extreme cases for the alignment of the dipole moments can directly be compared in a single experiment. It was found that depending on the orientation of the dipole moments, the fluorescence intensity as function of the two-photon detuning either was composed by two or by three peaks. These results are in agreement with a theoretical analysis (Wang, Wiseman, & Ficek, 2000). There it was found that both one-step, two-photon and two-step, one-photon excitation processes must be present to obtain agreement with the experiment. Further analysis is provided in the study by Agarwal (1997) and Berman (1998). However, a repetition of the experiment by Xia et al. (1996) could not verify these results (Li et al., 2000b).

A different approach to verify the presence of spontaneous coherences is to use artificial quantum systems. Early works reported quantum interference in tunneling of intersubband transitions in quantum wells (Faist et al., 1997; Schmidt et al., 1997). The observed effects crucially rely on the presence of two nearby states, which decay to the same continuum of final states (Harris, 1989). A quantum dot (QD) implementation of a three-level system in Λ -type configuration was studied, see Figure 12, by Dutt et al. (2005). Without magnetic field, the quantum dot has two degenerate electronic ground states and two excited states $|t_{\pm}\rangle$, which are charged exciton states with spin aligned (anti-)parallel to the growth axis of the quantum dot denoted as the z -axis. In the experiment, a magnetic field along the x -axis is applied to the quantum dot, which leads to the formation

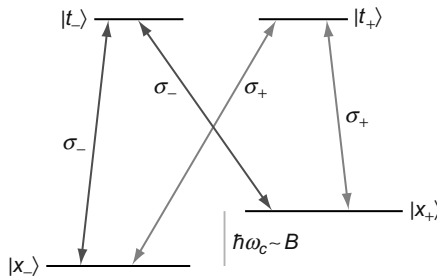


FIGURE 12 Spontaneously generated coherences in quantum dots. The figure shows the level scheme for the charged QD, with ground states $|x_{\pm}\rangle$ denoting electron spin projections along the x -axis split by $\hbar\omega_c$. The excited states $|t_{\pm}\rangle$ are trion exciton states. The arrows indicate different excitation channels, labeled with the polarization of the corresponding transition dipole moment.

of near-degenerate ground-state electron spin states $|x_{\pm}\rangle$ corresponding to the quantization axis defined by the magnetic field, see Figure 12. Initially, the two ground states are equally populated. The corresponding spin eigenstates with quantization axis along the z -axis can be written as $|z_{\pm}\rangle = (|x_{+}\rangle \pm |x_{-}\rangle)/\sqrt{2}$. The quantum dot is then excited using a short circularly (σ_{-}) polarized pump pulse propagating in z -direction, which excites population from the ground state $|z_{-}\rangle$ to the excited state $|t_{-}\rangle$. This leads to an optically induced *change* in the population of $|z_{-}\rangle$ given by $\Delta\rho_{z-z-}(\tau)$. Immediately after the pump pulse, $\Delta\rho_{z-z-}(\tau = 0) = -\rho_{t-,t-}$, where the initial excited-state population $\rho_{t-,t-}$ is proportional to the intensity of the pump pulse. Since the residual ground state after the pump pulse is not an eigenstate corresponding to the applied magnetic field, spin precession occurs, which leads to a time-dependent change in the population of $|z_{-}\rangle$ given by (Dutt et al., 2005)

$$\Delta\rho_{z-z-}(\tau) = -\frac{1}{2}\rho_{t-,t-}\{1 + e^{-\gamma_s\tau} \cos(\omega_c\tau - \phi)\}. \quad (3.44)$$

Quantum beats in the population change have the Larmor frequency ω_c and γ_s is the spin decoherence rate. If the coherence between the two ground state originates entirely from this optical pumping, then $\phi = 0$.

But ground-state coherences can also be created spontaneously. After the optical excitation, the excited state $|t_{-}\rangle$ decays back to $|z_{-}\rangle$, emitting a σ_{-} polarized photon. This gives rise to spontaneously generated coherences between $|x_{+}\rangle$ and $|x_{-}\rangle$, since the σ_{-} -polarized photon couples to both transitions $|x_{-}\rangle \leftrightarrow |t_{-}\rangle$ and $|x_{+}\rangle \leftrightarrow |t_{-}\rangle$, and since $|x_{\pm}\rangle$ are near-degenerate. Thus, the conditions for the creation of spontaneously generated coherences are fulfilled, similar to the case of an atom in a

polarization-selective cavity discussed in Section 3.2.7. But, in general, the spontaneously generated coherences are out of phase with the precessing laser-induced coherences, which leads to a nonzero phase ϕ in Equation (3.44). The time-dependent relative phase of the two contributions is determined by the ratio of the excited-state decay and the spin precession rates. If the spin precession is slow compared with the decay (weak magnetic field), then the SGC contributions cancel the optically induced coherences. If, on the other hand, the spin precession is fast compared with the decay (strong magnetic field), then the SGC contributions are averaged out. Since the spin precession is determined by the magnitude of the applied magnetic field, the presence of the SGC can be verified by observing the dependence of the quantum beats on the magnetic field. The experimental results clearly follow the theoretical predictions obtained by taking into account the SGC contributions, and therefore provide evidence for the presence of spontaneously generated coherences in QD systems (Dutt et al., 2005).

In the previous Section 3.2.1, we have shown that spontaneously generated coherences can modify the dynamics of a given quantum system to a large extent. SGC, however, only occur in selected realistic level schemes, and, therefore, in many cases cannot be facilitated in a straightforward way to manipulate the system to one's advantage. This observation motivated a number of attempts to induce similar coherences externally, i.e., to simulate the presence of SGC. In the following, we outline three different approaches to this, which are based on incoherent driving fields, coherent driving fields, or a breaking of the symmetry of the mode structure of the surrounding vacuum.

3.2.5. Interference Induced by Incoherent Driving

Since spontaneously generated coherences are closely related to the incoherent process of spontaneous emission, one might conclude that the coupling to the vacuum field cannot give rise to the buildup of coherences. Therefore, although it is obvious that coherent driving fields may generate atomic coherences, it is somewhat surprising that vacuum-mediated processes such as SGC can also lead to the creation of coherences. This motivates the question, whether phenomena associated with SGC can also be induced via suitable incoherent pumping fields. The answer is positive. It turns out that both the coherent and the incoherent dynamics can be modified via incoherent driving sources. Moreover, decay-induced cross-couplings can be engineered via a suitable incoherent pumping. One advantage of this approach is that it in principle also applies to systems that violate the conditions for SGC. Note that also other incoherent processes such as collisions or Doppler broadening can

induce extra-coherences, which may give rise to both constructive and destructive interference effects, see, e.g., Grynberg (1981), Grynberg and Berman (1990), Prior, Bogdan, Dagenais, and Bloembergen (1981), Wang and Gao (1995), and Yang, Sun, Zhang, Ding, and Wang (2005).

In the study by Fleischhauer, Keitel, Scully, and Su (1992) and Fleischhauer, Keitel, Scully, Su, Ulrich, and Zhu (1992), it was shown that coherences can be induced between a pair of atomic states by driving both states incoherently to an auxiliary state. This additional coherence was then shown to favorably affect lasing without inversion and enhancement of the index of refraction without absorption. Finite bandwidth driving was later studied in the same context by Sultana and Zubairy (1994) and Wilson, Meduri, Sellin, and Mossberg (1994). Both three-level V - and Λ -systems may exhibit coherence effects even if they are driven with incoherent fields only. This was shown for the case of the intensity correlation function $g_2(\tau)$ by Hegerfeldt and Plenio (1993), which oscillates at a characteristic frequency under incoherent driving. A similar effect was later discussed by Kohler (1996) for the fluorescence light on the Lyman- α transition of hydrogen-like systems driven by an incoherent field together with a constant electric field. Here, however, the coherence is induced by the constant field, but preserved in the presence of the incoherent field. Incoherent broadband fields may also significantly modify the system properties even if they are weak as compared with the applied coherent fields. This was shown in the study by Li, Peng, and Huang (2000a), where the steady-state population and the absorption spectrum of a three-level system in V -configuration were investigated. Both the population inversion and the absorption properties depend on the field intensities and on the central frequency of the stochastic broadband field. Also the question of thermodynamic equilibrium was analyzed (Agarwal & Menon, 2001; Macovei, Evers, & Keitel, 2005b). Different sources of interference are studied, and it was found that a steady state not corresponding to the thermodynamic equilibrium can be reached if spontaneous and stimulated processes are asymmetric, a realization of which is incoherent broadband pumping. It was then recognized that such incoherently induced interferences can also modify the spontaneous emission spectrum and rate of a given system (Bullock, Evers, & Keitel, 2003; Kapale, Scully, Zhu, & Zubairy, 2003). This will be discussed in more detail below. In Plenio and Huelga (2002), it was shown how entanglement can be created in an atomic system coupled to two cavities and driven exclusively by incoherent fields. Finally, also collections of atoms can be controlled to some extent via incoherent pump fields (Macovei & Evers, 2004).

The modification of spontaneous emission with incoherent pump processes involves incoherently induced interference (Agarwal & Menon, 2001; Bullock et al., 2003; Kapale et al., 2003). To explain the role

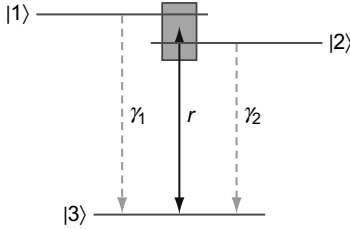


FIGURE 13 Atomic three-level system in V -configuration pumped incoherently with the rate r . γ_1 and γ_2 are the corresponding spontaneous decay rates. The box indicates the width of the broadband incoherent driving.

of interference in incoherent pump processes, we consider an atomic three-level system in V -configuration with two upper states $|1\rangle$ and $|2\rangle$, and one lower state $|3\rangle$. The corresponding transition dipole moments are \vec{d}_{13} and \vec{d}_{23} . We apply an incoherent pumping field with amplitude $\epsilon(t)$, center frequency ω_l , and polarization vector \hat{e} (see Figure 13). The Hamiltonian is (Fleischhauer, Keitel, Scully, and Su, 1992)

$$H_{\text{pump}} = \epsilon(t) \hat{e} \left(\vec{d}_{23} S_{23} + \vec{d}_{13} S_{13} \right) e^{-i\omega_l t} + \text{H.c.} \quad (3.45)$$

As the field is considered as incoherent, we assume the field amplitude $\epsilon(t)$ to be of zero mean value and δ -correlated,

$$\langle \epsilon(t) \rangle = 0, \quad \langle \epsilon(t)^* \rangle = 0, \quad \langle \epsilon(t) \epsilon^*(t') \rangle = \zeta \delta(t - t'), \quad (3.46)$$

where ζ describes the strength of the incoherent pumping process. As the free energy part H_0 of the total Hamiltonian is much larger than the incoherent pump part ($|H_{\text{pump}}| \ll |H_0|$), we can invoke standard perturbative techniques to eliminate the variables $\epsilon(t)$ (Puri, 2001). Thus, the contribution to the master equation that characterizes the incoherent pump process can be represented as (Puri, 2001)

$$\dot{\rho}_{\text{pump}}(t) = -\frac{1}{\hbar^2} \text{Tr} \int_0^t dt' [H_{\text{pump}}(t), [H_{\text{pump}}(t'), \rho_{\text{pump}}(t')]], \quad (3.47)$$

where the trace Tr is taken over the variables describing the subsystem of the incoherent pump field. By introducing Equation (3.45) in Equation (3.47), it is easy to obtain the pump field contribution to the master equation of the system as

$$\dot{\rho}_{\text{pump}}(t) = - \sum_{\alpha \in \{1,2\}} r_\alpha [S_{\alpha 3}, [S_{3\alpha}, \rho]] - \sum_{\alpha \neq \beta \in \{1,2\}} r_{\alpha\beta} [S_{\alpha 3}, [S_{3\beta}, \rho]] + \text{H.c..} \quad (3.48)$$

Here, $r_\alpha = \xi |\vec{d}_{\alpha 3} \cdot \hat{e}|^2 / \hbar^2$ ($\alpha = 1, 2$) are the incoherent pump rates, and $r_{\alpha\beta} = p e^{i\omega_{\alpha\beta} t} \sqrt{r_\alpha r_\beta}$ is a contribution arising from the interference amongst the two pump transitions. The parameter p is introduced manually in order to study the influence of the interference terms. As before, $S_{\alpha\beta} = |\alpha\rangle\langle\beta|$ are atomic population and transition operators. Note that the corresponding master equation describing an incoherently driven Λ -type system can be obtained from Equation (3.48) via interchanging the indices of the atomic operators, i.e., $3 \leftrightarrow \{\alpha, \beta\}$ (Macovei & Evers, 2004).

Comparing Equation (3.48) with the master equation describing spontaneous emission (SE) and vacuum-mediated cross couplings Equation (2.43), it is natural to interpret the interference induced by incoherent pumping fields along the same lines as interference among different spontaneous-emission channels. The effect occurs if a photon emitted on one transition into the pumping field mode can be reabsorbed by a second transition. A crucial difference to the SE case is that interference induced by an incoherent field can couple two transitions with perpendicular dipole moments, which is not possible for SE in a plain vacuum field. For example, the polarization direction of the incoherent field could be set in the plane spanned by the two orthogonal dipole moments, such that the projection on both dipole moments is nonzero. Thus, the stringent requirement of nonorthogonal dipole moments is not required for interference induced by incoherent driving fields (but c.f. Section 3.2.7, where it is shown that an anisotropic vacuum field can induce spontaneous emission interference between transitions with orthogonal dipole moments). Also, different transition frequencies do not prohibit this type of coupling, as long as the spectral width of the driving field is larger than the frequency separation.

It should be noted that in the literature, two different types of incoherent pump rates are considered. The first one is the direct incoherent pumping discussed above, which works in both directions. A second type of pumping is indirect pumping via an auxiliary state, which typically involves spontaneous emission from the auxiliary state to the final state. In contrast to the direct pumping, this process is unidirectional.

In the study by Kapale et al. (2003), it was demonstrated how the incoherently induced interference can modify spontaneous decay, i.e., how one incoherent process can influence another incoherent process. While the scheme in Kapale et al. (2003) still uses a coherent field to repump population from the lower to the two intermediate states, similar effects can also be observed in systems driven entirely by incoherent fields (Bullock et al., 2003). There, the resonance fluorescence of the level scheme shown in Figure 14(a) was studied. Both the spontaneous emission interference between the two lower transitions and the interference of the incoherent driving fields on the two upper transitions were considered. Here,

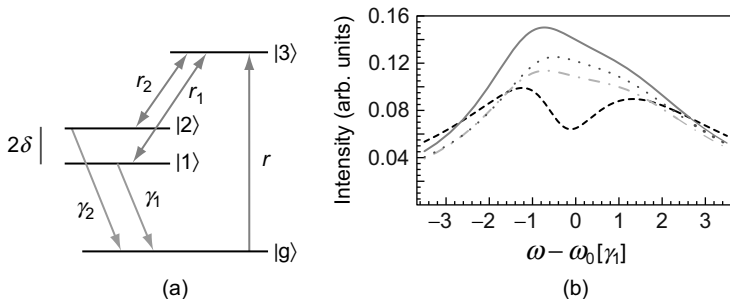


FIGURE 14 (a) Interference induced by incoherent driving fields in a system free of any coherent external fields. r_1 and r_2 are the interfering direct incoherent broadband pumping rates, whereas r is a one-way indirect repumping via an auxiliary level to avoid a trivial steady state. The studied spontaneous decay is from $|1\rangle, |2\rangle$ with rates γ_1, γ_2 . (b) Spontaneous emission spectrum. The average transition frequency of the two lower transitions is ω_0 . Parameters are $\gamma_1 = \gamma_2 =: \gamma, \delta = \gamma, r = \gamma$, and $r_1 = \gamma, r_2 = 3\gamma$. The solid line is without taking into account any interference effects. The dotted line includes interference between the incoherent pump rates, the dot-dashed line shows interference between the spontaneous emission channels, and the dashed line shows the case with both interferences. Reprinted from Bullock et al. (2003), Copyright (2003), with permission from Elsevier.

r_1 and r_2 are direct incoherent pump rates, whereas r is a one-way indirect pumping rate. Typical results for the resonance fluorescence spectrum are shown in Figure 14(b). It can be seen that the interference contributions can considerably modify the spontaneous emission spectrum from the case without any interference contribution shown as the solid line. While the most pronounced changes in the spectra can be achieved for the case with spontaneous emission interference, already the incoherently induced interference alone modifies the result notably. Furthermore, the qualitative shape of the spectrum can be modified via the interference effects, see Figure 14(b).

3.2.6. Interference Induced via Coherent Fields

From the previous sections, it became apparent that quantum coherence and interference are the key to many approaches to modify vacuum-induced processes such as spontaneous emission. Thus, it is not surprising that the modification of vacuum-induced processes by coherent driving fields has been studied in many settings. Often, the applied fields induce additional interference. For example, it was shown that interference can be generated in two-level atoms driven by polychromatic fields (Ficek & Freedhoff, 1996, 2000; Greentree, Wei, & Manson, 1999). Also, the multiphoton pathway interference discussed in Section 3.1.2.2 is a way of inducing quantum interference by means of a coherent driving field. In

two-particle systems, quantum interference is determined by the spatial dependence of the laser phase on the positions of the atoms (Das, Agarwal, & Scully, 2008). Applying a dc-field to the upper levels of a three-level V-type scheme with orthogonal dipole moments can to a certain extent simulate a corresponding setup with nonorthogonal dipole moments (Dalton & Gagen, 1985; Ficek & Swain, 2004; Hakuta, Marmet, & Stoicheff, 1992). The idea of inducing quantum interference in order to control the dynamics is also at the heart of coherent quantum control and adiabatic passage (Král et al., 2007), as of many other setups in quantum optics not directly related to vacuum-induced processes (Ficek & Swain, 2005) such as electromagnetically induced transparency (Fleischhauer et al., 2005).

A particular class of interference induced by coherent driving fields occurs in so-called closed-loop systems (Agarwal, Dey, & Menon, 2001a; Buckle, Barnett, Knight, Lauder, & Pegg, 1986; Kajari-Schröder, Morigi, Franke-Arnold, & Oppo, 2007; Kosachiov, Matisov, & Rozhdestvensky, 1992; Mahmoudi & Evers, 2006; Malinovsky & Sola, 2004; Morigi, Franke-Arnold, and Oppo, 2002; Paspalakis, Keitel, & Knight, 1998; Shpaisman, Wilson-Gordon, & Friedmann, 2005). These are setups in which laser fields are applied in such a way that the atom can undergo a nontrivial loop sequence of transitions from an initial state via different intermediate states back to the initial state. Alternatively, such setups allow to evolve from an initial to a final state via different pathways, which is a direct signature for quantum interference. For example, in Figure 15, the dynamics depends on the relative phase $\Delta\phi = \arg(\Omega_1) + \arg(\Omega_2) - \arg(\Omega_3)$ of two different pathways, the so-called closed-loop phase, where $\arg(z)$ is the argument or phase of the complex number z . The precise nature of the pathway interference can be elucidated via a quantized treatment of the applied laser fields (Evers, 2005). The phase-dependence in closed-loop systems has been observed experimentally in a number of setups (Kang, Hernandez, Zhang, & Zhu, 2006; Korsunsky, Leinfellner, Huss, Baluschev, & Windholz, 1999; Li et al., 2009b; Shahriar & Hemmer, 1990). Among many other applications, such pathway interference has also been suggested as a means to modify spontaneous emission. Part of these setups still rely on the presence of spontaneously generated coherences and thus of near-degenerate nonorthogonal transition dipole moments (Martinez et al., 1997; Menon & Agarwal, 1998; Paspalakis & Knight, 1998). But interestingly, phase control can already be achieved in more realistic level schemes with orthogonal transition dipole moments (Ghafoor, Zhu, & Zubairy, 2000; Morigi et al., 2002).

In the following, we outline the main idea of the phase control of spontaneous emission in a setup with orthogonal dipole moments analyzed by Ghafoor et al. (2000), see Figure 15. The applied laser fields form a closed interaction loop $|1\rangle \rightarrow |2\rangle \rightarrow |3\rangle \rightarrow |1\rangle$. The relative phase $\Delta\phi$ of the three

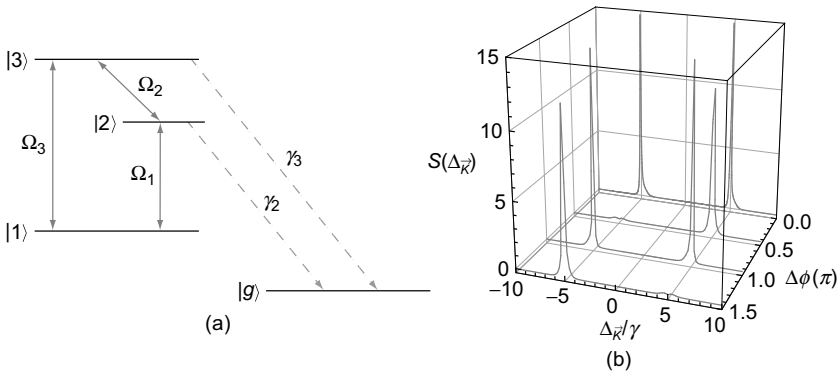


FIGURE 15 Phase control of spontaneous emission. (a) Level scheme. The laser fields applied to transitions between states $|1\rangle$ – $|3\rangle$ with Rabi frequencies Ω_i ($i \in \{1, 2, 3\}$) form a closed interaction loop. The two upper states spontaneously decay to state $|g\rangle$ with rates γ_i ($i \in \{2, 3\}$). (b) Results for the phase-dependent total fluorescence spectrum $S(\Delta)$. Parameters are $\gamma_2 = \gamma_3 = \gamma$, $\Omega_1 = \Omega_3 = 0.2\gamma$, and $\Omega_2 = 0.5 e^{i\phi} \gamma$. The closed loop phase $\Delta\phi$ thus coincides with ϕ . The figure shows the spectra corresponding to four different values of $\Delta\phi$. In all cases, the atom initially is in the state $|2\rangle$.

applied laser fields determines the population distribution among these three states. Eventually, the population spontaneously decays to $|g\rangle$. In general, six spectral lines can be expected in the obtained resonance fluorescence spectrum, as both $|2\rangle$ and $|3\rangle$ split up into three dressed states upon application of the driving laser fields. Defining the state vector as

$$|\Psi(t)\rangle = \sum_{i=1}^3 c_i(t)|i, \{0\}\rangle + \sum_{\vec{k}} c_{\vec{k}}(t)|g, \vec{k}\rangle, \quad (3.49)$$

where $|\{0\}\rangle$ denotes a state without photons and $|\vec{k}\rangle$ as state with one photon in mode \vec{k} , the equations of motion for the state amplitudes can be written as,

$$\frac{d}{dt}c_1(t) = -i\Omega_1^*c_2(t) - i\Omega_3^*c_3(t), \quad (3.50a)$$

$$\frac{d}{dt}c_2(t) = -\frac{\gamma_2}{2}c_2(t) - i\Omega_1c_1(t) - i\Omega_2^*c_3(t), \quad (3.50b)$$

$$\frac{d}{dt}c_3(t) = -\frac{\gamma_3}{2}c_3(t) - i\Omega_3c_1(t) - i\Omega_2c_2(t), \quad (3.50c)$$

$$\frac{d}{dt}c_{\vec{k}}(t) = -ic_2(t)g_{\vec{k}}^{(2)}e^{i(v_{\vec{k}}-\omega_{2g})t} - ic_3(t)g_{\vec{k}}^{(3)}e^{i(v_{\vec{k}}-\omega_{3g})t}. \quad (3.50d)$$

Here, $\nu_{\vec{k}}$ is the frequency corresponding to mode \vec{k} , ω_{ij} are transition frequencies between states $|i\rangle$ and $|j\rangle$, and $g_{\vec{k}}^{(i)}$ is the atom-vacuum coupling constant corresponding to mode i . In deriving Equations (3.50), the Wigner–Weisskopf approximation has been used. In steady state, using the Laplace transformation, one obtains (Ghafoor et al., 2000)

$$c_{\vec{k}}(t \rightarrow \infty) = -i \int_0^{\infty} g_{\vec{k}}^{(2)} c_2(t) e^{i(\Delta_{\vec{k}} - \omega_{32}/2)t} + g_{\vec{k}}^{(3)} c_3(t) e^{i(\Delta_{\vec{k}} + \omega_{32}/2)t} dt, \quad (3.51)$$

where $\Delta_{\vec{k}} = \nu_{\vec{k}} - \omega_{2g} + \omega_{32}/2$. The resonance fluorescence spectrum can then be calculated via

$$S(\Delta_{\vec{k}}) \sim |c_{\vec{k}}(t \rightarrow \infty)|^2. \quad (3.52)$$

An example is shown in Figure 15(b). For the particular choice of parameters, only one or two narrow peaks appear in the spectrum, depending on the closed-loop phase $\Delta\phi$. In particular, for $\Delta\phi = \pi/2$, only a single narrow peak appears at around $\Delta_{\vec{k}} = 5\gamma$, while for $\Delta\phi = 3\pi/2$, the spectrum contains a single peak at $\Delta_{\vec{k}} = -5\gamma$. This shows that phase control offers a convenient tool to significantly alter the spontaneous emission properties of closed-loop systems.

3.2.7. Interference Induced via Breaking the Symmetry

In the previous sections, we have seen that the generation of coherences via the vacuum is restricted by stringent conditions. One of these conditions is the nonorthogonality of transition dipole moments of the two transitions, which are coupled via the vacuum to give rise to the SGC. In the following, we show that this condition in some sense relates to the symmetry or isotropy of the surrounding vacuum field. If conditions are such that asymmetries or anisotropies occur, then SGC may be induced via transitions with *orthogonal* dipole moments.

The consequences of an anisotropic vacuum field were considered by Agarwal (2000) and Zhou, Gan, and Li (2004). The vacuum field experienced by an atom can be rendered anisotropic, e.g., by placing it between two parallel conducting plates. We consider a V –type three-level atom, whose two upper levels are two Zeeman sublevels $|1\rangle = |j=1, m=1\rangle$ with energy $\hbar\omega_1$, $|2\rangle = |j=1, m=-1\rangle$ with energy $\hbar\omega_2$, and one ground level $|3\rangle = |j=0, m=0\rangle$ with energy equal to zero. The quantization axis is chosen along the y -axis, and the conducting plates are aligned perpendicular to the z -axis at $z=0$ and $z=-d$, respectively. The atom is located at $z=-b$, where $0 \leq b \leq d$. The two transition dipole moments are in the

$x - z$ plane. The atomic dipole moment operator is represented by

$$\mathbf{d} = d_0(S_{13}\hat{\epsilon}_- + S_{23}\hat{\epsilon}_+) + \text{H.c.}, \quad (3.53)$$

where $\hat{\epsilon}_{\pm} = (1/\sqrt{2})(\hat{\epsilon}_z \pm i\hat{\epsilon}_x)$, and d_0 is chosen to be real. The equations of motion follow from Equation (2.43) as (Agarwal, 2000)

$$\frac{d}{dt}\langle S_{nn} \rangle = -\gamma_n \langle S_{nn} \rangle - \kappa_m \{ \langle S_{nm} \rangle + \langle S_{mn} \rangle \}, \quad (3.54a)$$

$$\frac{d}{dt}\langle S_{n3} \rangle = -(\gamma_n/2 - i\omega_n)\langle S_{13} \rangle - \kappa_m \langle S_{m3} \rangle, \quad (3.54b)$$

$$\frac{d}{dt}\langle S_{12} \rangle = -[\gamma_1/2 + \gamma_2/2 + i(\omega_2 - \omega_1)]\langle S_{12} \rangle - \kappa_1 \langle S_{11} \rangle - \kappa_2 \langle S_{22} \rangle. \quad (3.54c)$$

In Equations (3.54), $n, m \in \{1, 2\}$, and m must be chosen such that $m \neq n$. The spontaneous emission rate is γ_n , and κ_n characterizes the quantum interference induced by spontaneous emission, respectively. Both are related to the antinormally ordered correlation functions of the vacuum field $\mathbf{C}(\omega) = \int_0^\infty \langle \mathbf{E}^{(+)}(\tau) \mathbf{E}^{(-)}(0) \rangle e^{i\omega\tau} dt$ as follows:

$$\begin{aligned} \gamma_1 &= \frac{d_0^2}{\hbar^2} \hat{\epsilon}_+^* \cdot \mathbf{C}(\omega_1) \cdot \hat{\epsilon}_+, \quad \gamma_2 = \frac{d_0^2}{\hbar^2} \hat{\epsilon}_-^* \cdot \mathbf{C}(\omega_2) \cdot \hat{\epsilon}_-, \\ \kappa_1 &= \frac{d_0^2}{\hbar^2} \hat{\epsilon}_-^* \cdot \mathbf{C}(\omega_1) \cdot \hat{\epsilon}_+, \quad \kappa_2 = \frac{d_0^2}{\hbar^2} \hat{\epsilon}_+^* \cdot \mathbf{C}(\omega_2) \cdot \hat{\epsilon}_-. \end{aligned} \quad (3.55)$$

$\mathbf{E}^{(\pm)}$ is the positive/negative frequency parts of the anisotropic vacuum. From the expressions for $\kappa_{1,2}$ in Equation (3.55), it is clear that they are responsible for quantum interference between the two decay channels $|1\rangle \rightarrow |3\rangle$ and $|2\rangle \rightarrow |3\rangle$. In isotropic free space, $C_{zz}^{(+)}(\omega) = C_{xx}^{(+)}(\omega)$, $C_{zx}^{(+)}(\omega) = C_{xz}^{(+)}(\omega) = 0$. Hence, $\kappa_1 = \kappa_2 = 0$, and no interferences occur. In contrast, anisotropy leads to nonvanishing κ_1 and κ_2 . In particular, for the considered geometry, one finds (Agarwal, 2000)

$$\gamma_i = \gamma_i^{(0)} [\Gamma_{\perp}(\omega_i) + \Gamma_{\parallel}(\omega_i)]/2, \quad (3.56a)$$

$$\kappa_i = \gamma_i^{(0)} [\Gamma_{\perp}(\omega_i) - \Gamma_{\parallel}(\omega_i)]/2, \quad (3.56b)$$

where $\gamma_{1,2}^{(0)} = 2\omega_{1,2}^3 d_0^2 / (3c^3 \hbar)$, and

$$\Gamma_{\perp}(\omega) = \frac{3\pi}{2kd} + \frac{3\pi}{kd} \sum_{n=1}^N \left(1 - \frac{\pi^2 n^2}{k^2 d^2} \right) \cos^2 \left(\frac{b\pi n}{d} \right), \quad (3.57a)$$

$$\Gamma_{\parallel}(\omega) = \frac{3\pi}{2kd} \sum_{n=1}^N \left(1 + \frac{\pi^2 n^2}{k^2 d^2} \right) \sin^2 \left(\frac{b\pi n}{d} \right), \quad (3.57b)$$

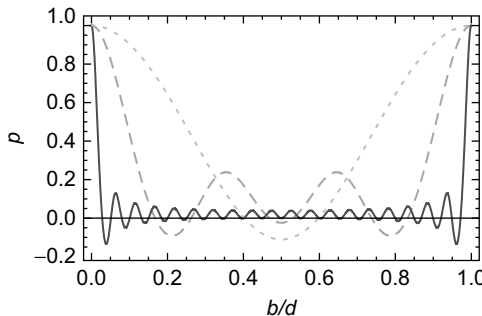


FIGURE 16 The quantum interference parameter p as function of atomic position b/d . Here, $d = 10\lambda$ (solid line), $d = 2\lambda$ (dashed line), and $d = \lambda$ (dotted curve).

where $k = \omega/c$, and N is the largest integer smaller than kd/π . Further, for simplicity, we assume that the two upper levels of the atom are nearly degenerate ($\omega_1 \approx \omega_2 = \omega$), such that $\gamma_1 \approx \gamma_2 = \gamma$, $\kappa_1 \approx \kappa_2 = \kappa$. We also define the relative strength of quantum interference as $p = \kappa/\gamma$. In free space, if the two atomic dipole moments are perpendicular to each other, $p = 0$. Maximum interference is obtained if the two atomic dipole moments are parallel [antiparallel], with $p = 1$ [$p = -1$]. In the anisotropic case with orthogonal dipole moments, below the cutoff frequency $kd/\pi < 1$, we find that $\Gamma_{||} \rightarrow 0$, $\Gamma_{\perp} \rightarrow 3\pi/(2kd)$, and, hence, $p \rightarrow 1$. Thus, near-maximum quantum interference can be achieved even for orthogonal transition dipole moments. Figure 16 shows the quantum interference parameter p as function of the atomic position b . By changing the atomic position or the interplate distance suitably, one can engineer different magnitudes and both signs for p , thus simulating various atomic dipole orientations. In particular, near the conducting plates, the quantum interferences are maximal.

A similar simulation of SGC can also be achieved by placing the atom close to a metallic nanostructure (Yannopapas et al., 2009), in a left-handed material (Li et al., 2009a; Yang, Xu, Chen, & Zhu, 2008), or in a lossy single-mode cavity, which supports only one out of two possible polarizations for the cavity field (Zhou & Swain, 2000). To illustrate the latter idea, we again consider a three-level atom in V -type configuration with orthogonal transition dipole moments. In deriving the equations of motion, one finds vacuum-induced couplings between the two transition dipole moments characterized by the coupling constant $\gamma_{12} \propto \sum_s g_1 g_2^*$, where g_1 and g_2 are coupling constants between the two atomic transitions and the cavity field, and s is a polarization index. This is in complete analogy to the polarization sum in the expression for the Cartesian components of the tensor F in Equation (2.54), which enters the expressions for the coupling constants in the master equation Equation (2.45).

If the cavity-field polarization is not preselected, as in free space, summing over both polarizations yields $\sum_s g_1 g_2^* \propto \mathbf{d}_{13} \cdot \mathbf{d}_{23}^*$, which is proportional to the scalar product of the two involved transition dipole moments. As in Equation (2.45), only nonorthogonal transition dipole moments lead to vacuum-induced interferences, and the maximum interference effect occurs with the two dipoles parallel or antiparallel. In contrast, if the cavity only supports one polarization, say $e_s = e_x$ along the x-quantization axis, then $g_1 g_2^* \propto (\mathbf{d}_{13})_x (\mathbf{d}_{23})_x$, which can be nonvanishing, regardless of the relative orientation of the atomic dipole matrix elements (Zhou & Swain, 2000). In this way, maximal quantum interference can be achieved even for the case of orthogonal transition dipole moments, if the atom is coupled to a single-mode, frequency-tunable cavity field with a preselected polarization in the bad cavity limit.

4. COLLECTIVE PROCESSES

In collections of nearby atoms, the various particles can interact via the common vacuum radiation field in a process where a photon emitted by one of the atoms is reabsorbed by another atom. If the distance between two particles does not significantly exceed the involved transition wavelength, this exchange of photons gives rise to a collective quantum dynamics of the system, which can significantly deviate from a corresponding single-particle dynamics.

The pioneering work by Dicke (1954) focuses on large ensembles of atoms. On the other hand, the archetype system for the study of collective effects is a pair of atoms, and our analysis places emphasis on this kind of systems. The aim of this section is to provide a thorough analysis of the physics of the dipole–dipole interaction, i.e., we want to provide a detailed description of the nature of this interaction and its effects on the quantum dynamics of the collective system.

From a conceptual point of view, the simplest collective system consists of a pair of two-level atoms. Although this system has been studied in great detail in the literature, we present a brief analysis of it in Section 4.1. Here, we highlight the essential features of the dipole–dipole interaction and demonstrate how it affects the dynamics of the two-atom system. The tremendous progress in experimental techniques allowed to carry out experiments where the distance between two atoms can be controlled. This enabled the experimental verification of the simple model introduced in Section 4.1, and these experiments are described in Section 4.2. We then extend our treatment to dipole–dipole interacting multilevel atoms in Section 4.3. Here, we investigate in detail the dependence of the dipole–dipole interaction on the geometrical setup of the two atoms. The effect of the dipole–dipole interaction on various physical observables has been

studied in great detail in the literature. An overview of these activities and outline of potential applications of the dipole–dipole interaction is presented in Section 4.4. Finally, we briefly review related phenomena in multiparticle quantum dynamics in Section 4.5.

4.1. Pair of Dipole–Dipole Interacting Two-Level Atoms

In this section, we study the dipole–dipole interaction between a pair of identical two-level atoms. In general, we consider arbitrary geometrical alignments of the atoms as shown in Figure 17(a). The relative position of the atoms with respect to each other is described by the separation vector $\mathbf{R} = \mathbf{r}_2 - \mathbf{r}_1$. Figure 17(b) shows the internal level structure of each atom. The energy difference between the ground state $|0\rangle$ and the excited state $|1\rangle$ is $\hbar\omega_0$, and the dipole moment of the $|1\rangle \leftrightarrow |0\rangle$ transition is denoted

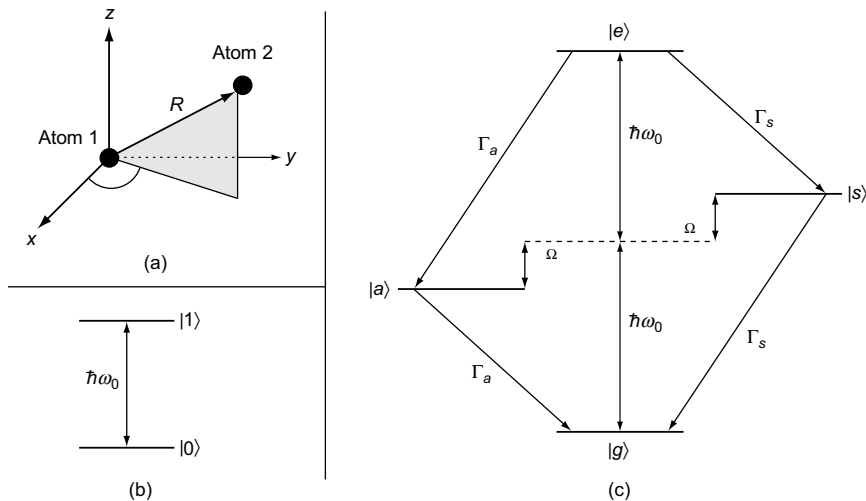


FIGURE 17 A pair of dipole–dipole interacting two-level atoms. (a) This shows the general setup of the two atoms at positions \mathbf{r}_1 and \mathbf{r}_2 , and the relative position of atom 2 with respect to atom 1 is given by the separation vector $\mathbf{R} = \mathbf{r}_2 - \mathbf{r}_1$. (b) This is the level scheme of each of the atoms. The transition frequency between the excited state $|1\rangle$ and the ground state $|0\rangle$ is ω_0 . The effective level scheme of the dipole–dipole interacting system is displayed in (c). The coherent part of the dipole–dipole interaction is represented by the parameter Ω and leads to an energy shift of the symmetric and the antisymmetric states $|s\rangle$ and $|a\rangle$, respectively. Note that the order of $|s\rangle$ and $|a\rangle$ in (c) corresponds to small interparticle separations such that $\Omega < 0$, see Figure 18(a). The incoherent part of the dipole–dipole interaction influences the decay rates of the excited states. The excited state $|e\rangle$ decays via $|a\rangle$ to the ground state $|g\rangle$ with decay rate Γ_a and via $|s\rangle$ to $|g\rangle$ with Γ_s .

by $d = \langle e | \hat{d} | g \rangle$. In order to determine the impact of the dipole–dipole interaction on the system of coupled two-level atoms, we specialize the general master Equation (2.43) to $M = 2$ atoms. Since we consider two-level atoms, the number of dipole transitions in each atom is $D = 1$, which allows to simplify the notation considerably. In particular, we introduce the abbreviations $S_+^{(\mu)} = S_{1+}^{(\mu)}$ and $S_-^{(\mu)} = S_{1-}^{(\mu)}$ for the transition operators, and the spontaneous decay of individual atoms is characterized by a single decay rate that we denote by $\gamma = \gamma_{11}$, where γ_{11} is given in Equation (2.45) with $d_1 = d$. Furthermore, the indices that distinguish the parameters $\Omega_{ij}^{\mu\nu}$ and $\Gamma_{ij}^{\mu\nu}$ can be omitted since for both of them there is only a single representative,

$$\Omega = \frac{1}{\hbar} \left[d^T \overset{\leftrightarrow}{\chi}_{\text{re}}(R) d^* \right] \quad \text{and} \quad \Gamma = \frac{1}{\hbar} \left[d^T \overset{\leftrightarrow}{\chi}_{\text{im}}(R) d^* \right], \quad (4.1)$$

where $\overset{\leftrightarrow}{\chi}_{\text{re}}$ and $\overset{\leftrightarrow}{\chi}_{\text{im}}$ denote the real and imaginary part of the tensor $\overset{\leftrightarrow}{\chi}$ defined in Equation (2.54). With these definitions, the master equation that describes the dynamics of the two atoms coupled to the radiation field in its vacuum state is given by

$$\begin{aligned} \partial_t \varrho &= -\frac{i}{\hbar} [H_A, \varrho] + i\Omega \sum_{\substack{\mu, v=1 \\ \mu \neq v}}^2 \left[S_+^{(\mu)} S_-^{(v)}, \varrho \right] \\ &\quad - \sum_{\mu=1}^2 \gamma \left(S_+^{(\mu)} S_-^{(\mu)} \varrho + \varrho S_+^{(\mu)} S_-^{(\mu)} - 2S_-^{(\mu)} \varrho S_+^{(\mu)} \right) \\ &\quad - \sum_{\substack{\mu, v=1 \\ \mu \neq v}}^2 \Gamma \left(S_+^{(\mu)} S_-^{(v)} \varrho + \varrho S_+^{(\mu)} S_-^{(v)} - 2S_-^{(v)} \varrho S_+^{(\mu)} \right). \end{aligned} \quad (4.2)$$

The first line of Equation (4.2) describes the unitary part of the time evolution and is governed by the atomic Hamiltonian H_A and the coherent part of the dipole–dipole interaction. If we choose the energy of the lower atomic state $|0\rangle$ to be zero, the general form of the atomic Hamiltonian in Equation (2.4) reduces to $H_A = \hbar\omega_0(|1_1\rangle\langle 1_1| + |1_2\rangle\langle 1_2|)$ for the considered pair of two-level atoms. It follows that the coherent part of the time evolution can be described by the total Hamiltonian

$$H_T = \hbar\omega_0(|1_1\rangle\langle 1_1| + |1_2\rangle\langle 1_2|) - \hbar\Omega \left(S_+^{(2)} S_-^{(1)} + S_+^{(1)} S_-^{(2)} \right). \quad (4.3)$$

The generic basis states that span the state space of the system are given by the eigenstates $\{|1, 1\rangle, |1, 0\rangle, |0, 1\rangle, |0, 0\rangle\}$ of the atomic Hamiltonian H_A ,

where $|k, l\rangle = |k_1\rangle \otimes |l_2\rangle$ and

$$\begin{aligned} H_A|1, 1\rangle &= 2\hbar\omega_0|1, 1\rangle, & H_A|1, 0\rangle &= \hbar\omega_0|1, 0\rangle, \\ H_A|0, 1\rangle &= \hbar\omega_0|0, 1\rangle, & H_A|0, 0\rangle &= 0. \end{aligned} \quad (4.4)$$

The collective ground and excited states $|0, 0\rangle$ and $|1, 1\rangle$ are not affected by the dipole–dipole interaction such that these states are simultaneous eigenstates of H_T and H_A . On the contrary, the states $|1, 0\rangle$ and $|0, 1\rangle$ are not eigenstates of H_T due to the contribution of the dipole–dipole interaction in Equation (4.3). Since it is convenient to analyze the system dynamics in the eigenbasis of H_T , we diagonalize this Hamiltonian in the subspace spanned by $|1, 0\rangle$ and $|0, 1\rangle$ and obtain the new basis set

$$\begin{aligned} |e\rangle &= |1, 1\rangle, & |g\rangle &= |0, 0\rangle, \\ |s\rangle &= \frac{1}{\sqrt{2}}(|1, 0\rangle + |0, 1\rangle), \\ |a\rangle &= \frac{1}{\sqrt{2}}(|1, 0\rangle - |0, 1\rangle). \end{aligned} \quad (4.5)$$

While the collective state $|s\rangle$ is symmetric with respect to an exchange of the atoms, the state $|a\rangle$ is antisymmetric. We find that the energies of $|s\rangle$ and $|a\rangle$ with respect to H_T are given by $\hbar(\omega_0 - \Omega)$ and $\hbar(\omega_0 + \Omega)$, respectively, and thus, the total Hamiltonian in Equation (4.3) can be written as

$$H_T = 2\hbar\omega_0|e\rangle\langle e| + \hbar(\omega_0 - \Omega)|s\rangle\langle s| + \hbar(\omega_0 + \Omega)|a\rangle\langle a|. \quad (4.6)$$

The effective level scheme of the two atoms in the presence of the dipole–dipole interaction is shown in Figure 17(c). It is comprised of the four levels in Equation (4.5), and the corresponding energies follow from Equation (4.6). In particular, note that the coherent part of the dipole–dipole interaction introduces a level shift of the states $|a\rangle$ and $|s\rangle$ with respect to each other that is given by $2|\Omega|$, where Ω is defined in Equation (4.1). The dependence of Ω on the interatomic distance is shown in Figure 18(a). It follows that the vacuum-induced level splitting between the collective states becomes important if the atomic separation is on the order of the transition wavelength or less.

Next we analyze the incoherent dynamics of the pair of two-level atoms in terms of the new basis states in Equation (4.5). To facilitate the interpretation, we introduce the transition operators $\sigma_{ij} = |i\rangle\langle j|$ with $i, j \in \{e, s, a, g\}$

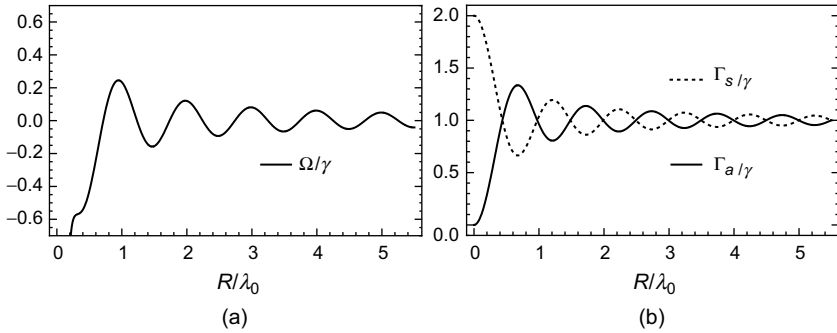


FIGURE 18 (a) Dependence of the parameter Ω that determines the level splitting between the collective states $|s\rangle$ and $|a\rangle$ on the atomic separation R . (b) Dependence of the collective decay rates Γ_s and Γ_a on the atomic separation. In (a) and (b), it is assumed that the dipole moment d of each two-level system is parallel to the z -axis, and that the separation vector R lies in the $x-y$ plane such that $d \perp R$.

and express the operators $S_{\pm}^{(\mu)}$ in terms of the σ_{ij} ,

$$S_{+}^{(1)} = \frac{1}{\sqrt{2}} (\sigma_{es} - \sigma_{ea} + \sigma_{sg} + \sigma_{ag}), \quad (4.7)$$

$$S_{+}^{(2)} = \frac{1}{\sqrt{2}} (\sigma_{es} + \sigma_{ea} + \sigma_{sg} - \sigma_{ag}). \quad (4.8)$$

With these relations and their adjoints, the master equation of the system can be written as

$$\begin{aligned} \partial_t \varrho = & -\frac{i}{\hbar} [H_T, \varrho] \\ & - \Gamma_s [(\sigma_{ee} + \sigma_{ss})\varrho + \varrho(\sigma_{ee} + \sigma_{ss}) - 2(\sigma_{se} + \sigma_{gs})\varrho(\sigma_{es} + \sigma_{sg})] \\ & - \Gamma_a [(\sigma_{ee} + \sigma_{aa})\varrho + \varrho(\sigma_{ee} + \sigma_{aa}) - 2(\sigma_{ga} - \sigma_{ae})\varrho(\sigma_{ag} - \sigma_{ea})], \end{aligned} \quad (4.9)$$

where H_T is defined in Equation (4.6). The coefficients Γ_s and Γ_a are decay rates that depend on the decay rate γ of the individual atoms and the parameter Γ introduced in Equation (4.1),

$$\Gamma_s = \gamma + \Gamma \quad \text{and} \quad \Gamma_a = \gamma - \Gamma. \quad (4.10)$$

The master equation in Equation (4.9) allows for a straightforward interpretation of the decay rates Γ_s and Γ_a . While Γ_s is the decay rate of the cascade from the collective excited state to the collective ground state $|g\rangle$ via the symmetric state $|s\rangle$, the parameter Γ_a describes the decay along the

cascade $|e\rangle \rightarrow |a\rangle \rightarrow |g\rangle$. It is important to note that Γ_s and Γ_a depend on the distance R between the two atoms via the collective parameter Γ in Equation (4.1), and this dependence is shown in Figure 18(b). Of particular interest is the so-called Dicke limit where R approaches zero. In this case, Γ_a tends to zero, which means that the antisymmetric state is completely decoupled from its environment. On the other hand, the excited state $|e\rangle$ and the symmetric state $|s\rangle$ decay twice as fast as compared with the single-atom decay since $\Gamma_s = 2\gamma$ for $R \rightarrow 0$. Although Figure 18(b) refers to a special alignment of the dipole moments with respect to the atomic separation vector R , it can be shown that the behavior of Γ_s and Γ_a in the Dicke limit does not depend on the orientation of R , see also Section 4.3.1.

4.2. Experimental Verification of the Dipole–Dipole Interaction

The analysis in the previous Section 4.1 revealed that the dipole–dipole interaction between a pair of emitters mainly has two effects. First, the coherent part of this exchange interaction results in the formation of collective states that experience a level shift. Second, the spontaneous emission of one atom is modified due to the presence of the other atom such that the decay rates of the various levels become a function of the distance between the emitters. In general, a measurement of the effects induced by the dipole–dipole interaction is challenging since it requires precise control over the interatomic separation. In Section 4.2.1, we describe an experiment that allowed to measure the coherent part of the dipole–dipole interaction, and the measurement of the collective decay rates as function of the interatomic distance is discussed in Section 4.2.2.

4.2.1. Measurement of the Level Shift

Experimental evidence for the dipole–dipole interaction between two molecules embedded in a crystal has been provided by Hettich et al. (2002). This experiment was carried out in a para-terphenyl crystal with a thickness of about 250 nm and contained a low concentration of terrylene molecules. The crystal was cooled down to a temperature of $T = 1.4$ K, such that the zero-phonon transition between the ground and excited singlet states becomes lifetime-limited. Since each molecule experiences a different environment in the crystal, the transition frequency of this effective two-level system varies from molecule to molecule. In the case of low doping concentrations, individual molecules can be excited independently. This was accomplished by a dye laser with a wavelength of $\lambda \approx 578$ nm that was scanned through the individual resonances of the molecules. The position of the molecules could be determined via the application of a strongly inhomogeneous field that gives rise to a

position-dependent Stark shift of the molecular transitions. This technique allowed to locate two terrylene molecules that were spaced by $R = 12\text{ nm}$, which is much less than the mean transition wavelength. At such small distances, both the coherent and the incoherent part of the dipole–dipole interaction contributes significantly to the system dynamics, and hence this system is an ideal candidate for quantitative measurements of the dipole–dipole interaction.

Apart from the zero-phonon line, the singlet excited state of each molecule can decay to vibrational states of the ground state. However, the strong phonon coupling of the vibrational states destroys the coherence of the dipole moment associated with this decay channel, and thus only the zero-phonon transitions in each molecule undergo an efficient coupling via the dipole–dipole interaction. It follows that the two molecules can be modeled by two 2-level systems with unequal transition frequencies, and the extension of our discussion in Section 4.1 to the case of nonidentical atoms is found in the studies by Akram et al. (2000); Ficek and Swain (2005); Ficek and Tanaś (2002); and Varada and Agarwal (1992). The resulting effective level scheme is similar to the one obtained for two identical two-level systems and is shown in Figure 19(a). In contrast to the case of two identical atoms as discussed in Section 4.1, the intermediate states $|I\rangle$ and $|J\rangle$ are not purely symmetric and antisymmetric states, but more complicated superpositions of the states $|0, 1\rangle$ and $|1, 0\rangle$. In addition, the decay constants of the various decay channels take on different values than in the case of identical atoms. The level splitting between the states $|I\rangle$ and $|J\rangle$ is given by (Akram et al. 2000; Ficek & Swain 2005; Ficek & Tanaś 2002; Hettich et al. 2002; Varada & Agarwal 1992)

$$|\omega_J - \omega_I| = 2\sqrt{(\omega_2 - \omega_1)^2/4 + |\Omega|^2}, \quad (4.11)$$

where ω_1 and ω_2 are the resonance frequencies of the independent molecules. The parameter Ω is given by Equation (4.1) with $\eta = k_0 n R$, where $k_0 c = (\omega_2 + \omega_1)/2$, and n is the index of refraction of the medium.

In the experiment by Hettich et al. (2002), the fluorescence intensity emitted by the two molecules was recorded as a function of the laser detuning and the laser intensity. The experimental results are shown in Figure 19(b), where the two outer peaks correspond to the resonances associated with the states $|I\rangle$ and $|J\rangle$. On the contrary, the third peak located exactly in the middle of the other resonances corresponds to a two-photon process in which both molecules are excited simultaneously. Since the two resonances associated with the states $|I\rangle$ and $|J\rangle$ do not overlap, such a two-photon absorption at the mean transition frequency $\omega_0 = (\omega_1 + \omega_2)/2$ could not be explained if the two molecules were

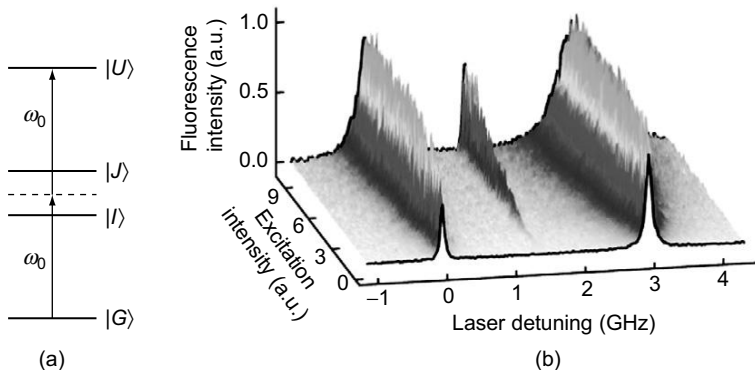


FIGURE 19 (a) Effective level scheme of two dipole–dipole interacting terrylene molecules. Since the two molecules experience a different environment in the crystal, their transition frequencies ω_1 and ω_2 are not identical. ω_0 is the mean transition frequency. (b) Experimental results for the excitation spectra of the two nearby molecules as a function of the laser detuning and the laser intensity. Zero detuning corresponds to resonant excitation of state $|I\rangle$. Reproduced from Hettich et al. (2002). Reprinted with permission from AAAS.

independent. In this case, the probability for simultaneous excitation is just the product of the excitation probability of the individual molecules and thus peaks at the transition frequencies ω_1 and ω_2 , but not at ω_0 . It follows that the additional peak in the middle results from a new excitation channel that is created by the dipole–dipole interaction between the molecules. In the level scheme shown in Figure 19(a), this channel corresponds to a direct excitation of the upper state $|U\rangle$ from the ground state $|G\rangle$ via a two-photon process. For a laser frequency ω_0 , one molecule is blue-detuned with respect to its resonance frequency and the other is red-detuned. Since the dipole–dipole interaction enables an energy exchange between the molecules, the excess energy of one molecule can be transferred to the other such that the total process is resonant. Energy conservation is clearly fulfilled if $\omega_L - \omega_1 = -(\omega_L - \omega_2)$, and hence the resonance occurs at $\omega_L = \omega_0$. The central peak in Figure 19(b) thus provides a direct signal of the dipole–dipole interaction between the molecules. Further experimental evidence for the two-photon excitation mechanism was gained by a measurement of the second-order intensity-correlation function $g^{(2)}(\tau)$ (Ficek & Swain, 2005). This time-resolved analysis showed that the photon statistics of the fluorescence light exhibits photon-bunching if the central resonance in Figure 19(b) is excited, which confirms that this peak originates from the decay of the doubly excited state $|U\rangle$ by the emission of two photons. The experimental value for the dipole–dipole

induced contribution to the frequency difference between states $|I\rangle$ and $|J\rangle$ in Equation (4.11) is $|\Omega| = 2\pi \times 0.95 \text{ GHz}$ (Hettich et al., 2002) and $|\omega_2 - \omega_1|/2 = 2\pi \times 1.16 \text{ GHz}$. In addition, the experiment revealed that the collective excited state $|U\rangle$ experiences a frequency shift of $\Delta_U = -2\pi \times 160 \text{ MHz}$. This effect cannot be explained within the framework of the dipole–dipole interaction and is believed to be caused by a slight change in size of the molecular electronic cloud in the excited state (Altner, Mitsunaga, Zumofen, & Wild, 1996; Brown & Orrit, 1997; Hettich et al., 2002). Finally, the experiment (Hettich et al., 2002) allowed to observe the phenomena of sub- and superradiance via the line widths of the resonances associated with states $|I\rangle$ and $|J\rangle$.

4.2.2. Measurement of Modified Spontaneous Emission

The modification of spontaneous emission induced by the dipole–dipole interaction between nearby emitters has been demonstrated by Barnes, Krstic, Kumar, Mehta, & Wells (2005). In this experiment, the emitters are represented by nanostructures from single molecules of semiconducting polymers. These structures are created by the application of a semiconducting polymer on a glass substrate by inkjet printing techniques. It is found that the transition dipole moments of individual nanostructures exhibit a highly uniform orientation perpendicular to the substrate plane. This alignment of the dipole moments manifests itself in the spatial intensity pattern of the emitted light, since no light is emitted in the direction of the dipole. In the experiment by Barnes et al. (2005), the radiative decay of pairs of oriented nanostructures with near-degenerate transition frequencies was investigated. A schematic setup of two nanostructures with dipole moments d_1 and d_2 is shown in Figure 20(a), where R denotes the relative position of the particles. Several pairs of molecules separated by distances ranging from 200 nm to $2 \mu\text{m}$ were excited with pulses of approximately 100 ps duration, and the decay rate of these systems was determined with time-correlated photon counting techniques. The experimental data for the dependence of the decay rate on the interparticle separation is shown in Figure 20(b). It follows that the decay of the two radiatively coupled nanostructures displays both sub- and superradiant features as compared with the decay of individual emitters.

The experimental results can be understood in a simple model. Since it is justified (Barnes et al., 2005) to treat the nanostructures as identical particles with the same resonance frequency, we can use the model established in Section 4.1. Furthermore, we can assume (Barnes et al., 2005) that the dipole moments d_1 and d_2 are parallel and oriented perpendicular to the substrate plane, and thus we have $d_1 \cdot d_2^*/(|d_1||d_2|) = 1$ and $R \cdot d_1 = R \cdot d_2 = 0$. If the laser that excites the nanostructures propagates

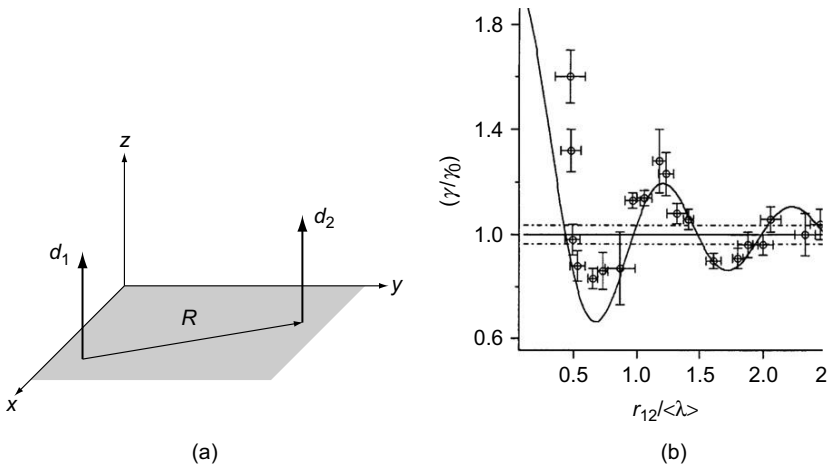


FIGURE 20 Observation of the dipole–dipole interaction in the fluorescence decay of pairs of oriented semiconducting polymer nanostructures. (a) Schematic setup of two nanostructures with dipole moments d_1 and d_2 oriented perpendicular to the substrate plane. (b) Experimental results for the fluorescence decay rate γ in relation to the decay rate γ_0 of isolated particles and as a function of the distance between the emitters relative to the mean transition wavelength $\langle\lambda\rangle$. Reproduced from Barnes et al. (2005). Copyright (2005) by the American Physical Society.

in a direction perpendicular to the separation vector R , both particles experience the same laser phase. In this case (Ficek & Swain, 2005; Ficek & Tanaš, 2002), only the symmetric state $|s\rangle$ is coupled to the ground state $|g\rangle$, and the antisymmetric state $|a\rangle$ remains empty. The decay rate of the coupled nanostructures is thus given by Γ_s in Equation (4.10). For the special alignment of the dipole moments as discussed above, we obtain

$$\Gamma_s = \gamma + \frac{3}{2}\gamma \left[\left(\frac{1}{\eta} - \frac{1}{\eta^3} \right) \sin \eta + \frac{1}{\eta^2} \cos \eta \right]. \quad (4.12)$$

In this equation, $\eta = 2\pi R/\langle\lambda\rangle$, and $\langle\lambda\rangle$ is the most probable transition wavelength (Barnes et al., 2005). The dependence of Γ_s on the distance R between the emitters is represented by the solid line in Figure 20(b) and thus in good agreement with the experimental data.

A similar measurement of the spontaneous emission rate as a function of the distance between two emitters was carried out with a pair of ions (DeVoe & Brewer, 1996). Here two positively charged barium ions were confined in a Paul trap. Although the energy levels of each ion are comprised of Zeeman sublevels, the authors argue (DeVoe & Brewer, 1996) that the essential features of their system can be understood within the simple model of two dipole–dipole interacting two-level

atoms as described in Section 4.1. The excitation scheme was designed in such a way that mostly the symmetric state $|s\rangle$ was excited, and the decay rate Γ_s was recorded as a function of the distance between the ions. In comparison with the previously described experiment with polymer nanostructures (Barnes et al., 2005), the distance between the ions could only be varied within a small range and in a region where the distance between the atoms is much larger than the transition wavelength. Due to the micromotion of the ions in the Paul trap and the presence of additional Zeeman sublevels, the analytical expression in Equation (4.12) for the decay rate Γ_s has to be modified. A theoretical model for the experiment by DeVoe and Brewer (1996) can be found in Brewer (1995). Related modifications of the spontaneous emission rate in many-particle systems are discussed in Section 4.5.

4.3. Dipole–Dipole Interaction beyond the Two-Level Approximation

In this section, we extend the treatment of the dipole–dipole interaction to pairs of multilevel atoms. In particular, the aim is to elucidate the dependence of the dipole–dipole interaction on the relative position of the atoms with respect to each other. Figure 21(a) shows the general setup of the two atoms that are located at positions r_1 and r_2 , respectively. In an environment with translational invariance such as the vacuum in free space,

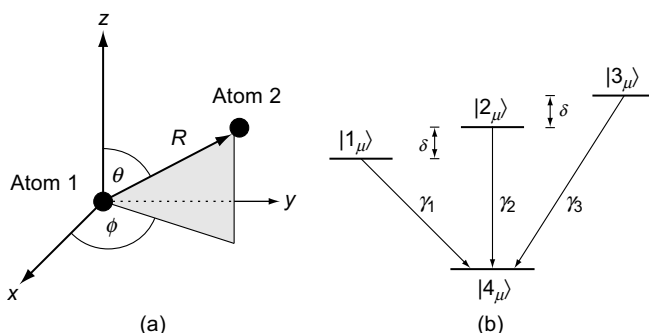


FIGURE 21 (a) The system under consideration is comprised of two atoms that are located at r_1 and r_2 , respectively. The relative position of atom 2 with respect to atom 1 is denoted by the separation vector $R = r_2 - r_1$. (b) Exemplary level structure of atom $\mu \in \{1,2\}$. The ground state of each of the atoms is a S_0 state, and the three excited levels are Zeeman sublevels of a P_1 triplet. The states $|1_\mu\rangle$, $|2_\mu\rangle$, and $|3_\mu\rangle$ correspond to the magnetic quantum numbers $m_j = -1, 0$, and 1 , respectively. The frequency splitting of the upper levels is denoted by $\delta = \omega_3 - \omega_2 = \omega_2 - \omega_1$, where $\hbar\omega_i$ is the energy of state $|i_\mu\rangle$, and $2\gamma_i$ is the decay rate of the excited state $|i_\mu\rangle$. Reproduced from Kiffner et al. (2007b). Copyright (2007) by the American Physical Society.

all physical observables of interest only depend on the relative position $\mathbf{R} = \mathbf{r}_2 - \mathbf{r}_1$ of the atoms with respect to each other. In particular, we investigate the dependence of the dipole–dipole interaction on the length of the atomic separation vector R and on its orientation. In contrast to Section 4.1, we now consider the more general situation of two identical atoms that are each comprised of an arbitrary number of D dipole transitions. In order to illustrate our results, we will frequently refer to the example system in Figure 21(b) that consists of two 4-level atoms.

The starting point of our discussion is the master equation

$$\partial_t \varrho_A(t) = -\frac{i}{\hbar} [H_A, \varrho_A(t)] + \mathcal{L}_\gamma \varrho_A(t) + \mathcal{L}_{\text{col}} \varrho_A(t) \quad (4.13)$$

introduced in Section 2.4 that we now specify to $M = 2$ identical multilevel atoms. In this equation, the Hamiltonian H_A describes the free evolution of the two atoms and is defined in Equation (2.4). The term $\mathcal{L}_\gamma \varrho$ in Equation (4.13) accounts for spontaneous emission of the individual atoms and reads

$$\begin{aligned} \mathcal{L}_\gamma \varrho = & - \sum_{i=1}^D \sum_{j=1}^D \gamma_{ij} \left(S_{i+}^{(1)} S_{j-}^{(1)} \varrho + \varrho S_{i+}^{(1)} S_{j-}^{(1)} - 2 S_{j-}^{(1)} \varrho S_{i+}^{(1)} \right) \\ & - \sum_{i=1}^D \sum_{j=1}^D \gamma_{ij} \left(S_{i+}^{(2)} S_{j-}^{(2)} \varrho + \varrho S_{i+}^{(2)} S_{j-}^{(2)} - 2 S_{j-}^{(2)} \varrho S_{i+}^{(2)} \right). \end{aligned}$$

Since this single-particle term and its physical implications are in the focus of Section 3, we will not discuss it here. Rather, the aim of this section is to investigate in detail the collective contribution

$$\mathcal{L}_{\text{col}} \varrho_A(t) = -\frac{i}{\hbar} [H_\Omega, \varrho_A(t)] + \mathcal{L}_\Gamma \varrho_A(t) \quad (4.14)$$

to the master Equation (4.13) that arises from the vacuum-mediated dipole–dipole coupling between the two atoms. In this equation, the Hamiltonian H_Ω represents the coherent part of the dipole–dipole interaction, and $\mathcal{L}_\Gamma \varrho_A$ describes the modification of spontaneous emission of one atom due to the presence of the other atom. The general definition of these two terms is provided in Equations (2.48) and (2.50) and involves the parameters $\Gamma_{ij}^{\mu\nu}$ and $\Omega_{ij}^{\mu\nu}$, respectively. Since we restrict the analysis to a single pair of atoms, we can omit the superscripts μ and ν in the description of the parameters $\Gamma_{ij}^{\mu\nu}$ and $\Omega_{ij}^{\mu\nu}$ and denote them by $\Gamma_{ij}(R)$ and $\Omega_{ij}(R)$, respectively. Note that this procedure is unambiguous because

the coupling parameters do not depend on the sign of the vector \mathbf{R} , see Equation (2.55). The Hamiltonian H_Ω can thus be written as

$$\begin{aligned} H_\Omega = & -\hbar \sum_{i=1}^D \left\{ \Omega_{ii} S_{i+}^{(2)} S_{i-}^{(1)} + \text{H.c.} \right\} \\ & - \hbar \sum_{\substack{i,j=1 \\ i>j}}^D \left\{ \Omega_{ij} \left(S_{i+}^{(2)} S_{j-}^{(1)} + S_{i+}^{(1)} S_{j-}^{(2)} \right) + \text{H.c.} \right\}, \end{aligned} \quad (4.15)$$

and the collective decay term $\mathcal{L}_\Gamma \varrho$ becomes

$$\begin{aligned} \mathcal{L}_\Gamma \varrho = & - \sum_{i=1}^D \left\{ \Gamma_{ii} \left(S_{i+}^{(2)} S_{i-}^{(1)} \varrho + \varrho S_{i+}^{(2)} S_{i-}^{(1)} - 2S_{i-}^{(1)} \varrho S_{i+}^{(2)} \right) + \text{H.c.} \right\} \\ & - \sum_{\substack{i,j=1 \\ i>j}}^D \left\{ \Gamma_{ij} \left(S_{i+}^{(2)} S_{j-}^{(1)} \varrho + \varrho S_{i+}^{(2)} S_{j-}^{(1)} - 2S_{j-}^{(1)} \varrho S_{i+}^{(2)} \right. \right. \\ & \left. \left. + S_{i+}^{(1)} S_{j-}^{(2)} \varrho + \varrho S_{i+}^{(1)} S_{j-}^{(2)} - 2S_{j-}^{(2)} \varrho S_{i+}^{(1)} \right) + \text{H.c.} \right\}. \end{aligned} \quad (4.16)$$

In Section 4.3.1, we begin with a general study of the dependence of the dipole–dipole interaction on the relative position of the two atoms with respect to each other. More specifically, we discuss its dependence on the distance between the atoms as well as on the orientation of the separation vector \mathbf{R} with respect to the various dipole moments. Our results are illustrated by means of the example system in Figure 21(b). The analysis in Section 4.3.1 singles out a special case of the dipole–dipole interaction that occurs between transitions with orthogonal dipole moments in different atoms. The importance of these transitions and their physical relevance will be discussed in Section 4.3.2. Finally, the dependence of the dipole–dipole interaction on the orientation of the separation vector \mathbf{R} displays interesting features in the special case of transitions between angular momentum multiplets. The influence of rotations of the atomic separation vector in this physically relevant systems will be discussed in Section 4.3.3.

4.3.1. Geometrical Considerations

The purpose of this section is to analyze the geometrical dependence of the parameters Ω_{ij} and Γ_{ij} that constitute H_Ω and $\mathcal{L}_\Gamma \varrho$ in Equations (4.15) and (4.16), respectively. For this, we rewrite the definitions of these parameters in Equations (2.49) and (2.51) such that they readily reveal their

dependence on the involved dipole moments and the atomic separation vector \vec{R} ,

$$\Omega_{ij} = \frac{3}{2} \sqrt{\gamma_i \gamma_j} \left[\vec{d}_i \cdot \vec{d}_j^* G_\Omega(\eta) - (\vec{d}_i \cdot \vec{R})(\vec{d}_j^* \cdot \vec{R}) H_\Omega(\eta) \right], \quad (4.17)$$

$$\Gamma_{ij} = \frac{3}{2} \sqrt{\gamma_i \gamma_j} \left[\vec{d}_i \cdot \vec{d}_j^* G_\Gamma(\eta) - (\vec{d}_i \cdot \vec{R})(\vec{d}_j^* \cdot \vec{R}) H_\Gamma(\eta) \right]. \quad (4.18)$$

In these equations, bold symbols with arrows denote unit vectors, $\vec{d}_i = \vec{d}_i / |\vec{d}_i|$, $\vec{R} = \vec{R} / |\vec{R}|$, $\eta = k_0 R$, and

$$G_\Omega(\eta) = \left[\left(\frac{1}{\eta} - \frac{1}{\eta^3} \right) \cos \eta - \frac{1}{\eta^2} \sin \eta \right], \quad (4.19)$$

$$H_\Omega(\eta) = \left[\left(\frac{1}{\eta} - \frac{3}{\eta^3} \right) \cos \eta - \frac{3}{\eta^2} \sin \eta \right], \quad (4.20)$$

$$G_\Gamma(\eta) = \left[\left(\frac{1}{\eta} - \frac{1}{\eta^3} \right) \sin \eta + \frac{1}{\eta^2} \cos \eta \right], \quad (4.21)$$

$$H_\Gamma(\eta) = \left[\left(\frac{1}{\eta} - \frac{3}{\eta^3} \right) \sin \eta + \frac{3}{\eta^2} \cos \eta \right]. \quad (4.22)$$

A number of important conclusions can be drawn from Equations (4.17) and (4.18). First of all, the dependence of the parameters Ω_{ij} and Γ_{ij} on the distance between the atoms via $\eta = k_0 R$ is entirely described by the functions G_Ω , H_Ω and G_Γ , H_Γ , respectively. Furthermore, the functions G_Ω and G_Γ share the same coefficient $\vec{d}_i \cdot \vec{d}_j^*$ in Equations (4.17) and (4.18) that depends on the alignment of the involved dipole moments with respect to each other. On the other hand, the common coefficient $(\vec{d}_i \cdot \vec{R})(\vec{d}_j^* \cdot \vec{R})$ of the functions H_Ω and H_Γ is determined by the relative orientation of both dipoles with respect to the atomic separation vector. It follows that the parameters Ω_{ij} and Γ_{ij} depend in exactly the same way on the alignment of the dipole moments and on the orientation of the separation vector R , but display a different behavior as a function of the interatomic distance.

Next we discuss the behavior of Ω_{ij} and Γ_{ij} for small and large values of the parameter η . For $\eta \gg 1$, the functions G_Ω , H_Ω , G_Γ , and H_Γ vanish and hence the coupling constants Ω_{ij} and Γ_{ij} are negligible. It follows that the two atoms can be treated as independent particles if the distance between them is much larger than the mean wavelength of the involved transitions. The opposite limit ($\eta \ll 1$) requires a separate treatment of the parameters Ω_{ij} and Γ_{ij} , and we begin with a discussion of the functions G_Ω and H_Ω for small distances as compared with the mean transition wavelength. The

leading terms in an expansion of these functions for $\eta \ll 1$ are

$$G_\Omega(\eta) = -\eta^{-3} + \mathcal{O}(\eta^{-1}), \quad H_\Omega(\eta) = -3\eta^{-3} + \mathcal{O}(\eta^{-1}). \quad (4.23)$$

It follows that the coherent part of the dipole–dipole interaction reduces to the static interaction between two dipoles and thus diverges as η^{-3} ,

$$\Omega_{ij} = -\frac{3}{2}\sqrt{\gamma_i\gamma_j}\frac{1}{\eta^3}\left[\vec{d}_i \cdot \vec{d}_j^* - 3(\vec{d}_i \cdot \vec{R})(\vec{d}_j^* \cdot \vec{R})\right]. \quad (4.24)$$

Here we recall that we limited the theory of the dipole–dipole interaction to atomic separations that are much larger than the inverse cutoff number k_C , see Section 2.1. It follows that the dipole–dipole interaction remains finite for all atomic separations that we consider here. Note that the dipole–dipole interaction can be regularized (Brooke et al., 2008) such that it remains finite in the limit $\eta \rightarrow 0$.

The functions G_Γ and H_Γ describe the dependence of Γ_{ij} on the atomic separation and have a well-defined limit as η approaches zero,

$$\lim_{\eta \rightarrow 0^+} G_\Gamma(\eta) = \frac{2}{3}, \quad \lim_{\eta \rightarrow 0^+} H_\Gamma(\eta) = 0. \quad (4.25)$$

The collective decay rates in Equation (4.18) thus reduce to

$$\Gamma_{ij} = \sqrt{\gamma_i\gamma_j} \vec{d}_i \cdot \vec{d}_j^* \quad (4.26)$$

if $\eta \ll 1$. In the limit $\eta \rightarrow 0$, collective decay thus occurs only between transitions with nonorthogonal dipole moments of different atoms. This is similar to single-atom systems, where the radiation field in free space does not induce collective decay between orthogonal transitions, see Section 3.2.

In Equations (4.15) and (4.16), we split the double sum over the indices i and j in two parts that contain terms with $i = j$ and $i \neq j$, respectively. Here we recall that these indices label the various dipole transitions in each atom, see Section 2.1. More specifically, the parameters Ω_{ij} and Γ_{ij} account for the dipole–dipole interaction between transition i in one atom and transition j in the other atom. Since we consider a pair of identical atoms, the parameters Ω_{ii} and Γ_{ii} describe the interaction of transition i in one atom with the corresponding transition in the other atom. On the other hand, the parameters Ω_{ij} and Γ_{ij} with $i \neq j$ describe the interaction of transition i in one atom with a different transition j in the other atom. It is physically meaningful to distinguish these cross-coupling terms from the diagonal terms with $i = j$ since either the dipole moments \vec{d}_i and \vec{d}_j ,

the involved transition frequencies, or both can be different for the terms Ω_{ij} and Γ_{ij} with $i \neq j$. In general, these cross-coupling terms are different from zero and have to be taken into account. Before we highlight the physical importance of these terms in Section 4.3.2, we single out two special situations where the cross-coupling terms are either equal to zero or negligible.

First, we argue that the cross-coupling terms are negligible provided that the difference between the transition energies $\hbar\omega_i$ and $\hbar\omega_j$ of the involved transitions i and j is sufficiently large. In this case, the vacuum-induced couplings between these transitions are suppressed because the exchanged photons which mediate the dipole-dipole interaction cannot be resonant with both involved transitions at the same time. Formally, this can be seen if the master Equation (4.13) is transformed into the interaction picture with respect to the free Hamiltonian H_A . Due to the energy difference between the transitions i and j , all parameters Ω_{ij} and Γ_{ij} with $i \neq j$ acquire a an exponential that oscillates in time with frequency $|\omega_i - \omega_j|$. If this frequency difference is large, i.e., $|\omega_i - \omega_j| \gg |\Omega_{ij}|, |\Gamma_{ij}|$, then the cross-coupling terms can be neglected in the context of a secular approximation. Alternatively, this result can also be obtained from the argument in Section 2.3, where we demonstrated that the parameters Ω_{ij} and Γ_{ij} can be obtained in second-order perturbation theory. In particular, Equation (2.40) demonstrates that the transition amplitude from the initial to the final state and hence the impact of Ω_{ij} and Γ_{ij} diminishes as the energy difference $\hbar|\omega_i - \omega_j|$ increases. Note that the frequency difference between atomic transitions can be influenced or even controlled externally by a magnetic field via the Zeeman splitting of magnetic sublevels.

Second, we demonstrate that the cross-coupling terms are exactly equal to zero provided that the orientation of the involved dipole moments and the separation vector meet the following two conditions simultaneously. If the dipole d_i of one atom is orthogonal to the dipole d_j of the other atom, the first term proportional to $\vec{d}_i \cdot \vec{d}_j^*$ in Equations (4.17) and (4.18) vanishes. However, this condition is not sufficient for the omission of the cross-coupling terms between transitions i and j . The reason is that the second term proportional to $(\vec{d}_i \cdot \vec{R})(\vec{d}_j^* \cdot \vec{R})$ is different from zero if the separation vector has a nonzero projection onto both dipole moments d_i and d_j . It follows that the coupling terms Ω_{ij} and Γ_{ij} with $i \neq j$ vanish if and only if the dipole moments d_i and d_j of the involved transitions are simultaneously orthogonal to each other and to the separation vector R , i.e.,

$$\vec{d}_i \cdot \vec{d}_j^* = 0 \quad \text{and} \quad \vec{d}_i \cdot \vec{R} = \vec{d}_j \cdot \vec{R} = 0. \quad (4.27)$$

For the illustration of this result, we discuss several example geometries on the basis of the two 4-level systems (see Figure 21) in the following paragraph.

4.3.1.1. Example System The exemplary level scheme in Figure 21(b) is described by an $S_0 \leftrightarrow P_1$ transition that can be found, e.g., in ^{40}Ca atoms. We choose the z -axis as the quantization axis, which is distinguished by an external magnetic field that induces a Zeeman splitting δ of the excited states. The orientation of \mathbf{R} is defined relative to this quantization axis. The internal state $|i_\mu\rangle$ of atom μ is an eigenstate of $J_z^{(\mu)}$, where $J^{(\mu)}$ is the angular momentum operator of atom μ ($\mu \in \{1, 2\}$). In particular, the P_1 multiplet with $J = 1$ corresponds to the excited states $|1_\mu\rangle$, $|2_\mu\rangle$, and $|3_\mu\rangle$ with magnetic quantum numbers $m = -1, 0$, and 1 , respectively, and the S_0 state is the ground state $|4_\mu\rangle$ with $J = m = 0$. The raising and lowering operators on the $|4_\mu\rangle \leftrightarrow |i_\mu\rangle$ transition of atom μ are ($i \in \{1, 2, 3\}$)

$$S_{i+}^{(\mu)} = |i_\mu\rangle\langle 4_\mu| \quad \text{and} \quad S_{i-}^{(\mu)} = |4_\mu\rangle\langle i_\mu|. \quad (4.28)$$

We determine the electric-dipole moment operator of atom μ via the Wigner–Eckart theorem (Sakurai, 1994) and arrive at

$$\hat{\mathbf{d}}^{(\mu)} = \sum_{i=1}^3 [d_i S_{i+}^{(\mu)} + \text{H.c.}], \quad (4.29)$$

where the dipole moments $d_i = \langle i | \hat{\mathbf{d}} | 4 \rangle$ are given by

$$\begin{aligned} d_1 &= \mathcal{D} \epsilon^{(+)}, & d_2 &= \mathcal{D} e_z, \\ d_3 &= -\mathcal{D} \epsilon^{(-)}; & \epsilon^{(\pm)} &= \frac{1}{\sqrt{2}}(e_x \pm ie_y), \end{aligned} \quad (4.30)$$

and \mathcal{D} is the reduced dipole matrix element. In order to evaluate the expressions for the various coupling terms Ω_{ij} and the decay rates Γ_{ij} in Equations (4.17) and (4.18), we express the relative position of the two atoms in spherical coordinates (see Figure 21),

$$\mathbf{R} = R(\sin \theta \cos \phi, \sin \theta \sin \phi, \cos \theta)^T. \quad (4.31)$$

With Equations (4.30) and (4.31), we can now evaluate the geometrical coefficients in Equations (4.17) and (4.18). The explicit expressions for the

parameters Ω_{ij} are given by

$$\Omega_{11} = \frac{3}{2}\gamma_1 \left[G_\Omega(\eta) - \sin^2 \theta H_\Omega(\eta)/2 \right], \quad (4.32a)$$

$$\Omega_{22} = \frac{3}{2}\gamma_2 \left[G_\Omega(\eta) - \cos^2 \theta H_\Omega(\eta) \right], \quad (4.32b)$$

$$\Omega_{33} = \frac{3}{2}\gamma_3 \left[G_\Omega(\eta) - \sin^2 \theta H_\Omega(\eta)/2 \right], \quad (4.32c)$$

$$\Omega_{31} = \frac{3}{4}\sqrt{\gamma_3\gamma_1} \sin^2 \theta e^{-2i\phi} H_\Omega(\eta), \quad (4.32d)$$

$$\Omega_{32} = \frac{3}{2\sqrt{2}}\sqrt{\gamma_3\gamma_2} \sin \theta \cos \theta e^{-i\phi} H_\Omega(\eta), \quad (4.32e)$$

$$\Omega_{21} = -\frac{3}{2\sqrt{2}}\sqrt{\gamma_2\gamma_1} \sin \theta \cos \theta e^{-i\phi} H_\Omega(\eta). \quad (4.32f)$$

Since Ω_{ij} and Γ_{ij} depend in the same way on the orientation of the dipole moments and the separation vector \mathbf{R} , the parameters Γ_{ij} can be obtained by the replacement rules $\Omega_{ij} \sim \Gamma_{ij}$, $G_\Omega \sim G_\Gamma$, and $H_\Omega \sim H_\Gamma$.

From Equation (4.30), we can conclude that the three dipole transitions of the exemplary level scheme in Figure 21(b) are mutually orthogonal. The first condition in Equation (4.27) is thus fulfilled for all cross-coupling terms. Next we discuss several geometries where the second condition in Equation (4.27) holds for all or some of the cross-coupling terms.

As a first example, we assume that the atoms are aligned along the z -axis, i.e., $\theta = 0$. In this case, Equation (4.32) imply that all cross-coupling terms vanish, and the $S_0 \leftrightarrow P_1$ transition may be reduced to a two-level system formed by an arbitrary sublevel of the P_1 triplet and the ground state S_0 .

As a second example, we assume the atoms to be aligned in the $x-y$ plane, i.e., $\theta = \pi/2$. Then, the terms Ω_{21} , Γ_{21} and Ω_{32} , Γ_{32} vanish. In effect, the excited state $|2\rangle$ may be disregarded such that the atomic level scheme simplifies to a V-system formed by the states $|1\rangle$ and $|3\rangle$ of the P_1 multiplet and the ground state S_0 . Alternatively, the states $|2\rangle$ and $|4\rangle$ can be regarded as an effective two-level system.

4.3.2. Cross-Coupling between Orthogonal Dipole Transitions

The discussion of the example in the Section 4.3.1 reveals that the cross-coupling terms between transitions with orthogonal dipole moments are equal to zero only in very special geometrical configurations. In general, these terms have to be taken into account for a proper description of the

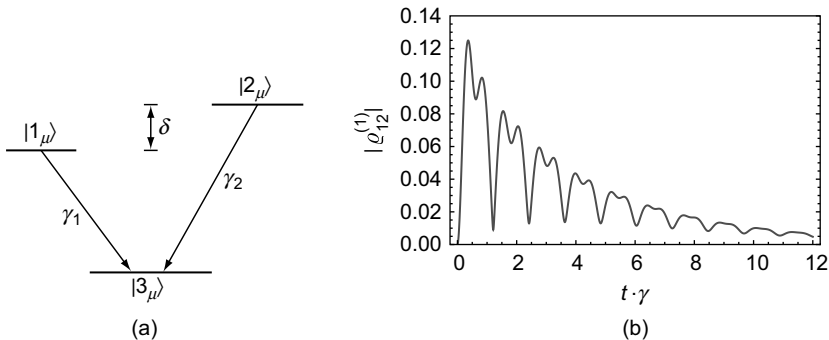


FIGURE 22 The system under consideration is comprised of two atoms as shown in Figure 21(a), where R denotes the relative position of the atoms with respect to each other. (a) The internal level scheme of each atom consists of three states in V -configuration. $2\gamma_i$ is the spontaneous decay rate of the excited state $|i\rangle$, and δ is the level splitting of the excited states. This level splitting is of the order of the spontaneous decay rates and not drawn to scale. (b) The absolute value of the matrix element $\varrho_{12}(t) = \langle 1,3| \varrho(t) | 2,3 \rangle$ is shown as a function of time. The initial state at $t = 0$ is $|1,3\rangle$, i.e., atom 1 is in the excited state $|1\rangle$ and atom 2 is in its ground state $|3\rangle$. We set $\gamma = \gamma_1 = \gamma_2$, and the parameters are $\delta = 2\gamma$ and $R = \lambda_0/6$. The geometrical setup of the atoms is characterized by the angles $\theta = \pi/2$ and $\phi = \pi/4$.

system dynamics. This fact is clarified in this section, where we highlight the impact of the cross-coupling terms on physical observables.

4.3.2.1. Vacuum-Induced Coherences The possibility to generate vacuum-induced coherences in single-atom systems was discussed in Section 3.2. There it was shown that decay-induced coherences in V -type systems as in Figure 6 can only occur if two conditions are met. First of all, the excited states have to be near-degenerate such that their frequency difference is at most of the order of the decay rate of these states. Second, the two dipole moments associated with the transitions between the ground and the excited states must be at least nonorthogonal. On the contrary, the situation is fundamentally different in a system of two dipole-dipole coupled V -type systems. Although the two upper levels must be near-degenerate as in single-atom systems, it has been shown (Agarwal & Patnaik, 2001) that the vacuum-induced dipole-dipole coupling is able to create a coherence between the excited states of an individual atom even if the two transitions in each atom are orthogonal. As we discuss below in more detail, this is rendered possible by the cross-coupling terms between transitions with orthogonal dipole moments that belong to different atoms.

The fundamental setup of the two-atom system is shown in Figure 21(a), and the level scheme of each atom is displayed in Figure 22(a). The dipole moments associated with the transitions $|1\rangle \leftrightarrow |3\rangle$

and $|2\rangle \leftrightarrow |3\rangle$ are assumed to be orthogonal, and the frequency splitting of the excited states is δ . At the initial time $t = 0$, atom 1 is in the excited state $|1\rangle$ and atom 2 is in its ground state $|3\rangle$, i.e., the initial state of the system is $|1,3\rangle$. We are interested in the time evolution of the coherence in the excited state of atom 1 under the condition that atom 2 is in its ground state. This observable is described by the density matrix element $\varrho_{12}^{(1)}(t) = \langle 1,3| \varrho(t) |2,3\rangle$, and its time evolution is shown in Figure 22(b). It can be seen that the collective decay creates a coherence between states $|1\rangle$ and $|2\rangle$ in atom 1.

This result can be understood as follows. The initially excited state $|1\rangle$ of atom 1 primarily decays via the transition $|1\rangle \leftrightarrow |3\rangle$ of atom 1. Since transitions with orthogonal dipole moments in a single atom are not coupled by the interaction with the isotropic vacuum field in free space (see Section 3.2), there is no direct coupling of the latter transition with its counterpart $|2\rangle \leftrightarrow |3\rangle$ in atom 1. However, the dipole–dipole interaction introduces an indirect coupling between these transitions that is mediated via the transitions of the second atom. In the geometrical setup considered for Figure 22(b), transition $|1_1\rangle \leftrightarrow |3_1\rangle$ is coupled via $|1_2\rangle \leftrightarrow |3_2\rangle$ of atom 2 to $|2_1\rangle \leftrightarrow |3_1\rangle$ of atom 1. In addition, $|1_1\rangle \leftrightarrow |3_1\rangle$ is coupled via $|2_2\rangle \leftrightarrow |3_2\rangle$ of atom 2 to $|2_1\rangle \leftrightarrow |3_1\rangle$ of atom 1. We emphasize that both of these coupling schemes only exist because of the cross-coupling between orthogonal transitions of different atoms. If these terms were absent, the decay-induced coherence between the upper states of atom 1 would be absent (Agarwal & Patnaik, 2001). In addition, the cross-coupling terms result in a population transfer between the two atoms (Agarwal & Patnaik; Kiffner, Evers, & Keitel, 2007a). We investigate this aspect and its consequences in more detail in Section 4.3.2.3.

4.3.2.2. Geometry-Dependent Dynamics The dependence of the dipole–dipole induced coupling terms on the relative position of the atoms has been investigated in Section 4.3.1. In particular, it has been shown that the cross-coupling terms vanish in particular geometrical configurations, but are nonzero otherwise. This feature can be used to control the quantum dynamics of a pair of atoms via their relative position with respect to each other (Evers, Kiffner, Macovei, & Keitel, 2006). This scheme (Evers et al., 2006) considers a pair of atoms that are driven by two classical laser fields propagating in z-direction, and each atom is modeled by a three-level system in Λ configuration, see Figures 23(a) and 23(b). The dipole moments of the two transitions are assumed to be orthogonal. All laser fields couple only to one transition in each of the atoms, and their frequency and intensity can be adjusted independently.

The physical observable is the time-dependent total fluorescence intensity emitted in the y -direction and is shown in Figure 23(c) for two different geometries. If the two atoms are aligned along the z -axis, then

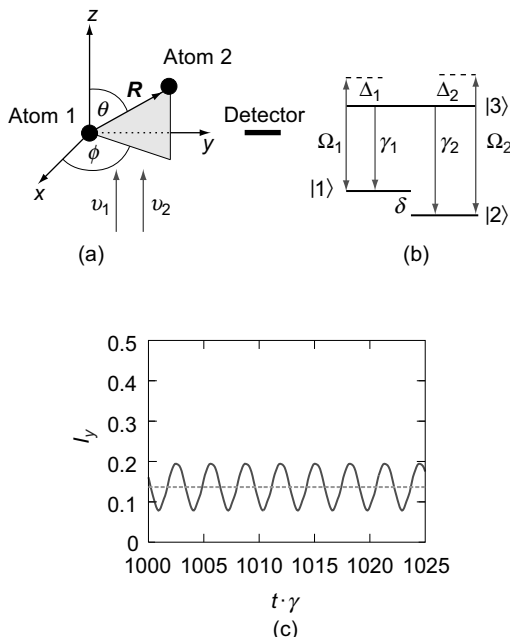


FIGURE 23 (a) A pair of nearby atoms is driven by two classical laser fields with frequencies ν_1 and ν_2 , respectively, and the relative position of the atoms is $R = r_2 - r_1$. The detector records the fluorescence intensity emitted in the y -direction. (b) Each atom is modeled by a three-level system in Λ configuration. Ω_1 (Ω_2) is the Rabi frequency of the laser field that drives transition $|1\rangle \leftrightarrow |3\rangle$ ($|2\rangle \leftrightarrow |3\rangle$) with detuning Δ_1 (Δ_2). The frequency difference of the two lower states is δ , and $2\gamma_i = 2\gamma$ is the spontaneous decay rate on the $|3\rangle \leftrightarrow |i\rangle$ transition. (c) The time-dependent fluorescence intensity I_y for the parameters $\Omega_1 = 3\gamma$, $\Omega_2 = 5\gamma$, $\delta = 0$, $\Delta_1 = 0$, $\Delta_2 = 2\gamma$, $R = 0.1\lambda$, and $\phi = \pi/4$. The solid line corresponds to $\theta = \pi/2$, and the dashed line is for $\theta = 0$. The oscillatory behavior of the intensity for $\theta = \pi/2$ remains undamped in the long-time limit. Reproduced from Evers et al. (2006). Copyright (2006) by the American Physical Society.

the system reaches a steady state (dashed line). If, however, the atoms are located in the $x-y$ plane, then the system never reaches a steady state, and the intensity exhibits periodic oscillations that persist even in the long-time limit (solid line).

The interpretation of this effect is straightforward. In general, the transition $|3\rangle \leftrightarrow |1\rangle$ of one atom is coupled to the transition $|3\rangle \leftrightarrow |2\rangle$ of the other atom via the dipole-dipole cross-coupling terms, see Section 4.3.1. The effect of this coupling is that each atomic transition does not only experience the direct driving of one laser field, but in addition an indirect driving via the second laser field. In general, the atomic response thus depends on the beat note of the two laser fields if their frequencies are

different. This effect is somewhat similar to a two-level system driven by a bichromatic field. Since the cross-coupling terms for the system under consideration are different from zero (Evers et al., 2006), if the atoms are located in the x - y plane, the system does not reach a true steady state such that the oscillations of the fluorescence intensity remain undamped in the long-time limit. For the special geometry where the atoms are aligned along the z -axis, the dipole–dipole cross-coupling terms vanish (Evers et al., 2006) and hence the fluorescence intensity is constant once the system has reached its steady state. It follows that the spatial orientation of the two-atom pair alone decides whether the system reaches a true constant steady state or not. In other words, the dynamics of the atom pair can be crucially modified by placing the second atom at a specific position with respect to the first atom.

So far, we assumed that the relative position of the two atoms is constant in time. However, in many relevant situations, such as in atomic gases, the position of the atoms is not fixed. It is, therefore, interesting to investigate whether the effects of the cross-coupling terms on the system dynamics persist if the relative position of the atoms changes in time. This question has been addressed in the study by Schmid and Evers (2008), where it is shown that these effects can survive, even if the atomic separation vector of pairs of atoms is extensively averaged in all three spatial dimensions.

4.3.2.3. Few-Level Approximation In this paragraph, we demonstrate that a negligent application of the few-level approximation in dipole–dipole interacting systems leads, in general, to substantial errors due to the presence of the cross-coupling terms. In this approximation, atomic few-level schemes like V -, Λ –type or even two-level systems are obtained by the deliberate omission of Zeeman sublevels of the full atomic angular momentum structure in the theoretical treatment. In order to illustrate that the few-level approximation is not compatible with the dipole–dipole interaction in general, we consider the geometrical setup shown in Figure 24. Here it is assumed that each atom can be modeled by the exemplary level scheme in Figure 21(b). The atom pair is aligned along the y -axis and interacts with a σ^+ polarized laser beam with frequency ω_L and Rabi frequency Ω_L . Since the laser polarization is σ^+ , it couples only to the transition $|3\rangle \leftrightarrow |4\rangle$ in each atom. This follows directly from the orientation of the dipole moments in the considered multiplet transition, see Equation (4.30). To describe this setup, one might be tempted to neglect the excited states $|1\rangle$ and $|2\rangle$ in each atom since they are not populated directly by the laser field. If this were correct, the seemingly relevant subsystem would be

$$\mathcal{C} = \text{Span}(|4, 4\rangle, |3, 3\rangle, |3, 4\rangle, |4, 3\rangle). \quad (4.33)$$

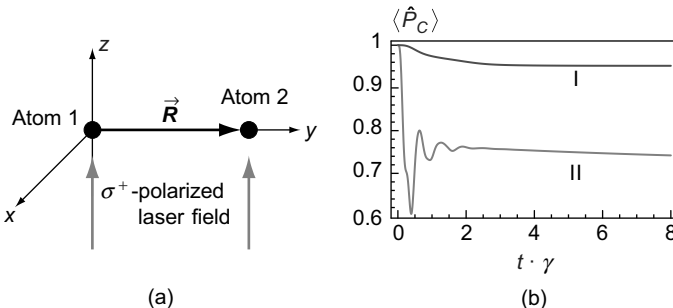


FIGURE 24 (a) The atoms are aligned along the y -axis, and the σ^+ polarized laser field with frequency ω_L and Rabi frequency Ω_L propagates in z -direction. (b) Population in the seemingly relevant subspace C [see Equation (4.33)]. The common parameters are $R = R\epsilon_y$, and the Zeeman splitting of the excited states is $\delta = 0$ [see Figure 21(b)]. ω_0 is the frequency of the $S_0 \leftrightarrow P_1$ transition, and we set $\gamma = \gamma_1 = \gamma_2 = \gamma_3$. In I, we have $\Omega_L = 2\gamma$, $R = 0.3\lambda_0$, and $\omega_L - \omega_0 = 0.58\gamma$. Curve II shows the case $\Omega_L = 5.4\gamma$, $R = 0.1\lambda_0$, and $\omega_L - \omega_0 = 5.2\gamma$. Reproduced from Kiffner et al. (2007a). Copyright (2007) by the American Physical Society.

However, it has been shown by Kiffner et al. (2007a) that the state space of the two atoms cannot be reduced to the subspace C , i.e., that the few-level approximation cannot be applied in its usual form. This result becomes apparent if the master Equation (4.13) with an additional term that accounts for the atom-laser interaction is integrated numerically. Figure 24(a) shows the resulting population confined to the subspace C ,

$$\langle \hat{P}_C \rangle = \text{Tr} [\varrho(t) \hat{P}_C], \quad (4.34)$$

where P_C is the projector onto the subspace C , and it was assumed that both atoms are initially in their ground states. Since population is lost from the subspace S , it is apparently not sufficient to take only the excited state $|3\rangle$ into account.

For the explanation of this outcome, we point out that the cross-coupling terms Ω_{31} and Γ_{31} are different from zero for the geometrical setup of Figure 24(a), see Equation (4.32). The transition $|3\rangle \leftrightarrow |4\rangle$ of one atom is thus coupled to the $|1\rangle \leftrightarrow |4\rangle$ transition of the other atom. Consequently, the dipole-dipole interaction results in a population of state $|1\rangle$ in each atom, although these states are not coupled directly to the laser field.

On the other hand, it can be verified via Equation (4.32) that the cross-coupling terms Ω_{21} , Γ_{21} and Ω_{32} , Γ_{32} vanish in the geometry chosen in Figure 24(a). The transition $|2\rangle \leftrightarrow |4\rangle$ of one atom is thus not coupled to the transitions $|1\rangle \leftrightarrow |4\rangle$ and $|3\rangle \leftrightarrow |4\rangle$ of the other atom, and the state $|2\rangle$ of each atom can be omitted. The study of the dipole-dipole coupling in

the chosen geometry and the polarization of the laser field suggests that the relevant subsystem is given by

$$\mathcal{G} = \text{Span}(|4,4\rangle, |3,3\rangle, |3,4\rangle, |4,3\rangle, |1,1\rangle, |1,3\rangle, |3,1\rangle, |1,4\rangle, |4,1\rangle) \quad (4.35)$$

rather than by the subspace \mathcal{S} in Equation (4.33). Since a numerical analysis (Kiffner et al., 2007a) shows that the population of \mathcal{G} remains unity at all times, this is indeed the case.

4.3.3. Rotations of the Atomic Separation Vector

A special situation arises if the ground- and excited-state manifolds are comprised of angular momentum multiplets. This is a physically relevant case that one encounters in atomic multiplets, where the states within each manifold can be identified with Zeeman sublevels. More specifically, we consider a pair of atoms and assume that the internal state $|i_\mu\rangle$ of atom μ is an eigenstate of $[J^{(\mu)}]^2$ and $J_z^{(\mu)}$, where $J^{(\mu)}$ is the angular momentum operator of atom μ ($\mu \in \{1, 2\}$). An example of such a level scheme is discussed in detail on the basis of Figure 21(b) in Section 4.3.1.1.

The primary concern of this section is to investigate the behavior of the dipole–dipole interaction under rotations of the atomic separation vector. In particular, we will show that the rotational symmetries of angular momentum eigenstates allow to draw extensive conclusions about the dipole–dipole interaction between a pair of atoms in the plain vacuum. For this, we consider two different geometrical configurations. In addition to a given relative position \mathbf{R} of the two atoms, we consider a second geometrical setup where the separation vector \mathbf{P} is obtained from \mathbf{R} by a rotation, $\mathbf{P} = \mathcal{R}_u(\alpha)\mathbf{R}$. Here, $\mathcal{R}_u(\alpha)$ is an orthogonal 3×3 matrix that describes a rotation in the three-dimensional real vector space \mathbb{R}^3 around the axis u by an angle α .

The first important consequence concerns the Hamiltonian H_Ω in Equation (4.15) that describes the coherent part of the dipole–dipole interaction. It can be shown (Kiffner et al., 2007a) that there exists a unitary operator W such that

$$H_\Omega(\mathbf{P}) = W H_\Omega(\mathbf{R}) W^\dagger, \quad (4.36)$$

where $W = W_u(\alpha)$ is given by

$$W_u(\alpha) = \exp[-i\alpha J^{(1)} \cdot u/\hbar] \exp[-i\alpha J^{(2)} \cdot u/\hbar]. \quad (4.37)$$

Here the operator $\exp[-i\alpha J^{(\mu)} \cdot u/\hbar]$ describes a rotation around the axis u by an angle α in the state space of atom μ . The notation $H_\Omega(\mathbf{R})$ means that the coupling constants in Equations (4.15) have to be evaluated at \mathbf{R} .

Equation (4.36) shows that the Hamiltonian $H_\Omega(\mathbf{P})$ is unitarily equivalent to $H_\Omega(\mathbf{R})$ if the separation vectors \mathbf{P} and \mathbf{R} are related by a rotation in the three-dimensional real space. Several important conclusions can be drawn from this result. First of all, it is immediately clear that the eigenvalues of H_Ω depend only on the interatomic distance, but not on the orientation of the separation vector \mathbf{R} . The reason is that the spectrum of two operators being related by a unitary transformation is identical. Here the Hamiltonian $H_\Omega(\mathbf{R})$ is related to $H_\Omega(\mathbf{P})$ by the unitary transformation W , and since \mathbf{P} is obtained from \mathbf{R} by an arbitrary rotation, the eigenvalues of H_Ω are identical for any orientation of the separation vector. Second, we point out that Equation (4.36) allows to diagonalize H_Ω in a special geometry where the eigenvectors and eigenenergies assume a particularly simple form. For example, we have shown in Section 4.3.1.1. that all cross-coupling terms for the system in Figure 21(b) vanish if the atoms are aligned along the z -axis, i.e., $\mathbf{R} = R \mathbf{e}_z$. In this situation, it is comparatively easy to find the eigenvalues and eigenstates of the system. Since the eigenvalues of H_Ω are identical for any geometry \mathbf{P} with $|\mathbf{P}| = R$, it remains to find the new eigenstates for arbitrary orientations of the separation vector. This can be achieved by a suitable choice of the rotation axis \mathbf{u} and the angle α such that $\mathbf{P} = \mathcal{R}_{\mathbf{u}}(\alpha)\mathbf{R}_z$, and the wanted Hamiltonian $H_\Omega(\mathbf{P})$ and its eigenstates can be generated via the corresponding transformation $W_{\mathbf{u}}(\alpha)$.

An additional conclusion can be drawn from Equation (4.36) if the atomic Hamiltonian H_A commutes with the transformation $W = W_{\mathbf{u}}(\alpha)$. Then, Equation (4.36) implies that $H_A + H_\Omega(\mathbf{P})$ is the unitary transform of $H_A + H_\Omega(\mathbf{R})$ by W . A straightforward realization of this is the case of degenerate Zeeman sublevels, in which the relation holds for an arbitrary orientation of \mathbf{P} . Then, the energy levels of the full-system Hamiltonian $H_A + H_\Omega$ do not depend on the orientation of the separation vector. This result can be understood as follows. Degenerate Zeeman manifolds are obtained in the absence of an external magnetic field, and hence there is no distinguished direction in space. Since the vacuum is isotropic in free space, one expects that the energy levels of the system are invariant under rotations of the separation vector \mathbf{R} . By contrast, the application of a magnetic field in z -direction leads to nondegenerate multiplets and breaks the full rotational symmetry. Since we chose the atomic states to be eigenstates of $J_z^{(\mu)}$, the atomic Hamiltonian H_A only commutes with transformations $W_{\mathbf{u}}(\alpha)$ that correspond to a rotation of the separation vector around the z -axis, $\mathbf{u} = \mathbf{e}_z$. If we express the atomic separation vector in terms of spherical coordinates as in Equation (4.31), this means that the eigenvalues of the full-system Hamiltonian $H_A + H_\Omega$ do only depend on the interatomic distance R and the angle θ , but not on the angle ϕ . This result reflects the symmetry of the system with respect to rotations around the z -axis. A direct verification of all these statements on the basis of the

exemplary level scheme in Figure 21(b) can be found the study by Kiffner et al. (2007a).

In addition to the result in Equation (4.36), it has been shown by Kiffner et al. (2007a) that the part of the master Equation (4.13) that describes the incoherent dynamics transforms according to

$$[\mathcal{L}_\gamma + \mathcal{L}_\Gamma(\mathbf{P})]W\varrho W^\dagger = W \{ [\mathcal{L}_\gamma + \mathcal{L}_\Gamma(\mathbf{R})]\varrho \} W^\dagger. \quad (4.38)$$

If the atomic Hamiltonian H_A commutes with the transformation $W = W_u(\alpha)$, Equations (4.36) and (4.38) imply that the density operator $W\varrho(\mathbf{R})W^\dagger$ obeys the same master equation than $\varrho(\mathbf{P})$ for $\mathbf{P} = \mathcal{R}_u(\alpha)\mathbf{R}$. We can thus conjecture that $\varrho(\mathbf{P})$ is the unitary transform of $\varrho(\mathbf{R})$ by W , i.e., $\varrho(\mathbf{P}) = W\varrho(\mathbf{R})W^\dagger$, provided that both density operators coincide at the initial time t_0 . If the initial conditions are invariant under the transformation W , it is thus sufficient to determine the solution of the master Equation (4.13) for only one particular geometry. Any other solution at any time t can then be generated via the transformation $W = W_u(\alpha)$ with suitable values of u and α . Another special situation arises if the steady-state solution of the master equation is independent of the initial conditions. In this frequently encountered case, the steady-state solutions for different orientations of the separation vector are also related by a properly chosen unitary transformation W .

Finally, we emphasize that the results in Equations (4.36) and (4.38) and all its implications cannot be recovered if any of the Zeeman sublevels of the ground- or excited-state manifold are removed. In this case, the unitary operator W does not exist since it is impossible to define an angular momentum or vector operator in a state space where magnetic sublevels have been removed artificially. In particular, the result that the energy levels of the two-atom system are invariant under rotations of the separation vector can only be established if complete and degenerate multiplets are considered and all cross-coupling terms are included in the analysis. On the contrary, the artificial omission of any of the Zeeman sublevels of a multiplet leads to a spurious dependence of the energy shifts on the orientation, and thus to incorrect predictions. As in Section 4.3.2.3, we thus arrive at the conclusion that the few-level approximation cannot be applied to dipole–dipole interacting systems in general.

4.4. Impact of the Dipole–Dipole Interaction

After the pioneering work by Dicke (1954) in 1954, the influence of the dipole–dipole interaction on physical processes has been investigated in great detail. A complete and exhaustive summary of these developments

is beyond the scope of this chapter, but we wish to highlight some examples where the dipole–dipole interaction gives rise to new physics and useful applications. In particular, we would like to connect the material discussed in Sections 4.1–4.3 to the pursued directions of research in the past and present.

Prominent examples for the impact of the dipole–dipole interaction are the phenomena of sub- and superradiance, see Sections 4.1 and 4.2. These phenomena were first studied in large ensembles of nearby atoms (Crubellier, Lieberman, & Pillet, 1980; Dicke, 1954; Gross & Haroche, 1982) and later in pairs of multilevel atoms (Barnes et al., 2005; Brewer, 1995; Chen & Freedhoff, 1991; DeVoe & Brewer, 1996; Fu & Gong, 1992; Hettich et al., 2002; Kurizki & Ben-Reuven, 1987; Macovei & Keitel, 2003). In addition to the rate of spontaneous emission, the dipole–dipole interaction modifies the frequency of the emitted light in spontaneous emission and resonance fluorescence (Agarwal et al., 1977; Chen & Freedhoff, 1991; Ficek & Sanders, 1990; Freedhoff, 1979, 1982; Guo & Cooper, 1995; Hettich et al., 2002; James, 1993; Lenz & Meystre, 1993; Macovei et al., 2003; Macovei, Evers, Li, & Keitel, 2007b; Östreich, 1994; Rudolph, Ficek, & Dalton, 1995; Trippenbach, Gao, Cooper, & Burnett, 1992b; Varada & Agarwal, 1991). Furthermore, other aspects like the radiation pattern of regularly aligned atoms (Brooke et al., 2008; Clemens, Horvath, Sanders, & Carmichael, 2003) and quantum jumps (Beige & Hegerfeldt, 1999; Hannstein & Hegerfeldt, 2003, 2004; Hegerfeldt & Plenio, 1992, 1995; Lewenstein & Javanainen, 1987; Plenio & Knight, 1998; Skornia, von Zanthier, Agarwal, Werner, & Walther, 2001) were investigated in dipole–dipole interacting systems.

Section 2 illustrates that the dipole–dipole interaction emerges from the interaction of atoms with the radiation field. Although the examples discussed in previous sections assume that the radiation field is in its vacuum state, other reservoirs will give rise to a modification of the dipole–dipole interaction. For example, the dipole–dipole interaction was studied in materials with negative refraction (Kästel & Fleischhauer, 2005), in photonic band gap materials (Lambropoulos, Nikolopoulos, Nielsen, & Bay, 2006), and squeezed reservoirs (Ficek, 1991; Ficek & Tanaś, 2002; Mundrarain & Orszag, 2007). Furthermore, the dipole–dipole interaction between two atoms can be mimicked by a single atom in front of a mirror (Eschner et al., 2001; Ficek & Swain, 2005; Morawitz, 1969). Couplings similar to the dipole–dipole interaction can be engineered between distant atoms by coupling them to a cavity, with applications, for example, in entangling the atoms (Angelakis, Bose, & Mancini, 2009; Cirac & Zoller, 1994; Natali & Ficek, 2007; Turchette et al., 1998).

The coherent part of the dipole–dipole interaction gives rise to a position-dependent potential between a pair of atoms, see Section 4.1. Consequently, the dipole–dipole interaction results in a force between the

atoms that can be either attractive or repulsive. These potentials and forces were mostly studied (Ellinger et al., 1994; Goldstein et al., 1996; Guo, 1994; Guo & Cooper, 1995; Smith & Burnett, 1991, 1992a,b; Smith et al., 1992) in the context of laser cooling, since they may alter the minimal temperature of a dense gas of laser-cooled atoms.

Section 4.3 investigates in detail the dependance of the dipole–dipole interaction on the geometrical alignment of the coupled atoms. The angular dependence of the dipole–dipole interaction was observed experimentally with Rydberg atoms (Carroll, Claringbould, Goodsell, Lim, & Noel, 2004). In the experiment, a nearly one-dimensional line of Rydberg atoms was produced, and the dipoles were aligned via static electric fields. On the other hand, the dependance of the dipole–dipole interaction on the interparticle spacing may be used as a sensitive probe of the distance between two interacting quantum particles on a lengthscale given by the wavelength of the optical transition (Chang, Evers, Scully, & Zubairy, 2006; Chang, Evers, & Zubairy, 2006; Gulfam & Evers, 2010; Hettich et al., 2002).

More recently, the dipole–dipole interaction was discussed in the context of quantum information theory (Nielsen & Chuang, 2000). The physical implementation of quantum computation and quantum information schemes involves the generation of entanglement and the realization of quantum gates. It has been shown that dipole–dipole interacting systems are both a resource for entanglement (Bargatin, Grishanin, & Zadkov, 2000; Ficek & Tanaś, 2002; Kiffner, Evers, & Keitel, 2007b) and suitable candidates for the implementation of gate operations between two qubits (Barenco, Deutsch, Ekert, & Jozsa, 1995; Beige, Huelga, Knight, Plenio, & Thompson, 2000; Brennen, Caves, Jessen, & Deutsch, 1999; Brennen, Deutsch, & Jessen, 2000; Jaksch et al., 2000; Lukin & Hemmer, 2000). Furthermore, an important concept in the field of quantum information theory are decoherence-free subspaces (DFS's) (Karasik, Marzlin, Sanders, & Whaley, 2008; Lidar, Chuang, & Whaley, 1998; Shabani and Lidar, 2005). A simple example for a one-dimensional DFS is the anti-symmetric state of a pair of two-level systems in the Dicke limit (see Section 4.1), and larger DFSs can be realized via the dipole–dipole interaction (Duan & Guo, 1998; Kiffner et al., 2007b; Mundrarin & Orszag, 2007; Zanardi, 1997). A general criterion for the existence of DFS's in dipole–dipole interacting systems is provided by Karasik, Marzlin, Sanders, and Whaley (2007): For translationally invariant reservoirs such as the vacuum, DFS's can only be realized in the Dicke limit where the interparticle distance approaches zero.

4.5. Multi-Particle Quantum Dynamics

In this final section, we turn to larger ensembles of atoms, in which more than two particles interact via the vacuum field. Even if the atoms

are initially independent, the coupling via the vacuum field can lead to a correlation or phasing of the individual particles, which subsequently leads to a collective dynamics. A key feature of such collective dynamics is superradiance, the cooperative spontaneous emission of radiation by an initially inverted ensemble of N two-level particles. In superradiance, the emission time scales with N^{-1} , the collective decay rates scale with N , and the emitted peak light intensity scales with N^2 (Agarwal, 1974; Andreev, Emel'yanov, & Il'inskii, 1993; Dicke, 1954; Gross & Haroche, 1982; Puri, 2001). Superradiance was first demonstrated experimentally in an optically pumped hydrogen fluoride gas (Skribanowitz, Herman, MacGillivray, & Feld, 1973), and the concept was transferred to other branches of physics (Brandes, 2005), including plasmas (Shvets, Fisch, Pukhov, & ter Vehn, 1998), multilevel systems with initial coherence (Brownell, Lu, & Hartmann, 1995), Bose-Einstein condensates (Inouye et al., 1999), micromasers (Orszag, Ramírez, Retamal, & Saavedra, 1994), molecular nanomagnets (Chudnovsky & Garanin, 2002), quantum dots (Scheibner et al., 2007), gamma ray lasers (Baldwin & Solem, 1997), collective cooling of atoms in a cavity (Chan, Black, & Vuletić, 2003; Domokos & Ritsch, 2002), band gap materials (John & Quang, 1995), long distance communication based on effective light-matter interfaces with ensembles of atoms (Duan, Lukin, Cirac, & Zoller, 2001), entanglement of macroscopic objects (Julsgaard, Kozhekin, & Polzik, 2001), localization of small dense ensembles of atoms (Macovei, Evers, Keitel, & Zubairy, 2007a), investigations devoted to quantum computation using collections of atoms (Duan, 2002; Duan, Cirac, Zoller, & Polzik, 2000; Lukin et al., 2001; Lukin, Yelin, & Fleischhauer, 2000; Macovei, Ficek, & Keitel, 2006; Saffman, Walker, & Molmer, 2010), nuclear forward scattering (Gerdau & deWaard, 1999; Pálffy, Keitel, & Evers, 2009), sonoluminescence (Mohanty & Khare, 1998), photon propagation in dense gases of atoms (Akkermans, Gero, & Kaiser, 2008), and single photons in extended clouds of atoms (Scully & Svidzinsky, 2009). Based on a thin solid sample, conditions close to those studied in the initial work by Dicke could be achieved experimentally (Greiner, Boggs, & Mossberg, 2000), in contrast to previous experiments which typically operated with optically thick and spatially extended samples, causing superfluorescent ringing (Heinzen, Thomas, & Feld, 1985). Superradiant states can be visualized as symmetric combinations of single-particle excitations, leading to constructive interference. Analogously, also antisymmetric combinations with destructive interference are possible (Dicke, 1954), even though they typically are more difficult to achieve experimentally. Subradiance was observed for the first time using gallium atoms which feature a suitable angular momentum structure (Pavolini, Crubellier, Pillet, Cabaret, & Liberman, 1985).

Just as in the single- and two-particle case considered in the previous sections, also the modification of the cooperative spontaneous decay by applying external fields or by modifying the external environment was studied (Andreev et al., 1993; Gross & Haroche, 1982; Puri, 2001). For example, the interference conditions leading to super- or subradiance can be modified by applying microwave pulses to the two lower levels of three-level atoms in a quasi-degenerate Λ -type configuration, allowing to switch the superradiant and sub-radiant processes from off to on and vice versa (Keitel, Scully, & Süssmann, 1992). Superfluorescence was shown to occur without inversion in such a coherently driven three-level system (Kozlov, Kocharovskaya, Rostovtsev, & Scully, 1999). Just as in cooperative spontaneous emission, also the output intensity and line width of a superradiant laser scale as N^2 and N^{-2} , respectively (Haake, Kolobov, Fabre, Giacobino, & Reynaud, 1993; Haake et al., 1996). Controlled by coherent light fields, collections of atomic few-level systems exhibit interesting steady-state characteristics like jumps and discontinuities (Andreev et al., 1993; Bogolubov, Quang, & Shumovsky, 1985; Puri, 2001; John & Quang, 1997; Kilin, 1982; Lawande & Jagatap, 1989). The relative phase of applied fields can be used to modify the steady-state population distribution and fluorescence intensity to a large degree in systems exhibiting spontaneously generated coherences (Macovei et al., 2003) or interferences from incoherent pumping (Macovei & Evers, 2004). Also the temperature of a thermal environment is suitable as control parameter (Macovei et al., 2004, 2005b).

In these examples, ensembles typically have the advantage over single- or few-particle systems that the system evolution is accelerated and that almost complete population transfer is possible between various system states. In this sense, cooperative effects complement the efforts in single- and two-atom systems to control or modify spontaneous decay summarized in the previous sections. In the following, we analyze a sample of three-level atoms in V -configuration in the Dicke setup, in order to demonstrate the basic techniques to analyze a many-particle ensemble and to explain the origin and the main features of cooperative dynamics. The two single-particle upper states of atom α are denoted as $|1\rangle_\alpha$ and $|2\rangle_\alpha$, the corresponding ground state as $|3\rangle_\alpha$ ($\alpha \in \{1, \dots, N\}$). To enable control, in our model, both transitions are driven by strong coherent fields, the atoms are incoherently pumped to the upper states with rates r_j , and we include spontaneously generated coherences γ_{jk} (Macovei et al., 2003). Following Dicke (1954), we assume that the atomic sample is confined in a small region compared with the wavelengths of the atomic transitions. Then, the antisymmetrical multiparticle states decouple from the interaction with the vacuum and the laser fields and can be omitted (see the

corresponding two-particle states and discussions in Section 4.1). Thus, the system reduces to symmetrized multiparticle states only and can be characterized by collective operators S_{jk} ,

$$S_{jk} = \sum_{\alpha=1}^N S_{jk}^{(\alpha)} = \sum_{\alpha=1}^N |j\rangle_{\alpha\alpha}\langle k|, \quad (4.39)$$

which are defined as the sum over the corresponding single-atom operators $S_{jk}^{(\alpha)}$ of atom α . The master equation describing such a system can be obtained in analogy to Equations (2.43) and (3.33) as (Macovei, Evers, & Keitel, 2005a)

$$\begin{aligned} \dot{\rho} + i \sum_{j \in \{1,2\}} \Omega_j [S_{j3} e^{i\phi_j} + S_{3j} e^{-i\phi_j}, \rho] \\ = - \sum_{j \in \{1,2\}} \gamma_j (S_{j3} S_{3j} \rho + \rho S_{j3} S_{3j} - 2 S_{3j} \rho S_{j3}) \\ - \sum_{j \neq k \in \{1,2\}} \gamma_{jk} (S_{j3} S_{3k} \rho + \rho S_{j3} S_{3k} - 2 S_{3k} \rho S_{j3}) \\ - \sum_{j \in \{1,2\}} r_j (S_{3j} S_{j3} \rho + \rho S_{3j} S_{j3} - 2 S_{j3} \rho S_{3j}). \end{aligned} \quad (4.40)$$

Regarding the coherent part, the dipole-allowed transitions between the states $|j\rangle \leftrightarrow |3\rangle$ are driven at resonance with Rabi frequencies $2\Omega_j$ by two strong coherent fields with phases ϕ_j , respectively ($j \in \{1, 2\}$). We have omitted the coherent part of the dipole-dipole interaction (see Section 4.1), which is justified if the Rabi frequencies dominate over the dipole-dipole induced energy shifts. Thus, the collective behavior we consider stems entirely from the mutual coupling of all the atoms with the common radiation field (Dicke, 1954). The degenerate upper states $|1\rangle$ and $|2\rangle$ decay to the ground state with decay rates $2\gamma_1$ and $2\gamma_2$, while two incoherent fields $2r_1$ and $2r_2$ are used to transfer population from the ground state to both upper states. $\gamma_{jk} = p \sqrt{\gamma_j \gamma_k}$ is the SGC contribution with p as a control parameter (see Section 3.2).

It is quite challenging to solve the Equation (4.40) for many atoms (Andreev et al., 1993; Macovei et al., 2003; Puri, 2001). Currently, only an approximate solution is known, valid in the secular approximation $\Omega_j \gg \{N\gamma_j, Nr_j\}$. Note that in realistic setups, the collective decay rates depend on the sample geometry as $\Gamma_j \propto \mu \gamma_j N$ with an additional geometrical factor μ (Andreev et al., 1993). Often, μ can be adjusted to be

much smaller than unity. Then, the condition $\Omega \gg \Gamma_j$ is satisfied, justifying the secular approximation. Leading corrections to the steady-state results obtained in the secular approximation are of the order of $N\gamma_j/\Omega$ and can be neglected in the intense field limit. We thus introduce single-particle dressed states $|\Psi_j\rangle_\alpha$ defined as in Equation (3.30), single-particle dressed state operators $R_{jk}^{(\alpha)} = |\Psi_j\rangle_\alpha\langle\Psi_k|$ and corresponding collective operators $R_{jk} = \sum_{\alpha=1}^N R_{jk}^{(\alpha)}$ and $R_z = R_{22} - R_{11}$. Assuming a compact notation using commutators, Equation (4.40) then becomes (Macovei et al., 2003)

$$\begin{aligned}\dot{\rho} + i\Omega[R_z, \rho] &= - \sum_{j \in \{1,2\}} (\gamma_- [R_{3j}, R_{j3}\rho] + f[R_{j3}, R_{3j}\rho] + \text{H.c.}) \\ &\quad - \sum_{j \neq k \in \{1,2\}} \left(\gamma_+ [R_{jk}, R_{kj}\rho] + \frac{1}{2} \gamma_+ [R_z, R_z\rho] + \text{H.c.} \right),\end{aligned}\quad (4.41)$$

where we have applied the unitary transformation $\tilde{S}_{j3} = S_{j3}e^{i\phi_j}$ and dropped the tilde afterwards. In secular approximation, we have neglected terms that oscillate with frequencies $\Omega = \sqrt{\Omega_1^2 + \Omega_2^2}$ and larger. The new coefficients in Equation (4.41) are given by ($\Delta\phi = \phi_2 - \phi_1$)

$$\gamma_- = (\gamma_1\Omega_2^2 + \gamma_2\Omega_1^2 - 2\gamma_{12}\Omega_1\Omega_2 \cos \Delta\phi)/(2\Omega^2), \quad (4.42a)$$

$$\gamma_+ = [(\gamma_1 + r_1)\Omega_1^2 + (\gamma_2 + r_2)\Omega_2^2 + 2\gamma_{12}\Omega_1\Omega_2 \cos \Delta\phi]/(4\Omega^2), \quad (4.42b)$$

$$f = (r_1\Omega_2^2 + r_2\Omega_1^2)/(2\Omega^2). \quad (4.42c)$$

The steady-state ρ_s of Equation (4.41) can be calculated using the ansatz

$$\rho_s = \frac{1}{Z} e^{-\xi R_{33}}, \quad (4.43)$$

where the normalization factor Z is determined by $\text{Tr}(\rho_s) = 1$. Inserting Equation (4.43) in Equation (4.41) and assuming steady-state $\dot{\rho}_s = 0$, one obtains $\xi = \ln(\gamma_-/f)$. In order to calculate the relevant expectation values, we introduce collective symmetrized atomic states $|N, n, m\rangle$ corresponding to the su(3) algebra of the operators R_{jk} (for details see, for instance, Macovei et al., 2005b). The state $|N, n, m\rangle$ describes a collection of atoms with n atoms in the dressed state $|\Psi_2\rangle$, $m - n$ atoms in state $|\Psi_3\rangle$, and $N - m$ atoms in state $|\Psi_1\rangle$, respectively. For example, one finds

$$\langle (R_{33})^l \rangle = Z^{-1} \left(-\frac{\partial}{\partial \xi} \right)^l Z, \quad (4.44a)$$

$$\langle R_{11} \rangle = \langle R_{22} \rangle = (N - \langle R_{33} \rangle)/2, \quad (4.44b)$$

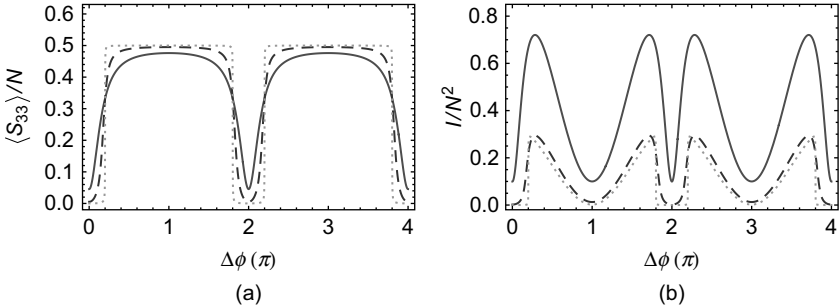


FIGURE 25 Collective ground-state population (a) and collective resonance fluorescence intensity (b) as function of $\Delta\phi$. Shown are particle numbers $N = 1$ (solid line), $N = 10$ (long-dashed line), and $N = 500$ (dotted line). Here, $p = 0.99$, $\Omega_1 = \Omega_2$, $\gamma_1 = \gamma_2 \equiv \gamma_0$, and $r_1 = r_2 \equiv r_0$ with $\gamma_0/r_0 = 5$.

where $l \in \{0, 1, \dots\}$ is an exponent and

$$Z = \frac{e^{-\xi N} (1 + (1+N)e^{(2+N)\xi} - (2+N)e^{(1+N)\xi})}{(1 - e^\xi)^2}. \quad (4.45)$$

The corresponding bare ground-state population is $\langle S_{33} \rangle = \langle R_{11} \rangle = \langle R_{22} \rangle$, and with $x = \gamma_-/f$, we obtain (Macovei et al., 2003)

$$\langle S_{33} \rangle = \frac{N(N+1)x^{N+3} - 2N(N+2)x^{N+2} + (2+3N+N^2)x^{N+1} - 2x}{2(x-1)[(1+N)x^{N+2} - (2+N)x^{N+1} + 1]}.$$

Figure 25(a) shows the steady-state population in the collective bare ground state $|3\rangle$ per atom for different numbers of atoms N versus the relative phase between the two applied strong resonant laser fields. The population ranges from 50% in the ground state as also found for a single strongly driven atom, up to all population trapped in the excited state. This trapping is due to the spontaneously generated coherences, and for single atoms, perfect trapping is only possible for $p = 1$ and $\Delta\phi = 2\pi n$ ($n \in \{0, 1, 2, \dots\}$). In contrast, for a collection of atoms ($N \gg 1$), upper-state trapping is possible with $p < 1$. Thus, cooperative effects allow to improve the effects of spontaneously generated coherences (Section 3.2). This can be useful in particular for engineered cross-couplings (Section 3.3), which often are restricted to $p < 1$. By increasing the number of atoms, the trapping range grows until in the limit $N \rightarrow \infty$, the system exhibits jumps between two states with either all or none of the population in the collective dressed state $|\Psi_3\rangle$ upon changing $\Delta\phi$. The discontinuities can be interpreted in terms of phase transitions (Andreev et al., 1993; Puri, 2001) and occur at the points where the dressed spontaneous decay out of [into] the collective dressed state $|\Psi_3\rangle$ is equal to the dressed pumping in the

reverse direction. Though true discontinuities require an infinite number of particles, Figure 25(a) shows that abrupt changes in the collective populations against suitable control parameters can already be observed with moderate particle numbers.

The corresponding total intensity I of the emitted fluorescence light divided by N^2 is shown in Figure 25(b). In the far-zone limit $|\vec{r}| \gg \lambda$, it is given by (Macovei et al., 2003)

$$I = \Phi(|\vec{r}|) \sum_{j,k \in \{1,2\}} (1 + (p - 1)(1 - \delta_{jk})) \langle S_{j3} S_{3k} \rangle e^{-i(\phi_j - \phi_k)}, \quad (4.46)$$

where $\Phi(|\vec{r}|)$ is a geometrical factor which we set equal to unity in the following. It can be seen from Figure 25(b) that the intensity scales with N^2 as predicted by Dicke. The intensity has minima at $\Delta\phi = \pi n$ ($n \in \{0, 1, 2, \dots\}$). The minima at even n are due to the trapping of the population in the collective upper bare states. But at odd n , the intensity has minima even though the population is not trapped in the upper states as for even n . Instead, 50% of the atomic population is in the bare ground state $|3\rangle$, and 25% of the population is in each of the upper bare states $|1\rangle$ and $|2\rangle$. As the inhibition of fluorescence does not occur in the single-atom case, these minima may be associated with subradiant states. It should be noted though that these subradiant states differ from the ones discussed in Section 4.1. In the present treatment, only symmetric multiparticle states are considered, while subradiant states commonly are associated with antisymmetric multiparticle states. The subradiance in Figure 25(b) arises from the trapping of the population in the excited states and quantum interference among the involved bare state transitions. At the maxima in Figure 25(b), again half of the population is in the ground and upper states, respectively, indicating superradiance.

ACKNOWLEDGMENTS

We are grateful to numerous scientists from whom we gained enormously during our years in this field of research, especially G. S. Agarwal, U. Akram, D. Browne, D. Bullock, J.-T. Chang, H. S. Chou, B. Dalton, T. N. Dey, N. A. Enaki, M. Erhard, J. Eschner, Z. Ficek, M. Fleischhauer, S. Q. Gong, M. Haas, O. Kocharovskaya, P. L. Knight, G. Kryuchkyan, G.-X. Li, G. Morigi, L. M. Narducci, Y. Niu, E. Paspalakis, M. B. Plenio, S. I. Schmid, M. O. Scully, C. Su, G. Süssmann, C. Szymanowski, K. Xia, L. Yin, G. Zeng, S. Y. Zhu, and M. S. Zubairy. In particular, we are indebted to Prof. Lorenzo M. Narducci for convincing us to write this review, which we would like to dedicate to his memory for his outstanding contributions to this field.

REFERENCES

- Abi-Salloum, T., Davis, J. P., Lehman, C., Elliott, E., & Narducci, F. A. (2007). Phase dynamics and interference in EIT. *Journal of Modern Optics*, 54, 2459.
- Agarwal, G. S. 1974. *Quantum statistical theories of spontaneous emission and their relation to other approaches*. Berlin: Springer.
- Agarwal, G. S. (1997). Physical picture for spontaneous-emission cancellation. *Physical Review A*, 55, 2457.
- Agarwal, G. S. (2000). Anisotropic vacuum-induced interference in decay channels. *Physical Review Letters*, 84(24), 5500.
- Agarwal, G. S., Brown, A. C., Narducci, L. M., & Vetri, G. (1977). Collective atomic effects in resonance fluorescence. *Physical Review A*, 15, 1613.
- Agarwal, G. S., Dey, T. N., & Menon, S. (2001a). Knob for changing light propagation from subluminal to superluminal. *Physical Review A*, 64(5), 053809.
- Agarwal, G. S., & Menon, S. (2001). Quantum interferences and the question of thermodynamic equilibrium. *Physical Review A*, 63, 023818.
- Agarwal, G. S., & Patnaik, A. K. (2001). Vacuum-induced coherences in radiatively coupled multilevel systems. *Physical Review A*, 63, 043805.
- Agarwal, G. S., Scully, M. O., & Walther, H. (2001b). Inhibition of decoherence due to decay in a continuum. *Physical Review Letters*, 86(19), 4271.
- Akkermans, E., Gero, A., & Kaiser, R. (2008). Photon localization and dicke superradiance in atomic gases. *Physical Review Letters*, 101(10), 103602.
- Akram, U., Evers, J., & Keitel, C. H. (2005). Multiphoton quantum interference on a dipole-forbidden transition. *Journal of Physics B*, 38, L69.
- Akram, U., Ficek, Z., & Swain, S. (2000). Decoherence and coherent population transfer between two coupled systems. *Physical Review A*, 62, 013413.
- Akulshin, A. M., Barreiro, S., & Lezama, A. (1998). Electromagnetically induced absorption and transparency due to resonant two-field excitation of quasidegenerate levels in rb vapor. *Physical Review A*, 57(4), 2996.
- Altner, S. B., Mitsunaga, M., Zumofen, G., & Wild, U. P. (1996). Dephasing-rephasing balancing in photon echoes by excitation induced frequency shifts. *Physical Review Letters*, 76, 1747.
- Andreev, A. V., Emel'yanov, V. I., & Il'inskii, Y. A. (1993). *Cooperative effects in optics. Superfluorescence and phase transitions*. London: IOP Publishing.
- Angelakis, D. G., Bose, S., & Mancini, S. (2009). Steady-state entanglement between hybrid light-matter qubits. *Europhysics Letters*, 85, 20007.
- Angelakis, D. G., Knight, P. L., & Paspalakis, E. (2004). Photonic crystals and inhibition of spontaneous emission: An introduction. *Contemporary Physics*, 45, 303.
- Angelakis, D. G., Paspalakis, E., & Knight, P. L. (2001). Coherent phenomena in photonic crystals. *Physical Review A*, 64, 013801.
- Anger, P., Bharadwaj, P., & Novotny, L. (2006). Enhancement and quenching of single-molecule fluorescence. *Physical Review Letters*, 96(11), 113002.
- Baldwin, G. C., & Solem, J. C. (1997). Recoilless gamma-ray lasers. *Reviews of Modern Physics*, 69, 1085.
- Barenco, A., Deutsch, D., Ekert, A., & Jozsa, R. (1995). Conditional quantum dynamics and logic gates. *Physical Review Letters*, 74, 4083.
- Bargatin, I. V., Grishanin, B. A., & Zadkov, V. N. (2000). Analysis of radiatively stable entanglement in a system of two dipole-interacting three-level atoms. *Physical Review A*, 61, 052305.
- Barnes, M. D., Krstic, P. S., Kumar, P., Mehta, A., & Wells, J. C. (2005). Far-field modulation of fluorescence decay rates in pairs of oriented semiconducting polymer nanostructures. *Physical Review B*, 71, 241303(R).

- Bay, S., Lambropoulos, P., & Molmer, K. (1997). Atom-atom interaction in strongly modified reservoirs. *Physical Review A*, 55, 1485.
- Beige, A., & Hegerfeldt, G. C. (1999). Cooperative effects in the light and dark periods of two dipole-interacting atoms. *Physical Review A*, 59, 2385.
- Beige, A., Huelga, S. F., Knight, P. L., Plenio, M. B., & Thompson, R. C. (2000). Coherent manipulation of two dipole-dipole interacting ions. *Journal of Modern Optics*, 47, 401.
- Benisty, H., & Weisbuch, C. (2006). Photonic crystals. In E. Wolf (Ed.), *Progress in optics* (Vol. 49, p. 177). Amsterdam: Elsevier.
- Berman, P. (1984). *Cavity quantum electrodynamics*. New York: Academic Press.
- Berman, P. R. (1998). Analysis of dynamical suppression of spontaneous emission. *Physical Review A*, 58, 4886.
- Berman, P. R. (2004). Comment on Physical Review Letters 89, p. 163601, 2002. *Physical Review Letters*, 92, 159301.
- Bogolubov, N. N., Jr. Quang, T., & Shumovsky, A. S. (1985). Double optical resonance in a system of atoms. *Physics Letters*, 112, 323.
- Bortman-Arbiv, D., Wilson-Gordon, A. D., & Friedmann, H. (2001). Phase control of group velocity: From subluminal to superluminal light propagation. *Physical Review A*, 63(4), 043818.
- Brandes, T. (2005). Coherent and collective quantum optical effects in mesoscopic systems. *Physics Reports*, 408, 315.
- Brennen, G. K., Caves, C. M., Jessen, P. S., & Deutsch, I. H. (1999). Quantum logic gates in optical lattices. *Physical Review Letters*, 82, 1060.
- Brennen, G. K., Deutsch, I. H., & Jessen, P. S. (2000). Entangling dipole-dipole interactions for quantum logic with neutral atoms. *Physical Review A*, 61, 062309.
- Breuer, H.-P., & Petruccione, F. 2006. *The theory of open quantum systems*. Oxford: Oxford University Press.
- Brewer, R. G. (1995). Two-ion superradiance theory. *Physical Review A*, 52(4), 2965.
- Brooke, P. G., Marzlin, K.-P., Cresser, J. D., & Sanders, B. C. (2008). Super- and subradiant emission of two-level systems in the near-dicke limit. *Physical Review A*, 77, 033844.
- Brown, R., & Orrit, M. (1997). Spectral jumps of single molecules. In T. Basche, W. E. Moerner, M. Orrit, & U. P. Wild (Eds.), *Single molecule optical detection, imaging and spectroscopy* (p. 109). Weinheim: VCH.
- Brownell, J. H., Lu, X., & Hartmann, S. R. (1995). Yoked superfluorescence. *Physical Review Letters*, 75, 3265.
- Buckle, S. J., Barnett, S. M., Knight, P. L., Lauder, M. A., & Pegg, D. T. (1986). Atomic interferometers - phase-dependence in multilevel atomic transitions. *Optica Acta*, 33, 2473.
- Bullock, D., Evers, J., & Keitel, C. H. (2003). Modifying spontaneous emission via interferences from incoherent pump fields. *Physics Letters A*, 307, 8.
- Bykov, V. (1972). Spontaneous emission in a periodic structure. *Soviet Physics JETP*, 35, 269.
- Cardimona, D. A., Kovanis, V., & Sharma, M. P. (1993). Stark effect in nonlinear jaynes-cummings models. *Physical Review A*, 47(2), 1227.
- Cardimona, D. A., Raymer, M. G., & Stroud, C. R., Jr. (1982). Steady-state quantum interference in resonance fluorescence. *Journal of Physics B*, 15, 55.
- Cardimona, D. A., & Stroud, C. R., Jr. (1983). Spontaneous radiative coupling of atomic energy levels. *Physical Review A*, 27, 2456.
- Carmichael, H. (1993). *An open systems approach to quantum optics*. Berlin: Springer.
- Carmichael, H. J., Lane, A. S., & Walls, D. F. (1987). Resonance fluorescence from an atom in a squeezed vacuum. *Physical Review Letters*, 58, 2539.
- Carroll, T. J., Claringbould, K., Goodsell, A., Lim, M. J., & Noel, M. W. (2004). Angular dependence of the dipole-dipole interaction in a nearly one-dimensional sample of rydberg atoms. *Physical Review Letters*, 93, 153001.

- Chan, H. W., Black, A. T., & Vuletić, V. (2003). Observation of collective-emission-induced cooling of atoms in an optical cavity. *Physical Review Letters*, 90(6), 063003.
- Chang, J.-T., Evers, J., Scully, M. O., & Zubairy, M. S. (2006a). Measurement of the separation between atoms beyond diffraction limit. *Physical Review A*, 73, 031803(R).
- Chang, J.-T., Evers, J., & Zubairy, M. S. (2006b). Distilling two-atom distance information from intensity-intensity correlation functions. *Physical Review A*, 74, 043820.
- Chen, Z., & Freedhoff, H. S. (1991). Cooperative effects in two-photon spontaneous emission and resonance fluorescence. *Physical Review A*, 44, 546.
- Chen, C., Yin, Y.-Y., & Elliott, D. S. (1990). Interference between optical transitions. *Physical Review Letters*, 64(5), 507.
- Chou, H.-S., & Evers, J. (2010). Dressed-atom multiphoton analysis of anomalous electromagnetically induced absorption. *Physical Review Letters*, 104, 213602.
- Chu, S., & Wieman, C. (Eds.). (1989). Feature issue on Laser cooling and trapping of atoms. *Journal of the Optical Society of America B-Optical Physics*, 6, 2020.
- Chudnovsky, E. M., & Garanin, D. A. (2002). Superradiance from crystals of molecular nanomagnets. *Physical Review Letters*, 89, 157201.
- Cirac, J. I., & Zoller, P. (1994). Preparation of macroscopic superpositions in many-atom systems. *Physical Review A*, 50(4), R2799.
- Clemens, J. P., Horvath, L., Sanders, B. C., & Carmichael, H. J. (2003). Collective spontaneous emission from a line of atoms. *Physical Review A*, 68, 023809.
- Cohen-Tannoudji, C. (1977). Atoms in strong resonant fields. In *Frontiers in laser spectroscopy*, Les Houches Session XXVII (1975). Amsterdam: North-Holland.
- Cohen-Tannoudji, C., Dupont-Roc, J., & Grynberg, G. (1997). *Photons and atoms*. New York: John Wiley & Sons.
- Cohen-Tannoudji, C., Dupont-Roc, J., & Grynberg, G. (1998). *Atom-Photon interactions*. New York: John Wiley & Sons.
- Cornelius, C. M., & Dowling, J. P. (1999). Modification of planck blackbody radiation by photonic band-gap structures. *Physical Review A*, 59(6), 4736.
- Craig, D. P., & Thirunamachandran, T. 1984. *Molecular quantum electrodynamics*. London: Dover.
- Crubellier, A., Lieberman, S., & Pillet, P. (1980). Superradiance and subradiance in three-level systems. *Optics Communications*, 33, 143.
- Dalton, B. J., & Gagen, M. (1985). Strongly driven stark coupled three-level systems and transitions at the rabi frequency. *Journal of Physics B: Atomic and Molecular Physics*, 18(22), 4403.
- Das, S., & Agarwal, G. S. (2008). Photon-photon correlations as a probe of vacuum-induced coherence effects. *Physical Review A*, 77, 033850.
- Das, S., Agarwal, G. S., & Scully, M. O. (2008). Quantum interferences in cooperative dicke emission from spatial variation of the laser phase. *Physical Review Letters*, 101(15), 153601.
- Davidovich, L. (1975). *On the Weisskopf-Wigner approximation in atomic physics*. Ph.D. Thesis, University of Rochester, Rochester, NY.
- Davies, E. B. (1974). Markovian master equations. *Communications in Mathematical Physics*, 39, 91.
- Derkacz, L., & Jakóbczyk, L. (2006). Quantum interference and evolution of entanglement in a system of three-level atoms. *Physical Review A*, 74(3), 032313.
- DeVoe, R. G., & Brewer, R. G. (1996). Observation of superradiant and subradiant spontaneous emission of two trapped ions. *Physical Review Letters*, 76(12), 2049.
- Dicke, R. H. (1954). Coherence in spontaneous radiation processes. *Physical Review*, 93, 99.
- Domokos, P., & Ritsch, H. (2002). Collective cooling and self-organization of atoms in a cavity. *Physical Review Letters*, 89(25), 253003.

- Duan, L.-M. (2002). Entangling many atomic ensembles through laser manipulation. *Physical Review Letters*, 88(17), 170402.
- Duan, L.-M., Cirac, J. I., Zoller, P., & Polzik, E. S. (2000). Quantum communication between atomic ensembles using coherent light. *Physical Review Letters*, 85(26), 5643.
- Duan, L.-M., & Guo, G.-C. (1998). Optimal quantum codes for preventing collective amplitude damping. *Physical Review A*, 58, 3491.
- Duan, L.-M., Lukin, M. D., Cirac, J. I., & Zoller, P. (2001). Long-distance quantum communication with atomic ensembles and linear optics. *Nature (London)*, 414, 413.
- Dümcke, R., & Spohn, H. (1979). The proper form of the generator in the weak coupling limit. *Zeitschrift für Physik B*, 34, 419.
- Dung, H. T., & Ujihara, K. (1999). Analytic solution for retardation in two-atom systems. *Physical Review A*, 59, 2524.
- Dutt, M. V. G., Cheng, J., Li, B., Xu, X., Li, X., Berman, P. R., et al., (2005). Stimulated and spontaneous optical generation of electron spin coherence in charged gaas quantum dots. *Physical Review Letters*, 94, 227403.
- Eichmann, U., Bergquist, J. C., Bollinger, J. J., Gilligan, J. M., Itano, W. M., Wineland, D. J., et al., (1993). Young's interference experiment with light scattered from two atoms. *Physical Review Letters*, 70(16), 2359.
- Ellinger, K., Cooper, J., & Zoller, P. (1994). Light-pressure force in n -atom sytems. *Physical Review A*, 49, 3909.
- Enaki, N. A., & Macovei, M. A. (2000). Resonance two-photon interaction of radiators with the broadband squeezed field. *Journal of Physics B*, 33, 2163.
- Eschner, J., Raab, C., Schmidt-Kaler, F., & Blatt, R. (2001). Light interference from single atoms and their mirror images. *Nature*, 413, 495.
- Evers, J. (2005). Phase-dependent interference mechanisms in a three-level system driven by a quantized laser field. *Journal of Modern Optics*, 52, 2699.
- Evers, J., Bullock, D., & Keitel, C. H. (2002). Dark state suppression and narrow fluorescent feature in a laser-driven lambda-atom. *Optics Communications*, 209, 173.
- Evers, J., & Keitel, C. H. (2002). Spontaneous emission suppression on arbitrary atomic transitions. *Physical Review Letters*, 89, 163601.
- Evers, J., & Keitel, C. H. (2004a). Reply to comment. *Physical Review Letters*, 92, 159303.
- Evers, J., & Keitel, C. H. (2004b). Spontaneous-emission suppression via multiphoton quantum interference. *Journal of Physics B*, 37, 2771.
- Evers, J., Kiffner, M., Macovei, M., & Keitel, C. H. (2006). Geometry-dependent dynamics of two Λ -type atoms via vacuum-induced coherences. *Physical Review A*, 73, 023804.
- Facchi, P., & Pascazio, S. (2001). Quantum zeno and inverse quantum zeno effects. In E. Wolf (Ed.), *Progress in optics* (Vol. 42, p. 147). Amsterdam: Elsevier.
- Failache, H., Valente, P., Ban, G., Lorent, V., & Lezama, A. (2003). Inhibition of electromagnetically induced absorption due to excited-state decoherence in rb vapor. *Physical Review A*, 67, 043810.
- Faist, J., Capasso, F., Sirtori, C., West, K. W., & Pfeiffer, L. N. (1997). Controlling the sign of quantum interference by tunneling from quantum wells. *Nature*, 390, 589.
- Feranchuk, I. D., Komarov, L. I., & Ulyanenkov, A. (2002). Control of the atom (nucleus) lifetime in the excited state by means of a low-frequency external field. *Journal of Physics B: Atomic, Molecular and Optical Physics*, 35(19), 3957.
- Ficek, Z. (1991). Pairwise atomic states: Two-atom system in a three-dimensional squeezed vacuum field. *Physical Review A*, 44(11), 7759.
- Ficek, Z., & Freedhoff, H. S. (1996). Fluorescence and absorption by a two-level atom in a bichromatic field with one strong and one weak component. *Physical Review A*, 53(6), 4275.
- Ficek, Z., & Freedhoff, H. S. (2000). Spectroscopy in polychromatic fields. In E. Wolf (Ed.), *Progress in optics* (Vol. 40, p. 391). Amsterdam: Elsevier.

- Ficek, Z., & Sanders, B. C. (1990). Quantum beats in two-atom resonance fluorescence. *Physical Review A*, 41, 359.
- Ficek, Z., & Swain, S. (2004). Simulating quantum interference in a three-level system with perpendicular transition dipole moments. *Physical Review A*, 69, 023401.
- Ficek, Z., & Swain, S. (2005). *Quantum interference and coherence*. New York: Springer.
- Ficek, Z., & Tanaś, R. (2002). Entangled states and collective nonclassical effects in two-atom systems. *Physics Reports*, 372, 369.
- Fleischhauer, M., Imamoglu, A., & Marangos, J. P. (2005). Electromagnetically induced transparency: Optics in coherent media. *Reviews of Modern Physics*, 77(2), 633.
- Fleischhauer, M., Keitel, C. H., Narducci, L. M., Scully, M. O., Zhu, S.-Y., & Zubairy, M. (1992). Lasing without inversion: Interference of radiatively broadened resonances in dressed atomic systems. *Optics Communications*, 94, 599.
- Fleischhauer, M., Keitel, C. H., Scully, M. O., & Su, C. (1992). Lasing without inversion and enhancement of the index of refraction via interference of incoherent pump processes. *Optics Communications*, 87, 109.
- Fleischhauer, M., Keitel, C. H., Scully, M. O., Su, C., Ulrich, B. T., & Zhu, S.-Y. (1992). Resonantly enhanced refractive index without absorption via atomic coherence. *Physical Review A*, 46, 1468.
- Fleming, J. G., Lin, S. Y., El-Kady, I., Biswas, R., & Ho, K. M. (2002). All-metallic three-dimensional photonic crystals with a large infrared bandgap. *Nature*, 417, 52.
- Florescu, M., & John, S. 2004. Resonance fluorescence in photonic band gap waveguide architectures: Engineering the vacuum for all-optical switching. *Physical Review A*, 69(5), 053810.
- Freedhoff, H., & Quang, T. (1994). Ultrasharp lines in the absorption and fluorescence spectra of an atom in a cavity. *Physical Review Letters*, 72, 474.
- Freedhoff, H. S. (1979). Collective atomic effects in resonance fluorescence: Dipole-dipole interaction. *Physical Review A*, 19, 1132.
- Freedhoff, H. S. (1982). Collective atomic effects in resonance fluorescence: The scaling factor. *Physical Review A*, 26, 684.
- Friedberg, R., Hartmann, S. R., & Manassah, J. T. (1973). Frequency shifts in emission and absorption by resonant systems of two-level atoms. *Physics Reports*, 7, 101.
- Frishman, E., & Shapiro, M. (2001). Complete suppression of spontaneous decay of a manifold of states by infrequent interruptions. *Physical Review Letters*, 87(25), 253001.
- Fu, C., & Gong, C. (1992). Spontaneous emission by two three-level atoms. *Physical Review A*, 45, 5095.
- Gabrielse, G., & Dehmelt, H. (1985). Observation of inhibited spontaneous emission. *Physical Review Letters*, 55(1), 67.
- Gao, S.-y., Li, F.-l., & Zhu, S.-y. (2002). Quantum interference and phase-dependent spectrum of resonance fluorescence of a three-level v-type atom. *Physical Review A*, 66(4), 043806.
- Gardiner, C. W. (1986). Inhibition of atomic phase decays by squeezed light: A direct effect of squeezing. *Physical Review Letters*, 56, 1917.
- Gardiner, C. W., & Collet, M. J. (1985). Input and output in damped quantum systems: Quantum stochastic differential equations and the master equation. *Physical Review A*, 31, 3761.
- Garraway, B. M., Kim, M. S., & Knight, P. L. (1995). Quantum jumps, atomic shelving and monte carlo fluorescence spectra. *Optics Communications*, 117, 560.
- Garraway, B. M., & Knight, P. L. (1996). Cavity modified quantum beats. *Physical Review A*, 54(4), 3592.
- Gerdau, E., & deWaard, H. (Eds.). (1999). Special issue on nuclear resonant scattering of synchrotron radiation. *Hyperfine Interactions*, 123–125, 1.

- Ghafoor, F., Zhu, S.-Y., & Zubairy, M. S. (2000). Amplitude and phase control of spontaneous emission. *Physical Review A*, 62(1), 013811.
- Goldstein, E. V., Pax, P., & Meystre, P. (1996). Dipole-dipole interaction in three-dimensional optical lattices. *Physical Review A*, 53, 2604.
- Gong, S. Q., Paspalakis, E., & Knight, P. L. (1998). Effects of spontaneous emission interference on population inversions of a v-type atom. *Journal of Modern Optics*, 45, 2433.
- Gonzalo, I., Antón, M. A., Carreño, F., & Calderón, O. G. (2005). Squeezing in a λ -type three-level atom via spontaneously generated coherence. *Physical Review A*, 72(3), 033809.
- Goy, P., Raimond, J. M., Gross, M., & Haroche, S. (1983). Observation of cavity-enhanced single-atom spontaneous emission. *Physical Review Letters*, 50(24), 1903.
- Greentree, A. D., Wei, C., & Manson, N. B. (1999). Polychromatic excitation of a two-level system. *Physical Review A*, 59(5), 4083.
- Greiner, C., Boggs, B., & Mossberg, T. W. (2000). Superradiant emission dynamics of an optically thin material sample in a short-decay-time optical cavity. *Physical Review Letters*, 85, 3793.
- Gross, M., & Haroche, S. (1982). Superradiance: An essay on the theory of collective spontaneous emission. *Physics Reports*, 93(5), 301.
- Grynberg, G. (1981). Resonances between 'unpopulated levels' in non-linear optics. *Journal of Physics B: Atomic and Molecular Physics*, 14(12), 2089.
- Grynberg, G., & Berman, P. R. (1990). Pressure-induced extra resonances in nonlinear spectroscopy. *Physical Review A*, 41, 2677.
- Gulfam, Q., & Evers, J. (2010). Measurement of distance and orientation of two atoms in arbitrary geometry. *Journal of Physics B*, 43, 045501.
- Guo, J. (1994). Effects of resonant dipole interaction between atoms on laser cooling: The case of two identical atoms. *Physical Review A*, 50, R2830.
- Guo, J., & Cooper, J. (1995). Cooling and resonance fluorescence of two atoms in a one-dimensional optical molasses. *Physical Review A*, 51, 3128.
- Haake, F., Kolobov, M. I., Fabre, C., Giacobino, E., & Reynaud, S. (1993). Superradiant laser. *Physical Review Letters*, 71, 995.
- Haake, F., Kolobov, M. I., Seeger, C., Fabre, C., Giacobino, E., & Reynaud, S. (1996). Quantum noise reduction in stationary superradiance. *Physical Review A*, 54, 1625.
- Hakuta, K., Marmet, L., & Stoicheff, B. P. (1992). Nonlinear optical generation with reduced absorption using electric-field coupling in atomic hydrogen. *Physical Review A*, 45(7), 5152.
- Hannstein, V., & Hegerfeldt, G. C. (2003). Cooperative fluorescence effects for dipole-dipole interacting systems with experimentally relevant level configurations. *Physical Review A*, 68, 043836.
- Hannstein, V., & Hegerfeldt, G. C. (2004). Cooperative quantum jumps for three dipole-interacting atoms. *Physical Review A*, 70, 023820.
- Harris, S. E. (1989). Lasers without inversion: Interference of lifetime-broadened resonances. *Physical Review Letters*, 62(9), 1033.
- Harris, S. E. (1997). Electromagnetically induced transparency. *Physics Today*, 50, 36.
- Hegerfeldt, G. C., & Plenio, M. B. (1992). Macroscopic dark periods without a metastable state. *Physical Review A*, 46(1), 373.
- Hegerfeldt, G. C., & Plenio, M. B. (1993). Coherence with incoherent light: A new type of quantum beat for a single atom. *Physical Review A*, 47, 2186.
- Hegerfeldt, G. C., & Plenio, M. B. (1995). Spectral structures induced by electron shelving. *Physical Review A*, 52(4), 3333.
- Heinzen, D. J., Childs, J. J., Thomas, J. E., & Feld, M. S. (1987). Enhanced and inhibited visible spontaneous emission by atoms in a confocal resonator. *Physical Review Letters*, 58, 1320.
- Heinzen, D. J., Thomas, J. E., & Feld, M. S. (1985). Coherent ringing in superfluorescence. *Physical Review Letters*, 54(7), 677.

- Hettich, C., Schmitt, C., Zitzmann, J., Kühn, S., Gerhardt, I., & Sandoghdar, V. (2002). Nanometer resolution and coherent optical dipole coupling of two individual molecules. *Nature*, 298, 385.
- Hulet, R. G., Hilfer, E. S., & Kleppner, D. (1985). Inhibited spontaneous emission by a rydberg atom. *Physical Review Letters*, 55(20), 2137.
- Imamoglu, A. (1989). Interference of radiatively broadened resonances. *Physical Review A*, 40(5), 2835.
- Inouye, S., Chikkatur, A. P., Stamper-Kurn, D. M., Stenger, J., Pritchard, D. E., & Ketterle, W. (1999). Superradiant rayleigh scattering from a bose-einstein condensate. *Science*, 285, 571.
- Itano, W. M., Bergquist, J. C., Bollinger, J. J., Wineland, D. J., Eichmann, U., & Raizen, M. G. (1998). Complementarity and young's interference fringes from two atoms. *Physical Review A*, 57(6), 4176.
- Jakob, M., & Bergou, J. (1999). Resonance fluorescence spectra and squeezing properties of a bichromatically driven four-level atom. *Physical Review A*, 60(5), 4179.
- Jaksch, D., Cirac, J. I., Zoller, P., Rolston, S. L., Côté, R., & Lukin, M. D. (2000). Fast quantum gates for neutral atoms. *Physical Review Letters*, 85(10), 2208.
- James, D. F. V. (1993). Frequency shifts in spontaneous emission from two interacting atoms. *Physical Review A*, 47(2), 1336.
- Javanainen, J. (1992). Effect of state superpositions created by spontaneous emission on laser-driven transitions. *Europhysics Letters*, 17, 407.
- Jhe, W., Anderson, A., Hinds, E. A., Meschede, D., Moi, L., & Haroche, S. (1987). Suppression of spontaneous decay at optical frequencies: Test of vacuum-field anisotropy in confined space. *Physical Review Letters*, 58, 666.
- Joannopoulos, J. D., Johnson, S. G., Winn, J. N., & Meade, R. D. (2008). *Photonic crystals: Molding the flow of light*. Princeton, NJ: Princeton University Press.
- John, S. (1987). Strong localization of photons in certain disordered dielectric superlattices. *Physical Review Letters*, 58, 2486.
- John, S., & Quang, T. (1994). Spontaneous emission near the edge of a photonic band gap. *Physical Review A*, 50, 1764.
- John, S., & Quang, T. (1995). Localization of superradiance near a photonic band gap. *Physical Review Letters*, 74, 3419.
- John, S., & Quang, T. (1997). Collective switching and inversion without fluctuation of two-level atoms in confined photonic systems. *Physical Review Letters*, 78(10), 1888.
- John, S., & Wang, J. (1990). Quantum electrodynamics near a photonic band gap: Photon bound states and dressed atoms. *Physical Review Letters*, 64(20), 2418.
- Joshi, A., Yang, W. G., & Xiao, M. (2003). Effect of spontaneously generated coherence on optical bistability in three-level Λ -type atomic system. *Physics Letters A*, 315, 203.
- Julsgaard, B., Kozhekin, A., & Polzik, E. S. (2001). Experimental long-lived entanglement of two macroscopic objects. *Nature (London)*, 413, 400.
- Kajari-Schröder, S., Morigi, G., Franke-Arnold, S., & Oppo, G.-L. (2007). Phase-dependent light propagation in atomic vapors. *Physical Review A*, 75, 013816.
- Kang, H., Hernandez, G., Zhang, J., & Zhu, Y. (2006). Phase-controlled light switching at low light levels. *Physical Review A*, 73(1), 011802.
- Kapale, K. T., Scully, M. O., Zhu, S. Y., & Zubairy, M. S. (2003). Quenching of spontaneous emission through interference of incoherent pump processes. *Physical Review A*, 67, 023804.
- Karasik, R. I., Marzlin, K.-P., Sanders, B. C., & Whaley, K. B. (2007). Multiparticle decoherence-free subspaces in extended systems. *Physical Review A*, 76, 012331.
- Karasik, R. I., Marzlin, K.-P., Sanders, B. C., & Whaley, K. B. (2008). Criteria for dynamically stable decoherence-free subspaces and incoherently generated coherences. *Physical Review A*, 77, 052301.

- Kästel, J., & Fleischhauer, M. (2005). Suppression of spontaneous emission and superradiance over macroscopic distances in media with negative refraction. *Physical Review A*, 71, 011804(R).
- Keitel, C. H. (1999). Narrowing spontaneous emission without intensity reduction. *Physical Review Letters*, 83(7), 1307.
- Keitel, C. H., Knight, P. L., Narducci, L. M., & Scully, M. O. (1995). Resonance fluorescence in a tailored vacuum. *Optics Communications*, 118, 143.
- Keitel, C. H., Narducci, L. M., & Scully, M. O. (1995). Origin of the sub-natural line-narrowing effect in resonance fluorescence. *Applied Physics B*, 60, S153.
- Keitel, C. H., Scully, M. O., & Süßmann, G. (1992). Triggered superradiance. *Physical Review A*, 45(5), 3242.
- Kiffner, M., Evers, J., & Keitel, C. H. (2006a). Interference in the resonance fluorescence of two incoherently coupled transitions. *Physical Review A*, 73, 063814.
- Kiffner, M., Evers, J., & Keitel, C. H. (2006b). Quantum interference enforced by time-energy complementarity. *Physical Review Letters*, 96, 100403.
- Kiffner, M., Evers, J., & Keitel, C. H. (2007a). Breakdown of the few-level approximation in collective systems. *Physical Review A*, 76, 013807.
- Kiffner, M., Evers, J., & Keitel, C. H. (2007b). Coherent control in a decoherence-free subspace of a collective multilevel system. *Physical Review A*, 75, 032313.
- Kilin, S. J. (1982). Critical phenomena in the cooperative resonance fluorescence of a system of interacting atoms. *Soviet Physics JETP*, 55, 38, [Zhurnal eksperimental'noi i Teoreticheskoi fiziki, 82, 63 (1982)].
- Kim, S. K., Moon, H. S., Kim, K., & Kim, J. B. (2003). Observation of electromagnetically induced absorption in open systems regardless of angular momentum. *Physical Review A*, 68(6), 063813.
- Kleppner, D. (1981). Inhibited spontaneous emission. *Physical Review Letters*, 47, 233.
- Knight, P. (1981). Radiative frustration by vacuum manipulation. *Nature*, 293, 514.
- Kocharovskaya, O., Mandel, P., & Scully, M. O. (1995). Atomic coherence via modified spontaneous relaxation of driven three-level atoms. *Physical Review Letters*, 74(13), 2451.
- Kocharovskaya, O., Radeonychev, Y. V., Mandel, P., & Scully, M. O. (1999). Field-dependent relaxation effects in a three-level system driven by a strong coherent field. *Physical Review A*, 60(4), 3091.
- Kofman, A. G. (2004). Comment on *Physical Review Letters*, 89, 163601, (2002). *Physical Review Letters*, 92, 159302.
- Kofman, A. G., & Kurizki, G. (2000). Acceleration of quantum decay processes by frequent observations. *Nature (London)*, 405, 546.
- Kofman, A. G., Kurizki, G., & Sherman, B. (1994). Spontaneous and induced atomic decay in photonic band structures. *Journal of Modern Optics*, 41, 353.
- Kohler, T. (1996). Coherence with incoherent light in hydrogen-like systems. *Zeitschrift für Physik D*, 38, 321.
- Korsunsky, E. A., Leinfellner, N., Huss, A., Baluschev, S., & Windholz, L. (1999). Phase-dependent electromagnetically induced transparency. *Physical Review A*, 59(3), 2302.
- Kosachiov, D. V., Matisov, B. G., & Rozhdestvensky, Y. V. (1992). Coherent phenomena in multilevel systems with closed interaction contour. *Journal of Physics B*, 25, 2473.
- Kozlov, V., Kocharovskaya, O., Rostovtsev, Y., & Scully, M. (1999). Superfluorescence without inversion in coherently driven three-level systems. *Physical Review A*, 60, 1598.
- Král, P., Thanopoulos, I., & Shapiro, M. (2007). Colloquium: Coherently controlled adiabatic passage. *Reviews of Modern Physics*, 79(1), 53.
- Kreuter, A., Becher, C., Lancaster, G. P. T., Mundt, A. B., Russo, C., Haffner, H., et al., (2004). Spontaneous emission lifetime of a single trapped ca^+ ion in a high finesse cavity. *Physical Review Letters*, 92(20), 203002.

- Kurizki, G., & Ben-Reuven, A. (1987). Theory of cooperative fluorescence from products of reactions of collisions: Identical neutral atomic fragments. *Physical Review A*, 36, 90.
- Lambropoulos, P., Nikolopoulos, G. M., Nielsen, T. R., & Bay, S. (2006). Fundamental quantum optics in structured reservoirs. *Physical Review A*, 74, 043820.
- Landau, L. (1927). Das dämpfungsproblem in der wellenmechanik. *Zeitschrift fr Physik A*, 45, 430.
- Lawande, S. V., & Jagatap, B. N. (1989). Cooperative effects in a system of strongly driven three-level atoms. *Physical Review A*, 39, 683.
- Lax, M. (1963). Formal theory of quantum fluctuations from a driven state. *Physical Review*, 129(5), 2342.
- Lee, H., Polynkin, P., Scully, M. O., & Zhu, S.-Y. (1997). Quenching of spontaneous emission via quantum interference. *Physical Review A*, 55(6), 4454.
- Lehmberg, R. H. (1970a). Radiation from an n -atom system. i. general formalism. *Physical Review A*, 2(3), 883.
- Lehmberg, R. H. (1970b). Radiation from an n -atom system. ii. spontaneous emission from a pair of atoms. *Physical Review A*, 2(3), 889.
- Lenz, G., & Meystre, P. (1993). Resonance fluorescence from two identical atoms in a standing-wave field. *Physical Review A*, 48, 3365.
- Lewenstein, M., & Javanainen, J. (1987). Cooperative quantum jumps with two atoms. *Physical Review Letters*, 59(12), 1289.
- Lezama, A., Barreiro, S., & Akulshin, A. M. (1999). Electromagnetically induced absorption. *Physical Review A*, 59(6), 4732.
- Li, G.-x., Evers, J., & Keitel, C. H. (2009a). Spontaneous emission interference in negative-refractive-index waveguides. *Physical Review B*, 80(4), 045102.
- Li, G.-X., Peng, J. S., & Huang, G. M. (2000a). Population inversion and absorption spectrum of a v-type three-level atom driven by coherent and stochastic fields. *Journal of Physics B*, 33, 3743.
- Li, H., Sautenkov, V. A., Rostovtsev, Y. V., Welch, G. R., Hemmer, P. R., & Scully, M. O. (2009b). Electromagnetically induced transparency controlled by a microwave field. *Physical Review A*, 80(2), 023820.
- Li, L., Wang, X., Yang, J., Lazarow, G., Qi, J., & Lyyra, A. M. (2000b). Comment on Physical Review Letters, 77, 1032, 1996. *Physical Review Letters*, 84, 4016.
- Lidar, D. A., Chuang, I. L., & Whaley, K. B. (1998). Decoherence-free subspaces for quantum computation. *Physical Review Letters*, 81, 2594.
- Lindner, F., Schätzel, M. G., Walther, H., Baltuška, A., Goulielmakis, E., Krausz, F., et al., (2005). Attosecond double-slit experiment. *Physical Review Letters*, 95(4), 040401.
- Liu, C. P., Gong, S. Q., Fan, X. J., & Xu, Z. Z. (2004). Phase control of spontaneously generated coherence induced bistability. *Optics Communications*, 239, 383.
- Lodahl, P., van Driel, A. F., Nikolaev, I. S., Irman, A., Overgaag, K., Vanmaekelbergh, D., et al., (2004). Controlling the dynamics of spontaneous emission from quantum dots by photonic crystals. *Nature*, 430, 654.
- Löffler, M., Nikonorov, D. E., Kocharovskaya, O. A., & Scully, M. O. (1997). Strong-field index enhancement via selective population of dressed states. *Physical Review A*, 56(6), 5014.
- Lukin, M. D., Fleischhauer, M., Cote, R., Duan, L. M., Jaksch, D., Cirac, J. I., et al., (2001). Dipole blockade and quantum information processing in mesoscopic atomic ensembles. *Physical Review Letters*, 87, 037901.
- Lukin, M. D., & Hemmer, P. R. (2000). Quantum entanglement via optical control of atom-atom interactions. *Physical Review Letters*, 84, 2818.
- Lukin, M. D., Yelin, S. F., & Fleischhauer, M. (2000). Entanglement of atomic ensembles by trapping correlated photon states. *Physical Review Letters*, 84(18), 4232.

- Lütkenhaus, N., Cirac, J. I., & Zoller, P. (1998). Mimicking a squeezed-bath interaction: Quantum-reservoir engineering with atoms. *Physical Review A*, 57(1), 548.
- Macovei, M., Evers, J., & Keitel, C. H. (2003). Phase control of collective quantum dynamics. *Physical Review Letters*, 91(23), 233601.
- Macovei, M., Evers, J., & Keitel, C. H. (2004). Magnetic and thermal influences on collective resonance fluorescence. *Europhysics Letters*, 68, 391.
- Macovei, M., Evers, J., & Keitel, C. H. (2005a). Coherent manipulation of collective three-level systems. *Physical Review A*, 71(3), 033802.
- Macovei, M., Evers, J., & Keitel, C. H. (2005b). Quantum correlations of an atomic ensemble via an incoherent bath. *Physical Review A*, 72(6), 063809.
- Macovei, M., Evers, J., Keitel, C. H., & Zubairy, M. S. (2007). Localization of atomic ensembles via superfluorescence. *Physical Review A*, 75(3), 033801.
- Macovei, M., Evers, J., Li, G.-X., & Keitel, C. H. (2007). Strong-field spatial interference in a tailored electromagnetic bath. *Physical Review Letters*, 98, 043602.
- Macovei, M., Ficek, Z., & Keitel, C. H. (2006). Collective coherent population trapping in a thermal field. *Physical Review A*, 73(6), 063821.
- Macovei, M., & Keitel, C. H. (2003). Laser control of collective spontaneous emission. *Physical Review Letters*, 91(12), 123601.
- Macovei, M. A., & Evers, J. (2004). Phase dependence of collective fluorescence via interferences from incoherent pumping. *Optics Communications*, 240, 379.
- Mahmoudi, M., & Evers, J. (2006). Light propagation through closed-loop atomic media beyond the multiphoton resonance condition. *Physical Review A*, 74(6), 063827.
- Malinovsky, V. S., & Sola, I. R. (2004). Quantum phase control of entanglement. *Physical Review Letters*, 93(19), 190502.
- Mandel, L., & Wolf, E. (1995). *Optical coherence and quantum optics*. London: Cambridge University Press.
- Manka, A. S., Doss, H. M., Narducci, L. M., Ru, P., & Oppo, G.-L. (1991). Spontaneous emission and absorption properties of a driven three-level system. ii. the Λ and cascade models. *Physical Review A*, 43(7), 3748.
- Martinez, M. A. G., Herczfeld, P. R., Samuels, C., Narducci, L. M., & Keitel, C. H. (1997). Quantum interference effects in spontaneous atomic emission: Dependence of the resonance fluorescence spectrum on the phase of the driving field. *Physical Review A*, 55, 4483.
- Martini, F. D., Innocenti, G., Jacobovitz, G. R., & Mataloni, P. (1987). Anomalous spontaneous emission time in a microscopic optical cavity. *Physical Review Letters*, 59, 2955.
- McLone, R. R., & Power, E. A. (1965). The long range van der waals forces between non-identical systems. *Proceedings of the Royal Society of London Series A*, 286, 573.
- Megens, M., Wijnhoven, J. E. G. J., Lagendijk, A., & Vos, W. L. (1999). Fluorescence lifetimes and linewidths of dye in photonic crystals. *Physical Review A*, 59, 4727.
- Menon, S., & Agarwal, G. S. (1998). Effects of spontaneously generated coherence on the pump-probe response of a Λ system. *Physical Review A*, 57(5), 4014.
- Milonni, P. W., & Knight, P. L. (1974). Retardation in the resonant interaction of two identical atoms. *Physical Review A*, 10, 1096.
- Milonni, P. W., & Knight, P. L. (1975). Retarded interaction of two nonidentical atoms. *Physical Review A*, 11, 1090.
- Misra, B., & Sudarshan, E. C. G. (1977). The zeno's paradox in quantum theory. *Journal of Mathematical Physics*, 18, 756.
- Mohanty, P., & Khare, S. V. (1998). Sonoluminescence as a cooperative many body phenomenon. *Physical Review Letters*, 80(1), 189.
- Morawitz, H. (1969). Self-coupling of a two-level system by a mirror. *Physical Review*, 187(5), 1792.

- Morigi, G., Franke-Arnold, S., & Oppo, G.-L. (2002). Phase-dependent interaction in a four-level atomic configuration. *Physical Review A*, 66(5), 053409.
- Mundrarain, D., & Orszag, M. (2007). Decoherence-free subspace and entanglement by interaction with a common squeezed bath. *Physical Review A*, 75, 040303(R).
- Narducci, L. M., Scully, M. O., Oppo, G.-L., Ru, P., & Tredicce, J. R. (1990). Spontaneous emission and absorption properties of a driven three-level system. *Physical Review A*, 42(3), 1630.
- Natali, S., & Ficek, Z. (2007). Temporal and diffraction effects in entanglement creation in an optical cavity. *Physical Review A*, 75(4), 042307.
- Nielsen, M. A., & Chuang, I. L. (2000). *Quantum Computation and Quantum Information*. Cambridge, MA: Cambridge University Press.
- Niu, Y., & Gong, S. (2006). Enhancing kerr nonlinearity via spontaneously generated coherence. *Physical Review A*, 73(5), 053811.
- Orszag, M., Ramírez, R., Retamal, J. C., & Saavedra, C. (1994). Quantum cooperative effects in a micromaser. *Physical Review A*, 49(4), 2933.
- Östreich, T. (1994). Exchange effects on cooperative radiation interaction in a two-atom model. *Physical Review A*, 50, 2621.
- Pálffy, A., Keitel, C. H., & Evers, J. (2009). Single-photon entanglement in the kev regime via coherent control of nuclear forward scattering. *Physical Review Letters*, 103(1), 017401.
- Paspalakis, E., Keitel, C. H., & Knight, P. L. (1998). Fluorescence control through multiple interference mechanisms. *Physical Review A*, 58(6), 4868.
- Paspalakis, E., & Knight, P. L. (1998). Phase control of spontaneous emission. *Physical Review Letters*, 81(2), 293.
- Pavolini, D., Crubellier, A., Pillet, P., Cabaret, L., & Liberman, S. (1985). Experimental evidence for subradiance. *Physical Review Letters*, 54, 1917.
- Petrov, E. P., Bogomolov, V. N., Kalosha, I. I., & Gaponenko, S. V. (1998). Spontaneous emission of organic molecules embedded in a photonic crystal. *Physical Review Letters*, 81, 77.
- Plenio, M. B., & Huelga, S. F. (2002). Entangled light from white noise. *Physical Review Letters*, 88, 197901.
- Plenio, M. B., & Knight, P. L. (1998). The quantum-jump approach to dissipative dynamics in quantum optics. *Reviews of Modern Physics*, 70(1), 101.
- Polder, D., & Schuurmans, M. F. H. (1976). Resonance fluorescence from a $j = 1/2$ to $j = 1/2$ transition. *Physical Review A*, 14(4), 1468.
- Power, E. A., & Zienau, S. (1959). Coulomb gauge in non-relativistic quantum electrodynamics and the shape of spectral lines. *Philosophical transactions of the Royal Society of London. Series A*, 251, 427.
- Prior, Y., Bogdan, A. R., Dagenais, M., & Bloembergen, N. (1981). Pressure-induced extra resonances in four-wave mixing. *Physical Review Letters*, 46, 111.
- Protopapas, M., & Knight, P. L. (1995). Phase control in two-colour multiphoton ionization. *Journal of Physics B*, 28, 4459.
- Purcell, E. M. (1946). Spontaneous emission probabilities at radio frequencies. *Physical Review*, 69, 681.
- Puri, R. R. (2001). *Mathematical methods of quantum optics*. Berlin: Springer.
- Quang, T., Woldeyohannes, M., John, S., & Agarwal, G. S. (1997). Coherent control of spontaneous emission near a photonic band edge: A single-atom optical memory device. *Physical Review Letters*, 79(26), 5238.
- Rudolph, T. G., Ficek, Z., & Dalton, B. J. (1995). Two-atom resonance fluorescence in running- and standing-wave laser fields. *Physical Review A*, 52(1), 636.
- Saffman, M., Walker, T. G., & Molmer, K. (2010). Quantum information with rydberg atoms. *Review of Modern Physics*, 82, 2313.

- Sakurai, J. J. (1994). *Modern quantum mechanics*. Reading, MA: Addison-Wesley.
- Scheibner, M., Schmidt, T., Worschech, L., Forchel, A., Bacher, G., Passow, T., et al., (2007). Superradiance of quantum dots. *Nature Physics*, 3, 106.
- Schmid, S. I., & Evers, J. (2008). Dipole-dipole interaction between orthogonal dipole moments in time-dependent geometries. *Physical Review A*, 77, 013822.
- Schmid, S. I., & Evers, J. (2009). Interplay of vacuum-mediated inter- and intraatomic couplings in a pair of atoms. *Physical Review A*, 81, 063805.
- Schmidt, H., Campman, K. L., Gossard, A. C., & Imamoğlu, A. (1997). Tunneling induced transparency: Fano interference in intersubband transitions. *Applied Physics Letters*, 70(25), 3455.
- Schriemer, H. P., van Driel, H. M., Koenderink, A. F., & Vos, W. L. (2001). Modified spontaneous emission spectra of laser dye in inverse opal photonic crystals. *Physical Review A*, 63, 011801.
- Schulman, L. S. (1997). Observational line broadening and the duration of a quantum jump. *Journal of Physics A: Mathematical and General*, 30, L293.
- Schumacher, D. W., Weihe, F., Muller, H. G., & Bucksbaum, P. H. (1994). Phase dependence of intense field ionization: A study using two colors. *Physical Review Letters*, 73(10), 1344.
- Scully, M. O., & Svidzinsky, A. A. (2009). The super of superradiance. *Science*, 325, 1510.
- Scully, M. O., & Zhu, S. Y. (1998). Anisotropic vacuum-induced interference in decay channels. *Science*, 281, 1973.
- Scully, M. O., & Zubairy, M. S. (1997). *Quantum Optics*. Cambridge, MA: Cambridge University Press.
- Shabani, A., & Lidar, D. A. (2005). Theory of initialization-free decoherence-free subspaces and subsystems. *Physical Review A*, 72, 042303.
- Shahriar, M. S., & Hemmer, P. R. (1990). Direct excitation of microwave-spin dressed states using a laser-excited resonance raman interaction. *Physical Review Letters*, 65(15), 1865.
- Shpaisman, H., Wilson-Gordon, A. D., & Friedmann, H. (2005). Electromagnetically induced waveguiding in double- Λ systems. *Physical Review A*, 71(4), 043812.
- Shvets, G., Fisch, N. J., Pukhov, A., & ter Vehn, J. M. (1998). Superradiant amplification of an ultrashort laser pulse in a plasma by a counterpropagating pump. *Physical Review Letters*, 81, 4879.
- Skornia, C., von Zanthier, J., Agarwal, G. S., Werner, E., & Walther, H. (2001). Monitoring the dipole-dipole interaction via quantum jumps of individual atoms. *Physical Review A*, 64, 053803.
- Skribanowitz, N., Herman, I. P., MacGillivray, J. C., & Feld, M. S. (1973). Observation of dicke superradiance in optically pumped hf gas. *Physical Review Letters*, 30, 309.
- Smith, A. M., & Burnett, K. (1991). Effect of long-range collisions between atoms on laser cooling. *Journal of the Optical Society of America B*, 8, 1592.
- Smith, A. M., & Burnett, K. (1992a). Analytical study of long-range collisions between two atoms undergoing laser cooling. *Journal of the Optical Society of America B*, 9, 1256.
- Smith, A. M., & Burnett, K. (1992b). Effect of diffusion on laser cooling of atoms with long-range collisions. *Journal of the Optical Society of America B*, 9, 1240.
- Smith, A. M., Burnett, K., & Cooper, J. (1992). Calculating the diffusion coefficient for laser cooling of atoms with long-range collisions. *Physical Review A*, 46, 4065.
- Spani Molella, L., Rinkleff, R.-H., & Danzmann, K. (2005). Role of the coupling laser in electromagnetically induced absorption. *Physical Review A*, 72, 041802.
- Sultana, S., & Zubairy, M. S. (1994). Effect of finite bandwidth on refractive-index enhancement and lasing without inversion. *Physical Review A*, 49, 438.
- Taichenachev, A. V., Tumaikin, A. M., & Yudin, V. I. (1999a). Electromagnetically induced absorption in a four-state system. *Physical Review A*, 61(1), 011802.

- Taichenachev, A. V., Tumaikin, A. M., & Yudin, V. I. (1999b). Electromagnetically induced absorption in a four-state system. *Physical Review A*, 61(1), 011802.
- Tan, H.-t., Xia, H.-x., & Li, G.-x. (2009). Quantum interference and phase-dependent fluorescence spectrum of a four-level atom with antiparallel dipole moments. *Journal of Physics B*, 42, 125502.
- Trippenbach, M., Gao, B., Cooper, J., & Burnett, K. (1992a). Slow collisions between identical atoms in a laser field: Application of the born and markov approximations to the system of moving atoms. *Physical Review A*, 45, 6539.
- Trippenbach, M., Gao, B., Cooper, J., & Burnett, K. (1992b). Slow collisions between identical atoms in a laser field: The spectrum of redistributed light. *Physical Review A*, 45, 6555.
- Turchette, Q. A., Wood, C. S., King, B. E., Myatt, C. J., Leibfried, D., Itano, W. M., et al., (1998). Deterministic entanglement of two trapped ions. *Physical Review Letters*, 81(17), 3631.
- Varada, G. V., & Agarwal, G. S. (1991). Microscopic approach to correlation-induced frequency shifts. *Physical Review A*, 44(11), 7626.
- Varada, G. V., & Agarwal, G. S. (1992). Two-photon resonance induced by the dipole-dipole interaction. *Physical Review A*, 45(9), 6721.
- Wang, D.-Z., & Gao, J.-Y. (1995). Effect of doppler broadening on optical gain without inversion in a four-level model. *Physical Review A*, 52, 3201.
- Wang, J., Wiseman, H. M., & Ficek, Z. (2000). Quantum interference in the fluorescence of a molecular system. *Physical Review A*, 62, 013818.
- Weisskopf, V., & Wigner, E. (1930). Berechnung der natürlichen linienbreite auf grund der diracschen lichttheorie. *Zeitschrift fr Physik A*, 63, 54.
- Wilson, G. A., Meduri, K. K., Sellin, P. B., & Mossberg, T. W. (1994). Inversionless gain in driven three-level ssv-type atoms: A comparison of broadband and monochromatic excitation. *Physical Review A*, 50, 3394.
- Woolley, R. G. (1971). Molecular quantum electrodynamics. *Proceedings of the Royal Society of London A*, 321, 557.
- Xia, H.-R., Ye, C.-Y., & Zhu, S.-Y. (1996). Experimental observation of spontaneous emission cancellation. *Physical Review Letters*, 77(6), 1032.
- Xu, J.-P., Yang, Y.-P., Lin, Q., & Zhu, S.-Y. (2009). Spontaneous decay of a two-level atom near the left-handed slab. *Physical Review A*, 79(4), 043812.
- Yablonovitch, E. (1987). Inhibited spontaneous emission in solid-state physics and electronics. *Physical Review Letters*, 58, 2059.
- Yang, Y., Fleischhauer, M., & Zhu, S.-Y. (2003). Spontaneous emission in a photonic crystal near the band edge: Field versus population dynamics. *Physical Review E*, 68(1), 015602.
- Yang, X., Sun, Z., Zhang, S., Ding, L., & Wang, Z. (2005). Collision-induced destructive quantum interference. *Journal of Physics B: Atomic, Molecular and Optical Physics*, 38(14), 2519.
- Yang, Y., Xu, J., Chen, H., & Zhu, S. (2008). Quantum interference enhancement with left-handed materials. *Physical Review Letters*, 100, 043601.
- Yannopapas, V., Paspalakis, E., & Vitanov, N. V. (2009). Plasmon-induced enhancement of quantum interference near metallic nanostructures. *Physical Review Letters*, 103(6), 063602.
- Zanardi, P. (1997). Dissipative dynamics in a quantum register. *Physical Review A*, 56, 4445.
- Zhang, Y., Khadka, U., Anderson, B., & Xiao, M. (2009). Temporal and spatial interference between four-wave mixing and six-wave mixing channels. *Physical Review Letters*, 102(1), 013601.
- Zheng, H., Zhu, S. Y., & Zubairy, M. S. (2008). Quantum zeno and anti-zeno effects: Without the rotating-wave approximation. *Physical Review Letters*, 101(20), 200404.
- Zhou, L., Gan, Z.-W., & Li, G.-X. (2004). Quantum interference between decay channels of a three-level atom placed between two parallel plates. *Chinese Physics Letters*, 21, 1518.

- Zhou, P., & Swain, S. (1996). Ultranarrow spectral lines via quantum interference. *Physical Review Letters*, 77(19), 3995.
- Zhou, P., & Swain, S. (1997). Quantum interference in probe absorption: Narrow resonances, transparency, and gain without population inversion. *Physical Review Letters*, 78, 832.
- Zhou, P., & Swain, S. (2000). Cavity engineering of quantum interference. *Optics Communications*, 179, 267.
- Zhu, S.-Y., Chan, R. C. F., & Lee, C. P. (1995). Spontaneous emission from a three-level atom. *Physical Review A*, 52(1), 710.
- Zhu, S.-Y., Chen, H., & Huang, H. (1997). Quantum interference effects in spontaneous emission from an atom embedded in a photonic band gap structure. *Physical Review Letters*, 79(2), 205.
- Zhu, S.-Y., & Scully, M. O. (1996). Spectral line elimination and spontaneous emission cancellation via quantum interference. *Physical Review Letters*, 76(3), 388.
- Zhu, S.-Y., Yang, Y., Chen, H., Zheng, H., & Zubairy, M. S. (2000). Spontaneous radiation and lamb shift in three-dimensional photonic crystals. *Physical Review Letters*, 84, 2136.
- Zhu, S. Y., Li, G. X., Yang, Y. P., & Li, F. L. (2003a). Spontaneous emission in three-dimensional photonic crystals with an incomplete band gap. *Europhysics Letters*, 62, 210.
- Zwanzig, R. (1961). Statistical Mechanics of Irreversibility. In W. E. Brittin, B. W. Downs, & J. Downs (Eds.), *Lectures in theoretical physics* (Vol. 3, p. 106). New York: Interscience.

This page intentionally left blank

CHAPTER 4

Adaptive Lens

Guoqiang Li

*University of Missouri – St. Louis, College of Optometry,
Department of Physics and Astronomy,
St. Louis, USA*

Contents		
1.	Introduction	200
2.	Adaptive Liquid Crystal Lens	203
2.1.	Liquid Crystal Cell	203
2.2.	Liquid Crystal Lens	207
2.3.	Refractive Liquid Crystal Lens Using Discrete Electrodes	208
2.4.	Diffractive Liquid Crystal Lens Using Discrete Electrodes	211
2.5.	Liquid Crystal Lens Based on Hole-Patterned Electrode	242
2.6.	Liquid Crystal Lens Formed by a Glass/Polymer Lens/Shell and Flat LC Layer(s)	249
2.7.	Modal Liquid Crystal Lens Based on Resistive Electrode	252
2.8.	Lens Using Polymer/Liquid Crystal Composites	254
2.9.	Microlens with Hybrid Alignment	256
2.10.	Polarization-Independent LC Lens	258
3.	Adaptive Liquid Lens	258
3.1.	Liquid Lenses Based on Fluid-Membrane Interaction	259
3.2.	Liquid Lenses Based on Electrowetting Effect	264
3.3.	Liquid Microlenses Based on Dielectrophoretic Effect	268
3.4.	Liquid Microlenses Based on Hydrogel and Thermal Effect	273

4.	Examples of Applications of the Adaptive Lenses	274
4.1.	Correction of Presbyopia	274
4.2.	Zoom Lens, Optical Tweezer, and Biomedical Imaging	276
4.3.	Aberration Correction	277
5.	Conclusion	278
	Acknowledgments	278
	References	278

1. INTRODUCTION

Adaptive or varifocal lenses with variable focusing powers have attracted much attention in the last two decades because of their wide applications in vision care, consumer electronics such as digital cameras, aberration correction, optical interconnects, and three-dimensional biomedical imaging. The focal power of an optical system is usually changed by nonlinear movement of lenses with spherical or cylindrical powers along the optical axis and such a system consists of several lens components (Back & Lowen, 1954, 1958; Bergstein, 1958). It requires mechanic translation and might be bulky. Detailed discussion of optical zoom lenses is not covered here. In the late 1960s, Luis Alvarez and William Humphrey (Alvarez, 1967; Alvarez, 1978; Alvarez & Humphrey, 1970), and Adolf Lohmann (Lohmann, 1964) invented independently new types of varifocal composite lenses based on lateral rather than longitudinal shifts of two lenses with conjugate, rotationally asymmetric, aspheric surfaces. The Alvarez lens and the Lohmann lens contain two transmissive refractive plates, each having a plano surface and a surface shaped in a two-dimensional cubic profile. The sag or the z coordinate of the cubic-type surface can be represented by the following general expression

$$z_1 = A_x x^3 + A'_x x^2 y + A_y y^3 + A'_y x y^2 + B x^2 + C x y + D x + E, \quad (1.1)$$

where $A_x, A'_x, A_y, A'_y, B, C, D$, and E are the coefficients of the " x^3 ," " $x^2 y$," " y^3 ," " $x y^2$," " x^2 ," " $x y$," and " x " terms, respectively, while " E " is a term for constant thickness. In the case that the noncubic faces are planar surfaces, the second-order terms of Equation (1.1) (coefficients B, C , and D) are usually set to zero.

Alvarez lens satisfies: $A'_x = A_y = 0$, and Lohmann lens: $A'_x = A'_y = 0$.

Figure 1 illustrates two configurations for the Alvarez and Lohmann lenses (Barbero, 2009): the two cubic surfaces facing outward (the upper part) and the two cubic surfaces facing inward (the lower part). The two

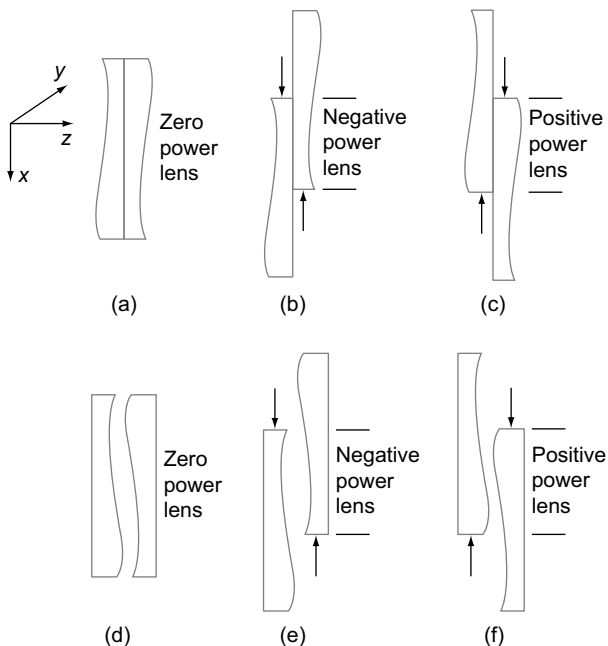


FIGURE 1 Alvarez–Lohmann lenses. Top, outer cubic surfaces configuration at: (a) neutral position. (b) Negative power addition. (c) Positive power addition. Bottom, inner cubic surfaces configuration at: (d) neutral position. (e) Negative power addition. (f) Positive power addition. Note that for the outer cubic surfaces configuration, there must be a space between both lenses to avoid collision when the shift is done to achieve positive power addition (f).

cubic surfaces are made to be the inverse of each other, so that when both plates are placed with their vertices on the optical axis, the induced phase variations cancel out and there is no power. This state is also called a “do-nothing machine” (Caulfield, 2002). However, if the two plates undergo a relative lateral translation, a phase variation is induced that is the differential of the cubic surface profiles, resulting in a quadratic phase profile – or, in other words, optical power. Relative movements in the x or y direction induce cylindrical power independently in orthogonal directions. Combined movements can produce circular, elliptical, or cylindrical phase profiles. For example, if both lens components of the Alvarez lens are moved by a distance Δ in the opposite directions along the x coordinate and assume $A_x = A'_y = A$, it can be deduced (using Equation (1.1)) that all terms containing “ x ” and “ y ” cancel out leaving only the $(x^2 + y^2)$ term and some constants. The total thickness is equal to $2A\Delta(x^2 + y^2)$,

indicating that symmetrical movement of the two plates results in a varifocal spherical lens and the focal length is a function of the coefficient "A" and the displacement "Δ." Based on the property of a thin lens in phase transformation (Goodman, 2005), the paraxial focal length can be written as

$$f = \frac{1}{4A\Delta(n - n')}, \quad (1.2)$$

where n is the refractive index of the lens material and n' is the refractive index of the surrounding medium. It should be noted that for the configuration with the cubic surfaces facing inward, there needs to be a space between the two components to avoid collision during the shifts.

The Alvarez lens has been applied to Humphrey analyzer (Humphrey, 1976), scanning microscope (Rege, Tkaczyk, & Descour, 2004), intraocular accommodative lens (Simonov, Vdovin, & Rombach, 2006), and spectacle lenses (Spivey, 2008). Recent analysis (Barbero, 2009) shows that for the same power and lateral shifts, the Lohmann lens is thinner and provides better optical performance. It also shows that the inner cubic surface configuration provides slightly better optical performance. Recent advances in microfabrication technologies allow us to make both refractive and diffractive Alvarez or Lohmann lenses.

In the late 1960s, Lohmann and Paris also described varifocal spherical zone plates as a moiré effect created by translations and rotations of the basic grids, as well as varifocal cylindrical zone plates formed by translations (Lohmann & Paris, 1967). By adding a linear carrier frequency to the basic grids described by curves of cube functions, the focusing power can be varied over a considerable range by relative translation of the grids, and it increases the clarity of moiré fringes by making their period more uniform (Burch & Williams, 1977; Lohmann, 1970). Elliptical and hyperbolic moiré patterns can be generated too. For binary amplitude basic grids, the light efficiency of the moiré diffractive optical elements is low ($1/\pi^4 \approx 1.03\%$) and it can be increased to $16/\pi^4 (\approx 16.43\%)$ if binary phase basic grids are used. Further improvement of the light efficiency to the values up to 100% by superposition of two conjugated kinoforms was first proposed by Lohmann (1970) and then realized experimentally (Barton et al., 2000; Kołodziejczyk & Jaroszewicz, 1993). Equilateral hyperbolic zone plates with variable focal length has been formed as moiré patterns by a mutual rotation of two identical basic grids by a proper choice of the basic grid's particular form (Jaroszewicz, Kołodziejczyk, Mira, Henao, & Bará, 2005). Advantages of this approach include a constant aperture of the created element during the mutual movement of basic grids, lack of aberrations because of their undesired mutual lateral displacements

and high-diffraction efficiency of the binary phase version. Very recently optical power can be adjusted continuously by a mutual rotation of one diffractive optical element with respect to the other without eccentric displacements (Bernet & Ritsch-Marte, 2008).

Although the Alvarez and Lohmann lenses use only two conjugate lenses and the relative movement is linear and simpler in comparison with the traditional varifocal lens system based on longitudinal movements of the lenses, it is attractive to develop single-element adaptive lenses. There are two kinds of adaptive lenses: liquid crystal (LC) lens and liquid lens. The former is based on tuning the refractive index of the liquid crystal, and the latter is based on changing the shape of the liquid. These two kinds of adaptive lenses and their applications are reviewed below. Although the majority of the articles on adaptive lenses are covered here, the list is by no means complete.

2. ADAPTIVE LIQUID CRYSTAL LENS

2.1. Liquid Crystal Cell

Liquid crystals are mesophases between isotropic liquids and crystalline solids (Yang & Wu, 2006). They can flow and take the shape like regular liquids and exhibit optical birefringence like crystalline solids. The constituents are elongated rod-like or disc-like organic molecules. Nematic phase (Figure 2(a)) is the most common LC phase, and the molecules have orientational order but no positional order. Nematic LC cells consisting of rod-like molecules are most suited for phase modulation and high transmission of light. Orientational order is the most important property of the LCs. The orientation of the rod-like molecule can be represented by a unit vector \vec{a} , which is along the long axis of the molecule. It has preferred direction, and the average directions of the long axis of the rod-like molecules are parallel to each other at the macroscopic scale. The average direction of the long molecular axis is denoted by the unit vector \vec{n} and called LC director. There is no preferred direction for the short axes and hence the nematic LC is usually optical uniaxial. Because of this feature, nematic LC possesses optical anisotropy property manifested by different indices of refraction. The birefringence is defined by $\Delta n = n_e - n_o$, where n_e and n_o are refractive indices for the extraordinary and ordinary beams, respectively. The electrical properties of the LC are represented by the dielectric permittivities parallel and perpendicular to the long molecular axis \vec{a} , $\varepsilon_{||}$, and ε_{\perp} . The difference $\Delta\varepsilon = \varepsilon_{||} - \varepsilon_{\perp}$ is the dielectric anisotropy, which can be either positive or negative. LCs respond to the rms value of an applied AC field. The elastic properties of the LC are

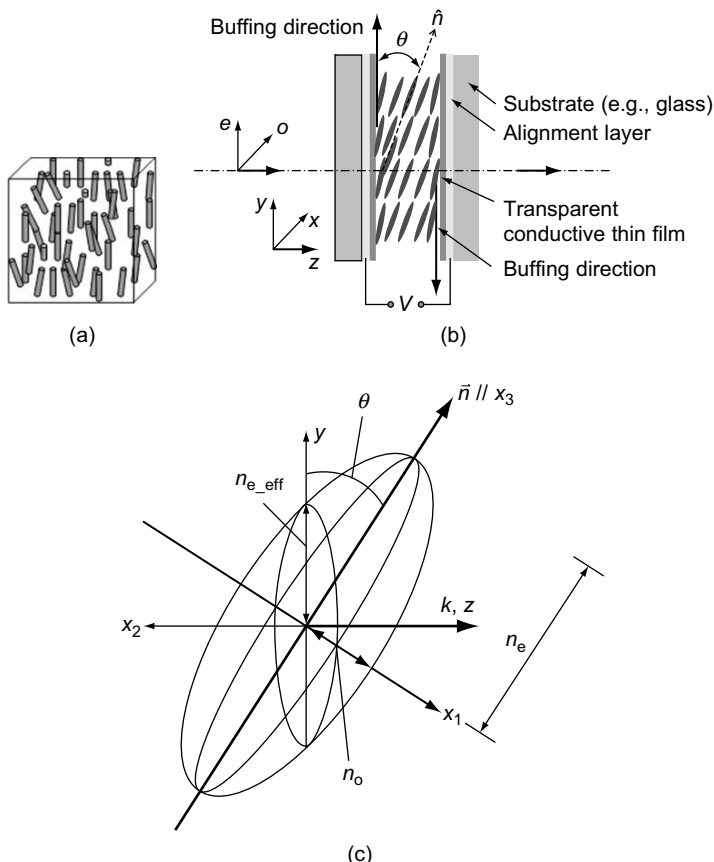


FIGURE 2 (a) Nematic phase of rod-like LC molecules. (b) Homogeneously aligned nematic LC cell. (c) Uniaxial LC molecule ellipsoid of refractive index.

characterized by the elastic constants K_{11} , K_{22} , and K_{33} for splay, twist, and bend, respectively, and they are temperature dependent.

Homogeneously aligned nematic LCs with positive dielectric anisotropy are most widely used for tunable devices based on phase modulation. Figure 2(b) shows a typical LC cell of this kind. LCs are sandwiched between two substrates coated with transparent conductive thin films such as indium tin oxide (ITO) and an alignment layer. The alignment layer can be polyimide, polyvinyl alcohol (PVA), or nylon. In the absence of external electrical fields, orientation of the LC in the cell is determined by the anchoring condition of the alignment layer. By rubbing the surface of the alignment layer, microgrooves along the rubbing direction

can be generated, and the LCs will be homogeneously aligned along the grooves. The LC cell is assembled with antiparallel configuration of the alignment layer. At the boundary between the LC and the alignment layer, pretilt angles of a few degrees can be generated. An LC cell is usually driven by an ac electric field in the lower kHz regime. When an external electrical field is applied to the two ITO electrodes, the LC will reorient because of their dielectric anisotropies. For LCs with positive dielectric anisotropy ($\Delta\epsilon > 0$), they tend to align parallel to the electrical field. For LCs with negative dielectric anisotropy ($\Delta\epsilon < 0$), they tend to align perpendicular to the electrical field. The field-induced reorientation is called *Freedericksz transition*. The reorientation of the LC happens when the amplitude of the applied voltage is higher than the threshold voltage given by

$$V_{\text{th}} = dE_{\text{th}} = \pi \sqrt{\frac{K_{11}}{\epsilon_0 \Delta\epsilon}}, \quad (2.3)$$

where E_{th} is the threshold field and ϵ_0 is the permittivity of free space. The orientation of the LC director in the applied electrical field determines the electric energy, which is part of the total free energy. The total free energy is the summation of the electric energy and the elastic energy. The equilibrium director configuration is obtained by minimizing the total free energy of the system. Finite difference method or finite-element method can be used to model the electric field distribution, and the LC director map across the LC cell based on the continuum theory. Details for the analysis are not discussed here. One important parameter for LC cells is the response time, including the turn-on time and the turn-off time. In a first approximation, the turn-on time can be approximated as

$$\tau_{\text{on}} = \frac{\gamma_1 d^2}{K\pi^2}, \quad (2.4)$$

where γ_1 is the rotational viscosity of the LC. And the turn-off time is

$$\tau_{\text{off}} = \frac{\gamma_1}{K} \frac{d^2}{\pi^2 [(V/V_{\text{th}})^2 - 1]}, \quad (2.5)$$

where V is the applied voltage. Equations (2.4) and (2.5) imply that the response and recovery time of LC cell is proportional to the square of the thickness of the cell. Typical nematic LC cells have a response time in the order of millisecond.

As shown in Figure 2(b), the original orientation of the liquid crystal molecule is determined by the buffering direction. The long axis (optic axis) of the liquid crystal molecule is close to the y axis (vertical direction in the figure). Light is normally incident to the LC cell and propagates along the z direction. When an appropriate voltage is applied, the LC director is titled in the YOZ plane by an angle θ from the y axis. The LC director pattern is symmetric in the z direction. Based on the ellipsoid of the wave vector or the ellipsoid of the refractive index (Born & Wolf, 1999, Figure 2(c)), the effective refractive index of the extraordinary beam (with a polarization state parallel to the y axis) is given by

$$n'_e(\theta) = \frac{n_o n_e}{\sqrt{(n_e^2 \sin^2 \theta + n_o^2 \cos^2 \theta)}}. \quad (2.6)$$

For an extraordinary beam, initially it has the maximum refractive index n_e . With the increase of the applied voltage, the tilt angle θ at a particular location (r, z) increases and the effective refractive index n'_e decreases, and when a saturation voltage is reached, the optic axis of the molecule is aligned horizontally, and the effective refractive index of n'_e reaches the minimum and equals to n_o . The refractive index for the ordinary beam (horizontally polarized) is always the same. So the electro-optic effect modulates the effective refractive index of the extraordinary beam. Because the effective refractive index n'_e is a spatially variant as a function of r and z , at a particular location with radius r from the center of the device, the average refractive index for the extraordinary beam is

$$n_{e,\text{avg}} = \frac{1}{d} \int_0^d n'_e(\theta(r, z)) dz, \quad (2.7)$$

and the average birefringence is given by

$$\Delta n_{\text{avg}} = \frac{1}{d} \int_0^d n'_e(\theta(r, z)) dz - n_o. \quad (2.8)$$

The phase retardation between the extraordinary beam and the ordinary beam takes the form

$$\Delta\varphi(r) = k \left[\int n'_e(\theta) dz - n_o d \right]. \quad (2.9)$$

2.2. Liquid Crystal Lens

The concept of LC adaptive lens was first published by Bricot, Hareng, and Spitz (1977) in their patent, where LCs are filled in the refractive lens chamber and the substrate has no power. Two uniform conductive electrodes and alignment layers are coated on the inner surfaces of the lens chamber, and the LCs are homogeneously aligned by rubbing the surfaces of the alignment layers. The LC lens power is determined by the effective refractive index. In 1979, Sato reported LC composite lens by immersing LC into a lens-shaped cell as shown in Figure 3 (Sato, 1979). The glass lens substrate can be either plano-convex or plano-concave shape, and the LC cell is processed in the same manner. In both cases, the focal length of the LC lens is given by

$$f_{LC} = \frac{R}{n_{e,eff} - 1}, \quad (2.10)$$

where R is the radius of the curved surface of the LC lens. Assuming $n_{e,eff}$ can be tuned from n_e to n_o for the extraordinary beam, the focal length of the LC lens can be varied from $f_e = R/(n_e - 1)$ to $f_o = R/(n_o - 1)$, and the focal length of the composite lens equals to

$$f = \left(\frac{1}{f_{LC}} + \frac{1}{f_{glass}} \right)^{-1}. \quad (2.11)$$

These two LC lens structures are relatively simple. However, there are several disadvantages. The thickness of the LC lens becomes very large

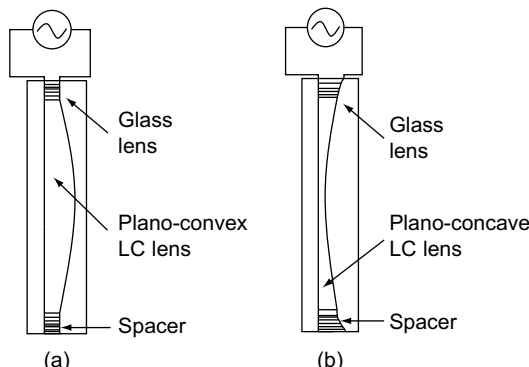


FIGURE 3 Lens-shaped LC cell. (a) Plano-convex LC lens. (b) Plano-concave LC lens (Sato, 1979).

at the center of the plano-convex lens or the peripheral region of the plano-concave lens, and this increase in thickness results in very slow speed of the response and recovery properties. For example, for a typical plano-convex LC lens with an aperture of 20 mm and a focal length of 20 cm, the thickness at the center is about 0.5 mm. As a result of the large variation of the thickness of the LC layer from the center to the periphery, the electric field inside the LC lens is not uniform, and thus, the effective refractive index is not uniform across the lens aperture. This means that the focal length at the center may be different from that at the periphery. Furthermore, the transmission of the lens is reduced by absorption and scattering of the light when the LC lens is thick. These issues can be overcome by using a Fresnel lens as the substrate for the LC lens (Fowler & Pateras, 1990; Sato, Sugiyama, & Sato, 1985). If the thickness of the LC lens is reduced by 10 times, the response time can be improved by two orders of magnitude.

Since then various adaptive LC lenses have been demonstrated by using different techniques to generate the phase profile for the lens. The phase profile can be induced by homogeneous LC but inhomogeneous electric field using discrete electrodes, hole-patterned electrode, resistive control electrode, spherical-shaped electrode, or homogeneous electric field but inhomogeneous LC based on polymer/LC composites, patterned or hybrid alignment of LCs on the cell walls. By using inhomogeneous electric field and inhomogeneous LCs, polarization-independent lenses are made possible.

2.3. Refractive Liquid Crystal Lens Using Discrete Electrodes

Consider a material of thickness d and refractive index distribution $n(x, y)$ centered on the z axis. The phase retardation is given by

$$\varphi(x, y) = kdn(x, y), \quad (2.12)$$

In order to form a lens, we assume the refractive index can be varied as

$$n(r) = A + Br^2, \quad (2.13)$$

where $r^2 = x^2 + y^2$.

At the center of the cell ($r = 0$), the refractive index reaches the maximum value

$$n(r = 0) = n_e. \quad (2.14)$$

At the edge of the cell, the refractive index is an intermediate value between n_e and n_o :

$$n(r = r_0) = n_i, (n_o \leq n_i < n_e). \quad (2.15)$$

Using the boundary conditions in Equations (2.14) and (2.15), Equation (2.13) becomes

$$n(r) = n_e + \left(\frac{n_i - n_e}{r_0^2} \right) r^2 = n_e - \frac{n_e - n_i}{r_0^2} r^2. \quad (2.16)$$

Thus the transmission function is

$$\begin{aligned} t(r) &= \exp[jkd_n(r)] = \exp\left[jkd\left(n_e - \frac{n_e - n_i}{r_0^2}\right)r^2\right] \\ &= \exp(jkd_n) \exp\left(-jkd\frac{n_e - n_i}{r_0^2}r^2\right). \end{aligned} \quad (2.17)$$

As we know, the phase transformation of a thin lens takes the following form (Goodman, 2005):

$$t(x, y) = \exp(jknd_0) \exp\left(-jk\frac{x^2 + y^2}{2f}\right), \quad (2.18)$$

where k is the wave number, n is the refractive index of the lens material, d_0 is the thickness of the center of the lens, and f is the paraxial focal length. The first term is a constant, and the second term represents the phase profile.

Comparing Equations (2.17) and (2.18), we have the focal length of the lens

$$f = \frac{r_0^2}{2d(n_e - n_i)}. \quad (2.19)$$

Because $n_o \leq n_i < n_e$, the range of the lens power is given by

$$0 < \frac{1}{f} \leq \frac{2d(n_e - n_o)}{r_0^2}. \quad (2.20)$$

Therefore, the power of the refractive lens is determined by the birefringence $\Delta n = n_e - n_o$. For the commonly used nematic LC material E7 (from Merck), at 20°C, $n_o = 1.5252$, $n_e = 1.7578$, and $\Delta n = 0.2326$ for the wavelength 546.1 nm. According to Equations (2.19) and (2.20), the focal length (power) of the refractive LC lens is limited by Δn . For large aperture (r_0) lens, the focal length is long, i.e., the power is small. Some high birefringence LCs exist, but their viscosity is too high, resulting in slow response. Therefore, LC lenses based on refractive principle are more suitable for small aperture cases such as microlenses.

The phase modulation of a homogeneously or homeotropically aligned LC cell can be measured by placing the cell in between two crossed polarizers. The normalized light transmittance is given by the general equation:

$$T = \cos^2 \chi - \sin 2\beta \sin 2(\beta - \chi) \sin^2 (\varphi/2), \quad (2.21)$$

where χ is the angle between the polarizer and the analyzer, β is the angle between the polarizer and the initial orientation of the LC director, and $\varphi = 2\pi d \Delta n / \lambda$ is the phase retardation. For crossed polarizer, $\chi = 90^\circ$. If $\beta = 0^\circ$ or 90° , $T = 0$. If $\beta = 45^\circ$, we have

$$T = \sin^2 (\varphi/2). \quad (2.22)$$

Therefore, the phase retardation φ can be calculated from the transmittance measurement.

Because

$$t(x, y) = \exp\left(-jk \frac{x^2 + y^2}{2f}\right) = \exp\left(-jk \frac{x^2}{2f}\right) \exp\left(-jk \frac{y^2}{2f}\right), \quad (2.23)$$

we can use a 1-D array of electrode strips to form a LC cell to achieve the phase transformation of a cylindrical lens and use two orthogonal array of electrodes to achieve the phase transformation of a spherical lens. But the two cylindrical lenses need to be carefully aligned. Both beam focusing and steering can be implemented by LC cells using discrete electrodes (Brinkley, Kowal, & Chu, 1988; Kowal, Cleverly, & Kornreich, 1984; Nouhi & Kowal, 1984).

Using the discrete isolated electrodes, there is a meshing phase error at the boundary of the electrodes because of the fringe field of the electrodes, especially when the interelectrode gap is relatively big. In order to make smooth phase profile and eliminate the need for complicated electronic drivers, several techniques based on resistive network have been proposed. In the article by Chan and Kowal (1997), conductive meshing and conductive ladder meshing methods were used. The conducting meshing design has a uniformly conducting electrode with multiple driving points, and a linear drop of voltage can be generated across the lens aperture. Conductive ladder meshing is a hybrid of conductive meshing and the conventional architecture. It divides a lens into sections, and each section is formed by two addressable electrodes and interpolating electrodes between these two addressable electrodes. A set of discrete linear voltage drops is yielded across the aperture of the lens. Circular electrodes

based on conductive ladder meshing method were fabricated to produce a spherical lens (Sun, Nordin, Kowal, & Wang, 2003). Another nematic LC three-terminal device for optical beam focusing has been proposed by Riza and DeJule (1994). A thin-film-resistor network on the device substrate layer is used to control the voltages on the 98 internal lens electrodes by the use of only one variable external driver. By using a high-resistance thin-film layer of amorphous silicon under the 98-element parallel electrode structure layer, a near-continuous index distribution is generated to form a cylindrical lens. The focal length of this lens is continuously variable from infinity to 12 cm by the use of a variable 1-4-V-peak, 1-kHz square-wave, external terminal control signal. However, the area of the active device that has been demonstrated was only 1×1 mm. It is not easy to fabricate large aperture LC lenses using this technique. In addition, the concept of "hybrid electrode" was also proposed to generate gray-scale electric field and simplify both the electrode design and the requirements on the electrical driver (Klaus, Ide, Hayano, Morokawa, & Arimoto, 1999). A bundle of parallel, very narrow, transparent, low-resistive, stripe-shaped electrodes is connected by means of two lateral, narrow, high-resistive electrodes forming together a broad, stripe-shaped "superelectrode." By applying two different voltages to each terminal of the lateral electrodes, a linear voltage gradient is generated along the lateral electrode as well as across the superelectrode. Two lateral electrodes with respect to a single superelectrode are connected in parallel to guarantee the uniform distribution of the voltage gradient anywhere within the superelectrode. Again only microlenses were fabricated, and it is difficult to apply this approach to LC lenses with larger apertures. It is possible to adopt simplified resistor network for locally linear phase modulation.

2.4. Diffractive Liquid Crystal Lens Using Discrete Electrodes

Recently we have successfully designed, fabricated, and characterized large-aperture, high-performance switchable LC diffractive lenses with discrete ring electrodes and bus lines for power supply.

2.4.1. Background and Analysis

The function of the diffractive lens is based on near-field diffraction by a Fresnel zone pattern. Each point emerging from the structure serves as an emitter of a spherical wave. The optical field at a particular observing point is a summation of the contributions of the emitted spherical waves over the whole structure. Constructive interference of the spherical waves coming from the various points creates a high intensity at the observation point, corresponding to high-diffraction efficiency.

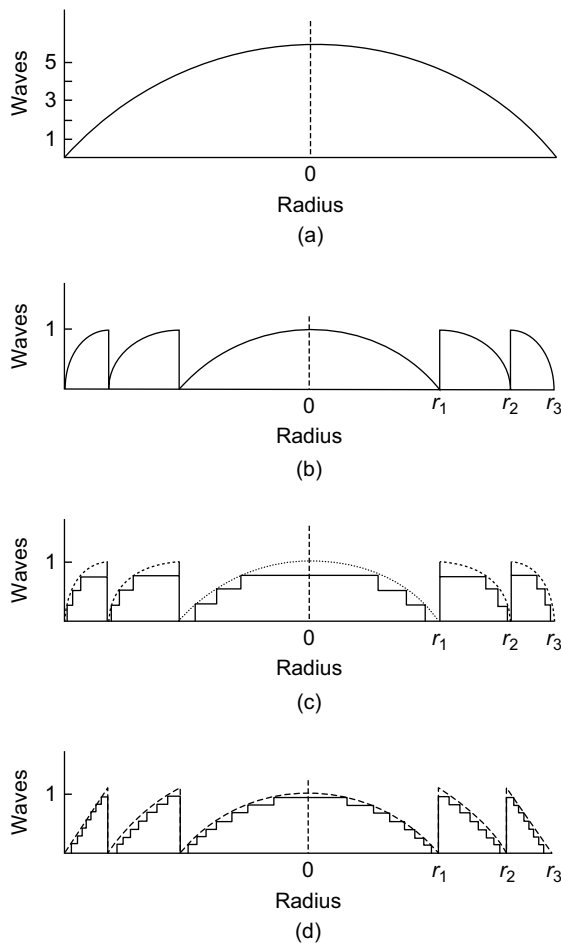


FIGURE 4 Illustration of a diffractive lens: (a) conventional refractive lens. (b) Diffractive lens with continuous quadratic blaze profile. (c) Binary diffractive lens. (d) Fourth-level approximation of the diffractive lens.

The basic structure of a diffractive lens is illustrated in Figure 4. Figure 4(a) shows a part of a refractive lens. By removing the multiple 2π phase retardation from the refractive lens, we obtain a diffractive lens as shown in Figure 4(b). The phase jump at each zone boundary is 2π for the design wavelength λ_0 , and the blazing profile in each zone makes perfect constructive interference at the focal point. Figures 4(c) and 4(d) show fourth-level and eighth-level approximations of the desired phase profile in Figure 4(b), respectively.

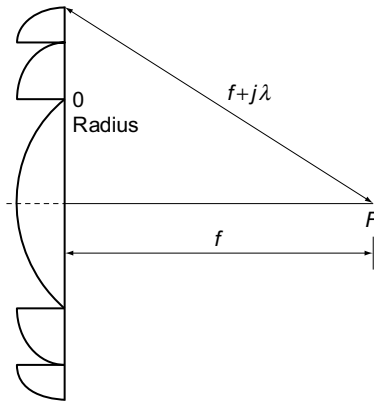


FIGURE 5 Construction of a diffractive lens.

The focal length of the diffractive lens is determined by the period of the zones. As shown in Figure 5, the optical path length differences are multiples of the wavelength. For the j th zone, we have

$$r_j^2 + f^2 = (f + j\lambda)^2. \quad (2.24)$$

For paraxial approximation, $f \gg j\lambda$, the radii of the zones are given by

$$r_j^2 = 2j\lambda f. \quad (2.25)$$

This determines the Fresnel zone pattern, which is periodic in r^2 . The period equals to r_1^2 . The focal length of the diffractive lens is

$$f = \frac{r_1^2}{2\lambda}. \quad (2.26)$$

Usually, the blaze profile in Figure 1(b) is generated by controlling the thickness of the material and it can be reproduced by single-point diamond turning or laser pattern generation. The discrete-step phase profile shown in Figure 1(c) and 1(d) can be reproduced by binary or grayscale photolithography technology. With the rapid progress in microfabrication, high-diffraction lens can be made with these technologies. The diffraction efficiency of an ideal multilevel diffractive lens is given by (Kress & Mey, 2000)

$$\eta = \sin c^2 \left(\frac{1}{L} \right) = \left[\frac{\sin(\pi/L)}{\pi/L} \right]^2, \quad (2.27)$$

where L is the number of phase steps in each zone.

The most important performance parameter for a diffractive lens is diffraction efficiency, which is determined by the phase profile across the lens. Although high-efficiency liquid crystal-based diffractive devices have been demonstrated for beam-steering (e.g., Ferstl & Frisch, 1996; Jepsen & Gerritsen, 1996; Lester, Coulston, & Strudwick, 2006; McManamon et al., 1996; Resler, Hobbs, Sharp, Friedman, & Dorschner, 1996; Slinger et al., 1997; Wang, Wilson, Muller, Maker, & Psaltis, 2000), less effort was given to the development of switchable diffractive lenses. The diffraction efficiencies of the lenses achieved for imaging and other applications were too low, typically around 36% (Dance, 1992; Ferstl and Frisch 1996; Hain et al., 2001; McOwan, Gordon, & Hossack, 1993; Laude, 1998; Ren, Fan, & Wu, 2003; Patel & Rastani, 1991; Williams, Powell, & Purvis, 1989; Wiltshire, 1993). One of the most important applications of the adaptive LC lens is for vision correction. The use of nematic LCs to implement switchable lenses has been proposed earlier but had limited success for ophthalmic applications (Charman, 1993; Smith & Atchison, 1997). The ophthalmic lens has stringent requirements, including high light efficiency, relatively large aperture, fast switching time, low driving voltage, and power-failure-safe configuration. Power-failure-safe configuration means that a loss of electrical power should be safe for critical distance vision task such as driving. None of the previous demonstrations satisfies these requirements simultaneously. The lens-shaped LC cell described above has long response and recovery times resulting from the large thickness of the LC layers (typically $>400\text{ }\mu\text{m}$), and the surface-relief Fresnel lens is optically active in the electrically off-state. The other lens structures to be described later are mainly suitable for micro- or mini-aperture lenses. Some of them require high driving voltages and some of them do not provide the range of focal length needed for ophthalmic applications. Here we use photolithographically patterned ring electrodes to form thin flat diffractive lens with large aperture, fast response time, and a power-failure-safe configuration and overcome these limitations. The first thing to consider is the phase profile of the LC cell formed by multiple discrete electrodes in each zone when each ring electrode is applied a different voltage and the corresponding diffraction efficiency.

The phase profile may be affected by various factors, including the number of phase levels in each zone, the gaps between the electrodes, fringing field effect in the transition area of neighboring zones (the elastic properties of the liquid crystal prohibit a sharp phase wrap between zones; Apter, Efron, & Bahat-Treidel, 2004; Brinkley et al., 1988; Wang et al., 2005), and fabrication errors. The effects of the gaps between the ring electrodes and the fringing field on the lens performance have been analyzed (Li, 2008). The amplitude (intensity) in the focal plane can be calculated

using Fresnel diffraction integral:

$$U(x, y) = \frac{e^{ikz}}{i\lambda z} e^{i\frac{k}{2z}(x^2+y^2)} \iint U(x_1, y_1) e^{i\frac{k}{2z}(x_1^2+y_1^2)} e^{-i\frac{2\pi}{\lambda z}(xx_1+yy_1)} dx_1 dy_1. \quad (2.28)$$

For axially symmetric system, the above expression becomes

$$U(r) = \frac{e^{ikz}}{i\lambda z} e^{i\frac{k}{2z}r^2} \cdot 2\pi \int_0^R J_0\left(\frac{2\pi rr_1}{\lambda z}\right) U(r_1) e^{i\frac{k}{2z}r_1^2} r dr. \quad (2.29)$$

Here, we just show an example. Assume the focal length is 1 m, and the diameter of the lens is 10 mm. Figure 6(a) depicts the normalized intensity distribution around the main focal point for no gap and gaps of various values. When the aperture of the lens is large, the gaps distort the phase profile and hence reduce the diffraction efficiency. The gaps should be kept small. Figure 6(b) illustrates the deviation of the phase profile of one zone from the ideal case caused by the fringing field effect. Type B transition reduces the diffraction efficiency too. The phase modulation for type A and type B can be represented by

$$-\frac{\pi}{4} \frac{e^{a(r-R)} - e^{-a(r-R)}}{e^{a(r-R)} + e^{-a(r-R)}} + c \quad (2.30)$$

and

$$\frac{3\pi}{4} \frac{e^{a(r-R)} - e^{-a(r-R)}}{e^{a(r-R)} + e^{-a(r-R)}} + \frac{3\pi}{4} \quad (2.31)$$

respectively.

With this model, we estimated that for eighth-level LC diffractive lens, if the gap between the neighboring ring electrodes is 1 μ m, the diffraction efficiency can be more than 91% for 10-mm aperture. Detailed analysis and experimental verification of the effect of the interelectrode gaps will be published elsewhere. In order to eliminate the gaps between the electrodes, the odd- and even-numbered electrodes can be interleaved into two layers, which are separated by a SiO₂ insulator layer.

Correspondingly, lenses with three different designs have been demonstrated:

1. All the ring electrodes for modulating the multilevel phase profile are patterned in one layer with a 1- μ m gap between the neighboring electrodes. Lenses with eight phase levels, 10-mm diameters, and focal

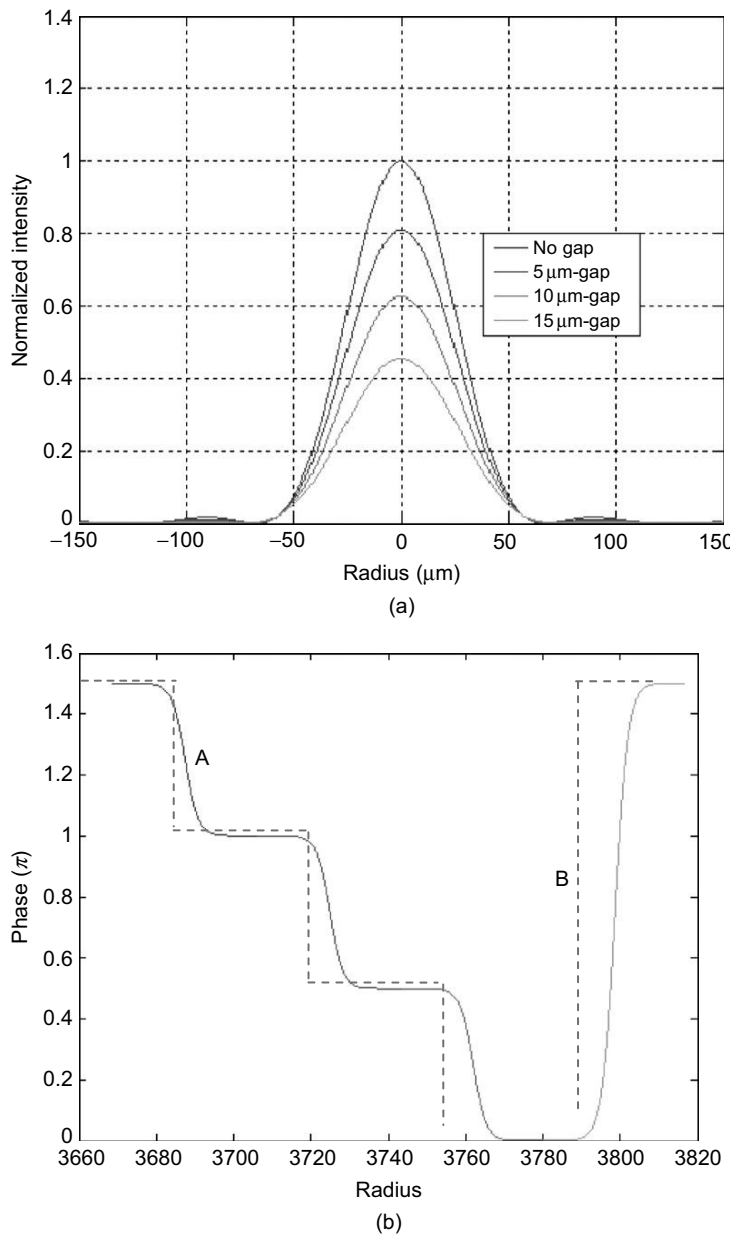


FIGURE 6 Effects of the gaps between the neighboring ring electrodes and the fringing field. (a) Intensity distribution at the focal plane for no gap and gaps of various values. (b) Illustration of the phase profile caused by the fringing field. Dashed line is the ideal phase profile.

lengths of 1 m and 0.5 m (+1.0 diopter and +2 diopter of add power, respectively) have been demonstrated (Li et al., 2006).

2. In order to avoid the lateral gaps between the electrodes and allow high-diffraction efficiency, the odd- and even-numbered ring electrodes are separated in two layers. A preliminary experiment with interleaved electrode pattern has been performed for a fourth-level, 15-mm aperture, 2-diopter lens with the expected performance (Li et al., 2006).
3. A robust design is given with three-layer electrode pattern and two-layer via structures for flexible interconnection and no-gap pattern (Li, Valley, Äyräs, Honkanen, & Peyghambarian, 2007). The microfabricated transparent concentric ring electrodes are distributed in two layers and different voltages are applied to each electrode through bus lines in another layer. Connection between the electrodes and the bus lines is achieved by vias in the third dimension. This design makes it easier to fabricate lenses with higher-level phase steps and larger aperture and overcome the shorts between the electrodes. This method can be used for design of LC lens of any phase levels. It should be noted that, unlike the conventional binary optics, in this design the increase of the phase levels (e.g., to 16 levels) in each zone does not increase the fabrication steps.

2.4.2. Switchable Electro-Optic Diffractive Lens with High Efficiency Based on One-Layer Patterned Electrodes

Here we report on new switchable, flat, liquid crystal diffractive lenses that can adaptively change their focusing power. The operation of these spectacle lenses is based on electrical control of the refractive index of a 5- μm -thick layer of nematic liquid crystal using a circular array of photolithographically defined transparent electrodes. It operates with high transmission, low voltage ($< 2 V_{\text{RMS}}$), fast response ($< 1 \text{ s}$), diffraction efficiency exceeding 90%, small aberrations, and a power-failure-safe configuration. These results represent significant advancement in the state-of-the-art in liquid crystal diffractive lenses for vision care and other applications (Li et al., 2006).

The phase jump at each zone boundary is 2π for the design wavelength. The outer radius of each zone is given by

$$r_m = \sqrt{2m\lambda f}, \quad m = 1, 2, \dots, M, \quad (2.32)$$

where m is a counting index that refers to successive Fresnel zone starting in the center, λ is the wavelength, and f is the focal length. To digitize the

process, the continuous phase profile in each zone is divided into multiple subzones with a series of discrete phase levels ("staircase" structure, Figure 4(d)). The outer radius of each subzone is given by

$$r_{m,n} = \sqrt{2[(m-1) + n/L]\lambda f}, \quad n = 1, 2, \dots, L, \quad (2.33)$$

where L is the number of phase levels per zone and n is the counting index of the individual phase levels. Diffraction efficiency increases by increasing the number of subzones L , reaching maximum values of 40.5, 81.1, and 95.0% for lenses with 2-, 4-, and 8-phase levels per zone, respectively.

Diffractive lenses with eight subzones, 10-mm diameters and focal lengths of 1 m and 0.5 m (+1.0 diopter and +2 diopter of add power, respectively) were demonstrated at the peak of the human photopic response, 555 nm. The schematic drawing of the electrode pattern is shown in Figure 7, and the fabrication procedure is shown in Figure 8. Using photolithographic techniques, concentric and rotationally symmetric transparent indium tin oxide (ITO) electrodes (50 nm in thickness), whose radii were determined by Equation (2.33), were patterned on a float-glass substrate. A 1- μm gap was required between adjacent electrodes to maintain electrical isolation and ensure a smooth transition of the phase profile introduced by the liquid crystal. Over the patterned ITO, a 200-nm-thick electrically insulating layer of SiO_2 is sputtered into which small via openings ($3 \times 3 \mu\text{m}$) were etched, allowing electrical contact to be made to the underlying electrodes. An electrically conductive layer of Al is subsequently sputtered over the insulating layer to fill the vias and contact the electrodes and patterned to form eight independent electrical bus bars (6- μm wide within the lens). Each bus bar connects the discrete phase level electrodes of equal counting index n in all Fresnel zones (as shown in Figure 7) such that only eight external electrical connections (plus one ground connection) are required per lens.

The patterned substrate, as well as an additional substrate with a continuous ITO electrode that acts as the electrical ground, were spin coated with poly(vinyl alcohol) to act as liquid crystal alignment layer. The alignment layers were rubbed with a velvet cloth to achieve homogeneous alignment, and the two substrates were assembled. The commercial nematic liquid crystal E7 (Merck) was used as the electro-optic medium and was filled by capillary action into the empty cell at a temperature more than the clearing point (60°C) and then cooled at 1°C/min to room temperature. The cell was then sealed with epoxy and connected to the drive electronics. The drive electronics consist of custom fabricated integrated circuits that contain eight independently controlled output channels. Each channel generates a modified square waveform with variable peak-to-peak amplitude between 0 and 5 V.

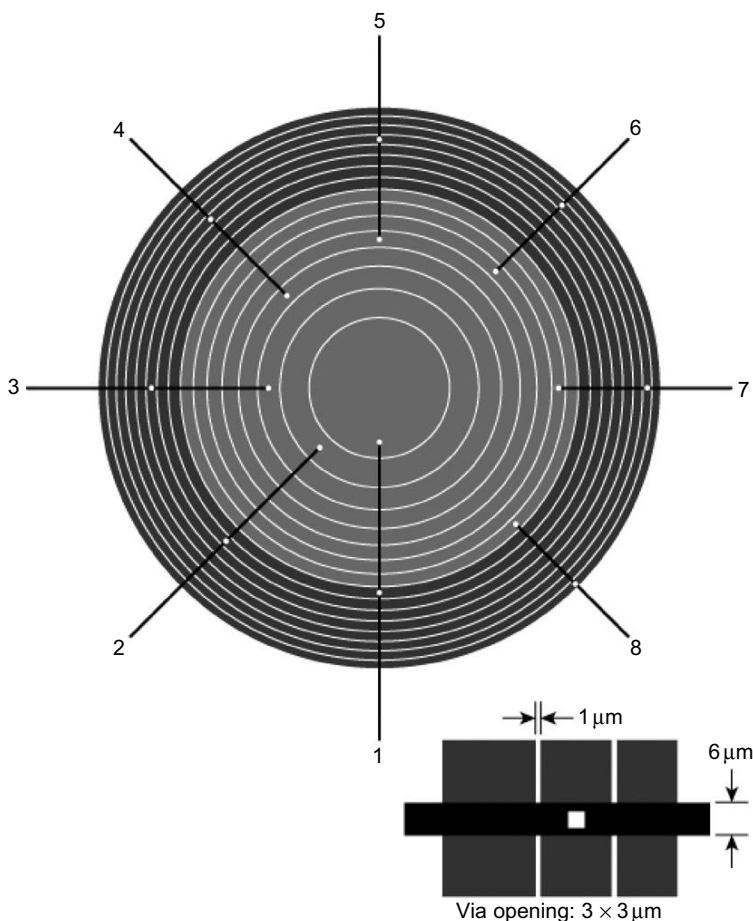


FIGURE 7 Layout of the one-layer electrode pattern (two central zones shown) for adaptive LC diffractive lens adjacent zones are distinguished by color. An electrical insulation layer with vias is added (vias shown with white dots). Each bus connects to one electrode (subzone) in each zone. Dimensions of the vias, the bus line, and the gap between electrodes are illustrated in the bottom right corner of the figure.

The lens showed excellent performance (because of space limitations, we only describe the results for 1-diopter lens). In the optically inactive state (voltage off) in which the lens has no focusing power, optical transmission is 85% over the visible spectrum, a value that can be increased by the use of ophthalmic quality substrates and antireflection coatings. A computer-interfaced polarized optical microscope with a laser source at 543.5 nm (Figure 9) was constructed on the optical bench and used to

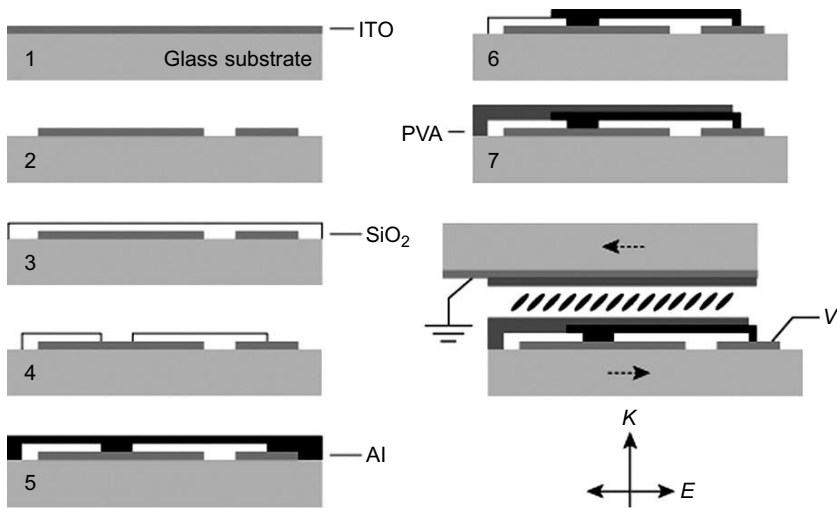


FIGURE 8 Processing steps for fabrication of the patterned electrodes and the conductive lines. The structure of the liquid crystal lens is shown in the bottom right of the figure, where k is the wave vector and E is the polarization state of the incident light.

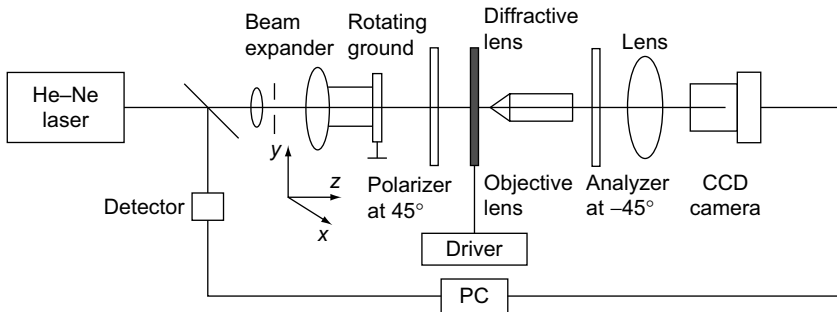


FIGURE 9 Schematic diagram of the polarizing microscope.

inspect the lenses on a microscopic scale and to verify that all electrodes were operating properly. The lens was placed between crossed polarizers where the transmission axes are oriented at angles of 45° and -45° with respect to the liquid crystal alignment layer rub direction. For each position on the lens, the intensity seen by the CCD camera is a function of the voltage-dependent phase retardation $\phi(V)$ between the ordinary

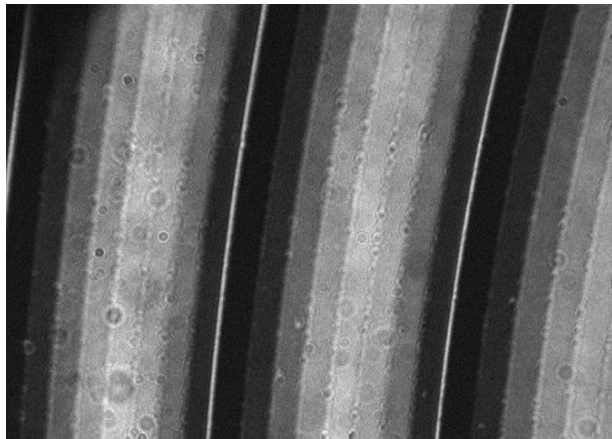


FIGURE 10 Electro-optic response of the eighth-phase level lens obtained with polarizing microscope.

and extraordinary wave components at the exit surface of the lens. Therefore, the voltage-dependent phase retardation of each electrode can be inspected by observing the intensity variations over its area. Monochromatic polarized microscopy images of the lens under operation indicate that all eight electrode sets operated properly and provided discrete phase changes (Figure 10).

Eight optimized drive voltages with amplitudes between 0 and $2V_{\text{rms}}$ produced a maximum first-order diffraction efficiency of 91%, near the 95% predicted by scalar diffraction theory. The measured diffraction efficiency as a function of lens area reaches 94% near the center of the lens, decreasing monotonically as the area is increased (Figure 11). The decrease is because of the fact that phase distortion caused by the fringing field at the zone boundaries has more significant effect at the outer zones as the width of each electrode becomes smaller. At the edges of the electrodes, the electric field lines are not perpendicular to the liquid crystal lens substrate and the fringing fields cause the phase transitions at the zone boundaries to be not as sharp as in the ideal case; thus inducing phase distortions and reducing the diffraction efficiencies. The diffraction efficiency as a function of incidence angle is related to practical application of the adaptive lens for vision correction. The measurement is depicted in Figure 12. It drops about 3% when the incidence angle is 20° . The focused spot size is about $135 \mu\text{m}$, which is also close to the diffraction-limit value of $133 \mu\text{m}$. The lens shows subsecond switching time.

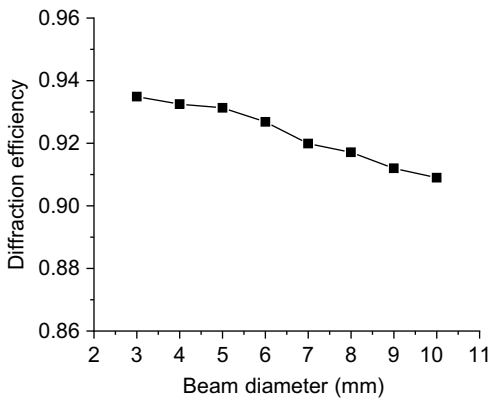


FIGURE 11 Diffraction efficiency as a function of the beam diameter.

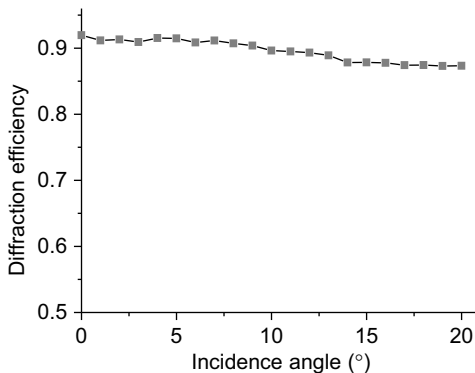


FIGURE 12 Diffraction efficiency as a function of the incidence angle.

The performance of the diffractive lenses was also evaluated using a computer-interfaced, phase-shifting Mach-Zehnder interferometer with a linearly polarized 543.5-nm laser source (Figure 13). The lens under test was placed in the object arm of the interferometer and then imaged onto a CCD camera such that the captured interference patterns are formed by the converging wavefront generated at the exit face of the lens and the reference plane wave. A small aperture was placed between the imaging lens and the camera at the point of focus in order to isolate and test only the wavefront generated by the first-diffracted order. Multiple $\pi/2$ phase shifts are generated in the reference arm using a PZT-actuated mirror, and a phase-unwrapping algorithm is then used to generate a phase map of the diffracted wavefront. The data is processed using IntelliWave

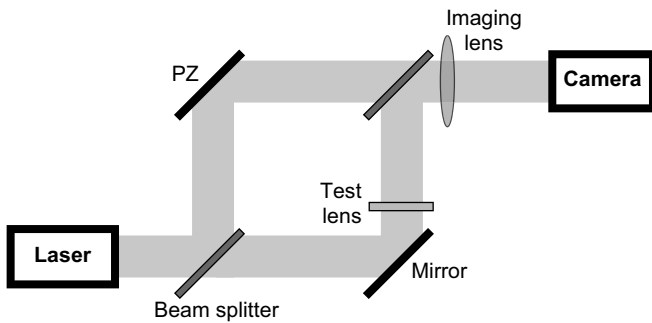


FIGURE 13 Schematic drawing of the Mach–Zehnder interferometer for measurement of the wavefront coming out of the lens.

(Engineering Synthesis Design, Inc). From this unwrapped phase map of the wavefront immediately behind the diffractive lens, the focal length (f) of the diffractive lens is calculated using

$$f = \frac{\rho^2}{2\text{OPD}}, \quad (2.34)$$

where OPD is the peak-to-valley optical path difference from center to edge and ρ is the radius of the test area (Born & Wolf, 1999). As the lenses were designed for operation at 555 nm but tested at 543.5 nm, correction of the extracted focal length value was made by

$$f(\lambda) = f_0 \frac{\lambda_0}{\lambda}, \quad (2.35)$$

where f_0 and λ_0 are the design focal length and wavelength, respectively, and λ is the measurement wavelength. Measurement of the peak-to-valley and RMS errors in the wavefront were made subsequent to removing the best fit sphere and any tilt from the phase map.

The imaging performance of the lens can be evaluated in terms of the modulation transfer function, which represents the ratio of the image modulation to the object modulation at all frequencies. The wavefront of the first-order diffraction can be expressed by a sum of Zernike polynomials (Born & Wolf, 1999), and the modulation transfer function can, thus, be calculated by normalized autocorrelation of the generalized pupil function.

Interferometric measurements at 543.5 nm show excellent imaging capability of the lens. Strong modulation of the optical power is observed in interferogram of the lens in the optically active state (Figure 14).

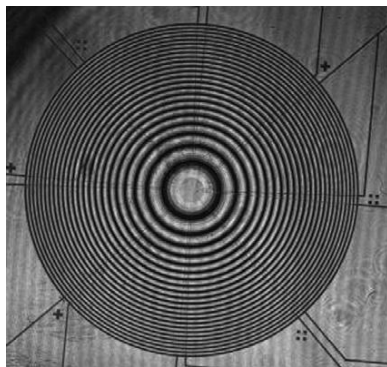


FIGURE 14 Interferogram obtained with the Mach-Zehnder interferometer. The interference pattern has very good fringe modulation across the lens. A close-up of the interferogram shows that the eight subzones in each zone have different grayscale intensities and the pattern is periodic.

The unwrapped phase map of the lens is shown in Figure 15(a) with a peak-to-valley optical path length of 23.05λ . The focusing power was estimated to be 1.002 diopter in excellent agreement with the design value. Very good spherical profiles were obtained in both x and y cross sections, indicating small aberrations. Higher-order aberrations were estimated by analyzing the difference between the measured wavefront and a best-fit spherical wave and tilt (Figure 15(b)). The peak-to-valley range of the difference is 0.241λ and the RMS value is 0.039λ , which is comparable with a high-quality reading glass. The modulation transfer function indicated near diffraction-limited performance (Figure 15(c)). All properties of the lens, as shown in Figures 11 and 14, make the switchable lens suitable for ophthalmic applications.

For vision correction of presbyopic eyes, polarization insensitive switchable lenses are needed. As homogeneously aligned nematic liquid crystals are polarization sensitive, two lenses with orthogonal alignment directions were used in series to create a single polarization insensitive lens. Two such lenses were aligned and cemented together. Figure 16 depicts the alignment of the two lenses. The two lenses are mounted on translation stages. The incident light is linearly polarized at 45° . A CCD detector is put at the focal plane. When the two lenses are displaced, the two focal spots are separated (see upper right of Figure 16). When the two lenses are well aligned, the two focal spots are overlapped (see lower right of Figure 16) and the lenses are cemented together.

For real application, the lenses will be centered on the line of sight when the user is looking at a near object, i.e., the locations of the centers of the LC

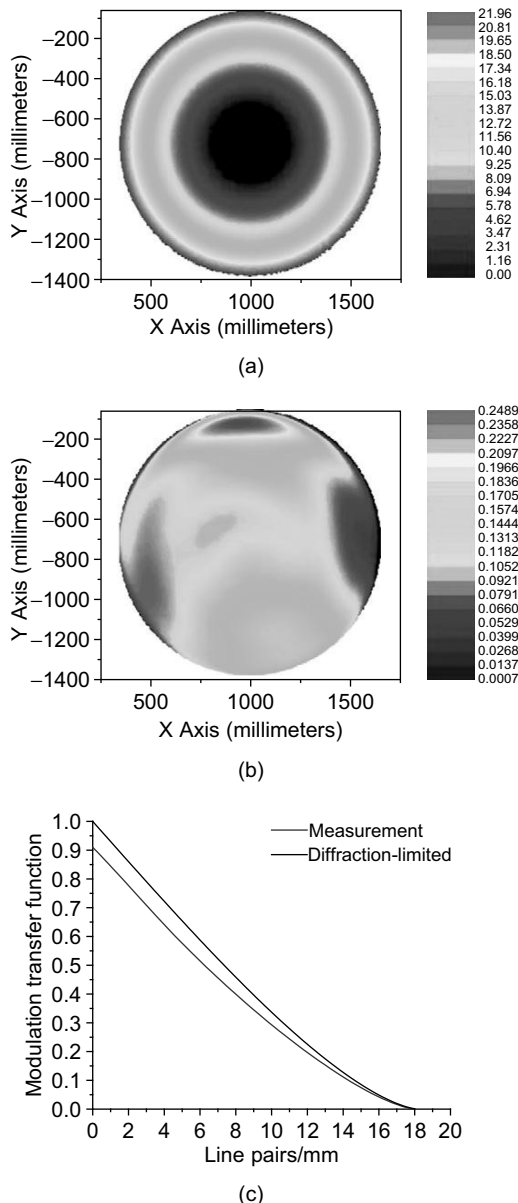


FIGURE 15 Phase map of the lens working at 1-diopter. (a) Unwrapped phase map for a 10-mm aperture. (b) Phase map of the unwrapped phase minus tilting and focusing. (c) Modulation transfer function of the lens. The green line is obtained from the measurement data, while the blue line is for a diffraction-limited lens. The value at low spatial frequency is determined by the diffraction efficiency of the lens.

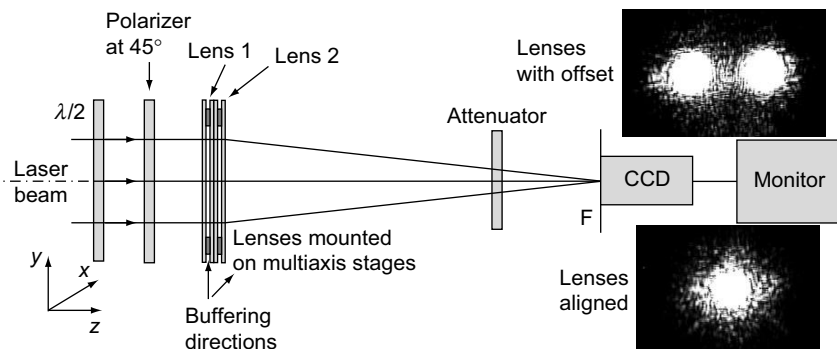


FIGURE 16 Setup for assembly of a complete lens.

lenses should be made to coincide with where the optical axes of the eyes pass through the spectacles when viewing a near object. In this way, any off-axis component is minimized, and the optical performance is maximized. Optical simulation showed that the two lenses and the human eye model can generate good image spots. To demonstrate vision correction, a model eye was constructed using a fixed +60-diopter achromatic doublet glass lens and a CCD with a filter to match the human photopic response. The chromatic aberration of this system is ~ 0.5 diopter. To simulate a typical near vision task such as reading, a double-element lens was placed in front of the model eye and used to image a test object illuminated with unpolarized white light placed 30 cm in front of the lens. As can be seen in Figure 17(a), the model eye has insufficient power to form a sharp image, but by switching on the diffractive lens the image is brought into focus (Figure 17(b)). The double-element lens has excellent optical transmission. When the electro-optic lenses are both in the inactive state, there is no noticeable degradation in the quality of the distant vision. For chromatic aberration, an achromatic diffractive lens can be designed by introducing $p2\pi$ ($p > 1$, integer) phase jump at the zone boundaries for the design wavelength (Faklis & Morris, 1995). In practice, the ocular lens itself has a chromatic aberration, which is less than the diffractive lens. Assuming the brain is adapted to a certain degree of chromatic aberration, balancing the dispersion of the diffractive lens and the eye is less desirable. More clinical study will be performed on this.

In this section, we have demonstrated switchable liquid crystal diffractive lenses with high-diffraction efficiency, high optical quality, rapid response time, and diffraction limited performance. These flat lenses are highly promising to replace conventional area division refractive, multifocal spectacle lenses used by presbyopes. They have the potential of

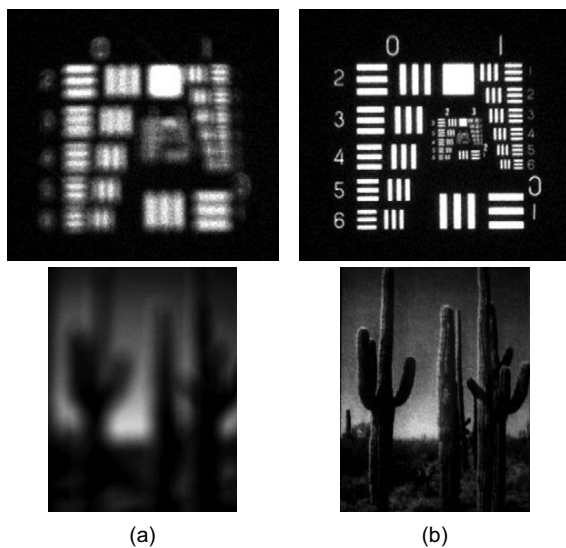


FIGURE 17 Hybrid imaging using the 1-diopter electro-active diffractive lens with the model eye. The function of the diffractive lens is to provide near vision correction to the model eye. (a) The object is placed at a reading distance (~ 30 cm). The image is severely out of focus in the model eye when the diffractive lens is OFF (b) When the diffractive lens is activated, the object is imaged clearly.

revolutionizing the field of presbyopia correction when it is combined with automatic adjustable focusing power. Negative focusing powers can also be achieved with the same lenses by changing the sign of the slope of the applied voltages. The use of these lenses is not limited to ophthalmology but can be extended to numerous other applications where switchable lens elements with relatively large diameters are desirable.

2.4.3. Switchable Electro-Optic Diffractive Lens with High Efficiency Based on Two-Layer Patterned Electrodes for Ophthalmic Applications

In order to develop various approaches that allow large aperture, fast response time, low-operating voltages, high-diffraction efficiency, and power-failure-safe configuration, we presented a design for high-efficiency switchable diffractive lens by separating odd- and even-numbered ring electrodes into two layers and thus eliminating the gaps between the neighboring electrodes (Li et al., 2006). Compared to the design with the one-layer electrode pattern, another advantage of this concept is that it is easier to overcome shorts between neighboring conductive electrodes and fabricate lenses with larger aperture and smaller feature

size. The thickness of the LC is only $5\text{ }\mu\text{m}$. Diffraction efficiency of 75% has been achieved in fourth-level phase modulation lenses with 15 mm diameter and a focusing power of two diopters. The response time and the decay time were measured to be 180 and 120 ms, respectively. The operating voltages are less than 2 V.

Figure 4(c) shows a fourth-level approximation (solid line) of the desired phase profile (dashed line). In each zone, multiple steps are used to approximate the desired phase profile. The structure is periodic in r^2 (r is the radius), and the period is equal to r_1^2 , where r_1 is the radius of the first zone. Each zone (subzone) has the same area as $r_1^2(r_1^2/N$, where N is the discrete phase levels). Here we consider the nematic LC lens (Figure 18(a)), where the phase profile is obtained by the electrically controlled birefringence effect. A nematic LC layer (E7 from Merck with birefringence greater than 0.2) is sandwiched between a patterned electrode substrate and a ground electrode substrate. The patterned electrode is fabricated by photolithographic processing of an indium-tin-oxide (ITO) film deposited on a glass substrate, and the ground electrode substrate contains a uniform conductive ITO layer. The patterned electrodes consist of a circular array of rings. Both of the two electrode surfaces are coated with polyvinyl alcohol (PVA) as an alignment layer and are treated by rubbing to give a homogeneous molecular orientation. The refractive index experienced by the extraordinary beam is changed because of the reorientation of the LC molecule when a voltage is applied to the medium. The phase profile across the lens is tailored by applying proper voltages to the patterned electrodes and as such, determines the diffraction efficiency. The phase profile may be affected by various factors, including the quantization error (number of phase levels in each zone), the gaps between the electrodes, fringing field effects in the transition area of neighboring zones, and fabrication errors. The quantization error can be reduced by increasing the number of phase levels in each zone. For instance, an ideal diffractive lens with 2- and 4-level digitization corresponds to efficiency of 40.5 and 81.1%, respectively. Simulations show that the gaps between the electrodes and different types of phase distortion at the electrode boundaries greatly affect diffraction efficiency and other performance parameters. To alleviate this effect, the odd- and even-numbered rings can be interleaved into two layers that are separated by an insulating layer such as SiO_2 . In this demonstration, all the subzones having the same counting index $n(n = 1, 2, \dots, N)$ are connected together by a bus line, i.e., applied the same voltage, and thus have the same phase value. Figure 18(b) shows the cross section of the two-layer electrode pattern, where odd- and even-numbered rings are distributed in two layers, and there are no gaps between two neighboring electrodes.

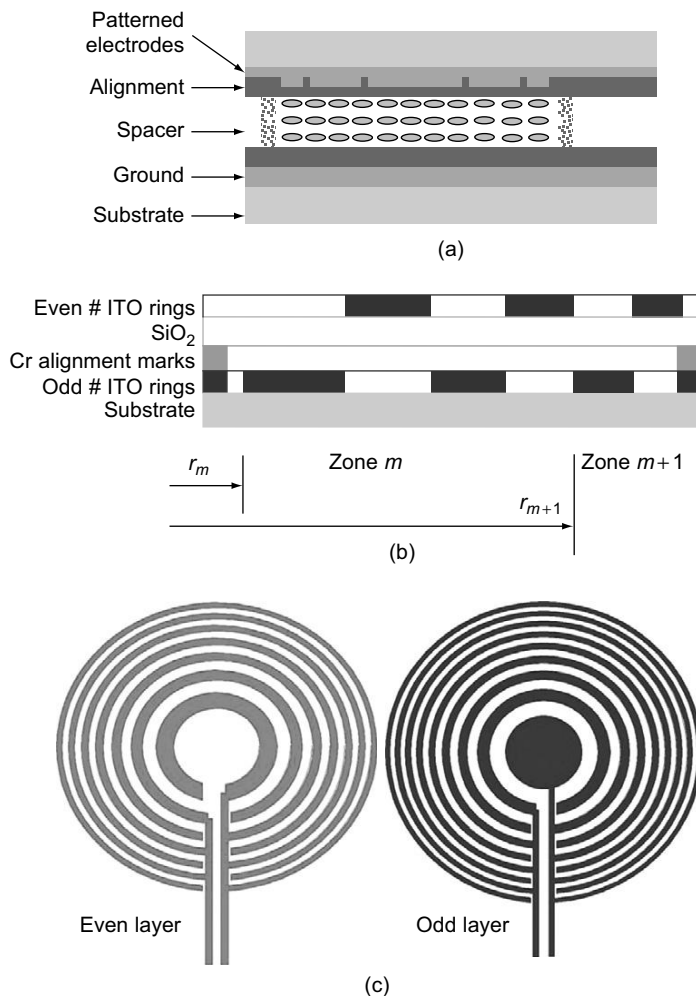


FIGURE 18 Switchable LC diffractive lens. (a) Structure of the flat LC lens. (b) Structure of the two-layer electrode pattern for fourth-level lens. (c) Patterns for odd-number electrodes and even-numbered electrodes.

The schematic diagrams for the pattern of the odd-numbered electrodes and for the pattern of the even-numbered electrodes are shown in Figure 18(c). The fabrication procedure for the interleaved electrode pattern is illustrated in Figure 19. With this design, it is easier to avoid shorts between neighboring ITO electrodes and fabricate lenses with larger aperture and smaller subzones.

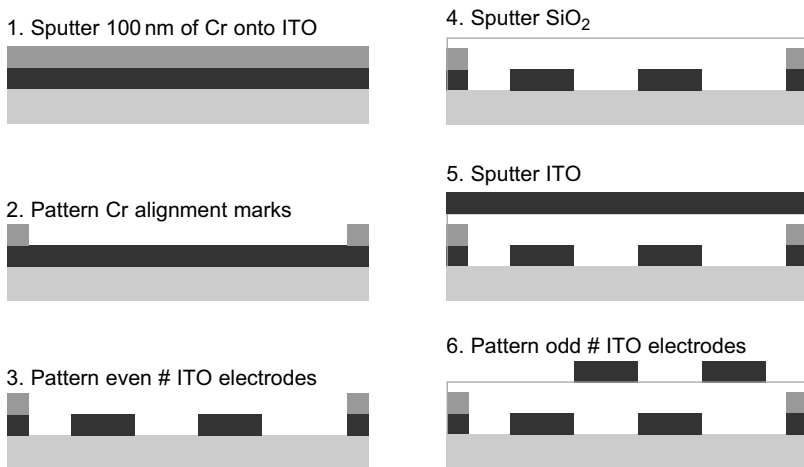


FIGURE 19 Fabrication procedure for the interleaved electrode pattern.

Here, we demonstrate a fourth-level, 15-mm-aperture lens with a 2-diopter focusing power at 555 nm, the peak of the human photopic vision response. The width of the last subzone at the edge is $9.2\text{ }\mu\text{m}$. After the lens is fabricated, various optical characterizations are performed. In the off state, transmission of the lens over the visible spectrum is more than 85% if there is no antireflection coating on the surfaces. A polarized microscope is used to check the electro-optic function of each electrode. The lens is placed between two crossed polarizers, which are aligned with their transmission axes at 45° and -45° , respectively, to the horizontal axis. For each position, the intensity at the detector changes with the change of the phase difference (ϕ) between the ordinary and extraordinary components at the exit surface of the lens. The operation of each electrode can be inspected by observing the intensity variations over the area of said electrode. Figure 20 shows the intensity variation on electrode 1 when electrodes 2, 3, 4 were set to certain voltages, respectively, and the voltage applied to electrode 1 was adjusted. The electrode boundaries can be clearly observed in the images.

To determine the diffraction efficiency as a function of lens area, an iris is placed at the center of the lens and the diffraction efficiency is measured for various beam sizes. Variation of the diffraction efficiency is depicted in Figure 21(a). The efficiency for the 15-mm-diameter area is more than 75%. As we expect, the lens without gaps has only a little decrease in efficiency when the activated area increases. The decrease is because the phase distortion caused by the fringing field has more significant effect on the outer

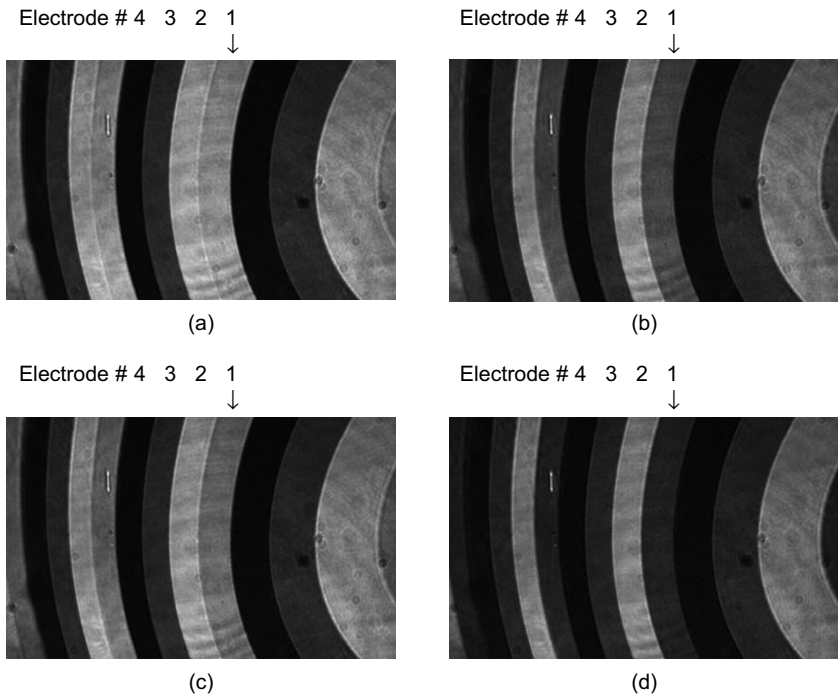


FIGURE 20 Operation of the electrodes. Electrodes 2, 3, 4 are set to certain voltages respectively, while the voltage applied to electrode 1 was adjusted.

zones. The efficiency of the center area is close to the theoretical value as the fringing field effect is negligible in this area. Dependence of the diffraction efficiency on the incidence angle is related to the field-of-view effect for normal use of the spectacle lenses. From the experiment, the diffraction efficiency decreases monotonically as the increase of the incidence angle. It drops about 4% when the lens is tilted 20° about the lateral axis.

A Mach-Zehnder interferometer operating at 543.5 nm was used to measure wave-front quality immediately behind the lens and to determine the focal length. The technique is based on interference between the spherical wave after the lens and a reference plane wave. Figure 21(b) shows an example of the measured interferograms. Five interferograms were taken with a phase shift between each interferogram and the wrapped phase map can be produced. The unwrapped phase map represents the actual optical path difference profile generated by the diffractive lens. It is generated from the wrapped phase by removing the 2π discontinuities. The unwrapped phase map of the lens is shown in Figure 21(c). A good spherical wave was obtained with very few higher-order aberrations as indicated

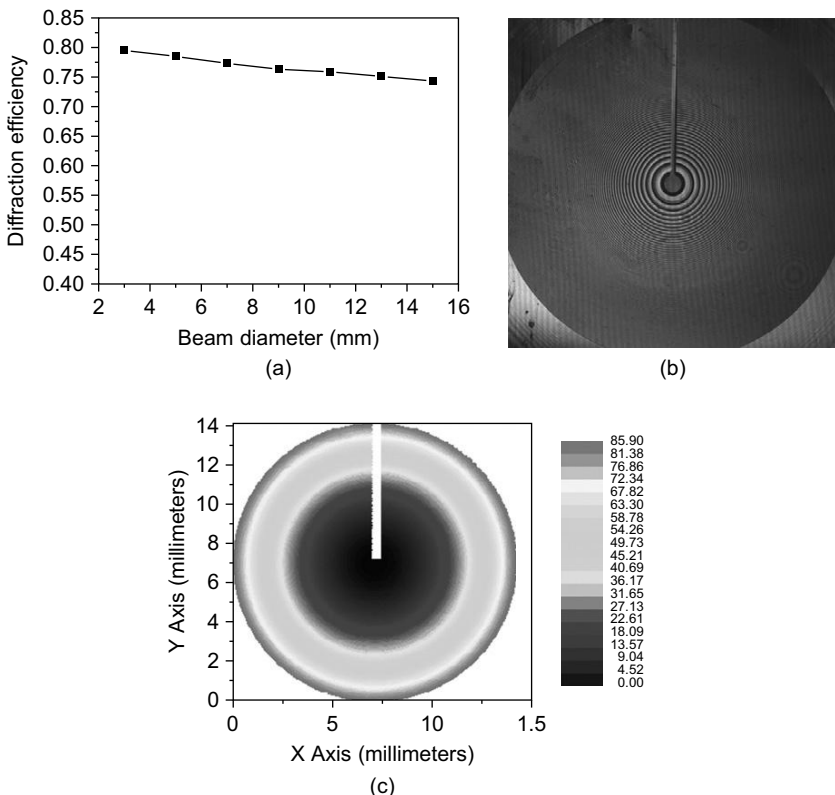


FIGURE 21 Some characterization results of the 15-mm-aperture, fourth-level, 2-diopter lens. (a) Diffraction efficiency as a function of the beam diameter. (b) Interferogram obtained with the Mach-Zehnder interferometer. (c) Unwrapped phase map for a 14-mm aperture.

by an RMS wave front error of 0.0889λ . The focal length was found to be 50.855 cm and by using Equation (2.35), the focal length at 555 nm was calculated as 49.80 cm, which corresponds to a focusing power of 2.008 diopter and indicates that accurate focusing power can be achieved. The focused spot size was also measured and found to be $47.9 \mu\text{m}$, close to the diffraction-limited spot size of $45.1 \mu\text{m}$. The response time and the decay time were measured to be 180 and 120 ms, respectively. All these parameters indicate high performance of the lens. In addition, we also verified that, by changing the slope of the applied voltages to each zone, a negative 2-diopter focusing power can be obtained with the same lens, and the diffraction efficiency is the same as the positive 2-diopter case.

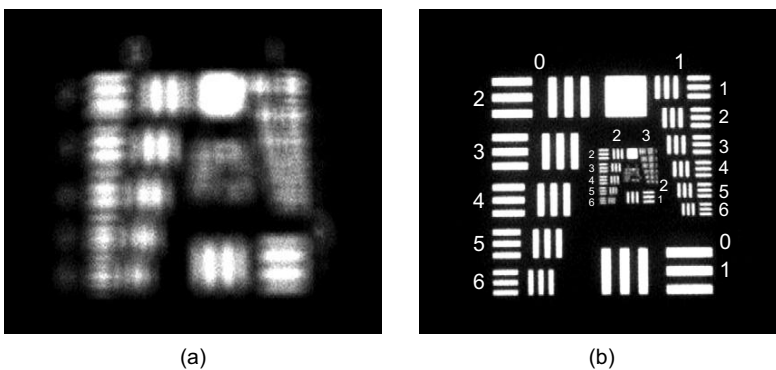


FIGURE 22 Imaging using the 2-diopter electro-active diffractive lens with the model eye. The object is placed at a reading distance (~ 30 cm). (a) The image is severely out of focus in the model eye when the diffractive lens is OFF. (b) When the diffractive lens is activated, the object is imaged clearly.

As nematic liquid crystal is polarization sensitive, two LC lenses with orthogonal alignment directions are required to form a complete lens that works for randomly polarized light. The double-element complete lens has been demonstrated to provide near vision correction for an accommodation free model eye consisting of a 60-D refractive lens, an iris, and a CCD array. A white light source illuminates the object placed at a typical reading distance of approximately 30 cm. When the diffractive lens is not activated, the image is blurred (Figure 22(a)) but when the diffractive lens is turned on, the object is imaged clearly (Figure 22(b)). The ON- and OFF-state of the lens allow near- and distance-vision, respectively.

In this section, we have demonstrated a high-performance switchable electro-optic adaptive diffractive lens for vision correction of presbyopia. By interleaving the odd-numbered and even-numbered electrodes into two layers, there is no gap between the neighboring electrodes. This helps to maintain the desired diffraction efficiency, and it makes it easier to fabricate lenses with large aperture and small feature size without shorts between the ring electrodes. Diffraction efficiency of more than 75% has been achieved for fourth-level lenses with 15-mm aperture. This design methodology can be extended to phase steps larger than four, where the electrodes can be addressed from an additional layer through vias. However, more fabrication steps are required. The focusing power of the lens can be adjusted to be either positive or negative, depending on the voltages applied to the patterned electrodes. Other advantages of this lens include compact, lighter weight, low cost, and easier operation with low voltages and low-power dissipation. For people those who also

need correction for distance vision, an additional refractive lens can be integrated with the switchable diffractive lens. Using nematic LC, two LC lenses set in orthogonal direction are required to make it polarization insensitive. In order to avoid light loss as a result of back reflections at the substrate interfaces, antireflection coating is necessary.

2.4.4. Robust Structure with Three-Layer Electrode Pattern and Two-Layer via Structures for Flexible Interconnection and No-Gap Pattern

In Section 2.4.3, we demonstrated a switchable diffractive LC lens with high performance. In that design, the ring electrodes for modulating the eighth-level (number of phase digitization) phase profile are patterned in one layer with a 1- μm gap between the neighboring electrodes. In order to avoid the lateral gaps between the electrodes, we did a preliminary experiment with interleaved electrode pattern. However, with that design, the number of phase levels is limited only to four. Here we show a novel and general design for flat thin diffractive lens with high performance and powerful functions for vision care. It has three-layer microfabricated electrode pattern and two-layer via structures for flexible interconnection and no-gap pattern (Li, Valley, Äyräs, Honkanen, & Peyghambarian, 2007). It allows any even-numbered phase levels greater than four and provides the capability of correction for near-, intermediate-, and distance-vision. Such a lens has potential of revolutionizing the field of presbyopia correction.

The diffractive lens is designed at the peak of the human photopic response, 555 nm. The radii of each zone and subzone are given by Equations (2.32) and (2.33). A nematic LC layer is sandwiched between a ground electrode substrate and a patterned electrode substrate. The ground electrode substrate contains a uniform conductive indium-tin-oxide (ITO) layer and the patterned electrodes are fabricated by photolithographic processing. For higher diffraction efficiency and ease of control, the patterned electrodes have a ring shape defined by Equation (2.33). If all the ring electrodes for tailoring the refractive index are patterned in one layer, there must be gaps between neighboring electrodes. When the aperture of the lens is large, the gaps will distort the desired phase profile and hence reduce the diffraction efficiency. In order to avoid this effect, the odd- and even-numbered electrodes are interleaved into two layers. The discrete electrodes for equal phase level in different zones are connected by a bus line through vias. The module was fabricated from the bottom to the top. All the bus lines are distributed in one layer in the bottom, and the number of the bus lines is equal to the number of phase levels in each zone. Therefore, there are three layers of

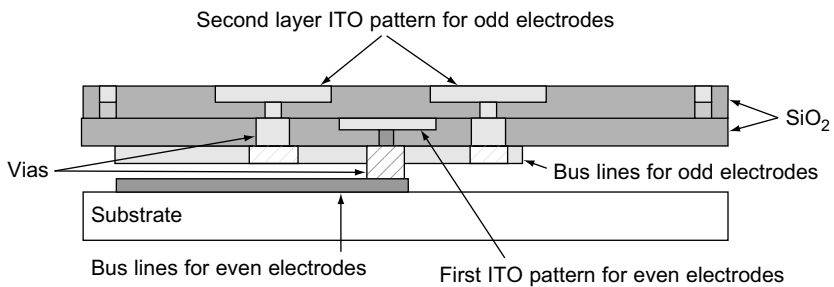


FIGURE 23 Structure of the three-layer patterned electrodes and two-layer vias. It eliminates gaps between neighboring ring electrodes for arbitrary phase levels.

electrodes and two layers of vias in total, as shown in Figure 23. The layer for the bus lines, the layer for the odd-numbered electrodes, and the layer for the even-numbered electrodes are isolated by two insulator layers of SiO_2 , where vias are made for conduction between the bus lines and the ring electrodes. The fabrication procedure for the module is illustrated in sequences in Figure 24. The etching time for SiO_2 is optimized by checking the conductivity between ITO test structures, while the etching time for ITO is optimized by eliminating the electric shorts between different electrodes, i.e., electrodes for different phase levels. The new design makes it easier to fabricate lenses with higher-level phase steps and larger aperture and overcome the shorts between the electrodes. This method can be used for design of LC lens of any phase levels. It should be noted that, unlike the conventional binary optics, in this design, the increase of the phase levels (e.g., to 16 levels) in each zone does not increase the fabrication steps. The lens assembly procedure has been described earlier. The initial orientation of the molecules is parallel to the polarization of the incident beam, which is an extraordinary beam, and its effective refractive index can be changed in the range from n_e to n_o due to the reorientation of the LC molecule when a voltage is applied. The material has a positive dielectric anisotropy (> 0.2), which provides enough phase modulation for the visible wavelength with the 5- μm -thick cell.

The polarized optical microscope (Figure 9) was used to inspect the lenses on a microscopic scale. Images of the eighth-level 1-diopter lens under operation indicate that all eight electrode sets operated properly and provided discrete phase changes (Figure 25(a)). Eight drive voltages with amplitudes between 0 and 2 V_{rms} were optimized and the maximum first-order diffraction efficiency (ratio of first-order diffracted power to the total transmitted power) of 92.5% was obtained for the whole lens area. The diffraction efficiency was measured as a function of the beam diameter. It reaches 94% near the center of the lens and decreases monotonically as

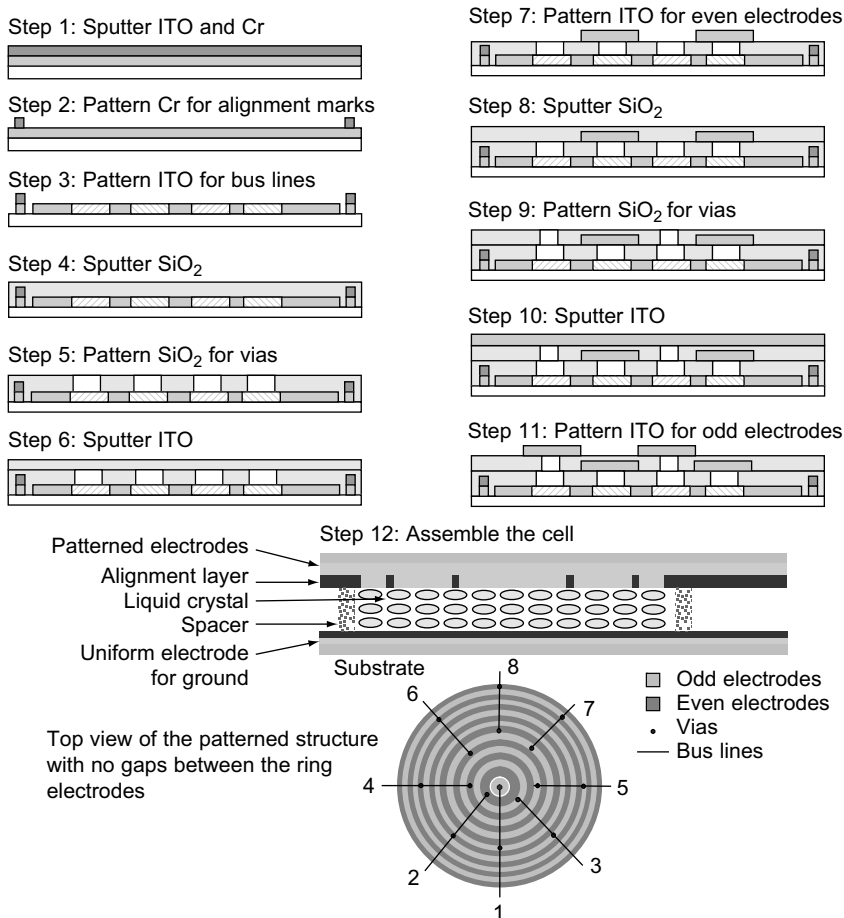


FIGURE 24 Processing steps for fabrication of the LC diffractive lens with three-layer patterned electrodes and two-layer via structures. At the bottom of the figure, the top view of the finished layers is shown with eight bus lines as an example. The design can be used for any higher phase levels.

the beam diameter is increased (Figure 25(b)). The diffraction efficiency at different location of the lens is shown in Figure 25(c). Although there is a small decrease due to the phase distortion caused by the fringing field at the zone boundaries, it is flatter than that of the design with gaps between the electrodes. The diffraction efficiency as a function of incidence angle is depicted in Figure 25(d). It drops about 4% when the incidence angle is 20° . As shown in Figure 25(e), switching of the lens is relatively fast. The rise time between 10 and 90% of the diffraction efficiencies was 150 ms and

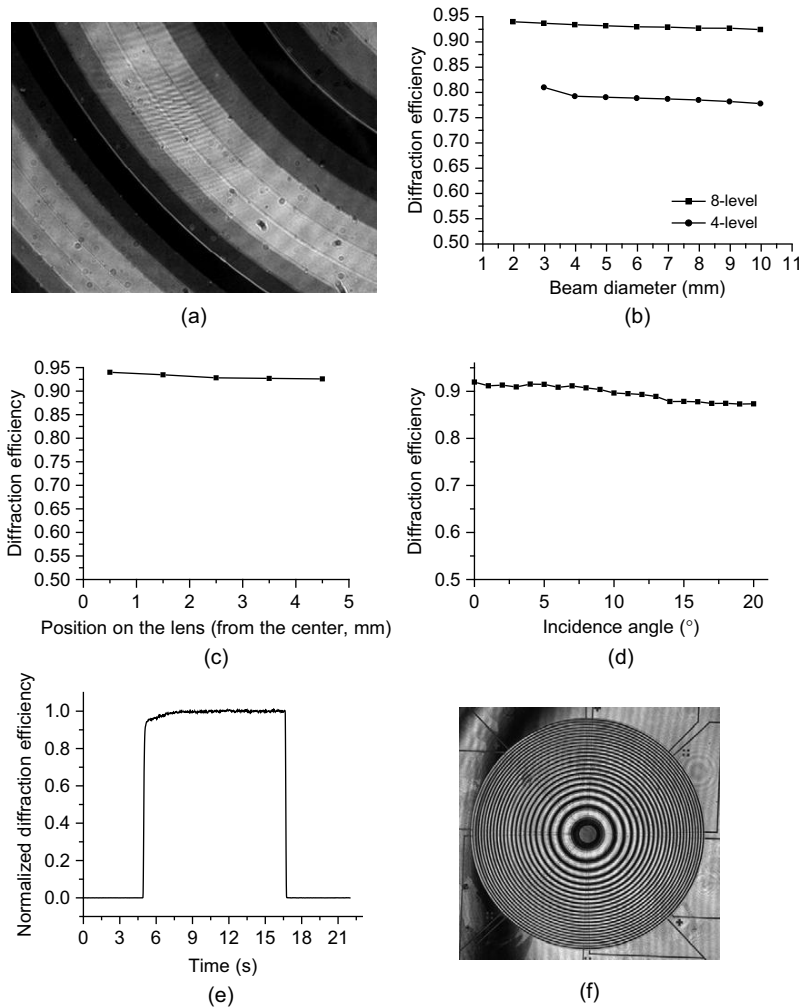


FIGURE 25 Characterization of the LC lens. (a) Electro-optic response of individual electrode rings. (b), (c), (d), Diffraction efficiency as a function of the beam diameter, position on the lens, and incidence angle, respectively. (e) Switching dynamics of the lens. (f) Interferogram.

the full decay time was 134 ms. The wavefront immediately behind the lens can be measured using a phase-shift interferometer. Figure 25(f) shows one interferogram formed by the test wave and the reference wave. The RMS error of the spherical wavefront was measured to be 0.0688 waves. The parallelism between the two substrates of the lens may cause variation

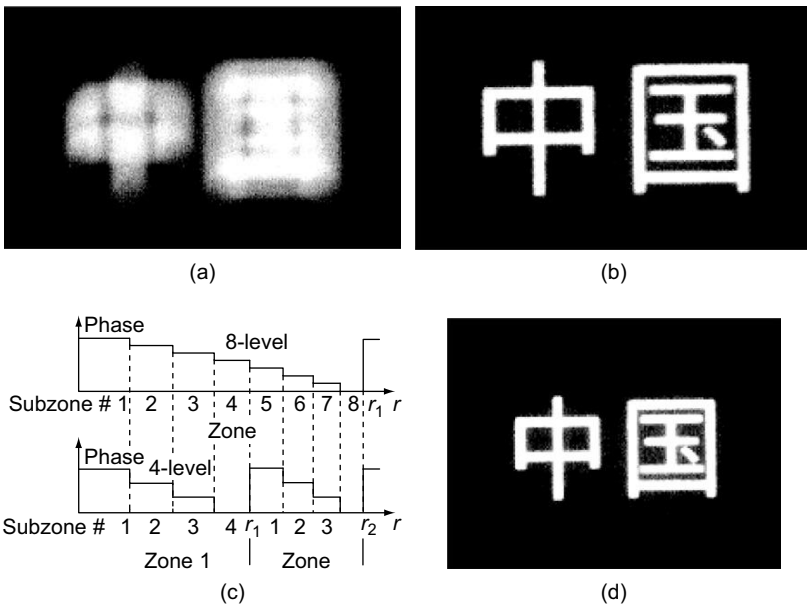


FIGURE 26 Hybrid imaging using the varifocal LC lens. The LC lens is (a) OFF and (b) activated with 1-diopter power. (c) An eighth-level 1-diopter LC lens can be reconfigured to a fourth-level 2-diopter lens. (d) Hybrid imaging with the 2-diopter power.

of the RMS error. In addition, for the same lens, negative focusing power (-1 diopter) can also be achieved with the same diffraction efficiency by changing the sign of the slope of the applied voltages.

To demonstrate the vision correction capability, the double-element LC lens was put in front of the model eye and an object was placed ~ 35 cm in front of the lens with unpolarized white light illumination. When the complete LC lens is off, the model eye has insufficient power to form a sharp image (Figure 26(a)). But by switching on the diffractive lens, the image is brought into focus with excellent contrast (Figure 26(b)).

Based on the current design, the focal length of the lens can be switched between a few digital values by reducing the zone period digitally, and each corresponds to different diffraction efficiency. Assume an 8-level lens with the design focal length $f = F$ (Figure 26(c)). If each zone is divided into two, and voltage V_1 is applied to all the first and the fifth subzones, V_2 to all the second and the sixth subzones, V_3 to all the third and the seventh subzones, and V_4 to all the fourth and the eighth subzones, then the lens has a focal length of $F/2$ with an efficiency corresponding to 4-level phase digitization (lower part of Figure 26(c)). Actually every four subzones form

a new zone for the lens with the focal length $F/2$. Furthermore, if each zone is divided into four, the lens has a focal length of $F/4$ with an efficiency corresponding to a 2-level device. In this case, every two subzones form a new zone. With the 8-level 1-diopter lens described earlier, diffraction efficiency of 78% was obtained when it is optimized for the 4-level 2-diopter case. The diffraction efficiency as a function of the lens aperture is shown in Figure 25(b), and hybrid imaging with the model eye is shown in Figure 26(d). For the same condition, the 2-diopter LC lens would allow the model eye to see objects at a closer distance than the 1-diopter lens. The main effect on the image is the brightness. Therefore, the same electro-optic LC lens can be switched for near-, intermediate-, and distant-vision with each using the whole lens aperture.

Similarly, the focal length F of a 12-level diffractive lens can be adjusted to $F/2$, $F/3$, $F/4$, and $F/6$, with diffraction efficiency corresponding to a 6-, 3-, 4-, and 2-level device, respectively. For 6-level case, all the subzones of (1 and 7), (2 and 8), (3 and 9), (4 and 10), (5 and 11), (6 and 12) from each zone are applied the same voltages, respectively. For the 4-level case, all the subzones (1, 5, and 9), (2, 6, and 10), (3, 7, and 11), (4, 8, and 12) from each zone are applied the same voltages, respectively. For the 3-level case, all the subzones of (1, 4, 7, and 10), (2, 5, 8, and 11), (3, 6, 9, and 12) from each zone are applied the same voltages, respectively. For the 2-level case, all the subzones (1, 3, 5, 7, 9, and 11), (2, 4, 6, 8, 10, and 12) from each zone are applied the same voltages, respectively.

In this section, we have demonstrated flat, thin, switchable LC diffractive lens with three-layer-patterned electrodes and two-layer via structures, which is a general design for multilevel phase modulation. The lens has high-optical quality, good response time, and this design allows larger aperture. The focusing powers of the whole aperture can be switched between different values. This kind of lens may afford an alternative to replace area division multifocal spectacle lenses. Antireflection coatings can be used to avoid light loss at the substrates. Usually correction of presbyopia needs an add power less than 3 diopters, and a 15-mm aperture for the center area is enough. In this case for an eighth-level lens, the smallest subzone is $\sim 3.1 \mu\text{m}$. With the state-of-the-art facilities, it is feasible to make such lenses. For correcting a residual refractive error for myopia or hyperopia, a curved substrate can be used or the lens can be used together with a contact lens for eyes that need minor correction for distance vision. The other concern is the temperature dependence of the lens performance. The refractive indices of the LC change as a result of the temperature variation (n_e has a larger change than n_o). A temperature sensor and a variable voltage circuit are needed for compensation. The birefringence disappears above the clearing point in the isotropic phase.

2.4.5. Improved Design with Individually Addressed Electrode Pattern

Although connecting the corresponding subzones together is easy to operate at the design focal length, it results in some disadvantages for ophthalmic application. First, if the design focal length F is for near-vision correction, it cannot provide intermediate vision because the switchable focal lengths are F and a few values smaller than F . Second, the diffraction efficiency is different for each switchable focal length. When the lens is adjusted to work with second- or third-level phase modulation within each zone, the efficiency is relatively low for vision.

In order to overcome the above-mentioned disadvantages, each electrode (subzone) must be individually addressed, as shown in Figure 27 (Li, Ayras, & Peyghambarian, 2006). Assume the geometry of the electrode pattern is designed for focal length F with L -level phase modulation. The flexibility of this architecture is to increase the zone period. For instance, based on Equations (2.32) and (2.33), if the zone period r_1^2 is increased to $2r_1^2$ by grouping every two neighboring subzones into one, i.e., applying the same voltage to the two neighboring electrodes, then the focal length is changed to $2F$ without change of diffraction efficiency (Figure 28). Similarly, with the fixed electrode pattern, the focal length can be varied to $3F, 4F, \dots$, by increasing the zone period to $3r_1^2, 4r_1^2, \dots$, respectively. This provides the lens with the adaptive capability to near, intermediate (e.g., computer screen), and distance vision for presbyopia eyes. Because the F value cannot be too small (when F is small, the feature size of the electrodes becomes very small for a 15-mm-aperture lens, and it is impossible

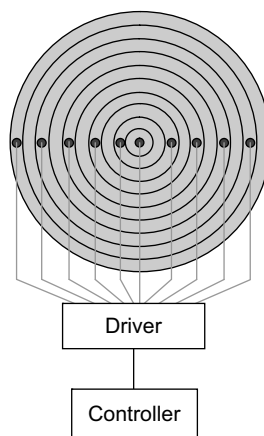


FIGURE 27 Schematic diagram for driving the individually addressable electrodes.

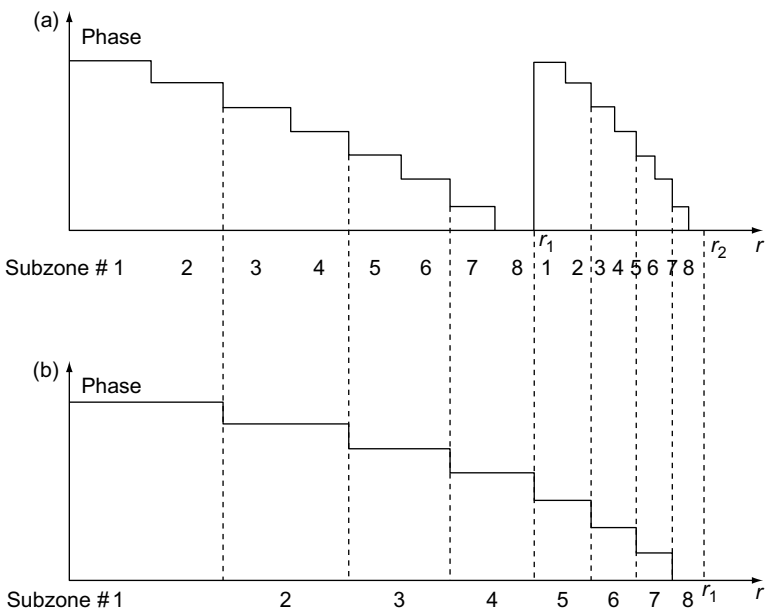


FIGURE 28 With individually addressable electrodes, multiple focal lengths F , $2F$, $3F$, ..., can be obtained while the light efficiency is kept the same.

to make them with low cost), one design can only be used by subjects who need the corresponding correction.

It will be more attractive to design the adaptive lens that can be used by all the subjects. This requires the lens have the capability to quasi-continuously change the focal length. Here we propose a new general design that allows continuous change of the focal length. The patterned electrodes are a circular array of rings of particular size. A proper resolution of the ring can be determined by the focal length range to be adjusted. Each ring can be individually addressed. For each desired focal length, the size of each subzone of all the zones can be calculated using Equation (2.33). A certain number of rings can be chosen to form each subzone and appropriate voltage can be applied. If the resolution of the rings is good enough, the lens can always have high efficiency with no significant change. With this design, lenses of various powers can be obtained using the same electrode pattern. To avoid the gaps between the electrodes, even- and odd-numbered electrodes can be interleaved into two layers. Because the zones that are close to the center have larger size, sparser electrodes can be used in that area (the size of the electrodes close

to the center can be bigger than those in the other area). With current fabrication technology, the array of ring electrodes with a small feature size (less than 5 μm) can be made. The proposed structure is easier to control than the spatial light modulator. Simplified resistor network may be used to generate locally linear drops of voltage so that a small number of electrodes can produce the desired phase modulation.

2.5. Liquid Crystal Lens Based on Hole-Patterned Electrode

2.5.1. Basic Structure

Axially symmetric, continuous inhomogeneous electric field can be generated by a hole-patterned electrode and a uniform counter-electrode, and homogeneously aligned LC cell can be used to function as an adaptive lens (Nose & Sato, 1989). Figure 29(a) shows the cross section of the nonuniform electric field inside the cell. The hole-patterned electrode (top view shown in Figure 29(b)) was made photolithographically from thin aluminum film deposited on the glass substrate. Both electrode surfaces were treated with homogeneous alignment layers for LCs with positive dielectric anisotropy. The optical property of the LC cell would depend on the orientation of the LC directors resulting from the nonuniform electric field. In Figure 29(a), the electric field is represented by arrows. The length of each arrow corresponds to the field strength and the direction coincides with that of the local electric field. It should be noted that the strength of the electric field reaches the maximum at the edge of the hole pattern and becomes smaller at the center of the hole. The angle between the direction of the field and the normal to the substrates also approaches the maximum at the edge of the hole.

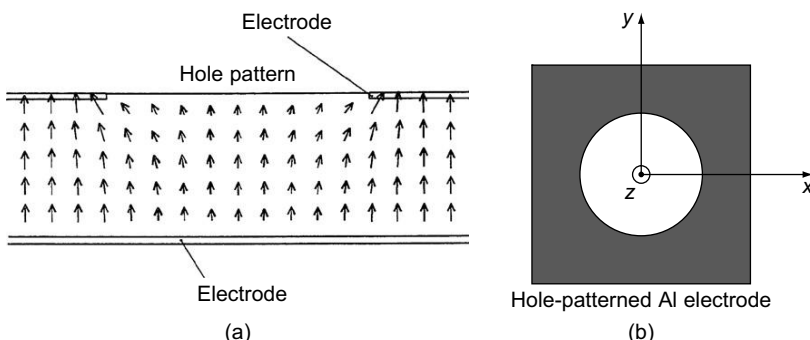


FIGURE 29 Cross section of the nonuniform electric field produced by a hole-patterned electrode. (a) Cross section of the cell. (b) Top view of the hole pattern (Nose & Sato, 1989).

When there is no electric field applied, the directors of the LC are uniformly parallel to the substrates and the refractive index is equal to n_e . When a voltage more than the threshold is applied, the directors near the edge of the hole start to reorient and the directors close to the center remain parallel to the substrate. Therefore, the refractive index near the edge is smaller than n_e . This leads to a gradient refractive index distribution across the hole with the maximum value at the center and the LC cell operates as a converging lens. When the applied voltage increases, the gradient of the refractive index decreases and the focal length becomes longer according to Equation (2.19). If the applied voltage further increases to a high value, the refractive index profile can be opposite, and the LC cell functions as a diverging lens. By changing the shape of the hole from a circle to a rectangle or an ellipse, cylindrical, and anamorphic lenses can be achieved, respectively (He, Nose, & Sato, 1995; Honma, Nose, & Sato, 1999; Ren, Fan, Gauza, & Wu, 2004b). By dividing the electrode with circular hole into several subelectrodes and applying appropriate potentials to each subelectrode, anamorphic lens can also be obtained (Ye & Sato, 2005). Besides homogeneous LC cell, adaptive microlens formed by homeotropic aligned LC with positive dielectric anisotropy has also been studied (Scharf, Fontannaz, Bouvier, & Grupp, 1999). Comparative study of the lens with different alignment was conducted by Gvozdarev and Nevskaia (1999, 2001a, 2001b). It turns out that under low voltages the LC microlenses with a homeotropical alignment possess defocusing properties and the microlenses with planar and hybrid alignments possess focusing properties. With the increase of the ratio of lens diameter to the LC thickness, the applied voltage increases. At higher voltages, planar- and hybrid-aligned microlenses become defocusing.

The above LC cell is termed as the asymmetric electrode structure. With homogeneous alignment of the LC, a disclination line is usually observed in the direction perpendicular to the director of the LC. Such a disclination line can be eliminated by hybrid alignment of the LC (Nose, Masuda, & Sato, 1991a), where the surface of the hole-patterned electrode is treated with homeotropic alignment while the surface of the continuous electrode is still treated with homogeneous alignment. But the lens properties are not improved much because the center of the lens shifts. To overcome these issues, homogeneous LC lens with a symmetric electrode structure has been proposed where cocentered hole-patterned electrodes are used for both substrates (Nose, Masuda, & Sato, 1991b, 1992). Yanase, Ouchi, and Sato (2002) also investigated the effect of the ratio of the diameter of the hole in the bottom electrode to that of the hole in the top electrode on the lens property under various applied voltages. Interestingly, when the ratio is about 1:2 and the applied voltage is above certain value, the phase profiles at the center and the outer regions are approximated by

near-parabolic curves of different coefficients, which mean bifocal lengths. With these symmetric and nonsymmetric hole-patterned LC structure, the ratio D/t of the lens diameter (D) to the thickness of the LC layer (t) should be less than 10 for good optical performance. The optimum ratio of D/t is about 2:3. Diffraction-limited LC microlenses with lens diameters 120 and 110 μm and D/t ratio about 2.4 have been demonstrated (Scharf, Kipfer, Bouvier, & Grupp, 2000). Because the thickness is typically limited to a few tens of micrometers for fast response time, the lens diameter can only be a few hundred micrometers. This limitation has been broken by inserting a dielectric slab between the hole-patterned electrode and the LC layer (Ye & Sato, 2002).

2.5.2. Liquid Crystal Lens with Circular Hole-Patterned Electrode Detached from the LC Layer

As shown in Figure 30 (Ye & Sato, 2002), LC is sandwiched between two glass substrates and treated with homogeneous alignment. The top surface of the lower glass is coated with conductive thin film, and the top surface of the upper glass substrate is coated with a circular hole-patterned electrode. The difference between this structure and the structure described above is that there is an insulating glass layer between the LC layer and the hole-patterned electrode, and because there is distance between the hole-patterned electrode and the LC layer, a nonuniform electrical field produced by the free electric charges in the electrodes and the induced electric charges at the glass surfaces is distributed over a larger area in the LC, allowing a larger aperture of the lens. Experiment with a 7-mm-lens aperture, 130- μm -thick LC layer, and 1.3-mm-thick glass substrate has been demonstrated. The phase profile can be adjusted by the diameter of the lens and the thickness of the substrate. However, the required voltage is 70 V_{rms} . It is also possible to use the symmetric two hole-patterned electrodes structure, but the driving voltage will be doubled.

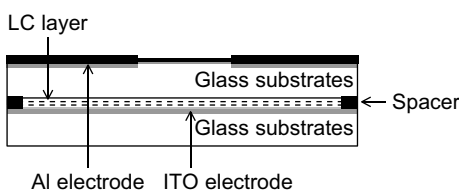


FIGURE 30 Cell structure with the hole-patterned electrode detached from the LC layer (Ye & Sato, 2002).

However, as the directions of the LC directors are spatially variant, the boundary of the different domains of rotation appears as a disclination line that greatly degrades the optical quality of the lens. A new driving method has been proposed, which allows all the directors in the cell to rotate in the same direction (Ye, Wang, & Sato, 2003). In this approach, an electric current flows in one of the electrodes for a short time interval at the beginning of voltage application. The electric field associated with the current tilts the electric field lines in the LC to one side, making the angles between the directors and the electric lines acute in most locations in the cell. The directors then tend to align with the electric field in the same direction. Defects therefore do not appear. With this driving technology, the application of a temporal high voltage to accelerate the response of an LC lens to the applied voltage is also realized (Ye & Sato, 2005).

In order to increase the tunable range of the lens power, two LC layers can be incorporated into this structure by putting the hole-patterned electrode in the center of the device, as shown in Figure 31 (Ye, Wang, & Sato, 2004a). The power enhancement is because of the electrical interaction between the components at two sides of the Al electrode through the open hole. The focusing power of the lens becomes much larger than two times that of the LC lens with one LC layer. If the buffering directions of the alignment layers for the two LC layers are perpendicular to each other, the lens becomes polarization independent, i.e., the lens can focus incident light of arbitrary polarization state (Ye & Sato, 2003). To further enhance the tunable range, a new design that drives the LC cell using two voltages has been proposed (Ye, Wang, & Sato, 2004b). With reference to Figure 30, another ITO electrode is placed on the hole-patterned Al electrode with a 70- μm -thick glass slide between them (Figure 32). The geometrical sizes of the components in the cell are the same as those in Figure 30, except that

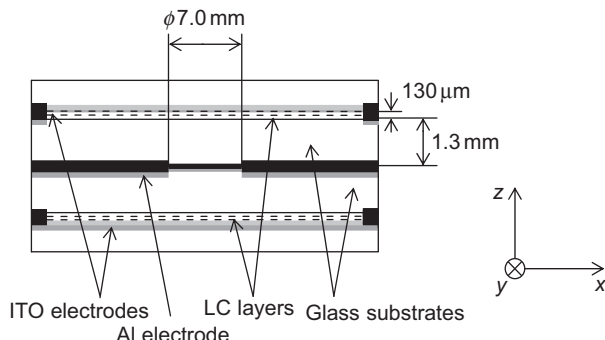


FIGURE 31 Cell structure with the hole-patterned electrode at the center and two LC layers on its sides (Ye et al., 2004a).

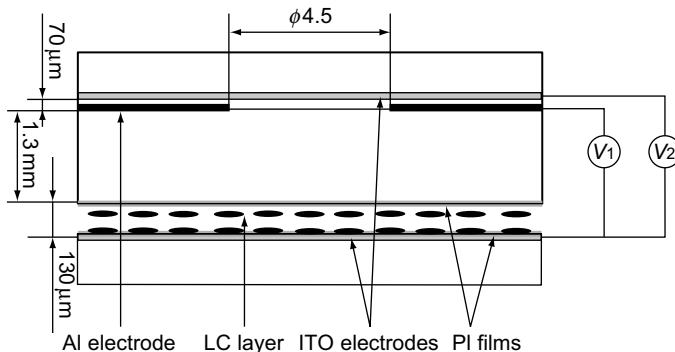


FIGURE 32 LC cell with three electrodes driven by two voltages for wider tunable range (Ye et al., 2004b).

the diameter of the circular hole becomes 4.5 mm. Two voltages V_1 and V_2 drive the cell. V_1 is maintained to be 70 V_{rms} , and V_2 changes from 0 to 70 V_{rms} to tune the lens power. The spatial variation of E in the hole area decreases with increasing V_2 , and hence so does the power. The range of the variable power is very wide, covering 0.8–10.7 D . When $V_1 < V_2$, the electric field in the LC layer increases from the edge to the center of the hole area, and so does the refractive index, and then the cell becomes a negative lens. So by adjusting V_1 and V_2 , the power of the LC cell can be variable from negative to positive values (Wang, Ye, & Sato, 2005a, 2006a). An example is presented here. For the cell with 75- μm -thick LC layer, 3-mm-lens aperture, 1.3-mm-thick glass between the hole-patterned electrode and the LC layer, and 50- μm -thick thin glass slide between the hole-patterned electrode and the upper ITO electrode, when V_1 is maintained at 35 V_{rms} and V_2 is tuned in the range from 0 to 40 V_{rms} , the LC cell works as a positive lens. However, when V_2 is maintained at 60 V_{rms} and V_1 is tuned in the range from 0 to 50 V_{rms} , the cell works as a negative lens. The data is shown in Figure 33. Aberrations of the two-voltage-driven LC lens were measured using a Fizeau interferometer and optimum conditions for operation as positive or negative lens were discussed (Takahashi, Ye, & Sato, 2007). If the LC layer in Figure 24 is replaced by two thin LC layers as shown in Figure 34 (Wang, Ye, & Sato, 2005b, 2006b), the operation speed of the lens will be improved and the focus range will be wider. Experiments show that the lens power of the two-LC-layer lens is approximately twofold larger than that of the single-LC-layer lens. On this basis, if two more LC layers are added to the other side of the hole-patterned electrode but with orthogonal homogeneous alignment, a polarization-independent LC lens with a large tenability can be produced (Ye, Wang, & Sato, 2006).

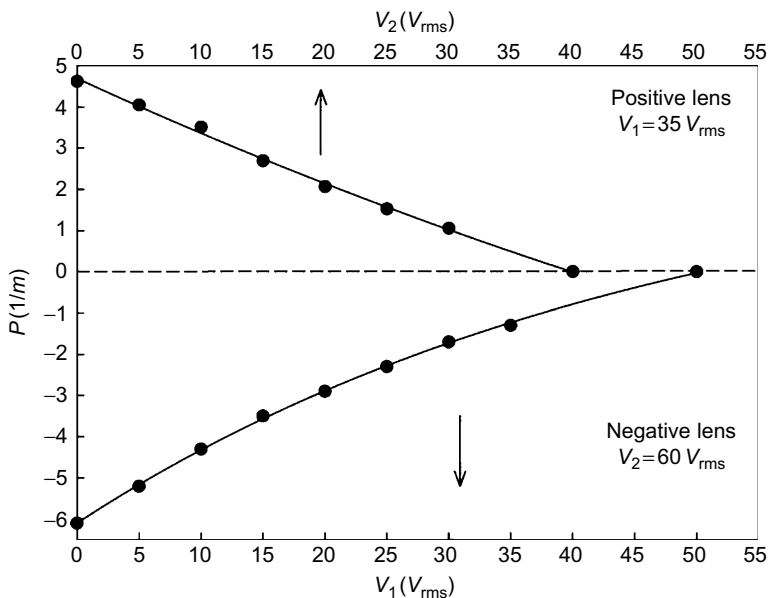


FIGURE 33 Tunable power of the lens driven by two voltages. When V_1 is fixed at $35 V_{rms}$, positive powers are tunable as a function of V_2 ; When V_2 is fixed at $60 V_{rms}$, negative powers are tunable as a function of V_1 (Wang et al., 2006a).

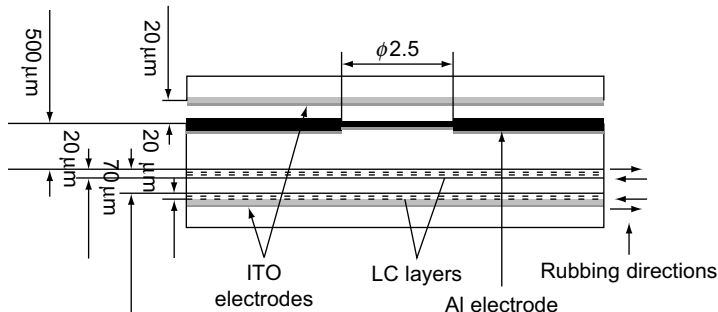


FIGURE 34 LC cell driven by two voltages for fast operation and wider power range by stacking two thin LC layers (Wang et al., 2005b).

There are two additional LC lens structures that are driven by two voltages and they allow increased focusing power for mini aperture lenses. One structure is shown in Figure 35 with (a) for the cross section of the lens and (b) for the patterned electrode (Ye, Wang, & Sato, 2008). The lens has two layers of LC for higher power. For the patterned electrode, the outer

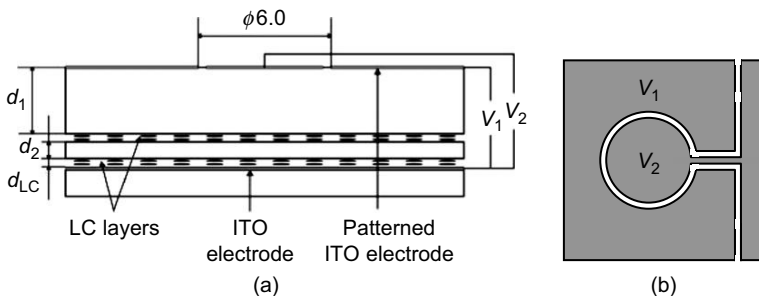


FIGURE 35 LC lens structure driven by two voltages with a circular electrode in the center surrounded by a hole-patterned electrode. (a) Cross section. (b) Electrode pattern (Ye et al., 2008).

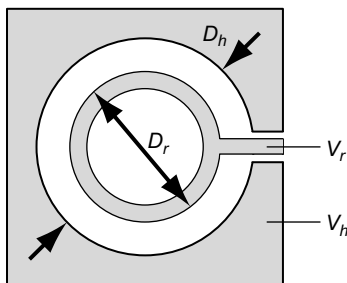


FIGURE 36 Electrode pattern with a ring electrode inside a hole-patterned electrode. The lens structure can be the same as shown in Figure 30 (Chiu et al., 2008).

part has a hole (6 mm in diameter in the example) in the center and the inner part is a circular electrode (5.92 mm in diameter). There is a gap between the two parts so that two different voltages V_1 and V_2 can be applied to the outer and inner electrodes, respectively. Similar to the structure described earlier, both positive and negative powers can be obtained. In the positive lens state, V_1 is maintained to $120 V_{rms}$ and V_2 varies from 30 to $120 V_{rms}$, and in the negative lens state, V_2 is maintained to $120 V_{rms}$ and V_1 varies from 40 to $120 V_{rms}$. The power is tuned from 1.5 to -1.1 diopter. To increase the focusing capability of the conventional hole type lens, one approach is to improve the intensity of electric field at the central hollow area. Correspondingly, Chiu, Lin, Chao, and Fuh (2008) proposed a new hole-and-ring type electrode (Figure 36) to improve the distribution of electric field, and it requires lower applied voltage than the conventional one. In the example, the diameter of the hole of the outer electrode is 4 mm, and the ring electrode is inside and cocentered with the hole. The outer radius of the ring electrode is 1 mm. The overall thickness of the LC

lens can be as thin as 1.2 mm and the shortest focal length of the 4-mm-aperture lens occurs at 20 cm (5 diopter) under an applied voltage of 30 V at 1 kHz. The inner ring electrode requires only 40% of applied voltage of the external hole electrode.

Using the above hole-pattern electrode structure, although it is possible to increase the lens aperture by increasing the thickness of the substrate between the hole-patterned electrode and the top surface of the LC layer (the ratio of the two parameters are kept between 2 and 3, e.g., 2.6), it is not a practical approach because the driving voltages are almost linearly proportional to the thickness of the substrate, making the voltages too high. A higher dielectric constant substrate may help, but the voltages are still high for lens apertures close to 10 mm. The problem can be alleviated by inserting a layer of material of weak conductivity between the patterned electrode and the LC layer (Ye et al., 2008). The nonuniform electric field induced by the patterned electrode in the cell generates a radial electric current that redistributes the electric charges in the weakly conductive layer. An electric field resulting from the charge redistribution then occurs in the conductive layer in the direction opposite to that of the radial component of the nonuniform electric field created by the patterned electrode. As a result, the abruptly changing potential caused by the patterned electrode is smoothed by the conductive layer. With this structure, for a 15-mm-aperture lens, the thickness between the patterned electrode and the LC layer was reduced from 6 to 0.475 mm (Ye et al., 2008). However, the power of the lens was too low and was tunable only from plano to 0.2 diopter.

2.6. Liquid Crystal Lens Formed by a Glass/Polymer Lens/Shell and Flat LC Layer(s)

When a glass/polymer lens and a LC layer are sandwiched between two electrodes, the thickness variance of the glass/polymer lens gives rise to an inhomogeneous electric field in the LC layer. Different geometries can be used.

Figure 37 shows the LC lens where LC is sandwiched between a flat glass substrate and a plano-convex glass lens (Wang, Ye, Honma, Nose, & Sato, 2002; Wang, Ye, & Sato, 2005c,d). ITO is coated on the top surface of the flat substrate and the spherical surface of the lens. The LC is homogeneously aligned. The spherical electrode generates a gradient electric field distribution in the LC layer. The field is the smallest at the center and the largest at the edge. The tilt of the LC directors near the edge is larger than that of the directors at the center, and the effective refractive index for an extraordinary incident beam is smaller at the edge, producing a parabolic phase profile. The advantage of this structure is that the LC

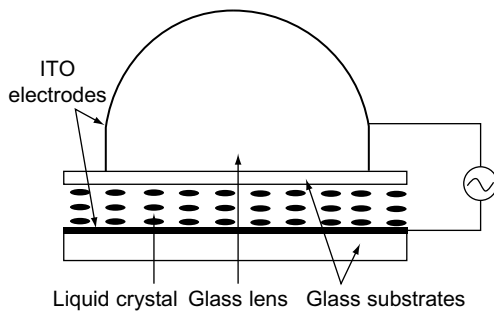


FIGURE 37 LC cell with a spherical electrode (Wang et al., 2002).

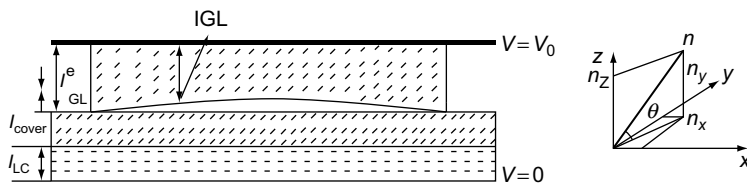


FIGURE 38 LC lens formed by a plano-concave lens with conductive coating on the plano surface and a flat LC layer (Wang et al., 2004).

lens aperture can be much larger than that of the lens based on the hole-patterned electrodes. The power tunable range is relatively small, but it can be increased by using thinner substrate between the LC layer and the plano-convex lens, thick LC layer, and spherical electrode of smaller radius of curvature. If the spherical electrode is covered by another substrate with the same curvature and the refractive indices of the materials on both sides are matched (Ren, Fan, Gauza, & Wu, 2004b), the power of the plano-convex lens will be canceled, leaving only the tunable power of the LC cell. Very recently Asatryan et al. (2010) adopted this structure and deliberately selected the dielectric constants of two materials, composing the doublet to improve the performance of the lens with an aperture of 2.5 mm.

An alternative structure based on a plano-concave glass lens is shown in Figure 38 (Wang, Ye, & Sato, 2004). The concave lens is placed on a LC cell with another flat glass substrate between them. The LC directors are homogeneously aligned parallel to the x axis. One electrode is in the LC cell, and the other one is on the top of the glass lens. When a voltage V_0 is applied across the electrodes, an electric field builds up between the electrodes. In the LC, the electric field is weakest at the center and strongest around the aperture edge and is nearly symmetrical about the center.

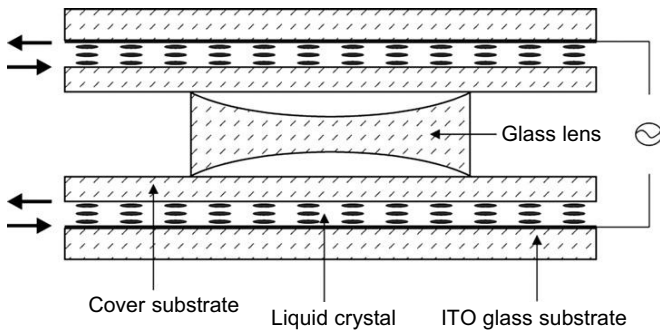


FIGURE 39 LC lens with two concave surfaces and two LC layers (Wang et al., 2004).

Analogous to the above analysis, the bell-like shape of the phase retardation changes with the applied voltage V_0 . If it takes a quadratic form, then the LC cell behaves as an optical lens with a focal length that is electrically tunable. To enforce the effect, two identical LC layers are used. The structure of the system is shown in Figure 39 (Wang et al.). The LC directors are then aligned homogeneously in one direction. The applied voltage is relatively high and the tunable range of the power is limited (about 1 diopter for a 10-mm aperture with a voltage higher than 100 V).

In the lens structure shown in Figure 37 and that in Ren, Fan, Gauza, and Wu (2004), there is a dielectric material (glass or polymer) between the spherical electrode and the flat glass above the LC layer. The effect of the dielectric material on the electric field is the increased strength of the electric field at the center of the lens, and this reduces the gradient of the electric field within the LC layer. This limits the maximum power of the LC lens for a fixed LC layer thickness. Of course, the lens power can be increased by increasing the thickness of the LC layer for larger phase retardation between the center and the edge of the lens, but that increase results in slower response. The ideal case is that when the LC directors at the border start to reorient with an initial voltage, the distributed voltage at the center is less than or near the threshold. When the voltage gradually increases, the reorientation of the LC directors spread toward the center. In order to achieve this, the region between the spherical electrode and the flat glass (0.55-mm thick) is kept empty (Ren & Wu, 2006), and the ITO electrode is coated on the inner surface of a spherical glass shell. For a 6-mm-aperture lens and 25- μm -thick LC layer, the shortest focal length was 0.96 m at 140 V_{rms} with a response time in the order of 1 s. However, the glass shell is fragile. To improve the mechanic stability, another approach was proposed (Ren, Fox, Wu, & Wu, 2007), where a droplet of UV curable optical adhesive forms a parabolic shape, and a thin layer of

conductive polymer is coated on its surface. In this approach, although region between the curved electrode and the flat substrate is still filled with the polymer, the sag of the polymer was increased, and the thickness of the flat substrate was reduced to 0.2 mm, simultaneously. For a lens with 4.2-mm diameter and 60- μm -thick LC layer, the shorted focal length was 15.4 cm at a much reduced voltage 23 V_{rms} . The response time was about 4 s.

2.7. Modal Liquid Crystal Lens Based on Resistive Electrode

Apart from the hole-patterned electrode, another modal approach to generate smooth continuous electric field distribution and hence the refractive index profile is to use resistive electrode. This method is referred to modal addressing or modal control, which is characterized by a high-resistance transparent electrode (control electrode) and a low-resistance contact at the periphery of the control electrode. Lenses made based on this approach are called modal LC lenses (MLCLs) (Naumov, Loktev, Guralnik, & Vdovin, 1998; Vdovin, Gural'nik, Kotova, Loktev, & Naumov, 1999a,b; Yu et al., 2000).

Figure 40(a) shows the schematic drawing of the MLCL. The LC layer is sandwiched between two glass substrates on which the resistive electrode and the continuous electrode are deposited respectively. The surface resistance of the control electrode is much higher than the resistance of the continuous electrode. The initial uniform orientation of the LC layer is determined by the alignment coatings. The control voltage is applied to

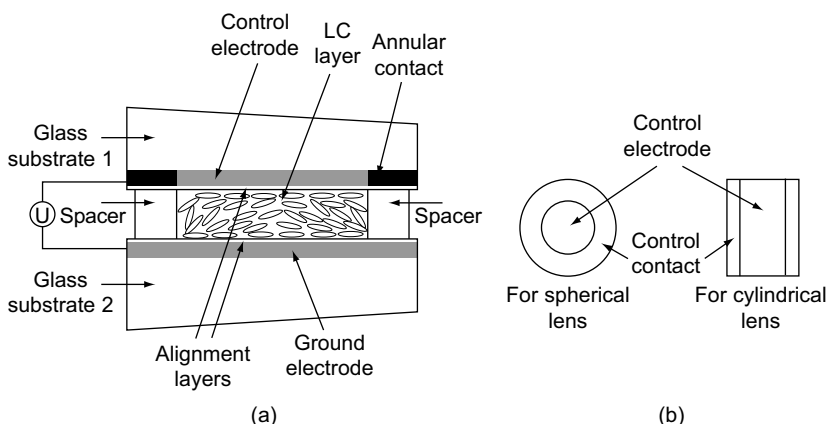


FIGURE 40 (a) Modal LC lens structure. (b) Resistive electrode patterns for the spherical lens and the cylindrical lens (Naumov et al., 1998).

contacts located at the control electrode periphery. The contact configuration determinates the type of lens. For spherical lenses, an annular contact is used, and for a cylindrical lens, two linear parallel contacts are used, as shown in Figure 40(b). The control voltage is applied to a low-resistance annular electrode around the active area of the lens. The resultant system with distributed resistance (control electrode) and capacitance (LC layer) is reactive. This makes it possible to control the parameters of an LC cell utilizing both the amplitude and the frequency of the applied voltage. When an AC control voltage is applied to the contacts, the changes in the voltage at the center of the control electrode lag behind the changes in the voltage applied to the contact electrodes because of the resistive-capacitative nature of the system. An increase in the frequency of the applied voltage increases the delay and reduces the rms value of the voltage at the center of the aperture. Under steady-state conditions, the distribution of the rms voltage in the LC layer decreases radially toward the center of the lens because of the potential divider that is formed by the high-resistance control electrode and the capacitance of the LC layer, and the refractive index for the incident extraordinary beam increases from the periphery to the aperture center, forming the phase profile for a lens. In contrast to the lens based on hole-patterned electrode, MLCL responds to both amplitude and frequency of the control voltages, and this offers additional freedom in optimizing the performance of the lens. However, these values need to be carefully selected in order to minimize phase aberrations, caused by both the nonideal distribution of the electrical field across the lens aperture, and the nonlinear electro-optical response of the LC against the applied field. Algorithms for optimization of the applied voltages are presented in Loktev et al. (2000) and Naumov, Love, Loktev, and Vladimirov (1999). For a 5-mm-aperture lens, the focusing power can be tuned from 0 to 3D. Possibility of using the MLCL for intraocular lens has been considered with wireless control (Simonov, Vdovin, & Loktev, 2007; Vdovin, Loktev, & Naumov, 2003; Zhang, Loktev, & Vdovin, 2005). Using this method, large-aperture lenses can be made. However, the maximum power of the lens that can be realized is limited. It should also be noted that the transmission of the high-resistance electrode may affect the light efficiency of the LC lens.

If the high-resistance control electrode is replaced by a photoconducting layer, whose surface resistance depends on the intensity of the incident radiation, the shape of the wavefront of the new lens can be controlled by varying not only the amplitude and frequency of the applied voltage, but also by changing the profile of the incident intensity. A circular contact can be used to generate a spherical lens while a rectangular contact can be used for a cylindrical lens. Such a lens is called optically addressable modal LC lens (Gural'nik & Samagin, 2003).

2.8. Lens Using Polymer/Liquid Crystal Composites

Addition of a small amount of monomer (about 3%) into LC cell and its in-situ photopolymerization allows controlling the spatial orientation of LC molecules. Such polymer-stabilized LC (PSLC) can be used to fabricate tunable lens with circular-hole-patterned electrodes on one or both substrates of the cell. There is another kind of PSLC that can be used for tunable focus using nonuniform illumination and uniform electric field (Presnyakov, Asatryan, Galstian, & Tork, 2002). In this case, the mixture is homogeneous oriented LC (E7) and few percent (about 3%) of photopolymerizable monomer (e.g., bisphenol-A-dimethacrylate) doped with photoinitiating complex. Homogeneous LC cell with alignment layer was prepared. Exposition of a UV or green laser beam with Gaussian spatial intensity distribution to such a mixture induces a spatially inhomogeneous polymer network (Figure 41, Presnyakov & Galstian, 2005). The higher exposure region results in a higher polymer concentration and smaller LC domains, so the threshold voltage in that region is higher. The electro-optical response of this system to a uniform electrical field creates a nonhomogeneous, centrally symmetric character, and a gradient refractive index lens can be obtained. The Gaussian spatial intensity distribution gives a convex lens. In the previous study, for a lens with 1.5-mm aperture and 10- μm -thick cell, the minimum values of the focal length are 1.6 and 0.8 m for the field frequencies 1 kHz and 60 Hz, respectively. The applied voltage is only a few V_{rms} . In another experiment (Ren & Wu, 2003), a circularly symmetric, continuously variable optical density filter was used as the photomask for illumination. Three percent UV-curable monomer BAB6 (containing 2 wt% photoinitiator IRG184) was mixed in a LC host and the mixture is also named polymer network LC (PNLC). The transmission at the center was the lowest, so a concave phase profile was formed. The radius of the lens was 0.8 cm and the focal length of the lens

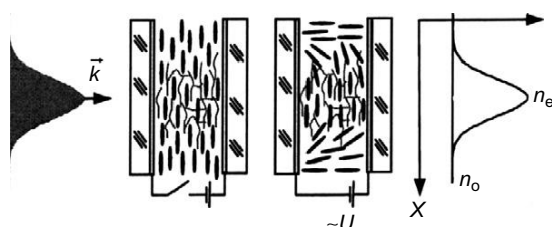


FIGURE 41 Illustration of the principle of polymer stabilized LC lens fabrication and refractive index distribution with a uniform voltage (Presnyakov & Galstian, 2005).

was very long, \sim 310 m. Binary Fresnel zone plate using polymer-stabilized LC was also reported (Fan, Ren, & Wu, 2003).

Polymer-dispersed LC (PDLC) is a composite material consisting of LC droplets dispersed in a polymer matrix. The principle of a PDLC lens is based on inhomogeneous droplet size distribution, which is also obtained by exposing the LC/monomer mixture with a gradient UV light. In this case, the UV-curable monomer has a much larger concentration. In one example (Ren & Wu, 2002), monomer NOA-81 (Norland) and LC (E7) was mixed at 70:30 wt% ratio. The area exposed to higher irradiance generates smaller LC droplet size. The driving voltage of PDLC is inversely proportional to the square root of the LC droplet size. When a uniform voltage is applied to the cell, the LC directors have different degrees of reorientation, and a gradient phase profile can be generated. Depending on the pattern of the irradiance, both positive and negative lens can be formed. If the photomask has the transmission like a binary amplitude Fresnel zone plate, when a uniform voltage is applied, a switchable phase Fresnel zone plate can be formed. Because the nanoscale LC droplets in the polymer matrix are randomly distributed, the lens is polarization independent and exhibits a fast switching time.

Another mechanism of adaptive lens using LC/polymer composite is based on electrically induced LC/monomer concentration redistribution (Ren, Lin, & Wu, 2006). LC/monomer mixture consisting of 50 wt% negative nematic LC (ZLI-4788-000, $\Delta\epsilon = -5.7$) and 50 wt% liquid monomer (N-vinylpyrrollidone, NVP) was injected into the homogeneous cell. This structure avoids any electric-field induced molecular reorientation. In the absence of an electric field, the LC/monomer mixture is homogeneously distributed. Application of an inhomogeneous electric field causes the LC molecules to diffuse toward the high-field region and the liquid monomer toward the low field region. However, the LC molecules tend to diffuse from high to low concentration direction in order to balance the concentration change. A gradient LC concentration is thus obtained. In the LC-rich region, the surface rubbing aligns the LC molecules and gives an increased refractive index, while the monomer-rich region exhibits a lower refractive index. A tunable-focus lens can be produced. Spherical electrode was used to generate inhomogeneous electric field. However, the focus tunable range is small and the response time of a 25- μm -thick cell has a response time about 3 min for a 9-mm aperture.

A switchable Fresnel zone plate lens was demonstrated using a phase-separated composite film (Fan, Ren, & Wu, 2005). UV curable prepolymer (e.g., NOA 65, Norland) is mixed with a nematic LC (e.g., E48, Merck) with a ratio of 70:30 wt%. The mixture is illuminated by a uniform UV light through an amplitude chromium mask. Phase separation is executed at a

temperature of around 100 °C. The phase retardation between the neighboring zones is determined by the effective refractive index of the LC, the thickness of the LC layer, and the thickness of the polymer layer. The effective refractive index of the LC is tuned by the applied voltage. Since the LC and polymer are separated completely to become two layers, there is no light scattering and a relatively low operating voltage is required.

2.9. Microlens with Hybrid Alignment

Two groups developed microlenses based on the patterned orientations of the LC on cell walls (Cheng, Chang, Liu, & Yeh, 2006; Ye, Yokoyama, & Sato, 2006). In the design by Ye et al., the LC lens is prepared using a thin LC layer sandwiched between two planar glass substrates with a transparent electrode on each. The alignment films on the cell walls are treated so that the LC molecules in the overlapped circular areas on both walls align parallel, while those outside the circular areas are perpendicular, to the cell walls (Figure 42). The LC directors inside the layer then gradually change their direction of alignment between the parallel and perpendicular states; a spatially inhomogeneous distribution of refractive index that is nearly axially symmetrical for an incident extraordinary light wave is consequently formed and a spherical lens is produced. An applied voltage changes the refractive index distribution and hence the optical powers. This method is suitable to make LC lenses of very small size from

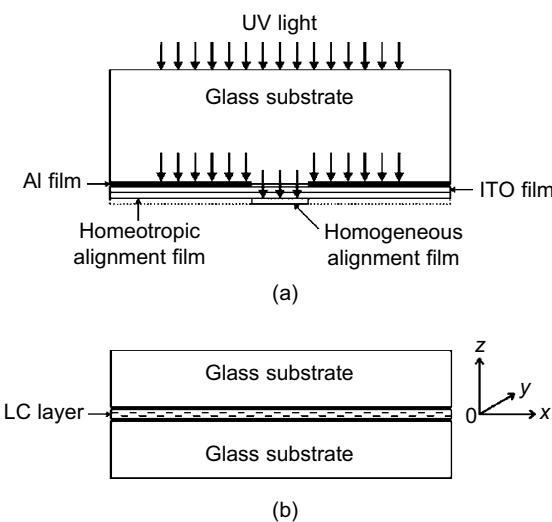


FIGURE 42 LC microlens formed by patterned molecular orientations on cell walls.
(a) Substrate treatment. (b) LC cell (Ye et al., 2006).

several to several tens of micrometers with planar LC layers of thickness of approximately $100\text{ }\mu\text{m}$. Calculated director orientations in plane $y = 0$ at $V = 0$ and $V = 1\text{ V}$ are shown in Figure 43.

In the design by Cheng, Chang, Liu, and Yeh (2006), hybrid alignment of the LC in the central region is processed with micro-imprinting technology. The imprinted hybrid alignment, which was surrounded by homogeneous (homeotropic) alignment (Figure 44), resulted in spatial

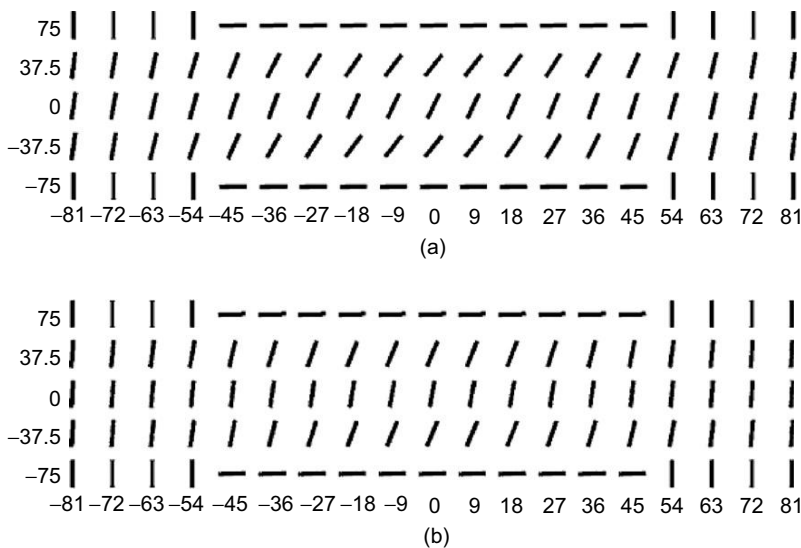


FIGURE 43 Calculated director orientations in plane $y = 0$ at (a) $V = 0$ and (b) $V = 1\text{ V}$ (Ye et al., 2006).

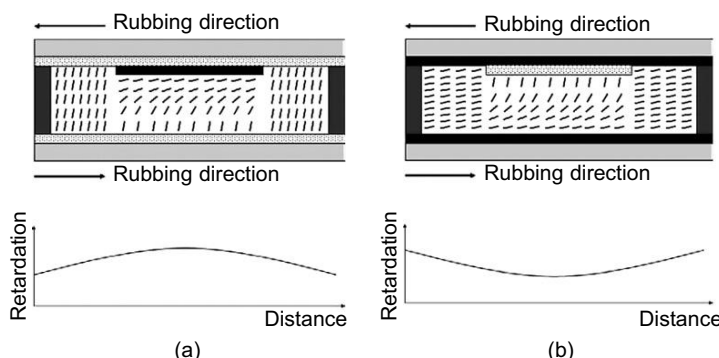


FIGURE 44 Microlens based on hybrid LC alignment. (a) The convex lens configuration. (b) The concave lens configuration (Cheng, Chang, & Yeh, 2006).

refractive-index distribution of liquid-crystal molecules in the microlens. With different hybrid-alignment configurations, the microlens functioned either as a convex (Figure 44(a)) or concave (Figure 44(b)) lens. The focal length of the microlens was electrically controlled at applied voltages of less than 4 V. The focal length was adjusted from 7.8 to 8.6 mm and from -10 to -35 mm for a convex and a concave lens, respectively. The rising response time was 0.5 s, and the falling response time was 5 s.

2.10. Polarization-Independent LC Lens

We have shown that high-performance, polarization-independent lens can be achieved by using orthogonal alignment of two LC layers. For binary phase Fresnel zone plate, several articles have addressed this issue by using orthogonal alignment of the LCs in the neighboring subzones. One technique is to control the alignment layer of the neighboring subzones for the side of patterned electrode and use homeotropic alignment on the other side with continuous electrode (Kim, Yu, Kim, Kim, & Lee, 2006; Patel & Rastani, 1991). The other technique is based on double-side photocalignment of azo-dye (Methyl Red) doped LCs (e.g., E7) (Lin, Jau, Lin, & Fuh, 2007). Before the LC cell is assembled, the two ITO-coated glass substrates are slightly rubbed with cloth. Methyl Red dyes may undergo photo-isomerization between the trans-isomer and the cis-isomer. Azo-dyes are usually in the stable trans-state in the dark. When the dye-doped LC cell is excited by light in the absorption spectrum range at the room temperature, the dyes are transformed from the trans to the cis form, inducing the diffusion, and adsorption onto the substrate facing the incident pump beam with the long axes of dyes being perpendicular to the pump-beam polarization after many trans–cis transformation cycles. The adsorbed dyes then align LCs. The adsorption of dyes can be made onto both of the two substrates of the cell, if the cell is optically excited at a temperature just above the clear temperature of LC. Detailed procedures can be found in Lin et al. (2007). Other materials such as polymer-dispersed LCs and cholesteric LCs may be used for polarization-independent lens. However, the required voltage is high and the general performance is not good enough.

3. ADAPTIVE LIQUID LENS

Adaptive liquid lens offers the variable focus by changing the shape of the liquid. Based on the operation mechanism, adaptive liquid lenses can be classified into four types: fluid-membrane interaction, electrowetting effect, dielectrophoretic effect, and thermal effect.

3.1. Liquid Lenses Based on Fluid-Membrane Interaction

This kind of liquid lens consists of a liquid-filled chamber, which is formed by two elastic membranes or one membrane and one support frame. The principle of this lens is similar to that of the accommodating lens inside the human eye or other animal eyes, and sometimes it is called bio-inspired fluidic lens. By changing the pressure of the liquid, the shape of the liquid lens is changed as a result of the deformation of the membrane and hence the focal length can be varied. The most widely used flexible polymer membrane material is poly(dimethyl siloxane) (PDMS, (10:1 mixing ratio of the monomer and a curing agent, Sylgard 184, Dow Corning, MI). In 1968, Wright proposed the idea of liquid-filled varifocal lens (Wright, 1968). Shortly after that Knollman, Bellin, and Weaver (1970) investigated theoretically the shape of the membrane-encapsulated liquid-filled lens and it is a parabola. Later on Sugiura and Morita (1993) analyzed the effect of gravity on the lens shape and the aberration of the lens. The effect of gravity and the aberration can be negligibly small by selection of optimized materials and parameters such as the lens diameter, hydraulic pressure, and liquid density. Rawicz and Mikhailyenko (1996) developed a mathematical model that calculates the absolute value of the tension in the membrane and experimentally verified it. Chronis, Liu, Jeong, and Lee (2003) fabricated tunable liquid microlens array by soft lithographic technique, and simultaneous control of the focal length of all the microlenses was accomplished by pneumatically regulating the pressure of the microfluidic network. Tunable microdoublet lens array capable of creating dual modes of biconvex or meniscus lens was demonstrated (Jeong, Liu, Chronis, & Lee, 2004). Zhang, Lien, Berdichevsky, Choi, and Lo (2003) demonstrated a 20-mm-aperture lens with wide range focal length (41–172 mm) adjusted and controlled by a syringe pump. Lenses based on the similar mechanism were also reported in Marks, Mathine, Peyman, Schwiegerling, and Peyghambarian (2009). In 2004, Zhang also demonstrated plano-convex and biconvex lenses with a tunable focus range from 30 mm to infinity (Zhang, Justis, Lien, Berdichevsky, & Lo, 2004). Chen, Wang, Fang, and Varahramyan (2004) designed a polymer microlens with higher numerical aperture (up to 0.24) by using a thin PDMS diaphragm with 3D convex lens, a silicon chamber, and a PDMS chamber block with an inlet channel. For 1.4-mm aperture, the focal length can be tuned from 3.8 to 10.6 mm. Agarwal, Gunasekaran, Coane, and Varahramyan designed and fabricated microlenses with a wide field-of-view (FOV) and large numerical aperture using standard photolithographic and silicon micromachining techniques. Fluidic pressure was applied by an external syringe pump. This lens system is capable of working in dual mode, forming either a double convex (DCX) or a

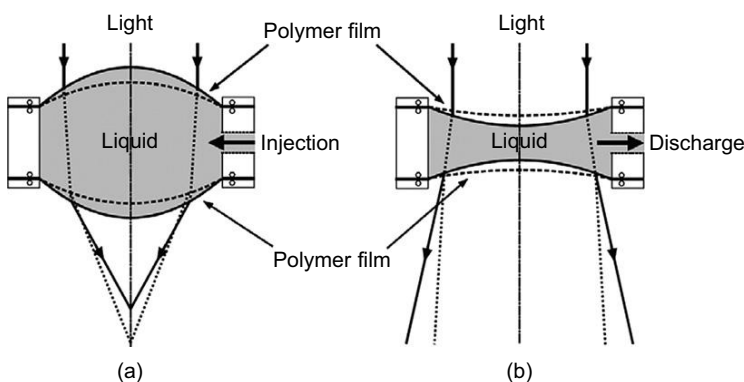


FIGURE 45 Principle of liquid pressure varifocus lens: (a) biconvex lens and (b) biconcave lens.

double concave (DCV) lens. The focal length could be tuned in the range from 75.9 to 3.1 mm and from -75.9 to -3.3 mm for the DCX and DCV lens configurations, respectively. The FOV for this lens system was found to be in the range of $0.12\text{--}61^\circ$ for DCX lens and $7\text{--}69^\circ$ for DCV lens. The smallest *F*-number that could be achieved using this dynamic lens is 0.61, which corresponds to the numerical aperture value of 0.64. Based on the same mechanism, Kuwano, Tokunaga, Otani, and Umeda (2005) were able to continuously change the shape of the lens from concave to convex. A schematic diagram is shown in Figure 45. When the liquid is injected into the lens, the pressure increases as shown in Figure 45(a), and both lens surfaces expand into a convex shape. When the liquid is discharged from the lens, the refraction surface is reformed to a concave shape as shown in Figure 45(b). This kind of lens was also demonstrated by Moran et al. (2006). A microfluidic device that operates as a set of two adaptive cylindrical lenses focusing light along two orthogonal axes was demonstrated by Pang, Levy, Campbell, Groisman, and Fainman (2005). The device is made out of PDMS using soft lithography, and consists of a few chambers separated by flexible membranes and filled with liquids of different refractive indices. The cylindrical lenses can be both converging and diverging; their focal lengths are varied independently and continuously adjusted between -40 and 23 mm by setting pressure in the chambers. An adaptive lens by changing the effective aperture of the liquid was proposed by Ren and Wu (2005). The lens consists of an elastic membrane, a solid plate, and an annular sealing ring which looks like an iris diaphragm; a liquid with a fixed volume is stored in lens chamber. The surfaces of annular sealing ring are sealed with an elastic membrane. The radius of the annular sealing ring is changeable. By tuning the radius of

the annular sealing ring, the stored liquid in the lens will be redistributed, thus changing the curvature of the elastic membrane. Therefore, the lens cell causes light to converge or diverge.

The lens cell may consist of a lens chamber connected to a reservoir, both covered by elastic membranes. By pushing the membrane of the reservoir, the liquid of the fixed volume will be redistributed and consequently the fluid pressure deforms the membrane of the lens chamber. Various techniques for implementation of the fluidic pressure have been proposed. For example, a servo-motor can be used to push the membrane of the reservoir from the side of the lens (Ren, Fox, Anderson, Wu, & Wu, 2006). Deformation of the membrane can also be implemented by a piece of photo-polymer, which can bend under the influence of polarized light (Yu, Nakano, & Ikeda, 2003). Such a polymer contains azobenzene LC moieties. When the photo-sensitive polymer is attached to the membrane of the reservoir and exposed to polarized blue light, the polymer is bent, exerting fluid pressure for the change the focal length of the plano-convex lens (Xu et al., 2009). However, the response of the lens is slow (approximately a few seconds). In order to achieve high-speed focusing, a piezo stack actuator with a built-in motion amplifier has been used to rapidly deform the membrane and 1-kHz bandwidth was achieved (Oku, Hashimoto, & Ishikawa, 2004). Two pneumatically actuated adaptive lenses with a 2-ms response time and a 4-diopter variation of power have been demonstrated (Campbell, Fainman, & Groisman, 2007). The two membranes are 18 and 12 mm in diameter and the effective aperture of the two lenses are 5 and 3.3 mm, respectively. A pinned-contact oscillating liquid lens working at 100 Hz with a small scale (1–2 mm aperture) has been reported (López & Hirsa, 2008). Electrochemical (López, Lee, & Hirsa, 2005) and electromagnetic (Lee & Lee, 2007) actuators have also been proposed for implementation of small-scale lens. Recently, Li and Fang (2010) have demonstrated compact, low-cost adaptive lenses actuated by electromagnetic solenoid. The lens apertures are all larger than 10 mm and the lenses show large tunable power (over 30 diopters) and high performance. A novel structure for electromagnetic solenoids was designed, which allows much larger electromagnetic force. As shown in Figure 46, there are two holes in the plastic substrate and they are connected by a channel. They serve as the reservoir and the lens chambers respectively. The top surfaces of the two chambers are covered by soft materials such as elastic rubber or PDMS membrane. The bottom surface of the lens is covered by glass or another PDMS membrane. The required DC voltage is only a few volts.

Apart from the continuously tunable lens, a 4-bit digital liquid lens for variable focal length using a 4-bit actuator (b_1, b_2, b_3 , and b_4 bit actuators) has been demonstrated (Lee & Cho, 2010). The 4-bit actuator, where

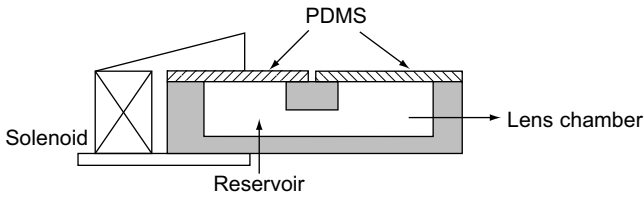


FIGURE 46 The compact liquid lens actuated by the modified electromagnetic solenoids.

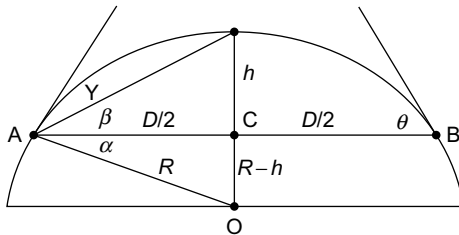


FIGURE 47 A schematic diagram for the plano-convex lens shape.

1, 2, 4, and 8 unit pneumatic actuators are serially connected with binary-combination, pushes a discrete fluidic volume into the lens in 2^4 different levels. Thus, the 4-bit digital actuation mode ($b_4 b_3 b_2 b_1$) from (0000) to (1111) makes $2^4 = 16$ different levels of lens curvature and focal length.

Most of the adaptive liquid lenses focus light perpendicular to the plane of the substrate (out-of-plane). A structure for tunable microlens that can focus light in the plane of the substrate (in-plane) was proposed by Shi, Stratton, Steven, Huang, and Huang (2010). The in-plane tunable microlens is critical for lab-on-a-chip devices.

In most of the systems demonstrated, simple models assuming spherical surfaces have been used.

Although this model is not accurate, to first order this approximation is useful in determining the basic focal length. A schematic drawing for the plano-convex lens shape is shown in Figure 47. The dependence of the focal length on the liquid volume and lens contact angle can be calculated using the lens formula. From thin lens equation,

$$\frac{1}{f} = (n - 1) \left(\frac{1}{R_1} - \frac{1}{R_2} \right), \quad (3.36)$$

when $R_2 \rightarrow \infty$, the following equation is obtained:

$$f = R_1 / (n - 1). \quad (3.37)$$

Referring to Figure 47, assume the lens diameter D , sag height h , and contact angle $\theta = \beta + \gamma$. We have

$$R = \frac{D^2 + 4h^2}{8h}, \quad (3.38)$$

$$\alpha = \tan^{-1} \left(\frac{R - h}{D/2} \right), \quad (3.39)$$

and

$$\beta = \tan^{-1} \left(\frac{h}{D/2} \right). \quad (3.40)$$

Then

$$\gamma = 90^\circ - \alpha - \beta = 90^\circ - \tan^{-1} \left(\frac{2R - 2h}{D} \right) - \tan^{-1} \left(\frac{2h}{D} \right). \quad (3.41)$$

Therefore, the contact angle θ equals to

$$\begin{aligned} \theta &= \beta + \gamma = 90^\circ - \tan^{-1} \frac{2R - 2h}{D} \\ &= 90^\circ - \tan^{-1} \left[\frac{2 \left(\frac{D^2 + 4h^2}{8h} \right) - 2h}{D} \right] \\ &= 90^\circ - \tan^{-1} \left[\frac{1 - \left(\frac{h}{D} \right)^2}{4 \frac{h}{D}} \right]. \end{aligned} \quad (3.42)$$

The volume of the liquid that enters the lens chamber can be express by

$$\Omega = \frac{\pi R^3}{3} (2 + \cos \theta)(1 - \cos \theta)^2, \quad (3.43)$$

and the focal length f is equal to

$$f^3 = \frac{3\Omega}{\pi (1 - \cos \theta)(2 - \cos^2 \theta - \cos \theta)(n_L - 1)^3}, \quad (3.44)$$

where n_L is the refractive index of the liquid.

The maximum deflection h of the membrane is derived by

$$w_0 = 0.662 \left(\frac{a \Delta P}{Et} \right)^{1/3}, \quad (3.45)$$

where P is the pressure drop, a is the radius, t is the thickness, and E is the elastic modulus of a membrane. The equation shows that the maximum deflection is proportional to the cube root of the pressure and inversely proportional to the cube root of the thickness.

As a result of edge-bonding conditions and finite film stiffness, the surface of the membrane is not exactly a sphere. A higher-order shape function is needed to design precise optical systems. A parametric mechanical model is first developed for the deformation by Yang, Kobrin, Seabury, Narayanaswamy, and Christian (2008), based on the geometric dimensions and film properties including thickness, boundary conditions, modulus, and prestrain. The material constants are then extracted from a comparison with simple point measurements on real devices at various pressures. Those values are then inserted into a finite-element model to predict the precise shape over a wide range of operating conditions. This form is then fitted with a standard optical lens shape function to obtain the radius of curvature and the conic constant, which are used for accurate optical design. Several articles have characterized the aberrations of the liquid lenses (Feng & Chou, 2009; Schneider, Draheim, Kammerer, Waibel, & Wallrabe, 2009; Schneider, Müller, & Wallrabe, 2008; Shaw & Sun, 2007; Werber & Zappe, 2005). A design method for correcting chromatic as well as spherical aberrations of variable-focus, multichamber liquid lenses was presented by Reichelt and Zappe (2007). By combining suitable optical liquids with appropriate radii of the liquid's interfaces, liquid lenses with superior, diffraction-limited resolution over a wide focal tuning range are possible. Wang, Xu, and Zhao (2007) showed that a two-group liquid lens system is the simplest one that contains no moving mechanical parts and has enough parameters to correct all chromatic aberrations for any focal length and most monochromatic aberrations for certain focal lengths.

3.2. Liquid Lenses Based on Electrowetting Effect

The electrowetting effect (Minnema, Barneveld, & Rinkel, 1980) can be explained with reference to Figure 48, where a droplet of conductive liquid partially wets a solid insulator film of thickness d and dielectric constant ϵ_r and a voltage is applied between the liquid and a counter-electrode beneath the insulator. The contact angle θ of the droplet on the surface will be modified according to the Young–Laplace equation (Vallet, Berge, &

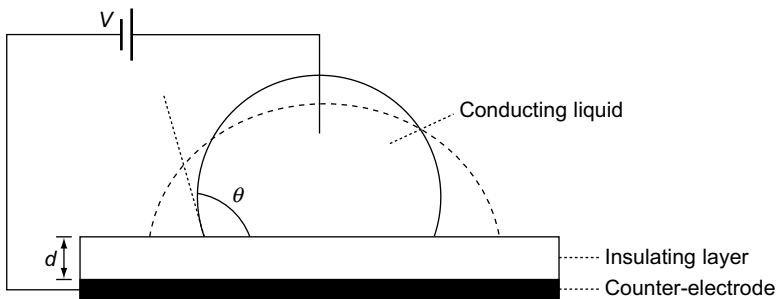


FIGURE 48 Schematic drawing of an electrowetting experiment. A droplet of a conducting liquid is placed on an insulating layer of thickness d , which is deposited on a metal counter electrode. Application of a potential V between the droplet and the metal electrode changes the free energy of the droplet and results in a decrease of the contact angle θ . The resulting droplet shape is indicated by the dashed line (Minnema et al., 1980).

(Volvelle, 1996)

$$\cos \theta(V) = \cos \theta_0 + \frac{\varepsilon_0 \varepsilon_r}{2d\gamma_{LV}} V^2, \quad (3.46)$$

where V is the applied voltage, θ_0 is the initial contact angle at 0 V, γ_{LV} is the surface tension of the liquid-surrounding media interface, ε_r is the permittivity of the dielectric substrate, ε_0 is the permittivity of the vacuum, and d is the distance that separates the electrode and the liquid-solid interface. This effect has been studied in other articles such as Gorman, Biebuyck, and Whitesides (1995), Verheijen and Prins (1999), and Welters and Fokkink (1998). The contact angle can be modified by more than 50°. The insulating layer minimizes the electrolysis of the conductive liquid and reduces the Joule heating effect and the microbubbles.

A direct application of this effect is to use the liquid drop as an optical lens (Figure 49(a), Krupenkin, Yang, & Mach, 2003). Changes of the contact angle of the drop induce changes of the radius of curvature of a liquid-liquid interface, changing its resulting focal length, which is determined by the contact angle θ , the droplet volume Ω , and the refractive indices of the liquid and the surrounding media as

$$f^3 = \frac{3\Omega}{\pi(1 - \cos \theta)(2 - \cos^2 \theta - \cos \theta)(n_L - n_V)^3}, \quad (3.47)$$

where n_L is the refractive index of the liquid and n_V is the refractive index of the surrounding media. The counter-electrode can also be divided into

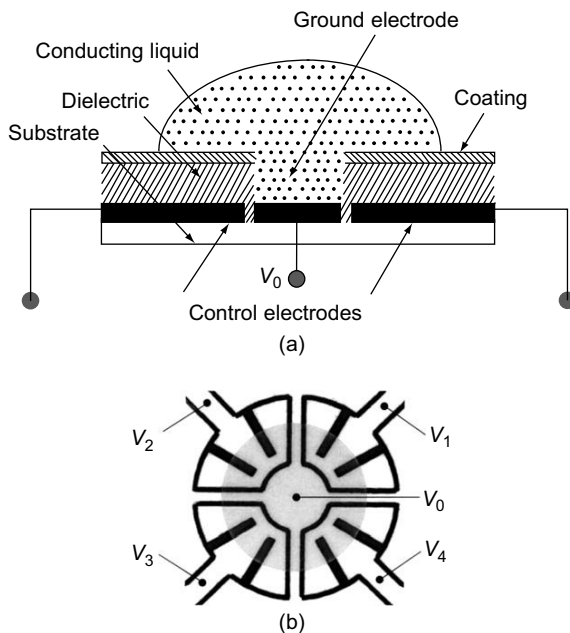


FIGURE 49 Schematic diagram of the tunable liquid microlens based on the electrowetting effect. (a) Electrode design. Black lines indicate etched areas on ITO. Applied voltages are indicated as V_0 through V_4 . Lightly shaded area represents an approximate droplet position. (b) Device cross section. Voltage applied to the ground electrode is indicated as V_0 (Krupenkin et al., 2003).

several subelectrodes and ground electrode (Figure 49(b)), and by applying different voltages to these subelectrodes, the droplet can be moved toward the higher-voltage electrode, and hence, the location of the droplet can be adjusted. However, the conductive liquid is exposed to the air, and the evaporation of the liquid could be a problem. To overcome the problem, electrowetting lenses using two immiscible liquids inside a chamber have been studied as described later (Berge & Peseux, 2000; Kuiper & Hendriks, 2004; Liu, Park, & Choi, 2008).

Figure 50 (Berge & Peseux, 2000) shows the schematic drawing of the lens cell with two nonmiscible liquids, one insulating and nonpolar, and the other a conducting water solution. The liquids are transparent with different indices of refraction, but with the same density so that gravity does not deform the liquid–liquid interface, which remains spherical to any orientation of the cell. The insulating liquid has the shape of a drop in contact with a thin insulating window (in gray in Figure 50), which is hydrophobic so that naturally the insulating liquid will sit on it.

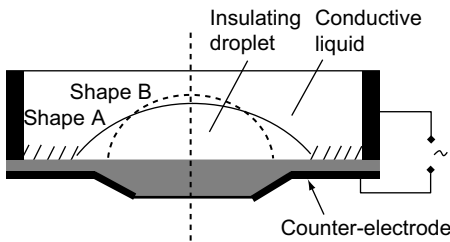


FIGURE 50 Tunable lens using two immiscible liquids. The cell is filled with a conductive sealing liquid. A drop of an insulating and nonpolar liquid is deposited on the bottom wall, which is made of an insulating and transparent material, in gray. The central disc on the bottom wall surface is hydrophobic, in order to trap the drop. The outer zone (hatched area) is hydrophilic (Berge & Peseux, 2000).

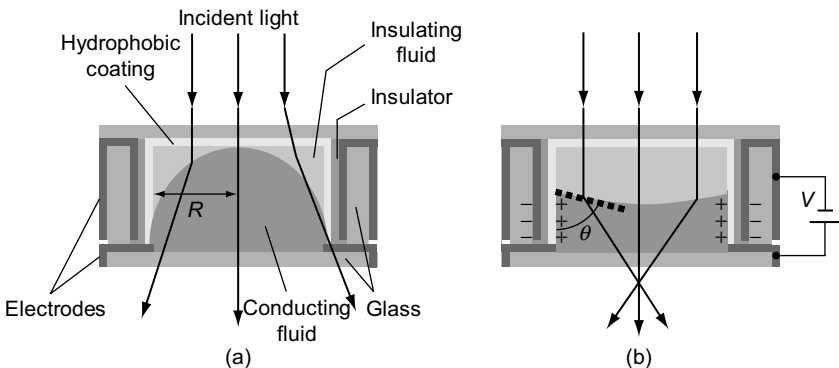


FIGURE 51 (a) Schematic cross section of a liquid-based variable lens in a cylindrical glass housing. (b) When a voltage is applied, the contact angle of the conducting liquid is changed at the interface of the insulator (Kuiper & Hendriks, 2004).

The transparent counter-electrode is deposited on the external side of the window. The outer zone is treated to be hydrophilic so that when no voltage is applied, the drop maintains in shape A. Application of a voltage between the counter-electrode and the conducting liquid favors the wettability of the surface by the same liquid. This deforms the interface from shape A to shape B and thus changes the focal length. Figure 51 (Kuiper & Hendriks, 2004) shows a self-centered lens using two immiscible liquids. The cylindrical glass housing is coated with a transparent electrode, which is formed of 50-nm ITO. The inside of the cylinder is coated with a hydrophobic insulator (The insulator is a 3-mm-parylene-N layer, and the 10-nm-hydrophobic top coating is a dipcoated fluoropolymer, AF1600 supplied by Dupont). The counter electrode is in direct contact with

the conducting liquid. The top and bottom glass plates are glued onto the glass cylinder with epoxy glue. When a voltage is applied between the electrodes, charges accumulate in the wall electrode and opposite charges collect near the solid/liquid interface in the conducting liquid and this results in an electric field across the insulator, which effectively lowers the interfacial tension between the conductive liquid and the insulator and hence the contact angle. The resulting change in contact angle of the conducting liquid with the wall changes the focal length of the lens. However, the out-of-plane electrode in the lens design limited its application in integrated microsystems as vertical metal deposition in microfabrication is often difficult to achieve. To avoid this issue, a planar liquid lens design based on electrowetting of two immiscible liquids with two ring-type electrodes beneath the hydrophobic surface has been reported (Figure 52, Liu et al., 2008). As shown in Figure 52, the outer ring electrode, when applied with an electric potential, electrowets the area above it and changes the surface property. This provides an initial boundary to confine the insoluble oil droplet. If this voltage was not applied before the placement of the oil, it could easily disperse on the hydrophobic surface. The inner ring, however, is the actuation electrode of the lens. When an electric voltage is applied to the inner electrode, the surface above becomes hydrophilic and attracts the surrounding aqueous solution. The aqueous solution deforms the shape of the confined oil droplet, which means changing the focal length of the optical lens.

These electrowetting lenses typically have an aperture about 3 mm and the tunable focal range about 10 mm. But the insulating layer induces electric field shielding effect and increases the driving voltage. Usually they require high voltages up to a few hundred voltages. Very recently an electrode-less and circuitless microlens array configuration was proposed based on the electrowetting effect in pyroelectric periodically poled crystals (Grilli et al., 2008; Miccio et al., 2009; Miccio, Paturzo, Grilli, Vespi, & Ferraro, 2009). Lens effect was obtained in an open microfluidic system by using a thin layer of liquid on a polar electric crystal like LiNbO₃. Because of the pyroelectric effect of the crystals, a temporary voltage is generated when they are heated or cooled. An array of liquid micro-lenses was observed during heating and cooling treatments. The response time is in the order of seconds, which is slower than the earlier lenses using external applied voltages.

3.3. Liquid Microlenses Based on Dielectrophoretic Effect

Nonuniform electric fields exert a dielectrophoretic force on polarizable media including liquids (Jones, Gunji, Washizu, & Feldman, 2001). The liquids respond to a nonuniform electric field by collecting preferentially

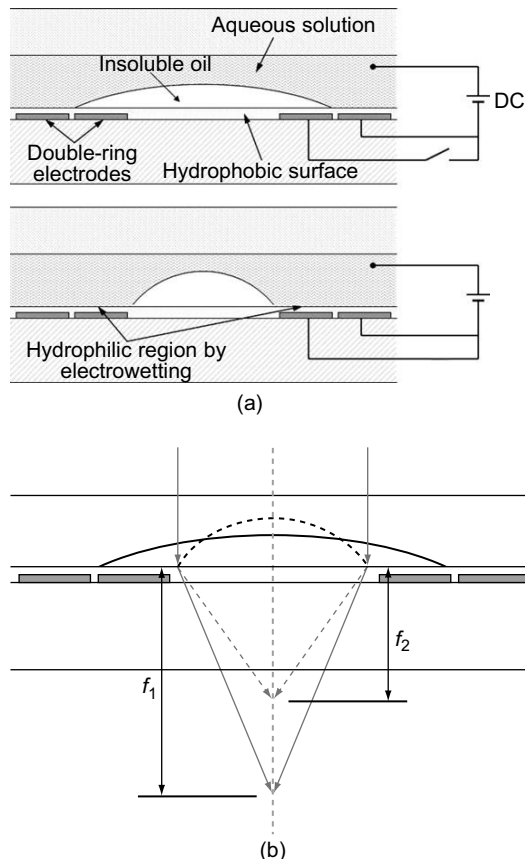


FIGURE 52 Schematic illustrations of the planar liquid lens design: (a) curvature change of the liquid lens by electrowetting and (b) focal length change of the liquid lens. After the application of a dc voltage, the insoluble oil droplet becomes more curved and the focal length is shortened from f_1 to f_2 (Liu et al., 2008).

in regions of maximum field intensity. With properly designed electrodes, the DEP effect may be exploited to control and manipulate small water volumes. The structures of the microlenses based on the dielectrophoretic effect have some similarities to those based on the electrowetting effect. Either one liquid or two immiscible liquids can be used. However, for electrowetting lenses, one liquid must be conductive. In contrast, the liquid(s) used for dielectrophoretic lenses are nonconductive, and when two liquids are used, they have different dielectric constants. Moreover, there are no electrolysis, microbubbles and Joule heat that may appear in electrowetting lenses. Several kinds of dielectrophoretic microlenses

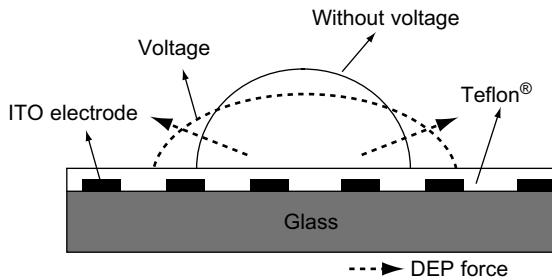


FIGURE 53 (a) Schematic view of deformation mechanism of a deformable liquid crystal droplet lens (not to scale). (b) Design of concentric ITO electrode of 50 μm in width and 50 μm in spacing (Cheng, Chang, & Yeh, 2006).

have been demonstrated using different methods to generate inhomogeneous electric field, including patterned ring electrodes, hole-patterned electrode, continuous flat electrode, and curved electrode on a concave lens surface.

The first dielectric microlens (Cheng, Chang, & Yeh, 2006) used nonconductive LC as the high-dielectric medium and patterned ring electrodes to generate the inhomogeneous field, as shown in Figure 53. Because of the birefringence of the LC, it must be operated in the isotropic phase (temperature exceeding 23.5° of the transition temperature between the nematic phase and the isotropic phase). The ITO electrodes of 50 μm in width and 50 μm in spacing were fabricated on a glass wafer, followed by Teflon coating, which functions as a hydrophobic layer to increase the contact angle of the LC droplet. The dielectric force is given by the Kelvin theory (Haus & Melcher online material)

$$F = \frac{\varepsilon_0}{2} (\varepsilon_{\parallel\parallel} - 1) \nabla(E \bullet E), \quad (3.48)$$

where $\varepsilon_{\parallel\parallel}$ and ε_0 are the permittivities of the LC and free space, respectively. E denotes the electric field intensity. For a lens aperture less than 2 mm, the focal length varied from 1.6 to 2.6 mm in the voltage range of 0–200 V at 1 kHz. In order to allow for operation of the dielectric lens at the ambient temperature that is less than the transition temperature of the LC, two new liquids were used to replace LC (Cheng & Yeh, 2007). As shown in Figure 54, the new lens consists of a liquid droplet with a low-dielectric constant and a sealing liquid with a high-dielectric constant. The bottom diameter of the droplet was 7 mm when no voltage was applied. The two liquids were injected inside a 3-mm-thick PMMA (polymethyl methacrylate) chamber that was sealed between two ITO glass substrates.

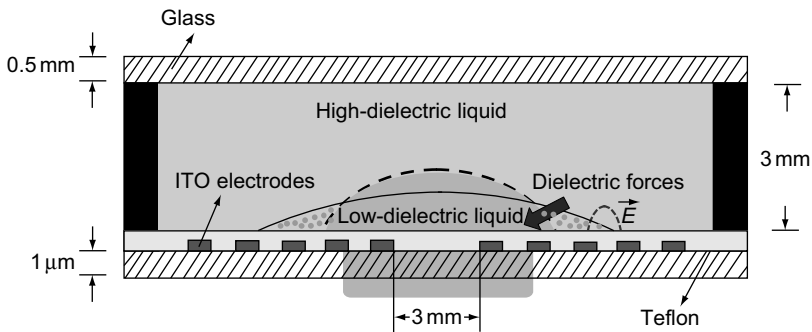


FIGURE 54 Illustration of a dielectric liquid lens. The droplet shrunk to a new state (dashed line) due to the dielectric force (Cheng & Yeh, 2007).

The mass density of the sealing liquid was matched to that of the droplet to minimize the gravitational effect for better optical quality. As the voltage was applied, a dielectric force exerts on the droplet because of the difference in the dielectric constant between the two liquids. In this case, the dielectric force is given by

$$F = \frac{\varepsilon_0}{2}(\varepsilon_1 - \varepsilon_2)\nabla(E \bullet E), \quad (3.49)$$

where ε_1 and ε_2 are the permittivities of the sealing liquid and the droplet, respectively. The dielectric force shrinks the droplet toward the region where the electric field is weaker, increasing the droplet's contact angle and shortening the focal length of the liquid lens. The refractive indices were 1.4 and 1.6 for the sealing liquid and the droplet (optical fluids SL-5267, SantoLight™), respectively. The two liquids had a difference in dielectric constant of about 35. The focal length of the 3-mm-aperture lens was tuned from 34 to 12 mm in the range of 0–200 V. The rise time was measured to be about 650 ms and the measured fall time was 300 ms. To reduce the applied voltage, two liquids with a large difference in dielectric constants should be used. Following this operation mechanism, a hole-patterned array electrode is used to substitute for the patterned ring electrodes to make dielectric microlens array (Ren & Wu, 2008). The aperture of each hole is 140 μm and the gap between the adjacent holes is 100 μm. A thin polyimide layer was coated on the hole-patterned electrode surface, and two liquids were chosen: diacrylate monomer AE-93 ($n \sim 1.46$ and $\varepsilon_1 \sim 5$) for the droplet and deionized water ($n = 1.33$, $\varepsilon_2 \sim 80$) for the sealing liquid. The focal length can be changed from 1.45 to 2.1 mm. The rise time was measured to be ~30 ms and the fall time ~250 ms.

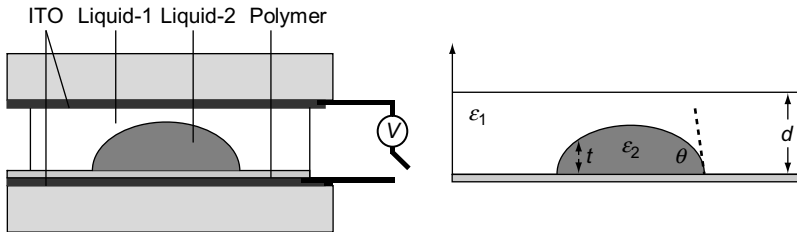


FIGURE 55 Dielectric liquid lens using two flat electrodes. (a) Side view of the lens. (b) Definition of the parameters (Ren et al., 2008).

Ren, Xianyu, Xu, and Wu (2008) also showed that if the droplet and the sealing liquid are sandwiched between two flat electrodes as shown in Figure 55, the electric field across the droplet is inhomogeneous. The electric field inside the droplet with a height t is given by

$$E_t = \frac{V/\varepsilon_2}{t/\varepsilon_2 + (d-t)/\varepsilon_1 + d_p/\varepsilon_p}, \quad (3.50)$$

where ε_p is the dielectric constant of the polymer layer, d is the cell gap, and d_p is the thickness of the polymer layer. If the polymer layer is very thin, i.e., $d_p \rightarrow 0$, the effect of d_p/ε_p on E_t is negligible. Then, the electric field at the boundary of the droplet can be approximated as

$$E_{t \rightarrow 0} = \frac{V\varepsilon_1}{d\varepsilon_2}. \quad (3.51)$$

If the sag of the droplet approaches the cell gap, i.e., $t \rightarrow d$, the electric field at the center of the droplet can be approximated as

$$E_{t \rightarrow d} = \frac{V}{d}. \quad (3.52)$$

The above two equations indicate that the electric field at the boundary of the droplet is $\varepsilon_1/\varepsilon_2$ times stronger than that at its center. The electric field changes continuously in between them. With $\varepsilon_p = 4$, $d_p = 0.8 \mu\text{m}$, $\varepsilon_1 = 47$ (NOA81), $\varepsilon_2 = 1.672$ (SantoLight Optical Fluids SL-5267), $d = 110 \mu\text{m}$, droplet diameter = $230 \mu\text{m}$, the focal length was changed from $620 \mu\text{m}$ at $V = 0 \text{ V}_{\text{rms}}$ to $500 \mu\text{m}$ at $V = 90 \text{ V}_{\text{rms}}$. To enhance the gradient of the electric field across the droplet and hence the dielectric force (Figure 56, Xu et al., 2009), the bottom electrode is replaced by a curved electrode on a plano-concave polymer lens base formed by a glass plano-convex microlens array stamper. The curved electrode not only fixes the position of the microlens, but also reduces the driving voltage.

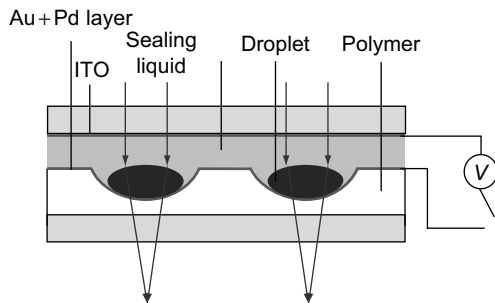


FIGURE 56 Dielectric liquid lens using a spherical electrode (Xu et al., 2009).

Furthermore, the polymer layer is not necessarily required in this case, which simplifies the fabrication process and minimizes the electric field-shielding effects. Using the same liquids and the concave polymer lens with a radius of curvature of 1 mm and an aperture of 0.75 mm, the focal length was tuned from 2.5 mm at $V = 0$ to 1.39 mm at $V = 88 V_{rms}$. The relaxing speed is slow (~ 0.5 s), which can be improved using low-viscosity liquids.

3.4. Liquid Microlenses Based on Hydrogel and Thermal Effect

Liquid microlenses actuated by hydrogel responding to pH, temperature, or infrared light have been demonstrated (Dong, Agarwal, Beebe, & Jiang, 2006, 2007; Zeng & Jiang, 2008). In these devices, microstructures made of pH-, thermal-, or light-responsive hydrogel were used to regulate the curvature of a liquid–liquid interface to form tunable microlenses. An example is shown in Figure 57. The basic design consists of a stimuli-responsive hydrogel ring placed within a microfluidic channel system, and sandwiched between a glass plate and an aperture slip, the latter with an opening centered over the ring. The microchannels are filled with water, and oil is placed on top of this structure and capped with a glass coverslip. The sidewall and bottom surface of the aperture ('ca' in Figure 57(b)) are hydrophilic and the top surface ('ts' in Figure 57(b)) is hydrophobic, which ensures that the water–oil meniscus is pinned along the hydrophobic–hydrophilic contact line 'ca-ts' (that is, the top edge of the aperture opening). When exposed to an appropriate stimulus (which could be pH, temperature, light, an electric field, and so on), the hydrogel ring underneath the aperture opening responds by expanding or shrinking, owing to the absorption or release of water via the hydrogel network interstitials; this leads to a change in the volume of the water droplet located in the middle of the ring. The net volume changes – the change in the volume

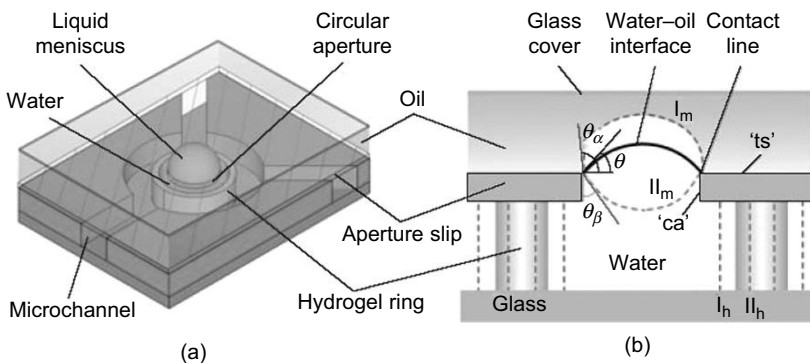


FIGURE 57 Liquid microlens using stimuli-responsive hydrogel. (a) The water–oil interface forms the liquid microlens. The microchannels allow the flow of fluids to the microlens structure. (b) Smart variable-focus mechanism (Dong et al., 2006).

enclosed by the ring, and the change in water droplet volume – cause a change in the pressure difference P across the water–oil interface, with P directly determining the geometry of the liquid meniscus. Because the contact line of the meniscus is pinned and stationary, volume changes are translated into a change in curvature and hence angle (Figure 57(b)), which determines the focal length of the microlens. Another thermal responsive material poly-*N*-isopropylacrylamide (PNIPAAm) has been encapsulated into monodisperse microcapsules for microlens array (Yang, Han, Zhao, Nagai, & Gu, 2006). The size, embedding efficiency, and wall thickness of the microcapsules are controllable. The monodisperse microcapsules were hexagonally packed to form microlens array via a self-assembly process. The imaging capability is controlled by temperature.

4. EXAMPLES OF APPLICATIONS OF THE ADAPTIVE LENSES

Adaptive liquid crystal and liquid lenses have been applied for ophthalmic lens, zoon lens, aberration compensation, biomedical imaging, optical tweezers, beam steering, fiber coupling, and so on. Here we only list a few examples.

4.1. Correction of Presbyopia

Presbyopia is an age-related loss of accommodation of the human eye that manifests itself as inability to shift focus from distant to near objects. Assuming no refractive error, presbyopes have clear vision of distant objects; they require reading glasses for viewing near objects.

Area-divided bifocal lenses are one example of a treatment for this problem. However, the field of view is limited in such eyeglasses except the bifocal diffractive lens (Futhey, 1989), requiring the user to gaze down to accomplish near vision tasks and in some cases, causing dizziness and discomfort. Some users need three different eyeglasses for reading, computer, and driving. Progressive lenses cause some distortion. By using the new switchable, flat, liquid crystal diffractive lenses that can adaptively change their focusing power, we have assembled the prototypes of adaptive eyewear, one can be switched between plano, 1-diopter and 2-diopter (Figure 58), and the other can be switched between plano, 2-diopter, and 4-diopter (Figure 59). The operation of these spectacle lenses is based on electrical control of the refractive index of a 5- μm -thick layer of nematic liquid crystal using a circular array of photolithographically defined transparent electrodes. It operates with high transmission, low voltage ($< 2 \text{ V}_{\text{RMS}}$), fast response ($< 1 \text{ s}$), diffraction efficiency exceeding 90% at eight phase levels, small aberrations, and a power-failure-safe configuration. These results represent significant advance in the state-of-the-art in liquid crystal diffractive lenses for vision care and other applications. They have the potential of revolutionizing the field of presbyopia correction when it is combined with automatic adjustable focusing power. In addition, Professor Josh Silver at Oxford University has developed adaptive eyewear using liquid lens and it has been commercialized with the main market in the undeveloped countries. Besides the adaptive spectacle lenses, accommodative intraocular lens has been proposed using the tunable liquid lens (Qiao, Tsai, Cho, Yan, & Lo, 2009).

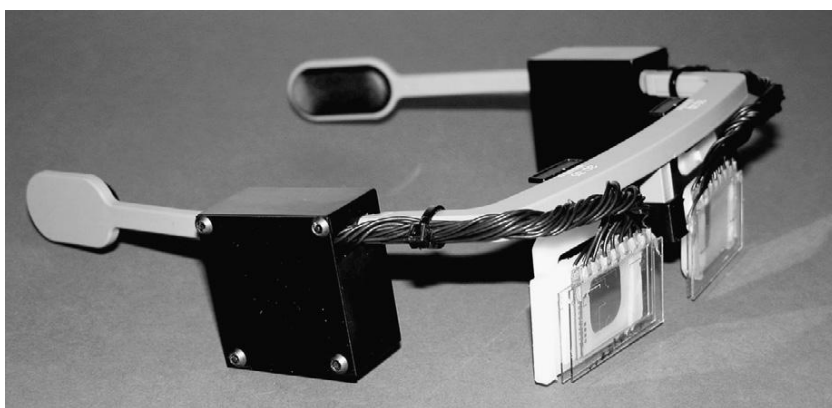


FIGURE 58 A prototype of the assembled adaptive eyewear whose power can be switched between plano, 1D, and 2D.

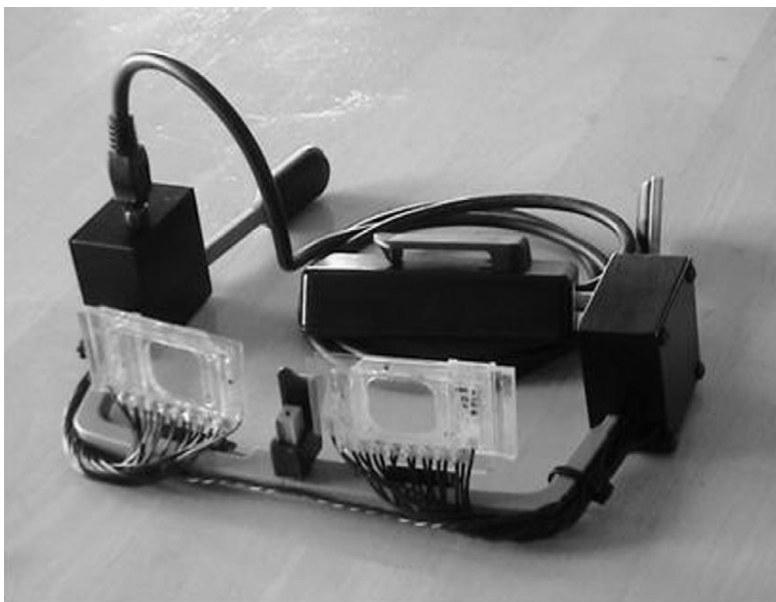


FIGURE 59 A prototype of the assembled adaptive eyewear whose power can be switched between plano, 2D, and 4D.

4.2. Zoom Lens, Optical Tweezer, and Biomedical Imaging

An optical zoom lens is a system that can vary the magnification of focal length while keeping the image plane fixed. As described in the introduction section, replacing the moving optics with stationary adaptive lens can simplify the system, reduce the size and power consumption, and eliminate vibration caused by conventional mechanic movement. Changing the magnification or focal length of an imaging system can be accomplished by using one or multiple adaptive lenses. An optical zoom lens based on two LC spatial light modulators and a few more conventional lenses has been analyzed by Tam (1992), and a design with $3.9\times$ zoom was presented by Wick and Martinez (2004). In the design by Zhang, Justis, and Lo (2005), two fluidic lenses were used to achieve a zoom ratio higher than 4.0. In another design, the zoom lens system consists of one lens with fixed power followed by two double-liquid variable-focus lenses (Peng, Chen, Zhu, & Zhuang, 2007). Recently Ye, Noguchi, Wang, and Sato (2009) demonstrated a zoom lens system by using one glass lens in between two LC lenses and a zoom ratio 1.5 was achieved. Micro-zoom arrays have been used for parallel focusing in integral imaging (Tolosa et al., 2010).

A laser-manipulation system using a LC lens with variable-focusing and beam deflection functions for the transmitted laser beam has been demonstrated by Kawamura, Ye, and Sato (2005). Three-dimensional trapping and manipulation of microscopic particles can be realized by focusing and deflecting the laser beam, and the position of the captured particles can be controlled by adjusting the applied voltage without any mechanical movements. Hands, Tatarkova, Kirby, and Love (2006) used different LC elements to provide full three-dimensional particle control in an optical tweezer. The transmissive LC devices could be retro-fitted to an existing microscope system. An adaptive modal LC lens is used to vary the z -focal position over a range of up to $100\text{ }\mu\text{m}$ and an adaptive LC beam-steering device is used to deflect the beam (and trapped particle) in the $x-y$ plane within an available radius of $10\text{ }\mu\text{m}$.

Confocal laser scanning fluorescence microscopy has been an indispensable tool for live cell imaging. Rapid data acquisition with high resolution and nontranslational components is extremely important for 3D microscopic imaging, especially live-cell imaging where dynamic behaviors inside cells need to be recorded in real time for better understanding of the cell functions. Very recently a nontranslational parallel 3D confocal optical imaging system equipped with an electro-optic varifocal lens for rapid depth scanning and digital micromirror device for parallel transverse confocal scanning and hence fast image acquisition has been presented by Li, Fang, and Zhao (2010).

4.3. Aberration Correction

The next-generation data storage system will use shorter wavelength (blue light), multiple recording layers, and objective lens with higher numerical aperture. These factors increase the sensitivity of the optical pickup to the spherical aberration, which is mainly due to the variation of the substrate thickness and the switching between layers, as the objective lens can be compensated only for a single-layer thickness. LC lenses have been used as a nonmechanical device to compensate the spherical aberration (Hain et al., 2001; Ohtaki, Murao, Ogasawara, & Iwasaki, 1999; Stallinga, Vrehen, Wals, Stapert, & Verstegen, 2000), but they have low tolerance with regard to lateral adjustments of the LC device into the light path and a comparatively high number of driving electrodes is required. For example, in the latter case, a convex LC lens and a circular electrode structure with 64 ring electrodes were used in dual-layer digital versatile discs (DVDs). Somalingam et al. (2004) proposed a method for effective compensation of spherical aberration by utilizing a novel LC device that generates a parabolic wave front. This particular shape makes the element highly tolerant against lateral movements. By enhancing the method

of conductive ladder meshing for electrode design, the number of driving electrodes is reduced to only two. Chung, Choi, Kim, Ahn, and Baik (2006) designed and fabricated a novel structure of the LC lens having both the concave and convex surfaces for spherical aberration compensation. The structure was able to improve the shift tolerance characteristics of the objective lens and increase the compensation range to a three-layer recording disk. Examples of the other applications of adaptive lens include beam steering, (Masuda, Takahashi, Nose, Sato, & Ito, 1997), fiber optic device (Reza & Riza, 2009), and so on. Spatial light modulators have been used as a programmable lens for imaging (Gruneisen, DeSandre, Rotge, Dymale, & Lubin, 2004; Laude, 1998), information processing (Davis, Valadéz, & Cottrell, 2003; Love et al., 2009; Takaki & Ohzu 1996), and vision correction (Fernández, Prieto, & Artal, 2009). Quite a few articles are on fabrication and applications of adaptive microlens array and the details are not presented here. Adaptive microlenses are very useful for optofluidic, lab-on-a-chip, and micro-total-analysis systems.

5. CONCLUSION

A lot of efforts have been devoted to the research in adaptive lens. Recent advances in this field have been reviewed in this article. For liquid crystal lens, refractive and diffractive LC lenses based on discrete electrodes, hole-patterned electrodes, modal control electrode, hybrid alignment, polymer/LC materials have been discussed in detail. For liquid lenses, lenses based on mechanic pressure, electrowetting effect, dielectric effect, hydrogel and thermal effect have been reviewed. Examples of applications in vision care, aberration compensation, zoom lens, and optical tweezers have been discussed. To fabricate large-aperture low-aberration adaptive LC and liquid lenses are still challenging. We look forward to new developments in this active area.

ACKNOWLEDGMENTS

I would like to acknowledge the Wallace H. Coulter Foundation, National Institutes of Health, and University of Missouri Research Board for partially supporting my current research.

REFERENCES

- Agarwal, M., Gunasekaran, R. A., Coane, P., & Varahramyan, K. (2004). *Journal of Micro-mechanics and Microengineering*, 14, 1665.
Alvarez, L. W. (1967). U.S. Patent No. 3,305,294.
Alvarez, L. W. (1978). *Journal of the American Optometric Association*, 49(1), 24.

- Alvarez, L. W., & Humphrey, W. E. (1970). U.S. Patent No. 3,507,565.
- Apter, B., Efron, U., & Bahat-Treidel, E. (2004). *Applied Optics*, 43, 11.
- Asatryan, K., Presnyakov, V., Tork, A., Zohrabyan, A., Bagramyan, A., & Galstian, T. (2010). *Optics Express*, 18, 13981.
- Back, F. G., & Lowen, H. (1954). *Journal of the Optical Society of America*, 44, 684.
- Back, F. G., & Lowen, H. (1958). *Journal of the Optical Society of America*, 48, 149.
- Barbero, S. (2009). *Optics Express*, 17, 9376.
- Barton, I. M., Dixit, S. N., Summers, L. J., Thompson, C. A., Avicola, K., & Wilhelmsen, J. (2000). *Optics Letters*, 25, 1.
- Berge, B., & Peseux, J. (2000). *European Physical Journal E*, 3, 159.
- Bergstein, L. (1958). *Journal of the Optical Society of America*, 48, 154.
- Bernet, S., & Ritsch-Marte, M. (2008). *Applied Optics*, 47, 3722.
- Born, M., & Wolf, E. (1999). *Principles of optics*. Oxford: Pergamon.
- Bricot, C., Hareng, M., & Spitz, F. (1977). U.S. Patent No. 4,037,929.
- Brinkley, P. F., Kowal, S. T., & Chu, C. (1988). *Applied Optics*, 27, 4578.
- Burch, J. M., & Williams, D. C. (1977). *Applied Optics*, 16, 2445.
- Campbell, K., Fainman, Y., & Groisman, A. (2007). *Applied Physics Letters*, 91, 171111.
- Caulfield, H. J. (2002). *Optics Laser Technology*, 34, 1.
- Chan, W. W., & Kowal, S. T. (1997). *Applied Optics*, 36, 8958.
- Charman, W. N. (1993). *Ophthalmic and Physiological Optics*, 13, 427.
- Chen, J., Wang, W., Fang, J., & Varahramyan, K. (2004). *Journal of Micromechanics and Microengineering*, 14, 675.
- Cheng, C. C., & Yeh, J. A. (2007). *Optics Express*, 15, 7140.
- Cheng, C. C., Chang, C. A., & Yeh, J. A. (2006). *Optics Express*, 14, 4101.
- Cheng, C. C., Chang, C. A., Liu, C. H., & Yeh, J. A. (2006). *Journal of Optics A: Pure Applied Optics*, 8, S365.
- Chiu, C. W., Lin, Y.-C., Chao, P. C.-P., & Fuh, A. Y.-G. (2008). *Optics Express*, 16, 19277.
- Chronis, N., Liu, G. L., Jeong, K.-H., & Lee, L. P. (2003). *Optics Express*, 11, 2370.
- Chung, S. H., Choi, S. W., Kim, Y. J., Ahn, H. J., & Baik, H. K. (2006). *Japanese Journal of Applied Physics*, 45, 1152.
- Dance, B. (1992). *Laser Focus World*, 28, 34.
- Davis, J. A., Valadéz, K. O., & Cottrell, D. M. (2003). *Applied Optics*, 42, 2003.
- Dong, L., Agarwal, A. K., Beebe, D. J., & Jiang, H. (2006). *Nature*, 442, 551.
- Dong, L., Agarwal, A. K., Beebe, D. J., & Jiang, H. (2007). *Advanced Materials*, 19, 401.
- Faklis, D., & Morris, G. M. (1995). *Applied Optics*, 34, 2462.
- Fan, Y.-H., Ren, H., & Wu, S.-T. (2003). *Optics Express*, 11, 3080.
- Fan, Y.-H., Ren, H., & Wu, S.-T. (2005). *Optics Express*, 13, 4141.
- Feng, G.-H., & Chou, Y.-C. (2009). *Applied Optics*, 48, 3284.
- Fernández, E. J., Prieto, P. M., & Artal, P. (2009). *Optics Letters*, 34, 2628.
- Ferstl, M., & Frisch, A.-M. (1996). *Journal of Modern Optics*, 43, 1451.
- Fowler, C. W., & Pateras, E. S. (1990). *Ophthalmic and Physiological Optics*, 10, 186.
- Futhey, J. A. (1989). *Proceedings of SPIE*, 1052, 142.
- Goodman, J. W. (2005). *Introduction to Fourier optics*. Roberts & Company Publishers.
- Gorman, C. B., Biebuyck, H. A., & Whitesides, G. M. (1995). *Langmuir*, 11, 2242.
- Gural'nik, I. P., & Samagin, S. A. (2003). *Quantum Electronics*, 33, 430.
- Grilli, S., Miccio, L., Vespi, V., Finizio, A., De Nicola, S., & Ferraro, P. (2008). *Optics Express*, 16, 8084.
- Gruneisen, M. T., DeSandre, L. F., Rotge, J. R., Dymale, R. C., & Lubin, D. L. (2004). *Optical Engineering*, 43, 1387.
- Gvozdarev, A., & Nevskaya, G. E. (1999). *Molecular Crystallization Liquid Crystallization Science Technology, Section A*, 329, 81.

- Gvozdarev, A., & Nevskaya, G. E. (2001a). *Molecular Crystallization Liquid Crystallization Science Technology, Section A*, 4, 364.
- Gvozdarev, A., & Nevskaya, G. E. (2001b). *Molecular Crystallization Liquid Crystallization Science Technology, Section B: Nonlinear Optics*, 4, 358.
- Hain, M., Glöckner, R., Bhattacharya, S., Dias, D., Stankovic, S., & Tschudi, T. (2001). *Optics Communications*, 188, 291.
- Hands, P. J. W., Tatarkova, S. A., Kirby, A. K., & Love, G. D. (2006). *Optics Express*, 14, 4525.
- Haus, H. A., & Melcher, J. R. (1998). *Electromagnetic fields and energy* (chap. 11). http://web.mit.edu/6.013_book/www/chapter11/11.9.html.
- He, Z., Nose, T., & Sato, S. (1995). *Japanese Journal of Applied Physics*, 34, 2392.
- Honma, M., Nose, T., & Sato, S. (1999). *Japanese Journal of Applied Physics*, 38, 89.
- Humphrey, W. E. (1976). *Optical Engineering*, 15, 286.
- Jaroszewicz, Z., Kołodziejczyk, A., Mira, A., Henao, R., & Bará, S. (2005). *Optics Express*, 13, 918.
- Jeong, K. H., Liu, G. L., Chronis, N., & Lee, L. P. (2004). *Optics Express*, 12, 2494.
- Jepsen, M. L., & Gerritsen, H. J. (1996). *Optics Letters*, 21, 1081.
- Jones, T. B., Gunji, M., Washizu, M., & Feldman, M. J. (2001). *Journal of Applied Physics*, 89, 1441.
- Kawamura, M., Ye, M., & Sato, S. (2005). *Japanese Journal of Applied Physics*, 44, 6098.
- Kim, D.-W., Yu, C.-J., Kim, H.-R., Kim, S.-J., & Lee, S.-D. (2006). *Applied Physics Letters*, 88, 203505.
- Klaus, W., Ide, M., Hayano, Y., Morokawa, S., & Arimoto, Y. (1999). *Proceedings of SPIE*, 3635, 66.
- Knollman, G. C., Bellin, J. L. S., & Weaver, J. L. (1970). *Journal of the Acoustical Society of America*, 49, 253.
- Kolodziejczyk, A., & Jaroszewicz, Z. (1993). *Applied Optics*, 32, 4317.
- Kowal, S. T., Cleverly, D. S., & Kornreich, P. G. (1984). *Applied Optics*, 23, 278.
- Kress, B., & Mey, P. (2000). *Digital diffractive optics*. England: John Wiley & Sons Ltd.
- Krupenkin, T., Yang, S., & Mach, P. (2003). *Applied Physics Letters*, 82, 316.
- Kuiper, S., & Hendriks, B. H. W. (2004). *Applied Physics Letters*, 85, 1128.
- Kuwano, R., Tokunaga, T., Otani, Y., & Umeda, N. (2005). *Optical Review*, 12, 405.
- Laude, V. (1998). *Optics Communications*, 153, 134.
- Lee, D. W., & Cho, Y.-H. (2010). *Journal of Micromechanics and Microengineering*, 20, 035029.
- Lee, S. W., & Lee, S. S. (2007). *Applied Physics Letters*, 90, 121129.
- Lester, G. A., Coulston, S. J., & Strudwick, A. M. (2006). *Applied Optics*, 45, 110.
- Li, G. (2008). Liquid crystal lenses for correction of presbyopia. In J. C. Dainty (Ed.), *Adaptive optics for industry and medicine: Proceedings of the Sixth International Workshop* (pp. 3–8). London: Imperial College Press.
- Li, G., Ayras, P., & Peyghambarian, N. (2006) U.S. Patent No. 0164593.
- Li, G., & Fang, H. (2010). *Frontiers in optics*. Rochester, New York: Optical Society of America.
- Li, G., Fang, X., & Zhao, D. (2010). *Frontiers in optics*. Rochester, New York: Optical Society of America.
- Li, G., Mathine, D. L., Valley, P., Ayras, P., Haddock, J. N., Giridhar, M. S., et al. (2006). *Proceedings of the National Academy of Sciences of the United States of America*, 103, 6100.
- Li, G., Valley, P., Åyräs, P., Honkanen, S., & Peyghambarian, N. (2007). *Applied Physics Letters*, 90, 111105.
- Li, G., Valley, P., Giridhar, M. S., Mathine, D., Meredith, G., Haddock, J., et al. (2006). *Applied Physics Letters*, 89, 141120.
- Lin, L.-C., Jau, H.-C., Lin, T.-H., & Fuh, A. Y.-G. (2007). *Optics Express*, 15, 2900.
- Liu, C.-X., Park, J., & Choi, J.-W. (2008). *Journal of Micromechanics and Microengineering*, 18, 035023.

- Lohmann, A. W. (1964). *British Patent*, 998, 191.
- Lohmann, A. W. (1970). *Applied Optics*, 9, 1669.
- Lohmann, A. W., & Paris, D. P. (1967). *Applied Optics*, 6, 1567.
- Loktev, M. Y., Belopukhov, V. N., Vladimirov, F. L., Vdovin, G. V., Love, G. D., & Naumov, A. F. (2000). *Review of Scientific Instruments*, 71, 3290.
- López, C. A., & Hirsa, A. H. (2008). *Nature Photonics*, 2, 610.
- López, C. A., Lee, C. C., & Hirsa, A. H. (2005). *Applied Physics Letters*, 87, 134102.
- Love, G. D., Hoffman, D. M., Hands, P. J. W., Gao, J., Kirby, A. K., & Banks, M. S. (2009). *Optics Express*, 17, 15716.
- Marks, R., Mathine, D. L., Peyman, G., Schwiegerling, J., & Peyghambarian, N. (2009). *Optics Letters*, 34, 515.
- Masuda, S., Takahashi, S., Nose, T., Sato, S., & Ito, H. (1997). *Applied Optics*, 36, 4772.
- McManamon, P. F., Dorschner, T. A., Corkum, D. L., Friedman, L. J., Holz, M., Liberman, S., et al. (1996). *Proceedings of IEEE*, 84, 268.
- McOwan, P. W., Gordon, M. S., & Hossack, W. J. (1993). *Optics Communications*, 103, 189.
- Miccio, L., Finizio, A., Grilli, S., Vespini, V., Paturzo, M., De Nicola, S., et al. (2009). *Optics Express*, 17(4), 2487.
- Miccio, L., Paturzo, M., Grilli, S., Vespini, V., & Ferraro, P. (2009). *Optics Letters*, 34, 1075.
- Minnema, L., Barneveld, H. A., & Rinkel, P. D. (1980). *IEEE Transactions on Electrical Insulation*, EI-15(6), 461.
- Moran, P. M., Dharmatilleke, S., Khaw, A. H., Tan, K. W., Chan, M. L., & Rodriguez, I. (2006). *Applied Physics Letters*, 88, 041120.
- Naumov, A. F., Loktev, M. Y., Guralnik, I. R., & Vdovin, G. (1998). *Optics Letters*, 23, 992.
- Naumov, A. F., Love, G. D., Yu, M. L., & Vladimirov, F. L. (1999). *Optics Express*, 4, 344.
- Nose, T., Masuda, S., & Sato, S. (1991a). *Molecular Crystallization Liquid Crystallization*, 199, 27.
- Nose, T., Masuda, S., & Sato, S. (1991b). *Japanese Journal of Applied Physics*, 30, 2110.
- Nose, T., Masuda, S., & Sato, S. (1992). *Japanese Journal of Applied Physics*, 31, 1643.
- Nose, T., & Sato, S. (1989). *Liquid Crystallization*, 5, 1425.
- Nouhi, A., & Kowal, S. T. (1984). *Applied Optics*, 23, 2774.
- Ohtaki, S., Murao, N., Ogasawara, M., & Iwasaki, M. (1999). *Japanese Journal of Applied Physics*, 38, 1744.
- Oku, H., Hashimoto, K., & Ishikawa, M. (2004). *Optics Express*, 12, 2138.
- Pang, L., Levy, U., Campbell, K., Groisman, A., & Fainman, Y. (2005). *Optics Express*, 13, 9003.
- Patel, J. S., & Rastani, K. (1991). *Optics Letters*, 16, 532.
- Peng, R., Chen, J., Zhu, C., & Zhuang, S. (2007). *Optics Express*, 15, 6664.
- Presnyakov, V. V., Asatryan, K. E., Galstian, T. V., & Tork, A. (2002). *Optics Express*, 10, 865.
- Presnyakov, V. V., & Galstian, T. V. (2005). *Journal of Applied Physics*, 97, 103101.
- Qiao, W., Tsai, F. S., Cho, S. H., Yan, H., & Lo, Y.-H. (2009). *IEEE Photonics Technology Letters*, 21, 304.
- Rawicz, A. H., & Mikhailenko, I. (1996). *Applied Optics*, 35, 1587.
- Rege, S. S., Tkaczyk, T. S., & Descour, M. R. (2004). *Optics Express*, 12, 2574.
- Reichelt, S., & Zappe, H. (2007). *Optics Express*, 15, 14146.
- Ren, H., & Wu, S.-T. (2002). *Applied Physics Letters*, 81, 3537.
- Ren, H., & Wu, S. T. (2003). *Applied Physics Letters*, 82, 22.
- Ren, H., & Wu, S. T. (2005). *Applied Physics Letters*, 86, 211107.
- Ren, H., & Wu, S. T. (2006). *Optics Express*, 14, 11292.
- Ren, H., & Wu, S. T. (2008). *Optics Express*, 16, 2646.
- Ren, H., Fan, Y.-H., Gauza, S., & Wu, S. T. (2004a). *Japanese Journal of Applied Physics*, 43, 652.
- Ren, H., Fan, Y.-H., Gauza, S., & Wu, S.-T. (2004b). *Applied Physics Letters*, 84, 4789.
- Ren, H., Fan, Y.-H., & Wu, S.-T. (2003). *Applied Physics Letters*, 83, 1515.
- Ren, H., Fox, D., Anderson, P. A., Wu, B., & Wu, S.-T. (2006). *Optics Express*, 14, 8031.

- Ren, H., Fox, D. W., Wu, B., & Wu, S.-T. (2007). *Optics Express*, 15, 11328.
- Ren, H., Lin, Y.-H., & Wu, S.-T. (2006). *Applied Physics Letters*, 88, 1911116.
- Ren, H., Xianyu, H., Xu, S., & Wu, S. T. (2008). *Optics Express*, 16, 14954.
- Resler, D. P., Hobbs, D. S., Sharp, R. C., Friedman, L. J., & Dorschner, T. A. (1996). *Optics Letters*, 21, 689.
- Reza, S., & Riza, N. A. (2009). *Optics Communications*, 282, 1298.
- Riza, N. A., & DeJule, M. C. (1994). *Optics Letters*, 19, 1013.
- Sato, S. (1979). *Japanese Journal of Applied Physics*, 18, 1679.
- Sato, S., Sugiyama, A., & Sato, R. (1985). *Japanese Journal of Applied Physics*, 24, L626.
- Sato, S., & Ye, M. (2005). *Proceedings of SPIE*, 5936, 113.
- Scharf, T., Kipfer, P., Bouvier, M., & Grupp, J. (2000). *Japanese Journal of Applied Physics*, 39, 6629.
- Scharf, T., Fontannaz, J., Bouvier, M., & Grupp, J. (1999). *Molecular Crystallization Liquid Crystallization*, 331, 235.
- Schneider, F., Draheim, J., Kammerer, R., Waibel, P., & Wallrabe, U. (2009). *Optics Express*, 17, 11813.
- Schneider, F., Müller, C., & Wallrabe, U. (2008). *Journal of Optics A: Pure Applied Optics*, 10, 044002.
- Shaw, D., & Sun, T. E. (2007). *Optical Engineering*, 46, 024002.
- Shi, J., Stratton, Z., Steven, S.-C., Huang, L.-H., & Huang, T.-J. (2010). *Microfluidics and Nanofluidics*, 9, 313.
- Simonov, A. N., Vdovin, G., & Loktev, M. (2007). *Optics Express*, 15, 7468.
- Simonov, A. N., Vdovin, G., & Rombach, M. C. (2006). *Optics Express*, 14, 7757.
- Slinger, C., Brett, P., Hui, V., Monnington, G., Pain, D., & Sage, I. (1997). *Optics Letters*, 22, 1113.
- Smith, G., & Atchison, D. A. (1997). *The eye and visual optical instruments*. United Kingdom: Cambridge University Press.
- Somalingam, S., Dressbach, K., Hain, M., Stankovic, S., Tschudi, T., Knittel, J., et al. (2004). *Applied Optics*, 43, 2722.
- Spivey, B. (2008). U.S. Patent No. 151184.
- Stallinga, S., Vrehen, J. J., Wals, J., Stapert, H., & Versteegen, E. (2000). *Proceedings of SPIE*, 4081, 50.
- Sugiura, N., & Morita, S. (1993). *Applied Optics*, 32, 4181.
- Sun, Y., Nordin, G. P., Kowal, S. T., & Wang, B. (2003). *Proceedings of SPIE*, 4987, 209.
- Takahashi, T., Ye, M., & Sato, S. (2007). *Japanese Journal of Applied Physics*, 46, 2926.
- Takaki, Y., & Ohzu, H. (1996). *Applied Optics*, 35, 6896.
- Tam, E. C. (1992). *Optics Letters*, 17, 369.
- Tolosa, A., Martinez-Cuenca, R., Pons, A., Saavedra, G., Martinez-Corral, M., & Javadi, B. (2010). *Journal of the Optical Society of America A*, 27, 495.
- Vallet, M., Berge, B., & Volvelle, L. (1996). *Polymer (Guildf)*, 37, 2465.
- Vdovin, G. V., Gural'nik, I. R., Kotova, S. P., Yu, M. L., & Naumov, A. F. (1999a). *Quantum Electronics*, 29, 256.
- Vdovin, G. V., Gural'nik, I. R., Kotova, S. P., Yu, M. L., & Naumov, A. F. (1999b). *Quantum Electronics*, 29, 261.
- Vdovin, G., Loktev, M., & Naumov, A. (2003). *Optics Express*, 11, 810.
- Verheijen, H. J. J., & Prins, N. W. J. (1999). *Langmuir*, 15, 6616.
- Wang, X., Wang, B., Bos, P. J., Anderson, J. E., Pouch, J. J., & Miranda, F. A. (2005). *Journal of the Optical Society of America A*, 22, 346.
- Wang, X., Wilson, D., Muller, R., Maker, P., & Psaltis, D. (2000). *Applied Optics*, 39, 6545.
- Wang, B., Ye, M., Honma, M., Nose, T., & Sato, S. (2002). *Japanese Journal of Applied Physics*, 41, L1232.
- Wang, B., Ye, M., & Sato, S. (2004). *Applied Optics*, 43, 3420.

- Wang, B., Ye, M., & Sato, S. (2005a). *Japanese Journal of Applied Physics*, 44, 4979.
- Wang, B., Ye, M., & Sato, S. (2005b). *Optics Communications*, 250, 266.
- Wang, B., Ye, M., & Sato, S. (2005c). *Molecular Crystallization Liquid Crystallization*, 433, 217.
- Wang, B., Ye, M., & Sato, S. (2005d). *Proceedings of SPIE*, 6018, 324.
- Wang, B., Ye, M., & Sato, S. (2006a). *IEEE Photonics Technology Letters*, 18, 79.
- Wang, B., Ye, M., & Sato, S. (2006b). *Japanese Journal of Applied Physics*, 45, 7813.
- Wang, Z., Xu, Y., & Zhao, Y. (2007). *Optics Communications*, 275, 22.
- Welters, W. J. J., & Fokkink, L. G. J. (1998). *Langmuir*, 14, 1535.
- Werber, A., & Zappe, H. (2005). *Applied Optics*, 44, 3238.
- Wick, D. V., & Martinez, T. (2004). *Optical Engineering*, 43, 8.
- Williams, G., Powell, N. J., & Purvis, A. (1989). *Proceedings of SPIE*, 1168, 352.
- Wiltshire, M. C. K. (1993). *GEC Journal of Research* 10, 119.
- Wright, B. M. (1968). UK Patent No. 1,209,234.
- Xu, S., Lin, Y. J., & Wu, S. T. (2009). *Optics Express*, 17, 10499.
- Xu, S., Ren, H., Lin, Y.-J., Moharam, M. G. J., Wu, S.-T., & Tabiryan, N. (2009). *Optics Express*, 17, 17590.
- Yanase, S., Ouchi, K., & Sato, S. (2002). *Japanese Journal of Applied Physics*, 41, L1482.
- Yang, H., Han, Y.-H., Zhao, X.-W., Nagai, K., & Gu, Z.-Z. (2006). *Applied Physics Letters*, 89, 111121.
- Yang, Q., Kobrin, P., Seabury, C., Narayanaswamy, S., & Christian, W. (2008). *Applied Optics*, 47, 3658.
- Yang, D.-K., & Wu, S.-T. (2006). *Fundamentals of liquid crystal devices*. England: John Wiley & Sons.
- Ye, M., Noguchi, M., Wang, B., & Sato, S. (2009). *Electronics Letters*, 46, 646.
- Ye, M., & Sato, S. (2002). *Japanese Journal of Applied Physics*, 41, L571.
- Ye, M., & Sato, S. (2003). *Japanese Journal of Applied Physics*, 42, 6439.
- Ye, M., & Sato, S. (2005). *Molecular Crystallization Liquid Crystallization*, 433, 229.
- Ye, M., Wang, B., & Sato, S. (2003). *Japanese Journal of Applied Physics*, 42, 5086.
- Ye, M., Wang, B., & Sato, S. (2004a). *Japanese Journal of Applied Physics*, 43, L352.
- Ye, M., Wang, B., & Sato, S. (2004b). *Applied Optics*, 43, 6407.
- Ye, M., Wang, B., & Sato, S. (2006). *IEEE Photonics Technology Letters*, 18, 505.
- Ye, M., Wang, B., & Sato, S. (2008). *Optics Express*, 16, 4302.
- Ye, M., Yokoyama, Y., & Sato, S. (2005). *Japanese Journal of Applied Physics*, 44, 235.
- Ye, M., Yokoyama, Y., & Sato, S. (2006). *Applied Physics Letters*, 89, 141112.
- Yu, M. L., Belopukhov, V. N., Vladimirov, F. L., Vdovin, G. V., Love, G. D., & Naumov, A. F. (2000). *The Review of Scientific Instruments*, 71, 3290.
- Yu, Y., Nakano, M., & Ikeda, T. (2003). *Nature* 425, 145.
- Zeng, X., & Jiang, H. (2008). *Applied Physics Letters*, 93, 151101.
- Zhang, D. Y., Justis, N., Lien, V., Berdichevsky, Y., & Lo, Y.-H. (2004). *Applied Optics*, 43, 783.
- Zhang, D. Y., Justis, N., & Lo, Y. H. (2005). *Optics Communications*, 249, 175.
- Zhang, D. Y., Lien, V., Berdichevsky, Y., Choi, J., & Lo, Y. H. (2003). *Applied Physics Letters*, 82, 3171.
- Zhang, X., Loktev, M., & Vdovin, G. (2005). *Review of Scientific Instruments*, 76, 043109.

This page intentionally left blank

CHAPTER 5

The Structure of Partially Coherent Fields

G. Gbur^a and T.D. Visser^b

^a*University of North Carolina at Charlotte, Charlotte NC, USA*

^b*Delft University of Technology and Free University Amsterdam,
The Netherlands*

Contents		
1.	Preface	285
2.	The Space-Frequency Representation	287
3.	Partially Coherent Fields in Young's Experiment	291
4.	The Evolution of Partially Coherent Beams	296
5.	Focusing of Partially Coherent Wave Fields	302
6.	Scattering of Partially Coherent Wave Fields by Random and Deterministic Media	308
7.	Phase Singularities of Coherence Functions	314
8.	The Coherent Mode Representation	320
9.	Numerical Simulation of Partially Coherent Fields	324
10.	Direct Applications of Coherence Theory	326
	References	329

1. PREFACE

The general framework of optical coherence theory is now well established and has been described in numerous publications (see Beran & Parrent, 1964; Born & Wolf, 1999; Goodman, 1985; Mandel & Wolf, 1995; Marathay, 1982; Perina, 1985; Schouten & Visser, 2008; Troup, 1967; Wolf, 2007b). In this article, we provide an overview of recent advances, both theoretical and experimental, that have been made in a number of areas of classical optical coherence. These advances have been spurred on by the introduction of the space-frequency representation of partially coherent fields, to be discussed in Section 2, and an increased emphasis on the

spatial coherence properties of wave fields. The fundamental experiment to measure spatial coherence is, of course, Young's double-slit experiment, which still provides many insights to this day; recent developments will be discussed in Section 3.

A number of important optical processes are influenced by the coherence properties of the wave field. Results relating to the propagation of partially coherent wavefields are too numerous to be comprehensively covered here, but Section 4 highlights some of the significant results relating to optical beams. In Section 5, the influence of coherence on focusing is summarized and reviewed. In Section 6, the scattering of partially coherent wave fields, and its relation to inverse scattering problems, is discussed.

In recent years, it has been shown that spatial correlation functions have interesting topological properties associated with their phase singularities; these properties and the relevant literature are discussed in Section 7. The coherent mode representation and its applications are described in Section 8. Several techniques for the numerical simulation of wave fields with a prescribed statistical behavior are explained in Section 9. Many novel applications of partially coherent fields are described in the concluding Section 10.

As noted, optical coherence is a mature field of study, and a single review article cannot comprehensively cover all of the important developments. This article is restricted to results from the classical theory of optical coherence, and excludes discussion of the quantum theory. A number of other developments are discussed only in the context of the specific topics mentioned earlier. Among these are *correlation-induced spectral changes* and the relatively recent *unified theory of coherence and polarization*. "Correlation-induced spectral changes" refers to the important observation that the spectrum of a partially coherent wave field can change on propagation or scattering; a thorough review of research on the phenomenon was undertaken by Wolf and James (1996). The "unified theory of coherence and polarization" refers to a new formulation of the electromagnetic theory of optical coherence that has been used, among other things, to characterize the changes in the state and degree of polarization of electromagnetic fields on propagation; the fundamental results are reviewed by Wolf (2007b).

The topics discussed in this review are unified, in part, by the realization that the ability to manipulate the spatial coherence of a wave field provides an additional degree of control over the properties of that wave field. Many of the advances in optical coherence have come from the design of fields with unusual structural properties that are optimized for different applications.

2. THE SPACE-FREQUENCY REPRESENTATION

Optical coherence theory is the study of the statistical properties of light and their influence on the observable characteristics of optical fields. The beginnings of coherence theory can be traced back to Verdet (1865), who estimated the spatial coherence of sunlight on the Earth's surface, and van Cittert (1934) and Zernike (1948), who calculated the evolution of the spatial coherence of light propagating from an incoherent source.¹

The modern theory of optical coherence, as championed by Wolf and others, began with the study of the mutual coherence function $\Gamma(\mathbf{r}_1, \mathbf{r}_2, \tau)$ of wide-sense statistically stationary optical fields, defined as

$$\Gamma(\mathbf{r}_1, \mathbf{r}_2, \tau) = \langle U^*(\mathbf{r}_1, t_1)U(\mathbf{r}_2, t_2) \rangle, \quad (2.1)$$

where the time difference $\tau \equiv t_2 - t_1$ and the angle brackets represent time averaging or, equivalently for ergodic fields, ensemble averaging. The field $U(\mathbf{r}, t)$ is typically taken to be scalar, with polarization effects neglected, but the formalism can be readily extended to the fully electromagnetic case, as discussed in detail in Wolf (2007b). It was shown by Wolf (1955) that the mutual coherence function satisfies a pair of wave equations in free space, namely,

$$\left(\nabla_1^2 - \frac{1}{c^2} \frac{\partial^2}{\partial \tau^2} \right) \Gamma(\mathbf{r}_1, \mathbf{r}_2, \tau) = 0, \quad (2.2)$$

$$\left(\nabla_2^2 - \frac{1}{c^2} \frac{\partial^2}{\partial \tau^2} \right) \Gamma(\mathbf{r}_1, \mathbf{r}_2, \tau) = 0, \quad (2.3)$$

where ∇_i^2 is the Laplacian with respect to the Cartesian coordinates of position vector \mathbf{r}_i and c is the speed of light. From these equations one can see that the statistical properties of light evolve in a well-defined way on propagation, and much of the research in optical coherence theory has involved the study of the consequences of these equations of evolution.

Just as it is possible to study the behavior of deterministic wave fields in the time domain or the frequency domain, it is also possible to study the behavior of partially coherent wave fields in either time or frequency. The *cross-spectral density function* $W(\mathbf{r}_1, \mathbf{r}_2, \omega)$ is defined as the temporal

¹More details on the history of optical coherence theory can be found in Born and Wolf (1999), section 10.1, and Wolf (2001). Reprints of a number of classic articles can be found in Mandel and Wolf (1990).

Fourier transform of the mutual coherence function with respect to the time variable τ , i.e.,

$$W(\mathbf{r}_1, \mathbf{r}_2, \omega) = \frac{1}{2\pi} \int_{-\infty}^{\infty} \Gamma(\mathbf{r}_1, \mathbf{r}_2, \tau) e^{-i\omega\tau} d\tau. \quad (2.4)$$

The cross-spectral density will then satisfy a pair of Helmholtz equations,

$$\left(\nabla_1^2 + k^2 \right) W(\mathbf{r}_1, \mathbf{r}_2, \omega) = 0, \quad (2.5)$$

$$\left(\nabla_2^2 + k^2 \right) W(\mathbf{r}_1, \mathbf{r}_2, \omega) = 0, \quad (2.6)$$

where $k = \omega/c$ is the wave number of light corresponding to frequency ω . This pair of elliptic partial differential equations for the cross-spectral density function is, in general, easier to solve than the pair of hyperbolic wave equations for the mutual coherence function; the mutual coherence function can, however, be readily determined by taking an inverse Fourier transform of the cross-spectral density.

The cross-spectral density is commonly written in terms of two other functions, the *spectral density* $S(\mathbf{r}, \omega)$ and the *spectral degree of coherence* $\mu(\mathbf{r}_1, \mathbf{r}_2, \omega)$, as

$$W(\mathbf{r}_1, \mathbf{r}_2, \omega) = \sqrt{S(\mathbf{r}_1, \omega)} \sqrt{S(\mathbf{r}_2, \omega)} \mu(\mathbf{r}_1, \mathbf{r}_2, \omega). \quad (2.7)$$

The spectral density $S(\mathbf{r}, \omega)$ represents the intensity of the wave field at position \mathbf{r} and frequency ω , and it may be written in terms of the cross-spectral density function as

$$S(\mathbf{r}, \omega) \equiv W(\mathbf{r}, \mathbf{r}, \omega). \quad (2.8)$$

The spectral degree of coherence $\mu(\mathbf{r}_1, \mathbf{r}_2, \omega)$ is a measure of the degree of correlation of the field at the two positions \mathbf{r}_1 and \mathbf{r}_2 and at frequency ω , and may be written in terms of the cross-spectral density function and spectral density as

$$\mu(\mathbf{r}_1, \mathbf{r}_2, \omega) \equiv \frac{W(\mathbf{r}_1, \mathbf{r}_2, \omega)}{\sqrt{S(\mathbf{r}_1, \omega) S(\mathbf{r}_2, \omega)}}. \quad (2.9)$$

It can be shown that the absolute value of the spectral degree of coherence is restricted to the values

$$0 \leq |\mu(\mathbf{r}_1, \mathbf{r}_2, \omega)| \leq 1, \quad (2.10)$$

where 0 represents complete spatial incoherence, and 1 represents full spatial coherence. The physical significance of $\mu(\mathbf{r}_1, \mathbf{r}_2, \omega)$ will be discussed in more detail in Section 3.

An important milestone in the development of coherence theory in the space-frequency domain was the observation by Wolf (1982) that the cross-spectral density itself may be represented as a correlation function derived from an ensemble of monochromatic realizations of the field. This can be proven by first noting that the cross-spectral density is Hermitian, i.e.,

$$W(\mathbf{r}_2, \mathbf{r}_1, \omega) = W^*(\mathbf{r}_1, \mathbf{r}_2, \omega), \quad (2.11)$$

and that it is non-negative definite, such that

$$\int_D \int_D W(\mathbf{r}_1, \mathbf{r}_2, \omega) f^*(\mathbf{r}_1) f(\mathbf{r}_2) d^2 r_1 d^2 r_2 \geq 0, \quad (2.12)$$

where $f(\mathbf{r})$ is an arbitrary square-integrable function and, for a secondary source with a field propagating from $z = 0$, the domain of integration D is the source plane. Assuming that the cross-spectral density is also square-integrable over this domain, it represents a *Hilbert–Schmidt kernel*; by *Mercer’s theorem*², it may be expanded in a series of orthogonal functions of the form

$$W(\mathbf{r}_1, \mathbf{r}_2, \omega) = \sum_n \lambda_n(\omega) \phi_n^*(\mathbf{r}_1, \omega) \phi_n(\mathbf{r}_2, \omega), \quad (2.13)$$

where the eigenvalues $\lambda_n(\omega)$ and the eigenfunctions $\phi_n(\mathbf{r}, \omega)$ satisfy the integral equation

$$\int_D W(\mathbf{r}_1, \mathbf{r}_2, \omega) \phi(\mathbf{r}_1, \omega) d^2 r_1 = \lambda_n(\omega) \phi_n(\mathbf{r}_2, \omega). \quad (2.14)$$

The summation, in general, may be over multiple indices, and may be a finite or infinite sum. The eigenvalues are non-negative, and the eigenfunctions are orthogonal and typically taken to be orthonormal. Equation (2.13) represents what is now known as the *coherent mode representation* of the cross-spectral density, to be discussed further in Section 8.

The coherent mode representation may be used to construct an ensemble of monochromatic wave fields whose second-order average reproduces

²Mercer’s theorem and Hilbert–Schmidt kernels are introduced in the theory of integral equations; see, for instance, Moisewitsch (1977).

a given cross-spectral density. To do so, we introduce an ensemble of fields defined by

$$U(\mathbf{r}, \omega) = \sum_n a_n(\omega) \phi_n(\mathbf{r}, \omega), \quad (2.15)$$

where the coefficients a_n are random variables. We choose these variables such that the average of them over the entire ensemble of fields (denoted by $\langle \dots \rangle_\omega$) satisfies the condition

$$\langle a_n^*(\omega) a_m(\omega) \rangle_\omega = \lambda_n(\omega) \delta_{nm}. \quad (2.16)$$

It then follows that the cross-spectral density function may be written as

$$W(\mathbf{r}_1, \mathbf{r}_2, \omega) = \langle U^*(\mathbf{r}_1, \omega) U(\mathbf{r}_2, \omega) \rangle_\omega. \quad (2.17)$$

On substitution from Equation (2.15) into Equation (2.17), we readily find that Equation (2.13) is satisfied. Furthermore, on substitution from Equation (2.17) into Equations (2.5) and (2.6), it follows that the individual realizations $U(\mathbf{r}, \omega)$ each satisfy the Helmholtz equation and represent valid monochromatic, and therefore coherent, wave fields.

This result, which seems very formal and almost trivial at first glance, is perhaps one of the most useful results in modern coherence theory, because it implies that a valid cross-spectral density can be found by any suitable averaging process over a set of monochromatic realizations. This is used, for instance, in the “beam wander” model discussed in Section 7.

It is to be noted that it is possible to extend the space-frequency theory to higher-order correlation functions, as done by Wolf (1986b) and Agarwal and Wolf (1993); the formalism becomes significantly more complicated, however.

The theory of optical coherence has developed rapidly with the introduction of the space-frequency representation. Perhaps the most significant result to arise as yet is the theory of correlation-induced spectral changes, in which the degree of spatial coherence of a source can affect the properties of the radiated spectral density. The results arising from this theory are too numerous to be included here; a comprehensive review was provided some time ago by Wolf and James (1996).

At its heart, the theory of optical coherence may be said to be the *optics of observable quantities*. Although traditional optics focuses on the behavior of wave fields $U(\mathbf{r}, t)$ that are not directly observable, coherence theory describes the behavior of second-order and higher moments of the wave field such as the mutual coherence function and the cross-spectral density function, which can be measured through interference experiments. An early discussion of this point of view was given by Wolf (1954).

3. PARTIALLY COHERENT FIELDS IN YOUNG'S EXPERIMENT

The state of coherence of a wave field is intimately related to its ability to form an interference pattern. The relation between the visibility of the fringes that are produced in Young's celebrated experiment (see Young, 1804 and Young, 1807) and the state of coherence of the field at the two pinholes was first studied by Zernike (1938).³ To see this relation in the space-frequency domain, let us first consider the case of a partially coherent, scalar wave field that impinges on an opaque screen \mathcal{A} with two identical small apertures at positions $Q(\mathbf{r}'_1)$ and $Q(\mathbf{r}'_2)$. (See Figure 1.) The field at a point $P(\mathbf{r})$ on the observation screen \mathcal{B} is given by the formula

$$U(\mathbf{r}, \omega) = K_1 U(\mathbf{r}'_1, \omega) + K_2 U(\mathbf{r}'_2, \omega), \quad (3.1)$$

where

$$K_i = -\frac{ikA}{2\pi} \frac{\exp(ikR_i)}{R_i} \quad (i = 1, 2) \quad (3.2)$$

is the propagator that relates the field at $Q(\mathbf{r}'_i)$ to the field at $P(\mathbf{r})$. Here A is the area of each pinhole, R_i denotes the distance from $Q(\mathbf{r}'_i)$ to P , and k is the wave number associated with the angular frequency ω . It follows from Equation (3.1) that the spectral density of the field at P equals

$$\begin{aligned} S(\mathbf{r}, \omega) = & |K_1|^2 S(\mathbf{r}'_1, \omega) + |K_2|^2 S(\mathbf{r}'_2, \omega) \\ & + 2\sqrt{S(\mathbf{r}'_1, \omega)S(\mathbf{r}'_2, \omega)} \operatorname{Re}\{K_1^* K_2 \mu_{12}(\omega)\}, \end{aligned} \quad (3.3)$$

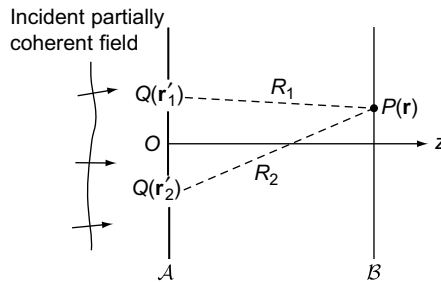


FIGURE 1 Young's interference experiment with partially coherent light. The perforated screen is situated in the plane $z = 0$, and the origin O of the coordinate system is taken in between the two pinholes.

³ A historical overview of the role of Young's experiment in the development of coherence theory was given by Wolf (2007a).

where

$$\mu_{12}(\omega) = \frac{\langle U^*(\mathbf{r}'_1, \omega)U(\mathbf{r}'_2, \omega) \rangle}{\sqrt{S(\mathbf{r}'_1, \omega)S(\mathbf{r}'_2, \omega)}} \quad (3.4)$$

is the spectral degree of coherence of the field at the two pinholes. Equation (3.3) is the so-called *spectral interference law* for partially coherent fields.

In the often occurring case that $|K_1| \approx |K_2| = K$ and $S(\mathbf{r}'_1, \omega) \approx S(\mathbf{r}'_2, \omega) = S(\omega)$, and on writing

$$\mu_{12}(\omega) = |\mu_{12}(\omega)| e^{i\phi}, \quad (3.5)$$

and

$$K_1^* K_2 = K^2 e^{ik(R_2 - R_1)}, \quad (3.6)$$

Equation (3.3) reduces to

$$S(\mathbf{r}, \omega) = 2K^2 S(\omega) \{1 + |\mu_{12}(\omega)| \cos[\phi + k(R_2 - R_1)]\}. \quad (3.7)$$

In the immediate neighborhood of the observation point P on the plane \mathcal{B} , the phase factor $k(R_2 - R_1)$ will take on all values between 0 and 2π , whereas K remains approximately unchanged. Hence, in the vicinity of P , the maximum spectral density equals

$$S_{\max}(\omega) = 2K^2 S(\omega) (1 + |\mu_{12}(\omega)|), \quad (3.8)$$

and the minimum spectral density equals

$$S_{\min}(\omega) = 2K^2 S(\omega) (1 - |\mu_{12}(\omega)|). \quad (3.9)$$

Suppose now that the two pinholes are covered by narrow-band filters, centered around the frequency ω . If we define the spectral visibility (or "sharpness") of the interference fringe that is formed near P as

$$\mathcal{V}(P, \omega) = \frac{S_{\max}(\omega) - S_{\min}(\omega)}{S_{\max}(\omega) + S_{\min}(\omega)}, \quad (3.10)$$

it immediately follows that

$$\mathcal{V}(P, \omega) = |\mu_{12}(\omega)|. \quad (3.11)$$

Hence, as derived by Mandel & Wolf (1976), *the visibility of the fringes that are produced in Young's interference experiment is a direct measure of the modulus of the spectral degree of coherence of the field at the two pinholes.*

It is readily seen from Equation (3.7) that, in general, the spectral density of the field that is observed on the screen \mathcal{B} differs from that of the field at the pinholes. This is due to (a) the appearance of the wave number k in the propagators K_i and (b) the modulus and phase of the spectral degree of coherence $\mu_{12}(\omega)$. Such spectral changes were analyzed in James and Wolf (1991a,b) for both filtered and broadband thermal light. In the latter case, significant spectral changes may occur. Experimental observations of spectral changes in a double-slit setup were presented by Santarsiero and Gori (1992). It is clear that Equation (3.7) can also be used to determine the spectral degree of coherence of the field at the apertures by comparing the spectral density in the far zone with that at the perforated screen. Such a study was carried out by Kandpal, Vaishya, Chander, Saxena, and Joshi (1992), and Kandpal and Vaishya (2000).

Another consequence of the spectral interference law, as expressed by Equation (3.3), is that the state of coherence of the field in the region of superposition may be different from that at the two pinholes. One might expect that when the incident field is partially coherent, i.e., $0 < |\mu_{12}(\omega)| < 1$, the same holds true for the field on the observation screen \mathcal{B} . This turns out not always to be the case. Extending the work of Ponomarenko and Wolf (1999), it was predicted by Schouten, Visser, and Wolf (2003) that at certain pairs of points the light is fully coherent, i.e., $|\mu(\mathbf{r}_1, \mathbf{r}_2, \omega)| = 1$, regardless of the state of coherence of the light at the two pinholes. The other extreme, namely the complete absence of coherence can also occur. This was demonstrated by Schouten, Gbur, Visser, and Wolf (2003) who found that at certain pairs of observation points $\mu(\mathbf{r}_1, \mathbf{r}_2, \omega) = 0$. This means that at these points, the spectral degree of coherence is singular. It is important to realize that such a *coherence singularity* occurs in a six-dimensional $(\mathbf{r}_1, \mathbf{r}_2)$ -space, in contrast to the classical phase singularities that are found in two or three dimensions. A fuller discussion of coherence singularities is presented in Section 7.

Next we turn our attention to Young's experiment with stochastic, electromagnetic beams. A study by Wang and Lü (2002) described how covering the apertures with linear polarizers can lead to changes in the spectral density and the state of polarization. Their work was based on the "beam coherence-polarization matrix" approach as developed by Gori (1998). Here we concentrate on the recently developed "unified theory of coherence and polarization," described in Wolf (2003b) and Wolf (2003a). In that theory, the state of coherence and polarization of a random beam is characterized by the *electric cross-spectral density matrix*, which is

defined as

$$\mathbf{W}(\mathbf{r}_1, \mathbf{r}_2, \omega) = \begin{bmatrix} W_{xx}(\mathbf{r}_1, \mathbf{r}_2, \omega) & W_{xy}(\mathbf{r}_1, \mathbf{r}_2, \omega) \\ W_{yx}(\mathbf{r}_1, \mathbf{r}_2, \omega) & W_{yy}(\mathbf{r}_1, \mathbf{r}_2, \omega) \end{bmatrix}, \quad (3.12)$$

where

$$W_{ij}(\mathbf{r}_1, \mathbf{r}_2, \omega) = \langle E_i^*(\mathbf{r}_1, \omega) E_j(\mathbf{r}_2, \omega) \rangle, \quad (i, j = x, y). \quad (3.13)$$

Here $E_i(\mathbf{r}, \omega)$ is a Cartesian component of the electric field at a point specified by a position vector \mathbf{r} at frequency ω , of a typical realization of the statistical ensemble representing the beam. A method to determine the elements of the matrix $\mathbf{W}(\mathbf{r}_1, \mathbf{r}_2, \omega)$ is described by Roychowdhury and Wolf (2004). Several observables can be derived from knowledge of the cross-spectral density matrix. The spectral density is given by the expression

$$S(\mathbf{r}, \omega) = \text{Tr } \mathbf{W}(\mathbf{r}, \mathbf{r}, \omega), \quad (3.14)$$

where Tr denotes the trace. The degree of coherence $\eta(\mathbf{r}_1, \mathbf{r}_2, \omega)$ of the field is defined as

$$\eta(\mathbf{r}_1, \mathbf{r}_2, \omega) = \frac{\text{Tr } \mathbf{W}(\mathbf{r}_1, \mathbf{r}_2, \omega)}{[\text{Tr } \mathbf{W}(\mathbf{r}_1, \mathbf{r}_1, \omega) \text{Tr } \mathbf{W}(\mathbf{r}_2, \mathbf{r}_2, \omega)]^{1/2}}. \quad (3.15)$$

In a manner quite similar to that for the spectral degree of coherence of scalar wave fields (see Section 2), one can show that

$$0 \leq |\eta(\mathbf{r}_1, \mathbf{r}_2, \omega)| \leq 1, \quad (3.16)$$

with the extreme values 0 and 1 corresponding to complete incoherence and complete coherence, respectively. The sharpness of the interference fringes that are produced in Young's experiment are related to the modulus of $\eta(\mathbf{r}_1, \mathbf{r}_2, \omega)$ in complete analogy to the scalar case described in the first part of this section. The absence of off-diagonal matrix elements in the definition of the spectral degree of coherence reflects a generalization of the classical Fresnel-Arago interference laws, according to which mutually orthogonal components of the electric field do not give rise to interference. A third observable is the (spectral) degree of polarization $\mathcal{P}(\mathbf{r}, \omega)$. This is defined as the ratio of the spectral density of the polarized part of the beam and its total spectral density (see Born & Wolf, 1999). One can show that

$$\mathcal{P}(\mathbf{r}, \omega) = \sqrt{1 - \frac{4 \text{Det } \mathbf{W}(\mathbf{r}, \mathbf{r}, \omega)}{[\text{Tr } \mathbf{W}(\mathbf{r}, \mathbf{r}, \omega)]^2}}, \quad (3.17)$$

where Det denotes the determinant.

As pointed out in Wolf (2003a), the elements of the electric cross-spectral density matrix change as the beam propagates. It is therefore to be expected that the observable quantities $S(\mathbf{r}, \omega)$, $\eta(\mathbf{r}_1, \mathbf{r}_2, \omega)$, and $\mathcal{P}(\mathbf{r}, \omega)$, which are derived from the matrix, will also change on propagation. Examples of such correlation-induced changes are discussed in Section 4.

Within the present context, that of Young's experiment, we need to know the electric field at two points $P(\mathbf{r}_1)$ and $P(\mathbf{r}_2)$, both located on the observation screen depicted in Figure 1. It is given by the expressions

$$E_x(\mathbf{r}_1, \omega) = K_{11}E_x(\mathbf{r}'_1, \omega) + K_{21}E_x(\mathbf{r}'_2, \omega), \quad (3.18)$$

$$E_y(\mathbf{r}_1, \omega) = K_{11}E_y(\mathbf{r}'_1, \omega) + K_{21}E_y(\mathbf{r}'_2, \omega), \quad (3.19)$$

$$E_x(\mathbf{r}_2, \omega) = K_{12}E_x(\mathbf{r}'_1, \omega) + K_{22}E_x(\mathbf{r}'_2, \omega), \quad (3.20)$$

$$E_y(\mathbf{r}_2, \omega) = K_{12}E_y(\mathbf{r}'_1, \omega) + K_{22}E_y(\mathbf{r}'_2, \omega), \quad (3.21)$$

with the propagators K_{ij} defined as

$$K_{ij} = -\frac{ikA}{2\pi} \frac{e^{ikR_{ij}}}{R_{ij}}, \quad (i, j = 1, 2), \quad (3.22)$$

and where R_{ij} denotes the distance from the pinhole $Q(\mathbf{r}'_i)$ to the point $P(\mathbf{r}_j)$. As was shown by Roychowdhury and Wolf (2005b), substitution from Equations (3.18)–(3.21) into definition (3.12) yields the cross-spectral density matrix in the region of superposition, expressed entirely in terms of that matrix at the two pinholes. They applied this formalism to the case of incident Gaussian Schell-model beams (see Section 4) and found that the degree of polarization of the field on the observation screen depends on (1) the position of observation, (2) the degree of polarization of the incident light, and (3) the degree of coherence of the field at the pinholes. The degree of coherence of the field that is observed, however, only depends on the degree of coherence of the incident field. Another striking prediction made by Roychowdhury and Wolf is that light that is completely unpolarized at the pinholes may become partially polarized across the fringe pattern. Experimental confirmation of this prediction was presented in Gori, Santarsiero, Borghi, and Wolf (2006). A further study of the observable quantities in the region of superposition was presented by Li, Lee, and Wolf (2006).

Generalizing the work concerning scalar fields of Schouten et al. (2003), it was shown by Agarwal, Dogariu, Visser, and Wolf (2005) that there exist special pairs of points at which the field is spatially fully coherent, irrespective of the state of coherence and polarization of the field that is incident at the two pinholes.

4. THE EVOLUTION OF PARTIALLY COHERENT BEAMS

It was noted in Section 2 that coherence functions obey certain propagation equations: the mutual coherence function $\Gamma(\mathbf{r}_1, \mathbf{r}_2, \tau)$ satisfies a pair of wave equations and the cross-spectral density function $W(\mathbf{r}_1, \mathbf{r}_2, \omega)$ satisfies a pair of Helmholtz equations. The coherence functions therefore have a well-defined behavior as they propagate; however, other properties derived from those coherence functions are not solutions of a differential equation and can evolve in nontrivial and unexpected ways on propagation. Among the properties that can change on propagation are the spectrum and the spectral degree of coherence of a wave field, defined by Equations (2.8) and (2.9), respectively, as well as the state of polarization and degree of polarization of an electromagnetic wave field.

Of particular interest is the propagation and evolution of partially coherent beams, i.e., wave fields that are highly directional. Partially coherent beams can be generated, for instance, by the distortion of a fully coherent laser beam, using a rotating ground-glass plate or a liquid crystal spatial light modulator. Numerous articles have been published on the behavior of partially coherent beams, in fact, more than can reasonably be covered here. In this section, we highlight some of the most significant results and discuss their theoretical foundations.

We consider first a partial coherent scalar wave field propagating from the plane $z = 0$ into the half-space $z > 0$; in the plane $z = 0$, the cross-spectral density has the form $W_0(\rho_1, \rho_2, \omega)$, where ρ_1 and ρ_2 represent transverse coordinates in the plane. Using the space-frequency representation of partially coherent wave fields, it can be readily shown that the cross-spectral density at points \mathbf{r}_1 and \mathbf{r}_2 in the half-space may be written in integral form as

$$W(\mathbf{r}_1, \mathbf{r}_2, \omega) = \iint W_0(\rho'_1, \rho'_2, \omega) G^*(\rho'_1, \mathbf{r}_1, \omega) G(\rho'_2, \mathbf{r}_2, \omega) d^2\rho'_1 d^2\rho'_2, \quad (4.1)$$

where $G(\rho', \mathbf{r}, \omega)$ is the free-space propagator for the Helmholtz equation. The propagator may be written as

$$G(\rho', \mathbf{r}, \omega) = \frac{1}{2\pi} \frac{\partial}{\partial z} \left(\frac{e^{iks}}{s} \right), \quad (4.2)$$

with $s \equiv |\mathbf{r} - \rho'|$ and $\mathbf{r} = (\rho, z)$.

If we assume for the moment that the field is highly directional, it follows that the cross-spectral density must be negligible outside of a narrow

cone centered on the z -axis. The propagator may then be approximated by its paraxial form,

$$G(\rho', \mathbf{r}, \omega) = -\frac{ik}{2\pi z} \exp[ik[(x - x')^2 + (y - y')^2]/2z]. \quad (4.3)$$

It is to be noted that there is no precise criterion for what constitutes a “beamlike” wave field. For a monochromatic wave field, a beam condition is typically formulated using the angular spectrum representation of the wave field. With this representation, the field in the half-space $z > 0$ can be written as

$$U(\mathbf{r}, \omega) = \int a(\mathbf{k}_\perp) \exp[i\mathbf{k} \cdot \mathbf{r}] d^2 k, \quad (4.4)$$

where $\mathbf{k} = (\mathbf{k}_\perp, k_z)$, $|\mathbf{k}| = k$, and

$$k_z = \sqrt{k^2 - k_\perp^2}. \quad (4.5)$$

The quantity $a(\mathbf{k}_\perp)$ is the *angular spectrum* of the wave field, defined as

$$a(\mathbf{k}_\perp) = \frac{1}{(2\pi)^2} \int U_0(\rho', \omega) \exp[-i\mathbf{k}_\perp \cdot \rho'] d^2 \rho', \quad (4.6)$$

where $U_0(\rho, \omega)$ is the wave field in the plane $z = 0$. Equation (4.4) expresses the field as a coherent superposition of plane waves propagating into the positive half-space. For $|\mathbf{k}_\perp| \leq k$, the quantity k_z is real-valued, and the plane wave has a constant amplitude on propagation. For $|\mathbf{k}_\perp| > k$, however, k_z is imaginary and the plane wave decays exponentially in the z -direction; it is an evanescent wave. The total wave of Equation (4.4) is said to be beamlike if

$$|a(\mathbf{k}_\perp)| \approx 0 \text{ unless } |\mathbf{k}_\perp| \ll k. \quad (4.7)$$

A similar definition exists, almost by analogy, for a partially coherent field. We introduce the angular spectrum of the cross-spectral density function as

$$\begin{aligned} \mathcal{A}(\mathbf{k}_{1\perp}, \mathbf{k}_{2\perp}) &= \frac{1}{(2\pi)^2} \iint W_0(\rho'_1, \rho'_2, \omega) \exp[i\mathbf{k}_{1\perp} \cdot \rho'_1] \\ &\quad \times \exp[-i\mathbf{k}_{2\perp} \cdot \rho'_2] d^2 \rho'_1 d^2 \rho'_2. \end{aligned} \quad (4.8)$$

The cross-spectral density may be written in terms of plane waves as

$$W(\mathbf{r}_1, \mathbf{r}_2, \omega) = \iint \mathcal{A}(\mathbf{k}_{1\perp}, \mathbf{k}_{2\perp}) \exp[-i\mathbf{k}_1 \cdot \mathbf{r}_1] \exp[i\mathbf{k}_2 \cdot \mathbf{r}_2] d^2k_{1\perp} d^2k_{2\perp}. \quad (4.9)$$

It can be shown (for details see, for instance, section 5.6.3 of Mandel & Wolf, 1995) that the field will be beamlike if

$$|\mathcal{A}(\mathbf{k}_\perp, \mathbf{k}_\perp)| \approx 0 \text{ unless } |\mathbf{k}_\perp| \ll k. \quad (4.10)$$

A number of special classes of fields have been used because of their analytic simplicity and their relevance to physically realizable optical fields. The first of these is produced by a so-called Schell-model source (Schell, 1961), for which the spectral degree of coherence is a function of the spatial difference variable alone, i.e.,

$$\mu_0(\mathbf{r}_1, \mathbf{r}_2, \omega) = \mu_0(\mathbf{r}_2 - \mathbf{r}_1, \omega). \quad (4.11)$$

The most analytically tractable class of partially coherent sources are known as *Gaussian Schell-model sources*, for which the spectral density and spectral degree of coherence in the plane $z = 0$ are both of Gaussian shape, namely

$$S_0(\rho, \omega) = A^2 e^{-\rho^2/2\sigma_S^2}, \quad (4.12)$$

$$\mu_0(\rho', \omega) = e^{-\rho'^2/2\sigma_\mu^2}. \quad (4.13)$$

Here A represents the amplitude of the wave, σ_S represents the width of the source and σ_μ represents the transverse correlation length of the source; all quantities are in general frequency dependent. It can be readily shown that the spectral density and spectral degree of coherence retain a Gaussian form on propagation. An early study of the directionality of beams produced by such sources was done by Foley and Zubairy (1978).

When the width of the spectral degree of coherence function is much narrower than the width of the spectral density function, one may further approximate a Schell-model source by using the *quasi-homogeneous* approximation, such that

$$W_0(\mathbf{r}_1, \mathbf{r}_2, \omega) \approx S_0\left(\frac{\mathbf{r}_1 + \mathbf{r}_2}{2}, \omega\right) \mu_0(\mathbf{r}_2 - \mathbf{r}_1, \omega). \quad (4.14)$$

A study of the propagation characteristics of Gaussian quasi-homogeneous beams was undertaken by Collett and Wolf (1980); the concept of quasi-homogeneity is also used to describe scatterers, and it will be further discussed in Section 6.

Directionality is often assumed to require a high degree of spatial coherence, as in a laser, and it would seem to exclude the possibility of beamlike fields from quasi-homogeneous sources. It was shown in Collett and Wolf (1978) and Wolf and Collett (1978) that one can create partially coherent sources of nearly any degree of spatial coherence that produce the same directionality as a laser. The far-field spatial coherence properties of such laser-equivalent sources was studied in Shirai and Wolf (2002).

The earliest studies of the evolution of partially coherent fields investigated the change in spatial coherence on propagation; most notable are those of van Cittert (1934) and Zernike (1948), who investigated the coherence of light emanating from a spatially incoherent planar source. More generally, it has been shown by Friberg and Wolf (1983) that there exist reciprocity relations between the intensity and spatial coherence of the source and the spatial coherence and intensity of the radiation in the far zone, respectively. Another investigation of the reciprocal relationship between source and far zone has been undertaken by Friberg, Visser, and Wolf (2000).

Although typically the spatial coherence of a field increases on propagation, it was shown by Devaney, Friberg, Kumar, and Wolf (1997) that it is possible to produce fields whose spatial coherence decreases on propagation through the mechanism of phase conjugation. Furthermore, Pedersen and Stammes (2000) used a radiometric approach to show that if on propagation an increase of the intensity occurs, i.e., when the light is being concentrated, the spatial degree of coherence decreases.

An unusual class of spatially coherent beams are the so-called non-diffracting or Bessel beams; a review of the subject was presented by Bouchal (2003). It was shown by Turunen, Vasara, and Friberg (1991) that fields that have Bessel *correlations* can also possess a degree of propagation-invariance, or even revivals of spatial coherence on propagation.

We have already noted that the spectrum of light of a partially coherent field can change on propagation, even in free space, a phenomenon known as a correlation-induced spectral change. An early study of the spectral changes of beams on propagation was done by Dačić and Wolf (1988).

One can readily extend the formalism of partially coherent scalar beams to partially coherent electromagnetic beams. Within the paraxial limit, the electric and magnetic fields will be completely transverse to the direction of propagation, formally chosen as the z -axis. The second-order coherence properties of the electromagnetic beam can then be characterized by the 2×2 cross-spectral density matrix,

$$\mathbf{W}(\mathbf{r}_1, \mathbf{r}_2, \omega) = \begin{bmatrix} \langle E_x^*(\mathbf{r}_1, \omega) E_x(\mathbf{r}_2, \omega) \rangle & \langle E_x^*(\mathbf{r}_1, \omega) E_y(\mathbf{r}_2, \omega) \rangle \\ \langle E_y^*(\mathbf{r}_1, \omega) E_x(\mathbf{r}_2, \omega) \rangle & \langle E_y^*(\mathbf{r}_1, \omega) E_y(\mathbf{r}_2, \omega) \rangle \end{bmatrix}, \quad (4.15)$$

where $E_x(\mathbf{r}, \omega)$ and $E_y(\mathbf{r}, \omega)$ are monochromatic realizations of the x and y -components of the electric field, respectively. Each component of this matrix can be propagated using Equation (4.1) for a scalar partially coherent wave field.

At any point in the wave field, the degree of polarization is defined by the following expression, previously noted in Section 3,

$$\mathcal{P}(\mathbf{r}, \omega) = \sqrt{1 - \frac{4\text{Det}\{\mathbf{W}(\mathbf{r}, \mathbf{r}, \omega)\}}{[\text{Tr}\{\mathbf{W}(\mathbf{r}, \mathbf{r}, \omega)\}]^2}}, \quad (4.16)$$

where Det indicates the determinant and Tr the trace of the cross-spectral density matrix. The value $\mathcal{P} = 0$ indicates a completely unpolarized field, while the value $\mathcal{P} = 1$ indicates a completely polarized field.

When the correlation and polarization properties of the source are spatially-varying, it is possible for the degree of polarization of the light field to change on propagation; this seems to have first been observed by James (1994), and was later discussed by Agrawal and Wolf (2000), well before a unified theory of coherence and polarization was introduced by Wolf (2003b) (and discussed in detail in Wolf, 2007b). This unified theory was used by Wolf (2003a) to study the correlation-induced changes in coherence, polarization, and spectrum of a partially coherent electromagnetic beam. The far zone behavior of these properties in quasi-homogeneous electromagnetic beams was investigated by Korotkova, Hoover, Gamiz, and Wolf (2005). It has also been shown by Korotkova and Wolf (2005) that the state of polarization (ellipticity, orientation and handedness of the polarization ellipse) of an electromagnetic beam may change on propagation in free space. A further study of the changes in the degree of polarization was done by Salem and Wolf (2008).

There is a well-known theorem due to Stokes (1852) regarding the decomposition of an arbitrary beam into polarized and unpolarized components, in which he states,

...it is always possible to represent the given group by a stream of common light combined with a stream of elliptically polarized light independent of the former.

It has recently been shown that this assertion is incorrect (Wolf, 2008): the decomposition of a beam into a polarized part and an unpolarized part was further shown by Korotkova, Visser, and Wolf (2008) to be a local, rather than global, property of the field (i.e., the decomposition may be different at different points).

From the definition (4.16) of the degree of polarization, it is to be noted that it depends only on the diagonal elements ($\mathbf{r}_1 = \mathbf{r}_2 = \mathbf{r}$) of the cross-spectral density matrix. This implies that there are many different

coherence matrices that can produce the same degree of polarization; in particular, Visser, Kuebel, Lahiri, Shirai, and Wolf (2009) demonstrated that completely unpolarized beams may have a variety of coherence properties. Gbur and James (2000) used a similar observation to theoretically construct three-dimensional unpolarized primary radiation sources that produce nearly fully polarized fields.

Additional effects can arise when a partially coherent electromagnetic beam propagates through a homogeneous and isotropic weakly scattering medium such as the turbulent atmosphere. The effect of atmospheric turbulence on beam propagation can be made analytically tractable by treating the scattered wave field by a perturbative approximation such as the Born or Rytov series. A more direct connection to the earlier equations of this section may be made by using the so-called extended Huygens–Fresnel principle, in which the effect of turbulence is treated as a perturbation of the free-space Green’s function. Equation (4.1) can then be written in the form,

$$\begin{aligned} W(\mathbf{r}_1, \mathbf{r}_2, \omega) = & \iint W_0(\rho'_1, \rho'_2, \omega) C_\psi(\rho'_1, \rho'_2, \mathbf{r}_1, \mathbf{r}_2) \\ & \times G^*(\rho'_1, \mathbf{r}_1, \omega) G(\rho'_2, \mathbf{r}_2, \omega) d^2\rho'_1 d^2\rho'_2, \end{aligned} \quad (4.17)$$

where $\psi(\rho, \mathbf{r})$ is the phase distortion induced by the turbulence on the field on propagation from ρ to \mathbf{r} , and

$$C_\psi(\rho'_1, \rho'_2, \mathbf{r}_1, \mathbf{r}_2) = \langle \exp[\psi^*(\rho'_1, \mathbf{r}_1)] \exp[\psi(\rho'_2, \mathbf{r}_2)] \rangle_T \quad (4.18)$$

is the correlation function of that phase distortion. The average $\langle \dots \rangle_T$ is an ensemble average over realizations of the atmospheric turbulence, and this average is, in general, independent of the ensemble average of the wave field. The calculation of C_ψ is nontrivial and requires a number of simplifying, sometimes dubious, assumptions; details can be found in Lutomirski and Yura (1971) and the book by Andrews and Phillips (2005). Equation (4.17) can be used to propagate each component of the cross-spectral density matrix to study the effects of turbulence on polarization.

Polarization changes of beams in turbulence were first studied by Roychowdhury, Ponomarenko, and Wolf (2005) and Salem, Korotkova, Dogariu, and Wolf (2004); it was surprisingly shown that the degree of polarization tends to its initial value after propagation over a sufficiently long distance. The far zone behavior of the degree of polarization was investigated by Korotkova, Salem, and Wolf (2004). Changes in the state of polarization in turbulence, and its return to the initial state, were discussed by Korotkova, Salem, Dogariu, and Wolf (2005). Spectral changes of

electromagnetic beams in turbulence were considered by Korotkova, Pu, and Wolf (2008).

Propagation through other types of random media have also been considered; Gao and Korotkova (2007) considered the changes of polarization on propagation through tissue.

Discussions of the behavior of the scintillation of partially coherent beams in turbulence will be considered in Section 10.

5. FOCUSING OF PARTIALLY COHERENT WAVE FIELDS

The classical theory of focusing deals with monochromatic wave fields that can be scalar or vectorial in nature; an excellent overview is given by Stamnes (1986). In the present section, we examine the focusing of partially coherent scalar fields. In particular, the effect of the state of coherence of the field in the exit pupil on the distribution of the spectral density and the coherence properties of the field in the focal region will be discussed. In addition, the focal shift phenomenon will also be addressed.

We consider first a monochromatic, spherical wave of frequency ω that emerges from a circular aperture with radius a , and which converges toward a geometrical focus O (see Figure 2). The field in the focal region is, according to the Huygens–Fresnel principle (see Born & Wolf, 1999, chapter 8), given by the expression

$$U(\mathbf{r}, \omega) = -\frac{i}{\lambda} \int_S U^{(0)}(\mathbf{r}', \omega) \frac{e^{iks}}{s} dS. \quad (5.1)$$

Here $U^{(0)}(\mathbf{r}', \omega)$ is the field on the wavefront S that fills the aperture, $k = \omega/c = 2\pi/\lambda$ is the wave number associated with frequency ω , with c the speed of light and λ the wavelength. Furthermore, $s = |\mathbf{r}' - \mathbf{r}|$ denotes the distance from a point of integration $Q(\mathbf{r}')$ to the observation point $P(\mathbf{r})$. From Equation (5.1), one can derive the so-called Debye

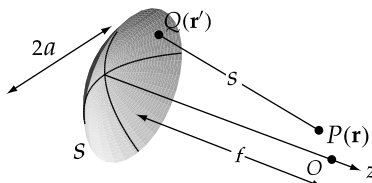


FIGURE 2 Illustrating the focusing configuration. The origin of a right-handed cartesian coordinate system is taken at the geometrical focus O .

integral (see Born & Wolf, 1999, chapter 8)

$$U(\mathbf{r}, \omega) = -\frac{i}{\lambda} \int_{\Omega} a(\mathbf{s}, \omega) e^{ik\mathbf{s} \cdot \mathbf{r}} d\Omega, \quad (5.2)$$

where Ω is the solid angle subtended by the aperture at the geometrical focus, which is spanned by the real unit vectors $\mathbf{s} = (s_x, s_y, s_z > 0)$. The amplitude function $a(\mathbf{s}, \omega)$ is assumed to be real, apart from a possible constant phase factor. The Debye integral expresses the field in the focal region as a superposition of plane waves, with direction-dependent amplitudes. Equations (5.1) and (5.2) are valid provided that $\lambda \ll a \ll f$, where f is the radius of curvature of the wavefront. In addition, the Fresnel number $N = a^2/\lambda f$ must be large compared with unity.

The above two expressions can both be generalized to deal with partially coherent fields. Recall the definition (2.17) of the cross-spectral density function of the field at a pair of points \mathbf{r}_1 and \mathbf{r}_2 ,

$$W(\mathbf{r}_1, \mathbf{r}_2, \omega) = \langle U^*(\mathbf{r}_1, \omega) U(\mathbf{r}_2, \omega) \rangle_{\omega}. \quad (5.3)$$

On substituting from Equation (5.1) into Equation (5.3) and interchanging the order of integration and ensemble averaging, we obtain the following formula for the cross-spectral density in the focal region,

$$W(\mathbf{r}_1, \mathbf{r}_2, \omega) = \frac{1}{\lambda^2} \iint_S W^{(0)}(\mathbf{r}'_1, \mathbf{r}'_2, \omega) \frac{e^{ik(s_2 - s_1)}}{s_1 s_2} dS_1 dS_2, \quad (5.4)$$

where

$$W^{(0)}(\mathbf{r}'_1, \mathbf{r}'_2, \omega) = \langle U^{(0)*}(\mathbf{r}'_1, \omega) U^{(0)}(\mathbf{r}'_2, \omega) \rangle_{\omega} \quad (5.5)$$

denotes the cross-spectral density of the field in the exit pupil, and

$$s_1 = |\mathbf{r}'_1 - \mathbf{r}_1|, \quad (5.6)$$

$$s_2 = |\mathbf{r}'_2 - \mathbf{r}_2|. \quad (5.7)$$

The spectral density $S(\mathbf{r}, \omega) = W(\mathbf{r}, \mathbf{r}, \omega)$ in the focal region is then given by the expression

$$S(\mathbf{r}, \omega) = \frac{1}{\lambda^2} \iint_S W^{(0)}(\mathbf{r}'_1, \mathbf{r}'_2, \omega) \frac{e^{ik(s'_2 - s'_1)}}{s'_1 s'_2} dS_1 dS_2, \quad (5.8)$$

with

$$s'_1 = |\mathbf{r}'_1 - \mathbf{r}|, \quad (5.9)$$

$$s'_2 = |\mathbf{r}'_2 - \mathbf{r}|. \quad (5.10)$$

Alternatively, one can use the *angular correlation function* defined as

$$\mathcal{A}(\mathbf{s}_1, \mathbf{s}_2, \omega) = \langle a^*(\mathbf{s}_1, \omega) a(\mathbf{s}_2, \omega) \rangle_\omega. \quad (5.11)$$

On substituting from Equations (5.2) and (5.11) into Equation (5.3), we obtain the expression

$$W(\mathbf{r}_1, \mathbf{r}_2, \omega) = \frac{1}{\lambda^2} \iint_{\Omega} \mathcal{A}(\mathbf{s}_1, \mathbf{s}_2, \omega) e^{ik(\mathbf{s}_2 \cdot \mathbf{r}_2 - \mathbf{s}_1 \cdot \mathbf{r}_2)} d\Omega_1 d\Omega_2. \quad (5.12)$$

Expression (5.12) is known as the *generalized Debye integral*. The spectral density $S(\mathbf{r}, \omega) = W(\mathbf{r}, \mathbf{r}, \omega)$ in the focal region is now given by the formula

$$S(\mathbf{r}, \omega) = \frac{1}{\lambda^2} \iint_{\Omega} \mathcal{A}(\mathbf{s}_1, \mathbf{s}_2, \omega) e^{ik\mathbf{r} \cdot (\mathbf{s}_2 - \mathbf{s}_1)} d\Omega_1 d\Omega_2. \quad (5.13)$$

Equations (5.4) and (5.8) allow one to study the state of coherence and the spectral density of the field in the focal region for a given cross-spectral density $W^{(0)}(\mathbf{r}'_1, \mathbf{r}'_2, \omega)$ of the field in the aperture. Alternatively, Equations (5.12) and (5.13) can be used for the same purpose when the angular correlation function $\mathcal{A}(\mathbf{s}_1, \mathbf{s}_2, \omega)$ of the field in the aperture is known.

To specify the position of an observation point near the geometrical focus we use the dimensionless Lommel variables, which are defined as

$$u = k \left(\frac{a}{f} \right)^2 z, \quad (5.14)$$

$$v = k \left(\frac{a}{f} \right) \sqrt{x^2 + y^2}. \quad (5.15)$$

Friberg and Turunen (1988) studied the imaging of Gaussian Schell-model sources by generalizing the familiar *ABCD* ray-transfer formalism. They derived expressions for the size and position of the image waist. Wang, Friberg, and Wolf (1997) used the generalized Debye integral, Equation (5.12), to calculate the axial spectral density distribution of focused, partially coherent cylindrical waves with a Gaussian angular correlation function. They noticed that the peak intensity decreases as the coherence

of the field in the aperture is reduced. Also, the focal spot size was seen to increase in that case. The effect of the state of coherence on the full three-dimensional spectral density near focus was examined by Visser, Gbur, and Wolf (2002). Starting from Equation (5.4), the field in the exit pupil was assumed to be of the Gaussian Schell-model type, i.e.,

$$W^{(0)}(\rho'_1, \rho'_2, \omega) = S^{(0)}(\omega) e^{-(\rho'_2 - \rho'_1)^2 / 2\sigma_g^2}. \quad (5.16)$$

Here $S^{(0)}(\omega)$ denotes the spectral density and σ_g the effective coherence length of the field in the aperture. Furthermore, $\rho' = (x', y')$ is the two-dimensional projection, considered as a two-dimensional vector, of the position vector r' of the point Q onto the xy -plane (see Figure 2). It was shown for such fields that the spectral density distribution is symmetric about the geometrical focus. Also, the maximum spectral density, which occurs at the geometrical focal point, decreases when σ_g decreases. The intricate focal field structure that is typical of coherent fields gradually disappears when σ_g becomes smaller than the aperture radius a . In addition, the maximum spectral density decreases with decreasing coherence length. These trends can be seen from Figures 3 and 4. The focusing of twisted anisotropic Gaussian-Schell model beams was examined by Cai and Lin (2003). The coupling of partially coherent light into a planar waveguide was discussed by Saastamoinen, Kuittinen, Vahimaa, and Turunen (2004).

It was noted by Visser et al. (2002) that cross-spectral density functions that are not positive for all values of their spatial arguments may

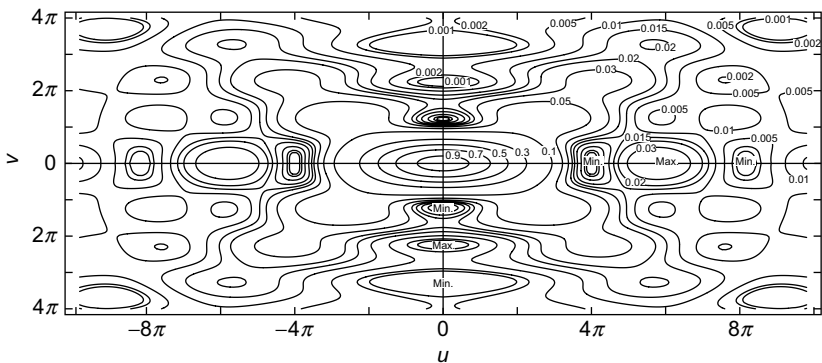


FIGURE 3 Contours of constant spectral density of a fully coherent field in the neighborhood of the geometrical focus. Positions are indicated using Lommel variables as defined in Equations (5.14) and (5.15) (Adapted from Visser, Gbur, & Wolf, 2002).

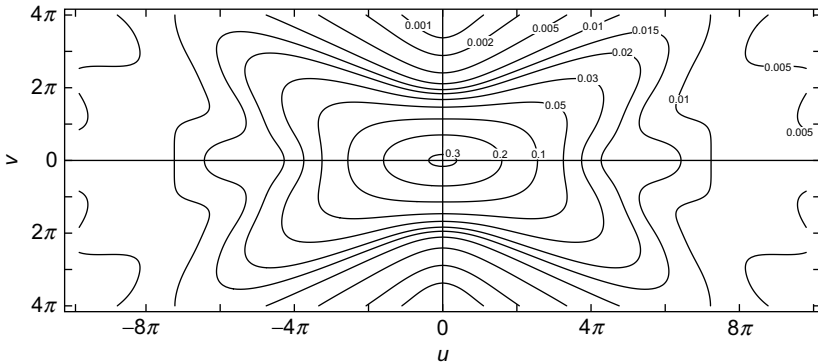


FIGURE 4 Contours of constant spectral density of a converging partially coherent Gaussian Schell-model field with $\sigma_g/a = 0.25$, in the neighborhood of the geometrical focus. The normalization is equal to that used in Figure 3. (Adapted from Visser, Gbur and Wolf, 2002.)

produce a spectral density distribution that is still symmetric about the focal plane, but with a maximum that does not coincide with the geometrical focus. Following up on this observation, cross-spectral densities of the type

$$W^{(0)}(\mathbf{r}_1', \mathbf{r}_2', \omega) = S^{(0)}(\omega) J_0[\beta(r_2 - r_1)], \quad (5.17)$$

were studied by Gbur and Visser (2003a), Pu, Nemoto, and Liu (2004), and van Dijk, Gbur, and Visser (2008). In Equation (5.17), $S^{(0)}(\omega)$ denotes the (uniform) spectral density of the aperture field, J_0 is the Bessel function of zeroth order, and β is, roughly speaking, the inverse effective coherence length. Using a coherent mode decomposition (see Section 8), it was calculated how the spectral density distribution in the focal region changes as the parameter $a\beta$, with a the aperture radius, is varied. It was indeed found that the spectral density at focus can be a local minimum, rather than a maximum, when $a\beta < 1$. This is illustrated in Figure 5. An experimental observation of such a partially coherent “bottle beam” was made by Pu, Dong, and Wang (2006).

Thus far, we have discussed focusing configurations for which the Fresnel number $N = a^2/\lambda f \gg 1$. For systems with $N \approx 1$, the location of maximum spectral density is no longer at the geometrical focus, but it occurs closer toward the aperture. This so-called focal shift phenomenon is described in detail in Stammes (1986). Lü, Zhang, and Cai (1995) and later Friberg, Visser, Wang, and Wolf (2001) analyzed this effect for converging partially coherent fields. It was found that the focal shift depends not just on the Fresnel number, as it does for fully coherent fields, but also

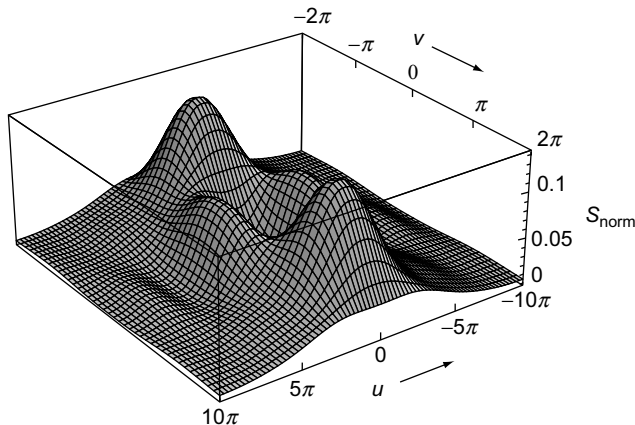


FIGURE 5 Example of the three-dimensional normalized spectral density distribution near focus, produced by a converging, Bessel-correlated field. The minimum at the geometrical focus is clearly visible. (Adapted from van Dijk, Gbur, & Visser, 2008.)

on the state of coherence. Experimental confirmation of these predictions was reported by Wang, Cai, and Korotkova (2009).

It has long been known that the focusing and diffraction of polychromatic light generally results in spectral changes. In studying the diffraction of partially coherent light, Pu, Zhang, and Nemoto (1999) noted that the spectrum can, in fact, change very rapidly under a gradual change of system parameters. Such “spectral switches” on diffraction were studied in more detail by Pu and Nemoto (2000) and Pu and Nemoto (2002). Similar spectral switches that arise on focusing were investigated by Gbur, Visser, and Wolf (2002a), Gbur, Visser, and Wolf (2002b), and Visser and Wolf (2003); it was pointed out that the switches can be associated with the phase singularities of coherent waves (to be discussed in Section 7). These spectral anomalies at focus were experimentally measured by Popescu and Dogariu (2002), and the connection between phase singularities and spectral changes was described further by Foley and Wolf (2002). The spectral changes associated with the focusing of high-order Bessel beams was discussed by Hu and Pu (2006).

The above-mentioned studies dealt exclusively with spectral densities (intensities) of focused, partially coherent fields. The coherence properties of such fields were studied by Fischer and Visser (2004). It was found for Gaussian-correlated fields that, depending on the effective coherence length of the field in the aperture, the effective width of the spectral degree of coherence can be either larger or smaller than that of the spectral density distribution. Moreover, the spectral degree of coherence was shown to possess phase singularities, even though such singularities are

not present in the aperture field (see also Section 7). The coherence properties of focused, Bessel-correlated fields were analyzed by van Dijk et al. (2008).

In this section, we have restricted ourselves to scalar waves, but we do mention that a few studies have been devoted to the focusing of partially coherent electromagnetic fields, e.g., Zhang, Pu, and Wang (2008), Foreman and Török (2009), Salem and Agrawal (2009a), and Salem and Agrawal (2009b).

6. SCATTERING OF PARTIALLY COHERENT WAVE FIELDS BY RANDOM AND DETERMINISTIC MEDIA

The scattering of wave fields by a particulate medium such as, for example, a colloidal suspension, is a problem of fundamental importance. The seminal work by Mie (1908) laid the groundwork for an entire field of study. Here we review the scattering of partially coherent fields from both deterministic and random media. Also, the role of coherence in inverse problems is explained.

We consider first a fully coherent field, propagating in free space, that is incident on a deterministic scatterer. The total field $U(\mathbf{r}, \omega)$ can be written as the sum of the incident field, $U^{(i)}(\mathbf{r}, \omega)$, and the scattered field, $U^{(s)}(\mathbf{r}, \omega)$, i.e.,

$$U(\mathbf{r}, \omega) = U^{(i)}(\mathbf{r}, \omega) + U^{(s)}(\mathbf{r}, \omega). \quad (6.1)$$

Here \mathbf{r} denotes the position and ω the frequency. The total field satisfies the following integral equation (see Born & Wolf, 1999, section 13.1):

$$U(\mathbf{r}, \omega) = U^{(i)}(\mathbf{r}, \omega) + \int_V F(\mathbf{r}', \omega) U(\mathbf{r}', \omega) G(\mathbf{r} - \mathbf{r}', \omega) d^3 r', \quad (6.2)$$

where V is the volume occupied by the scatterer,

$$F(\mathbf{r}, \omega) = \frac{k^2}{4\pi} [n^2(\mathbf{r}, \omega) - 1] \quad (6.3)$$

is the *scattering potential* and $n(\mathbf{r}, \omega)$ the refractive index. Furthermore,

$$G(\mathbf{r} - \mathbf{r}', \omega) = \frac{e^{ik|\mathbf{r}-\mathbf{r}'|}}{|\mathbf{r} - \mathbf{r}'|} \quad (6.4)$$

is the outgoing free-space Green's function associated with the Helmholtz operator. For weak scatterers, i.e., scatterers whose refractive index differs

only slightly from unity, we may approximate the total field $U(\mathbf{r}', \omega)$ in the integral of Equation (6.2) by the incident field $U^{(i)}(\mathbf{r}', \omega)$. This so-called first-order Born approximation yields the expression

$$U(\mathbf{r}, \omega) = U^{(i)}(\mathbf{r}, \omega) + \int_V F(\mathbf{r}', \omega) U^{(i)}(\mathbf{r}', \omega) G(\mathbf{r} - \mathbf{r}', \omega) d^3 r'. \quad (6.5)$$

We notice that Equation (6.5) involves an ordinary integral, and is therefore typically easier to solve than an integral equation of the form of Equation (6.2).

Let us now consider the case where the incident field is not fully coherent, but partially coherent. Such a field is characterized by a cross-spectral density function (see Section 2)

$$W^{(i)}(\mathbf{r}_1, \mathbf{r}_2, \omega) = \langle U^{(i)*}(\mathbf{r}_1, \omega) U^{(i)}(\mathbf{r}_2, \omega) \rangle_\omega. \quad (6.6)$$

Because the incident field is random, the scattered field, represented by the last term of Equation (6.5), will also be random. Its cross-spectral density function

$$W^{(s)}(\mathbf{r}_1, \mathbf{r}_2, \omega) = \langle U^{(s)*}(\mathbf{r}_1, \omega) U^{(s)}(\mathbf{r}_2, \omega) \rangle_\omega \quad (6.7)$$

can readily be found by substituting from Equation (6.5) into Equation (6.7) and interchanging the order of averaging and integration. The resulting expression is

$$\begin{aligned} W^{(s)}(\mathbf{r}_1, \mathbf{r}_2, \omega) &= \iint_V F^*(\mathbf{r}'_1, \omega) F(\mathbf{r}'_2, \omega) W^{(i)}(\mathbf{r}'_1, \mathbf{r}'_2, \omega) \\ &\quad \times G^*(\mathbf{r}_1 - \mathbf{r}'_1, \omega) G(\mathbf{r}_2 - \mathbf{r}'_2, \omega) d^3 r'_1 d^3 r'_2. \end{aligned} \quad (6.8)$$

Expression (6.8) pertains to the scattering of a partially coherent field by a deterministic scatterer. It can easily be generalized to scatterers whose refractive index, and hence also their scattering potential $F(\mathbf{r}, \omega)$, is a random function of position. This is achieved by replacing the product $F^*(\mathbf{r}'_1, \omega) F(\mathbf{r}'_2, \omega)$ by the correlation function

$$C_F(\mathbf{r}'_1, \mathbf{r}'_2, \omega) = \langle F^*(\mathbf{r}'_1, \omega) F(\mathbf{r}'_2, \omega) \rangle_F, \quad (6.9)$$

where the symbol $\langle \dots \rangle_F$ denotes an average taken over an ensemble of scatterers. On making use of Equation (6.9) and again interchanging the

order of averaging and integration, we obtain the formula

$$\begin{aligned} W^{(s)}(\mathbf{r}_1, \mathbf{r}_2, \omega) &= \iint_V C_F(\mathbf{r}'_1, \mathbf{r}'_2, \omega) W^{(i)}(\mathbf{r}'_1, \mathbf{r}'_2, \omega) \\ &\quad \times G^*(\mathbf{r}_1 - \mathbf{r}'_1, \omega) G(\mathbf{r}_2 - \mathbf{r}'_2, \omega) d^3 r'_1 d^3 r'_2. \end{aligned} \quad (6.10)$$

The radiant intensity (the rate at which the field radiates energy at frequency ω in direction s per unit solid angle) of the scattered field in a direction specified by the unit vector s equals

$$J(r\mathbf{s}, \omega) = r^2 W^{(s)}(r\mathbf{s}, r\mathbf{s}, \omega), \quad (6.11)$$

$$\begin{aligned} &= r^2 \iint_V C_F(\mathbf{r}'_1, \mathbf{r}'_2, \omega) W^{(i)}(\mathbf{r}'_1, \mathbf{r}'_2, \omega) \\ &\quad \times G^*(r\mathbf{s} - \mathbf{r}'_1, \omega) G(r\mathbf{s} - \mathbf{r}'_2, \omega) d^3 r'_1 d^3 r'_2. \end{aligned} \quad (6.12)$$

Equation (6.12) brings into evidence that the radiant intensity depends on both the statistical properties of the scatterer [represented by the function $C_F(\mathbf{r}'_1, \mathbf{r}'_2, \omega)$] and those of the incident field [represented by the function $W^{(i)}(\mathbf{r}'_1, \mathbf{r}'_2, \omega)$]. Using the above formalism, Jannson, Jannson, and Wolf (1988) studied how the degree of coherence of the incident field affects the directionality of the field scattered by a Gaussian-correlated medium. They found that the effective angular width of the radiant intensity increases as the correlation length of the scatterer decreases. Furthermore, the radiant intensity was found to be more peaked in the forward direction for a fully coherent beam than for a partially coherent field. Gori, Palma, and Santarsiero (1990) confirmed experimentally that for a planar random medium (in their case, a rotating ground-glass plate), the width of the radiant intensity distribution of the scattered field indeed increases when the spectral degree of coherence of the incident field decreases.

An important class of scatterers is formed by so-called *quasi-homogeneous media*. These were introduced by Carter and Wolf (1988), who defined the degree of spatial correlation of the scattering potential [given by Equation (6.9)] as

$$\mu_F(\mathbf{r}_1, \mathbf{r}_2, \omega) \equiv \frac{C_F(\mathbf{r}_1, \mathbf{r}_2, \omega)}{\sqrt{I_F(\mathbf{r}_1, \omega) I_F(\mathbf{r}_2, \omega)}}. \quad (6.13)$$

Here the quantity $I_F(\mathbf{r}, \omega) \equiv C_F(\mathbf{r}, \mathbf{r}, \omega)$ represents the average value of the second moment of the scattering potential. Just as for the spectral degree of coherence of a wave field, one can show that

$$0 \leq |\mu_F(\mathbf{r}_1, \mathbf{r}_2, \omega)| \leq 1. \quad (6.14)$$

The extreme values $|\mu_F(\mathbf{r}_1, \mathbf{r}_2, \omega)| = 1$ and $\mu_F(\mathbf{r}_1, \mathbf{r}_2, \omega) = 0$ correspond to complete correlation and the total absence of correlation, respectively. As discussed by Silverman (1958), for many scatterers such as fluids, plasmas, or the atmosphere, the degree of spatial correlation of the scattering potential will depend only on the two positions \mathbf{r}_1 and \mathbf{r}_2 through the difference $\mathbf{r}_2 - \mathbf{r}_1$. We can then write

$$\mu_F(\mathbf{r}_1, \mathbf{r}_2, \omega) = g_F(\mathbf{r}_2 - \mathbf{r}_1, \omega) \quad (6.15)$$

A scatterer is said to be quasi-homogeneous if the function $g_F(\mathbf{r}, \omega)$ varies much faster with \mathbf{r} than the function $I_F(\mathbf{r}', \omega)$ varies with \mathbf{r}' . Carter and Wolf (1988) studied the scattering of a monochromatic plane wave by a quasi-homogeneous medium. They showed that, within the validity of the first-order Born approximation, the far zone field satisfies two reciprocity relations, namely

$$J(r\mathbf{s}, \omega) = \tilde{I}_F(\mathbf{0}, \omega) \tilde{g}_F[k(\mathbf{s} - \mathbf{s}_0), \omega], \quad (6.16)$$

$$\mu(r\mathbf{s}_1, r\mathbf{s}_2, \omega) = \tilde{I}_F[k(\mathbf{s}_2 - \mathbf{s}_1), \omega] / \tilde{I}_F(\mathbf{0}, \omega). \quad (6.17)$$

Here \mathbf{s}_0 is the direction of propagation of the incident field, and $\tilde{I}_F(\mathbf{K}, \omega)$ and $\tilde{g}_F(\mathbf{K}, \omega)$ are the three-dimensional spatial Fourier transforms of $I_F(\mathbf{r}, \omega)$ and $g_F(\mathbf{r}, \omega)$, respectively. Equation (6.16) states that the radiant intensity is proportional to the Fourier transform of the degree of spatial correlation of the scattering potential. Equation (6.17) states that degree of coherence is proportional to the Fourier transform of the second moment of the scattering potential. It is to be noted that these relations are similar to the reciprocity relations satisfied by the fields of quasi-homogeneous beams, which are mentioned in Section 4.

Fischer and Wolf (1994) described how these two reciprocity relations can be used to reconstruct both the correlation function $g_F(\mathbf{r}, \omega)$, and the second moment $I_F(\mathbf{r}, \omega)$ of the scattering potential of a quasi-homogeneous medium from far-zone field data. Fischer and Cairns (1995) showed that by using pulses, rather than an incident monochromatic plane wave, the second moment of the dielectric susceptibility of a quasi-homogeneous medium can be reconstructed from far-zone intensity measurements alone. A theory of diffraction tomography for quasi-homogeneous media was later developed by Fischer and Wolf (1997), and generalized by Fischer (1998). Visser, Fischer, and Wolf (2006) examined how radiation generated by a quasi-homogeneous source (discussed in Section 4) is scattered by a quasi-homogeneous medium. They derived reciprocity relations for both the spectral degree of coherence and the spectral density of the field in the far zone. Recently, an “Ewald-sphere construction” for determining

the structure of random media was proposed by Lahiri, Wolf, Fischer, and Shirai (2009).

The scattering of a two-dimensional electromagnetic field by a slit or a groove was studied by Huttunen, Friberg, and Turunen (1995). By using a coherent mode decomposition (see Section 8), the scattered field can be considered as an incoherent superposition of the field scattered by each individual mode. A strong decrease in the directionality of the scattered radiant intensity with decreasing spatial coherence was found.

As discussed in Section 4 (see also Wolf & James, 1996), the spectral density of the field that is generated by a partially coherent source can change on propagation, even when this propagation takes place in free space. Because of the well-known analogy that exists between radiation and scattering, one might expect that a similar effect will arise when a polychromatic wave is scattered by a medium whose dielectric susceptibility is a random function of position. Wolf, Foley, and Gori (1989) showed that, within the validity of the first-order Born approximation, this is indeed the case. In particular, if the two-point correlation function $C_F(\mathbf{r}_1', \mathbf{r}_2', \omega)$ of Equation (6.9) is a Gaussian, and if the spectrum of the incident light has a Gaussian profile, then the spectral density of the scattered field may be effectively blue-shifted or red-shifted, depending on the scattering angle. The analysis was extended to multiple scattering using the Rytov approximation by Shirai and Asakura (1995). Zhao, Korotkova, and Wolf (2007) discussed how the observation of these spectral changes in the far zone of the scatterer may be used to determine the correlation function of its scattering potential.

The spectral changes described above involve what may be referred to as a redistribution of the spectral density, in that light of different frequencies is scattered in different directions; no new frequencies are generated by the scattering. When the scattering medium is itself explicitly varying in time, however, it is possible to get true changes of the spectrum on scattering, including Doppler-like frequency shifts. This latter possibility was first introduced by Wolf (1989), and suggested by James, Savedoff, and Wolf (1990) as a possible explanation for some observed anomalies in quasar spectra. These Doppler-like shifts were further investigated by James and Wolf (1990).

Inverse scattering techniques have been developed that exploit the relationship between coherence and scattering. Baleine and Dogariu (2004a) developed the “variable coherence tomography” method. In this approach, the spatial coherence properties of the incident beam are tuned such that two separate volumes are created in which the field is strongly correlated. The correlation function of the scattering potential can then be determined by recording the spectral density of the scattered field in

a single direction. An experimental demonstration of this method was presented by Baleine and Dogariu (2004b).

A general expression for the rate at which energy is removed by scattering and absorption from a partially coherent beam that is incident on a deterministic scatterer was derived by Carney, Wolf, and Agarwal (1997). Their result can be considered as a generalization of the optical cross-section theorem. This generalization was applied to derive an energy theorem for partially coherent beams by Carney and Wolf (1998), and it was used as the basis for a new diffraction tomography technique by Carney and Wolf (2001).

The scattering of a partially coherent wave field by a sphere, i.e., a generalization of the so-called Mie scattering, has been considered by several authors. Greffet, Cruz-Gutierrez, Ignatovich, and Radunsky (2003) applied the results from Carney et al. (1997) to study rotationally invariant scatterers. Using the Wigner transform, they showed that the extinction cross section does not depend on the coherence of the incident field. van Dijk, Fischer, Visser, and Wolf (2010) generalized the method of partial waves to the case of partially coherent fields. They predicted that when the correlation length of the incident field is comparable with or is smaller than the radius of the sphere, the angular distribution of the radiant intensity depends strongly on the degree of coherence. The occurrence of coherence vortices (see Section 7) in Mie scattering was studied by Marasinghe, Premaratne, and Paganin (2010). By varying the so-called “pointing stability” of the incident field, such singularities were found to be created or annihilated.

An inverse problem of fundamental importance is the determination of crystalline structures from diffraction experiments. Because of the small distances involved, one uses X-rays rather than radiation in the visible spectrum. The basis of this method, for which knowledge of both the phases and amplitudes of the diffracted beams is necessary, was provided by Laue (1912). This approach, however, suffers from a serious limitation because of the inability to measure these phases. It was explained in Wolf (2009) and Wolf (2010) that the phase of any physically realizable wave field is a meaningless concept due to the inherent fluctuations that the field undergoes. He pointed out that for a spatially coherent beam (which is not necessarily the same as a monochromatic beam, as was noted earlier by Roychowdhury and Wolf (2005a)), there exists an “equivalent” monochromatic beam whose phase can be determined from correlation measurements as in Young’s two-slit experiment (see Section 3). Because spatially coherent X-ray beams can indeed be generated, as was shown by Liu et al. (2001), such an experiment can indeed be carried out. Knowledge of this phase then, together with the amplitude

of the diffracted beams, allows one to reconstruct the crystal's structure unambiguously.

Interesting effects can also arise from the scattering of partially coherent wave fields from crystalline structures. Such effects were considered by Dušek (1995) and Sinha, Tolan, and Gibaud (1998).

7. PHASE SINGULARITIES OF COHERENCE FUNCTIONS

Researchers have long noticed that the phase of a wave field has an unusual behavior in the neighborhood of its zeros of amplitude; an early instance of this was described by Sommerfeld (1964) in his textbook on optics. Looking at the structure of a wave field consisting of plane waves of different frequency and direction, he noted that in most regions the field behaves locally like a plane wave, the exception being the behavior in the neighborhood of zeros. He concluded,

However, just because the amplitude vanishes there, they do not produce any stronger effect than other points of varying intensity.

This view changed in the mid-1970s with the publication of an article by Nye and Berry (1974), in which it was noted that the zeros of wave fields and their phase have a well-defined structure that is analogous to dislocations in crystal structures. These zeros are generally referred to as *phase singularities*, and the study of these and comparable phenomena is now its own subfield, referred to as *singular optics*. Several review articles have been published on the subject, such as Soskin and Vasnetsov (2001) and Dennis, O'Holleran, and Padgett (2009), and singular optics is also discussed in the book by Nye (1999).

Philosophically, singular optics is distinct from other fields of optics in that it emphasizes the study of "common" or "generic" features of wave fields over the study of "possible" features, the latter of which require special circumstances, such as rotational symmetry, to occur. For instance, the most commonly-described interference experiment is Young's two-pinhole experiment, illustrated in Figure 6, and previously discussed in Section 3. The (approximate) zeros of the interference pattern observed on the screen are lines, which correspond to zero surfaces in three-dimensional space. If an interference experiment is done with three or more pinholes, however, the interference pattern has a fundamentally different behavior, also illustrated in Figure 6: the zeros on the measurement screen are points, which correspond to lines of zeros in three-dimensional space. These zero lines are said to be the typical, or *generic*, features of interference patterns; for instance, laser speckle patterns contain a large number of these zero lines.

A typical example of a phase singularity is present in a Laguerre–Gauss laser mode of azimuthal order $m = 1$ and radial order $n = 0$ propagating

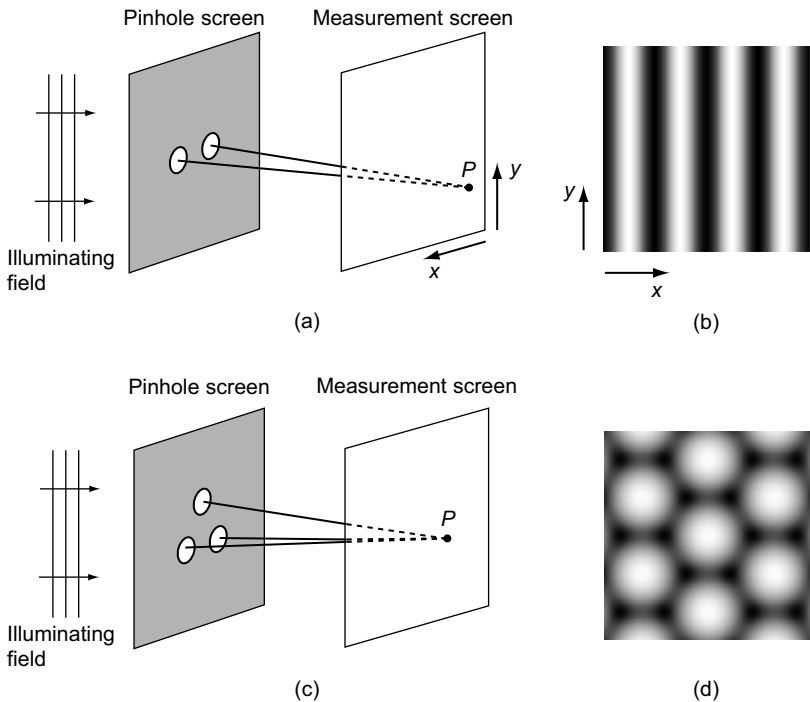


FIGURE 6 (a) Young's two-pinhole experiment. (b) The intensity of light observed on the measurement screen. (c) Young's three-pinhole experiment. (d) The intensity of light observed on the measurement screen. The zeros form a hexagonal pattern.

in the z -direction, which in the waist plane $z = 0$ has the form

$$U_0^1(\rho, \phi, 0) = \sqrt{2} U^{(0)} \frac{\rho}{w_0} e^{i\phi} \exp[-\rho^2/w_0^2], \quad (7.1)$$

where (ρ, ϕ) are polar coordinates in the transverse (x, y) -plane, w_0 is the width of the beam in the waist plane and $U^{(0)}$ is the field amplitude. The phase and intensity of this mode are illustrated in Figure 7. It can be seen that there is a zero of intensity on the central axis $\rho = 0$, and that the phase increases continuously by 2π as one traverses a closed path counterclockwise around the axis; for this reason, such phase singularities are commonly referred to as *optical vortices*.

More generally, it has become clear that nearly every property of a wave field that can be characterized by a spatially dependent amplitude and phase can also have singularities of that phase and associated generic features. For instance, vortices of the Poynting vector have been observed (see, for instance, Braunbek & Laukien, 1952; Boivin, Dow, & Wolf, 1967;

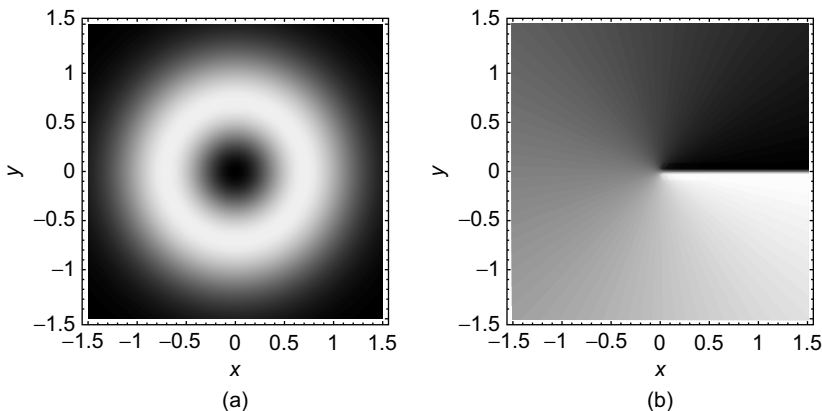


FIGURE 7 The (a) intensity and (b) phase of a Laguerre–Gauss beam of order $m = 1$, $n = 0$ in the waist plane $z = 0$.

Schouten, Visser, Gbur, Lenstra, & Blok, 2003), where the “phase” is, in this case, the direction of power flow. For inhomogeneously polarized light, singularities of the ellipticity and orientation axis of the polarization ellipse can arise; see, for instance, Nye (1983b), Nye (1983a), and Schoonover and Visser (2006).

Coherence functions of wave fields also possess spatially varying amplitude and phase structures, albeit more complicated ones, and it was natural for researchers to investigate the properties of such *correlation vortices* (also referred to as *coherence vortices*). Most studies have centered on singularities of the cross-spectral density function, i.e., regions in $(\mathbf{r}_1, \mathbf{r}_2)$ -space such that $W(\mathbf{r}_1, \mathbf{r}_2, \omega) = 0$, and the phase structure of the cross-spectral density in the neighborhood of such regions. A complete description of the behavior of zeros requires the analysis of the cross-spectral density in six variables, $(\mathbf{r}_1, \mathbf{r}_2)$, a difficult prospect, and most research to date has involved studying lower-dimensional projections of the correlation function.

The earliest article on this subject seems to be that of Schouten et al. (2003), who studied singularities of the cross-spectral density of Young’s interference experiment. It is to be noted, however, that these singularities are not generic features of the cross-spectral density.

Soon after, a number of authors approached the idea of correlation singularities from different viewpoints. Freund (2003), in the context of studying singularities of bichromatic optical fields, noted that correlation singularities could arise in correlations between orthogonal polarizations of the field. Gbur and Visser (2003b) studied the structure of correlation

singularities in partially coherent beams in the special case in which one of the observation points is fixed, i.e., the behavior of $W(\mathbf{r}_1, \mathbf{r}_2)$ as a function of \mathbf{r}_2 . Bogatyryova et al. (2003) performed a theoretical and experimental investigation of a class of partially coherent vortex beams, and observed singularities in the spectral degree of coherence. Palacios, Maleev, Marathay, and Swartzlander (2004) experimentally studied correlation singularities of the so-called cross-correlation function, the case such that $\mathbf{r}_2 = -\mathbf{r}_1$; this work was soon followed up with a theoretical analysis by Maleev, Palacios, Marathay, and Swartzlander (2004). An experimental observation of the fixed point correlation singularities, which possess a vortex structure and have been dubbed *correlation vortices*, was undertaken by Wang, Duan, Hanson, Miyamoto, and Takeda (2006).

A characteristic example of a correlation singularity can be derived from the Laguerre–Gauss beam of Equation (7.1) using the so-called beam wander model, introduced by Gbur, Visser, and Wolf (2004b). A partially coherent vortex beam is modeled by a Laguerre–Gauss beam with a central axis that is a random function of position; the cross-spectral density in the plane $z = 0$ is defined as

$$W(\rho_1, \rho_2, \omega) = \int U_0^{1*}(\rho_1 - \rho', 0) U_0^1(\rho_2 - \rho', 0) f(\rho') d^2\rho', \quad (7.2)$$

where

$$f(\rho') = \frac{1}{\delta\sqrt{\pi}} e^{-\rho'^2/\delta^2} \quad (7.3)$$

is the probability density of the position of the central axis, and δ characterizes the average variance of the beam wander. This integral can be evaluated analytically, and takes on the form

$$\begin{aligned} W(\rho_1, \rho_2, \omega) &= \frac{2\sqrt{\pi}|U^{(0)}|^2}{w_0^6 A^3 \delta} \exp[-(\rho_1 - \rho_2)^2/w_0^4 A] \exp[-(\rho_1^2 + \rho_2^2)/\delta^2 w_0^2 A] \\ &\times \left\{ \left[\gamma^2(x_1 + iy_1) + (x_1 - x_2) + i(y_1 - y_2) \right] \right. \\ &\left. \times \left[\gamma^2(x_2 - iy_2) - (x_1 - x_2) + i(y_1 - y_2) \right] + w_0^4 A \right\}, \end{aligned} \quad (7.4)$$

where $\gamma \equiv w_0/\delta$, $\rho \equiv (x, y)$ and

$$A \equiv \left(\frac{2}{w_0^2} + \frac{1}{\delta^2} \right). \quad (7.5)$$

The typical projections of correlation singularities are exhibited by this simple model. For instance, a plot of the cross-spectral density when \mathbf{r}_1 is fixed and \mathbf{r}_2 is varied is shown in Figure 8. It can be seen that a pair of correlation vortices are present, one associated with the original optical vortex of the Laguerre–Gauss beam and one that travels from the point at infinity. Figure 9 shows the cross-spectral density for the case when $\mathbf{r}_2 = -\mathbf{r}_1$. It can be seen that the correlation singularity is a zero ring centered on the origin, referred to as a *ring dislocation*; the phase jumps discontinuously by π across the boundary of the singularity. It is to be noted that these two very different behaviors – correlation vortex and ring dislocation – are different manifestations of the general correlation singularity in all variables $\mathbf{r}_1, \mathbf{r}_2$.

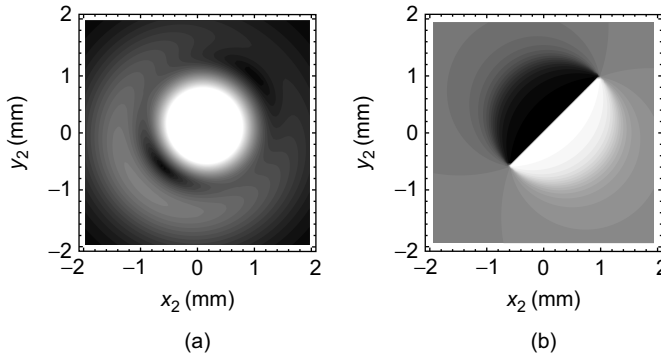


FIGURE 8 The (a) amplitude and (b) phase of the cross-spectral density $W(\mathbf{r}_1, \mathbf{r}_2, \omega)$, with \mathbf{r}_1 fixed. Here $w_0 = 1.0$ mm, $\delta = 0.6$ mm, $x_1 = 0.1$ mm, and $y_1 = 0.1$ mm. The phase runs over 2π , with lower values darker.

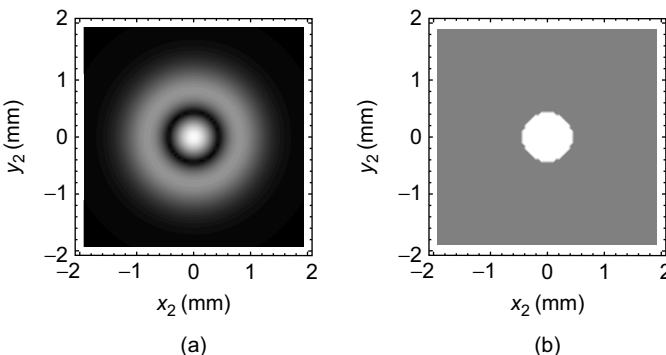


FIGURE 9 The (a) intensity and (b) phase of the cross-spectral density $W(\mathbf{r}_1, \mathbf{r}_2, \omega)$, with $\mathbf{r}_2 = -\mathbf{r}_1$. Here $w_0 = 1.0$ mm, $\delta = 0.6$ mm, $x_1 = 0.1$ mm, and $y_1 = 0.1$ mm. The phase runs over 2π , with lower values darker.

The presence of correlation singularities in a variety of optical systems has been noted. Fischer and Visser (2004) observed singularities of the correlation function in the focusing of partially coherent light, and Motsek, Kivshar, Shih, and Swartzlander (2005) noted such singularities in a nonlinear photorefractive crystal. Far-zone characteristics of Schell-model vortex beams were studied by Liu and Lü (2007), and correlation vortices in superpositions of vortex beams were studied by Cheng and Lü (2008). The behavior of correlation vortices in the focusing of partially coherent vortex beams was considered by Liu, Yang, Rong, Wang, and Yan (2010).

Because of the complexity of correlation singularities, a significant amount of effort has been directed toward characterizing them and their propagation and conservation properties. Wang and Takeda (2006) introduced the idea of a “coherence current” and a conservation law of coherence. Swartzlander and Hernandez-Aranda (2007) made an analogy between Rankine vortices of fluid dynamics and correlation singularities. Gbur and Swartzlander (2008) described the complete structure of a correlation vortex in a single transverse plane, a “surface” in the four transverse coordinates. Ren, Zhu, and Duan (2008) characterized the behavior of correlation vortices using their topological characteristics. Maleev and Swartzlander (2008) investigated the evolution of a correlation singularity on propagation, as did van Dijk and Visser (2009). The topology of correlation singularities in the far zone of a quasi-homogeneous source was studied by van Dijk, Schouten, and Visser (2009).

It can be shown that there is a strong relationship between the correlation vortices of a partially coherent field and the optical vortices of the corresponding fully coherent field. This relationship seems to have been first noted by Gbur et al. (2004b), an article which also elaborates on the concept of spectral changes related to vortices. Gbur and Visser (2006) demonstrated that this relationship holds for variable coherence fields in any linear optical system. Additional work by Gu and Gbur (2009) investigated the behavior of higher-order vortices and topological reactions of such vortices.

Gbur et al. (2004b) also observed that zeros of intensity are not generic features of partially coherent fields, but it is still possible to specially prepare fields that are partially coherent and possess such zeros. Gbur, Visser, and Wolf (2004a) determined conditions under which complete destructive interference can be achieved with a partially coherent field in a three-pinhole interferometer; these results were confirmed experimentally both acoustically by Basano and Ottonello (2005) and optically by Ambrosini, Gori, and Paoletti (2005). The phase structure of such nongeneric fields, including both phase and coherence singularities, was studied theoretically by Gan and Gbur (2007). Extending the relationship between different classes of singularities further, Visser and Schoonover

(2008) demonstrated that it is possible to smoothly transform between phase, correlation, and polarization singularities in Young's interferometer, a process referred to as a "cascade" of singularities.

It is also possible to introduce correlation singularities of temporal coherence functions, such as the mutual coherence function $\Gamma(\mathbf{r}_1, \mathbf{r}_2, \tau)$. Swartzlander and Schmit (2004) introduced and experimentally studied singularities of the function $\Gamma(\mathbf{r}, \mathbf{r}, \tau)$, with variable position \mathbf{r} and fixed τ . The resulting singularities have the form of vortices.

Recently, there have been some studies of the polarization singularities of partially coherent beams; this is discussed in Chernyshov, Felde, Bogatyryova, Polyanskii, and Soskin (2009) and Chernyshov, Fel'de, Bogatyreva, Polyanskii, and Soskin (2009).

8. THE COHERENT MODE REPRESENTATION

The coherent mode representation introduced by Wolf (1982)⁴ is the expansion of the cross-spectral density function of a partially coherent source or partially coherent field into a diagonal representation of orthogonal modes, of the form

$$W(\mathbf{r}_1, \mathbf{r}_2, \omega) = \sum_n \lambda_n(\omega) \phi_n^*(\mathbf{r}_1, \omega) \phi_n(\mathbf{r}_2, \omega), \quad (8.1)$$

where the eigenvalues $\lambda_n(\omega)$ are non-negative quantities. The modes $\phi_n(\mathbf{r}, \omega)$ are orthogonal with respect to a given domain; for a primary radiation source, the domain is typically taken to be the volume of the source, while for a secondary planar source, the domain is the planar area of the source. The index n may represent multiple indices of summation; the mode decomposition of a field in a region of three-dimensional space, for instance, usually requires two summation indices, while the mode decomposition of a source in three-dimensional space typically requires three.

The coherent mode representation has become an excellent tool for computationally evaluating the propagation of a wave field. Before its introduction, finding the evolution of the cross-spectral density of a wave field on propagation through an optical system required the evaluation of an integral of the form

$$W(\mathbf{r}_1, \mathbf{r}_2, \omega) = \iint W_0(\mathbf{r}'_1, \mathbf{r}'_2, \omega) G^*(\mathbf{r}_1, \mathbf{r}'_1, \omega) G(\mathbf{r}_2, \mathbf{r}'_2, \omega) d^2 r'_1 d^2 r'_2, \quad (8.2)$$

⁴It is worth noting that a very similar representation was introduced earlier for the mutual intensity function by Gori (1980).

where the integrations are over the input plane of the optical system, $W_0(\mathbf{r}_1, \mathbf{r}_2, \omega)$ is the cross-spectral density of the field on this input plane, and $G(\mathbf{r}, \mathbf{r}', \omega)$ is the Green's function of the optical system.

A numeric solution to this equation would require the evaluation of a four-fold complex integral, a very difficult prospect. Using the coherent mode representation for the field on the input plane, Equation (8.2) may be written as

$$W(\mathbf{r}_1, \mathbf{r}_2, \omega) = \sum_n \lambda_n(\omega) \left[\int \phi_n(\mathbf{r}'_1, \omega) G(\mathbf{r}_1, \mathbf{r}'_1, \omega) d^2 r'_1 \right]^* \\ \times \left[\int \phi_n(\mathbf{r}'_2, \omega) G(\mathbf{r}_2, \mathbf{r}'_2, \omega) d^2 r'_2 \right]. \quad (8.3)$$

The four-fold integral has been reduced to a sum over the product of identical two-fold integrals. Typically a partially coherent field can be represented to a good approximation by a small number of modes; this is illustrated in Figure 10 using the eigenvalues of a Bessel-correlated field. By using the coherent mode representation, the propagation of the cross-spectral density can be evaluated by the determination of a relatively small number of two-fold integrals.

Research related to the coherent mode representation can be broadly broken into four parts: extensions of the basic theory, the determination of mode representations for model fields or sources, methods for determining the mode representation for arbitrary fields, and application of the mode representation to wave propagation problems.

One of the first extensions of the basic theory was by Starikov (1982), who used the representation to define an effective number of degrees of freedom of the source. Wolf (1986a) derived a number of theorems for modes of spatially bandlimited wave fields.

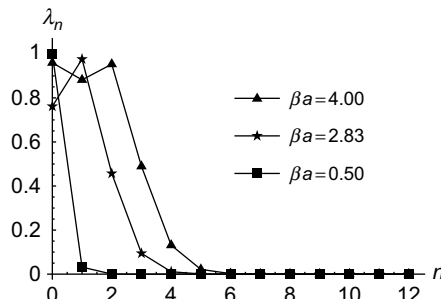


FIGURE 10 Eigenvalues λ_n versus n for a J_0 -correlated field such as described by Equation (5.17).

The original coherent mode calculations were done for scalar wave fields, but there have been a number of extensions of the theory to fully electromagnetic wave fields. The earliest of these was by Pask and Stacey (1988), who used electromagnetic plane waves as the mode functions. The first general theory for characterizing an electromagnetic coherent mode representation was presented much later by Gori et al. (2003). At about the same time, Tervo, Setälä, and Friberg (2004) constructed a representation based on their theory of coherence for electromagnetic waves; another representation was provided by Kim (2005). Kim and Wolf (2006) introduced a scalar mode representation of an electromagnetic wave field, using a biorthogonal expansion of modes.

A number of alternatives to the original scalar coherent mode representation have also been suggested. Sung, Kim, and Park (1996) introduced a “P-representation” of the cross-spectral density, based on analogy with the expansion of a density operator in coherent state vectors. Withington, Hobson, and Berry (2004) introduced a representation based on an overcomplete set of Gabor basis functions. Martinsson, Lajunen, and Friberg (2007) have suggested the use of “communication modes” of a linear optical system, namely the functions arising from the singular value decomposition of the propagation kernel.

It is, in general, quite difficult to derive the coherent mode representation for a particular wave field; there has been much success, however, in deriving the modal representation for a variety of model wave fields, particularly beams. The most important of these, Gaussian Schell-model beams, was determined by Starikov and Wolf (1982); these beams were interpreted as multimode laser radiation by Gase (1991). The mode representation of Bessel-correlated Schell-model sources was derived by Gori, Guattari, and Padovani (1987). Flat-topped partially coherent beams were treated by Borghi and Santarsiero (1998), and a special class of beams carrying optical vortices was introduced by Ponomarenko (2001). The mode representation of anisotropic Gaussian Schell-model beams was evaluated by Sundar, Makunda, and Simon (1995).

A new and intriguing class of partially coherent Gaussian beams incorporating a “twist” in the azimuthal phase structure was introduced by Simon and Mukunda (1993) and are referred to as twisted Gaussian Schell-model beams; in relatively short order their mode decomposition was derived (Simon & Sundar, 1993) and their propagation characteristics determined (Sundar, Simon, & Mukunda, 1993). An intuitive model of twisted beams as the incoherent superposition of ordinary Gaussian beams was related by Ambrosini, Bagini, Gori, and Santarsiero (1994).

The mode representations of three-dimensional sources and fields have also been considered. Gori, Palma, and Padovani (1989) introduced a modal expansion for blackbody radiation in a spherical cavity. Setälä,

Lindberg, Blomstedt, Tervo, and Friberg (2005) applied their aforementioned electromagnetic coherent mode representation to study the full vector properties of blackbody radiation. Gori and Korotkova (2009) have studied the general mode representation of spherical homogeneous sources.

A number of other mode representations of broad physical interest have been derived, including the representation of Lambertian sources (Starikov & Friberg, 1984), the representation of propagation-invariant fields (Ostrovsky, Martinez-Niconoff, & Ramirez-San-Juan, 2001), and that of thin annular sources (Gori, Santarsiero, Borghi, & Li, 2008).

As noted, it is in general difficult to derive the coherent mode representation for an arbitrary wave field. A number of techniques have been proposed, both experimental and theoretical, for extracting the mode behavior from a given partially coherent field. The earliest of these seems to be by Kim and Park (1992), who developed an approximate method for determining the eigenvalues and eigenfunctions of the representation; this method was tested numerically by Hong, Kang, and Kim (1993). For the special case when the modes are known to be of Hermite-Gaussian form, Gori, Santarsiero, Borghi, and Guattari (1998) demonstrated that knowledge of the intensity of the field is sufficient to determine the mode weights. Xue, Wei, and Kirk (2000) further suggested that the weights could be determined by the evolution of the intensity on propagation. Another experimental technique for extracting the mode structure from intensities was recently introduced by Flewett, Quiney, Tran, and Nugent (2009).

Alternative modal decompositions have been shown to be easier to calculate both experimentally and theoretically. Ostrovsky, Zemliak, and Hernández-García (2005) introduced an alternative representation that can be determined experimentally from radiometric measurements. An “elementary source model” was described by Vahimaa and Turunen (2006) for efficient propagation of partially coherent fields. Davis and Schoonover (2009) have introduced a computationally efficient modal decomposition based on the LDL^\dagger factorization, while Martinex-Herrero, Mejias, and Gori (2009) have given a nonorthogonal “pseudo-modal” decomposition of the cross-spectral density.

The coherent mode representation has been shown to be directly useful in a number of optical applications, foremost among them, as noted, the propagation of partially coherent wave fields. The first use of coherent modes for propagation appears to be due to Gori (1983), who investigated the free-space propagation of Schell-model sources. Such a strategy has also been applied to the analysis of spectral changes on propagation (Gamliel, 1990), changes in the state of coherence on propagating through an optical system (Shirai & Asakura, 1993), and the evolution of

the generalized radiance (Ostrovsky & Rodriguez-Solid, 2000). The mode representation has also been applied to a class of inverse source problems (Habashy, Friberg, & Wolf, 1997).

A modal representation can also be applied to the propagation of fields through random media, as was demonstrated theoretically by Shirai, Dogariu, and Wolf (2003) in a study of the spreading of beams in turbulence. Schwartz and Dogariu (2006) have suggested that a mode-coupling approach could be used to study more general properties of a turbulence-degraded beam.

One interesting observation that has been made is that the coherent mode representation allows for the quasi-geometrical propagation of partially coherent wave fields. Zysk, Carney, and Schotland (2005) have demonstrated that a scalar partially coherent field could be propagated by ray-tracing the individual coherent modes; this method was later extended to electromagnetic partially coherent fields by Schoonover, Zysk, Carney, and Wolf (2008).

Several other applications of the coherent mode representation are worth noting. Gbur and Wolf (1997) used the representation to construct theoretically a primary source that is globally incoherent but produces a fully coherent field. Withington and Murphy (1998) applied the representation to study submillimeter-wave quasi-optical systems. The modal representation has been applied to the development of a near-field measurement technique by Fourestie, Altman, Bolomey, Wiart, and Brouaye (2002).

Although they do not directly apply the coherent mode representation, Salem and Agrawal (2009a) recently described a modal technique for analyzing the coupling of stochastic beams into optical fibers. The technique was used to study the effects of this coupling on the coherence and polarization of the coupled field by Salem and Agrawal (2009b).

9. NUMERICAL SIMULATION OF PARTIALLY COHERENT FIELDS

As already noted, determining the free-space propagation of a partially coherent field typically involves the evaluation of one or more four-fold integrals, a difficult prospect even with modern computing power. The application of the coherent mode representation (described in Section 8) allows one to reduce the problem to a finite sum of two-fold integrals, but even these integrals may be difficult to evaluate – and the coherent mode representation of the field may not be available. Because of this, a variety of techniques have been proposed for the numerical evaluation of the propagation of a partially coherent field.

These techniques may be broadly divided into two classes: efficient simulation of the average properties of the optical field and generation of realizations of a wave field with prescribed statistical behavior. The second class is of interest for evaluating the properties of systems in which detectors can respond fast enough to measure instantaneous field properties.

Of the first class of techniques, a number of methods have been developed for propagating correlation functions using the framework of geometrical optics. We have already noted the propagation of partially coherent fields using geometrical optics and the coherent mode representation, as done by Zysk et al. (2005); this method was later extended by Schoonover et al. (2008) to encompass partially coherent electromagnetic fields. Another ray-based propagation method was introduced by Petruccielli and Alonso (2008), based on their earlier work on generalized radiometry (see Alonso, 2001; Petruccielli & Alonso, 2007, and references therein) that allows the propagation of the cross-spectral density through complex optical systems. Very recently, a third method was developed by Riechert, Dürr, Rohlfing, and Lemmer (2009) to propagate the temporal coherence function by means of rays; this method, however, does not as yet include diffraction effects. Pedersen and Stammes (2000) introduced another method of propagation based on radiometric concepts.

Monte Carlo methods have also been combined with geometric techniques for the efficient propagation of coherence functions. Fischer, Prahl, and Duncan (2008) introduced a Monte Carlo propagation technique based on the Huygens–Fresnel principle; later work (Prahl, Fischer, & Duncan, 2009) investigated the construction of the Green's function for an entire optical system using Monte Carlo methods.

The second class of techniques involves determining realizations, in space and time, of partially coherent fields of given average properties. An early technique of this type was given by Davis, Kim, and Piepmeier (2004), who described a method of generating realizations of stationary electromagnetic random processes in time; the method was later extended to generating full vectorial spatio-temporal realizations by Davis (2007). Another technique for generating spatio-temporal realizations was introduced by Gbur (2006), who constructed the realizations from a collection of pulses of appropriate spatial and temporal shape. Around the same time another method was introduced by Rydberg and Bengtsson (2006) in which realizations are generated from a finite superposition of independent monochromatic fields.

Somewhere between the first and second class of techniques lies the works of Voelz, Bush, and Idell (1997) and Xiao and Voelz (2006), in which the average properties of a partially coherent field are determined by constructing temporal and spatial realizations of the field, respectively, and averaging over these properties.

10. DIRECT APPLICATIONS OF COHERENCE THEORY

The theory of optical coherence plays an important indirect role in many optical applications in which the statistical properties of light must be understood in order to evaluate their effect on system performance. There are also a number of applications, however, based directly on the manipulation of the state of spatial and temporal coherence.

Several of these applications have been touched upon in previous sections. For instance, it has been suggested by Gbur and Visser (2003a), Pu et al. (2004), and van Dijk et al. (2008) that the ability to shape the intensity in the focal region by spatial coherence could be used to develop novel optical trapping and optical manipulation schemes. In particular, Arlt and Padgett (2000) introduced the term “bottle beam” to characterize a focused coherent field with an intensity minimum at the geometric focus; this term has also been adopted for describing partially coherent beams of this type by Pu, Liu, and Nemoto (2005).

The most well-known application involving coherence theory is *optical coherence tomography* (OCT), a low-coherence interferometric technique which can be used to image subsurface features of a biological specimen. OCT has become a very important medical diagnostic tool, and references to it are far too numerous to exhaustively discuss here; we mention the review article by Fercher and Hitzenberger (2002) and the text by Brezinski (2006). It is also worth noting more recent research that improves on the standard OCT modality by treating it as an inverse scattering problem (see Ralston, Marks, Carney, and Boppart, 2006; Marks, Ralston, Carney, and Boppart, 2007 for details).

Laser beams with high spatial and temporal coherence produce speckle patterns on reflection or scattering that can be detrimental for many applications; appropriately chosen partially coherent fields can provide superior performance in many of these cases. Because the high brightness and directionality of laser light is usually required, the strategy for producing partially coherent light is typically to distort a fully coherent laser beam. An overall review of the techniques of speckle reduction was given by Iwai and Asakura (1996); we also list a few illustrative applications. Kato, Nakayama, and Suzuki (1975) used an extended incoherent source to reduce speckle in the recording of holograms; other studies of the effects of coherence in holography include the work of Lurie (1966), Lurie (1968), Wolf, Shirai, Agarwal, and Mandel (1999), and Gopinathan, Pedrini, and Osten (2008). Wang, Tschudi, Halldórsson, and Pétursson (1998) reduced speckle in a laser projection system by introducing a time-varying diffractive optical element. Speckle reduction in OCT was achieved using a partially coherent source by Kim et al. (2005). A number of authors have investigated the usefulness of partially coherent fields in

inertial confinement fusion schemes, for instance, Lehmberg and Goldhar (1987), Rothenberg (1997), and Tsubakimoto, Nakatsuka, Miyanaga, and Jitsuno (1998).

Closely related to the goal of speckle reduction is the observation that partially coherent beams are often more useful than their fully coherent counterparts for applications involving propagation through random media such as the turbulent atmosphere. It has been demonstrated that such “prerandomized” beams have less scintillations (intensity fluctuations) in turbulence, making them of interest for free-space laser communications and sensing.

Early articles, such as those by Beran (1966), Taylor (1967), Yura (1972), Belenkii, Kon, and Mironov (1977), and Fante (1981b), looked at the general evolution of the mutual coherence function in turbulence. Other articles, such as those by Kon and Tatarskii (1972) and Leader (1978), studied the propagation characteristics of partially coherent beams. During the same period, the focus of research seems to have gradually shifted to the study of the scintillation characteristics of partially coherent beams. Leader (1979), Fante (1981a), and Banakh, Buldakov, and Mironov (1983) looked at the fluctuations of beams with partial spatial coherence. Fante (1979) noted that a decrease in temporal coherence could also significantly reduce scintillations.

Through the 1990s, the study of such effects seems to have been mostly ignored, with the exception of articles by Wu (1990) and Wu and Boardman (1991) on the propagation and coherence properties of model beams in turbulence.

At the turn of the millennium, interest in partial coherence-based turbulence effects exploded again. Gbur and Wolf (2002) looked theoretically at the spreading of partially coherent beams in random media, and noted that they are “resistant” to turbulence; this was demonstrated experimentally by Dogariu and Amarande (2003). Similar theoretical results were found by Ponomarenko, Greffet, and Wolf (2002) using a Hilbert-space method, and by Shirai et al. (2003) using the coherent mode representation. Long-distance propagation of partially coherent beams was studied soon after by Salem, Shirai, Dogariu, and Wolf (2003). Baykal (2004) investigated the average transmittance of partially coherent beams in turbulence. Many other studies of beam spreading in turbulence have been performed since then for specific classes of beams.

Of most interest to those developing optical communications and sensing applications is the scintillation reduction associated with partially coherent beams. The application of Gaussian Schell-model beams to free-space communication was investigated by Ricklin and Davidson (2002), Ricklin and Davidson (2003), and Korotkova, Andrews, and Phillips (2004).

Much research since then has involved the study of a variety of strategies for reducing scintillation with partial coherence. A “pseudo-partially coherent beam” was introduced by Voelz and Fitzberry (2004) for free-space communication. Kiasaleh (2006) investigated the scintillation of a multiwavelength Gaussian beam; a spectral encoding strategy for scintillation reduction was introduced by Berman, Bishop, Chernobrod, Nguyen, and Gorshkov (2007). Baykal and Eyyuboglu (2007) studied the scintillation of incoherent flat-topped Gaussian beams. It was shown in Korotkova (2006) and Korotkova (2008) that appropriately chosen electromagnetic beams can have appreciably lower scintillation. Furthermore, Gu, Korotkova, and Gbur (2009) have demonstrated that nonuniform, fully polarized beams can have lower scintillation as well, as they become partially polarized on propagation; the propagation characteristics of such beams were studied by Wang and Pu (2008).

One of the most promising partially coherent sources for optical communications is an incoherent array of beams. The possibility of scintillation reduction with beams of different wavelengths was investigated in Peleg and Moloney (2006), Peleg and Moloney (2007), and Polynkin, Peleg, Klein, Rhoadarmer, and Moloney (2007). A study of a partially coherent array of Gaussian beams was performed in Baykal, Eyyuboglu, and Cai (2009), following up on work on coherent arrays done in Eyyuboglu, Baykal, and Cai (2008).

A number of mathematical tools have been developed for studying partially coherent beams in turbulence. The optimization of scintillation and propagation characteristics of beams was investigated in Schulz (2004) and Schulz (2005). An angular spectrum representation for propagation through turbulence was introduced by Gbur and Korotkova (2007); an electromagnetic version of this representation was done by Korotkova and Gbur (2007).

The relation between partial coherence and random media has also been used to probe the structure of the medium itself. Ponomarenko and Wolf (2002) developed a technique for deducing the turbulence correlations using measurements of the correlations of the scattered light. A strategy for determining the scattering parameter of an optically diffusive medium was tested by McKinney, Webster, Webb, and Weiner (2000). A technique called *variable coherence tomography* was introduced in Baleine and Dogariu (2004b) and Baleine and Dogariu (2005), which uses illumination with various states of coherence to deduce structure; this technique was adapted to include polarization effects by Tyo and Turner (2008). More recently, Gu and Gbur (2010) showed that the evolution of correlation singularities in turbulence can be used as a crude measure of turbulence strength.

REFERENCES

- Agarwal, G. S., Dogariu, A., Visser, T. D., & Wolf, E. (2005). Generation of complete coherence in Young's interference experiment with random mutually uncorrelated electromagnetic beams. *Optics Letters*, 30, 120–122.
- Agarwal, G. S., & Wolf, E. (1993). Higher-order coherence functions in the space-frequency domain. *Journal of Modern Optics*, 40, 1489–1496.
- Agrawal, G. P., & Wolf, E. (2000). Propagation-induced polarization changes in partially coherent optical beams. *Journal of the Optical Society of America A*, 17, 2019–2023.
- Alonso, M. A. (2001). Radiometry and wide-angle wave fields III: Partial coherence. *Journal of the Optical Society of America A*, 18, 2502–2511.
- Ambrosini, D., Bagini, V., Gori, F., & Santarsiero, M. (1994). Twisted Gaussian Schell-model beams: A superposition model. *Journal of Modern Optics*, 41, 1391–1399.
- Ambrosini, D., Gori, F., & Paoletti, D. (2005). Destructive interference from three partially coherent point sources. *Physical Review Letters*, 254, 30–39.
- Andrews, L. C., & Phillips, R. L. (2005). *Laser beam propagation through random media* (2nd ed.). Bellingham, WA: SPIE.
- Arlt, J., & Padgett, M. J. (2000). Generation of a beam with a dark focus surrounded by regions of higher intensity: The optical bottle beam. *Optics Letters*, 25, 191–193.
- Baleine, E., & Dogariu, A. (2004a). Variable coherence tomography. *Optics Letters*, 29, 1233–1235.
- Baleine, E., & Dogariu, A. (2004b). Variable-coherence tomography for inverse scattering problems. *Journal of the Optical Society of America A*, 21, 1917–1923.
- Baleine, E., & Dogariu, A. (2005). Variable coherence scattering microscopy. *Physical Review Letters*, 95, 193904.
- Banakh, V. A., Buldakov, V. M., & Mironov, V. L. (1983). Intensity fluctuations of a partially coherent light beam in a turbulent atmosphere. *Optics and Spectroscopy*, 54, 1054–1059.
- Basano, L., & Ottolengo, P. (2005). Complete destructive interference of partially coherent sources of acoustic waves. *Physical Review Letters*, 94, 173901.
- Baykal, Y. (2004). Average transmittance in turbulence for partially coherent sources. *Optics Communications*, 231, 129–136.
- Baykal, Y., & Eyyuboglu, H. T. (2007). Scintillations of incoherent flat-topped Gaussian source field in turbulence. *Applied Optics*, 46, 5044–5050.
- Baykal, Y., Eyyuboglu, H. T., & Cai, Y. (2009). Scintillation of partially coherent multiple gaussian beams in turbulence. *Applied Optics*, 48, 1943–1954.
- Belenkii, M. S., Kon, A. I., & Mironov, V. L. (1977). Turbulent distortions of the spatial coherence of a laser beam. *Soviet Journal of Quantum Electronics*, 7, 287–290.
- Beran, M. J. (1966). Propagation of the mutual coherence function through random media. *Journal of the Optical Society of America*, 56, 1475–1480.
- Beran, M. J., & Parrent, G. B., Jr. (1964). *Theory of partial coherence*. Englewood Cliffs, NJ: Prentice-Hall.
- Berman, G. P., Bishop, A. R., Chernobrod, B. M., Nguyen, P. C., & Gorshkov, V. N. (2007). Suppression of intensity fluctuations in free space high-speed optical communication based on spectral encoding of a partially coherent beam. *Optics Communications*, 280, 264–270.
- Bogatyryova, G. V., Fel'de, C. V., Polyanskii, P. V., Ponomarenko, S. A., Soskin, M. S., & Wolf, E. (2003). Partially coherent vortex beams with a separable phase. *Optics Letters*, 28, 878–880.
- Boivin, A., Dow, J., & Wolf, E. (1967). Energy flow in the neighborhood of the focus of a coherent beam. *Journal of the Optical Society of America*, 57, 1171–1175.

- Borghi, R., & Santarsiero, M. (1998). Modal decomposition of partially coherent flat-topped beams produced by multimode lasers. *Optics Letters*, 23, 313–315.
- Born, M., & Wolf, E. (1999). *Principles of optics* (7th (expanded) ed.). Cambridge, MA: Cambridge University Press.
- Bouchal, Z. (2003). Nondiffracting optical beams: Physical properties, experiments, and applications. *Czechoslovak Journal of Physics*, 53(7), 537–624.
- Braunbek, W., & Laukien, G. (1952). Einzelheiten zur Halbebenen-Beugung. *Optik*, 9, 174–179.
- Brezinski, M. (2006). *Optical coherence tomography: Principles and applications*. Burlington, MA: Academic Press.
- Cai, Y., & Lin, Q. (2003). Focusing properties of partially coherent twisted anisotropic gaussian-schell model beams. *Optics Communications*, 215, 239–245.
- Carney, P. S., & Wolf, E. (1998). An energy theorem for scattering of partially coherent beams. *Optics Communications*, 155, 1–6.
- Carney, P. S., & Wolf, E. (2001). Power-excitation diffraction tomography with partially coherent light. *Optics Letters*, 26, 1770–1772.
- Carney, P. S., Wolf, E., & Agarwal, G. S. (1997). Statistical generalizations of the optical cross-section theorem with application to inverse scattering. *Journal of the Optical Society of America A*, 14, 3366–3371.
- Carter, W. H., & Wolf, E. (1988). Scattering from quasi-homogeneous media. *Optics Communications*, 67, 85–90.
- Cheng, K., & Lü, B. (2008). Composite coherence vortices in coherent and incoherent superpositions of two off-axis partially coherent vortex beams. *Journal of Modern Optics*, 55, 2751–2764.
- Chernyshov, A. A., Felde, G. V., Bogatyryova, H. V., Polyanskii, P. V., & Soskin, M. S. (2009). Vector singularities of the combined beams assembled from mutually incoherent orthogonally polarized components. *Journal of Optics A: Pure and Applied Optics*, 11, 094010.
- Chernyshov, A. A., Fel'de, K. V., Bogatyreva, G. V., Polyanskii, P. V., & Soskin, M. S. (2009). Vector singularities of superposition of mutually incoherent orthogonally polarized beams. *Optics and Spectroscopy*, 107, 645–650.
- Collett, E., & Wolf, E. (1978). Is complete spatial coherence necessary for the generation of highly directional light beams? *Optics Letters*, 2, 27–29.
- Collett, E., & Wolf, E. (1980). Beams generated by Gaussian quasi-homogeneous sources. *Optics Communications*, 32, 27–31.
- Dačić, Z., & Wolf, E. (1988). Changes in the spectrum of a partially coherent light beam propagating in free space. *Journal of the Optical Society of America A*, 5, 1118–1126.
- Davis, B. (2007). Simulation of vector fields with arbitrary second-order correlations. *Optics Express*, 15, 2837–2846.
- Davis, B., Kim, E., & Piepmeyer, J. R. (2004). Stochastic modeling and generation of partially polarized or partially coherent electromagnetic waves. *Radio Science*, 39, RS1001.
- Davis, B. J., & Schoonover, R. W. (2009). Computationally efficient coherent-mode representations. *Optics Letters*, 34, 923–925.
- Dennis, M. R., O'Holleran, K., & Padgett, M. J. (2009). Singular optics: Optical vortices and polarization singularities. In E. Wolf (Ed.), *Progress in optics* (vol. 53, pp. 293–364). Amsterdam: Elsevier.
- Devaney, A. J., Friberg, A. T., Kumar, A., & Wolf, E. (1997). Decrease in spatial coherence of light propagating in free space. *Optics Letters*, 22, 1672–1673.
- Dogariu, A., & Amarde, S. (2003). Propagation of partially coherent beams: Turbulence-induced degradation. *Optics Letters*, 28, 10–12.
- Dušek, M. (1995). Diffraction of partially coherent beams on 3-dimensional periodic structures and the angular shifts of the diffraction maxima. *Physical Review E, Statistical Physics, Plasmas, Fluids, and Related Interdisciplinary Topics*, 52, 6833–6840.

- Eyyuboglu, H. T., Baykal, Y., & Cai, Y. (2008). Scintillations of laser array beams. *Applied Physics B*, 91, 265–271.
- Fante, R. L. (1979). The effect of source temporal coherence on light scintillation in weak turbulence. *Journal of the Optical Society of America*, 69, 71–73.
- Fante, R. L. (1981a). Intensity fluctuations of an optical wave in a turbulent medium. Effect of source coherence. *Optica Acta*, 28, 1203–1207.
- Fante, R. L. (1981b). Two-position, two-frequency mutual-coherence function in turbulence. *Journal of the Optical Society of America*, 71, 1446–1451.
- Fercher, A. F., & Hitzenberger, C. K. (2002). Optical coherence tomography. In E. Wolf (Ed.), *Progress in optics* (vol. 44, pp. 215–301). Amsterdam: Elsevier.
- Fischer, D. G. (1998). Generalized theory of diffraction tomography for random media. *Pure and Applied Optics*, 7, 1151–1160.
- Fischer, D. G., & Cairns, B. (1995). Inverse problems with quasi-homogeneous random media utilizing scattered pulses. *Journal of Modern Optics*, 42, 655–666.
- Fischer, D. G., & Wolf, E. (1994). Inverse problems with quasi-homogeneous random media. *Journal of the Optical Society of America A*, 11, 1128–1135.
- Fischer, D. G., & Wolf, E. (1997). Theory of diffraction tomography for quasi-homogeneous random objects. *Optics Communications*, 133, 17–21.
- Fischer, D. G., Prahl, S. A., & Duncan, D. D. (2008). Monte Carlo modeling of spatial coherence: Free-space diffraction. *Journal of the Optical Society of America A*, 25, 2571–2581.
- Fischer, D. G., & Visser, T. D. (2004). Spatial correlation properties of focused partially coherent light. *Journal of the Optical Society of America A*, 21, 2097–2102.
- Flewett, S., Quiney, H. M., Tran, C. Q., & Nugent, K. A. (2009). Extracting coherent modes from partially coherent wavefields. *Optics Letters*, 34, 2198–2200.
- Foley, J. T., & Wolf, E. (2002). The phenomenon of spectral switches as a new effect in singular optics with polychromatic light. *Journal of the Optical Society of America A*, 19, 2510–2516.
- Foley, J. T., & Zubairy, M. S. (1978). The directionality of Gaussian Schell-model beams. *Optics Communications*, 26, 297–300.
- Foreman, M. R., & Török, P. (2009). Focusing of spatially inhomogeneous partially coherent, partially polarized electromagnetic fields. *Journal of the Optical Society of America A*, 26, 2470–2479.
- Fourestie, B., Altman, Z., Bolomey, J.-C., Wiart, J., & Brouaye, F. (2002). Statistical modal analysis applied to near-field measurements of random emissions. *IEEE Transactions on Antennas and Propagation*, 50, 1803–1812.
- Freund, I. (2003). Bichromatic optical Lissajous fields. *Optics Communications*, 226, 351–376.
- Friberg, A. T., & Turunen, J. (1988). Imaging of Gaussian Schell-model sources. *Journal of the Optical Society of America A*, 5, 713–720.
- Friberg, A. T., & Wolf, E. (1983). Reciprocity relations with partially coherent sources. *Optica Acta*, 30, 1417–1435.
- Friberg, A. T., Visser, T. D., Wang, W., & Wolf, E. (2001). Focal shifts of converging diffracted waves of any state of spatial coherence. *Optics Communications*, 196, 1–7.
- Friberg, A. T., Visser, T. D., & Wolf, E. (2000). A reciprocity inequality for Gaussian Schell-model beams and some of its consequences. *Optics Letters*, 25, 366–368.
- Gamliel, A. (1990). Mode analysis of spectral changes in light-propagation from sources of any state of coherence. *Journal of the Optical Society of America A*, 7, 1591–1597.
- Gan, C. H., & Gbur, G. (2007). Phase and coherence singularities generated by the interference of partially coherent fields. *Optics Communications*, 280, 249–255.
- Gao, W., & Korotkova, O. (2007). Changes in the state of polarization of a random electromagnetic beam propagating through tissue. *Optics Communications*, 270, 474–478.
- Gase, R. (1991). The multimode laser-radiation as a Gaussian-Schell model beam. *Journal of Modern Optics*, 38, 1107–1115.

- Gbur, G. (2006). Simulating fields of arbitrary spatial and temporal coherence. *Optics Express*, 14, 7567–7578.
- Gbur, G., & James, D. F. V. (2000). Unpolarized sources that generate highly polarized fields outside the source. *Journal of Modern Optics*, 47, 1171–1177.
- Gbur, G., & Korotkova, O. (2007). Angular spectrum representation for the propagation of arbitrary coherent and partially coherent beams through atmospheric turbulence. *Journal of the Optical Society of America A*, 24, 745–752.
- Gbur, G., & Swartzlander, G. A. (2008). Complete transverse representation of a correlation singularity of a partially coherent field. *Journal of the Optical Society of America B*, 25, 1422–1429.
- Gbur, G., & Visser, T. D., (2003a). Can spatial coherence effects produce a local minimum of intensity at focus? *Optics Letters*, 28, 1627–1629.
- Gbur, G., & Visser, T. D. (2003b). Coherence vortices in partially coherent beams. *Optics Communications*, 222, 117–125.
- Gbur, G., & Visser, T. D. (2006). Phase singularities and coherence vortices in linear optical systems. *Optics Communications*, 259, 428–435.
- Gbur, G., Visser, T. D., and Wolf, E. (2002a). Anomalous behavior of spectra near phase singularities of focused waves. *Physical Review Letters*, 88, 013901.
- Gbur, G., Visser, T. D., & Wolf, E. (2002b). Singular behavior of the spectrum in the neighborhood of focus. *Journal of the Optical Society of America A*, 19, 1694–1700.
- Gbur, G., Visser, T. D., & Wolf, E. (2004a). Complete destructive interference of partially coherent fields. *Optics Communications*, 239, 15–23.
- Gbur, G., Visser, T. D., & Wolf, E. (2004b). 'Hidden' singularities in partially coherent wavefields. *Journal of Optics A: Pure and Applied Optics*, 6, S239–S242.
- Gbur, G., & Wolf, E. (1997). Sources of arbitrary states of coherence that generate completely coherent fields outside the source. *Optics Letters*, 22, 943–945.
- Gbur, G., & Wolf, E. (2002). Spreading of partially coherent beams in random media. *Journal of the Optical Society of America A*, 19, 1592–1598.
- Goodman, J. W. (1985). *Statistical optics*. New York: Wiley.
- Gopinathan, U., Pedrini, G., & Osten, W. (2008). Coherence effects in digital in-line holographic microscopy. *Journal of the Optical Society of America A*, 25, 2459.
- Gori, F. (1980). Collett-Wolf sources and multimode lasers. *Optics Communications*, 34, 301–305.
- Gori, F. (1983). Mode propagation of the field generated by Collett-Wolf Schell-model sources. *Optics Communications*, 46, 149–154.
- Gori, F. (1998). Matrix treatment for partially polarized partially coherent beams. *Optics Letters*, 23, 241–243.
- Gori, F., Guattari, G., & Padovani, C. (1987). Modal expansion for j_0 -correlated Schell-model sources. *Optics Communications*, 64, 311–316.
- Gori, F., & Korotkova, O. (2009). Modal expansion for spherical homogeneous sources. *Optics Communications*, 282, 2859–3861.
- Gori, F., Palma, C., & Padovani, C. (1989). Modal expansion of the blackbody cross spectral density. *Atti Fondaz G Ronchi*, 44, 1–7.
- Gori, F., Palma, C., & Santarsiero, M. (1990). A scattering experiment with partially coherent light. *Optics Communications*, 74, 353–356.
- Gori, F., Santarsiero, M., Borghi, R., & Li, C. F. (2008). Partially correlated thin annular sources: The scalar case. *Journal of the Optical Society of America A*, 25, 2826–2832.
- Gori, F., Santarsiero, M., Borghi, R., & Guattari, G. (1998). Intensity-based modal analysis of partially coherent beams with hermite-gaussian modes. *Optics Letters*, 23, 989–991.

- Gori, F., Santarsiero, M., Borghi, R., & Wolf, E. (2006). Effects of coherence on the degree of polarization in a young interference pattern. *Optics Letters*, 31, 688–690.
- Gori, F., Santarsiero, M., Simon, R., Piquero, G., Borghi, R., & Guattari, G. (2003). Coherent-mode decomposition of partially polarized, partially coherent sources. *Journal of the Optical Society of America A*, 20, 78–84.
- Greffet, J.-J., De La Cruz-Gutierrez, M., Ignatovich, P. V., & Radunsky, A. (2003). Influence of spatial coherence on scattering by a particle. *Journal of the Optical Society of America A*, 20, 2315–2320.
- Gu, Y., & Gbur, G. (2009). Topological reactions of correlation vortices. *Optics Communications*, 282, 709–716.
- Gu, Y., & Gbur, G. (2010). Measurement of atmospheric turbulence strength by vortex beam. *Optics Communications*, 283, 1209–1212.
- Gu, Y., Korotkova, O., & Gbur, G. (2009). Scintillation of nonuniformly polarized beams in atmospheric turbulence. *Optics Letters*, 34, 2261–2263.
- Habashy, T., Friberg, A. T., & Wolf, E. (1997). Application of the coherent-mode representation to a class of inverse source problems. *Inverse Problems*, 13, 47–61.
- Hong, J. P., Kang, K., & Kim, K. S. (1993). Numerical-analysis in the coherent mode representation. *Journal of the Korean Physical Society*, 26, 592–596.
- Hu, X., & Pu, J. (2006). Spectral anomalies of focused high order Bessel beams in the neighborhood of focus. *Optics Communications*, 266, 413–418.
- Huttunen, J., Friberg, A. T., & Turunen, J. (1995). Scattering of partially coherent electromagnetic fields by microstructured media. *Physical Review A*, 52, 3081–3092.
- Iwai, T., & Asakura, T. (1996). Speckle reduction in coherent information processing. *Proceedings of IEEE*, 84, 765–781.
- James, D. F. V. (1994). Change of polarization of light beams on propagation in free space. *Journal of the Optical Society of America A*, 11, 1641–1643.
- James, D. F. V., & Wolf, E. (1990). Doppler-like frequency shifts generated by dynamic scattering. *Optics Letters A*, 146, 167–171.
- James, D. F. V., & Wolf, E. (1991a). Some new aspects of Young's interference experiment. *Physics Letters A*, 157, 6–10.
- James, D. F. V., & Wolf, E. (1991b). Spectral changes produced in Young's interference experiment. *Optics Communications*, 81, 150–154.
- James, D. F. V., Savedoff, M., & Wolf, E. (1990). Shifts of spectral lines caused by scattering from fluctuating random media. *The Astrophysical Journal*, 359, 67–71.
- Jannson, J., Jannson, T., & Wolf, E. (1988). Spatial coherence discrimination in scattering. *Optics Letters*, 13, 1060–1062.
- Kandpal, H. C., & Vaishya, J. S. (2000). Experimental study of coherence properties of light fields in the region of superposition in Young's interference experiment. *Optics Communications*, 186, 15–20.
- Kandpal, H. C., Vaishya, J. S., Chander, M., Saxena, K., & Joshi, K. C. (1992). Field correlations from spectral measurements in Young's interference experiment. *Physics Letters A*, 167, 120–122.
- Kato, M., Nakayama, Y., & Suzuki, T. (1975). Speckle reduction in holography with a spatially incoherent source. *Applied Optics*, 14, 1093–1099.
- Kiasaleh, K. (2006). On the scintillation index of a multiwavelength Gaussian beam in a turbulent free-space optical communications channel. *Journal of the Optical Society of America A*, 23, 557–566.
- Kim, K. (2005). An orthogonal-mode representation of stochastic electromagnetic beams. *The journal of the Korean Physical Society*, 47, 228–234.

- Kim, J., Miller, D. T., Kim, E., Oh, S., Oh, J., & Milner, T. E. (2005). Optical coherence tomography speckle reduction by a partially spatially coherent source. *Journal of Biomedical Optics*, 10, 064034.
- Kim, K., & Park, D. (1992). Approximate method in coherent-mode representation. *Optics Letters*, 17, 1043–1045.
- Kim, K., & Wolf, E. (2006). A scalar-mode representation of stochastic, planar, electromagnetic sources. *Optics Communications*, 261, 19–22.
- Kon, A. I., & Tatarskii, V. I. (1972). On the theory of the propagation of partially coherent light beams in a turbulent atmosphere. *Radiophysics and Quantum Electronics*, 15, 1187–1192.
- Korotkova, O. (2006). Changes in the intensity fluctuations of a class of random electromagnetic beams on propagation. *Journal of Optics A: Pure and Applied Optics*, 8, 30–37.
- Korotkova, O. (2008). Scintillation index of a stochastic electromagnetic beam propagating in random media. *Optics Communications*, 281, 2342–2348.
- Korotkova, O., Andrews, L. C., & Phillips, R. L. (2004). Model for a partially coherent Gaussian beam in atmospheric turbulence with application in Lasercom. *Optical Engineering*, 43, 330–341.
- Korotkova, O., & Gbur, G. (2007). Angular spectrum representation for propagation of random electromagnetic beams in a turbulent atmosphere. *Journal of the Optical Society of America A*, 24, 2728–2736.
- Korotkova, O., Hoover, B., Gamiz, V., & Wolf, E. (2005). Coherence and polarization properties of far-fields generated by quasi-homogeneous electromagnetic sources. *Journal of the Optical Society of America A*, 22, 2547–2556.
- Korotkova, O., Pu, J., & Wolf, E. (2008). Spectral changes in electromagnetic stochastic beams propagating through turbulent atmosphere. *Journal of Modern Optics*, 55, 1199–1208.
- Korotkova, O., Salem, M., Dogariu, A., & Wolf, E. (2005). Changes in the polarization ellipse of random electromagnetic beams propagating through the turbulent atmosphere. *Waves in Complex and Random Media*, 15, 353–364.
- Korotkova, O., Salem, M., & Wolf, E. (2004). The far-zone behavior of the degree of polarization of electromagnetic beams propagating through atmospheric turbulence. *Optics Communications*, 233, 225–230.
- Korotkova, O., Visser, T. D., & Wolf, E. (2008). Polarization properties of stochastic electromagnetic beams. *Optics Communications*, 281, 515–520.
- Korotkova, O., & Wolf, E. (2005). Changes in the state of polarization of a random electromagnetic beam on propagation. *Optics Communications*, 246, 35–43.
- Lahiri, M., Wolf, E., Fischer, D. G., & Shirai, T. (2009). Determination of correlation functions of scattering potentials of stochastic media from scattering experiments. *Physics Review Letters*, 102, 123901.
- Laue, M. (1912). Interferenzerscheinungen bei Röntgenstrahlen. *Sitzungsberichte der Bayrische Akademie der Wissenschaften*. An English translation can be found in G. E. Bacon's (Eds.), *X-Ray and neutron diffraction* (pp. 303–322). Oxford: Pergamon, 1966.
- Leader, J. C. (1978). Atmospheric propagation of partially coherent radiation. *Journal of the Optical Society of America*, 68, 175–185.
- Leader, J. C. (1979). Intensity fluctuations resulting from partially coherent light propagating through atmospheric turbulence. *Journal of the Optical Society of America*, 69, 73–84.
- Lehmberg, R. H., & Goldhar, J. (1987). Use of incoherence to produce smooth and controllable irradiation profiles with KrF fusion lasers. *Fusion Technology*, 11, 532–541.
- Li, Y., Lee, H., & Wolf, E. (2006). Spectra, coherence and polarization in Young's interference pattern formed by stochastic electromagnetic beams. *Optics Communications*, 265, 63–72.
- Liu, P.-S., & Lü, B. (2007). Coherence vortices of partially coherent beams in the far field. *Chinese Physics*, 16, 411–415.

- Liu, Y., Seminario, M., Tomasel, F. G., Chang, C., Rocca, J. J., & Attwood, D. T. (2001). Achievement of essentially full spatial coherence in a high-average-power soft-x-ray laser. *Physical Review A*, 63, 033802.
- Liu, P., Yang, H., Rong, J., Wang, G., & Yan, Y. (2010). Coherence vortex evolution of partially coherent vortex beams in the focal region. *Optics and Laser Technology*, 42, 99–104.
- Lü, B., Zhang, B., & Cai, B. (1995). Focusing of a Gaussian Schell-model beam through a circular lens. *Journal of Modern Optics*, 42, 289–298.
- Lurie, M. (1966). Effects of partial coherence on holography with diffuse illumination. *Journal of the Optical Society of America*, 56, 1369–1372.
- Lurie, M. (1968). Fourier-transform holograms with partially coherent light: Holographic measurement of spatial coherence. *Journal of the Optical Society of America*, 58, 614–619.
- Lutomirski, R. F., & Yura, H. T. (1971). Propagation of a finite optical beam in an inhomogeneous medium. *Applied Optics*, 10, 1652–1658.
- Maleev, I. D., Palacios, D. M., Marathay, A. S., & Swartzlander, G. A. (2004). Spatial correlation vortices in partially coherent light: Theory. *Journal of the Optical Society of America B*, 21, 1895–1900.
- Maleev, I. D., & Swartzlander, G. A. (2008). Propagation of spatial correlation vortices. *Journal of the Optical Society of America B*, 25, 915–922.
- Mandel, L., & Wolf, E. (1976). Spectral coherence and the concept of cross-spectral purity. *Journal of the Optical Society of America*, 66, 529–535.
- Mandel, L., & Wolf, E. (1995). *Optical coherence and quantum optics*. Cambridge, UK: Cambridge University Press.
- Mandel, L., & Wolf, E. (Eds.). (1990). *Selected papers on coherence and fluctuations of light (1850–1966)*. Bellingham, WA: SPIE.
- Marasinghe, M. L., Premaratne, M., & Paganin, D. M. (2010). Coherence vortices in Mie scattering of statistically stationary partially coherent fields. *Optics Express*, 18, 6628–6641.
- Marathay, A. S. (1982). *Elements of optical coherence theory*. New York: Wiley.
- Marks, D. L., Ralston, T. S., Carney, P. S., & Boppart, S. A. (2007). Inverse scattering for frequency-scanned full-field optical coherence tomography. *Journal of the Optical Society of America A*, 24, 1034–1041.
- Martinex-Herrero, R., Mejias, P. M., & Gori, F. (2009). Genuine cross-spectral densities and pseudo-modal expansions. *Optics Letters*, 34, 1399–1401.
- Martinsson, P., Lajunen, H., & Friberg, A. T. (2007). Communication modes with partially coherent fields. *Journal of the Optical Society of America A*, 24, 3336–3342.
- McKinney, J. D., Webster, M. A., Webb, K. J., & Weiner, A. M. (2000). Characterization and imaging in optically scattering media by use of laser speckle and a variable-coherence source. *Optics Letters*, 25, 4–6.
- Mie, G. (1908). Beiträge zur Optik trüber Medien, speziell kolloidaler Metallösungen. *Annalen der Physik*, 25, 377–445.
- Moisewitsch, B. L. (1977). *Integral equations*. London: Longman Group Limited.
- Motsek, K., Kivshar, Y. S., Shih, M.-F., & Swartzlander, G. A. (2005). Spatial coherence singularities and incoherent vortex solitons. *Journal of the Optical Society of America B*, 22, 1437–1442.
- Nye, J. F. (1983a). Lines of circular polarization in electromagnetic wave fields. *Proceedings of the Royal Society of London A*, 389, 279–290.
- Nye, J. F. (1983b). Polarization effects in the diffraction of electromagnetic waves: The role of disclinations. *Proceedings of the Royal Society of London A*, 387, 279–290.
- Nye, J. F. (1999). *Natural focusing and fine structure of light*. Bristol: IOP Publishing.
- Nye, J. F., & Berry, M. V. (1974). Dislocations in wave trains. *Proceedings of the Royal Society of London A*, 336, 165–190.

- Ostrovsky, A. S., Martinez-Niconoff, G., & Ramirez-San-Juan, J. C. (2001). Coherent-mode representation of propagation-invariant fields. *Optics Communications*, 195, 27–34.
- Ostrovsky, A. S., & Rodriguez-Solid, M. V. (2000). Free-space propagation of the generalized radiance defined in terms of the coherent-mode representation of cross-spectral density function. *Optical Review*, 7, 112–114.
- Ostrovsky, A. S., Zemliak, A. M., & Hernández-García, E. (2005). Alternative coherent-mode representation of a planar source. *Optics Communications*, 249, 1–6.
- Palacios, D. M., Maleev, I. D., Marathay, A. S., & Swartzlander, G. A. (2004). Spatial correlation singularity of a vortex field. *Physical Review Letters*, 92, 143905.
- Pask, C., & Stacey, A. (1988). Optical coherence and Wolf's theory for electromagnetic waves. *Journal of the Optical Society of America A*, 5, 1688–1693.
- Pedersen, H. M., & Stamnes, J. J. (2000). Radiometric theory of spatial coherence in free-space propagation. *Journal of the Optical Society of America A*, 17, 1413–1420.
- Peleg, A., & Moloney, J. V. (2006). Scintillation reduction for two Gaussian laser beams with different wavelengths in weak atmospheric turbulence. *Journal of the Optical Society of America A*, 23, 3114–3122.
- Peleg, A., & Moloney, J. V. (2007). Scintillation reduction by use of multiple Gaussian laser beams with different wavelengths. *IEEE Photonics Technology Letters*, 19, 883–885.
- Perina, J. (1985). *Coherence of light*. (2nd ed.). Dordrecht: Reidel.
- Petrucelli, J. C., & Alonso, M. A. (2007). Propagation of partially coherent fields through planar dielectric boundaries using angle-impact Wigner functions I. Two dimensions. *Journal of the Optical Society of America A*, 24, 2590–2603.
- Petrucelli, J. C., & Alonso, M. A. (2008). Ray-based propagation of the cross-spectral density. *Journal of the Optical Society of America A*, 25, 1395–1405.
- Polynkin, P., Peleg, A., Klein, L., Rhoadarmer, T., & Moloney, J. (2007). Optimized multiemitter beams for free-space optical communication through turbulent atmosphere. *Optics Letters*, 32, 885–887.
- Ponomarenko, S. A. (2001). A class of partially coherent beams carrying optical vortices. *Journal of the Optical Society of America A*, 18, 150–156.
- Ponomarenko, S. A., Greffet, J. J., & Wolf, E. (2002). The diffusion of partially coherent beams in turbulent media. *Optics Communications*, 208, 1–8.
- Ponomarenko, S. A., & Wolf, E. (1999). Coherence properties of light in Young's interference pattern formed with partially coherent light. *Optics Communications*, 170, 1–8.
- Ponomarenko, S. A., & Wolf, E. (2002). Solution for the inverse scattering problem for strongly fluctuating media. *Optics Letters*, 27, 1770–1772.
- Popescu, G., & Dogariu, A. (2002). Spectral anomalies at wave-front dislocations. *Physical Review Letters*, 88, 183902.
- Prahl, S. A., Fischer, D. G., & Duncan, D. D. (2009). Monte Carlo Green's function formalism for the propagation of partially coherent light. *Journal of the Optical Society of America A*, 26, 1533–1543.
- Pu, J., Dong, M., & Wang, T. (2006). Generation of adjustable partially coherent bottle beams by use of an axicon-lens system. *Applied Optics*, 45, 7553–7556.
- Pu, J., Liu, X., & Nemoto, S. (2005). Partially coherent bottle beams. *Optics Communications*, 252, 7–11.
- Pu, J., & Nemoto, S. (2000). Spectral shifts and spectral switches in diffraction of partially coherent light by a circular aperture. *IEEE Journal of Quantum Electronics*, 36, 1407–1411.
- Pu, J., & Nemoto, S. (2002). Spectral changes and $1 \times n$ spectral switches in the diffraction of partially coherent light by an aperture. *Journal of the Optical Society of America A*, 19, 339–344.
- Pu, J., Nemoto, S., & Liu, X. (2004). Beam shaping of focused partially coherent beams by use of the spatial coherence effect. *Applied Optics*, 32, 5281–5286.

- Pu, J., Zhang, H., & Nemoto, S. (1999). Spectral shifts and spectral switches of partially coherent light passing through an aperture. *Optics Communications*, 162, 57–63.
- Ralston, T. S., Marks, D. L., Carney, P. S., & Boppart, S. A. (2006). Inverse scattering for optical coherence tomography. *Journal of the Optical Society of America A*, 23, 1027–1037.
- Ren, J.-R., Zhu, T., & Duan, Y.-S. (2008). Topological properties of spatial coherence function. *Chinese Physics Letters*, 25, 367–370.
- Ricklin, J. C., & Davidson, F. M. (2002). Atmospheric turbulence effects on a partially coherent Gaussian beam: Implications for free-space laser communication. *Journal of the Optical Society of America A*, 19, 1794–1802.
- Ricklin, J. C., & Davidson, F. M. (2003). Atmospheric optical communication with a Gaussian-Schell beam. *Journal of the Optical Society of America A*, 20, 856–866.
- Riechert, F., Dürr, F., Rohlffing, U., & Lemmer, U. (2009). Ray-based simulation of the propagation of light with different degrees of coherence through complex optical systems. *Applied Optics*, 48, 1527–1534.
- Rothenberg, J. E. (1997). Comparison of beam-smoothing methods for direct-drive inertial confinement fusion. *Journal of the Optical Society of America B*, 14, 1664–1671.
- Roychowdhury, H., Ponomarenko, S., & Wolf, E. (2005). Change of polarization of partially coherent electromagnetic beams propagating through the turbulent atmosphere. *Journal of Modern Optics*, 52, 1611–1618.
- Roychowdhury, H., & Wolf, E. (2004). Determination of the electric cross-spectral density matrix of a random electromagnetic beam. *Optics Communications*, 226, 57–60.
- Roychowdhury, H., & Wolf, E. (2005a). Statistical similarity and the physical significance of complete spatial coherence and complete polarization of random electromagnetic beams. *Optics Communications*, 248, 327–332.
- Roychowdhury, H., & Wolf, E. (2005b). Young's interference experiment with light of any state of coherence and of polarization. *Optics Communications*, 252, 268–274.
- Rydberg, C., & Bengtsson, J. (2006). Efficient numerical representation of the optical field for the propagation of partially coherent radiation with a specified spatial and temporal coherence function. *Journal of the Optical Society of America A*, 23, 1616–1625.
- Saastamoinen, T., Kuittinen, M., Vahimaa, P., & Turunen, J. (2004). Focusing of partially coherent light into planar waveguides. *Optics Express*, 12, 4511–4522.
- Salem, M., & Wolf, E. (2008). Coherence-induced polarization changes in light beams. *Optics Letters*, 33, 1180–1182.
- Salem, M., & Agrawal, G. P. (2009a). Coupling of stochastic electromagnetic beams into optical fibers. *Optics Letters*, 34, 2829–2831.
- Salem, M., & Agrawal, G. P. (2009b). Effects of coherence and polarization on the coupling of stochastic electromagnetic beams into optical fibers. *Journal of the Optical Society of America A*, 26, 2452–2458.
- Salem, M., Korotkova, O., Dogariu, A., & Wolf, E. (2004). Polarization changes in partially coherent electromagnetic beams propagating through turbulent atmosphere. *Waves in Random Media*, 14, 513–523.
- Salem, M., Shirai, T., Dogariu, A., & Wolf, E. (2003). Long-distance propagation of partially coherent beams through atmospheric turbulence. *Optics Communications*, 216, 261–265.
- Santarsiero, M., & Gori, F. (1992). Spectral changes in a Young interference pattern. *Physics Letters A*, 167, 123–128.
- Schell, A. C. (1961). *The multiple plate antenna*. PhD thesis, Massachusetts Institute of Technology.
- Schoonover, R. W., & Visser, T. D. (2006). Polarization singularities of focused, radially polarized fields. *Optics Express*, 14, 5733–5745.
- Schoonover, R. W., Zysk, A. M., Carney, P. S., & Wolf, E. (2008). Geometrical optics limit of stochastic electromagnetic fields. *Physical Review A*, 77, 043831.

- Schouten, H. F., Gbur, G., Visser, T. D., & Wolf, E. (2003). Phase singularities of the coherence functions in Young's interference pattern. *Optics Letters*, 28, 968–970.
- Schouten, H. F., & Visser, T. D. (2008). The role of correlation functions in the theory of optical wave fields. *American Journal of Physics*, 76, 867–871.
- Schouten, H. F., Visser, T. D., Gbur, G., Lenstra, D., & Blok, H. (2003). Creation and annihilation of phase singularities near a sub-wavelength slit. *Optics Express*, 11, 371–380.
- Schouten, H. F., Visser, T. D., & Wolf, E. (2003). New effects in Young's interference experiment with partially coherent light. *Optics Letters*, 28, 1182–1184.
- Schulz, T. J. (2004). Iterative transform algorithm for the computation of optimal beams. *Journal of the Optical Society of America A*, 21, 1970–1974.
- Schulz, T. J. (2005). Optimal beams for propagation through random media. *Optics Letters*, 30, 1093–1095.
- Schwartz, C., & Dogariu, A. (2006). Mode coupling approach to beam propagation in atmospheric turbulence. *Journal of the Optical Society of America A*, 23, 329–338.
- Setälä, T., Lindberg, J., Blomstedt, K., Tervo, J., & Friberg, A. T. (2005). Coherent-mode representation of a statistically homogeneous and isotropic electromagnetic field in spherical volume. *Physical Review E*, 71, 036618.
- Shirai, T., & Asakura, T. (1993). Mode analysis of changes in spatial coherence of light passing through a periodic sequence of lenses. *Optik*, 94, 123–131.
- Shirai, T., & Asakura, T. (1995). Spectral changes of light induced by scattering from spatially random media under the Rytov approximation. *Journal of the Optical Society of America A*, 12, 1354–1363.
- Shirai, T., Dogariu, A., & Wolf, E. (2003). Mode analysis of spreading of partially coherent beams propagating through atmospheric turbulence. *Journal of the Optical Society of America A*, 20, 1094–1102.
- Shirai, T., & Wolf, E. (2002). Spatial coherence properties of the far field of a class of partially coherent beams which have the same directionality as a fully coherent laser beam. *Optics Communications*, 204, 25–31.
- Silverman, R. A. (1958). Scattering of plane waves by locally homogeneous dielectric noise. *Proceedings of the Cambridge Philosophical Society*, 54, 530–537.
- Simon, R., & Sundar, K. (1993). Twisted Gaussian Schell-model beams. i. symmetry structure and normal-mode spectrum. *Journal of the Optical Society of America A*, 10, 2008–2016.
- Simon, R., & Mukunda, N. (1993). Twisted Gaussian Schell-model beams. *Journal of the Optical Society of America A*, 10, 95–109.
- Sinha, S. K., Tolan, M., & Gibaud, A. (1998). Effects of partial coherence on the scattering of x rays by matter. *Physical Review B*, 57, 2740–2758.
- Sommerfeld, A. (1964). *Optics*. New York: Academic Press.
- Soskin, M. S., & Vasnetsov, M. V. (2001). Singular optics. In E. Wolf (Ed.), *Progress in Optics* (vol. 42, pp. 83–110). Amsterdam: Elsevier.
- Stamnes, J. J. (1986). *Waves in focal regions*. Bristol: Adam Hilger.
- Starikov, A. (1982). Effective number of degrees of freedom of partially coherent sources. *Journal of the Optical Society of America*, 72, 1538–1544.
- Starikov, A., & Friberg, A. T. (1984). One-dimensional Lambertian sources and the associated coherent-mode representation. *Applied Optics*, 23, 4261–4268.
- Starikov, A., & Wolf, E. (1982). Coherent-mode representation of Gaussian Schell-model sources and of their radiation fields. *Journal of the Optical Society of America*, 72, 923–928.
- Stokes, G. G. (1852). On the composition and resolution of streams of polarized light from different sources. *Transactions of the Cambridge Philosophical Society*, 9, 399–416. Reprinted in Swindell, W. (Ed.). (1975). *Polarized light*. Stroudsburg, PA: Halsted Press.

- Sundar, K., Makunda, N., & Simon, R. (1995). Coherent-mode decomposition of general anisotropic Gaussian Schell-model beams. *Journal of the Optical Society of America A*, 12, 560–569.
- Sundar, K., Simon, R., & Mukunda, N. (1993). Twisted Gaussian Schell-model beams. II. Spectrum analysis and propagation characteristics. *Journal of the Optical Society of America A*, 10, 2017–2023.
- Sung, D., Kim, K., & Park, D. Y. (1996). P-representation of the cross-spectral density. *The Journal of the Korean Physical Society*, 29, 719–723.
- Swartzlander, G. A., & Hernandez-Aranda, R. I. (2007). Optical Rankine vortex and anomalous circulation of light. *Physical Review Letters*, 99, 163901.
- Swartzlander, G. A., & Schmit, J. (2004). Temporal correlation vortices and topological dispersion. *Physical Review Letters*, 93, 093901.
- Taylor, L. S. (1967). Decay of mutual coherence in turbulent media. *Journal of the Optical Society of America*, 57, 304–308.
- Tervo, J., Setälä, T., & Friberg, A. T. (2004). Theory of partially coherent electromagnetic fields in the space-frequency domain. *Journal of the Optical Society of America A*, 21, 2205–2215.
- Troup, G. J. (1967). *Optical coherence theory – recent developments*. Methuen, London.
- Tsubakimoto, K., Nakatsuka, M., Miyanaga, N., & Jitsuno, T. (1998). Analysis of spherical target illumination with partially coherent light through random phase plate. *Japanese Journal of Applied Physics*, 37, 5560–5568.
- Turunen, J., Vasara, A., & Friberg, A. T. (1991). Propagation invariance and self-imaging in variable-coherence optics. *Journal of the Optical Society of America A*, 28, 282–289.
- Tyo, J. S., & Turner, T. S. (2008). Sensing polarization with variable coherence tomography. *Journal of the Optical Society of America A*, 25, 2383–2389.
- Vahimaa, P., & Turunen, J. (2006). Finite-elementary-source model for partially coherent radiation. *Optics Express*, 14, 1376–1381.
- van Cittert, P. H. (1934). Die wahrscheinliche Schwingungsverteilung in einer von einer Lichtquelle direkt oder mittels einer Linse beleuchteten Ebene. *Physica*, 1, 201–210.
- van Dijk, T., Fischer, D. G., Visser, T. D., & Wolf, E. (2010). The effects of spatial coherence on the angular distribution of radiant intensity generated by scattering on a sphere. *Physical Review Letters*, 104, 173902.
- van Dijk, T., Gbur, G., & Visser, T. D. (2008). Shaping the focal intensity distribution using spatial coherence. *Journal of the Optical Society of America A*, 25, 575–581.
- van Dijk, T., Schouten, H. F., & Visser, T. D. (2009). Coherence singularities in the far field generated by partially coherent sources. *Physical Review A*, 79, 033805.
- van Dijk, T., & Visser, T. D. (2009). Evolution of singularities in a partially coherent vortex beam. *Journal of the Optical Society of America A*, 26, 741–744.
- Verdet, E. (1865). Etude sur la constitution de la lumière non polarisée et de la lumière partiellement polarisée. *Annales Scientifiques de l'E.N.S.*, 2, 291–316.
- Visser, T. D., Kuebel, D., Lahiri, M., Shirai, T., & Wolf, E. (2009). Unpolarized light beams with different coherence properties. *Journal of Modern Optics*, 56, 1369–1374.
- Visser, T. D., Fischer, D. G., & Wolf, E. (2006). Scattering of light from quasi-homogeneous sources by quasi-homogeneous media. *Journal of the Optical Society of America A*, 23, 1631–1638.
- Visser, T. D., & Wolf, E. (2003). Spectral anomalies near phase singularities in partially coherent focused wavefields. *Journal of Optics A*, 5, 371–373.
- Visser, T. D., Gbur, G., & Wolf, E. (2002). Effect of the state of coherence on the three-dimensional spectral intensity distribution near focus. *Optics Communications*, 213, 13–19.
- Visser, T. D., & Schoonover, R. W. (2008). A cascade of singular field patterns in Young's interference experiment. *Optics Communications*, 281, 1–6.

- Voelz, D. G., Bush, R. A., & Idell, P. S. (1997). Illumination coherence effects in laser-speckle imaging: Modeling and experimental demonstration. *Applied Optics*, 36, 1781–1788.
- Voelz, D., & Fitzberry, K. (2004). Pseudo-partially coherent beam for free-space laser communication. In Proceedings of SPIE (vol. 5550, pp. 218–224). Bellingham, WA: SPIE.
- Wang, F., Cai, Y., & Korotkova, O. (2009). Experimental observation of focal shifts in focused partially coherent beams. *Optics Communications*, 282, 3408–3413.
- Wang, W., Duan, Z., Hanson, S. G., Miyamoto, Y., & Takeda, M. (2006). Experimental study of coherence vortices: Local properties of phase singularities in a spatial coherence function. *Physical Review Letters*, 96, 073902.
- Wang, W., Friberg, A. T., & Wolf, E. (1997). Focusing of partially coherent light in systems of large Fresnel numbers. *Journal of the Optical Society of America A*, 14, 491–496.
- Wang, L., & Lü, B. (2002). Intensity and polarization changes of partially coherent and partially polarized light in Young's experiment. *Optik*, 113, 277–283.
- Wang, T., & Pu, J. (2008). Propagation of non-uniformly polarized beams in a turbulent atmosphere. *Optics Communications*, 281, 3617–3622.
- Wang, W., & Takeda, M. (2006). Coherence current, coherence vortex, and the conservation law of coherence. *Physical Review Letters*, 96, 223904.
- Wang, L., Tschudi, T., Halldórrsson, T., & Pétrusson, P. R. (1998). Speckle reduction in laser projection systems by diffractive optical elements. *Applied Optics*, 37, 1770–1775.
- Withington, S., & Murphy, J. A. (1998). Modal analysis of partially coherent submillimeter-wave quasi-optical systems. *IEEE Transactions on Antennas and Propagation*, 46, 1651–1659.
- Withington, S., Hobson, M. P., & Berry, R. H. (2004). Representing the behavior of partially coherent optical systems by using overcomplete basis sets. *Journal of the Optical Society of America A*, 21, 207–217.
- Wolf, E. (1954). Optics in terms of observable quantities. *Nuovo Cimento C* 12, 884–888.
- Wolf, E. (1955). A macroscopic theory of interference and diffraction of light from finite sources II. Fields with a spectral range of arbitrary width. *Proceedings of the Royal Society of London*, 230, 246–265.
- Wolf, E. (1982). New theory of partial coherence in the space-frequency domain. Part I: Spectra and cross spectra of steady-state sources. *Journal of the Optical Society of America*, 72, 343–351.
- Wolf, E. (1986a). Coherent-mode representation in spatially band-limited wave fields. *Journal of the Optical Society of America A*, 3, 1920–1924.
- Wolf, E. (1986b). New theory of partial coherence in the space-frequency domain. Part II: Steady-state fields and higher-order correlations. *Journal of the Optical Society of America*, 73, 76–85.
- Wolf, E. (1989). Correlation-induced Doppler-like frequency shifts of spectral lines. *Physical Review Letters*, 63, 2220–2223.
- Wolf, E. (2001). The development of optical coherence theory. In *Selected works of Emil Wolf with commentary* (pp. 620–633). Singapore: World Scientific.
- Wolf, E. (2003a). Correlation-induced changes in the degree of polarization, the degree of coherence and the spectrum of random electromagnetic beams on propagation. *Optics Letters*, 28, 1078–1080.
- Wolf, E. (2003b). Unified theory of coherence and polarization of random electromagnetic beams. *Physics Letters A*, 312, 263–267.
- Wolf, E. (2007a). The influence of Young's interference experiment on the development of statistical optics. In E. Wolf (Ed.), *Progress in Optics* (vol. 50, pp. 251–273). Amsterdam: Elsevier.
- Wolf, E. (2007b). *Introduction to the theory of coherence and polarization of light*. Cambridge, UK: Cambridge University Press.

- Wolf, E. (2008). Can a light beam be considered to be the sum of a completely polarized and a completely unpolarized beam? *Optics Letters*, 33, 642–644.
- Wolf, E. (2009). Solution of the phase problem in the theory of structure determination of crystals from x-ray diffraction experiments. *Physical Review Letters*, 103, 075501.
- Wolf, E. (2010). Determination of phases of diffracted x-ray beams in investigations of structure of crystals. *Physics Letters A*, 374, 491–495.
- Wolf, E., & Collett, E. (1978). Partially coherent sources which produce the same far-field intensity distribution as a laser. *Optics Communications*, 25, 293–296.
- Wolf, E., Foley, J. T., & Gori, F. (1989). Frequency shifts of spectral lines produced by scattering from spatially random media. *Journal of the Optical Society of America A*, 6, 1142–1149.
- Wolf, E., & James, D. F. V. (1996). Correlation-induced spectral changes. *Reports on Progress in Physics*, 59, 771–818.
- Wolf, E., Shirai, T., Agarwal, G., & Mandel, L. (1999). Storage and retrieval of correlation functions of partially coherent fields. *Optics Letters*, 24, 367–369.
- Wu, J. (1990). Propagation of a Gaussian-Schell beam through turbulent media. *Journal of Modern Optics*, 37, 671–684.
- Wu, J., & Boardman, A. D. (1991). Coherence length of a Gaussian-Schell beam and atmospheric turbulence. *Journal of Modern Optics*, 38, 1355–1363.
- Xiao, X., & Voelz, D. (2006). Wave optics simulation approach for partial spatially coherent beams. *Optics Express*, 14, 6986–6992.
- Xue, X., Wei, H., & Kirk, A. G. (2000). Intensity-based modal decomposition of optical beams in terms of Hermite-Gaussian functions. *Journal of the Optical Society of America A*, 17, 1086–1090.
- Young, T. (1804). The Bakerian Lecture. Experiments and calculations relative to physical optics. *Philosophical Transactions of the Royal Society of London*, 94, 1–16.
- Young, T. (1807). *A course of lectures on natural philosophy and the mechanical arts*. London: Johnson.
- Yura, H. T. (1972). Mutual coherence function of a finite cross section optical beam propagating in a turbulent medium. *Applied Optics*, 11, 1399–1406.
- Zernike, F. (1938). The concept of degree of coherence and its applications to optical problems. *Physica*, 5, 785–795.
- Zernike, F. (1948). Diffraction and optical image formation. *Proceedings of the Physical Society*, 61, 158–164.
- Zhang, Z., Pu, J., & Wang, X. (2008). Focusing of partially coherent Bessel-Gaussian beams through a high-numerical aperture objective. *Optics Letters*, 33, 49–51.
- Zhao, D., Korotkova, O., & Wolf, E. (2007). Application of correlation-induced spectral changes to inverse scattering. *Optics Letters*, 32, 3483–3485.
- Zysk, A. M., Carney, P. S., & Schotland, J. C. (2005). Eikonal method for calculation of coherence functions. *Physical Review Letters*, 95, 043904.

This page intentionally left blank

AUTHOR INDEX FOR VOLUME 55

A

Abi-Salloum, T., 121
Abramomitz, M., 25
Adesso, G., 43
Agarwal, A.K., 273
Agarwal, G., 326
Agarwal, G.S., 42, 44, 49, 54, 59, 87, 92, 96,
 98, 106, 109, 111, 112, 114, 118, 120, 126,
 127, 129, 130, 131, 132, 138, 141, 145, 147,
 148, 156, 168, 169, 176, 178, 290, 295, 313
Agrawal, G.P., 300, 308, 324
Ahn, H.J., 277
Aichele, T., 45, 51, 52, 56
Akkermans, E., 178
Akram, U., 101, 121, 122, 123, 156
Akulshin, A.M., 134
Alberts, B., 6
Alfano, R.R., 7
Alonso, M.A., 325
Alter, C.A., 17
Altman, Z., 324
Altner, S.B., 158
Alvarez, L.W., 200
Amarande, S., 327
Ambrose, M., 19
Ambrosini, D., 319, 322
Anderson, B., 121
Anderson, P.A., 260
Andreev, A.V., 178, 179, 180, 182
Andrews, L.C., 301, 327
Angelakis, D.G., 114, 176
Anger, P., 117
Anhut, T., 44
Antón, M.A., 128
Apter, B., 214
Arecchi, F.T., 51, 54, 79
Arimoto, Y., 211
Arinc, F., 29
Arlt, J., 326
Arridge, S.R., 3

B

Artal, P., 278
Asakura, T., 312, 324, 326
Asatryan, K.E., 250, 254
Asboth, J.K., 59
Atchison, D.A., 214
Ayrancı, I., 29
Ayras, P., 240
Äyräs, P., 217, 234
Babichev, S.A., 79
Back, F.G., 200
Bagini, V., 322
Bahat-Treidel, E., 214
Baierlein, R., 8
Baik, H.K., 277
Bal, G., 7
Baldwin, G.C., 178
Baleine, E., 312, 313, 328
Baluschev, S., 145
Ban, G., 134
Banakh, V.A., 327
Banaszek, K., 43, 78
Bará, S., 202
Barbero, S., 200, 202
Barencova, A., 177
Bargatin, I.V., 177
Barnes, F.S., 7
Barnes, M.D., 158, 159, 160, 176
Barnett, S.M., 145
Barneveld, H.A., 264
Barreiro, S., 134
Barron, L., 5
Basano, L., 319
Basu, S., 7, 8
Bay, S., 114, 176
Bayazitoglu, Y., 25
Baykal, Y., 327, 328
Beebe, D.J., 273
Beige, A., 176, 177

- Belenkii, M.S., 327
 Bellin, J.L.S., 259
 Bellini, M., 43, 44, 45, 48, 50, 51, 52, 53,
 55, 57, 58, 59, 60, 61, 64, 72, 74, 76, 79
 Bengtsson, J., 325
 Benisty, H., 114
 Ben-Reuven, A., 176
 Benson, O., 45, 52, 56
 Beran, M.J., 285, 327
 Berdichevsky, Y., 259
 Berge, B., 266
 Bergou, J., 132
 Bergstein, L., 200
 Berman, G.P., 328
 Berman, P.R., 113, 121, 123, 138, 141
 Bernet, S., 203
 Berry, M.V., 314
 Berry, R.H., 322
 Bhan, K., 20
 Bharadwaj, P., 117
 Biebuyck, H.A., 265
 Bishop, A.R., 328
 Biswas, R., 114
 Black, A.T., 178
 Blatt, R., 114
 Bloembergen, N., 141
 Blok, H., 316
 Blomstedt, K., 323
 Boardman, A.D., 327
 Bogatyryova, G.V., 317, 320
 Bogatyryova, H.V., 320
 Bogdan, A.R., 141
 Boggs, B., 178
 Bogolubov, N.N., 179
 Bogomolov, V.N., 114
 Bohren, C.F., 5
 Boivin, A., 316
 Bolomey, J.-C., 324
 Bonifacio, R., 44, 70, 74
 Boppert, S.A., 326
 Borghi, R., 295, 322, 323
 Born, M., 5, 10, 206, 223, 285, 287n, 294,
 302, 303, 308
 Bortman-Arbiv, D., 128
 Bose, S., 176
 Bouchal, Z., 299
 Boulanger, J., 19
 Bouma, B.E., 7, 8
 Bouvier, M., 243, 244
 Brandes, T., 178
 Braunbek, W., 316
 Braunstein, S.L., 43, 56, 70
 Bray, D., 7
 Brennen, G.K., 177
 Breuer, H.-P., 87, 88, 92, 96, 97, 98, 112
 Brewer, R.G., 159, 160, 176
 Brezinski, M., 326
 Bricot, C., 207
 Briggs, L.L., 27
 Brinkley, P.F., 210, 214
 Brooke, P.G., 109, 164, 176
 Brouaye, F., 324
 Brown, A.C., 126
 Brown, R., 158
 Brownell, J.H., 178
 Buckle, S.J., 145
 Bucksbaum, P.H., 121
 Bužek, V., 56
 Buksas, M.W., 19
 Buldakov, V.M., 327
 Bullock, D., 141, 143, 144
 Burch, J.M., 202
 Burnett, K., 97, 111, 176, 177
 Bush, R.A., 325
 Busnaina, A.A., 19
 Bykov, V., 114
- C**
- Cabaret, L., 178
 Cai, B., 306
 Cai, Y., 305, 307, 328
 Cairns, B., 311
 Caldas, M., 14
 Calderón, O.G., 128
 Calsamiglia, J., 59
 Campbell, K., 260, 261
 Campman, K.L., 127
 Canuto, C., 24
 Capasso, F., 127
 Cardimona, D.A., 101, 106, 122, 125, 127
 Carmichael, H., 88
 Carmichael, H.J., 70, 125, 176
 Carney, P.S., 313, 324, 325, 326
 Carreño, F., 128
 Carroll, T.J., 177
 Carter, W.H., 310, 311
 Caulfield, H.J., 201
 Caves, C.M., 177
 Cayan, F.N., 29
 Cerf, N.J., 43, 44, 70
 Chai, J.C., 27, 28, 29

- Chan, H.W., 178
Chan, R.C.F., 127
Chan, T.F., 24
Chan, W.W., 210
Chander, M., 293
Chandrasekhar, S., 7, 20
Chang, C.A., 256, 257, 270
Chang, J.-T., 177
Chang, W., 3, 4
Chao, P.C.-P., 248
Charette, A., 19
Charman, W.N., 214
Chavez-Cerda, S., 42
Chefles, A., 70
Chen, C., 121
Chen, H., 114, 149
Chen, J., 259, 276
Chen, S., 74
Chen, Y.-A., 74
Chen, Z., 176
Cheng, C.C., 256, 257, 270, 271
Cheng, K., 319
Chernobrod, B.M., 328
Chernyshov, A.A., 320
Childs, J.J., 113
Chin, J.H., 22
Chiu, C.W., 248
Cho, S.H., 276
Choi, J., 259
Choi, J.-W., 266
Choi, S.W., 277
Chou, H.-S., 135
Chou, Y.-C., 264
Christian, W., 263
Chronis, N., 259
Chu, C., 210
Chu, C.M., 22
Chu, S., 110
Chuang, I.L., 177
Chudnovsky, E.M., 178
Chugh, P., 19
Chui, E.H., 27, 29
Chung, S.H., 277
Churchill, S.W., 22
Cirac, I.J., 43
Cirac, J.I., 132, 176, 178
Claringbould, K., 177
Clausen, J., 44
Clemens, J.P., 176
Cleverly, D.S., 210
Clouet, J.F., 20
Cochrane, P.T., 44, 70
Cohen-Tannoudji, C., 90, 91, 92, 96, 97,
103, 104, 105, 109, 112, 126, 131
Collet, M.J., 96
Collett, E., 298, 299
Cooper, J., 97, 110, 111, 176, 177
Cornelius, C.M., 114
Cornette, W.M., 17
Coulston, S.J., 214
Craig, D.P., 100, 102, 109
Cresser, J.D., 109
Crubellier, A., 176, 178
- D**
- Dačić, Z., 299
Dagenais, M., 141
Dakna, M., 44, 54
Dalton, B.J., 145, 176
Dance, B., 214
D'Angelo, M., 74
Daniel, K.J., 22
Dantan, A., 44, 71, 74
Danzmann, K., 134
D'Ariano, G.M., 58, 78
Das, S., 132, 145
Davidovich, L., 91
Davidson, F.M., 327
Davies, E.B., 42, 61, 98
Davis, B., 325
Davis, B.J., 323
Davis, J.P., 121
de Boer, J.F., 7, 8
Dehmelt, H., 113
DeJule, M.C., 211
De La Cruz-Gutierrez, M., 313
Dell'Anno, F., 43
Demirkaya, G., 29
Dennis, M.R., 314
Densmore, J.D., 19
Derkacz, L., 128
DeSandre, L.F., 278
Descour, M.R., 202
Deutsch, D., 177
Deutsch, I.H., 177
Devaney, A.J., 299
DeVoe, R.G., 159, 160, 176
deWaard, H., 178
Dey, T.N., 145
Dicke, R.H., 131, 150, 175, 176, 178, 179, 180
DiGuglielmo, J., 43

- Ding, L., 141
 Diósi, L., 54, 58
 Dodonov, A.V., 48
 Dodonov, V.V., 61
 Dogariu, A., 295, 301, 307, 312, 313, 324,
 327, 328
 Domokos, P., 178
 Dong, L., 273
 Dong, M., 306
 Dong, R., 43
 Dorschner, T.A., 214
 Doss, H.M., 125
 Dow, J., 316
 Dowling, J.P., 114
 Draheim, J., 264
 Draine, B.T., 17
 Duan, L.-M., 177, 178
 Duan, Y.-S., 319
 Duan, Z., 317
 Ducci, S., 51
 Dümcke, R., 98
 Duncan, D.D., 325
 Dung, H.T., 98
 Dupont-Roc, J., 90
 Dürr, F., 325
 Dušek, M., 314
 Dutt, M.V.G., 138, 139, 140
 Dymale, R.C., 278
- E**
 Efron, U., 214
 Eichmann, U., 132
 Eisert, J., 43
 Ekert, A., 177
 El-Kady, I., 114
 Ellinger, K., 110, 177
 Elliott, D.S., 121
 Elliott, E., 121
 Emel'yanov, V.I., 178
 Enaki, N.A., 96
 Eschner, J., 114, 176
 Evans, T.M., 19
 Evers, J., 114, 121, 122, 123, 124, 125, 126,
 127, 128, 134, 135, 141, 143, 145, 169, 170,
 171, 177, 178, 179, 180
 Eyyuboglu, H.T., 328
- F**
 Fabre, C., 52, 179
 Facchi, P., 117, 118
 Fadeev, V.V., 49
 Failache, P., 134
 Fainman, Y., 260, 261
 Faist, J., 127, 138
 Faklis, D., 226
 Fan, X.J., 128
 Fan, Y.-H., 214, 243, 250, 251, 255
 Fang, H., 277
 Fang, J., 259
 Fante, R.L., 327
 Feld, M.S., 113, 178
 Felde, G.V., 320
 Fel'de, K.V., 320
 Feldman, M.J., 269
 Feng, G.-H., 264
 Feranchuk, I.D., 121
 Fercher, A.F., 7, 326
 Fernández, E.J., 278
 Ferraro, P., 269
 Ferreyrol, F., 44, 74
 Ferstl, M., 214
 Fićek, Z., 87, 96, 101, 111, 125, 127,
 129, 130, 134, 138, 144, 145, 156, 157,
 159, 176, 177, 178
 Filip, R., 43, 44
 Fisch, N.J., 178
 Fischer, D.G., 307, 311, 312, 313, 319, 325
 Fitzberry, K., 328
 Fiurášek, J., 43, 44, 70
 Flannery, B.P., 29, 30
 Fleischhauer, M., 106, 114, 127, 134, 141,
 142, 145, 178
 Fleming, J.G., 114
 Flewett, S., 323
 Flock, S.T., 18
 Florescu, M., 114
 Fokkink, L.G.J., 265
 Foley, J.T., 298, 307, 312
 Fontannaz, J., 243
 Foreman, M.R., 308
 Foster, K.R., 7
 Fourestie, B., 324
 Fox, D., 260
 Fox, D.W., 251
 Frank, S., 22
 Franke-Arnold, S., 145
 Franzen, A., 43
 Freedhoff, H., 125
 Freedhoff, H.S., 144, 176
 Freund, I., 316
 Friberg, A.T., 299, 304, 306, 312, 323,
 323, 324

- Friedberg, R., 100
 Friedman, L.J., 214
 Friedmann, H., 128, 145
 Friend, J., 19, 24, 25
 Frisch, A.-M., 214
 Frishman, E., 121
 Fu, C., 176
 Fuchs, C.A., 70
 Fuh, A.Y.-G., 248, 258
 Furusawa, A., 43, 44, 66, 68, 69, 70
 Futhey, J.A., 274
- G**
- Gabrielse, G., 113
 Gagen, M., 145
 Galstian, T.V., 254
 Galyukov, A.O., 32
 Gamiz, V., 300
 Gamliel, A., 323
 Gan, C.H., 319
 Gan, Z.-W., 147
 Gao, B., 97, 176
 Gao, J.-Y., 141
 Gao, S.-Y., 128
 Gao, W., 302
 Gaponenko, S.V., 114
 Gaposchkin, S.I., 20
 Garanin, D.A., 178
 García-Patrón, R., 44, 70
 Gardiner, C.W., 96
 Garraway, B.M., 113, 125
 Gase, R., 322
 Gauza, S., 243, 250, 251
 Gbur, G., 293, 301, 305, 306, 307, 316,
 317, 319, 324, 325, 326, 327, 328
 Genoni, M.G., 43
 Gerdau, E., 178
 Gero, A., 178
 Gerritsen, H.J., 214
 Ghafoor, F., 145, 147
 Giacobino, E., 52, 179
 Gibaud, A., 314
 Giedke, G., 43
 Glauber, R.J., 49, 57, 60, 62, 64
 Gobin, A.M., 2
 Goldbach, T., 6, 17, 18
 Goldhar, J., 327
 Goldstein, E.V., 111, 177
 Gomer, C.J., 20
 Gong, C., 176
 Gong, S., 128
- Gong, S.Q., 127, 128
 Gonzalo, I., 128
 Goodman, J.W., 202, 209, 285
 Goodsell, A., 177
 Gopinathan, U., 326
 Gordon, M.S., 214
 Gori, F., 293, 295, 310, 312, 319, 320n,
 322, 323
 Gorman, C.B., 265
 Gorshkov, V.N., 328
 Gossard, A.C., 127
 Goy, P., 113
 Graaff, R., 6
 Grabow, J., 61
 Grangier, P., 42, 44
 Greenebaum, B., 7
 Greenstein, J.L., 6, 15
 Greentree, A.D., 144
 Greffet, J.J., 313, 327
 Greiner, C., 178
 Greiner, W., 8
 Grilli, S., 269
 Grishanin, B.A., 177
 Groisman, A., 260, 261
 Gross, M., 113, 176, 178, 179
 Gruneisen, M.T., 278
 Grupp, J., 243, 244
 Grynpberg, G., 90, 141
 Gu, Y., 319, 328
 Gu, Z.-Z., 274
 Guattari, G., 322, 323
 Gulfam, Q., 177
 Gunji, M., 269
 Guo, G.-C., 177
 Guo, J., 111, 176, 177
 Guo, Z., 19
 Gural'nik, I.P., 252, 254
 Gural'nik, I.R., 252
 Gvozdarev, A., 243
- H**
- Haake, F., 179
 Habashy, T., 324
 Hage, B., 43
 Haught, J., 54
 Hain, M., 214, 277
 Hakuta, K., 145
 Halldórsson, T., 326
 Ham, B.S., 69
 Hammer, M., 18
 Han, Y.-H., 274

- Handapangoda, C.C., 19, 24, 25
Hands, P.J.W., 276
Hannstein, V., 176
Hansen, H., 45, 52, 56
Hanson, S.G., 317
Hareng, M., 207
Haroche, S., 113, 176, 178, 179
Harris, S.E., 134, 138
Hartmann, S.R., 100, 178
Hashimoto, K., 261
Hayano, Y., 211
Hayasaka, K., 43, 69
Hayrynen, T., 48
He, Z., 243
Heersink, J., 43
Hegerfeldt, G.C., 125, 141, 176
Heidmann, A., 52
Heinzen, D.J., 113, 178
Hemmer, P.R., 145, 177
Henao, R., 202
Hendriks, B.H.W., 266, 267
Henryy, L.G., 6, 15
Hercules, D.M., 5
Herczfeld, P.R., 125
Herman, I.P., 178
Hernandez, G., 145
Hernandez-Aranda, R.I., 319
Hernández-García, E., 323
Hettich, C., 44, 155, 156, 157, 158, 176, 177
Higenyi, J., 25
Hilfer, E.S., 113
Hirano, M., 79
Hirano, T., 79
Hirsia, A.H., 261
Hitzenberger, C.K., 7, 326
Ho, K.M., 114
Hobbs, D.S., 214
Hobson, M.P., 322
Hoffman, J.D., 5
Hong, J.P., 323
Honkanen, S., 217, 234
Honma, M., 243, 249
Hoover, B., 300
Horvath, L., 176
Hossack, W.J., 214
Hradil, Z., 78, 79
Hsu, P.-F., 19, 32, 33
Hu, X., 307
Huang, D., 3, 4
Huang, G.M., 141
Huang, H., 114
Huang, L.-H., 262
Huang, T.-J., 262
Huelga, S.F., 141, 177
Huffman, D.R., 5
Huisman, S.R., 79
Hulet, R.G., 113
Humphrey, W.E., 200, 202
Huss, A., 145
Hussaini, M.Y., 24
Huttunen, J., 312
- I**
- Ide, M., 211
Idell, P.S., 325
Iftimia, N., 7, 8
Ignatovich, P.V., 313
Ikeda, T., 260
Il'inskii, Y.A., 178
Illuminati, F., 43
Imamoğlu, A., 106, 127, 134
Imoto, N., 61
Incropera, F.P., 22
Innocenti, G., 113
Inouye, S., 178
Irvin, W.M., 16
Ishikawa, M., 261
Ishimaru, A., 24
Itano, W.M., 132
Ito, H., 277
Iwai, T., 326
Iwasaki, M., 277
- J**
- Jacobovitz, G.R., 113
Jacques, S.L., 17
Jagatap, B.N., 179
Jain, N., 79
Jakóbczyk, L., 128
Jakob, M., 132
Jaksch, D., 177
James, D.F.V., 176, 286, 290, 293, 300,
 301, 312
Jannson, J., 310
Jannson, T., 310
Jaroszewicz, Z., 202
Jau, H.-C., 258
Javanainen, J., 127, 176
Jeong, H., 43, 44, 54, 56, 69, 74, 76
Jeong, K.H., 259

- Jepsen, M.L., 214
Jessen, P.S., 177
Jhe, W., 113
Jiang, H., 273
Jitsuno, T., 327
Joannopoulos, J.D., 114
John, S., 114, 115, 116, 117, 178, 179
Johnson, A., 7
Johnson, S.G., 114
Jones, G.N., 54
Jones, T.B., 269
Joshi, A., 128
Joshi, K.C., 293
Jozsa, R., 177
Julsgaard, B., 178
Justis, N., 276
- K**
- Kaiser, R., 178
Kajari-Schröder, S., 145
Kalosha, I.I., 114
Kamberger, R., 264
Kandpal, H.C., 293
Kang, H., 145
Kang, K., 323
Kanwal, R.P., 15
Kapale, K.T., 141, 143
Karasik, R.I., 177
Kästel, J., 114
Katika, K.M., 19, 32
Kato, M., 326
Kattawar, G.W., 16
Kawamura, M., 276
Keitel, C.H., 114, 121, 122, 123, 124, 125,
 126, 127, 128, 141, 145, 169, 176, 177, 178,
 179, 180
Khadka, U., 121
Khare, S.V., 178
Kiasaleh, K., 328
Kiesel, T., 60
Kiffner, M., 126, 128, 132, 132, 133, 134,
 135, 160, 169, 172, 173, 175, 177
Kilin, S.J., 179
Kim, A.D., 24
Kim, D.-W., 258
Kim, E., 325
Kim, H.-R., 258
Kim, J., 326
Kim, J.B., 135
Kim, K., 135, 322, 323
Kim, K.S., 323
Kim, M., 44, 47, 62
Kim, M.S., 43, 44, 54, 56, 59, 61, 64, 69, 72,
 74, 76, 125
Kim, S.-J., 258
Kim, S.K., 135
Kim, Y.J., 278
Kimble, H.J., 70, 74
Kipfer, P., 244
Kirby, A.K., 276
Kirk, A.G., 323
Kitaeva, G.K., 49
Kitagawa, A., 70
Kivshar, Y.S., 319
Klaus, W., 211
Klein, L., 328
Kleppner, D., 111, 113
Klose, A.D., 19
Klyshko, D.N., 49, 58
Knight, P., 113
Knight, P.L., 44, 54, 56, 97, 113, 114, 121,
 125, 127, 145, 176, 177
Knill, E., 45
Knöll, L., 44, 54
Knollman, G.C., 259
Kobrin, P., 263
Kocharovskaya, O., 124, 125, 179
Kocharovskaya, O.A., 124
Koenderink, A.F., 114
Kofman, A.G., 114, 118, 121, 124
Kohler, T., 141
Kokhanovsky, A.A., 5
Kolb, A., 18
Kolobov, M.I., 179
Kołodziejczyk, A., 202
Komarov, L.I., 121
Kon, A.I., 327
Kong, R., 19
Konigsdorff, R., 22
Kornreich, P.G., 210
Korotkova, O., 300, 301, 302, 307, 312, 323,
 327, 328
Korsunsky, E.A., 145
Kosachiov, D.V., 145
Kotova, S.P., 252
Kourganoff, V., 25, 26
Kovanis, V., 122
Kowal, S.T., 210, 211
Kozhekin, A., 178
Kozlov, V., 179
Král, P., 121, 145

- Kress, B., 213
Kreuter, A., 113
Krstic, P.S., 158
Krüger, O., 43
Krupenkin, T., 265
Kuebel, D., 301
Kuiper, S., 266
Kuittinen, M., 305
Kumar, A., 299
Kumar, P., 19, 58, 158
Kumar, S., 19, 23, 26
Kurizki, G., 43, 70, 114, 118, 176
Kuwano, R., 259
- L**
- Lacis, A.A., 12, 20
Laflamme, R., 45
Lagendijk, A., 114
Lahiri, M., 301, 312
Lai, M.S., 26
Lajunen, H., 322
Lambropoulos, P., 114, 176
Landau, L., 127
Lane, A.S., 125
Larsen, E.W., 19
Lassen, M., 43
Laude, V., 214, 278
Lauder, M.A., 145
Laue, M., 313
Laukien, G., 316
Laurat, J., 44
Laurendeau, N.M., 22
Lawande, S.V., 179
Lax, M., 88
Leader, J.C., 327
Lee, C.C., 261
Lee, C.P., 127
Lee, C.T., 48, 54, 58
Lee, H., 127, 295
Lee, H.S., 27, 28, 29
Lee, J., 59
Lee, L.P., 259
Lee, S.-D., 258
Lee, S.S., 261
Lee, S.W., 261
Lehman, C., 121
Lehmberg, R.H., 87, 327
Leinfellner, N., 145
Leitgeb, R., 7
Lemmer, U., 325
- Lenstra, D., 316
Lenz, G., 176
Leonhardt, U., 78
Lester, G.A., 214
Leuchs, G., 43
Lev, B.I., 61
Levy, U., 260
Lewenstein, M., 176
Lewis, E.E., 27
Lewis, J., 7
Lezama, A., 134
Li, B.X., 21
Li, C.F., 323
Li, F.L., 70, 114
Li, F.-l., 128
Li, G., 214, 217, 227, 234, 240, 277
Li, G.-X., 114, 141, 147, 149
Li, H., 145
Li, L., 138
Li, Y., 295
Liberman, S., 178
Lidar, D.A., 177
Lieberman, S., 176
Lien, V., 259
Lightman, A.P., 7
Lim, M.J., 177
Lin, C.P., 3, 4
Lin, L.-C., 258
Lin, Q., 114, 305
Lin, S.Y., 114
Lin, T.-H., 258
Lin, Y.-C., 248
Lindberg, J., 323
Lindner, F., 133
Liou, K.-N., 12
Liu, C.H., 256, 257
Liu, C.P., 128
Liu, C.-X., 266, 268
Liu, F., 7
Liu, G.L., 259
Liu, L.H., 21, 32, 33
Liu, P., 14, 319
Liu, P.-S., 319
Liu, X., 306, 326
Liu, Y., 313
Lo, Y.H., 259, 276
Lodahl, P., 114
Löffler, M., 124
Lohmann, A.W., 200, 202
Loktev, M., 253
Loktev, M.Y., 252, 253

López, C.A., 261

Lorent, V., 134

Love, G.D., 253, 276, 278

Lowen, H., 200

Lowery, A., 7, 10, 11

Lü, B., 293, 306, 319

Lu, X., 19, 178

Lubin, D.L., 278

Lukin, M.D., 177, 178

Lund, A.P., 56, 69

Lurie, M., 326

Lütckenhaus, N., 132

Lutomirski, R.F., 301

Lvovsky, A.I., 45, 51, 52, 56, 57, 58, 59,
78, 79

M

MacGillivray, J.C., 178

Mach, P., 265

Macovei, M., 126, 127, 141, 169, 176, 178,
179, 180, 181, 182, 183

Macovei, M.A., 96, 141, 143, 179

Mahanta, P., 19

Mahmoudi, M., 145

Maker, P., 214

Makunda, N., 322

Maleev, I.D., 317, 319

Malinovsky, V.S., 145

Manassah, J.T., 100

Mancini, S., 176

Mandel, L., 57, 60, 92, 96, 285, 287n,
293, 326

Mandel, P., 124

Manka, A.S., 125

Manson, N.B., 144

Marangos, J.P., 134

Marasinghe, M.L., 313

Marathay, A.S., 285, 317

Marek, P., 44

Marin, F., 51, 79

Marks, D.L., 326

Marks, R., 259

Marmet, L., 145

Marquardt, C., 43, 44

Martinex-Herrero, R., 323

Martinez, M.A., 145

Martinez, M.A.G., 125

Martinez, T., 276

Martinez-Niconoff, G., 323

Martini, F.D., 113

Martinsson, P., 322

Marzlin, K.-P., 109, 177

Masuda, S., 243, 277

Mataloni, P., 113

Mathine, D.L., 259

Mathur, S.R., 29

Matisov, B.G., 145

McCormick, N.J., 15, 17, 18

McIntire, L.V., 7

McKinney, J.D., 328

McLone, R.R., 100

McManamon, P.F., 214

McOwan, P.W., 214

Meade, R.D., 114

Meduri, K.K., 141

Megens, M., 114

Mehta, A., 158

Mejias, P.M., 323

Menon, S., 141, 145

Mey, P., 213

Meystre, P., 111, 176

Miccio, L., 269

Michel, B., 18

Mie, G., 308

Migdall, A., 49

Mikhailenko, I., 259

Milburn, G.J., 44, 45, 70

Miller, J.G., 13

Miller, J.W.F., 27

Milonni, P.W., 97

Minnema, L., 264

Mira, A., 202

Mironov, V.L., 327

Mishchenko, M.I., 12, 13, 20

Mishra, S.C., 19

Misra, B., 117

Mitra, K., 7, 8, 19, 23, 26

Mitsunaga, M., 158

Miyamoto, Y., 317

Miyanaga, N., 327

Mizrahi, S.S., 48, 61

Mlynek, J., 45, 52, 56

Mobley, J., 13

Modest, M.F., 28, 29

Mogilevtsev, D., 78, 79

Mohanty, P., 178

Moiseiwitsch, B.L., 289n

Mollow, B.R., 42

Molmer, K., 44, 178

Mølmer, K., 114

Moloney, J., 328

Moloney, J.V., 328
 Moon, H.S., 135
 Moran, P.M., 260
 Morawitz, H., 114, 176
 Morigi, G., 145
 Morita, S., 259
 Morokawa, S., 211
 Morris, G.M., 226
 Moscoso, M., 24
 Mossberg, T.W., 141, 178
 Motsek, K., 319
 Mourant, J.R., 2, 3
 Moya-Cessa, H., 42
 Mueller, C.R., 44
 Mukunda, N., 322
 Müller, C., 264
 Muller, H.G., 121
 Muller, R., 214
 Mundrarin, D., 176
 Murao, N., 277
 Murphy, J.A., 324
 Murthy, J.Y., 29

N

Nagai, K., 274
 Nakano, M., 260
 Nakatsuka, M., 327
 Nakayama, Y., 326
 Narayanaswamy, S., 263
 Narducci, F.A., 121
 Narducci, L.M., 125, 126
 Natali, S., 176
 Naumov, A.F., 252, 253
 Navez, P., 43
 Neergaard-Nielsen, J.S., 44, 66, 67, 68, 69
 Nemoto, S., 306, 307, 326
 Nevskaya, G.E., 243
 Nguyen, P.C., 328
 Nha, H., 70
 Nicodemus, F.E., 9
 Nielsen, B.M., 44
 Nielsen, M.A., 177
 Nielsen, T.R., 176
 Niemz, M.H., 2, 3
 Nieto-Vesperinas, M., 6
 Nikolopoulos, G.M., 176
 Nikonorov, D.E., 124
 Niu, Y., 128
 Noel, M.W., 177
 Noguchi, M., 276

Nordin, G.P., 211
 Nose, T., 242, 243, 249, 277
 Nouhi, A., 210
 Novotny, L., 117
 Nugent, K.A., 323
 Nye, J.F., 314, 316

O

Ogasawara, M., 277
 Ogawa, T., 61
 O'Holleran, K., 314
 Ohtaki, S., 277
 Ohzu, H., 278
 Oksanen, J., 48
 Oku, H., 261
 Okubo, R., 79
 Okutucu, T., 19
 Olivares, S., 44, 70, 74
 Opatrný, T., 43, 44, 70
 Oppo, G.-L., 125, 145
 Orrit, M., 158
 Orszag, M., 176, 178
 Osten, W., 326
 Östreich, T., 176
 Ostrovsky, A.S., 323, 324
 Otani, Y., 259
 Ottanello, P., 319
 Ou, N.R., 26
 Ou, Z.Y., 51
 Ouchi, K., 243
 Ourjoumtsev, A., 44, 64, 65, 66, 67, 71, 74

P

Padgett, M.J., 314, 326
 Padovani, C., 322
 Paganin, D.M., 313
 Pal, G., 7, 8
 Palacios, D.M., 317
 Pálffy, A., 178
 Palma, C., 310, 322
 Pan, J.-W., 74
 Pang, L., 260
 Paoletti, D., 319
 Parigi, V., 43, 44, 48, 55, 58, 60, 61, 64, 72,
 74, 76
 Paris, D.P., 202
 Paris, M.G.A., 43, 44, 70, 74, 78
 Park, D., 323
 Park, D.Y., 322

- Park, E., 44, 54
Park, J., 266
Parrent, G.B.Jr., 285
Parthasarathy, G., 27, 28
Pascazio, S., 117, 118
Pask, C., 322
Paspalakis, E., 114, 125, 127, 145
Patankar, S.V., 27, 28, 29
Patel, J.S., 214, 258
Patnaik, A.K., 168, 169
Patterson, M.S., 18
Paturzo, M., 269
Pavolini, D., 178
Pax, P., 111
Pedersen, G.D., 15
Pedersen, H.M., 299, 325
Pedrini, G., 326
Pegg, D.T., 145
Peleg, A., 328
Peng, J.S., 141
Peng, R., 276
Penin, A.N., 49
Peraiah, A., 4
Perina, J., 285
Peseux, J., 266
Peskin, M.E., 8
Petrov, E.P., 114
Petrucelli, J.C., 325
Petruccione, F., 87, 96
Pétursson, P.R., 326
Peyghambarian, N., 217, 234, 240, 259
Peyman, G., 259
Pfeiffer, L.N., 127
Phillips, R.L., 301, 327
Piepmeyer, J.R., 325
Pillet, P., 176, 178
Pilon, L., 19, 32
Plenio, M.B., 43, 125, 141, 176, 177
Polder, D., 132
Polyanskii, P.V., 320
Polynkin, P., 127, 328
Polzik, E.S., 44, 178
Pomraning, G.C., 4, 7, 20
Ponomarenko, S., 301
Ponomarenko, S.A., 293, 322, 327, 328
Popescu, G., 307
Powell, N.J., 214
Power, E.A., 91, 100
Prahl, S.A., 17, 325
Prasad, P.N., 2
Premaratne, E., 7, 10, 11
Premaratne, M., 7, 10, 11, 19, 24, 25, 313
Presnyakov, V.V., 254
Press, W.H., 29, 30
Prieto, P.M., 278
Prins, N.W.J., 265
Prior, Y., 141
Protopapas, M., 121
Psaltis, D., 214
Pu, J., 302, 306, 307, 308, 326, 328
Pukhov, A., 178
Purcell, E.M., 111, 113
Puri, R.R., 142, 178, 179, 180, 182
Purvis, A., 214
- ## Q
- Qiao, W., 276
Quang, T., 114, 115, 116, 117, 125, 178, 179
Quarteroni, A., 24
Quiney, H.M., 323
- ## R
- Raab, C., 114
Radeonychev, Y.V., 124
Radunsky, A., 313
Raff, M., 7
Raimond, J.M., 113
Raithby, G.D., 27, 29
Ralph, T.C., 44, 56, 69, 70
Ralston, T.S., 326
Ramazza, P.L., 51, 79
Ramírez, R., 178
Ramirez-San-Juan, J.C., 323
Rastani, K., 214, 258
Rath, P., 19
Rawicz, A.H., 259
Raymer, M.G., 79, 106
Rege, S.S., 202
Rehacek, J., 78, 79
Reichelt, S., 264
Reinhardt, J., 8
Ren, H., 214, 243, 250, 251, 254, 255,
 260, 261, 271, 272
Ren, J.-R., 319
Resasco, D.C., 24
Resler, D.P., 214
Retamal, J.C., 178
Reynaud, S., 52, 179
Reynolds, L.O., 15, 17, 18
Reza, S., 277

- Rhoadarmer, T., 328
Richter, T., 58, 59, 60
Ricklin, J.C., 327
Riechert, F., 325
Rinkel, P.D., 264
Rinkleff, R.-H., 134
Riskin, H., 78
Ritsch, H., 59, 178
Ritsch-Marte, M., 203
Riza, N.A., 211, 277
Roberts, K., 7
Rodriguez-Solid, M.V., 324
Rohlfing, U., 325
Rombach, M.C., 202
Rong, J., 319
Rostovtsev, Y., 179
Rotge, J.R., 278
Rothenberg, J.E., 327
Roy, A.K., 14, 15
Roychowdhury, H., 294, 295, 301, 313
Rozhdestvensky, Y.V., 145
Ru, P., 125
Rudolph, T.G., 176
Rukolaine, S.A., 32
Rybicki, G.B., 7
Rydberg, C., 325
- S**
- Saastamoinen, T., 305
Saavedra, C., 178
Sacchi, M.F., 58, 78
Sadat, H., 21
Saffman, M., 178
Saha, U.K., 19
Sakami, M., 19
Sakami, S., 19
Sakurai, J.J., 166
Salem, M., 300, 301, 308, 324, 327
Samagin, S.A., 254
Samba, G., 20
Samblowski, A., 43
Samuels, C., 125
San, K.-C., 19
San, K.-Y., 7
Sanders, B.C., 109, 176, 177
Santarsiero, M., 293, 295, 310, 322, 323
Sasaki, M., 44, 66, 68, 70
Sasse, C., 22
Saterbak, A., 7
Sato, R., 208, 208, 242, 243, 244, 245, 246, 247, 249, 250, 251, 256, 276, 277
Savedoff, M., 312
Sawetprawichkul, A., 19
Saxena, K., 293
Scharf, T., 243, 244
Scheel, S., 43
Scheibner, M., 178
Schell, A.C., 298
Schiller, S., 45, 51, 52, 56
Schmid, S.I., 134, 171
Schmidt, H., 127, 138
Schmidt-Kaler, F., 114
Schmiedmayer, J., 74
Schmit, J., 320
Schnabel, R., 43
Schneider, F., 264
Schoonover, R.W., 316, 319, 323, 324, 325
Schotland, J.C., 324, 325
Schouten, H.F., 285, 293, 295, 316, 319
Schriemer, H.P., 114
Schroeder, D.V., 8
Schulman, L.S., 118
Schulz, T.J., 328
Schumacher, D.W., 121
Schuman, J.S., 3, 4
Schuster, A., 21
Schuurmans, M.F.H., 132
Schwan, H.P., 7
Schwartz, C., 324
Schwarzmaier, H.-J., 6, 17, 18
Schweitzer, D., 18
Schwiegerling, J., 259
Scully, M., 179
Scully, M.O., 96, 112, 118, 124, 125, 126, 127, 131, 141, 145, 177, 178, 179
Seabury, C., 263
Selcuk, N., 29
Selc-uk, N., 29
Sellin, P.B., 141
Semenov, A.A., 61
Semiao, V., 14
Setälä, T., 322
Shabani, A., 177
Shahriar, M.S., 145
Shanks, J.G., 17
Shapiro, J.H., 57, 58, 59
Shapiro, M., 121
Sharma, M.P., 122
Sharma, S.K., 14, 15
Sharp, R.C., 214

- Shaw, D., 264
Sherman, B., 114
Shi, J., 262
Shih, M.-F., 319
Shirai, T., 299, 301, 312, 324, 326, 327
Shpaisman, H., 145
Shumovsky, A.S., 179
Shvets, G., 178
Siena, S.D., 43
Silverman, R.A., 311
Simon, R., 322
Simonov, A.N., 202, 253
Sinha, S.K., 314
Sirtori, C., 127
Skornia, C., 176
Skribanowitz, N., 178
Slinger, C., 214
Smith, A.M., 111, 177
Smith, G., 214
Sobolev, V.V., 20
Sola, I.R., 145
Solem, J.C., 178
Somalingam, S., 277
Somerford, D.J., 14, 15
Sommerfeld, A., 314
Son, W., 56
Sörensen, J.L., 70
Soskin, M.S., 314, 320
Souza, L.A.M., 43
Spanier, J., 19, 20
Spani Molella, L., 134
Spitz, F., 207
Spivey, B., 202
Spohn, H., 98
Springer, S.C., 59
Srinivas, M.D., 42, 61
Stacey, A., 322
Stallinga, S., 277
Stamnes, J.J., 299, 302, 306, 325
Stamnes, K., 21
Stapert, H., 277
Starikov, A., 321, 322, 323
Stegun, I.A., 25
Steven, S.-C., 262
Stinson, W.G., 3, 4
Stoicheff, B.P., 145
Stokes, G.G., 300
Stratton, Z., 262
Stroud, C.R.Jr., 101, 106
Strudwick, A.M., 214
Sudarshan, E.C.G., 57, 117
Sugiura, N., 259
Sugiyama, A., 208
Sultana, S., 141
Sun, T.E., 264
Sun, Y., 211
Sun, Z., 141
Sundar, K., 322
Sung, D., 322
Süssmann, G., 179
Suzuki, S., 43, 69
Suzuki, T., 326
Svaasand, L.O., 20
Svidzinsky, A.A., 178
Swain, S., 87, 101, 111, 125, 127, 129, 130,
 134, 145, 156, 157, 159, 176
Swanson, E.A., 3, 4
Swartzlander, G.A., 317, 319, 320
- T**
- Taichenachev, A.V., 134, 135, 136, 137
Takahashi, H., 43, 44, 66, 68, 69, 246, 278
Takahashi, S., 277
Takahashi, T., 246
Takaki, Y., 278
Takeda, M., 317, 319
Takeoka, M., 43, 44, 69, 70
Tam, E.C., 276
Tan, J.Y., 21
Tan, Z.-M., 19
Tanaś, R., 96, 156, 159, 176, 177
Tanev, S., 2, 3
tang Tan, H., 132
Tara, K., 42, 44, 49, 54, 59
Tatarkova, S.A., 276
Tatarskii, V.I., 327
Taylor, L.S., 327
Tearney, B.J., 7, 8
ter Vehn, J.M., 178
Tervo, J., 323
Teukolsky, S.A., 29, 30
Thamm, E., 18
Thanopoulos, I., 121
Thirunamachandran, T., 100
Thomas, G.E., 21
Thomas, J.E., 113, 178
Thompson, R.C., 177
Titulaer, U.M., 57, 60
Tkaczyk, T.S., 202
Tokunaga, T., 259
Tolan, M., 314

- Tolosa, A., 276
 Tork, A., 254
 Török, P., 308
 Tran, C.Q., 323
 Travis, L.D., 12, 20
 Tredicce, J.R., 125
 Trippenbach, M., 97, 111, 176
 Troup, G.J., 285
 Tsai, F.S., 276
 Tschudi, T., 326
 Tsubakimoto, K., 327
 Tualle-Brouri, R., 42, 44
 Tuchin, V., 3
 Tuchin, V.V., 2, 3, 5
 Tulkki, J., 48
 Tumaikin, A.M., 135
 Turchette, Q.A., 176
 Turner, T.S., 328
 Turunen, J., 299, 304, 305, 312, 323
 Tyo, J.S., 328
- U**
- Ueda, M., 61
 Ujihara, K., 98
 Ulyanenkov, A., 121
 Umeda, N., 259
 Urbatsch, T.J., 19
 Usuga, M.A., 44
- V**
- Vahimaa, P., 305, 323
 Vaishya, J.S., 293
 Valente, P., 134
 Valley, P., 217, 234
 van Cittert, P.H., 287, 299
 van de Hulst, H.C., 6
 van Dijk, T., 306, 307, 308, 313, 319, 326
 van Driel, H.M., 114
 van Gemert, M.J.C., 3, 4, 6, 26
 van Loock, P., 43, 56
 Varada, G.V., 156, 176
 Varahramyan, K., 259
 Vasara, A., 299
 Vasilyev, M.G., 32
 Vasnetsov, M.V., 314
 Vasylyev, D.Y., 61
 Vdovin, G., 202, 252, 253
 Vdovin, G. V., 252
- Verdet, E., 287
 Verheijen, H.J.J., 265
 Versteegen, E., 277
 Vespiini, V., 269
 Vetri, G., 126
 Vetterling, W.T., 29, 30
 Vewinger, F., 79
 Viciani, S., 43, 44, 45, 48, 50, 51, 52, 53,
 55, 57
 Vidal, G., 59, 72
 Visser, T.D., 285, 293, 295, 299, 300, 301,
 305, 306, 307, 311, 313, 316, 317, 319, 326
 Vitanov, N.V., 114
 Vladimirov, F.L., 253
 Vo-Dinh, T., 7, 8
 Voelz, D., 325, 328
 Voelz, D.G., 325
 Vogel, K., 78
 Vogel, W., 42, 54, 57, 58, 59, 60, 61
 von Zanthier, J., 176
 Vos, W.L., 114
 Vrehen, J.J., 277
 Vuletić, V., 178
- W**
- Waibel, P., 264
 Wakui, K., 43, 44, 66, 68, 69
 Walker, T.G., 178
 Wallrabe, U., 264
 Walls, D.F., 125
 Wals, J., 277
 Walther, H., 118, 176
 Wang, B., 211, 245, 246, 247, 249, 250,
 251, 276
 Wang, D.-Z., 141
 Wang, F., 307
 Wang, G., 319
 Wang, J., 116, 138
 Wang, L., 293, 326
 Wang, T., 306, 328
 Wang, W., 259, 304, 306, 317, 319
 Wang, X., 214, 308
 Wang, Z., 141, 264
 Washizu, M., 269
 Waters, K.R., 13
 Weaver, J.L., 259
 Webb, K.J., 328
 Webb, R.H., 3
 Webster, M.A., 328

Wei, C., 144
 Wei, H., 323
 Weihe, F., 121
 Weiner, A.M., 328
 Weisbuch, C., 114
 Weisskopf, V., 112
 Welch, A.J., 3, 4, 6, 26
 Wells, J.C., 158
 Welsch, D.-G., 43, 44, 54, 59, 70
 Welters, W.J.J., 265
 Wenger, J., 42, 44, 64, 70
 Werber, A., 264
 Werner, E., 176
 Werner, R.F., 43, 59, 72
 West, K.W., 127
 Whaley, K.B., 177
 Whitesides, G.M., 265
 Wiart, J., 324
 Wick, D.V., 276
 Wieman, C., 110
 Wigner, E., 112
 Wijnhoven, J.E.G.J., 114
 Wild, U.P., 158
 Williams, D.C., 202
 Williams, G., 214
 Wilson, B.C., 18
 Wilson, C.B., 2, 3
 Wilson, D., 214
 Wilson, G.A., 141
 Wilson-Gordon, A.D., 128, 145
 Wiltshire, M.C.K., 214
 Windholz, L., 145
 Winn, J.N., 114
 Wiseman, H.M., 138
 Withington, S., 322, 324
 Wittmann, C., 44
 Woldeyohannes, M., 114
 Wolf, E., 5, 6, 10, 92, 96, 206, 223, 285, 286,
 287, 287n, 289, 290, 291n, 293, 294, 295,
 298, 299, 300, 301, 302, 303, 304, 305,
 306, 307, 308, 310, 311, 312, 313, 316, 317,
 319, 320, 321, 322, 324, 326, 327, 328
 Wolf, M.M., 43
 Woolley, R.G., 91
 Wu, B., 251, 260
 Wu, C.-Y., 18, 19, 26
 Wu, J., 327
 Wu, S.-H., 18, 19
 Wu, S.-T., 203, 214, 243, 250, 251, 254, 255,
 260, 261, 271, 272

X

Xia, H.-R., 137, 138
 xiang Li, G., 132
 Xianyu, H., 271
 Xiao, M., 121, 128
 Xiao, X., 325
 xing Xia, H., 132
 Xu, J., 149
 Xu, J.-P., 114
 Xu, S., 261, 271, 272
 Xu, Y., 264
 Xu, Z.Z., 128
 Xue, X., 323

Y

Yablonovitch, E., 114
 Yan, H., 276
 Yan, Y., 319
 Yanait, Y.A., 49
 Yanase, S., 243
 Yang, D.-K., 203
 Yang, H., 274, 319
 Yang, Q., 263
 Yang, S., 265
 Yang, W.G., 128
 Yang, X., 141
 Yang, Y., 70, 114, 149
 Yang, Y.P., 114
 Yannopapas, V., 114, 149
 Yaroslavsky, A.N., 6, 17, 18
 Yaroslavsky, I.V., 6, 17, 18
 Ye, C.-Y., 138
 Ye, M., 243, 244, 245, 246, 247, 248, 249,
 250, 251, 255, 257, 276, 277
 Yeh, J.A., 256, 257, 270, 271
 Yelin, S.F., 178
 Yener, Y., 19
 Yeo, L., 19, 24, 25
 Yin, Y.-Y., 121
 Yokoyama, Y., 256
 Yoo, K.M., 7
 Yoon, G., 17
 Youn, S.H., 79
 Young, T., 291
 Yu, C.-J., 258
 Yu, M.L., 252
 Yu, Y., 260
 Yuan, Z.-S., 74

- Yudin, V.I., 135
Yuferev, V.S., 32
Yun, S.H., 7, 8
Yura, H.T., 301, 327
- Z**
- Zadkov, V.N., 159, 160, 176, 177
Zanardi, P., 177
Zang, T.A., 24
Zappe, H., 264
Zavatta, A., 42, 43, 44, 45, 48, 50, 51, 52,
 53, 55, 57, 58, 60, 61, 64, 72, 74, 76, 79
Zemliak, A.M., 323
Zeng, X., 273
Zernike, F., 287, 291, 299
Zhang, A.N., 79
Zhang, B., 306
Zhang, D.Y., 259, 276
Zhang, H., 307
Zhang, J., 145
Zhang, S., 141
Zhang, X., 253
- Zhang, Y., 79, 121
Zhang, Z., 308
Zhao, B., 74
Zhao, D., 312
Zhao, X.-W., 274
Zhao, Y., 264
Zheng, H., 114, 121
Zhou, L., 147
Zhou, P., 125, 127, 149, 150
Zhu, C., 276
Zhu, S., 149
Zhu, S.-Y., 114, 121, 125, 127, 128, 138,
 143, 145
Zhu, T., 319
Zhu, Y., 145
Zhuang, S., 276
Zienau, S., 91
Zoller, P., 110, 132, 176, 178
Zubairy, M.S., 96, 112, 114, 121, 131, 141,
 143, 145, 177, 298
Zumofen, G., 158
Zwanzig, R., 92
Zysk, A.M., 324, 325

SUBJECT INDEX FOR VOLUME 55

Page numbers followed by "f" indicates figures and "t" indicates tables.

- Aberration correction, 277–278
- Adaptive liquid crystal lens
 - application of
 - aberration correction, 277–278
 - correction of presbyopia, 274–276
 - zoom lens, optical tweezer, and biomedical imaging, 276–277
 - diffractive liquid crystal lens
 - binary/grayscale photolithography technology, 213
 - construction of, 213, 213*f*
 - diffraction efficiency, 214, 221, 222*f*, 230, 236
 - double-element lens, 226
 - fabrication procedure, 218, 220*f*
 - Fresnel diffraction integral, 215
 - Fresnel zone pattern, 211
 - illustration of, 212, 212*f*
 - individually addressable electrodes, 240, 240*f*
 - interferogram, 223, 224*f*
 - interleaved electrode pattern, fabrication procedure, 229, 230*f*
 - Mach-Zehnder interferometer, 222, 223*f*
 - one-layer electrode pattern, 218, 219*f*, 227
 - ophthalmic application, disadvantages, 240
 - ophthalmic lens, 214
 - patterned electrodes, 228
 - phase map, 224, 225*f*
 - phase-shift interferometer, 237
 - polarized optical microscope, 220, 220*f*
 - quantization error, 228
 - scalar diffraction theory, 221
 - switchable LC diffractive lens, 228, 229*f*
 - three-layer patterned electrodes, 235, 235*f*
 - lens using polymer/liquid crystal composites, 254–255
 - liquid crystal cell
 - Freedericksz transition, 205
 - nematic cells, 203
 - nematic phase, 203, 204*f*
 - liquid crystal lens, 207–208, 207*f*
 - formation, 249–252
 - hole-patterned electrode, 244–259
 - polarization-independent, 258
 - microlens
 - formation, 256*f*
 - with hybrid alignment, 256–258
 - MLCLs on resistive electrode, 252–254
 - refractive liquid crystal lens
 - discrete isolated electrodes, 210
 - hybrid electrode, 211
 - phase retardation, 208
 - refractive index, 208
 - transmission function, 209
 - Adaptive liquid lens
 - application of
 - aberration correction, 277–278
 - correction of presbyopia, 274–276
 - zoom lens, optical tweezer, and biomedical imaging, 276–277
 - electrowetting effect, 264–269
 - application of, 265
 - fluid-membrane interaction, 259–264
 - microlenses based on
 - dielectrophoretic effect, 268–273
 - hydrogel and therma effect, 273–274
 - Adaptive modal LC lens, 277
 - Alvarez-Lohmann lenses, 200, 201*f*
 - Angular correlation function, 304
 - Angular dependence of dipole-dipole interaction, 177

- Annihilation operator, 42
 —sequences of creation and, 72–73
 Arbitrary light states, photon subtraction from, 61–64
 Artificial quantum systems, 128, 138
 Assembled adaptive eyewear, prototype of, 274, 275*f*, 276*f*
 Atomic Hamiltonian, 152
 —separation vector, rotations of, 173–175
 —subsystem, 87, 88, 92, 93
 —transition frequency, 113, 116, 121
 Avalanche on–off photodiode (APD), 65
 Azodyes, 258
- Back-scatter fraction, 23
 Beam coherence–polarization matrix approach, 293
 —wander model, 317
 —splitter (BS) operator, 46, 67
 Biomedical imaging, 276
 Blue light-induced infrared absorption (BLIIRA), 68
 Born approximation, 93, 94, 99, 109
 —Markov approximation, 98
 Bessel beams, 299
- Cartesian coordinates system, 20, 21*f*
 Characteristic curves, 30
 —method, 30–32
 Closed-loop systems, 145
 Coherence functions, phase singularities of, 314–320
 —singularity, 293
 —theory, direct applications of, 326–328
 Coherent beam
 —partially, evolution of, 296–302
 —pseudo partially, 328
 —mode representation, 289, 320–324
 —states, single-photon addition, 49–53
 Collective ground-state population, 182*f*
 —system, quantum dynamics of, 150
 Compact liquid lens, 262*f*
 Confocal laser scanning fluorescence microscopy, 277
 Continuous-variable (CV) quantum state engineering, 43–44
 Control voltage, 253
 Correlation vortices, 317
 —induced spectral changes, 286
- Cross-coupling, orthogonal dipole transitions, 167–173
 —spectral density, 288, 289
 —function, 287, 290
- Debye integral, 302–304
 Decoherence-free subspaces (DFSs), 177
 Deformable liquid crystal droplet lens, 270*f*
 De-Gaussification of squeezed states, 64–69
 Density matrix elements
 —reconstructed Wigner functions and, 53, 63*f*, 69*f*
 —for SPACSSs, 50, 53*f*
 Deterministic methods, 19
 Dicke limit, 155
 Dielectric liquid lens, 271–273, 271*f*
 —using spherical electrode, 273*f*
 —two flat electrodes, 271*f*
 Dielectrophoretic effect, adaptive liquid microlens, 268–273
 Diffraction tomography, theory of, 311
 Diffractive liquid crystal lens
 —binary/grayscale photolithography technology, 213
 —construction of, 213, 213*f*
 Diffraction efficiency, 214, 221, 222*f*, 230, 236
 —double-element lens, 226
 —fabrication procedure, 218, 220*f*
 —Fresnel diffraction integral, 215
 —zone pattern, 211
 —illustration of, 212, 212*f*
 —individually addressable electrodes, 240, 240*f*
 —interferogram, 223, 224*f*
 —interleaved electrode pattern, fabrication procedure, 229, 230*f*
 —Mach–Zehnder interferometer, 222, 223*f*
 —one-layer electrode pattern, 218, 219*f*, 227
 —ophthalmic application, disadvantages, 240
 —lens, 214
 —patterned electrodes, 228
 —phase map, 224, 225*f*
 —phase-shift interferometer, 237
 —polarized optical microscope, 220, 220*f*

- quantization error, 228
- scalar diffraction theory, 221
- switchable LC diffractive lens, 228, 229^f
- three-layer patterned electrodes, 235, 235^f
- Dipole–dipole interaction, 86, 103, 105, 109–110, 131, 150
- beyond two-level approximation, 160
- coherent part of, 153
- effective level scheme of, 157^f
- experimental verification
- level shift measurement, 155–158
- modified spontaneous emission measurement, 158–160
- few-level approximation in, 171–173
- geometrical considerations, 162–166
- impact of, 175–177
- multiparticle quantum dynamics, 177–183
- observation of, 159^f
- pair of identical two-level atoms, 151–155, 151^f
- Dipole-forbidden transition, 121, 123
- Discrete isolated electrodes, 210
- Double concave (DCV) lens, 260
- convex (DCX) lens, 259

- EIA, *see* Electromagnetically induced absorption
- EIT, *see* Electromagnetically induced transparency
- Electric cross-spectral density matrix, 293
- Electric-dipole coupling, 91, 105, 109
- moment operator, 166
- Electromagnetic solenoid, 261
- vacuum field, 86, 112
- Electromagnetically induced absorption (EIA), 134, 135
- induced transparency (EIT), 134
- Electro-optical response, 254
- Electrowetting
 - effect, adaptive liquid lens, 264–268
 - experiment, 265^f
 - lenses, 268
- Elementary source model, 323
- Entanglement potential (EP) of SPATSSs, 56, 59
- Extended Huygens–Fresnel principle, 301

- Few-level approximation in dipole–dipole interaction, 171–173
- Fibre coupler, 74
- Field-of-view (FOV), 259
- Finite volume method, 26–29
- First-order perturbation theory, 46
- Richter–Vogel (RV) criterion, 58
- Fluid-membrane interaction, adaptive liquid lens, 259–264
- Fluorescence, 5
- Fock states, 49, 50
- P*-function of single-photon, 57
- Fredericksz transition, 205
- Frequency domain methods, 7, 8
- Fresnel zone pattern, 211

- Gaussian beam, 328
- Gaussian quadrature-entangled light pulses, 71
- Schell-model, 305, 306, 322
- application of, 327
- beams, 295
- sources, 298
- spatial intensity distribution, 254
- Gaussian states, quantum information with, 43
- Wigner function, 43
- General reservoir theory, 92–94
- Generalized Debye integral, 304
- Glauber–Sudarshan *P*-function, 57

- Helmholtz equations, 288, 296
- Henyey–Greenstein phase function, 6, 15–17
- Hilbert–Schmidt kernel, 289
- Hilbert-space method, 327
- Homodyne detection, 53, 66, 67, 77
- Huygens–Fresnel principle, 301, 302
- Hybrid alignment, LC microlens with, 256–258
- Hybrid electrode, 211
- methods, 19–21

- Incoherent pump processes, 141–143
- In-situ photopolymerization, 254
- Interaction Hamiltonian, 90, 91, 92, 93, 98, 103
- Interferometric technique, low-coherence, 326
- Inverse scattering techniques, 312

- Kelvin theory, 270

- Laguerre Runge–Kutta–Fehlberg (LRKF)
—method, 19, 24
- Lamb shift, 101, 103, 113, 131
- Laser
—applications, 3
—beams, 326
—induced interstitial thermotherapy (LITT), 2
- Laser-manipulation system, 277
- LC lens, *see* Liquid crystal lens
- Light scattering
—classification of, 5–6
—phosphorescence, 5
—quantitative modeling, 6–8
—resonance scattering, 5
- Liquid crystal (LC) cell
—Fredericksz transition, 205
—nematic cells, 203
—phase, 203, 204^f
- Liquid crystal (LC) lens, 207–208, 207^f
—formation, 249–252
—hole-patterned electrode, 244–249,
 244^f–248^f
—lens using polymer, 254–255
—polarization-independent, 258
—polymer-dispersed, 255
—polymer-stabilized, 254
- Liquid crystal (LC) microlens
—formation, 256^f
—with hybrid alignment, 256–258
—lenses, aberrations of, 264
- Liquid microlens, hydrogel and thermal effect, 273–274
- pressure varifocus lens, principle of, 260^f
—based variable lens, 267^f
- LITT, *see* Laser-induced interstitial thermotherapy
- Liu phase function, 14–15
- Low-coherence interferometric technique, 326
- Low-frequency field (LFF) photon, 122, 123
- LRKF method, *see* Laguerre Runge–Kutta–Fehlberg method
- Mach–Zehnder interferometer, 222, 223^f
- Markov approximation, 96, 97, 117
- Mathematical model, 87–88
- Maxwell’s equations, 7
- Mercer’s theorem, 289
- Method of lines (MOL), 29
- Microfluidic device, 260
- Micro-zoom arrays, 276
- Mie scattering, 313
- Modal liquid crystal lens (MLCLs) on resistive electrode, 252–254
- Modified spontaneous emission, measurement of, 158–160
- MOL, *see* Method of lines
- Monte Carlo methods, 325
- Multiatom, multilevel system, 88–92
—derivation of master equation for, 94–105
- Multi-flux and two-flux methods, 21–23
- Multiparticle quantum dynamics, 177–183
- Multiphoton pathway interference, 121–124
- Nakajima–Zwanzig equation, 93
- Nematic LC cells, 203
- Nonclassical light, 56
- Nondiffracting, 299
- Non-Gaussian states, 43
- Nonuniform electric fields, 268
- Numerical methods
—Cartesian coordinates system, 20, 21^f
—characteristics method, 30–32
—deterministic methods, 19
—finite volume method, 26–29
—hybrid methods, 19–21
—MOL, 29
—spectral methods, 24–26
—stochastic/probabilistic methods, 19
—time shift and superposition method, 32–33
—two-flux and multi-flux methods, 21–23
- OCT, *see* Optical coherence tomography
- On–off photodetector, 51, 74, 79
- OPA, *see* Optical parametric amplifier
- OPOs, *see* Optical parametric oscillators
- Optical coherence theory, 287
—tomography (OCT), 3, 326
—speckle reduction in, 326
- fields, transient characteristics of, 4
- parametric amplifier (OPA), 67, 71
- parametric oscillators (OPOs), 66, 68
- vortices, 315
- zoom lens, 276

- Optically addressable modal LC lens, 253
 Orthogonal dipole transitions,
 cross-coupling, 167–173
- Parametric down-conversion (PDC), 45
 —mechanical model, 264
 Para-terphenyl crystal, 155
 Partially coherent beams, evolution of,
 296–302
 —coherent fields
 —numerical simulation of, 324–325
 —spectral interference law for, 292
 —in Young’s experiment, 291–295
 Partially coherent wave fields
 —focusing of, 302–308
 —scattering of, 308–314
 Pattern functions, 78
 PDC, *see* Parametric down-conversion
 PDMS membrane, 261
 Perturbation theory, 46, 165
P-function
 —reconstruction of, 60, 60^f
 —of single-photon Fock states, 57
 Phase singularities of coherence
 functions, 314–320
 Phosphorescence, 5
 Photoconducting layer, 253
 Photodynamic therapy, 2
 Photon subtraction
 —from arbitrary light states, 61–64
 —quantum processes of, 43
 —transport equation (PTE), 4
 —radiance
 —spectral radiance, 9
 —transport equation, 10–11
 —scattering phase function
 —Henyey–Greenstein phase function,
 15–17
 —Liu phase function, 14–15
 —probability density function, 12
 —Rayleigh phase function, 13–14
 —Reynolds–McCormick phase
 function, 17–18
 Photon transport theory, 7
 Photon-atom bound states, 114
 —band gap medium, 114
 Photon-number distribution, 58
 —subtracted squeezed vacuum states,
 68
 Pinned-contact oscillating liquid lens,
 261
- Planar liquid lens, design, 268, 269^f
 Plano-concave LC lens, 207, 207^f,
 208, 250^f
 Plano-convex LC lens, 207, 207^f, 208
 —convex lens, 262^f
 Polarization-independent LC lens, 258
 Polarized optical microscope, 220,
 220^f
- Polymer-dispersed liquid crystal
 (PDLC), 255
 —stabilized liquid crystal
 (PSLC), 254
 —fabrication, 254^f
 Potassium niobate (KNbO_3) crystals,
 67, 68
 Presbyopia, correction of, 274–276
 Probability density function, 12
 Pseudo partially coherent beam, 328
 PTE, *see* Photon transport equation
- QD, *see* Quantum dot
 Quadrature distributions, 73^f, 78
 —measured, 63
 —nonclassicality test based on, 57
 Quantitative modeling, 6–8
 Quantum anti-Zeno effect, 117–121
 —dot (QD), 138, 139^f
 —dynamics, multiparticle, 177–183
 —information
 —protocols, 43
 —theory, 177
 —interference, 134, 145, 148, 149^f
 —light state, nonclassicality of, 56–61
 —operators, 43
 —superpositions of, 73–76
 —processes, photon addition and
 subtraction, 43
 —tomography, 77–79
 —Zeno effect, 117–121
 Quasi-homogeneous approximation,
 298
- Rabi frequencies, 180
 Radiance, 8
 —spectral, 9
 —transport equation, 10–11
 Radiatively coupled multilevel systems
 —master equation for, 105–111
 Rapid data acquisition, 277
 Ray-based propagation method, 325
 Rayleigh phase function, 13–14

- Refractive liquid crystal lens
 —discrete isolated electrodes, 210
 —hybrid electrode, 211
 —phase retardation, 208
 —refractive index, 208
 —transmission function, 209
 Resistive electrode, MLCLs based on, 252–254
 Resonance fluorescence spectrum, 125–127, 132, 133*f*
 Resonance scattering, 5
 Reynolds–McCormick phase function, 17–18
 Richter–Vogel (RV) criterion, 58
 Rotating ground glass disk (RD), 54, 62
 Rotating-wave approximation (RWA), 98, 110
 RWA, *see* Rotating-wave approximation
 Rydberg atoms, 113, 177
- Scattering
 —of partially coherent wave fields, 308–314
 —phase function
 ——Henley–Greenstein phase function, 15–17
 ——Liu phase function, 14–15
 ——probability density function, 12
 ——Rayleigh phase function, 13–14
 ——Reynolds–McCormick phase function, 17–18
 Schell-model vortex beams, 319
 Schrödinger equation, 115
 Schrödinger’s cat paradox, 68
 —kittens, generation of, 64–69
 Scintillation reduction, 328
 SE, *see* Spontaneous emission
 Second-order perturbation theory, 165
 Single-photon addition, 42, 75*f*
 —coherent states, 49–53
 —experimental apparatus for, 52*f*
 —experimental, unified treatment of, 44–48
 —tests of nonclassicality, 56–61
 ——operators
 —for manipulating quantum information, 43–48
 —sequences and superpositions of, 72–76
 ——subtraction, 75*f*
 —from arbitrary light states, 61–64
 —de-Gaussification of squeezed states, 64–69
 —increasing entanglement and nonlocality by, 69–72
 —sequence of, 63
 —unified treatment of experimental, 44–48
 ——added coherent state (SPACS), 49–53
 —density matrix elements for, 50, 53*f*
 ——added thermal state (SPATSS), 53–56
 Space-frequency representation, 287–290
 SPACS, *see* Single-photon-added coherent state
 Spatio-temporal realizations, 325
 SPATSS, *see* Single-photon-added thermal state
 Speckle reduction, 327
 —in OCT, 326
 Spectral interference law, 293
 —for partially coherent fields, 292
 Spectral methods, 24–26
 —radiance, 9
 Spherical aberration, LC lens, 277
 Spontaneous decay
 —dynamic control of, 117, 118*f*
 —dressed-state level crossing, 124–125
 —multiphoton pathway interference, 121–124
 —quantum anti-Zeno effect, 117–121
 —quantum Zeno effect, 117–121
 —single-particle, 112
 —suppression of, 120, 121
 —surrounding vacuum modes, modifying, 114
 Spontaneous decay-induced coherences, 127–128
 —experimental evidence, 137–140
 —induced by coherent fields, 144–147
 —induced by incoherent driving, 140–144
 —via breaking symmetry, 147–150
 — $J = 1/2$ — $J = 1/2$ scheme, 131–134
 —N-type scheme, 134–137
 —three-level systems, 128–131, 129*f*
 Spontaneous emission (SE), 86, 111, 176
 —control of, 112
 —with incoherent pump processes, 141–143
 —measurement of, 158–160
 —phase control of, 145, 146*f*

- spectral control of, 125–127
- spectrum, 117, 141, 144*f*
- vacuum mode density modification, 113–117
- Spontaneous emission rate in single mode cavity, 113
- parametric down-conversion (SPDC), 51
- Spontaneously generated coherences (SGC), 111, 131, 132, 140
- in quantum dots, 139*f*
- Squeezed vacuum state, 65
- Starfleet Tricorder device, 2, 2*f*
- Static optical fields, 4
- Stochastic/probabilistic methods, 19
- Strongly scattering media, 6
- Superposition method and time shift, 32–33
- Surface resistance, 252

- Time shift and superposition method, 32–33
- Tomography, variable coherence, 312
- Transition dipole moments, 128, 135
- Tunable liquid microlens, 266*f*
- using immiscible liquids, 267*f*
- Two-flux and multi-flux methods, 21–23
- Two-level atoms, dipole-dipole interaction in, 151–155, 151*f*

- Unified theory of coherence and polarization, 286

- Vacuum state, radiation field in, 152
- Vacuum-induced coherences, 168–169
- processes in single multilevel atoms, 111–112
- Vacuum-mediated coupling, 131
- Variable coherence tomography, 312, 328

- Weakly scattering media, 6
- Wigner function, 78
 - and density matrix elements, 53
 - Gaussian, 43
 - of original thermal state, 77*f*
 - for SPACS, 50
 - for SPATSS, 54
- Wigner–Eckart theorem, 166
- Wigner–Weisskopf approximation, 115, 147

- Young–Laplace equation, 265
- Young’s experiment, partially coherent fields in, 291–295
- two-pinhole experiment, 315

- Zeeman splitting, 87, 165, 166
- Zero-phonon transition, 155, 156

This page intentionally left blank

CONTENTS OF PREVIOUS VOLUMES[☆]

VOLUME 1 (1961)

1	The modern development of Hamiltonian optics, <i>R.J. Pegis</i>	1–29
2	Wave optics and geometrical optics in optical design, <i>K. Miyamoto</i>	31–66
3	The intensity distribution and total illumination of aberration-free diffraction images, <i>R. Barakat</i>	67–108
4	Light and information, <i>D. Gabor</i>	109–153
5	On basic analogies and principal differences between optical and electronic information, <i>H. Wolter</i>	155–210
6	Interference color, <i>H. Kubota</i>	211–251
7	Dynamic characteristics of visual processes, <i>A. Fiorentini</i>	253–288
8	Modern alignment devices, <i>A.C.S. Van Heel</i>	289–329

VOLUME 2 (1963)

1	Ruling, testing and use of optical gratings for high-resolution spectroscopy, <i>G.W. Stroke</i>	1–72
2	The metrological applications of diffraction gratings, <i>J.M. Burch</i>	73–108
3	Diffusion through non-uniform media, <i>R.G. Giovanelli</i>	109–129
4	Correction of optical images by compensation of aberrations and by spatial frequency filtering, <i>J. Tsujuchi</i>	131–180
5	Fluctuations of light beams, <i>L. Mandel</i>	181–248
6	Methods for determining optical parameters of thin films, <i>F. Abelès</i>	249–288

VOLUME 3 (1964)

1	The elements of radiative transfer, <i>F. Kottler</i>	1–28
2	Apodisation, <i>P. Jacquinot, B. Roizen-Dossier</i>	29–186
3	Matrix treatment of partial coherence, <i>H. Gamo</i>	187–332

VOLUME 4 (1965)

1	Higher order aberration theory, <i>J. Focke</i>	1–36
2	Applications of shearing interferometry, <i>O. Bryngdahl</i>	37–83
3	Surface deterioration of optical glasses, <i>K. Kinoshita</i>	85–143

[☆]Volumes I–XL were previously distinguished by roman rather than by arabic numerals.

4	Optical constants of thin films, <i>P. Rouard, P. Bousquet</i>	145–197
5	The Miyamoto–Wolf diffraction wave, <i>A. Rubinowicz</i>	199–240
6	Aberration theory of gratings and grating mountings, <i>W.T. Welford</i>	241–280
7	Diffraction at a black screen, Part I: Kirchhoff's theory, <i>F. Kottler</i>	281–314

VOLUME 5 (1966)

1	Optical pumping, <i>C. Cohen-Tannoudji, A. Kastler</i>	1–81
2	Non-linear optics, <i>P.S. Pershan</i>	83–144
3	Two-beam interferometry, <i>W.H. Steel</i>	145–197
4	Instruments for the measuring of optical transfer functions, <i>K. Murata</i>	199–245
5	Light reflection from films of continuously varying refractive index, <i>R. Jacobsson</i>	247–286
6	X-ray crystal-structure determination as a branch of physical optics, <i>H. Lipson, C.A. Taylor</i>	287–350
7	The wave of a moving classical electron, <i>J. Picht</i>	351–370

VOLUME 6 (1967)

1	Recent advances in holography, <i>E.N. Leith, J. Upatnieks</i>	1–52
2	Scattering of light by rough surfaces, <i>P. Beckmann</i>	53–69
3	Measurement of the second order degree of coherence, <i>M. Françon, S. Mallick</i>	71–104
4	Design of zoom lenses, <i>K. Yamaji</i>	105–170
5	Some applications of lasers to interferometry, <i>D.R. Herriot</i>	171–209
6	Experimental studies of intensity fluctuations in lasers, <i>J.A. Armstrong, A.W. Smith</i>	211–257
7	Fourier spectroscopy, <i>G.A. Vanasse, H. Sakai</i>	259–330
8	Diffraction at a black screen, Part II: electromagnetic theory, <i>F. Kottler</i>	331–377

VOLUME 7 (1969)

1	Multiple-beam interference and natural modes in open resonators, <i>G. Koppelman</i>	1–66
2	Methods of synthesis for dielectric multilayer filters, <i>E. Delano, R.J. Pegis</i>	67–137
3	Echoes at optical frequencies, <i>I.D. Abella</i>	139–168
4	Image formation with partially coherent light, <i>B.J. Thompson</i>	169–230
5	Quasi-classical theory of laser radiation, <i>A.L. Mikaelian, M.L. Ter-Mikaelian</i>	231–297
6	The photographic image, <i>S. Ooue</i>	299–358
7	Interaction of very intense light with free electrons, <i>J.H. Eberly</i>	359–415

VOLUME 8 (1970)

1	Synthetic-aperture optics, <i>J.W. Goodman</i>	1–50
2	The optical performance of the human eye, <i>G.A. Fry</i>	51–131
3	Light beating spectroscopy, <i>H.Z. Cummins, H.L. Swinney</i>	133–200
4	Multilayer antireflection coatings, <i>A. Musset, A. Thelen</i>	201–237

5 Statistical properties of laser light, <i>H. Risken</i>	239–294
6 Coherence theory of source-size compensation in interference microscopy, <i>T. Yamamoto</i>	295–341
7 Vision in communication, <i>L. Levi</i>	343–372
8 Theory of photoelectron counting, <i>C.L. Mehta</i>	373–440

VOLUME 9 (1971)

1 Gas lasers and their application to precise length measurements, <i>A.L. Bloom</i>	1–30
2 Picosecond laser pulses, <i>A.J. Demaria</i>	31–71
3 Optical propagation through the turbulent atmosphere, <i>J.W. Strohbehn</i>	73–122
4 Synthesis of optical birefringent networks, <i>E.O. Ammann</i>	123–177
5 Mode locking in gas lasers, <i>L. Allen, D.G.C. Jones</i>	179–234
6 Crystal optics with spatial dispersion, <i>V.M. Agranovich, V.L. Ginzburg</i>	235–280
7 Applications of optical methods in the diffraction theory of elastic waves, <i>K. Gniadek, J. Petykiewicz</i>	281–310
8 Evaluation, design and extrapolation methods for optical signals, based on use of the prolate functions, <i>B.R. Frieden</i>	311–407

VOLUME 10 (1972)

1 Bandwidth compression of optical images, <i>T.S. Huang</i>	1–44
2 The use of image tubes as shutters, <i>R.W. Smith</i>	45–87
3 Tools of theoretical quantum optics, <i>M.O. Scully, K.G. Whitney</i>	89–135
4 Field correctors for astronomical telescopes, <i>C.G. Wynne</i>	137–164
5 Optical absorption strength of defects in insulators, <i>D.Y. Smith, D.L. Dexter</i>	165–228
6 Elastooptic light modulation and deflection, <i>E.K. Sittig</i>	229–288
7 Quantum detection theory, <i>C.W. Helstrom</i>	289–369

VOLUME 11 (1973)

1 Master equation methods in quantum optics, <i>G.S. Agarwal</i>	1–76
2 Recent developments in far infrared spectroscopic techniques, <i>H. Yoshinaga</i>	77–122
3 Interaction of light and acoustic surface waves, <i>E.G. Lean</i>	123–166
4 Evanescent waves in optical imaging, <i>O. Bryngdahl</i>	167–221
5 Production of electron probes using a field emission source, <i>A.V. Crewe</i>	223–246
6 Hamiltonian theory of beam mode propagation, <i>J.A. Arnaud</i>	247–304
7 Gradient index lenses, <i>E.W. Marchand</i>	305–337

VOLUME 12 (1974)

1 Self-focusing, self-trapping, and self-phase modulation of laser beams, <i>O. Svelto</i>	1–51
2 Self-induced transparency, <i>R.E. Slusher</i>	53–100
3 Modulation techniques in spectrometry, <i>M. Harwit, J.A. Decker Jr</i>	101–162
4 Interaction of light with monomolecular dye layers, <i>K.H. Drexhage</i>	163–232

5	The phase transition concept and coherence in atomic emission, <i>R. Graham</i>	233–286
6	Beam-foil spectroscopy, <i>S. Bashkin</i>	287–344

VOLUME 13 (1976)

1	On the validity of Kirchhoff's law of heat radiation for a body in a nonequilibrium environment, <i>H.P. Baltes</i>	1–25
2	The case for and against semiclassical radiation theory, <i>L. Mandel</i>	27–68
3	Objective and subjective spherical aberration measurements of the human eye, <i>W.M. Rosenblum, J.L. Christensen</i>	69–91
4	Interferometric testing of smooth surfaces, <i>G. Schulz, J. Schwider</i>	93–167
5	Self-focusing of laser beams in plasmas and semiconductors, <i>M.S. Sodha, A.K. Ghatak, V.K. Tripathi</i>	169–265
6	Aplanatism and isoplanatism, <i>W.T. Welford</i>	267–292

VOLUME 14 (1976)

1	The statistics of speckle patterns, <i>J.C. Dainty</i>	1–46
2	High-resolution techniques in optical astronomy, <i>A. Labeyrie</i>	47–87
3	Relaxation phenomena in rare-earth luminescence, <i>L.A. Riseberg, M.J. Weber</i>	89–159
4	The ultrafast optical Kerr shutter, <i>M.A. Duguay</i>	161–193
5	Holographic diffraction gratings, <i>G. Schmahl, D. Rudolph</i>	195–244
6	Photoemission, <i>P.J. Vernier</i>	245–325
7	Optical fibre waveguides – a review, <i>P.J.B. Clarricoats</i>	327–402

VOLUME 15 (1977)

1	Theory of optical parametric amplification and oscillation, <i>W. Brunner, H. Paul</i>	1–75
2	Optical properties of thin metal films, <i>P. Rouard, A. Meessen</i>	77–137
3	Projection-type holography, <i>T. Okoshi</i>	139–185
4	Quasi-optical techniques of radio astronomy, <i>T.W. Cole</i>	187–244
5	Foundations of the macroscopic electromagnetic theory of dielectric media, <i>J. Van Kranendonk, J.E. Sipe</i>	245–350

VOLUME 16 (1978)

1	Laser selective photophysics and photochemistry, <i>V.S. Letokhov</i>	1–69
2	Recent advances in phase profiles generation, <i>J.J. Clair, C.I. Abitbol</i>	71–117
3	Computer-generated holograms: techniques and applications, <i>W.-H. Lee</i>	119–232
4	Speckle interferometry, <i>A.E. Ennos</i>	233–288
5	Deformation invariant, space-variant optical pattern recognition, <i>D. Casasent, D. Psaltis</i>	289–356
6	Light emission from high-current surface-spark discharges, <i>R.E. Beverly III</i>	357–411
7	Semiclassical radiation theory within a quantum-mechanical framework, <i>I.R. Senitzky</i>	413–448

VOLUME 17 (1980)

- | | | |
|---|--|---------|
| 1 | Heterodyne holographic interferometry, <i>R. Dändliker</i> | 1–84 |
| 2 | Doppler-free multiphoton spectroscopy, <i>E. Giacobino, B. Cagnac</i> | 85–161 |
| 3 | The mutual dependence between coherence properties of light and nonlinear optical processes, <i>M. Schubert, B. Wilhelmi</i> | 163–238 |
| 4 | Michelson stellar interferometry, <i>W.J. Tango, R.Q. Twiss</i> | 239–277 |
| 5 | Self-focusing media with variable index of refraction, <i>A.L. Mikaelian</i> | 279–345 |

VOLUME 18 (1980)

- | | | |
|---|---|---------|
| 1 | Graded index optical waveguides: a review, <i>A. Ghatak, K. Thyagarajan</i> | 1–126 |
| 2 | Photocount statistics of radiation propagating through random and nonlinear media, <i>J. Peřina</i> | 127–203 |
| 3 | Strong fluctuations in light propagation in a randomly inhomogeneous medium, <i>V.I. Tatarskii, V.U. Zavorotnyi</i> | 204–256 |
| 4 | Catastrophe optics: morphologies of caustics and their diffraction patterns, <i>M.V. Berry, C. Upstill</i> | 257–346 |

VOLUME 19 (1981)

- | | | |
|---|---|---------|
| 1 | Theory of intensity dependent resonance light scattering and resonance fluorescence, <i>B.R. Mollow</i> | 1–43 |
| 2 | Surface and size effects on the light scattering spectra of solids, <i>D.L. Mills, K.R. Subbaswamy</i> | 45–137 |
| 3 | Light scattering spectroscopy of surface electromagnetic waves in solids, <i>S. Ushioda</i> | 139–210 |
| 4 | Principles of optical data-processing, <i>H.J. Butterweck</i> | 211–280 |
| 5 | The effects of atmospheric turbulence in optical astronomy, <i>F. Roddier</i> | 281–376 |

VOLUME 20 (1983)

- | | | |
|---|--|---------|
| 1 | Some new optical designs for ultra-violet bidimensional detection of astronomical objects, <i>G. Courtes, P. Cruvellier, M. Detaille</i> | 1–61 |
| 2 | Shaping and analysis of picosecond light pulses, <i>C. Froehly, B. Colombeau, M. Vampouille</i> | 63–153 |
| 3 | Multi-photon scattering molecular spectroscopy, <i>S. Kielich</i> | 155–261 |
| 4 | Colour holography, <i>P. Hariharan</i> | 263–324 |
| 5 | Generation of tunable coherent vacuum-ultraviolet radiation, <i>W. Jamroz, B.P. Stoicheff</i> | 325–380 |

VOLUME 21 (1984)

- | | | |
|---|---|---------|
| 1 | Rigorous vector theories of diffraction gratings, <i>D. Maystre</i> | 1–67 |
| 2 | Theory of optical bistability, <i>L.A. Lugiato</i> | 69–216 |
| 3 | The Radon transform and its applications, <i>H.H. Barrett</i> | 217–286 |
| 4 | Zone plate coded imaging: theory and applications, <i>N.M. Ceglio, D.W. Sweeney</i> | 287–354 |

- 5 Fluctuations, instabilities and chaos in the laser-driven nonlinear ring cavity,
J.C. Englund, R.R. Snapp, W.C. Schieve 355–428

VOLUME 22 (1985)

- 1 Optical and electronic processing of medical images, *D. Malacara* 1–76
- 2 Quantum fluctuations in vision, *M.A. Bouman, W.A. Van De Grind, P. Zuidema* 77–144
- 3 Spectral and temporal fluctuations of broad-band laser radiation,
A.V. Masalov 145–196
- 4 Holographic methods of plasma diagnostics, *G.V. Ostrovskaya,
 Yu.I. Ostrovsky* 197–270
- 5 Fringe formations in deformation and vibration measurements using laser
 light, *I. Yamaguchi* 271–340
- 6 Wave propagation in random media: a systems approach, *R.L. Fante* 341–398

VOLUME 23 (1986)

- 1 Analytical techniques for multiple scattering from rough surfaces,
J.A. DeSanto, G.S. Brown 1–62
- 2 Paraxial theory in optical design in terms of Gaussian brackets, *K. Tanaka* 63–111
- 3 Optical films produced by ion-based techniques, *P.J. Martin, R.P. Netterfield* 113–182
- 4 Electron holography, *A. Tonomura* 183–220
- 5 Principles of optical processing with partially coherent light, *F.T.S. Yu* 221–275

VOLUME 24 (1987)

- 1 Micro Fresnel lenses, *H. Nishihara, T. Suhara* 1–37
- 2 Dephasing-induced coherent phenomena, *L. Rothberg* 39–101
- 3 Interferometry with lasers, *P. Hariharan* 103–164
- 4 Unstable resonator modes, *K.E. Oughstun* 165–387
- 5 Information processing with spatially incoherent light, *I. Glaser* 389–509

VOLUME 25 (1988)

- 1 Dynamical instabilities and pulsations in lasers, *N.B. Abraham, P. Mandel,
 L.M. Narducci* 1–190
- 2 Coherence in semiconductor lasers, *M. Ohtsu, T. Tako* 191–278
- 3 Principles and design of optical arrays, *Wang Shaomin, L. Ronchi* 279–348
- 4 Aspheric surfaces, *G. Schulz* 349–415

VOLUME 26 (1988)

- 1 Photon bunching and antibunching, *M.C. Teich, B.E.A. Saleh* 1–104
- 2 Nonlinear optics of liquid crystals, *I.C. Khoo* 105–161
- 3 Single-longitudinal-mode semiconductor lasers, *G.P. Agrawal* 163–225
- 4 Rays and caustics as physical objects, *Yu.A. Kravtsov* 227–348
- 5 Phase-measurement interferometry techniques, *K. Creath* 349–393

VOLUME 27 (1989)

- | | | |
|---|---|---------|
| 1 | The self-imaging phenomenon and its applications, <i>K. Patorski</i> | 1–108 |
| 2 | Aicons and meso-optical imaging devices, <i>L.M. Soroko</i> | 109–160 |
| 3 | Nonimaging optics for flux concentration, <i>I.M. Bassett, W.T. Welford, R. Winston</i> | 161–226 |
| 4 | Nonlinear wave propagation in planar structures, <i>D. Mihalache, M. Bertolotti, C. Sibilia</i> | 227–313 |
| 5 | Generalized holography with application to inverse scattering and inverse source problems, <i>R.P. Porter</i> | 315–397 |

VOLUME 28 (1990)

- | | | |
|---|---|---------|
| 1 | Digital holography – computer-generated holograms, <i>O. Bryngdahl, F. Wyrowski</i> | 1–86 |
| 2 | Quantum mechanical limit in optical precision measurement and communication, <i>Y. Yamamoto, S. Machida, S. Saito, N. Imoto, T. Yanagawa, M. Kitagawa</i> | 87–179 |
| 3 | The quantum coherence properties of stimulated Raman scattering, <i>M.G. Raymer, I.A. Walmsley</i> | 181–270 |
| 4 | Advanced evaluation techniques in interferometry, <i>J. Schwider</i> | 271–359 |
| 5 | Quantum jumps, <i>R.J. Cook</i> | 361–416 |

VOLUME 29 (1991)

- | | | |
|---|---|---------|
| 1 | Optical waveguide diffraction gratings: coupling between guided modes, <i>D.G. Hall</i> | 1–63 |
| 2 | Enhanced backscattering in optics, <i>Yu.N. Barabanenkov, Yu.A. Kravtsov, V.D. Ozrin, A.I. Saichev</i> | 65–197 |
| 3 | Generation and propagation of ultrashort optical pulses, <i>I.P. Christov</i> | 199–291 |
| 4 | Triple-correlation imaging in optical astronomy, <i>G. Weigelt</i> | 293–319 |
| 5 | Nonlinear optics in composite materials. 1. Semiconductor and metal crystallites in dielectrics, <i>C. Flytzanis, F. Hache, M.C. Klein, D. Ricard, Ph. Roussignol</i> | 321–411 |

VOLUME 30 (1992)

- | | | |
|---|--|---------|
| 1 | Quantum fluctuations in optical systems, <i>S. Reynaud, A. Heidmann, E. Giacobino, C. Fabre</i> | 1–85 |
| 2 | Correlation holographic and speckle interferometry, <i>Yu.I. Ostrovsky, V.P. Shchepinov</i> | 87–135 |
| 3 | Localization of waves in media with one-dimensional disorder, <i>V.D. Freilikher, S.A. Gredeskul</i> | 137–203 |
| 4 | Theoretical foundation of optical-soliton concept in fibers, <i>Y. Kodama, A. Hasegawa</i> | 205–259 |
| 5 | Cavity quantum optics and the quantum measurement process, <i>P. Meystre</i> | 261–355 |

VOLUME 31 (1993)

- | | | |
|---|---|---------|
| 1 | Atoms in strong fields: photoionization and chaos, <i>P.W. Milonni, B. Sundaram</i> | 1–137 |
| 2 | Light diffraction by relief gratings: a macroscopic and microscopic view, <i>E. Popov</i> | 139–187 |
| 3 | Optical amplifiers, <i>N.K. Dutta, J.R. Simpson</i> | 189–226 |
| 4 | Adaptive multilayer optical networks, <i>D. Psaltis, Y. Qiao</i> | 227–261 |
| 5 | Optical atoms, <i>R.J.C. Spreeuw, J.P. Woerdman</i> | 263–319 |
| 6 | Theory of Compton free electron lasers, <i>G. Dattoli, L. Giannessi, A. Renieri, A. Torre</i> | 321–412 |

VOLUME 32 (1993)

- | | | |
|---|--|---------|
| 1 | Guided-wave optics on silicon: physics, technology and status, <i>B.P. Pal</i> | 1–59 |
| 2 | Optical neural networks: architecture, design and models, <i>F.T.S. Yu</i> | 61–144 |
| 3 | The theory of optimal methods for localization of objects in pictures, <i>L.P. Yaroslavsky</i> | 145–201 |
| 4 | Wave propagation theories in random media based on the path-integral approach, <i>M.I. Charnotskii, J. Gozani, V.I. Tatarskii, V.U. Zavorotny</i> | 203–266 |
| 5 | Radiation by uniformly moving sources. Vavilov–Cherenkov effect, Doppler effect in a medium, transition radiation and associated phenomena, <i>V.L. Ginzburg</i> | 267–312 |
| 6 | Nonlinear processes in atoms and in weakly relativistic plasmas, <i>G. Mainfray, C. Manus</i> | 313–361 |

VOLUME 33 (1994)

- | | | |
|---|---|---------|
| 1 | The imbedding method in statistical boundary-value wave problems, <i>V.I. Klyatskin</i> | 1–127 |
| 2 | Quantum statistics of dissipative nonlinear oscillators, <i>V. Peřinová, A. Lukš</i> | 129–202 |
| 3 | Gap solitons, <i>C.M. De Sterke, J.E. Sipe</i> | 203–260 |
| 4 | Direct spatial reconstruction of optical phase from phase-modulated images, <i>V.I. Vlad, D. Malacara</i> | 261–317 |
| 5 | Imaging through turbulence in the atmosphere, <i>M.J. Beran, I. Oz-Vogt</i> | 319–388 |
| 6 | Digital halftoning: synthesis of binary images, <i>O. Bryngdahl, T. Scheermesser, F. Wyrowski</i> | 389–463 |

VOLUME 34 (1995)

- | | | |
|---|---|---------|
| 1 | Quantum interference, superposition states of light, and nonclassical effects, <i>V. Bužek, P.L. Knight</i> | 1–158 |
| 2 | Wave propagation in inhomogeneous media: phase-shift approach, <i>L.P. Presnyakov</i> | 159–181 |
| 3 | The statistics of dynamic speckles, <i>T. Okamoto, T. Asakura</i> | 183–248 |
| 4 | Scattering of light from multilayer systems with rough boundaries, <i>I. Ohlídal, K. Navrátil, M. Ohlídal</i> | 249–331 |
| 5 | Random walk and diffusion-like models of photon migration in turbid media, <i>A.H. Gandomi, G.H. Weiss</i> | 333–402 |

VOLUME 35 (1996)

- | | | |
|---|--|---------|
| 1 | Transverse patterns in wide-aperture nonlinear optical systems,
<i>N.N. Rosanov</i> | 1–60 |
| 2 | Optical spectroscopy of single molecules in solids, <i>M. Orrit, J. Bernard, R. Brown, B. Lounis</i> | 61–144 |
| 3 | Interferometric multispectral imaging, <i>K. Itoh</i> | 145–196 |
| 4 | Interferometric methods for artwork diagnostics, <i>D. Paoletti, G. Schirripa Spagnolo</i> | 197–255 |
| 5 | Coherent population trapping in laser spectroscopy, <i>E. Arimondo</i> | 257–354 |
| 6 | Quantum phase properties of nonlinear optical phenomena, <i>R. Tanas, A. Miranowicz, Ts. Gantsog</i> | 355–446 |

VOLUME 36 (1996)

- | | | |
|---|--|---------|
| 1 | Nonlinear propagation of strong laser pulses in chalcogenide glass films, <i>V. Chumash, I. Cojocaru, E. Fazio, F. Michelotti, M. Bertolotti</i> | 1–47 |
| 2 | Quantum phenomena in optical interferometry, <i>P. Hariharan, B.C. Sanders</i> | 49–128 |
| 3 | Super-resolution by data inversion, <i>M. Bertero, C. De Mol</i> | 129–178 |
| 4 | Radiative transfer: new aspects of the old theory, <i>Yu.A. Kravtsov, L.A. Apresyan</i> | 179–244 |
| 5 | Photon wave function, <i>I. Bialynicki-Birula</i> | 245–294 |

VOLUME 37 (1997)

- | | | |
|---|--|---------|
| 1 | The Wigner distribution function in optics and optoelectronics, <i>D. Dragoman</i> | 1–56 |
| 2 | Dispersion relations and phase retrieval in optical spectroscopy, <i>K.-E. Peiponen, E.M. Vartiainen, T. Asakura</i> | 57–94 |
| 3 | Spectra of molecular scattering of light, <i>I.L. Fabelinskii</i> | 95–184 |
| 4 | Soliton communication systems, <i>R.-J. Essiambre, G.P. Agrawal</i> | 185–256 |
| 5 | Local fields in linear and nonlinear optics of mesoscopic systems, <i>O. Keller</i> | 257–343 |
| 6 | Tunneling times and superluminality, <i>R.Y. Chiao, A.M. Steinberg</i> | 345–405 |

VOLUME 38 (1998)

- | | | |
|---|--|---------|
| 1 | Nonlinear optics of stratified media, <i>S. Dutta Gupta</i> | 1–84 |
| 2 | Optical aspects of interferometric gravitational-wave detectors, <i>P. Hello</i> | 85–164 |
| 3 | Thermal properties of vertical-cavity surface-emitting semiconductor lasers, <i>W. Nakwasaki, M. Osiński</i> | 165–262 |
| 4 | Fractional transformations in optics, <i>A.W. Lohmann, D. Mendlovic, Z. Zalevsky</i> | 263–342 |
| 5 | Pattern recognition with nonlinear techniques in the Fourier domain, <i>B. Javidi, J.L. Horner</i> | 343–418 |
| 6 | Free-space optical digital computing and interconnection, <i>J. Jahns</i> | 419–513 |

VOLUME 39 (1999)

- | | | |
|---|--|------|
| 1 | Theory and applications of complex rays, <i>Yu.A. Kravtsov, G.W. Forbes, A.A. Asatryan</i> | 1–62 |
|---|--|------|

2	Homodyne detection and quantum-state reconstruction, <i>D.-G. Welsch, W. Vogel, T. Opatrný</i>	63–211
3	Scattering of light in the eikonal approximation, <i>S.K. Sharma, D.J. Somerford</i>	213–290
4	The orbital angular momentum of light, <i>L. Allen, M.J. Padgett, M. Babiker</i>	291–372
5	The optical Kerr effect and quantum optics in fibers, <i>A. Sizmann, G. Leuchs</i>	373–469

VOLUME 40 (2000)

1	Polarimetric optical fibers and sensors, <i>T.R. Woliński</i>	1–75
2	Digital optical computing, <i>J. Tanida, Y. Ichioka</i>	77–114
3	Continuous measurements in quantum optics, <i>V. Peřinová, A. Lukš</i>	115–269
4	Optical systems with improved resolving power, <i>Z. Zalevsky, D. Mendlovic, A.W. Lohmann</i>	271–341
5	Diffractive optics: electromagnetic approach, <i>J. Turunen, M. Kuittinen, F. Wyrowski</i>	343–388
6	Spectroscopy in polychromatic fields, <i>Z. Ficek, H.S. Freedhoff</i>	389–441

VOLUME 41 (2000)

1	Nonlinear optics in microspheres, <i>M.H. Fields, J. Popp, R.K. Chang</i>	1–95
2	Principles of optical disk data storage, <i>J. Carriere, R. Narayan, W.-H. Yeh, C. Peng, P. Khulbe, L. Li, R. Anderson, J. Choi, M. Mansuripur</i>	97–179
3	Ellipsometry of thin film systems, <i>I. Ohlídal, D. Franta</i>	181–282
4	Optical true-time delay control systems for wideband phased array antennas, <i>R.T. Chen, Z. Fu</i>	283–358
5	Quantum statistics of nonlinear optical couplers, <i>J. Peřina Jr, J. Peřina</i>	359–417
6	Quantum phase difference, phase measurements and Stokes operators, <i>A. Luis, L.L. Sánchez-Soto</i>	419–479
7	Optical solitons in media with a quadratic nonlinearity, <i>C. Etrich, F. Lederer, B.A. Malomed, T. Peschel, U. Peschel</i>	483–567

VOLUME 42 (2001)

1	Quanta and information, <i>S. Ya. Kilin</i>	1–91
2	Optical solitons in periodic media with resonant and off-resonant nonlinearities, <i>G. Kurizki, A.E. Kozhekin, T. Opatrný, B.A. Malomed</i>	93–146
3	Quantum Zeno and inverse quantum Zeno effects, <i>P. Facchi, S. Pascazio</i>	147–217
4	Singular optics, <i>M.S. Soskin, M.V. Vasnetsov</i>	219–276
5	Multi-photon quantum interferometry, <i>G. Jaeger, A.V. Sergienko</i>	277–324
6	Transverse mode shaping and selection in laser resonators, <i>R. Oron, N. Davidson, A.A. Friesem, E. Hasman</i>	325–386

VOLUME 43 (2002)

1	Active optics in modern large optical telescopes, <i>L. Noethe</i>	1–69
2	Variational methods in nonlinear fiber optics and related fields, <i>B.A. Malomed</i>	71–193

3	Optical works of L.V. Lorenz, <i>O. Keller</i>	195–294
4	Canonical quantum description of light propagation in dielectric media, <i>A. Lukš, V. Peřinová</i>	295–431
5	Phase space correspondence between classical optics and quantum mechanics, <i>D. Dragoman</i>	433–496
6	“Slow” and “fast” light, <i>R.W. Boyd, D.J. Gauthier</i>	497–530
7	The fractional Fourier transform and some of its applications to optics, <i>A. Torre</i>	531–596

VOLUME 44 (2002)

1	Chaotic dynamics in semiconductor lasers with optical feedback, <i>J. Ohtsubo</i>	1–84
2	Femtosecond pulses in optical fibers, <i>F.G. Omenetto</i>	85–141
3	Instantaneous optics of ultrashort broadband pulses and rapidly varying media, <i>A.B. Shwartsburg, G. Petite</i>	143–214
4	Optical coherence tomography, <i>A.F. Fercher, C.K. Hitzenberger</i>	215–301
5	Modulational instability of electromagnetic waves in inhomogeneous and in discrete media, <i>F.Kh. Abdullaev, S.A. Darmanyan, J. Garnier</i>	303–366

VOLUME 45 (2003)

1	Anamorphic beam shaping for laser and diffuse light, <i>N. Davidson, N. Bokor</i>	1–51
2	Ultra-fast all-optical switching in optical networks, <i>I. Glesk, B.C. Wang, L. Xu, V. Baby, P.R. Prucnal</i>	53–117
3	Generation of dark hollow beams and their applications, <i>J. Yin, W. Gao, Y. Zhu</i>	119–204
4	Two-photon lasers, <i>D.J. Gauthier</i>	205–272
5	Nonradiating sources and other “invisible” objects, <i>G. Gbur</i>	273–315
6	Lasing in disordered media, <i>H. Cao</i>	317–370

VOLUME 46 (2004)

1	Ultrastable solid-state lasers, <i>U. Keller</i>	1–115
2	Multiple scattering of light from randomly rough surfaces, <i>A.V. Shchegrov, A.A. Maradudin, E.R. Méndez</i>	117–241
3	Laser-diode interferometry, <i>Y. Ishii</i>	243–309
4	Optical realizations of quantum teleportation, <i>J. Gea-Banacloche</i>	311–353
5	Intensity-field correlations of non-classical light, <i>H.J. Carmichael, G.T. Foster, L.A. Orozco, J.E. Reiner, P.R. Rice</i>	355–404

VOLUME 47 (2005)

1	Multistep parametric processes in nonlinear optics, <i>S.M. Saltiel, A.A. Sukhorukov, Y.S. Kivshar</i>	1–73
2	Modes of wave-chaotic dielectric resonators, <i>H.E. Tütreci, H.G.L. Schwefel, Ph. Jacquod, A.D. Stone</i>	75–137
3	Nonlinear and quantum optics of atomic and molecular fields, <i>C.P. Search, P. Meystre</i>	139–214

4	Space-variant polarization manipulation, <i>E. Hasman, G. Biener, A. Niv, V. Kleiner</i>	215–289
5	Optical vortices and vortex solitons, <i>A.S. Desyatnikov, Y.S. Kivshar, L.L. Torner</i>	291–391
6	Phase imaging and refractive index tomography for X-rays and visible rays, <i>K. Iwata</i>	393–432

VOLUME 48 (2005)

1	Laboratory post-engineering of microstructured optical fibers, <i>B.J. Eggleton, P. Domachuk, C. Grillet, E.C. Mägi, H.C. Nguyen, P. Steinurzel, M.J. Steel</i>	1–34
2	Optical solitons in random media, <i>F. Abdullaev, J. Garnier</i>	35–106
3	Curved diffractive optical elements: Design and applications, <i>N. Bokor, N. Davidson</i>	107–148
4	The geometric phase, <i>P. Hariharan</i>	149–201
5	Synchronization and communication with chaotic laser systems, <i>A. Uchida, F. Rogister, J. García-Ojalvo, R. Roy</i>	203–341

VOLUME 49 (2006)

1	Gaussian apodization and beam propagation, <i>V.N. Mahajan</i>	1–96
2	Controlling nonlinear optical processes in multi-level atomic systems, <i>A. Joshi, M. Xiao</i>	97–175
3	Photonic crystals, <i>H. Benisty, C. Weisbuch</i>	177–313
4	Symmetry properties and polarization descriptors for an arbitrary electromagnetic wavefield, <i>C. Brosseau, A. Dogariu</i>	315–380
5	Quantum cryptography, <i>M. Dušek, N. Liittkenhaus, M. Hendrych</i>	381–454
6	Optical quantum cloning, <i>N.J. Cerf, J. Fiurášek</i>	455–545

VOLUME 50 (2007)

1	From millisecond to attosecond laser pulses, <i>N. Bloembergen</i>	1–12
2	Conical diffraction: Hamilton's diabolical point at the heart of crystal optics, <i>M.V. Berry, M.R. Jeffrey</i>	13–50
3	Historical papers on the particle concept of light, <i>O. Keller</i>	51–95
4	Field quantization in optics, <i>P.W. Milonni</i>	97–135
5	The history of near-field optics, <i>L. Novotny</i>	137–184
6	Light tunneling, <i>H.M. Nussenzveig</i>	185–250
7	The influence of Young's interference experiment on the development of statistical optics, <i>E. Wolf</i>	251–273
8	Planck, photon statistics, and Bose–Einstein condensation, <i>D.M. Greenberger, N. Erez, M.O. Scully, A.A. Svidzinsky, M.S. Zubairy</i>	275–330

VOLUME 51 (2008)

1	Negative refractive index metamaterials in optics, <i>N.M. Litchinitser, I.R. Gabitov, A.I. Maimistov, VM. Shalaev</i>	1–67
2	Polarization techniques for surface nonlinear optics, <i>M. Kauranen, S. Cattaneo</i>	69–120

3	Electromagnetic fields in linear bianisotropic media, <i>T.G. Mackay, A. Lakhtakia</i>	121–209
4	Ultrafast optical pulses, <i>C.R. Pollock</i>	211–249
5	Quantum imaging, <i>A. Gatti, E. Brambilla, L. Lugiato</i>	251–348
6	Assessment of optical systems by means of point-spread functions, <i>J.J.M. Braat, S. van Haver, A.J.E.M. Janssen, P. Dirksen</i>	349–468
7	The discrete Wigner function, <i>G. Björk, A.B. Klimov, L.L. Sánchez-Soto</i>	469–516

VOLUME 52 (2009)

1	Coherent backscattering and Anderson localization of light, <i>C.M. Aegerter, G. Maret</i>	1–62
2	Soliton shape and mobility control in optical lattices, <i>Y.V. Kartashov, V.A. Vysloukh, L. Torner</i>	63–148
3	Signal and quantum noise in optical communications and cryptography, <i>P. Gallion, F. Mendieta, S. Jiang</i>	149–259
4	Invisibility cloaking by coordinate transformation, <i>M. Yan, W. Yan, M. Qiu</i>	261–304

VOLUME 53 (2009)

1	The resolution challenge in 3D optical microscopy, <i>M. Martínez-Corral, G. Saavedra</i>	1–67
2	Transformation optics and the geometry of light, <i>U. Leonhardt, T.G. Philbin</i>	69–152
3	Photorefractive solitons and their underlying nonlocal physics, <i>E. DelRe, B. Crosignani, P. Di Porto</i>	153–200
4	Stimulated scattering effects of intense coherent light, <i>G.S. He</i>	201–292
5	Singular optics: Optical vortices and polarization singularities, <i>M.R. Dennis, K. O'Holleran, M.J. Padgett</i>	293–363
6	Quantum feed-forward control of light, <i>U.L. Andersen, R. Filip</i>	365–414

VOLUME 54 (2009)

1	Propagation-Invariant Optical Fields, <i>J. Turunen, A.T. Friberg</i>	1–88
2	Theoretical Tools for Quantum Optics in Structured Media, <i>D. Mogilevtsev, S. Kilin</i>	89–148
3	Polarization and Coherence Optics: Historical Perspective, Status, and Future Directions, <i>C. Brosseau</i>	149–208
4	Optical Quantum Computation, <i>T.C. Ralph, G.J. Pryde</i>	209–269
5	Science and Engineering of Photonic Crystals, <i>K. Sakoda, J.W. Haus</i>	271–317
6	The Mathematical Theory of Laser Beam-Splitting Gratings, <i>L.A. Romero, F.M. Dickey</i>	319–386

This page intentionally left blank

CUMULATIVE INDEX – VOLUMES 1–55[☆]

Abdullaev, F. and J. Garnier: Optical solitons in random media	48, 35
Abdullaev, F.Kh., S.A. Darmanyan and J. Garnier: Modulational instability of electromagnetic waves in inhomogeneous and in discrete media	44, 303
Abelès, F.: Methods for determining optical parameters of thin films	2, 249
Abella, I.D.: Echoes at optical frequencies	7, 139
Abitbol, C.I., <i>see</i> Clair, J.J.	16, 71
Abraham, N.B., P. Mandel and L.M. Narducci: Dynamical instabilities and pulsations in lasers	25, 1
Aegerter, C.M. and G. Maret: Coherent backscattering and Anderson localization of light	52, 1
Agarwal, G.S.: Master equation methods in quantum optics	11, 1
Agranovich, V.M. and V.L. Ginzburg: Crystal optics with spatial dispersion	9, 235
Agrawal, G.P.: Single-longitudinal-mode semiconductor lasers	26, 163
Agrawal, G.P., <i>see</i> Essiambre, R.-J.	37, 185
Allen, L. and D.G.C. Jones: Mode locking in gas lasers	9, 179
Allen, L., M.J. Padgett and M. Babiker: The orbital angular momentum of light	39, 291
Ammann, E.O.: Synthesis of optical birefringent networks	9, 123
Andersen, U.L. Filip, R.: Quantum feed-forward control of light	53, 365
Anderson, R., <i>see</i> Carriere, J.	41, 97
Apresyan, L.A., <i>see</i> Kravtsov, Yu.A.	36, 179
Arimondo, E.: Coherent population trapping in laser spectroscopy	35, 257
Armstrong, J.A. and A.W. Smith: Experimental studies of intensity fluctuations in lasers	6, 211
Arnaud, J.A.: Hamiltonian theory of beam mode propagation	11, 247
Asakura, T., <i>see</i> Okamoto, T.	34, 183
Asakura, T., <i>see</i> Peiponen, K.-E.	37, 57
Asatryan, A.A., <i>see</i> Kravtsov, Yu.A.	39, 1
Babiker, M., <i>see</i> Allen, L.	39, 291
Baby, V., <i>see</i> Glesk, I.	45, 53
Baltes, H.P.: On the validity of Kirchhoff's law of heat radiation for a body in a nonequilibrium environment	13, 1

[☆] Volumes I–XL were previously distinguished by roman rather than by arabic numerals.

Barabanenkov, Yu.N., Yu.A. Kravtsov, V.D. Ozrin and A.I. Saichev: Enhanced backscattering in optics	29, 65
Barakat, R.: The intensity distribution and total illumination of aberration-free diffraction images	1, 67
Barrett, H.H.: The Radon transform and its applications	21, 217
Bashkin, S.: Beam-foil spectroscopy	12, 287
Bassett, I.M., W.T. Welford and R. Winston: Nonimaging optics for flux concentration	27, 161
Beckmann, P.: Scattering of light by rough surfaces	6, 53
Bellini, M. and Zavatta, A.: Manipulating light states by single-photon addition and subtraction	55, 41
Benisty, H. and C. Weisbuch: Photonic crystals	49, 177
Beran, M.J. and J. Oz-Vogt: Imaging through turbulence in the atmosphere	33, 319
Bernard, J., <i>see</i> Orrit, M.	35, 61
Berry, M.V. and C. Upstill: Catastrophe optics: morphologies of caustics and their diffraction patterns	18, 257
Bertero, M. and C. De Mol: Super-resolution by data inversion	36, 129
Bertolotti, M., <i>see</i> Chumash, V.	36, 1
Bertolotti, M., <i>see</i> Mihalache, D.	27, 227
Beverly III, R.E.: Light emission from high-current surface-spark discharges	16, 357
Bialynicki-Birula, I.: Photon wave function	36, 245
Biener, G., <i>see</i> Hasman, E.	47, 215
Björk, G., A.B. Klimov and L.L. Sánchez-Soto: The discrete Wigner function	51, 469
Bloembergen, N.: From millisecond to attosecond laser pulses	50, 1
Bloom, A.L.: Gas lasers and their application to precise length measurements	9, 1
Bokor, N. and N. Davidson: Curved diffractive optical elements: Design and applications	48, 107
Bokor, N., <i>see</i> Davidson, N.	45, 1
Bouman, M.A., W.A. Van De Grind and P. Zuidema: Quantum fluctuations in vision	22, 77
Bousquet, P., <i>see</i> Rouard, P.	4, 145
Boyd, R.W. and D.J. Gauthier: "Slow" and "fast" light	43, 497
Braat, J.J.M., S. van Haver, A.J.E.M. Janssen and P. Dirksen: Assessment of optical systems by means of point-spread functions	51, 349
Brambilla, E., <i>see</i> Gatti, A.	51, 251
Brosseau, C. and A. Dogariu: Symmetry properties and polarization descriptors for an arbitrary electromagnetic wavefield	49, 315
Brosseau, C.: Polarization and coherence optics: Historical perspective, status, and future directions	54, 149
Brown, G.S., <i>see</i> DeSanto, J.A.	23, 1
Brown, R., <i>see</i> Orrit, M.	35, 61
Brunner, W. and H. Paul: Theory of optical parametric amplification and oscillation	15, 1
Bryngdahl, O.: Applications of shearing interferometry	4, 37
Bryngdahl, O.: Evanescent waves in optical imaging	11, 167

Bryngdahl, O., T. Scheermesser and F. Wyrowski: Digital halftoning: synthesis of binary images	33, 389
Bryngdahl, O. and F. Wyrowski: Digital holography – computer-generated holograms	28, 1 2, 73
Burch, J.M.: The metrological applications of diffraction gratings	19, 211
Butterweck, H.J.: Principles of optical data-processing	
Bužek, V. and P.L. Knight: Quantum interference, superposition states of light, and nonclassical effects	34, 1
Cagnac, B., <i>see</i> Giacobino, E.	17, 85
Cao, H.: Lasing in disordered media	45, 317
Carmichael, H.J., G.T. Foster, L.A. Orozco, J.E. Reiner and P.R. Rice: Intensity-field correlations of non-classical light	46, 355
Carriere, J., R. Narayan, W.-H. Yeh, C. Peng, P. Khulbe, L. Li, R. Anderson, J. Choi and M. Mansuripur: Principles of optical disk data storage	41, 97
Casasent, D. and D. Psaltis: Deformation invariant, space-variant optical pattern recognition	16, 289
Cattaneo, S., <i>see</i> Kauranen, M.	51, 69
Ceglio, N.M. and D.W. Sweeney: Zone plate coded imaging: theory and applications	21, 287
Cerf, N.J. and J. Fiurášek: Optical quantum cloning	49, 455
Chang, R.K., <i>see</i> Fields, M.H.	41, 1
Charnotskii, M.I., J. Gozani, V.I. Tatarskii and V.U. Zavorotny: Wave propagation theories in random media based on the path-integral approach	32, 203
Chen, R.T. and Z. Fu: Optical true-time delay control systems for wideband phased array antennas	41, 283
Chiao, R.Y. and A.M. Steinberg: Tunneling times and superluminality	37, 345
Choi, J., <i>see</i> Carriere, J.	41, 97
Christensen, J.L., <i>see</i> Rosenblum, W.M.	13, 69
Christov, I.P.: Generation and propagation of ultrashort optical pulses	29, 199
Chumash, V., I. Cojocaru, E. Fazio, F. Michelotti and M. Bertolotti: Nonlinear propagation of strong laser pulses in chalcogenide glass films	36, 1
Clair, J.J. and C.I. Abitbol: Recent advances in phase profiles generation	16, 71
Clarricoats, P.J.B.: Optical fibre waveguides – a review	14, 327
Cohen-Tannoudji, C. and A. Kastler: Optical pumping	5, 1
Cojocaru, I., <i>see</i> Chumash, V.	36, 1
Cole, T.W.: Quasi-optical techniques of radio astronomy	15, 187
Colombeau, B., <i>see</i> Froehly, C.	20, 63
Cook, R.J.: Quantum jumps	28, 361
Courtès, G., P. Cruvellier and M. Detaille: Some new optical designs for ultra-violet bidimensional detection of astronomical objects	20, 1
Creath, K.: Phase-measurement interferometry techniques	26, 349
Crewe, A.V.: Production of electron probes using a field emission source	11, 223
Crosignani, B., <i>see</i> DelRe, E.	53, 153

Cruvellier, P., <i>see</i> Courtès, G.	20, 1
Cummins, H.Z. and H.L. Swinney: Light beating spectroscopy	8, 133
Dainty, J.C.: The statistics of speckle patterns	14, 1
Dändliker, R.: Heterodyne holographic interferometry	17, 1
Darmanyan, S.A., <i>see</i> Abdullaev, F.Kh.	44, 303
Dattoli, G., L. Giannessi, A. Renieri and A. Torre: Theory of Compton free electron lasers	31, 321
Davidson, N. and N. Bokor: Anamorphic beam shaping for laser and diffuse light	45, 1
Davidson, N., <i>see</i> Bokor, N.	48, 107
Davidson, N., <i>see</i> Oron, R.	42, 325
De Mol, C., <i>see</i> Bertero, M.	36, 129
De Sterke, C.M. and J.E. Sipe: Gap solitons	33, 203
Decker Jr, J.A., <i>see</i> Harwit, M.	12, 101
Delano, E. and R.J. Pegis: Methods of synthesis for dielectric multilayer filters	7, 67
DelRe, E., Crosignani, B. and Di Porto, P.: Photorefractive solitons and their underlying nonlocal physics	53, 153
Demaria, A.J.: Picosecond laser pulses	9, 31
DeSanto, J.A. and G.S. Brown: Analytical techniques for multiple scattering from rough surfaces	23, 1
Dennis, M.R., O'Holleran, K. and Padgett, M.J.: Singular optics: Optical vortices and polarization singularities	53, 293
Desyatnikov, A.S., Y.S. Kivshar and L.L. Torner: Optical vortices and vortex solitons	47, 291
Detaille, M., <i>see</i> Courtès, G.	20, 1
Dexter, D.L., <i>see</i> Smith, D.Y.	10, 165
Di Porto, P., <i>see</i> DelRe, E.	53, 153
Dickey, F.M., <i>see</i> Romero, L.A.	54, 319
Dirksen, P., <i>see</i> Braat, J.J.M.	51, 349
Dogariu, A., <i>see</i> Brosseau, C.	49, 315
Domachuk, P., <i>see</i> Eggleton, B.J.	48, 1
Dragoman, D.: The Wigner distribution function in optics and optoelectronics	37, 1
Dragoman, D.: Phase space correspondence between classical optics and quantum mechanics	43, 433
Drexhage, K.H.: Interaction of light with monomolecular dye layers	12, 163
Duguay, M.A.: The ultrafast optical Kerr shutter	14, 161
Dušek M., N. Lütkenhaus and M. Hendrych: Quantum cryptography	49, 381
Dutta, N.K. and J.R. Simpson: Optical amplifiers	31, 189
Dutta Gupta, S.: Nonlinear optics of stratified media	38, 1
Eberly, J.H.: Interaction of very intense light with free electrons	7, 359
Eggleton, B.J., P. Domachuk, C. Grillet, E.C. Mägi, H.C. Nguyen, P. Steinurzel and M.J. Steel: Laboratory post-engineering of microstructured optical fibers	48, 1

Englund, J.C., R.R. Snapp and W.C. Schieve: Fluctuations, instabilities and chaos in the laser-driven nonlinear ring cavity	21, 355
Ennos, A.E.: Speckle interferometry	16, 233
Erez, N., <i>see</i> Greenberger, D.M.	50, 275
Essiambre, R.-J. and G.P. Agrawal: Soliton communication systems	37, 185
Etrich, C., F. Lederer, B.A. Malomed, T. Peschel and U. Peschel: Optical solitons in media with a quadratic nonlinearity	41, 483
Evers, J., <i>see</i> Kiffner, M.	55, 85
Fabelinskii, I.L.: Spectra of molecular scattering of light	37, 95
Fabre, C., <i>see</i> Reynaud, S.	30, 1
Facchi, P. and S. Pascazio: Quantum Zeno and inverse quantum Zeno effects	42, 147
Fante, R.L.: Wave propagation in random media: a systems approach	22, 341
Fazio, E., <i>see</i> Chumash, V.	36, 1
Fercher, A.F. and C.K. Hitzenberger: Optical coherence tomography	44, 215
Ficek, Z. and H.S. Freedhoff: Spectroscopy in polychromatic fields	40, 389
Fields, M.H., J. Popp and R.K. Chang: Nonlinear optics in microspheres	41, 1
Filip, R.: <i>see</i> Andersen, U.L.	53, 365
Fiorentini, A.: Dynamic characteristics of visual processes	1, 253
Fiurášek, J., <i>see</i> Cerf, N.J.	49, 455
Flytzanis, C., F. Hache, M.C. Klein, D. Ricard and Ph. Roussignol: Nonlinear optics in composite materials. 1. Semiconductor and metal crystallites in dielectrics	29, 321
Focke, J.: Higher order aberration theory	4, 1
Forbes, G.W., <i>see</i> Kravtsov, Yu.A.	39, 1
Foster, G.T., <i>see</i> Carmichael, H.J.	46, 355
Françon, M. and S. Mallick: Measurement of the second order degree of coherence	6, 71
Franta, D., <i>see</i> Ohlídal, I.	41, 181
Freedhoff, H.S., <i>see</i> Ficek, Z.	40, 389
Freilikher, V.D. and S.A. Gredeskul: Localization of waves in media with one-dimensional disorder	30, 137
Friberg, A.T., <i>see</i> Turunen, J.	54, 1
Frieden, B.R.: Evaluation, design and extrapolation methods for optical signals, based on use of the prolate functions	9, 311
Friesem, A.A., <i>see</i> Oron, R.	42, 325
Froehly, C., B. Colombeau and M. Vampouille: Shaping and analysis of picosecond light pulses	20, 63
Fry, G.A.: The optical performance of the human eye	8, 51
Fu, Z., <i>see</i> Chen, R.T.	41, 283
Gabitov, I.R., <i>see</i> Litchinitser, N.M.	51, 1
Gabor, D.: Light and information	1, 109
Gallion, P., F. Mendieta and S. Jiang: Signal and quantum noise in optical communications and cryptography	52, 149
Gamo, H.: Matrix treatment of partial coherence	3, 187

Gandjbakhche, A.H. and G.H. Weiss: Random walk and diffusion-like models of photon migration in turbid media	34, 333
Gantsog, Ts., <i>see</i> Tanaš, R.	35, 355
Gao, W., <i>see</i> Yin, J.	45, 119
García-Ojalvo, J., <i>see</i> Uchida, A.	48, 203
Garnier, J., <i>see</i> Abdullaev, F.	48, 35
Garnier, J., <i>see</i> Abdullaev, F.Kh.	44, 303
Gatti, A., E. Brambilla and L. Lugiato: Quantum imaging	51, 251
Gauthier, D.J.: Two-photon lasers	45, 205
Gauthier, D.J., <i>see</i> Boyd, R.W.	43, 497
Gbur, G.: Nonradiating sources and other “invisible” objects	45, 273
Gbur, G. and Visser, T.D.: The structure of partially coherent fields	55, 285
Gea-Banacloche, J.: Optical realizations of quantum teleportation	46, 311
Ghatak, A. and K. Thyagarajan: Graded index optical waveguides: a review	18, 1
Ghatak, A.K., <i>see</i> Sodha, M.S.	13, 169
Giacobino, E. and B. Cagnac: Doppler-free multiphoton spectroscopy	17, 85
Giacobino, E., <i>see</i> Reynaud, S.	30, 1
Giannessi, L., <i>see</i> Dattoli, G.	31, 321
Ginzburg, V.L.: Radiation by uniformly moving sources. Vavilov–Cherenkov effect, Doppler effect in a medium, transition radiation and associated phenomena	32, 267
Ginzburg, V.L., <i>see</i> Agranovich, V.M.	9, 235
Giovanelli, R.G.: Diffusion through non-uniform media	2, 109
Glaser, I.: Information processing with spatially incoherent light	24, 389
Glesk, I., B.C. Wang, L. Xu, V. Baby and P.R. Prucnal: Ultra-fast all-optical switching in optical networks	45, 53
Gniadek, K. and J. Petykiewicz: Applications of optical methods in the diffraction theory of elastic waves	9, 281
Goodman, J.W.: Synthetic-aperture optics	8, 1
Gozani, J., <i>see</i> Charnotskii, M.I.	32, 203
Graham, R.: The phase transition concept and coherence in atomic emission	12, 233
Gredeskul, S.A., <i>see</i> Freilikher, V.D.	30, 137
Greenberger, D.M., N. Erez, M.O. Scully, A.A. Svidzinsky and M.S. Zubairy: Planck, photon statistics, and Bose–Einstein condensation	50, 275
Grillet, C., <i>see</i> Eggleton, B.J.	48, 1
Hache, F., <i>see</i> Flytzanis, C.	29, 321
Hall, D.G.: Optical waveguide diffraction gratings: coupling between guided modes	29, 1
Hariharan, P.: Colour holography	20, 263
Hariharan, P.: Interferometry with lasers	24, 103
Hariharan, P.: The geometric phase	48, 149
Hariharan, P. and B.C. Sanders: Quantum phenomena in optical interferometry	36, 49
Harwit, M. and J.A. Decker Jr: Modulation techniques in spectrometry	12, 101

Hasegawa, A., <i>see</i> Kodama, Y.	30, 205
Hasman, E., G. Biener, A. Niv and V. Kleiner: Space-variant polarization manipulation	47, 215
Hasman, E., <i>see</i> Oron, R.	42, 325
Haus, J.W., <i>see</i> Sakoda, K.	54, 271
He, G.S.: Stimulated scattering effects of intense coherent light	53, 201
Heidmann, A., <i>see</i> Reynaud, S.	30, 1
Hello, P.: Optical aspects of interferometric gravitational-wave detectors	38, 85
Helstrom, C.W.: Quantum detection theory	10, 289
Hendrych, M., <i>see</i> Dušek, M.	49, 381
Herriot, D.R.: Some applications of lasers to interferometry	6, 171
Hitzenberger, C.K., <i>see</i> Fercher, A.F.	44, 215
Horner, J.L., <i>see</i> Javidi, B.	38, 343
Huang, T.S.: Bandwidth compression of optical images	10, 1
Ichioka, Y., <i>see</i> Tanida, J.	40, 77
Imoto, N., <i>see</i> Yamamoto, Y.	28, 87
Ishii, Y.: Laser-diode interferometry	46, 243
Itoh, K.: Interferometric multispectral imaging	35, 145
Iwata, K.: Phase imaging and refractive index tomography for X-rays and visible rays	47, 393
Jacobsson, R.: Light reflection from films of continuously varying refractive index	5, 247
Jacquinot, P. and B. Roizen-Dossier: Apodisation	3, 29
Jacquod, Ph., <i>see</i> Türeci, H.E.	47, 75
Jaeger, G. and A.V. Sergienko: Multi-photon quantum interferometry	42, 277
Jahns, J.: Free-space optical digital computing and interconnection	38, 419
Jamroz, W. and B.P. Stoicheff: Generation of tunable coherent vacuum-ultraviolet radiation	20, 325
Janssen, A.J.E.M., <i>see</i> Braat, J.J.M.	51, 349
Javidi, B. and J.L. Horner: Pattern recognition with nonlinear techniques in the Fourier domain	38, 343
Jiang, S., <i>see</i> Gallion, P.	52, 149
Jones, D.G.C., <i>see</i> Allen, L.	9, 179
Joshi, A. and M. Xiao: Controlling nonlinear optical processes in multi-level atomic systems	49, 97
Kartashov, Y.V., V.A. Vysloukh and L. Torner: Soliton shape and mobility control in optical lattices	52, 63
Kastler, A., <i>see</i> Cohen-Tannoudji, C.	5, 1
Kauranen, M. and S. Cattaneo: Polarization techniques for surface nonlinear optics	51, 69
Keitel, C.H., <i>see</i> Kiffner, M.	55, 85
Keller, O.: Local fields in linear and nonlinear optics of mesoscopic systems	37, 257

Keller, O.: Optical works of L.V. Lorenz	43, 195
Keller, O.: Historical papers on the particle concept of light	50, 51
Keller, U.: Ultrafast solid-state lasers	46, 1
Khoo, I.C.: Nonlinear optics of liquid crystals	26, 105
Khulbe, P., <i>see</i> Carriere, J.	41, 97
Kielich, S.: Multi-photon scattering molecular spectroscopy	20, 155
Kiffner, M., Macovei, M., Evers, J. and Keitel, C.H.: Vacuum-induced processes in multilevel atoms	55, 85
Kilin, S., <i>see</i> Mogilevtsev, D.	54, 89
Kilin, S.Ya.: Quanta and information	42, 1
Kinosita, K.: Surface deterioration of optical glasses	4, 85
Kitagawa, M., <i>see</i> Yamamoto, Y.	28, 87
Kivshar, Y.S., <i>see</i> Desyatnikov, A.S.	47, 291
Kivshar, Y.S., <i>see</i> Saltiel, S.M.	47, 1
Klein, M.C., <i>see</i> Flytzanis, C.	29, 321
Kleiner, V., <i>see</i> Hasman, E.	47, 215
Klimov, A.B., <i>see</i> Björk, G.	51, 469
Klyatskin, V.I.: The imbedding method in statistical boundary-value wave problems	33, 1
Knight, P.L., <i>see</i> Bužek, V.	34, 1
Kodama, Y. and A. Hasegawa: Theoretical foundation of optical-soliton concept in fibers	30, 205
Koppelman, G.: Multiple-beam interference and natural modes in open resonators	7, 1
Kottler, F.: The elements of radiative transfer	3, 1
Kottler, F.: Diffraction at a black screen, Part I: Kirchhoff's theory	4, 281
Kottler, F.: Diffraction at a black screen, Part II: electromagnetic theory	6, 331
Kozhekin, A.E., <i>see</i> Kurizki, G.	42, 93
Kravtsov, Yu.A.: Rays and caustics as physical objects	26, 227
Kravtsov, Yu.A. and L.A. Apresyan: Radiative transfer: new aspects of the old theory	36, 179
Kravtsov, Yu.A., G.W. Forbes and A.A. Asatryan: Theory and applications of complex rays	39, 1
Kravtsov, Yu.A., <i>see</i> Barabanenkov, Yu.N.	29, 65
Kubota, H.: Interference color	1, 211
Kuittinen, M., <i>see</i> Turunen, J.	40, 343
Kurizki, G., A.E. Kozhekin, T. Opatrný and B.A. Malomed: Optical solitons in periodic media with resonant and off-resonant nonlinearities	42, 93
Labeyrie, A.: High-resolution techniques in optical astronomy	14, 47
Lakhtakia, A., <i>see</i> Mackay, T.G.	51, 121
Lean, E.G.: Interaction of light and acoustic surface waves	11, 123
Lederer, F., <i>see</i> Etrich, C.	41, 483
Lee, W.-H.: Computer-generated holograms: techniques and applications	16, 119
Leith, E.N. and Upatnieks, J.: Recent advances in holography	6, 1

Leonhardt, U. and Philbin, T.G.: Transformation optics and the geometry of light	53, 69
Letokhov, V.S.: Laser selective photophysics and photochemistry	16, 1
Leuchs, G., <i>see</i> Sizmann, A.	39, 373
Levi, L.: Vision in communication	8, 343
Li, G.: Adaptive lens	55, 199
Li, L., <i>see</i> Carriere, J.	41, 97
Lipson, H. and C.A. Taylor: X-ray crystal-structure determination as a branch of physical optics	5, 287
Litchinitser, N.M., I.R. Gabitov, A.I. Maimistov and V.M. Shalaev: Negative refractive index metamaterials in optics	51, 1
Lohmann, A.W., D. Mendlovic and Z. Zalevsky: Fractional transformations in optics	38, 263
Lohmann, A.W., <i>see</i> Zalevsky, Z.	40, 271
Lounis, B., <i>see</i> Orrit, M.	35, 61
Lugiato, L., <i>see</i> Gatti, A.	51, 251
Lugiato, L.A.: Theory of optical bistability	21, 69
Luis, A. and L.L. Sánchez-Soto: Quantum phase difference, phase measurements and Stokes operators	41, 419
Lukš, A. and V. Peřinová: Canonical quantum description of light propagation in dielectric media	43, 295
Lukš, A., <i>see</i> Peřinová, V.	33, 129
Lukš, A., <i>see</i> Peřinová, V.	40, 115
Lütkenhaus, N., <i>see</i> Dušek, M.	49, 381
Machida, S., <i>see</i> Yamamoto, Y.	28, 87
Mackay, T.G. and A. Lakhtakia: Electromagnetic fields in linear bianisotropic media	51, 121
Macovei, M., <i>see</i> Kiffner, M.	55, 85
Mägi, E.C., <i>see</i> Eggleton, B.J.	48, 1
Mahajan, V.N.: Gaussian apodization and beam propagation	49, 1
Maimistov, A.I., <i>see</i> Litchinitser, N.M.	51, 1
Mainfray, G. and C. Manus: Nonlinear processes in atoms and in weakly relativistic plasmas	32, 313
Malacara, D.: Optical and electronic processing of medical images	22, 1
Malacara, D., <i>see</i> Vlad, V.I.	33, 261
Mallick, S., <i>see</i> Françon, M.	6, 71
Malomed, B.A.: Variational methods in nonlinear fiber optics and related fields	43, 71
Malomed, B.A., <i>see</i> Etrich, C.	41, 483
Malomed, B.A., <i>see</i> Kurizki, G.	42, 93
Mandel, L.: Fluctuations of light beams	2, 181
Mandel, L.: The case for and against semiclassical radiation theory	13, 27
Mandel, P., <i>see</i> Abraham, N.B.	25, 1
Mansuripur, M., <i>see</i> Carriere, J.	41, 97
Manus, C., <i>see</i> Mainfray, G.	32, 313

Maradudin, A.A., <i>see</i> Shchegrov, A.V.	46, 117
Marchand, E.W.: Gradient index lenses	11, 305
Maret, G., <i>see</i> Aegerter, C.M.	52, 1
Martin, P.J. and R.P. Netterfield: Optical films produced by ion-based techniques	23, 113
Martínez-Corral, M. and Saavedra, G.: The resolution challenge in 3D optical microscopy	53, 1
Masalov, A.V.: Spectral and temporal fluctuations of broad-band laser radiation	22, 145
Maystre, D.: Rigorous vector theories of diffraction gratings	21, 1
Meessen, A., <i>see</i> Rouard, P.	15, 77
Mehta, C.L.: Theory of photoelectron counting	8, 373
Méndez, E.R., <i>see</i> Shchegrov, A.V.	46, 117
Mendieta, F., <i>see</i> Gallion, P.	52, 149
Mendlovic, D., <i>see</i> Lohmann, A.W.	38, 263
Mendlovic, D., <i>see</i> Zalevsky, Z.	40, 271
Meystre, P.: Cavity quantum optics and the quantum measurement process	30, 261
Meystre, P., <i>see</i> Search, C.P.	47, 139
Michelotti, F., <i>see</i> Chumash, V.	36, 1
Mihalache, D., M. Bertolotti and C. Sibilia: Nonlinear wave propagation in planar structures	27, 227
Mikaelian, A.L.: Self-focusing media with variable index of refraction	17, 279
Mikaelian, A.L. and M.L. Ter-Mikaelian: Quasi-classical theory of laser radiation	7, 231
Mills, D.L. and K.R. Subbaswamy: Surface and size effects on the light scattering spectra of solids	19, 45
Milonni, P.W.: Field quantization in optics	50, 97
Milonni, P.W. and B. Sundaram: Atoms in strong fields: photoionization and chaos	31, 1
Miranowicz, A., <i>see</i> Tanaś, R.	35, 355
Miyamoto, K.: Wave optics and geometrical optics in optical design	1, 31
Mogilevtsev, D. and Kilin, S.: Theoretical tools for quantum optics in structured media	54, 89
Mollow, B.R.: Theory of intensity dependent resonance light scattering and resonance fluorescence	19, 1
Murata, K.: Instruments for the measuring of optical transfer functions	5, 199
Musset, A. and A. Thelen: Multilayer antireflection coatings	8, 201
Nakwaski, W. and M. Osiński: Thermal properties of vertical-cavity surface-emitting semiconductor lasers	38, 165
Narayan, R., <i>see</i> Carriere, J.	41, 97
Narducci, L.M., <i>see</i> Abraham, N.B.	25, 1
Navrátil, K., <i>see</i> Ohlídal, I.	34, 249
Netterfield, R.P., <i>see</i> Martin, P.J.	23, 113
Nguyen, H.C., <i>see</i> Eggleton, B.J.	48, 1
Nishihara, H. and T. Suhara: Micro Fresnel lenses	24, 1
Niv, A., <i>see</i> Hasman, E.	47, 215

Noethe, L.: Active optics in modern large optical telescopes	43, 1
Novotny, L.: The history of near-field optics	50, 137
Nussenzveig, H.M.: Light tunneling	50, 185
Ohlídal, I. and D. Franta: Ellipsometry of thin film systems	41, 181
Ohlídal, I., K. Navrátil and M. Ohlídal: Scattering of light from multilayer systems with rough boundaries	34, 249
Ohlídal, M., <i>see</i> Ohlídal, I.	34, 249
O'Holleran, K., <i>see</i> Dennis, M.R.	53, 293
Ohtsu, M. and T. Tako: Coherence in semiconductor lasers	25, 191
Ohtsubo, J.: Chaotic dynamics in semiconductor lasers with optical feedback	44, 1
Okamoto, T. and T. Asakura: The statistics of dynamic speckles	34, 183
Okoshi, T.: Projection-type holography	15, 139
Omenetto, F.G.: Femtosecond pulses in optical fibers	44, 85
Ooue, S.: The photographic image	7, 299
Opatrný, T., <i>see</i> Kurizki, G.	42, 93
Opatrný, T., <i>see</i> Welsch, D.-G.	39, 63
Oron, R., N. Davidson, A.A. Friesem and E. Hasman: Transverse mode shaping and selection in laser resonators	42, 325
Orozco, L.A., <i>see</i> Carmichael, H.J.	46, 355
Orrit, M., J. Bernard, R. Brown and B. Lounis: Optical spectroscopy of single molecules in solids	35, 61
Osiński, M., <i>see</i> Nakwaski, W.	38, 165
Ostrovskaya, G.V. and Yu.I. Ostrovsky: Holographic methods of plasma diagnostics	22, 197
Ostrovsky, Yu.I. and V.P. Shchepinov: Correlation holographic and speckle interferometry	30, 87
Ostrovsky, Yu.I., <i>see</i> Ostrovskaya, G.V.	22, 197
Oughstun, K.E.: Unstable resonator modes	24, 165
Oz-Vogt, J., <i>see</i> Beran, M.J.	33, 319
Ozrin, V.D., <i>see</i> Barabanenkov, Yu.N.	29, 65
Padgett, M.J., <i>see</i> Allen, L.	39, 291
Padgett, M.J., <i>see</i> Dennis, M.R.	53, 293
Pal, B.P.: Guided-wave optics on silicon: physics, technology and status	32, 1
Paoletti, D. and G. Schirripa Spagnolo: Interferometric methods for artwork diagnostics	35, 197
Pascazio, S., <i>see</i> Facchi, P.	42, 147
Patorski, K.: The self-imaging phenomenon and its applications	27, 1
Paul, H., <i>see</i> Brunner, W.	15, 1
Pegis, R.J.: The modern development of Hamiltonian optics	1, 1
Pegis, R.J., <i>see</i> Delano, E.	7, 67
Peiponen, K.-E., E.M. Vartiainen and T. Asakura: Dispersion relations and phase retrieval in optical spectroscopy	37, 57

Peng, C., <i>see</i> Carriere, J.	41, 97
Peřina Jr, J. and J. Peřina: Quantum statistics of nonlinear optical couplers	41, 359
Peřina, J.: Photocount statistics of radiation propagating through random and nonlinear media	18, 127
Peřina, J., <i>see</i> Peřina Jr, J.	41, 359
Peřinová, V. and A. Lukš: Quantum statistics of dissipative nonlinear oscillators	33, 129
Peřinová, V. and A. Lukš: Continuous measurements in quantum optics	40, 115
Peřinová, V., <i>see</i> Lukš, A.	43, 295
Pershaw, P.S.: Non-linear optics	5, 83
Peschel, T., <i>see</i> Etrich, C.	41, 483
Peschel, U., <i>see</i> Etrich, C.	41, 483
Petite, G., <i>see</i> Shvartsburg, A.B.	44, 143
Petykiewicz, J., <i>see</i> Gniadek, K.	9, 281
Philbin, T.G., <i>see</i> Leonhardt, U.	53, 69
Picht, J.: The wave of a moving classical electron	5, 351
Pollock, C.R.: Ultrafast optical pulses	51, 211
Popov, E.: Light diffraction by relief gratings: a macroscopic and microscopic view	31, 139
Popp, J., <i>see</i> Fields, M.H.	41, 1
Porter, R.P.: Generalized holography with application to inverse scattering and inverse source problems	27, 315
Premaratne, M.: Optical pulse propagation in biological media: theory and numerical methods	55, 1
Presnyakov, L.P.: Wave propagation in inhomogeneous media: phase-shift approach	34, 159
Prucnal, P.R., <i>see</i> Glesk, I.	45, 53
Pryde, G.J., <i>see</i> Ralph, T.C.	54, 209
Psaltis, D. and Y. Qiao: Adaptive multilayer optical networks	31, 227
Psaltis, D., <i>see</i> Casasent, D.	16, 289
Qiao, Y., <i>see</i> Psaltis, D.	31, 227
Qiu, M., <i>see</i> Yan, M.	52, 261
Ralph, T.C. and Pryde, G.J.: Optical quantum computation	54, 209
Raymer, M.G. and I.A. Walmsley: The quantum coherence properties of stimulated Raman scattering	28, 181
Reiner, J.E., <i>see</i> Carmichael, H.J.	46, 355
Renieri, A., <i>see</i> Dattoli, G.	31, 321
Reynaud, S., A. Heidmann, E. Giacobino and C. Fabre: Quantum fluctuations in optical systems	30, 1
Ricard, D., <i>see</i> Flytzanis, C.	29, 321
Rice, P.R., <i>see</i> Carmichael, H.J.	46, 355
Riseberg, L.A. and M.J. Weber: Relaxation phenomena in rare-earth luminescence	14, 89

Risken, H.: Statistical properties of laser light	8, 239
Roddier, F.: The effects of atmospheric turbulence in optical astronomy	19, 281
Rogister, F., <i>see</i> Uchida, A.	48, 203
Roizen-Dossier, B., <i>see</i> Jacquinot, P.	3, 29
Romero, L.A. and Dickey, F.M.: The mathematical theory of laser beam-splitting gratings	54, 319
Ronchi, L., <i>see</i> Wang Shaomin,	25, 279
Rosanov, N.N.: Transverse patterns in wide-aperture nonlinear optical systems	35, 1
Rosenblum, W.M. and J.L. Christensen: Objective and subjective spherical aberration measurements of the human eye	13, 69
Rothberg, L.: Dephasing-induced coherent phenomena	24, 39
Rouard, P. and P. Bousquet: Optical constants of thin films	4, 145
Rouard, P. and A. Meessen: Optical properties of thin metal films	15, 77
Roussignol, Ph., <i>see</i> Flytzanis, C.	29, 321
Roy, R., <i>see</i> Uchida, A.	48, 203
Rubinowicz, A.: The Miyamoto–Wolf diffraction wave	4, 199
Rudolph, D., <i>see</i> Schmahl, G.	14, 195
Saavedra, G., <i>see</i> Martínez-Corral, M.	53, 1
Saichev, A.I., <i>see</i> Barabanenkov, Yu.N.	29, 65
Saito, S., <i>see</i> Yamamoto, Y.	28, 87
Sakai, H., <i>see</i> Vanasse, G.A.	6, 259
Sakoda, K. and Haus, J.W.: Science and engineering of photonic crystals	54, 271
Saleh, B.E.A., <i>see</i> Teich, M.C.	26, 1
Saltiel, S.M., A.A. Sukhorukov and Y.S. Kivshar: Multistep parametric processes in nonlinear optics	47, 1
Sánchez-Soto, L.L., <i>see</i> Björk, G.	51, 469
Sánchez-Soto, L.L., <i>see</i> Luis, A.	41, 419
Sanders, B.C., <i>see</i> Hariharan, P.	36, 49
Scheermesser, T., <i>see</i> Bryngdahl, O.	33, 389
Schieve, W.C., <i>see</i> Englund, J.C.	21, 355
Schirripa Spagnolo, G., <i>see</i> Paoletti, D.	35, 197
Schmahl, G. and D. Rudolph: Holographic diffraction gratings	14, 195
Schubert, M. and B. Wilhelmi: The mutual dependence between coherence properties of light and nonlinear optical processes	17, 163
Schulz, G.: Aspheric surfaces	25, 349
Schulz, G. and J. Schwider: Interferometric testing of smooth surfaces	13, 93
Schwefel, H.G.L., <i>see</i> Türeci, H.E.	47, 75
Schwider, J.: Advanced evaluation techniques in interferometry	28, 271
Schwider, J., <i>see</i> Schulz, G.	13, 93
Scully, M.O. and K.G. Whitney: Tools of theoretical quantum optics	10, 89
Scully, M.O., <i>see</i> Greenberger, D.M.	50, 275

Search, C.P. and P. Meystre: Nonlinear and quantum optics of atomic and molecular fields	47, 139
Senitzky, I.R.: Semiclassical radiation theory within a quantum-mechanical framework	16, 413
Sergienko, A.V., <i>see</i> Jaeger, G.	42, 277
Shalaev, V.M., <i>see</i> Litchinitser, N.M.	51, 1
Sharma, S.K. and D.J. Somerford: Scattering of light in the eikonal approximation	39, 213
Shchegrov, A.V., A.A. Maradudin and E.R. Méndez: Multiple scattering of light from randomly rough surfaces	46, 117
Shchepinov, V.P., <i>see</i> Ostrovsky, Yu.I.	30, 87
Shvartsburg, A.B. and G. Petite: Instantaneous optics of ultrashort broadband pulses and rapidly varying media	44, 143
Sibilia, C., <i>see</i> Mihalache, D.	27, 227
Simpson, J.R., <i>see</i> Dutta, N.K.	31, 189
Sipe, J.E., <i>see</i> De Sterke, C.M.	33, 203
Sipe, J.E., <i>see</i> Van Kranendonk, J.	15, 245
Sittig, E.K.: Elastooptic light modulation and deflection	10, 229
Sizmann, A. and G. Leuchs: The optical Kerr effect and quantum optics in fibers	39, 373
Slusher, R.E.: Self-induced transparency	12, 53
Smith, A.W., <i>see</i> Armstrong, J.A.	6, 211
Smith, D.Y. and D.L. Dexter: Optical absorption strength of defects in insulators	10, 165
Smith, R.W.: The use of image tubes as shutters	10, 45
Snapp, R.R., <i>see</i> Englund, J.C.	21, 355
Sodha, M.S., A.K. Ghatak and V.K. Tripathi: Self-focusing of laser beams in plasmas and semiconductors	13, 169
Somerford, D.J., <i>see</i> Sharma, S.K.	39, 213
Soroko, L.M.: Axicons and meso-optical imaging devices	27, 109
Soskin, M.S. and M.V. Vasnetsov: Singular optics	42, 219
Spreeuw, R.J.C. and J.P. Woerdman: Optical atoms	31, 263
Steel, M.J., <i>see</i> Eggleton, B.J.	48, 1
Steel, W.H.: Two-beam interferometry	5, 145
Steinberg, A.M., <i>see</i> Chiao, R.Y.	37, 345
Steinvurzel, P., <i>see</i> Eggleton, B.J.	48, 1
Stoicheff, B.P., <i>see</i> Jamroz, W.	20, 325
Stone, A.D., <i>see</i> Türeci, H.E.	47, 75
Strohbehn, J.W.: Optical propagation through the turbulent atmosphere	9, 73
Stroke, G.W.: Ruling, testing and use of optical gratings for high-resolution spectroscopy	2, 1
Subbaswamy, K.R., <i>see</i> Mills, D.L.	19, 45
Suhara, T., <i>see</i> Nishihara, H.	24, 1
Sukhorukov, A.A., <i>see</i> Saltiel, S.M.	47, 1
Sundaram, B., <i>see</i> Milonni, P.W.	31, 1
Svelto, O.: Self-focusing, self-trapping, and self-phase modulation of laser beams	12, 1
Svidzinsky, A.A., <i>see</i> Greenberger, D.M.	50, 275

Sweeney, D.W., <i>see</i> Ceglio, N.M.	21 , 287
Swinney, H.L., <i>see</i> Cummins, H.Z.	8 , 133
Tako, T., <i>see</i> Ohtsu, M.	25 , 191
Tanaka, K.: Paraxial theory in optical design in terms of Gaussian brackets	23 , 63
Tanaś, R., A. Miranowicz and Ts. Gantsog: Quantum phase properties of nonlinear optical phenomena	35 , 355
Tango, W.J. and R.Q. Twiss: Michelson stellar interferometry	17 , 239
Tanida, J. and Y. Ichioka: Digital optical computing	40 , 77
Tatarskii, V.I. and V.U. Zavorotnyi: Strong fluctuations in light propagation in a randomly inhomogeneous medium	18 , 204
Tatarskii, V.I., <i>see</i> Charnotskii, M.I.	32 , 203
Taylor, C.A., <i>see</i> Lipson, H.	5 , 287
Teich, M.C. and B.E.A. Saleh: Photon bunching and antibunching	26 , 1
Ter-Mikaelian, M.L., <i>see</i> Mikaelian, A.L.	7 , 231
Thelen, A., <i>see</i> Musset, A.	8 , 201
Thompson, B.J.: Image formation with partially coherent light	7 , 169
Thyagarajan, K., <i>see</i> Ghatak, A.	18 , 1
Tonomura, A.: Electron holography	23 , 183
Torner, L., <i>see</i> Kartashov, Y.V.	52 , 63
Torner, L.L., <i>see</i> Desyatnikov, A.S.	47 , 291
Torre, A.: The fractional Fourier transform and some of its applications to optics	43 , 531
Torre, A., <i>see</i> Dattoli, G.	31 , 321
Tripathi, V.K., <i>see</i> Sodha, M.S.	13 , 169
Tsujiuchi, J.: Correction of optical images by compensation of aberrations and by spatial frequency filtering	2 , 131
Türeci, H.E., H.G.L. Schwefel, Ph. Jacquod and A.D. Stone: Modes of wave-chaotic dielectric resonators	47 , 75
Turunen, J., M. Kuittinen and F. Wyrowski: Diffractive optics: electromagnetic approach	40 , 343
Turunen, J. and Friberg, A.T.: Propagation-invariant optical fields	54 , 1
Twiss, R.Q., <i>see</i> Tango, W.J.	17 , 239
Uchida, A., F. Rogister, J. García-Ojalvo and R. Roy: Synchronization and communication with chaotic laser systems	48 , 203
Upatnieks, J., <i>see</i> Leith, E.N.	6 , 1
Upstill, C., <i>see</i> Berry, M.V.	18 , 257
Ushioda, S.: Light scattering spectroscopy of surface electromagnetic waves in solids	19 , 139
Vampouille, M., <i>see</i> Froehly, C.	20 , 63
Van De Grind, W.A., <i>see</i> Bouman, M.A.	22 , 77
van Haver, S., <i>see</i> Braat, J.J.M.	51 , 349
Van Heel, A.C.S.: Modern alignment devices	1 , 289

Van Kranendonk, J. and J.E. Sipe: Foundations of the macroscopic electromagnetic theory of dielectric media	15, 245
Vanasse, G.A. and H. Sakai: Fourier spectroscopy	6, 259
Vartiainen, E.M., <i>see</i> Peiponen, K.-E.	37, 57
Vasnetsov, M.V., <i>see</i> Soskin, M.S.	42, 219
Vernier, P.J.: Photoemission	14, 245
Visser, T.D., <i>see</i> Gbur, G.	55, 285
Vlad, V.I. and D. Malacara: Direct spatial reconstruction of optical phase from phase-modulated images	33, 261
Vogel, W., <i>see</i> Welsch, D.-G.	39, 63
Vysloukh, V.A., <i>see</i> Kartashov, Y.V.	52, 63
Walmsley, I.A., <i>see</i> Raymer, M.G.	28, 181
Wang Shaomin, and L. Ronchi: Principles and design of optical arrays	25, 279
Wang, B.C., <i>see</i> Glesk, I.	45, 53
Weber, M.J., <i>see</i> Riseberg, L.A.	14, 89
Weigelt, G.: Triple-correlation imaging in optical astronomy	29, 293
Weisbuch, C., <i>see</i> Benisty, H.	49, 177
Weiss, G.H., <i>see</i> Gandjbakhche, A.H.	34, 333
Welford, W.T.: Aberration theory of gratings and grating mountings	4, 241
Welford, W.T.: Aplanatism and isoplanatism	13, 267
Welford, W.T., <i>see</i> Bassett, I.M.	27, 161
Welsch, D.-G., W. Vogel and T. Opatrný: Homodyne detection and quantum-state reconstruction	39, 63
Whitney, K.G., <i>see</i> Scully, M.O.	10, 89
Wilhelmi, B., <i>see</i> Schubert, M.	17, 163
Winston, R., <i>see</i> Bassett, I.M.	27, 161
Woerdman, J.P., <i>see</i> Spreeuw, R.J.C.	31, 263
Wolf, E.: The influence of Young's interference experiment on the development of statistical optics	50, 251
Woliński, T.R.: Polarimetric optical fibers and sensors	40, 1
Wolter, H.: On basic analogies and principal differences between optical and electronic information	1, 155
Wynne, C.G.: Field correctors for astronomical telescopes	10, 137
Wyrowski, F., <i>see</i> Bryngdahl, O.	28, 1
Wyrowski, F., <i>see</i> Bryngdahl, O.	33, 389
Wyrowski, F., <i>see</i> Turunen, J.	40, 343
Xiao, M., <i>see</i> Joshi, A.	49, 97
Xu, L., <i>see</i> Glesk, I.	45, 53
Yan, M., W. Yan and M. Qiu: Invisibility cloaking by coordinate transformation	52, 261
Yan, W., <i>see</i> Yan, M.	52, 261

Yamaguchi, I.: Fringe formations in deformation and vibration measurements using laser light	22, 271
Yamaji, K.: Design of zoom lenses	6, 105
Yamamoto, T.: Coherence theory of source-size compensation in interference microscopy	8, 295
Yamamoto, Y., S. Machida, S. Saito, N. Imoto, T. Yanagawa and M. Kitagawa: Quantum mechanical limit in optical precision measurement and communication	28, 87
Yanagawa, T., <i>see</i> Yamamoto, Y.	28, 87
Yaroslavsky, L.P.: The theory of optimal methods for localization of objects in pictures	32, 145
Yeh, W.-H., <i>see</i> Carriere, J.	41, 97
Yin, J., W. Gao and Y. Zhu: Generation of dark hollow beams and their applications	45, 119
Yoshinaga, H.: Recent developments in far infrared spectroscopic techniques	11, 77
Yu, F.T.S.: Principles of optical processing with partially coherent light	23, 221
Yu, F.T.S.: Optical neural networks: architecture, design and models	32, 61
Zalevsky, Z., D. Mendlovic and A.W. Lohmann: Optical systems with improved resolving power	40, 271
Zalevsky, Z., <i>see</i> Lohmann, A.W.	38, 263
Zavatta, A., <i>see</i> Bellini, M.	55, 41
Zavorotny, V.U., <i>see</i> Charnotskii, M.I.	32, 203
Zavorotnyi, V.U., <i>see</i> Tatarskii, V.I.	18, 204
Zhu, Y., <i>see</i> Yin, J.	45, 119
Zubairy, M.S., <i>see</i> Greenberger, D.M.	50, 275
Zuidema, P., <i>see</i> Bouman, M.A.	22, 77

This page intentionally left blank